

**Synthesis of Highly-designed Functional
Periodic Mesoporous Organosilicas and
Their Applications**

MAEGAWA Yoshifumi

**Synthesis of Highly-designed Functional
Periodic Mesoporous Organosilicas and
Their Applications**

2020

MAEGAWA Yoshifumi

Abstract

Periodic mesoporous organosilicas (PMOs), synthesized by hydrolysis and polycondensation of organic-bridged alkoxysilane precursor in the presence of structure-directing agents, have attracted much attention for potential applications in various research fields. In this dissertation, the author describes the development of novel synthetic methods for functional organic-bridged alkoxysilane precursors and its synthetic equivalents, organic-bridged allylsilane precursors, toward high functionalization of PMOs. The author developed four synthetic approaches to diversify bridging organic groups in organosilane precursors. First, previously reported rhodium-catalyzed direct silylation of aryl halide with triethoxysilane was successfully applied for synthesis of high functional organic-bridged triethoxysilane precursors, which cannot be obtained by conventional methodologies using halogen-exchange reaction followed by alkoxysilylation. Second, a new synthetic method of high functional organic-bridged allylsilane precursors, which are stable during silica gel chromatography but are utilized for synthetic equivalents of alkoxysilane precursors, was developed. A variety type of building blocks possessing diallylethoxysilyl group were synthesized and applied to palladium-catalyzed cross-coupling reactions to synthesize high functional organic-bridged allylsilane precursors. Third, a synthetic method for high functional organic-bridged isopropoxysilane precursors having column stability and easy hydrolyzability was established. By using building blocks having triisopropoxysilyl groups, high functional organic-bridged isopropoxysilane precursors such as diketopyrrolopyrrole (DPP)- and dithienobenzothiadiazole (DTBT)-bridged isopropoxysilane precursors were successfully prepared by palladium-catalyzed coupling reactions. Finally, regioselective hydrosilylation was applied to synthesize organic-bridged alkoxysilane precursors bearing shortest alkyl spacer between the organic unit and alkoxysilyl groups which allowed densely packing of the organic chromophores into the organosilica frameworks. In this study, the author also investigated hydrolysis and condensation behaviors of model organoallylsilanes in various reaction solvents under acidic sol-gel polymerization conditions to enhance the hydrolyzability of allylsilyl groups.

By using established synthetic methods for high functional organic-bridged silane precursors, a variety of well-designed functional PMOs were synthesized. In this dissertation, the author describes the synthesis of high functional PMOs starting from newly designed functional

organic-bridged silane precursors and their applications for transparent and visible-light absorptive films, organic solar cells, and heterogeneous catalysts. Transparent and visible-light absorptive methylacridone (MeAcrid)-PMO films were prepared from newly designed MeAcrid-bridged ethoxysilane precursor in the presence of nonionic surfactant via evaporation-induced self-assembly. Visible-light absorption and fluorescence properties of MeAcrid-PMO films were measured and their visible-light harvesting antenna functions were investigated. Visible-light absorptive and hole-transporting DTBT-PMO films were prepared from DTBT-bridged isopropoxysilane precursors without addition of other silica precursors. The obtained DTBT-PMO films were applied to p-type material for organic solar cells and their photovoltaic performances were measured under simulated solar irradiation. A new class of crystal-like BPy-PMO, where 2,2'-bipyridine (BPy) ligands were densely and regularly arranged with a molecular-scale periodicity along with direction of mesochannels, was synthesized. The metal coordination ability of BPy-PMO was examined for various metal complex precursors and the catalytic performances of immobilized metal complexes were investigated for organic transformations and photocatalytic reaction.

Acknowledgements

The studies are concerned with the development of high functional periodic mesoporous organosilicas by design and synthesis of organic-bridged silane precursors. This work was mainly carried out at Toyota Central R&D Labs, Inc., and, in part, at Nara National College of Technology. This work was supported by JST CREST and JST ACT-C Grant Number JPMJCR12Y1, and, in part, by JSPS KAKENHI Grant Number JP24107002. The author would like to express his thanks to his company and college for the opportunity on carrying out these studies and publishing them as this dissertation.

The author would like to express his appreciation to Professor Takahiro Seki in Nagoya University, for supervising his Ph. D. studies, kind guidance and valuable discussions, and a careful reviewing of the thesis. The author would like to thank Professor Hiroshi Shinokubo, Professor Atsushi Satsuma, and Professor Jun Onoe in Nagoya University for agreeing to be co-supervisor and the interest shown in this manuscript by accepting to be referees.

The author greatly appreciates to Dr. Shinji Inagaki in Toyota Central R&D Labs, Inc. and Professor Toyoshi Shimada in Nara National College of Technology for their constant advices, valuable discussions, and encouragements during the course of this work.

The author is greatly thankful to Dr. Takao Tani, Mr. Mitsumasa Horii, Dr. Yoshihide Watanabe in Toyota Central R&D Labs, Inc. for their helpful advices and suggestions.

The author must make special mention of Dr. Norihiro Mizoshita, Dr. Yasutomo Goto, Dr. Minoru Waki, Dr. Masamichi Ikai, Dr. Soichi Shirai, Dr. Yuri Yamada, and Dr. Satoshi Ishikawa in Toyota Central R&D Labs, Inc. and Mr. Toyohiro Nagano, Mr. Tastuya Yabuno, Mr. Hiroki Nakagawa, and Mr. Akinari Umemoto in Nara National College of Technology for their great assistance and collaborations. The author is thankful to Ms. Momoe Ikami for her kind assistance and hearty encouragement. The author is deeply grateful to Dr. Sho Yamaguchi in Toyota Central R&D Labs, Inc. for his stimulating discussion and brilliant advices.

The author is deeply grateful to thank his former and present research members in Toyota Central R&D Labs, Inc., Nara National College of Technology, and other research groups who contributed on his research.

Finally, the author would like to express his deep appreciation to his family, Mr. Susumu Maegawa, Ms. Naoko Maegawa, Ms. Keiko Maegawa, and Mr. Ryusei (shibainu), especially, his wife, Ms. Yasuko Maegawa for their great constant support, confidence, encouragement, and love, throughout his Ph. D.–Thank you so much!

Yoshifumi Maegawa

2020

Table of Contents

	page
Abstract.....	i
Acknowledgements.....	iii
Table of Contents.....	v
List of Schemes.....	xii
List of Tables.....	xiv
List of Figures.....	xv
Abbreviations.....	xxvi
Chapter 1. General Introduction.....	1
1.1 Background.....	2
1.2 Literature Review.....	7
1.2.1 Organic-functionalized Mesoporous Silicas.....	7
1.2.2 Periodic Mesoporous Organosilicas (PMOs).....	9
1.2.3 Pioneer Researches of PMOs.....	9
1.2.4 Synthesis of Functional PMOs.....	14
1.2.5 Applications.....	20
<i>Solid acid and base catalysts</i>	20
<i>Heterogeneous metal complex catalysts</i>	22
<i>Heterogeneous organic molecular catalyst</i>	24
<i>Light-harvesting system</i>	25
<i>Photocatalysts</i>	27
<i>Luminescent materials</i>	29
<i>Photovoltaic devices</i>	31
1.3 The Aim and Outline of the Thesis.....	34

Chapter 2. Synthetic Methodologies for Functional Organosilane Precursors.....	37
2.1 Rh-catalyzed Silylation for Functional Organic-bridged Alkoxysilanes.....	38
2.1.1 Introduction.....	38
2.1.2 Experimental.....	39
<i>Materials and methods</i>	39
<i>General procedure for diiodination of carbazoles</i>	39
<i>Synthesis of carbazole-bridged triethoxysilane precursors</i>	40
<i>Preparation of carbazole-bridged periodic mesostructured organosilica under basic condition (Cbz-PMO-B)</i>	41
<i>Preparation of carbazole-bridged periodic mesostructured organosilica under acidic condition (Cbz-PMO-A)</i>	41
2.1.3 Results and Discussion.....	42
2.1.4 Conclusions.....	47
2.2 Pd-catalyzed Coupling Reactions for Highly Functional Organic-bridged Allylsilanes.....	48
2.2.1 Introduction.....	48
2.2.2 Experimental.....	50
<i>Materials and methods</i>	50
<i>Preparation of molecular building blocks</i>	50
<i>Coupling reaction of molecular building blocks with coupling partners</i>	55
<i>Preparation of functional sol–gel precursors with molecular building blocks</i>	59
2.2.3 Results and Discussion.....	61
<i>Preparation of molecular building blocks for allylsilane sol–gel precursors</i>	61
<i>Cross-coupling reactions of molecular building blocks with various coupling partners</i>	64
2.2.4 Conclusions.....	68

	page
2.3 Pd-catalyzed Coupling Reactions for Highly Functional Organic-bridged Alkoxysilanes.....	69
2.3.1 Introduction.....	69
2.3.2 Experimental.....	71
<i>Materials and methods</i>	71
<i>Synthesis of allylhalobenzene derivatives</i>	72
<i>Synthesis of molecular building blocks containing bulky alkoxyethyl group</i>	74
<i>Synthesis of molecular building blocks containing triallylsilyl group</i>	79
<i>Synthesis of DPP-bridged organosilane</i>	80
<i>Preparation of DPP-bridged organosilica film</i>	81
2.3.3 Results and Discussion.....	82
2.3.4 Conclusions.....	88
2.4 Synthetic Route to Functional Organic-bridged Alkoxysilanes with Short Linker.....	89
2.4.1 Introduction.....	89
2.4.2 Experimental.....	91
<i>Materials and methods</i>	91
<i>Synthesis of precursors</i>	92
<i>Preparation of organosilica films</i>	94
2.4.3 Results and Discussion.....	95
2.4.4 Conclusions.....	101
2.5 Sol-gel Polymerization Behavior of Organoallylsilanes.....	102
2.5.1 Introduction.....	102
2.5.2 Experimental.....	104
<i>Materials and methods</i>	104
<i>Synthesis of organoallylsilane precursors</i>	105

<i>Observation of sol–gel polymerization of model organoallylsilane precursors by ¹H NMR measurements</i>	106
<i>Identification of the generated gas during sol–gel polymerization of 1a and 1b</i>	106
<i>Preparation of spirobifluorene-bridged organosilica film</i>	107
2.5.3 Results and Discussion.....	107
<i>Sol–gel polymerization behavior of model organoallylsilane precursors by ¹H NMR spectroscopy</i>	107
<i>Mechanism of solvent effect on sol–gel polymerization of organoallylsilane precursors</i>	114
<i>Preparation of spirobifluorene-bridged organosilica film under a mild sol–gel polymerization condition</i>	117
2.5.4 Conclusions.....	118
Chapter 3. Transparent and Visible-Light Harvesting PMO Films.....	119
3.1 Introduction.....	120
3.2 Experimental.....	122
<i>Materials and methods</i>	122
<i>Synthesis of organosilane precursor</i>	123
<i>Preparation of organosilica films</i>	124
<i>Removal of the template surfactant from organosilica films</i>	124
3.3 Results and Discussion.....	125
<i>Synthesis of organosilane precursors</i>	125
<i>Preparation of mesoporous organosilica films</i>	126
<i>Optical properties of mesoporous organosilica films</i>	128
3.4 Conclusions.....	133

	page
Chapter 4. Visible-Light-Absorptive and Hole-Transporting PMO Films for Organic Solar Cells.....	135
4.1 Introduction.....	136
4.2 Experimental.....	138
<i>Materials and methods</i>	138
<i>Synthetic procedures and characterization</i>	139
<i>Preparation of sol mixtures and films</i>	141
<i>Fabrication methods of hole-only devices and the SCLC measurements</i>	142
<i>Fabrication methods of PMO-based solar cells</i>	143
4.3 Results and Discussion.....	143
<i>Synthesis of organosilane precursors</i>	143
<i>Preparation of PMO thin films</i>	145
<i>Structural analysis of PMO thin films</i>	147
<i>UV-vis absorption properties</i>	149
<i>Hole mobilities</i>	150
<i>Photovoltaic performance of PMO-based OSCs</i>	151
4.4 Conclusions.....	155
Chapter 5. Solid Chelating PMO for Heterogeneous Metal Complex Catalysts.....	157
5.1 Synthesis of Crystal-like Bipyridine-bridged PMO and Its Metalation Ability.....	158
5.1.1 Introduction.....	158
5.1.2 Experimental.....	161
<i>Materials and methods</i>	161
<i>Synthesis of organosilane precursors</i>	163
<i>Synthesis of BPy-PMO</i>	164
<i>Synthesis of BPy-PMO-TMS</i>	164
<i>Synthesis of metal-complexed BPy-PMO</i>	164

	page
<i>Synthesis of BPy-grafted mesoporous silica and silica gel</i>	165
<i>Synthesis of homogeneous Ir complex catalyst</i>	167
<i>General procedure for the direct C–H borylation of arenes catalyzed by Ir(OMe)(cod)(BPy-PMO-TMS)</i>	168
<i>Kinetic study of direct C–H borylation of benzene</i>	169
<i>Evaluation of photocatalytic hydrogen evolution</i>	170
5.1.3 Results and Discussion.....	170
<i>Synthesis of crystal-like BPy-PMO from 100% organosilane precursor</i>	170
<i>Metal complex formations using BPy-PMO as a ligand</i>	176
<i>Solid ligand properties for direct C–H borylation of arenes</i>	186
<i>A platform for integrated heterogeneous photocatalytic hydrogen evolution system</i>	192
5.1.4 Conclusions.....	195
5.2 Direct C–H Borylation of Arenes and Heteroarenes by Ir-immobilized BPy-PMO Catalyst.....	197
5.2.1 Introduction.....	197
5.2.2 Experimental.....	200
<i>Materials and methods</i>	200
<i>Preparation of Ir-BPy-PMO</i>	201
<i>General procedure for direct C–H borylation of arenes and heteroarenes</i>	201
<i>General procedure for multiple-direct C–H borylation of thiophene derivatives</i>	204
<i>Synthesis of triarylamine derivative</i>	205
<i>GC–MS analyses of side products after the reaction of Ir-BPy-PMO with boron reagent</i>	206
5.2.3 Results and Discussion.....	207
<i>Direct C–H borylation of benzene</i>	207
<i>Direct C–H borylation of substituted arenes and heteroarenes</i>	211

	page
<i>Multiple C–H borylation of thiophene derivatives</i>	214
5.2.4 Conclusions.....	217
5.3 Epoxidation of Olefins by Mo-immobilized BPy-PMO Catalyst.....	218
5.3.1 Introduction.....	218
5.3.2 Experimental.....	221
<i>Materials and methods</i>	221
<i>Immobilization of dichlorodioxomolybdenum(VI) complex</i>	222
<i>Epoxidation of cis-cyclooctene under undried conditions</i>	222
<i>Epoxidation of cis-cyclooctene under anhydrous conditions</i>	223
<i>General procedure for epoxidation of olefins</i>	224
5.3.3 Results and Discussion.....	224
<i>Synthesis and characterization</i>	224
<i>Catalytic activity in epoxidation of cis-cyclooctene under undried conditions</i>	232
<i>Catalytic activity in epoxidation of cis-cyclooctene under anhydrous condition.</i>	238
<i>Scope and limitations of Mo-BPy-PMO-TMS for epoxidation of olefins</i>	239
<i>Reusability of Mo-BPy-PMO-TMS.</i>	241
5.3.4 Conclusions.....	243
Chapter 6. Conclusions and Outlook.....	245
Conclusions.....	246
Outlook.....	252
List of publications.....	254
1. Original papers corresponding to this thesis.....	254
2. Related papers.....	255
3. Reviews.....	258

List of Schemes

page

Scheme 1.1. Functionalization of mesoporous silicas by a) post-synthetic treatment (grafting method) and b) co-condensation using tetraalkoxysilane and mono-organosilane.	8
Scheme 1.2. General synthetic pathway to PMOs starting from organic-bridged alkoxy silane precursor in the presence of structure-directing agents.	9
Scheme 1.3. Synthetic routes for aromatic- and aliphatic-bridged alkoxy silane precursors.	15
Scheme 1.4. Functionalization of crystal-like benzene-PMO by chemical modification.	19
Scheme 2.1. Synthetic route for carbazole-bridged triethoxysilane precursors starting from 3,6-dibromocarbazoles and 3,6-diiodocarbazoles.	42
Scheme 2.2. Rhodium-catalyzed disilylation of 3,6-diiodocarbazole derivatives 2a-c giving carbazole-bridged triethoxysilane precursors 4a-c .	46
Scheme 2.3. Synthesis of carbazole-bridged periodic mesostructured organosilicas (Cbz-PMO-B and Cbz-PMO-A) starting from carbazole-bridged triethoxysilane precursor 4a under basic and acidic conditions.	46
Scheme 2.4. Chemical structures of molecular building blocks for allylsilane sol-gel precursors (MBAS) and their palladium-catalyzed cross-coupling reactions giving sol-gel precursors.	49
Scheme 2.5. Preparation of molecular building blocks containing bromide (1a), iodide (1b), and triflate group (1c).	62
Scheme 2.6. Preparation of molecular building blocks containing magnesium (2a), stannyl (2b), and boryl group (2c).	62
Scheme 2.7. Preparation of molecular building blocks containing amino (3a), formyl (3b), and vinyl groups (3c).	63
Scheme 2.8. Synthesis of chiral BINAP-bridged sol-gel precursor 5a .	67
Scheme 2.9. Synthesis of oligophenylene-ethynylene-bridged sol-gel precursor 5b .	67
Scheme 2.10. Synthesis of benzidine-bridged sol-gel precursor 5c .	68

	page
Scheme 2.11. Synthetic method for functional organic-bridged triisopropoxysilanes using molecular building blocks.	71
Scheme 2.12. Synthesis of bromobenzene-based molecular building blocks containing various bulky trialkoxysilyl groups.	82
Scheme 2.13. Synthesis of magnesium-containing building blocks 2a–2c and borylated- 2d and stannylated building blocks 2e .	84
Scheme 2.14. Synthesis of functional molecular building blocks by cross-coupling reactions.	85
Scheme 2.15. Synthesis of DPP-bridged triisopropoxysilane 4a and triallylsilane 4b by Migita–Kosugi–Stille cross-coupling reaction between dibrominated DPP and building blocks, and preparation of organosilica films under acidic condition.	87
Scheme 2.16. Synthetic routes to newly designed TPPy-bridged alkoxy silane precursors 1-C3 and 1-C1 .	97
Scheme 2.17. Presumed deallylation mechanism of an allylsilyl group during acid-catalyzed a) hydrolysis and b) condensation.	104
Scheme 2.18 Acid-catalyzed sol–gel polymerization of 1a and 1b . The protons H ^a , H ^b , H ^c and H ^d were monitored by ¹ H NMR spectroscopy.	108
Scheme 3.1. Synthetic illustration of Acd- and MeAcd-bridged triethoxysilane precursors 1 and 2 .	125
Scheme 4.1. Synthesis route for two-armed DTBT-bridged organosilane precursor 1 .	144
Scheme 4.2. Synthesis route for four-armed DTBT-bridged organosilane precursor 2 .	144
Scheme 4.3. Synthesis route for DTBT-based PMO films.	145
Scheme 4.4. Schematic illustration of the fabrication steps for the OSC using p-type PMO film (orange) and PCBM (dark brown).	151
Scheme 5.1. Synthesis of 5,5'-bis(triisopropoxysilyl)-2,2'-bipyridine precursor 3 and schematic illustration of synthesis of BPy-PMO from precursor 3 by surfactant-templated supramolecular assembly.	171
Scheme 5.2. Synthesis of hole-transporting triarylamine derivative 5 by direct C–H borylation of 4 followed by Suzuki–Miyaura coupling reaction.	217

Scheme 5.3. Schematic illustration for $x\%$ Mo-BPy-PMO-TMS.	224
---	-----

List of Tables

Table 2.1. Iodination of <i>N</i> -unsubstituted carbazole.	44
Table 2.2. Iodination of <i>N</i> -substituted carbazoles.	45
Table 2.3. Palladium-catalyzed cross-coupling reactions between MBAS and coupling partners.	64-65
Table 2.4. Synthesis of halogen-substituted molecular building blocks containing one or two triisopropoxysilyl groups.	83
Table 2.5. Acidic sol-gel polymerization of model organoallylsilane precursors 1a and 1b in various organic solvents.	108
Table 3.1. Fluorescence quantum yields measured at excitation wavelengths of 380 nm and 475 nm for F-2 with different dye-doping.	132
Table 4.1. Optimization of reaction conditions for the formation of well-defined PMO films.	145
Table 5.1. Physical parameters of metal complexes prepared using BPy-PMO.	184
Table 5.2. Ligand effects in Ir-catalyzed direct C–H borylation of arenes with B ₂ pin ₂ .	188
Table 5.3. Catalytic activities of Ir-BPy-PMO catalyst in direct C–H borylation of benzene with HBpin and B ₂ pin ₂ .	208
Table 5.4. Direct C–H borylation of arenes and heteroarenes with HBpin catalyzed by Ir-BPy-PMO.	212
Table 5.5. Multiple borylation of heteroarenes with HBpin catalyzed by Ir-BPy-PMO	215
Table 5.6. Physicochemical properties of $x\%$ Mo-BPy-PMO-TMS.	225
Table 5.7. Curve-fitting parameters of Mo <i>K</i> -edge EXAFS Fourier transforms for MoO ₂ Cl ₂ (bpy) and 10% Mo-BPy-PMO-TMS.	231
Table 5.8. Catalytic activity of heterogeneous and homogeneous Mo-bipyridine catalysts for epoxidation of <i>cis</i> -cyclooctene (1a) with TBHP.	233
Table 5.9. Epoxidation of olefins with TBHP catalyzed by 10% Mo-BPy-PMO-TMS.	240

List of Figures

	page
Figure 1.1. Organic-bridged alkoxysilane precursors used in the PMO synthesis in early research.	11
Figure 1.2. Schematic illustration of amorphous and crystal-like frameworks PMOs.	12
Figure 1.3. Bis-silylated organosilane precursors used in synthesis of crystal-like PMOs.	13
Figure 1.4. Functional aromatic-bridged alkoxysilane precursors synthesized by method i).	16
Figure 1.5. Aliphatic-bridged alkoxysilane precursors synthesized by method ii).	16
Figure 1.6. Functional organic-bridged alkoxysilane precursor containing amide linkage and ionic	17
Figure 1.7. π -Conjugated aromatic-bridged alkoxysilane precursors synthesized by method iv).	17
Figure 1.8. Functional aromatic-bridged alkoxysilane precursors synthesized by method v).	18
Figure 1.9. Acid-base bifunctional PMO catalyst for acid-base sequential reaction.	22
Figure 1.10. Ligand and metal complex precursors used in the synthesis of PMOs.	23
Figure 1.11. Immobilized MacMillan PMO catalyst for asymmetric Diels–Alder reaction.	25
Figure 1.12. Schematic diagram of a light-harvesting antenna of a) red photosynthetic bacteria and b) BPh-PMO/coumarin dye system.	26
Figure 1.13. Schematic diagrams of a photocatalytic CO ₂ reduction system using Ru-Re@Acid-PMO.	28
Figure 1.14. Schematic diagrams of photocatalytic oxygen evolution system from water using Ru/IrO _x @Acid-PMO.	28
Figure 1.15. a) The emission spectral change of rubrene-doped hexyloxy-substituted OPV-bridged mesostructured organosilica films and b) schematic illustration of emission color control by dye doping.	30

- Figure 1.16.** Electroactive functional organic-bridged alkoxy silane precursors used in the synthesis of hole-transporting and electroactive PMOs. 32
- Figure 1.17.** Schematic illustration of photovoltaic devices based on hole-transporting PMO films infilling with electron-transporting materials. 33
- Figure 2.1.** XRD patterns of a) **Cbz-PMO-B** and b) **Cbz-PMO-A**. 47
- Figure 2.2.** a) Color change of sol-solution containing DPP-bridged triisopropoxysilane **4a** and triallylsilane **4b** before and after the hydrolysis in THF in the presence of HCl. b) UV-vis absorption spectra of organosilica films prepared from DPP-bridged silane precursors **4a** (solid line) and **4b** (broken line). 88
- Figure 2.3.** TPPy-bridged alkoxy silane precursors **1-U3**, **1-C3**, and **1-C1**. 90
- Figure 2.4.** Synthetic routes for olefinic aromatics by allylation of metalated aromatic compounds (method a), vinylation of aromatic dialdehydes (method b), and Suzuki–Miyaura coupling between aryl dihalides and olefin-substituted phenylboronic acid (method c). 95
- Figure 2.5.** Regioselective hydrosilylation of olefinic aromatics catalyzed by a) platinum- or b) palladium-catalyst followed by alkoxylation with alcohol. 96
- Figure 2.6.** Optical micrographs of a) **1-U3-F**, b) **1-C3-F** and c) **1-C1-F** (scale bar represents 20 μm). 98
- Figure 2.7.** a) UV-vis absorption spectra and b) fluorescence emission spectra of **1-U3** (green line), **1-C3** (blue line), and **1-C1** (red line) in *i*-PrOH (1.0×10^{-5} M). The spectra for TPPy (purple line) in CH_2Cl_2 (1.0×10^{-5} M) are also presented for comparison. 98
- Figure 2.8.** Dependence of the absorption coefficients for **1-U3-F** (green line), **1-C3-F** (blue line), **1-C1-F** (red line), and **TPPy-F** (purple line) on the wavelength. The absorption coefficients were obtained by normalizing the absorbance of the films at every wavelength according to the film thicknesses. 99
- Figure 2.9.** Normalized fluorescence emission spectra of **1-U3-F** (green line), **1-C3-F** (blue line), **1-C1-F** (red line), and **TPPy-F** (purple line). The excitation wavelength was 380 nm for all samples. 100

	page
Figure 2.10. Chemical structures of model organoallylsilane precursors 1a and 1b .	107
Figure 2.11. Changes in the ^1H NMR spectra of the sol-solution of 1a in MeCN- d_3 at 0 min, 10 min and 4 h after the addition of HCl.	109
Figure 2.12. Changes in the ^1H NMR spectra of the sol-solution of 1a in acetone- d_6 at 0 min, 10 min and 4 h after the addition of HCl.	110
Figure 2.13. Changes in the ^1H NMR spectra of the sol-solution of 1a in MeOH- d_4 at 0 min, 10 min and 4 h after the addition of HCl.	110
Figure 2.14. Changes in the ^1H NMR spectra of the sol-solutions of 1b in a) MeCN- d_3 and b) acetone- d_6 at 0 min and 4 h after the addition of HCl.	111
Figure 2.15. ^1H NMR spectrum of the generated gas dissolved in MeCN- d_3 .	111
Figure 2.16. Changes in the ^1H NMR spectra of the sol-solution of 1a in DMSO- d_6 at 0 min, 10 min and 4 h after the addition of HCl.	112
Figure 2.17. Changes in the ^1H NMR spectra of the sol-solution of 1a in THF- d_8 at 0 min, 10 min and 4 h after the addition of HCl.	112
Figure 2.18. Conversion of allyl groups in a) 1a and b) 1b with the reaction time for the sol solutions using various deuterated solvents. Solvents are labelled as follows: MeCN (\circ); acetone (Δ); MeOH (\diamond); THF (\square); and DMSO (\times) for 1a , MeCN (\bullet); acetone (\blacktriangle) for 1b .	113
Figure 2.19. Relationship between the initial deallylation rate (v_0) of 1a and a) solvent basicity (SB), b) dielectric constant (D_C), c) acceptor number (AN), d) Gutmann's donor number (DN) or e) Dimroth-Reichardt's E_T^N for various solvents. Solvents are labelled as follows: MeCN (\bullet); acetone (\blacktriangle); MeOH (\blacklozenge); THF (\blacksquare); and DMSO (\times).	115
Figure 2.20. Plots of a) D_C and b) AN vs. SB for DMF, TFE, MeCN, MeOH and THF. "Yes (X h)" and "No (X h)" denotes whether a solid organosilica film was formed or not from the sol solutions of 1a using the corresponding solvents after stirring for X h.	116
Figure 2.21. Chemical structure of spirobifluorene-bridged allylsilane precursor SBF-Si .	117

- Figure 2.22.** UV-vis absorption (solid line) and fluorescence emission (broken line, excited at 360 nm) spectra of the spirobifluorene-bridged organosilica film. 118
- Figure 3.1.** Acd- and MeAcd-bridged triethoxysilane precursors **1** and **2**. 121
- Figure 3.2.** IR absorption spectra of the precursor **1** at a) 2500–3500 cm^{-1} and b) 1300–1700 cm^{-1} . 126
- Figure 3.3.** UV-vis absorption spectra of the sol solution of **1** before (solid line) and after (broken line) the filtration. 126
- Figure 3.4.** a) Photograph of **F-1** (left) and **F-2** (right), and optical micrographs of b) **F-1** and c) **F-2** (scale bar represents 10 μm). d) optical micrograph of **F-2** after removal of surfactant template (scale bar represents 10 μm). 127
- Figure 3.5.** XRD patterns of a) **F-1** and b) **F-2** before (broken lines) and after (solid lines) the extraction of surfactant. 128
- Figure 3.6.** a) UV-vis absorption and b) fluorescence emission spectra of mesostructured organosilica film **F-2** (solid lines) and *i*-PrOH solutions of MAcd-bridged precursor **2** (broken lines). The excitation wavelength was 380 nm for all samples. 129
- Figure 3.7.** a) UV-vis absorption and b) fluorescence emission spectra of mesostructured organosilica film **F-1** (solid lines), *i*-PrOH solutions of Acd-bridged precursor **1** (broken lines), and aggregates of the precursor **1** (bold gray lines). The excitation wavelength was 380 nm for all samples. 129
- Figure 3.8.** Excitation spectra of a) **F-2** at 500 nm and b) **F-1** at 450 nm (broken line) and at 520 nm (solid line). 130
- Figure 3.9.** a) UV-vis absorption (broken lines) and fluorescence emission spectra (solid lines) of **F-2** (gray) and DCM (black) (10^{-5} M in *i*-PrOH). b) UV-vis absorption spectrum of 1 mol% DCM doped **F-2**. c) fluorescence emission spectra of 0 (blue line), 0.5 (orange line), 1 (red line), and 5 mol% (green line) DCM-doped **F-2**. The excitation wavelength was 380 nm for all samples. d) excitation energy transfer efficiency of **F-2**. 131

	page
Figure 4.1. Cross-sectional SEM images of PMO films. a)–f) correspond to entries 1 to 6 in Table 1.	146
Figure 4.2. Krypton adsorption–desorption isotherm of 1-PMO-F . Closed circles: adsorption, open circles: desorption.	148
Figure 4.3. Pore size distribution of mesopores for 1-PMO-F obtained from their top view SEM images (Samples a–c) using an image analysis software.	148
Figure 4.4. Normalized UV-vis absorption spectra of a) 1-PMO-F (red solid line) and precursor 1 (red dashed line), b) 2-PMO-F (black solid line) and precursor 2 (black dashed line). The concentration of the CHCl ₃ solutions for precursors 1 and 2 was 10 ⁻⁵ M.	149
Figure 4.5. Normalized absorbance of both 1-NP-F (red) and 2-NP-F (black) films.	150
Figure 4.6. <i>J–V</i> characteristics for hole-only devices with a) 1-NP-F (film thickness: 62 nm, open circles) and b) 2-NP-F (film thickness: 51 nm, open squares) films under the dark conditions. The dashed lines represent the prediction obtained using the SCLC model.	150
Figure 4.7. Cross-sectional SEM images of 1-PMO-F (top) and 2-PMO-F (bottom) on PEDOT:PSS/ITO before (left) and after (right) infiltration with PCBM.	152
Figure 4.8. a) External quantum efficiency (EQE) and b) <i>J–V</i> characteristics of the PMO-based OSCs (red: device A, black: device B) under 1 sun (AM 1.5G) simulated irradiation (solid lines) and in the dark (dashed lines). <i>J–V</i> characteristics of c) device A or d) device B without a buffer layer (black lines) and with 1'-NP-F buffer layer (red lines) in the dark (broken lines) and under 1 sun, AM1.5G illumination (solid lines).	153
Figure 4.9. EQE of the 1-PMO-F based solar cell (red, solid), and normalized absorbance of both 1-PMO-F (black, solid) and PCBM (black, dashed) films.	153
Figure 4.10. Ionization potentials of 1-NP-F and 2-NP-F measured by using AC-2.	154
Figure 5.1. ¹³ C CP MAS NMR spectra of a) L1 and b) L2 . Nitrogen adsorption/desorption isotherms of c) L1 and d) L2 . Closed circle: adsorption, open circle: desorption.	167

- Figure 5.2.** ^{29}Si DD MAS NMR spectra of BPy-PMO synthesized under a) 0.25 M OH^- , and b) 0.035 M OH^- conditions. c) ^{13}C CP MAS NMR spectrum of BPy-PMO (above) and ^{13}C NMR spectrum of precursor **3** (below). d) FT-IR spectrum of BPy-PMO before (black) and after (gray) the removal of surfactant. e) XRD patterns, and f) nitrogen adsorption/desorption isotherms (closed circles: adsorption, open circles: desorption) for BPy-PMO. 172
- Figure 5.3.** a) SEM and b–d) TEM images and (e) structural model of BPy-PMO. Silicon, yellow; oxygen, red; carbon, gray; nitrogen, blue; hydrogen, white. 174
- Figure 5.4.** Thermogravimetry (TG) (black) and differential thermal analysis (DTA) curves (gray line) of BPy-PMO in air stream. 175
- Figure 5.5.** FT-IR absorption spectra of BPy-PMO (black line) and BPy-PMO-TMS (gray line). 175
- Figure 5.6.** a) XRD patterns, b) nitrogen adsorption/desorption isotherms (closed circles: adsorption, open circles: desorption), c) ^{13}C CP MAS NMR, d) ^{29}Si DD MAS NMR spectra of BPy-PMO-TMS. 176
- Figure 5.7.** a) Schematic illustration of direct metal complex formation of the pore surface of BPy-PMO. b) Synthesis of $\text{Ru}(\text{bpy})_2(\text{BPy-PMO})$ starting from BPy-PMO and ruthenium precursor $\text{Ru}(\text{bpy})_2\text{Cl}_2 \cdot 2\text{H}_2\text{O}$. 177
- Figure 5.8.** Chemical structures of representative metal complexes immobilized on BPy-PMO as a solid chelating ligand. 177
- Figure 5.9.** a) UV-vis diffuse reflectance spectrum of $\text{Ru}(\text{bpy})_2(\text{BPy-PMO})$ (black line) and UV-vis absorption spectrum of $\text{Ru}(\text{bpy})_3\text{Cl}_2$ in CH_3CN (gray line), b) photoluminescence spectra of $\text{Ru}(\text{bpy})_2(\text{BPy-PMO})$ (black line) and $\text{Ru}(\text{bpy})_3\text{Cl}_2$ in CH_3CN (gray line). 178
- Figure 5.10.** Ru *K*-edge a, b) XANES spectra, c) EXAFS oscillations, and d) EXAFS Fourier transform ($k = 3\text{--}14 \text{ \AA}^{-1}$) of $\text{Ru}(\text{bpy})_2(\text{BPy-PMO})$ (black solid lines), $\text{Ru}(\text{bpy})_3\text{Cl}_2$ (gray solid lines), and Ru powder (black broken lines). 179
- Figure 5.11.** UV-vis diffuse reflectance spectrum (black line) and photoluminescence spectrum of $\text{Ir}(\text{ppy})_2(\text{BPy-PMO})$ excited at 385nm (gray line). 180

	page
Figure 5.12. Ir L_{III} -edge a, b) XANES spectra, c) EXAFS oscillations, and d) EXAFS Fourier transform of Ir(OMe)(cod)(BPy-PMO-TMS) (black lines) and Ir(OMe)(cod)(bpy) (gray lines).	180
Figure 5.13. XPS spectra of Ir(OMe)(cod)(BPy-PMO-TMS) (black line) and [Ir(OMe)(cod)(bpy)] (gray line).	181
Figure 5.14. a) UV-vis diffuse reflectance spectra of Re(CO) ₃ (BPy-PMO) (solid line) and BPy-PMO (broken line), b) FT-IR absorption spectrum of Re(CO) ₃ Cl(BPy-PMO) dispersed in CH ₃ CN (black line) and Re(bpy)(CO) ₃ Cl in CH ₃ CN solution (gray line).	182
Figure 5.15. Re L_{III} -edge a) XANES spectra and b) EXAFS oscillations of Re(CO) ₃ Cl(BPy-PMO) (black solid lines), Re(bpy)(CO) ₃ Cl (gray solid lines), and (NH ₄)ReO ₄ (black broken lines).	182
Figure 5.16. a) UV-vis diffuse reflectance spectra of Pd(OAc) ₂ (BPy-PMO) (solid line) and BPy-PMO (broken line), b) XPS spectra of Pd(OAc) ₂ (BPy-PMO) (solid line) and Pd(OAc) ₂ (broken line) for Pd _{3d5} .	183
Figure 5.17. a) Low-angle and b) high-angle XRD patterns for Ru(bpy) ₂ (BPy-PMO) (blue lines), Ir(ppy) ₂ (BPy-PMO) (red lines), Ir(OMe)(cod)(BPy-PMO-TMS) (green lines), Re(CO) ₃ Cl(BPy-PMO) (purple lines), and Pd(OAc) ₂ (BPy-PMO) (orange lines).	184
Figure 5.18. Nitrogen adsorption/desorption isotherms of a) Ru(bpy) ₂ (BPy-PMO), b) Ir(ppy) ₂ (BPy-PMO), c) Ir(OMe)(cod)(BPy-PMO-TMS), d) Re(CO) ₃ Cl(BPy-PMO), and e) Pd(OAc) ₂ (BPy-PMO). Closed circle: adsorption, open circle: desorption.	185
Figure 5.19. a) ¹³ C CP MAS NMR spectra and b) ²⁹ Si DD MAS NMR spectra of Ru(bpy) ₂ (BPy-PMO) (blue lines), Ir(ppy) ₂ (BPy-PMO) (red lines), Ir(OMe)(cod)(BPy-PMO-TMS) (green lines), Re(CO) ₃ Cl(BPy-PMO) (purple lines), and Pd(OAc) ₂ (BPy-PMO) (orange lines).	186
Figure 5.20. Chemical structure of solid bipyridine ligands L1 , L2 , and L3 .	187

Figure 5.21. a) Reaction kinetic curves of C–H borylation of benzene catalyzed by iridium catalysts based on BPy-PMO (red line), 2,2'-bipyridine (blue line), **L1** (purple line), **L2** (green line), and **L3** (gray line). b) Reusability of Ir@BPy-PMO-TMS catalyst, first cycle (original: 94%), second cycle (91%), third cycle (88%), and fourth cycle (78%), and other heterogeneous and homogeneous catalysts.

189

Figure 5.22. a) Reaction kinetic curves of direct C–H borylation of benzene with B_2pin_2 catalyzed by Ir(OMe)(cod)(BPy-PMO) and after the removal of Ir(OMe)(cod)(BPy-PMO) (red line). Photographs of reaction mixture b) before (Ir content was 835 ppm) and c) after the removal of homogeneous catalyst (left) and Ir@BPy-PMO-TMS (right) catalysts by filtration.

190

Figure 5.23. a) XRD profiles, b) nitrogen adsorption/desorption isotherms (closed circles: adsorption, open circles: desorption), and (c) ^{29}Si DD MAS NMR spectra of Ir@BPy-PMO-TMS before (black lines) and after (gray lines) the reactions. d) TEM image of recovered Ir@BPy-PMO-TMS.

191

Figure 5.24. Schematic illustration of a hydrogen evolution system based on Pt@Ru-BPy-PMO.

192

Figure 5.25. a) UV-vis diffuse reflectance spectra and b) ^{13}C CP MAS NMR spectra of Pt@Ru-BPy-PMO (gray lines) and Ru(bpy) $_2$ (BPy-PMO) (black lines). c, d) TEM images and e, f) XRD patterns of Pt@Ru-BPy-PMO.

193

Figure 5.26. a) Nitrogen adsorption/desorption isotherms of Pt@Ru-BPy-PMO. Closed circle: adsorption, open circle: desorption. b) ^{29}Si MAS NMR spectra of Pt@Ru-BPy-PMO (gray lines) and Ru-BPy-PMO (black lines).

194

Figure 5.27. Time-dependent hydrogen evolution curves of Pt@Ru-BPy-PMO (red line) and homogeneous Ru(bpy) $_3$ Cl $_2$ and colloidal platinum particles system (black line) under irradiation of visible light (> 385 nm).

195

Figure 5.28. Representative heterogeneous Ir–bipyridine complex catalysts based on well-defined bipyridine solid chelating ligands for direct C–H borylation of arenes with bis(pinacolato)diboron.

199

- Figure 5.29.** Reaction kinetic curves of C–H borylation of benzene catalyzed by a) Ir-BPy-PMO with HBpin (black line) or B₂pin₂ (blue line) and [Ir(bpy)(OMe)(cod)] with HBpin (red line) or B₂pin₂ (green line) under neat benzene conditions and b) Ir-BPy-PMO with HBpin (black broken line) or B₂pin₂ (blue broken line) under diluted conditions with cyclohexane. These reactions were conducted with benzene (**1a**, 30 equiv relative to boron atom in boron reagents) or benzene (**1a**, 2 equiv) in cyclohexane (2 mL) and HBpin (1 equiv) or B₂pin₂ (0.5 equiv) in the presence of Ir-BPy-PMO or [Ir(bpy)(OMe)(cod)] (0.75 mol% Ir). 209
- Figure 5.30.** Structural properties of Ir-BPy-PMO before (black line) and after 3rd reactions (gray line). a) XRD profiles and b) nitrogen adsorption/desorption isotherms (closed circle: adsorption, open circle: desorption). 211
- Figure 5.31.** Reaction kinetic curves of direct C–H borylation of benzene (●), 1,3-dichlorobenzene (■) catalyzed by Ir-BPy-PMO with HBpin under dilute condition in cyclohexane. 213
- Figure 5.32.** Reaction kinetic curves of direct C–H borylation of thiophene (▲), 2,2':5',2''-terthiophene (■), and benzene (●) catalyzed by Ir-BPy-PMO with HBpin under dilute condition in cyclohexane. 216
- Figure 5.33.** Heterogeneous MoO₂Cl₂(bpy)-based catalyst for epoxidation of olefins. 220
- Figure 5.34.** a) Relationship between preparative and observed Mo/BPy ratios determined by ICP analysis. b) CG image of pore surface of Mo-BPy-PMO-TMS with Mo/BPy molar ratio of approximately 23% (Mo/BPy_{surf} = approximately 35%). Mo: sky blue; Cl: pink; O: red; Si: orange; C: light gray; N: purple; H: omitted except for hydrogen atoms of OH ligands in Mo complexes. 225
- Figure 5.35.** a) Low-angle and b) high-angle XRD patterns for BPy-PMO-TMS (blue lines) and *x*% Mo-BPy-PMO-TMS (*x* = 5, red lines; 10, green lines; 20, purple lines; 23, orange lines). 227

- Figure 5.36.** Nitrogen adsorption/desorption isotherms for BPy-PMO-TMS (blue lines) and $x\%$ Mo-BPy-PMO-TMS ($x = 5$, red lines; 10, green lines; 20, purple lines; 23, orange lines). Closed symbols: adsorption; open symbols: desorption. 227
- Figure 5.37.** a) FT-IR and b) Raman spectra of BPy-PMO-TMS (blue lines), $x\%$ Mo-BPy-PMO-TMS ($x = 5$, red lines; 10, green lines; 20, purple lines; 23, orange lines), and MoO₂Cl₂(bpy) (sky blue lines). 228
- Figure 5.38.** FT-IR spectra of BPy-PMO (black line), BPy-PMO-TMS (blue line) and $x\%$ Mo-BPy-PMO-TMS ($x = 5$, red line; 10, green line; 20, purple line; 23, orange line). 229
- Figure 5.39.** a, b) Mo K -edge XANES spectra, c) EXAFS oscillations, and d) EXAFS Fourier transforms ($k = 2-13 \text{ \AA}^{-1}$) of 10% Mo-BPy-PMO-TMS (red lines), MoO₂Cl₂(bpy) (purple lines), MoO₂Cl₂ (orange lines), and MoO₃ (green lines). 230
- Figure 5.40.** Curve fitting of Mo K -edge EXAFS Fourier transform for a) MoO₂Cl₂(bpy) using the crystal data of MoO₂Cl₂(bpy) and b) Mo-BPy-PMO-TMS using the crystal data of MoO₂Cl(OEt)(bpy). 230
- Figure 5.41.** Mo K -edge a, b) XANES spectra, c) EXAFS oscillations and d) EXAFS Fourier transforms ($k = 2-13 \text{ \AA}^{-1}$) of $x\%$ Mo-BPy-PMO-TMS ($x = 5$, red lines; 10, green lines; 20, purple lines; 23, orange lines). 232
- Figure 5.42.** Epoxidation of *cis*-cyclooctene (**1a**) with TBHP under undried conditions catalyzed by various Mo-bipyridine complex catalysts at 75 °C. MoO₂Cl₂(bpy) (orange, ○), 10% Mo-BPy-PMO-TMS (blue, ●), Mo-BPy-FSM-TMS (red, ◆), Mo-PS-BPy (green, ■), 11% Mo-BPy-PMO (purple, ▲). 233
- Figure 5.43.** Hot filtration experiment for epoxidation of *cis*-cyclooctene (**1a**) with TBHP catalyzed by 10% Mo-BPy-PMO-TMS. Catalyst was not removed (black line). Catalyst was filtrated when reaction time reached 30 min and the reaction was continued without the catalyst (red line). 234
- Figure 5.44.** Schematic representations of 10% Mo-BPy-PMO-TMS, 11% Mo-BPy-PMO, Mo-BPy-FSM-TMS, and Mo-PS-BPy. 235

	page
Figure 5.45. a) Epoxidation of <i>cis</i> -cyclooctene (1a) with TBHP at 75 °C catalyzed by <i>x</i> % Mo-BPy-PMO-TMS (<i>x</i> = 5, red lines; 10, green lines; 20, purple lines; 23, orange lines). b) Yield changes of 2a up to 30 min from the start of the reaction.	236
Figure 5.46. TOF value per Mo in Mo-BPy-PMO-TMS (●) and Mo-BPy-Polymer (■). Immobilized Mo amounts were determined by ICP analysis.	237
Figure 5.47. Effect of water on epoxidation of <i>cis</i> -cyclooctene (1a) with TBHP at 75 °C in decane. Dry decane (◆), undried decane (●), and decane containing water (5 mmol) (■).	238
Figure 5.48. Solvent effect on epoxidation of <i>cis</i> -cyclooctene (1a) with TBHP at 75 °C in dry 1,2-DCE (blue, ●), dry CH ₃ CN (green, ▲), dry toluene (purple, ◆), dry decane (red, ■), dry EtOH (orange, ○).	239
Figure 5.49. Reusability of 10% Mo-BPy-PMO-TMS for epoxidation of <i>cis</i> -cyclooctene (1a) at 75 °C a) under undried conditions and b) under anhydrous conditions. For a), the recovered catalyst was reused for the recycle reaction under the same conditions. The reaction times were 8 h. For b), after the reaction, 1a and anhydrous TBHP were recharged. The reaction times were 1.5 h (1st), 1.5 h (2nd), 3 h (3rd), and 3.5 h (4th).	241
Figure 5.50. a) XRD patterns and b) nitrogen adsorption (closed circle)/desorption (open circle) isotherms of 10% Mo-BPy-PMO-TMS before the reaction (red line), after the 1st reaction run (blue line), after the 4th reaction run (green line).	242
Figure 5.51. IR spectra at (a) 2500–3500 cm ⁻¹ and (b) 1200–1400 cm ⁻¹ of BPy-PMO-TMS (gray line), 10% Mo-BPy-PMO-TMS before the reaction (red line), after the 1st reaction run (blue line), after the 2nd reaction run (green line).	243
Figure 6.1. Schematic illustration of roadmap from previous work (basic research) and this work (use-inspired & applied research) to future work toward industrial R&D and commercialization of highly-designed functional PMOs.	247

Abbreviations

AES	atomic emission spectroscopy
AM	air mass
AN	acceptor number
ATR	attenuated total reflection
Ac	acetyl
Acd	acridone
AllylMgBr	allylmagnesium bromide
BET	Brunauer-Emmett-Teller
BINAP	2,2'-bis(diphenylphosphino)-1,1'-binaphthyl
BSQ	bridged-silsesquioxane
Brij76	polyethylene(10) stearyl ether
Bu	butyl
C ₁₈ -C ₁₂ -C ₁₈	1,12-dodecanediaminium- <i>N</i> ¹ , <i>N</i> ¹ , <i>N</i> ¹² , <i>N</i> ¹² -tetramethyl- <i>N</i> ¹ , <i>N</i> ¹² -dioctadecyl dibromide
C ₁₈ TMACl	octadecyltrimethylammonium chloride
CN	coordination number
CP	cross polarization
CPME	cyclopentyl methyl ether
Cbz	carbazole
Cp*	pentamethylcyclopentadienyl
<i>D</i> _C	dielectric constant
DCE	dichloroethane
DCM	4-(dicyanomethylene)-2-methyl-6-(4-dimethylaminostyryl)-4H-pyran
DD	dipolar decoupling
DFT	density functional theory
DMF	<i>N,N</i> -dimethylformamide
DMSO	dimethyl sulfoxide
DN	donor number

DPP	1,4-diketo-3,6-dithienylpyrrolo[3,4- <i>c</i>]pyrrole
DTA	differential thermal analysis
DTBT	4,7-dithienyl-2,1,3-benzothiadiazole
EDTA	ethylenediaminetetraacetic acid
EDX	energy dispersive X-ray spectrometry
EI	electron ionization
EISA	evaporation-induced self-assembly
EO	ethylene oxide
EQE	external quantum efficiency
ESI	electrospray ionization
E_T^N	Dimroth–Reichardt’s ET parameter
EXAFS	extended X-ray absorption fine structure
Et	ethyl
EtOAc	ethyl acetate
FAB	fast atom bombardment
FF	fill factor
FI	field ionization
FID	flame ionization detector
FSM	folded sheet mechanism
FT	Fourier transform
GC–MS	gas chromatography–mass spectrometry
GI–SAXS	glazing incidence–small angle X-ray scattering
H-MOP	2-diphenylphosphino-1,1’-binaphthyl
HRMS	high resolution mass spectroscopy
ICP	inductively coupled plasma
IR	infra-red
ITO	indium tin oxide
J	coupling constant
J	current density
J_{sc}	short-circuit current density

JohnPhos	2-(di- <i>tert</i> -butylphosphino)biphenyl
M	molar concentration
MALDI	matrix assisted laser desorption/ionization
MAS	magic angle spinning
MBAS	molecular building blocks for allylsilane sol-gel precursors
MCM	Mobil composition of matter
MOF	metal-organic framework
MeAcid	methylacridone
NBS	<i>N</i> -bromosuccinimide
NLDFT	nonlinear density functional theory
NMP	<i>N</i> -methyl-2-pyrrolidone
NMR	nuclear magnetic resonance
NP	non-porous
OSC	organic solar cell
P123	Pluronic P123 poly(ethyleneglycol)-poly(propyleneglycol)-poly(ethyleneglycol)
PCBM	[6,6]-phenyl-C ₆₁ -butyric acid methyl ester
PCE	power conversion efficiency
PDI	polydispersity index
PEDOT:PSS	poly (3,4-ethylenedioxythiophene) doped with poly(4-styrenesulfonate)
PMO	Periodic Mesoporous Organosilica
PO	propylene oxide
PS-BPy	polystyrene-supported bipyridine
PS- <i>b</i> -PEO	polystyrene- <i>block</i> -polyethylene oxide
PTFE	polytetrafluoroethylene
Pa	pascal
Py	pyridine
QXAFS	quick X-ray absorption fine structure
<i>R</i>	interatomic distance
SB	solvent basicity
SBA	Santa Barbara Amorphous

S_{BET}	specific BET surface area
SCLC	space-charge-limited current
SDA	structure-directing agent
SEM	scanning electron microscope
TBHP	<i>tert</i> -butyl hydroperoxide
TEM	transmission electron microscope
TEOS	tetraethyl orthosilicate
TFE	2,2,2-trifluoroethanol
TG	thermal gravimetric analysis
THF	tetrahydrofuran
TMS	trimethylsilyl
TOF	turnover frequency
TON	turnover number
TPPy	1,3,6,8-tetraphenylpyrene
Tf	trifluoromethansulfonyl
UV-vis	ultraviolet-visible
UiO	University of Oslo
V	voltage
V_{oc}	open circuit voltage
$V_{t\text{-plot}}$	mesopore volume
XAFS	X-ray absorption fine structure
XANES	X-ray absorption near edge structure
XPS	X-ray photon spectroscopy
XRD	X-ray diffraction
a_0	lattice constant
bpy	2,2'-bipyridine
br	broad
brine	saturated sodium chloride aqueous solution
c	concentration
calcd	calculated

cat.	catalyst
cod	1,5-cyclooctadiene
d	doublet
<i>d</i>	spacing between diffracting planes
<i>d</i> _{DFT}	density functional theory pore diameter
dba	<i>trans,trans</i> -dibenzylideneacetone
dppf	1,1'-bis(diphenylphosphino)ferrocene
eV	electronvolt
equiv	equivalent
equiv	equivalent
h	hour
<i>i</i> -	iso
<i>i</i> -PrMgCl	isopropylmagnesium chloride
<i>m</i>	meta
m	multiplett
mM	millimolar concentration
min	minute
<i>n</i> -	normal
<i>o</i>	ortho
°C	degree Celsius
<i>p</i>	para
pin	pinacol
ppm	parts per million
ppy	2-phenylpyridine
q	quartet
quant.	quantitatively
<i>rac</i> -	racemic
rpm	revolutions per minute
s	singlet
sept	septet

t	triplet
t-	tertiary
ΔE_0	correction-of-edge energy
α	optical rotation
δ	chemical shift
ϵ	molar absorption coefficient
θ	incident angle
λ_{abs}	absorption wavelength
λ_{max}	maximum absorption wavelength
ν_{max}	frequency of maximum absorption
σ^2	Debye–Waller factor



Chapter 1
General Introduction

1.1 Background

Organic-inorganic hybrid materials are advanced functional materials obtained by combining organic components and inorganic components at the nano- or molecular level.¹ By combining the advantages of organic materials such as flexibility and lightweight, and the advantages of inorganic materials such as mechanical strength and heat resistance, the properties and functionalities of the organic-inorganic hybrid materials can be modulated.^{2,3} The merit of hybridization is that it not only adds individual functions but also can compensate for disadvantages to each other. For example, the incorporation of inorganic components enables to improve the mechanical strength and thermal stability and to induce the formation of a two-dimensional or three-dimensional structure that can be penetrated inside with accessibility. By introducing organic components into the inorganic matrix, it is possible to adjust the mechanical properties and the porosity and connectivity of the structure, and to modulate the hydrophobicity and hydrophilicity of organic-inorganic hybrid materials. Over the past two decades, these hybrid materials have been attracted in the fields of optics, microelectronics, transportation, health, energy, energy storage, environment, catalyst and developed on a large scale to realize their industrial and economical applications.⁴

Organic-inorganic hybrid materials can be categorized depending on connectivity between the organic and inorganic components. These components can generally be connected by covalent, coordination bonds, hydrogen bonds, electrostatic interactions, or π - π interactions.⁵

¹ Descalzo, A. B.; Martínez-Mañez, R.; Sancenón, F.; Hoffmann, K.; Rurack, K. *Angew. Chem., Int. Ed.* **2006**, *45*, 5924–5948.

² Owens, G. J.; Singh, R. K.; Foroutan, F.; Alqaysi, M.; Han, C.-M.; Mahapatra, C.; Kim, H.-W.; Knowles, J. C. *Prog. Mater. Sci.* **2016**, *77*, 1–79.

³ McCarthy, J. R.; Weissleder, R. *Adv. Drug Deliv. Rev.* **2008**, *60*, 1241–1251.

⁴ a) Guo, Y.; Mylonakis, A.; Zhang, Z.; Yang, G.; Lelkes, P. I.; Che, S.; Lu, Q.; Wei, Y. *Chem.–Eur. J.* **2008**, *14*, 2909–2917; b) Gun, J.; Lev, O. *Anal. Chim. Acta.* **1996**, *336*, 95–106; c) Avellaneda, C. O.; Dahmouche, K.; Bulhoes, L. O. S.; Pawlicka, A. *J. Sol-Gel. Sci. Technol.* **2000**, *19*, 447–451; d) Fei, J.; Lim, K. G.; Palmore, G. T. R. *Chem. Mater.* **2008**, *20*, 3832–3839; e) Ozer, N.; Cronin, J. P. *Key Eng. Mater.* **2004**, *264(I)*, 337–342; f) Yang, H.; Zhu, Y. *Biosens. Bioelectron.* **2007**, *22*, 2989–2993; g) Fang, Z.; Wang, S.; Zhao, L.; Dong, B.; Xu, Z.; Ren, J.; Yang, Q. *Mater. Lett.* **2008**, *62*, 1514–1517; h) Itoh, T.; Matsubara, I.; Shin, W.; Izu, N. *Mater. Lett.* **2007**, *61*, 4031–4034; i) Zhang, Y.; Shan, L.; Tu, Z.; Zhang, Y. *Sep. Purif. Technol.* **2008**, *63*, 207–212; j) Nam, S. E.; Kim, S. O.; Kang, Y.; Lee, J. W.; Lee, K. H. *J. Membr. Sci.*, **2008**, *322*, 466–474; k) Landi, E.; Martorana, S.; Tampieri, A.; Guicciardi, S.; Melandri, C. *Key Eng. Mater.* **2008**, *361* 547–550; l) Darder, M.; Aranda, P.; Ruiz-Hitzky, E. *Adv. Mater.* **2007**, *19*, 1309–1319; m) Tan, X. C.; Tian, Y. X.; Cai, P. X.; Zou, X. Y. *Anal. Bioanal. Chem.* **2005**, *381*, 500–507.

⁵ Mir, S. H.; Nagahara, L. A.; Thundat, T.; Mokarian-Tabari, P.; Furukawa, H.; Khosla, A. *J. Electrochem.*

Organic-inorganic hybrid materials synthesized by sol–gel or hydro/solvothermal methodologies have attracted much attention owing to unique physical and chemical properties of organic components, and mechanical and thermal stability thanks to covalent or ionic-covalent bonds between organic and inorganic components. This kind of hybrid materials can be readily prepared from mixture of metal alkoxides or halides ($M(OR')_n$ or MX_n , where $M = Si, Ti, Zr, Nb, Al$ etc., $R' =$ alkyl group) and organic-functionalized metal alkoxides ($RM(OR')_3$, where $R =$ functional organic group, $M = Si, Sn, R' =$ alkyl group).

Among organic-inorganic hybrid materials, organosilica hybrid materials prepared by sol–gel process have been attracted much attention and extensively studied owing to several advantages such as i) easy synthesis of organoalkoxysilanes, ii) introduction of various organic groups, iii) ease of reaction control of sol–gel polymerization (hydrolysis and condensation), iv) high flexibility for shaping, v) high chemical and structural stabilities due to the organic-inorganic hybrid frameworks. Historically, organosilica materials such as polysilsesquioxanes ($R-SiO_{1.5}$, where R : organic group) were already prepared from mono-organosilane precursors denoted as $R-Si(OR')_3$ (R : organic group, R' : Me, Et, etc.) in 1960s and 1970s.⁶ In the 1990s, research on functional organic silica hybrids, bridged-polysilsesquioxanes (BSQs, $O_{1.5}Si-R-SiO_{1.5}$), began to attract attention due to their high ability to control their processability.⁷ By using the organic-bridged alkoxysilane precursors denoted as $R-[Si(OR')_3]_n$ (R : organic group, R' : Me, Et, etc., $n \geq 2$) containing two or more hydrolyzable silyl groups, organic moieties can be directly incorporated in the three-dimensional structure of the silica matrix through robust covalent Si–C bonds without addition of pure silica source such as tetraalkoxysilane. Therefore, organic groups are distributed homogeneously and covalently bonded in the materials at the molecular level. This approach allows the synthesis of organosilica hybrids with high organic contents up to 30–70 wt%, maximizing the functionality of organic group on the overall properties of the hybrid materials.⁸ BSQs can be obtained as not only film and fiber shapes but also bulk and powder with large surface area and high porosity. The advances in the controlled synthesis of BSQs with various types of organic components, particles

Soc. **2018**, *165*, B3137–B3156.

⁶ a) Sprung, M.; Guenther, F. *J. Polym. Sci.* **1958**, *28*, 17–34; b) Katchman, A. U.S. Patent, 3162614, 1964; c) Cekada, J. J. U.S. Patent, 3355399, 1967.

⁷ Shea, K. J.; Loy, D. A. *Chem. Mater.* **2001**, *13*, 3306–3319

⁸ Loy, D. A.; Shea, K. J. *Chem. Rev.* **1995**, *95*, 1431–1442.

sizes, and morphologies accelerate their applications in optical materials,⁹ adsorbents,¹⁰ solid supports,¹¹ and catalysts.¹²

Over the time span of 1990–1993, synthetic route to periodic mesoporous silica with well-ordered pore size was reported by research groups in both Japan and United State independently.^{13–15} Yanagisawa et al. reported the first approach to form ordered mesoporous silica, so-called KSW-1, by mixing of a layered polysilicate kanemite and alkylammonium surfactant.¹³ Then, Inagaki et al. synthesized highly ordered mesoporous silica with two-dimensional (2D) hexagonal symmetry (FSM-16) by modification of Yanagisawa method.¹⁴ Mobil R&D Labs. introduced the synthetic route using alkylammonium surfactants as structure-directing agents to form well-ordered mesoporous (alumino-) silicate material with 2D-hexagonal symmetry, MCM-41.¹⁵ These synthetic approaches based on molding of a silica phase around the surfactant micelles expanded the field of molecular sieves from less than 1.4 nm for zeolite to more than 2 nm

⁹ a) Li, H.; Lin, J.; Zhang, H.; Fu, L.; Meng, Q.; Wang, S. *Chem. Mater.* **2002**, *14*, 3651–3655; b) Walcarius, A. *Chem. Mater.* **2001**, *13*, 3351–3372; c) Freitas, V. T.; Fu, L.; Cojocariu, A. M.; Cattoën, X.; Bartlett, J. R.; Le Parc, R.; Bantignies, J.-L.; Wong Chi Man, M.; André, P. S.; Ferreira, R. A. *ACS Appl. Mater. Interfaces* **2015**, *7*, 8770–8778; d) Nobre, S. S.; Cattoën, X.; Ferreira, R. A.; Carcel, C.; de Zea Bermudez, V.; Wong Chi Man, M.; Carlos, L. D. *Chem. Mater.* **2010**, *22*, 3599–3609; e) Nobre, S. S.; Brites, C. D.; Ferreira, R. A.; de Zea Bermudez, V.; Carcel, C.; Moreau, J. J. E.; Rocha, J.; Wong Chi Man, M.; Carlos, L. D. *J. Mater. Chem.* **2008**, *18*, 4172–4182; f) Guo, S.; Matsukawa, K.; Miyata, T.; Okubo, T.; Kuroda, K.; Shimojima, A. *J. Am. Chem. Soc.* **2015**, *137*, 15434–15440.

¹⁰ a) Dib, S.; Boufatit, M.; Chelouaou, S.; Sadi-Hassaine, F.; Croissant, J.; Long, J.; Raehm, L.; Charnay, C.; Durand, J. O.; **2014**, *4*, 24838–24841; b) Wu, M.; Wu, R. a.; Zhang, Z.; Zou, H. *Electrophoresis* **2011**, *32*, 105–115; c) Castricum, H. L.; Paradis, G. G.; Mittelmeijer-Hazeleger, M. C.; Kreiter, R.; Vente, J. F.; Ten Elshof, J. E. *Adv. Funct. Mater.* **2011**, *21*, 2319–2329; d) Tian, R. J.; Ye, M. L.; Hu, L. H.; Li, X.; Zou, H. F.; *J. Sep. Sci.* **2007**, *30*, 2204–2209.

¹¹ a) Biazotto, J. C.; Sacco, H. C.; Ciuffi, K. J.; Ferreira, A. G.; Serra, O. A. *J. Non-Cryst. Solids* **2000**, *273*, 186–192; b) Sacco, H. C.; Ciuffi, K. J.; Biazotto, J. C.; Zucchi, M. R.; Leite, C. A. P.; Nascimento, O. R.; Serra, O. A.; Iamamoto, Y. *J. Non-Cryst. Solids* **2000**, *273*, 150–158; c) Ciuffi, K. J.; Sacco, H. C.; Biazotto, J. C.; Vidoto, E. A.; Nascimento, O. R.; Leite, C. A.; Serra, O. A.; Iamamoto, Y. *J. Non-Cryst. Solids* **2000**, *273*, 100–108; d) Biazotto, J. C.; Sacco, H. C.; Ciuffi, K. J.; Neri, C. R.; Ferreira, A. G.; Iamamoto, Y.; Serra, O. A. *J. Non-Cryst. Solids* **1999**, *247*, 134–140; e) Hwang, K.-O.; Sasaki, T. *J. Mater. Chem.* **1998**, *8*, 2153–2156; f) Kloster, G. M.; Taylor, C. M.; Watton, S. P. *Inorg. Chem.* **1999**, *38*, 3954–3955.

¹² a) Croissant, J. G.; Cattoën, X.; Durand, J.-O.; Wong Chi Man, M.; Khashab, N. M. *Nanoscale*, **2016**, *8*, 19945–19972; b) Ferré, M.; Pleixats, R.; Wong Chi Man, M.; Cattoën, X. *Green Chem.* **2016**, *18*, 881–922; c) Adima, A.; Moreau, J. J. E.; Wong Chi Man, M. *J. Mater. Chem.* **1997**, *7*, 2331–2333; d) Adima, A.; Moreau, J. J. E.; Wong Chi Man, M. *Chirality* **2000**, *12*, 411–420; e) Moreau, J. J. E.; Wong Chi Man, M. *Coord. Chem. Rev.* **1998**, *178–180*, 1073–1084.

¹³ Yanagisawa, T.; Shimizu, T.; Kuroda, K.; Kato, C. *Bull. Chem. Soc. Jpn.* **1990**, *63*, 988–992.

¹⁴ Inagaki, S.; Fukushima, Y.; Kuroda, K. *J. Chem. Soc., Chem. Commun.* **1993**, 680–682.

¹⁵ a) Kresge, C. T.; Leonowicz, M. E.; Roth, W. J.; Vartuli, J. C.; Beck, J. S. *Nature* **1992**, *359*, 710–712; b) Beck, J. S.; Vartuli, J. C.; Roth, W. J.; Leonowicz, M. E.; Kresge, C. T.; Schmitt, K. D.; Chu, C. T.-W.; Olson, D. H.; Sheppard, E. W.; McCullen, S. B.; Higgins, J. B.; Schlenker, J. L. *J. Am. Chem. Soc.* **1992**, *114*, 10834–10843.

for mesoporous silica. Since the synthetic approach has been developed, extensive efforts have been devoted to expand to framework composition toward the enhancement of functionalities of mesoporous silicas.¹⁶ Research efforts in the field of mesoporous materials are shifting from hybrid materials containing metal oxides to those containing organic functionalities. In 1996, synthesis of organic-functionalized mesoporous silicas was demonstrated. These functional mesoporous silicas were synthesized by two approaches as follows: i) post-modification of mesoporous silica surface by organosilane precursors (grafting approach),¹⁷ ii) co-condensation of organosilane precursors and pure silica precursors in the presence of structure-directing agents (co-condensation approach).¹⁸ The meso-scale porous structures are available for modulation of surface properties by functionalization, which allows control of adsorption/desorption behaviors of gas or guest molecules in the mesopores, and design and construction of specific reaction fields for catalysts.

Introduction of meso-scale porous structure into organosilica hybrids can lead to increasing of surface area and high accessible porosity in the materials, which is effective for improvement of material properties toward their applications. In 1999, three research groups independently reported synthesis of periodic mesoporous organosilicas (PMOs) by direct condensation of organic-bridged alkoxy silane precursors in the presence of surfactant templates.^{19,20,21} By applying the concept of structure-directed synthesis of pure mesoporous silica, a well-ordered mesoporous structure was obtained from organic-bridged alkoxy silane precursors without addition of pure silica sources such as tetraethoxysilane. PMOs are fundamentally unique mesoporous materials possessing robust inorganic porous framework and high functionality of bridging organic group. The size of mesopores (1.5–30 nm) can be controlled by appropriate selecting of surfactant and additives. While the use of ionic surfactant templates usually forms PMOs with small-pore size, the combination of amphiphilic block copolymer and salts affords PMOs with large-pore size.²² A

¹⁶ a) He, X.; Antonelli, D. *Angew. Chem., Int. Ed.* **2002**, *41*, 214–229; b) Schüth, F. *Chem. Mater.* **2001**, *13*, 3184–3195.

¹⁷ a) Brühwiler, D. *Nanoscale*, **2010**, *2*, 887–892; b) Chen, J.; Li, Q.; Xu, R.; Xiao, F. *Angew. Chem., Int. Ed.* **1995**, *34*, 2694–2696.

¹⁸ a) Burkett, D. L.; Sims, S. D.; Mann, S. *Chem. Commun.* **1996**, 1367–1368; b) Macquarrie, D. J. *Chem. Commun.* **1996**, 1961–1962; c) Lim, M. H.; Blanford, C. F.; Stein, A. *J. Am. Chem. Soc.* **1997**, *119*, 4090–4091.

¹⁹ Inagaki, S.; Guan, S.; Fukushima, Y.; Ohsuna, T.; Terasaki, O. *J. Am. Chem. Soc.* **1999**, *121*, 9611–9614.

²⁰ Asefa, T.; MacLachlan, M. J.; Coombs, N.; Ozin, G. A. *Nature* **1999**, *402*, 867–871.

²¹ Melde, B. J.; Holland, B. T.; Blanford, C. F.; Stein, A. *Chem. Mater.* **1999**, *11*, 3302–3308.

²² a) Zhu, H.; Jones, D. J.; Zajac, J.; Rozière, J.; Dutartre, R. *Chem. Commun.* **2001**, 2568–2569; b) Muth,

variety of functional organic groups has been introduced to enhance the functionalities of PMOs. Although the simple aliphatic and aromatic bridging groups have been introduced in early research, recently advanced synthetic methods to prepare the organosilane precursors allowed introduction of a wide variety of organic groups ranging from hydrocarbons and π -conjugated aromatics to hetroaromatics and metal complexes.

Recent research on PMOs is motivated by its applications in material science. In PMOs, there are three clearly distinguishable regions for functionalization as follows: i) organosilica framework, ii) pore surface, and iii) mesopore space. Different functions can be introduced to each of these regions. It is expected to develop new functions that have never been seen. Since the function of an organic group can be imparted to the organosilica framework, it is possible to express a high level of function and unique properties by integration of functions of pore framework, the pore surface and the mesopore space. These numerous assets of PMOs encouraged synthetic chemists to synthesize the further functional PMOs. High functional PMOs have been studied for various potential applications such as optical materials,²³ adsorbents,²⁴ sensors,²⁵ low-*k* materials,²⁶ solid catalysts,²⁷ and biological drug delivery systems and controlled release materials.²⁸

O.; Schellbach, C.; Fröba, M. *Chem. Commun.* **2001**, 2032–2033

²³ a) Inagaki, S.; Ohtani, O.; Goto, Y.; Okamoto, K.; Ikai, M.; Yamanaka, K.-i.; Tani, T.; Okada, T. *Angew. Chem., Int. Ed.* **2009**, *48*, 4042–4046; b) Mizoshita, N.; Goto, Y.; Kapoor, M. P.; Shimada, T.; Tani, T.; Inagaki, S. *Chem.–Eur. J.* **2009**, *15*, 219–226; c) Takeda, H.; Goto, Y.; Maegawa, Y.; Ohsuna, T.; Tani, T.; Matsumoto, K.; Shimada, T.; Inagaki, S. *Chem. Commun.* **2009**, 6032–6034; d) Li, Y. J.; Wang, L.; Yan, B. *J. Mater. Chem.* **2011**, *21*, 1130–1138; e) Takeda, H.; Ohashi, M.; Tani, T.; Ishitani, O.; Inagaki, S. *Inorg. Chem.* **2010**, *49*, 4554–4559; f) Mizoshita, N.; Yamanaka, K.; Hiroto, S.; Shinokubo, H.; Tani, T.; Inagaki, S. *Langmuir* **2012**, *28*, 3987–3994.

²⁴ a) Hao, N.; Han, L.; Yang, Y. X.; Wang, H. T.; Webley, P. A.; Zhao, D. Y. *Appl. Surf. Sci.* **2010**, *256*, 5334–5342; b) Chandra, D.; Das, S. K.; Bhaumik, A. *Microporous Mesoporous Mater.* **2010**, *128*, 34–40; c) Wu, H.-Y.; Chen, C. T.; Hung, I.-M.; Liao, C.-H.; Vetrivel, S.; Kao, H.-M. *J. Phys. Chem. C* **2010**, *114*, 7021–7029; d) Moorthy, M. S.; Kim, M.-J.; Bae, J.-H.; Park, S. S.; Saravanan, N.; Kim, S.-H.; Ha, C.-S. *Eur. J. Inorg. Chem.* **2013**, 3028–3038; e) Kubo, M.; Ishiyama, K.; Shimojima, A.; Okubo, T. *Microporous Mesoporous Mater.* **2012**, *147*, 194–199; f) Ye, G.; Leng, Y.; Bai, F.; Wei, J.; Wang, J.; Chen, J. *Chem.–Asian J.* **2013**, *8*, 1482–1488.

²⁵ a) Melde, B. J.; Johnson, B. J. *Anal. Bioanal. Chem.* **2010**, *398*, 1565–1573; b) Borghard, W. G.; Calabro, D. C.; Disanzo, F. P.; Disko, M. M.; Diehl, J. W.; Fried, J. C.; Markowitz, M. A.; Zeinali, M.; Melde, B. J.; Riley, E. A. *Langmuir* **2009**, *25*, 12661–12669; c) Lofgreen, J. E.; Moudrakovski, I. L.; Ozin, G. A. *ACS Nano* **2011**, *5*, 2277–2287; d) Kang, C.; Li, W.; Tan, L.; Li, H.; Wei, C.; Tang, Y. *J. Mater. Chem. A* **2013**, *1*, 7147–7153; e) Du, J.; Cipet-Wechsler, J.; Lobe, J. M.; Looks, H.-P.; Crudden, C. M. *Small* **2010**, *6*, 1168–1172; e) Johnson, B. J.; Melde, B. J.; Charles, D. T.; Condon, D. C.; Dinderman, M. A.; Malanoski, A. P.; Qadri, S. B. *Langmuir* **2008**, *24*, 9024–9029.

²⁶ a) Wang, W.; Grozea, D.; Sandeep, K.; Perovic, D. D.; Ozin, G. A. *ACS Nano* **2011**, *5*, 1267–1275; b) Hatton, B. D.; Landskron, K.; Whitnall, W.; Perovic, D. D.; Ozin, G. A. *Adv. Funct. Mater.* **2005**, *15*, 823–829.

²⁷ a) Yang, Q.; Liu, J.; Zhang, L.; Li, C. *J. Mater. Chem.* **2009**, *19*, 1945–1955 and references therein; b)

1.2 Literature Review

1.2.1 Organic-functionalized Mesoporous Silicas

Organic-functionalized mesoporous silicas can be prepared by two pathways, i) grafting method and ii) co-condensation method (Scheme 1.1). The former method can be achieved by surface modification of mesoporous silica with silane coupling agents such as RSiX_3 (usually $\text{X} = \text{halide, alkoxy}$) in inert organic solvents.²⁹ The modification process was usually carried out under anhydrous condition at reflux temperature to induce the covalent bond formation between surface silanol groups and silane coupling agents.^{17b,30} The grafting method has several advantages as follows: i) synthetic operation is simple, ii) a variety of silane coupling agents are available, iii) mesoporous frameworks can be retained even after the process, iv) selective modification of internal/external surfaces or selective modification of pore opening can be achieved.³¹ It has been reported a variety of organically functionalized mesoporous silicas aimed for adsorbent materials and catalysts.³² However, this method has several disadvantages as follows: i) loading amount of organic groups is limited,³³ ii) it is difficult to control the distribution of organic groups on the pore surface,³⁴ iii) the pore size and volume are often reduced after introduction of organic functional groups.³⁵

Co-condensation method overcomes synthetic problems related to the grafting method. This approach can be achieved by hydrolysis and condensation of mono-organosilane precursor

Diaz, U.; Brunel, D.; Corma, A. *Chem. Soc. Rev.* **2013**, *42*, 4083–4097.

²⁸ a) Angelos, S.; Johansson, E.; Stoddart, D. F.; Zink, J. I. *Adv. Funct. Mater.* **2007**, *17*, 2261–2271; b) Liong, M.; Angelos, S.; Choi, E.; Patel, K.; Stoddart, J. F.; Zink, J. I. *J. Mater. Chem.* **2009**, *19*, 6251–6257.

²⁹ Zhao, X. S.; Lu, G. Q. *J. Phys. Chem. B* **1998**, *102*, 1556–1561.

³⁰ Zhao, X. S.; Lu, G. Q.; Whittaker, A. K.; Millar, G. J.; Zhu, H. Y. *J. Phys. Chem. B* **1997**, *10*, 6525–6531.

³¹ a) Shephard, D. S.; Zhou, W.; Maschmeyer, T.; Matters, J. M.; Roper, C. L.; Parsons, S.; Johnson, B. F. G.; Duer, M. J. *Angew. Chem., Int. Ed.* **1998**, *37*, 2719–2723; b) Mal, N. K.; Fujiwara, M.; Tanaka, Y. *Nature* **2003**, *421*, 350–353; c) Tourné-Péteilh, C.; Brunel, D.; Bégu, S.; Chiche, B.; Fajula, F.; Lerner, D. .; Devoisselle, J.-M. *New J. Chem.* **2003**, *27*, 1415–1418.

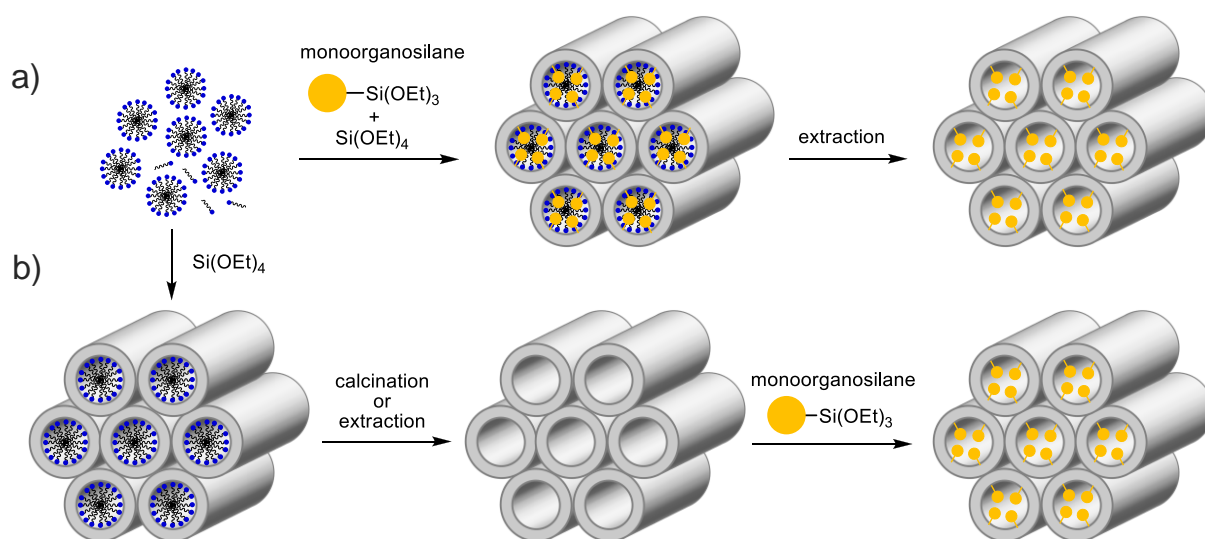
³² De Vos, D. E.; Dams, M.; Sels, B. F.; Jacobs, P. A. *Chem. Rev.* **2002**, *102*, 3615–3640; b) Wight, A. P.; Davis, M. E. *Chem. Rev.* **2002**, *102*, 3589–3614.

³³ Stein, A.; Melde, B. J.; Schroden, R. C. *Adv. Mater.* **2000**, *12*, 1403–1419.

³⁴ Gartmann, N.; Schütze, C.; Ritter, H.; Brühwiler, D. *J. Phys. Chem. Lett.* **2010**, *1*, 379–382.

³⁵ Walcarius, A.; Etienne, M.; Lebeau, B. *Chem. Mater.* **2003**, *15*, 2161–2173; b) Bourlinos, A. B.; Karakostas, T.; Petridis, D. *J. Phys. Chem. B* **2003**, *107*, 920–925.

(RSi(OR')₃) and pure silica sources such as TEOS in the presence of surfactant.^{18,36} A variety of synthetic methods such as hydrothermal synthesis and evaporation-induced self-assembly can be applied. In this case, functional organic groups are directly anchored through the siloxane bond into the pore framework. This synthetic method has some advantages as follows: i) the blocking of mesopore is not occurred during the synthesis of materials because organosilane precursors are components of pore frameworks, ii) homogeneous distribution of organic functional groups can be achieved compared to grafting approach.^{36a} However, this approach still suffers from several disadvantages as follows: i) the degree of ordered mesoporous structure decreases with increasing the loading amount of RSi(OR')₃,³⁷ ii) the proportion of organic functional groups in the materials is generally lower than starting concentration of RSi(OR')₃ in the reaction mixture. Consequently, the highest addition amount of the mono-organosilane precursor in the co-condensation method does not exceed 40 mol% relative to pure silica sources.



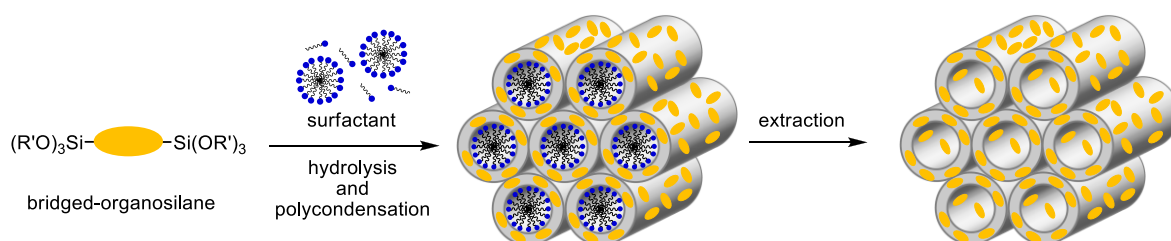
Scheme 1.1. Functionalization of mesoporous silicas by a) post-synthetic treatment (grafting method) and b) co-condensation using tetraalkoxysilane and mono-organosilane.

³⁶ a) Lim, M. H.; Stein, A. *Chem. Mater.* **1999**, *11*, 3285–3295; b) Hatton, B.; Landskron, K.; Whitnall, W.; Perovic, D.; Ozin, G. A. *Acc. Chem. Res.* **2005**, *38*, 305–312; c) Cauvel, A.; Renard, G.; Brunel, D. *J. Org. Chem.* **1997**, *62*, 749–751.

³⁷ Hatton, B.; Landskron, K.; Whitnall, W.; Perovic, D.; Ozin, G. A. *Acc. Chem. Res.* **2005**, *38*, 305–312.

1.2.2 Periodic Mesoporous Organosilicas (PMOs)

PMOs are new class of organic-inorganic hybrid materials synthesized by hydrolysis and polycondensation of organic-bridged alkoxy silane precursors containing two or more hydrolyzable alkoxy silyl groups ($R[(Si(OR')_3)_n]$, $n \geq 2$, R: organic group, R': Me, Et, etc.) in the presence of structure-directing agents (Scheme 1.2).³⁸ By using organic-bridged alkoxy silane precursors, well-ordered mesoporous structures were successfully formed without addition of pure silica sources such as TEOS and TMOS. A large amount of organic groups can be introduced into the pore wall. Also, the organic groups in the pore wall are uniformly dispersed and covalently embedded. Since the organic group is fixed inside the pore wall, no reduction in the pore diameter or decrease in the pore volume occurs during the formation of mesophases, which is not achieved by co-condensation of mono-organosilane precursors. As the pore wall is usually thin and most of the organic groups are exposed on the surface of the pores, guest molecules can be directly contact with organic groups through the pores. Hereinafter, pioneer researches on synthesis of aliphatic, aromatic and crystal-like PMOs, functionalization of PMOs, and applications of functional PMOs are introduced.



Scheme 1.2. General synthetic pathway to PMOs starting from organic-bridged alkoxy silane precursor in the presence of structure-directing agents.

1.2.3 Pioneer Researches of PMOs

In 1999, three research groups independently reported the synthetic method of PMOs. Inagaki and

³⁸ a) Hoffmann, F.; Cornelius, M.; Morell, J.; Fröba, M. *Angew. Chem.*, **2006**, *118*, 3290–3328; b) Fujita, S.; Inagaki, S. *Chem. Mater.* **2008**, *20*, 891–908; c) Mizoshita, N.; Tani, T.; Inagaki, S. *Chem. Soc. Rev.* **2011**, *40*, 789–800; d) Van Der Voort, P.; Esquivel, D.; De Canck, E.; Goethals, F.; Van Driessche, I.; Romero-Salguero, F. J. *Chem. Soc. Rev.* **2013**, *42*, 3913–3955

co-workers synthesized ethane-PMO by hydrolysis and polycondensation of bis-silylated organosilane precursor bridged with ethane groups (**1**) under basic conditions in the presence of a cationic surfactant template (Figure 1.1).¹⁹ By controlling the surfactant concentration, reaction temperature and basic concentration in the reaction mixture, ethane-PMO with symmetry of 2D hexagonal ($P6mm$) and 3D hexagonal ($P6_3/mmc$) were selectively synthesized, respectively. Ozin and co-workers reported the synthesis of PMO containing unsaturated bonds in the framework.²⁰ Bis-silylated ethene precursor (**3**) was successfully transformed into ethene-bridged PMO with 2D hexagonally ordered mesopores by using the CTAB as a structure-directing agent. They also investigated the molecular accessibility to ethene moieties in the materials by using bromine as a probe reagent. The ethene moieties were brominated without collapse of well-ordered mesoporous structure. Stein and co-workers synthesized not only ethane-bridged PMO but also ethene-bridged PMO by using the corresponding precursors (**2** and **3**) in the presence of cetyltrimethylammonium surfactant.²¹ The obtained PMOs have high surface areas of $\sim 1200 \text{ m}^2 \text{ g}^{-1}$ and narrow pore size distributions with diameters of 2.2–2.4 nm. TEM observation suggests that the pore structures consist of wormlike channels. It revealed that these PMOs are more hydrothermally stable than mesoporous silica. The ethene-bridged PMO was applied to gas-phase bromination to confirm the accessibility to the ethene groups in the materials as reported by Ozin and co-workers.

After these pioneer researches have been reported, aliphatic PMOs including ethane-PMO and periodic mesoporous dendrisilicas (PMDs) were synthesized from aliphatic-bridged precursor and dendrimer-like organosilane precursors, respectively.³⁹ In addition, nitrogen- and sulfur-contained aliphatic groups have been also introduced into PMO framework by co-condensation method.⁴⁰ In particular, ethane-PMO has been synthesized under various reaction conditions. Previously reported literatures indicated that the formation of ordered-mesoporous structures depends on various factors such as the type of hydrolyzable silyl group, bridging organic group, surfactant, catalyst, inorganic

³⁹ Landskron, K.; Ozin, G. A. *Science* **2004**, *306*, 1529–1532.

⁴⁰ a) Peng, H. S.; Tang, J.; Yang, L.; Pang, J. B.; Ashbaugh, H. S.; Brinker, C. J.; Yang, Z. Z.; Lu, Y. F. *J. Am. Chem. Soc.* **2006**, *128*, 5304–5305; b) Seo, Y.-K.; Park, S.-B.; Ho Park, D. *J. Solid State Chem.* **2006**, *179*, 1285–1288; c) Benitez, M.; Das, D.; Ferreira, R.; Pischel, U.; Garcia, H. *Chem. Mater.* **2006**, *18*, 5597–5603; d) Nunes, C. D.; Vaz, P. D.; Brandao, P.; Rocha, J.; Ferreira, P.; Bion, N.; Calhorda, M. J. *Microporous Mesoporous Mater.* **2006**, *95*, 104–111; e) Li, J. N.; Qi, T.; Wang, L.; Zhou, Y.; Liu, C. H.; Zhang, Y. *Microporous Mesoporous Mater.* **2007**, *103*, 184–189; f) Cho, E. B.; Han, O. H.; Kim, S.; Kim, D.; Jaroniec, M. *Chem. Commun.* **2010**, *46*, 4568–4570.

additive, swelling agent, synthetic composition and condition, post-treatment and etc.⁴¹ It has been also reported that ethane-PMO can be synthesized not only in bulk particles but also in the form of spherical particles, nanotubes, hollow nanoparticles and etc.⁴²

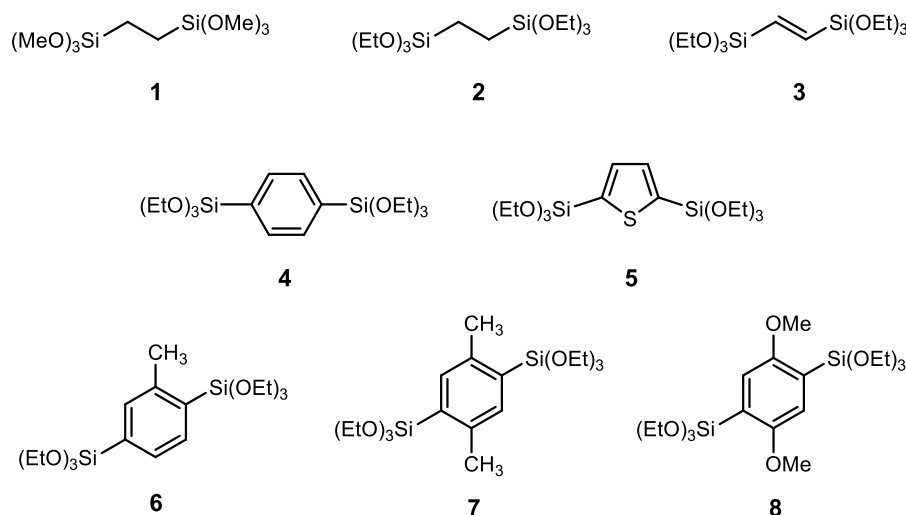


Figure 1.1. Organic-bridged alkoxy silane precursors used in the PMO synthesis in early research.

The synthesis of aromatic-bridged PMOs was reported by Yoshina-Ishii and co-workers in 1999 (Figure 1.1).⁴³ They succeeded in the introduction of benzene and thiophene groups into the organosilica framework of PMOs. Although the Si–C bonds of benzene- (**4**) and thiophene-bridged organosilane precursors (**5**) were cleaved during the hydrolysis and condensation processes under strong basic conditions, well-ordered benzene- and thiophene-PMOs were obtained by using a cationic pyridinium surfactant without cleavage of Si–C bonds under the mild acidic condition. It was also reported that benzene-PMO can be also synthesized by using cationic ammonium surfactant and nonionic surfactant under acidic condition.

After this report, Ozin and co-workers synthesized aromatic PMOs starting from bridged trialkoxysilane precursors of toluene (**6**), *p*-xylene (**7**), 1,4-dimethoxybenzene (**8**) as shown in Figure 1.1.⁴⁴ By using cationic pyridinium surfactant under acidic conditions, aromatic PMOs

⁴¹ Lin, H.-P.; Mou, C.-Y. *Acc. Chem. Res.* **2002**, *35*, 927–935.

⁴² Croissant, J. G.; Cattoën, X.; Wong Chi Man, M.; Durand, J.-O.; Khashab, N, M. *Nanoscale* **2015**, *7*, 20318–20334.

⁴³ Yoshina-Ishii, C.; Asefa, T.; Coombs, N.; MacLachlan, M. J.; Ozin, G. A. *Chem. Commun.* **1999**, 2539–2540.

⁴⁴ Temtsin, G.; Asefa, T.; Bittner, S.; Ozin, G. A. *J. Mater. Chem.* **2001**, *11*, 3202–3206.

having ordered 2D hexagonal mesoporous structures with diameters of 2.3 nm, surface areas of 560–1100 m² g⁻¹, and pore volumes of 0.3–0.6 cm³ g⁻¹ were obtained. XRD patterns of these PMOs suggested some degree of ordering of aromatic groups possibly due to π - π stacking in the pore channel.

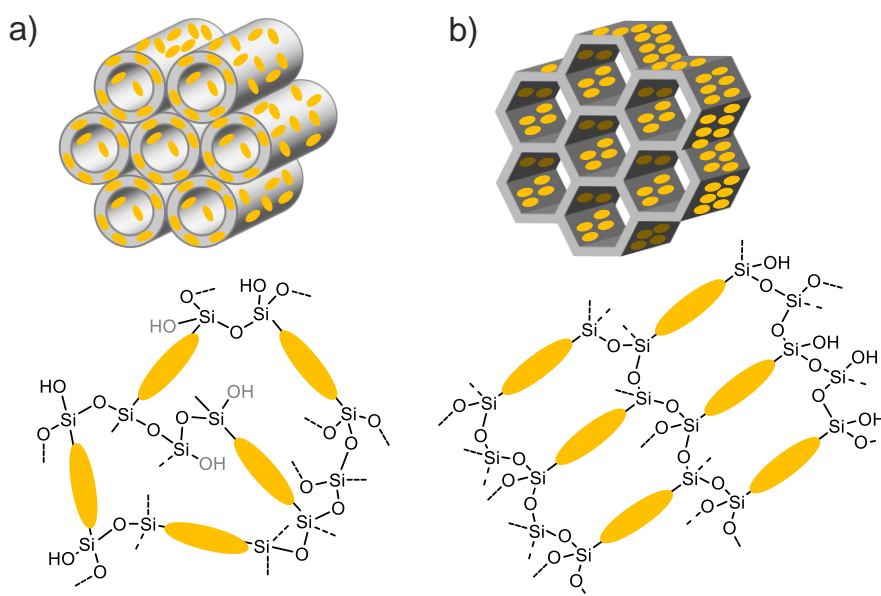


Figure 1.2. Schematic illustration of amorphous and crystal-like frameworks PMOs.

In 2002, Inagaki and co-workers reported first synthesis of benzene-PMO having a crystal-like organosilica pore wall.⁴⁵ The crystal-like benzene-PMO was synthesized from precursor **4** and cationic ammonium surfactant under basic conditions. The pore wall of conventional benzene-PMO reported by Ozin and co-workers was an amorphous structure where benzene groups were randomly dispersed in the siloxane networks (Figure 1.2a). In contrast, crystal-like benzene-PMO has not only an ordered mesoporous structure but also molecular-scale periodicity in the pore framework (Figure 1.2b). In this case, the benzene layer and the silica layer were alternately arranged with an interval of 7.6 Å along the pore channel direction. XRD patterns of crystal-like benzene-PMO showed reflections at low angles ($2\theta < 5^\circ$) corresponds to well-ordered 2D hexagonal structure and three reflections (10, 20, 30) at middle angles ($2\theta > 10^\circ$) assigned to a molecular-scale periodicity, respectively. TEM observation clearly indicated molecular-scale periodicity within the pore framework. The well-ordered pore channels with an interval of 7.6 Å

⁴⁵ Inagaki, S.; Guan, S.; Ohsuna, T.; Terasaki, O. *Nature* **2002**, *416*, 304–307.

and numerous lattice fringes along the channel axis were observed.

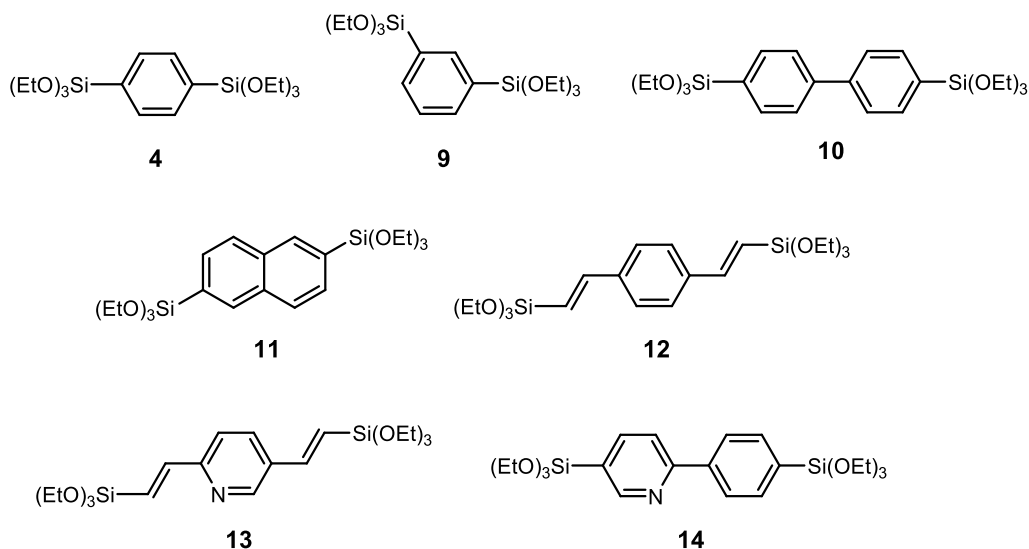


Figure 1.3. Bis-silylated organosilane precursors used in synthesis of crystal-like PMOs.

After this pioneering work, the series of crystal-like PMOs have been synthesized. For example, ethene (**3**),⁴⁶ 1,3-phenyl (**9**),⁴⁷ biphenyl (**10**),⁴⁸ naphthalene (**11**),⁴⁹ divinylbenzene (**12**),⁵⁰ divinylpyridine (**13**),⁵¹ and phenylpyridine groups (**14**)⁵² have been introduced into the framework of crystal-like PMOs (Figure 1.3). These crystal-like PMOs have been synthesized under basic conditions because the hydrophobic and hydrophilic interaction between hydrolyzed organosilane precursors would be induced the crystal-like organization of organic groups during the formation of mesophase. Morell and co-workers investigated the formation process of crystal-like biphenyl-PMO under basic conditions by in-situ SAXS measurements.⁵³ It indicated that formation of mesophase/mesopore and molecular-scale periodicity was simultaneously occurred after the

⁴⁶ Xia, Y.; Wang, W.; Mokaya, R. *J. Am. Chem. Soc.* **2005**, *127*, 790–798.

⁴⁷ Kapoor, M. P.; Yang, Q.; Inagaki, S. *Chem. Mater.* **2004**, *16*, 1209–1213

⁴⁸ Kapoor, M. P.; Yang, Q.; Inagaki, S. *J. Am. Chem. Soc.* **2002**, *124*, 15176–15177.

⁴⁹ Mizoshita, N.; Goto, Y.; Kapoor, M. P.; Shimada, T.; Tani, T.; Inagaki, S. *Chem.–Eur. J.* **2009**, *15*, 219–226.

⁵⁰ a) Sayari, A.; Wang, W. *J. Am. Chem. Soc.* **2005**, *127*, 12194–12195; b) Cornelius, M.; Hoffmann, F.; Fröba, M. *Chem. Mater.* **2005**, *17*, 6674–6678.

⁵¹ Waki, M.; Mizoshita, N.; Tani, T.; Inagaki, S. *Chem. Commun.* **2010**, *46*, 8163–8165.

⁵² Waki, M.; Mizoshita, N.; Tani, T.; Inagaki, S. *Angew. Chem., Int. Ed.* **2011**, *50*, 11667–11671.

⁵³ Morell, J.; Teixeira, C. V.; Cornelius, M.; Rebbin, V.; Tiemann, M.; Amenitsch, H.; Fröba, M.; Lindön, M. *Chem. Mater.* **2004**, *16*, 5564–5566.

formation of spherical micelles of surfactant.

Sayari and co-workers synthesized benzene-PMO, in which bridged benzene groups were partially arranged within the pore wall, by using nonionic oligomeric surfactant under acidic conditions.⁵⁴ Unlike the crystal-like benzene PMO synthesized under basic condition, the benzene groups are not aligned parallel to the pore channels but are arranged in a state inclined at about 57°. It is also reported that benzene-PMO having a large pore diameter and periodicity on the molecular scale can be synthesized using P123 as a surfactant under acidic conditions.

1.2.4 Synthesis of Functional PMOs

Chemical and physical properties of PMOs are directly linked to the functions of bridging organic groups in the framework. In order to obtain high functional PMOs, it is necessary to use organic-bridged alkoxy silane precursors having a desired organic functional group. In early research of PMO synthesis, bridging organic groups were limited to simple alkyl and aromatic groups, the types of bridging organic groups were greatly expanded and functionalized by progress of the synthetic method of organic-bridged alkoxy silane precursors.

Scheme 1.3 shows representative synthetic methods for organic-bridged alkoxy silane precursors. organic-bridged alkoxy silane precursors have been typically synthesized by i) metalation of aryl dihalides with organometallic reagents followed by treatment with tetraalkoxy silane or chlorotrialkoxy silane, ii) hydrosilylation of olefins, and iii) coupling reaction between silane coupling agents and bifunctional organic substrates.

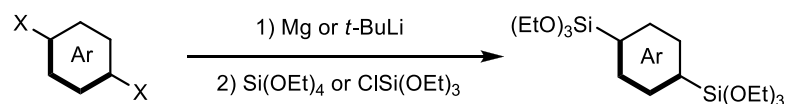
Method i) is commonly used to prepare the simple aromatic-bridged alkoxy silane precursors. The benzene- and biphenyl-bridged precursors were synthesized by Barbier-Grignard reaction between 1,4-dibromobenzene or 4,4'-dibromobiphenyl and TEOS in the presence of activated magnesium (Mg) turnings.⁵⁵ This reaction involves formation of Grignard reagent from aryl dibromide and nucleophilic substitution between the resulting Grignard reagent and TEOS. The terphenyl- (**15**) and anthracene-bridged precursors (**16**) were synthesized by lithiation of 4,4''-dibromoterpheny and 9,10-dibromoanthracene with *t*-butyllithium followed by addition of

⁵⁴ Wang, W. H.; Zhou, W. Z.; Sayari, A. *Chem. Mater.* **2003**, *15*, 4886–4889.

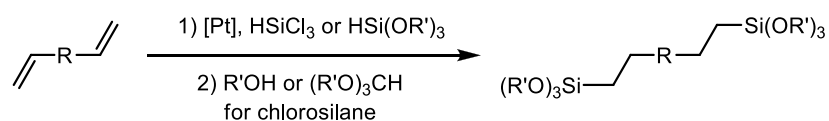
⁵⁵ Shea, K. J.; Loy, D. A.; Webster, O. W. *J. Am. Chem. Soc.* **1992**, *114*, 6700–6710.

chlorotriethoxysilane, respectively (Figure 1.4).⁵⁶

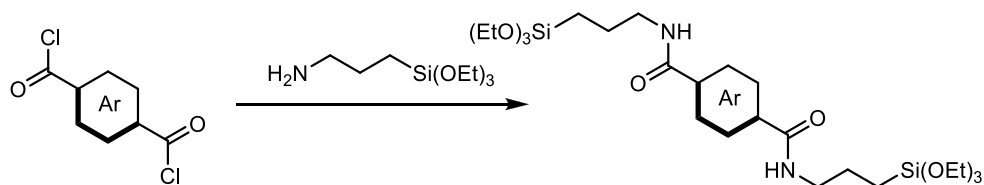
Method i) Metalation + Alkoxylation



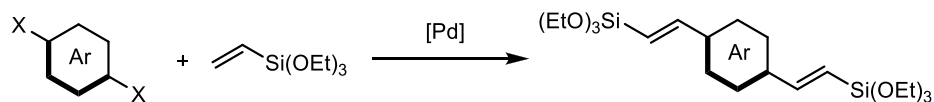
Method ii) Hydrosilylation



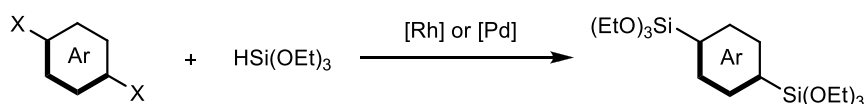
Method iii) Coupling reaction with silane coupling agent



Method iv) Pd-catalyzed Mizoroki–Heck reaction



Method v) Rh- and Pd-catalyzed direct disilylation



Scheme 1.3. Synthetic routes for aromatic- and aliphatic-bridged alkoxylation precursors.

⁵⁶ a) Corriu, R. J. P.; Moreau, J. J. E.; Thepot, P.; Wong Chi Man, M. *Chem. Mater.* **1992**, *4*, 1217–1224; b) Corriu, R. J. P.; Moreau, J. J. E.; Thepot, P.; Man, W. C. M.; Chorro, C.; Lere-Porte, J.-L.; Sauvajol, J.-L. *Chem. Mater.* **1994**, *6*, 640–649.

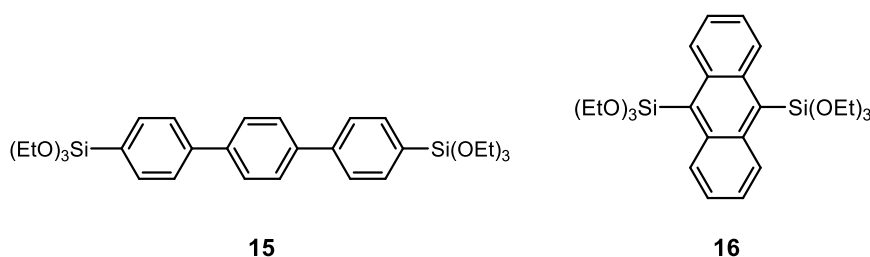


Figure 1.4. Functional aromatic-bridged alkoxy silane precursors synthesized by method i).

Method ii) is commonly used to prepare the aliphatic-bridged alkoxy silane precursors.⁵⁷ Hydrosilylation was generally carried out using trichlorosilane or trialkoxysilane as a hydrosilane source and precious metal complex as a catalyst.⁵⁸ In the case of trichlorosilane, the resulting hydrosilylated compounds were converted to trialkoxysilanes with trialkylorthoformate or alcohol in the presence of base. For example, butyl-bridged alkoxy silane precursor (17) was prepared by hydrosilylation of butadiene with trichlorosilane followed by alkoxylation with triethylorthoformate (Figure 1.5).⁵⁹ Hydrosilylation of 1,5-hexadiene with triethoxysilane gave 1,6-bis(triethoxysilyl)-hexane (18) in one step (Figure 1.5).

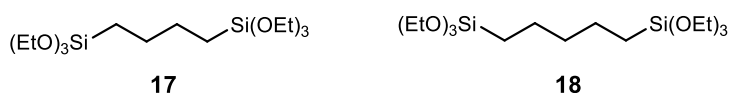


Figure 1.5. Aliphatic-bridged alkoxy silane precursors synthesized by method ii).

Method iii) has become increasingly common because organic-bridged alkoxy silane precursors were readily prepared from commercially available bifunctional organic substrates and silane coupling agents bearing amino group as an electrophilic moiety or isocyanate and halide groups as electrophilic moieties.⁶⁰ The reaction between 3-aminopropyltriethoxysilane and terephthaloyl

⁵⁷ Small, J. H.; Shea, K. J.; Loy, D. A. *J. Non-Cryst. Solids* **1993**, *160*, 234–246.

⁵⁸ Ojima, I. The Hydrosilylation Reaction. In *The Chemistry of Organic Silicon Compounds*; Patai, S., Rappoport, Z., Eds.; Wiley: Chichester, U.K.; 1989; Vol. 2, p 1479.

⁵⁹ Corriu, R. J. P.; Moreau, J. J. E.; Thepot, P.; Wong Chi Man, M. *J. Mater. Chem.* **1994**, *4*, 987–989.

⁶⁰ a) Corriu, R. J. P.; Hoarau, C.; Mehdi, A.; Reye, C. *Chem. Commun.* **2000**, 71–72; c) Bezombes, J.-P.; Chuit, C.; Corriu, R. J. P.; Reye, C. *J. Mater. Chem.* **1999**, *9*, 1727–1734; d) Jurado-Gonzalez, M.; Li Ou, D.; Ormsby, B.; Sullivan, A. C.; Wilson, J. R. H. *Chem. Commun.* **2000**, 67–68; e) Aliev, A.; Li Ou, D.; Ormsby, B.; Sullivan, A. C. *J. Mater. Chem.* **2000**, *10*, 2758–2764.

chloride gives organic-bridged alkoxy silane precursor containing amide linkages (**19**, Figure 1.6).⁶¹ 3-Halopropyltrialkoxysilane is useful silane coupling agent for S_N2 substitution reaction giving bridging linkages with ionic liquid moieties (**20**, Figure 1.6).⁶²

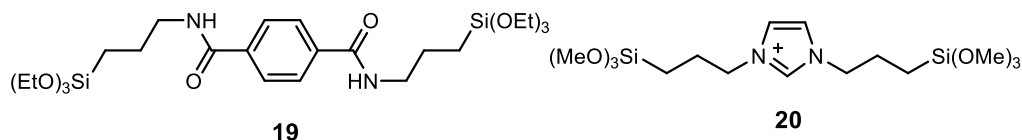


Figure 1.6. Functional organic-bridged alkoxy silane precursor containing amide linkage and ionic liquid moieties synthesized by method iii).

Recently, new synthetic approaches have been applied for synthesis of π -conjugated functional organosilane precursors by transition-metal catalyzed coupling reactions such as iv) Heck reaction between aryl halides and vinyltrialkoxysilanes and v) direct disilylation between aryl halides and trialkoxysilanes. Method iv) is useful synthetic method to synthesize the π -conjugated systems containing vinylene groups (Figure 1.7). For example, Sayari and Wang prepared 1,4-bis-((*E*)-2-(triethoxysilyl)vinyl)benzene by Heck reaction between 1,4-dibromobenzene and vinyltriethoxysilane.⁵⁰ This precursor is attractive precursor because π -conjugated system allows the synthesis of new PMO with 2D hexagonal mesophase and crystal-like pore walls. This approach is also applied to synthesize a highly π -conjugated organosilane precursor having 18 π -electron systems, namely 4,4'-bis((*E*)-2-(triethoxysilyl)vinyl)stilbene (**21**) and 1,2-bis(4-((*E*)-2-(triethoxysilyl)vinyl)phenyl)diazene (**22**).⁶³ These highly conjugated and elongated organosilane precursors allowed the synthesis of organosilica materials with UV-Vis absorption up to 600 nm.

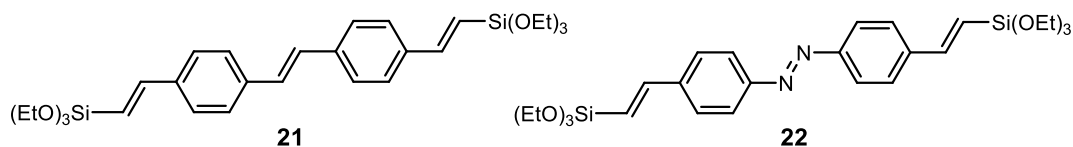


Figure 1.7. π -Conjugated aromatic-bridged alkoxy silane precursors synthesized by method iv).

⁶¹ Guizard, C.; Lacan, P. *New J. Chem.* **1994**, *18*, 1097–1107.

⁶² Lee, B.; Im, H.-J.; Luo, H.; Hagaman, E. W.; Dai, S. *Langmuir* **2005**, *21*, 5372–5376.

⁶³ Cornelius, M.; Hoffmann, F.; Ufer, B.; Behrens, P.; Fröba, M. *J. Mater. Chem.* **2008**, *18*, 2587–2592.

Method v) was a valuable synthetic method to prepare versatile organic-bridged alkoxy silane precursors having aromatic and heteroaromatics (Figure 1.8). Rhodium (Rh)- and palladium (Pd)-catalyzed direct disilylation of aryl and heteroaryl dihalides with trialkoxysilane allow the introduction of functional groups and large size organic groups, which cannot be achieved by classical method i).^{64,65} Especially, Rh-catalyzed direct disilylation, which was established by this study is a reliable synthetic method for functional organosilane precursors containing polycyclic aromatics such as 2,6-naphthalene^{23b} and 2,6-anthracene (**23**),⁶⁶ π -conjugated molecules such as oligo(phenylenevinylene)s (**24**, **25**),⁶⁷ ionic molecules such as methylacridinium (**26**)⁶⁸ and *N*-heterocyclic carbene (NHC),⁶⁹ chelating molecules such as 2-phenylpyridine,⁵² and visible-absorptive molecules such as acridone (**27**).^{23c}

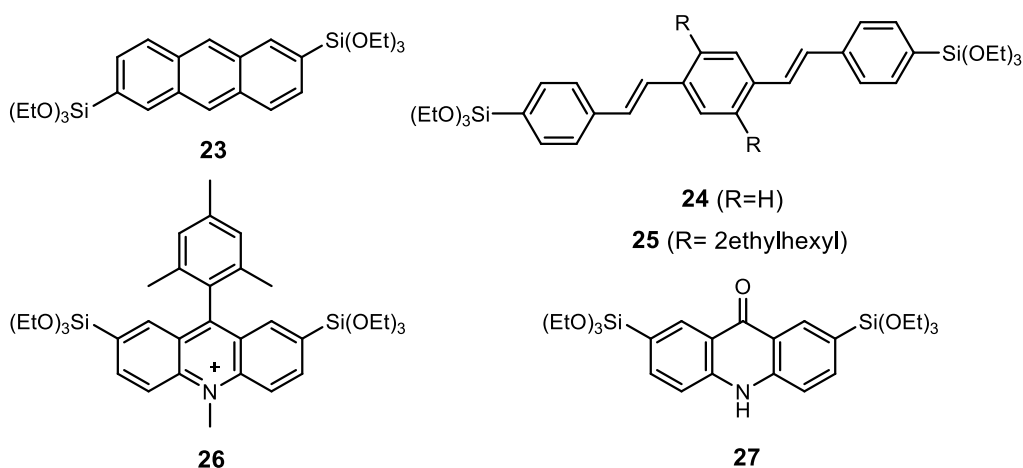


Figure 1.8. Functional aromatic-bridged alkoxy silane precursors synthesized by method v).

Post-functionalization of bridging organic group of PMOs by chemical modification is frequently an effective approach to introduce appropriate functions. Scheme 1.4 shows an example of post-modification of crystal-like benzene-PMO. The sulfonation and nitration of crystal-like benzene-PMO can be introduced sulfonic acid and nitro groups on the benzene moieties,

⁶⁴ Murata, M.; Ishikura, M.; Nagata, M.; Watanabe, S.; Masuda, Y. *Org. Lett.* **2002**, *4*, 1843–1845.

⁶⁵ a) Murata, M.; Suzuki, K.; Watanabe, S.; Masuda, Y. *J. Org. Chem.* **1997**, *62*, 8569–8571; b) Manoso, A. S.; DeShong, P. *J. Org. Chem.* **2001**, *66*, 7449–7455.

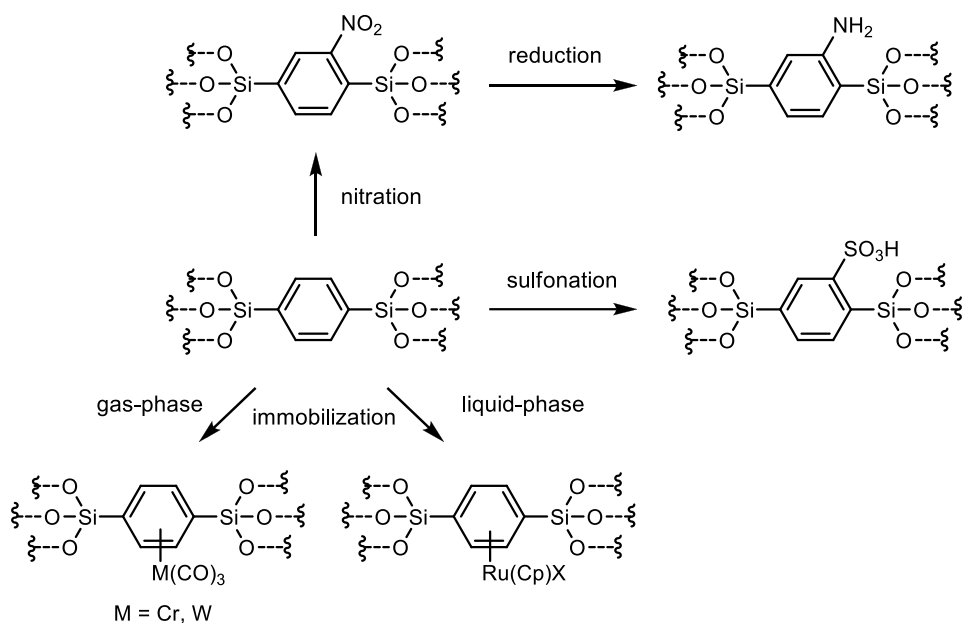
⁶⁶ Goto, Y.; Nakajima, K.; Mizoshita, N.; Suda, M.; Tanaka, N.; Hasegawa, T.; Shimada, T.; Tani, T.; Inagaki, S. *Microporous Mesoporous Materials*. **2009**, *117*, 535–540.

⁶⁷ a) Mizoshita, N.; Goto, Y.; Tani, T.; Inagaki, S. *Adv. Funct. Mater.* **2008**, *18*, 3699–3705; b) Mizoshita, N.; Goto, Y.; Tani, T.; Inagaki, S. *Adv. Mater.* **2009**, *21*, 4798–4801.

⁶⁸ Mizoshita, N.; Yamanak, K.-i.; Shimada, T.; Tani, T.; Inagaki, S. *Chem. Commun.* **2010**, *46*, 9235–9237.

⁶⁹ a) Nguyen, T. P.; Hesemann, P.; Gaveau, P.; Moreau, J. J. E. *J. Mater. Chem.* **2009**, *19*, 4164–4171 b) Yang, H.; Wang, Y.; Qin, Y.; Chong, Y.; Yang, Q.; Li, G.; Zhang, L.; Li, W. *Green Chem.* **2011**, *13*, 1352–1361.

respectively.^{52,70} The nitro group can be converted to the amino group by reduction. The ordered mesoporous structure and crystal-like pore walls were remained unchanged during the chemical modification. The obtained sulfonate- and amino-functionalized crystal-like benzene-PMOs can be used for solid acids and solid base catalysts. The amino groups on crystal-like benzene-PMO can be further modified by amidation, imidization and alkylation, respectively.⁷¹



Scheme 1.4. Functionalization of crystal-like benzene-PMO by chemical modification.

Crystal-like benzene PMO can be used as a ligand of metallocene complexes. Anpo and co-workers reported immobilization of metallocene complexes by chemical vapor deposition of chromium (Cr) and tungsten (W) carbonyl complex.⁷² In the case of $\text{Cr}(\text{CO})_3$ complex, about 15% of the benzene groups in the framework were converted to benzene chromium complex. Also, the metallocene complexes such as ruthenium (Ru) and molybdenum (Mo) can be immobilized by mixing a solution of metal complex precursors with crystal-like benzene-PMO.⁷³ The obtained Ru and Mo metallocene complexes can be used as heterogeneous catalyst for gas-phase hydrosilylation

⁷⁰ a) Ohashi, M.; Kapoor, M. P.; Inagaki, S. *Chem. Commun.* **2008**, 841–843; b) Lourenço, M. A. O.; Gomes, J. R. B.; Ferreira, P. *RSC Adv.* **2015**, 5, 9208–9216.

⁷¹ Lourenço, M. A. O.; Siegel, R.; Mafra, L.; Ferreira, P. *Dalton Trans.* **2013**, 42, 5631–5634.

⁷² Kamegawa, T.; Sakai, T.; Matsuoka, M.; Anpo, M. *J. Am. Chem. Soc.* **2005**, 127, 16784–16785.

⁷³ Kamegawa, T.; Saito, M.; Watanabe, T.; Uchihara, K.; Kondo, M.; Matsuoka, M.; Anpo, M. *J. Mater. Chem.* **2011**, 21, 12228–12231.

reaction and epoxidation of olefins with oxidants, respectively. In addition to crystal-like benzene-PMO, chemical modifications of ethene-PMO have been extensively studied. The double bond can be converted to functional moieties by bromination,⁷⁴ epoxidation,⁷⁵ ozonolysis,⁷⁶ Diels-Alder reaction, or Friedel-Crafts reaction.⁷⁷

1.2.5 Applications

There are many reports on applications of functional PMOs. Hereafter, advanced applications of PMOs for solid acid and base catalysts, heterogeneous metal complex catalysts, heterogeneous organic molecular catalysts, light-harvesting systems, luminescence materials, and photocatalysts were introduced.

Solid acid and base catalysts

Solid catalysts have been attracted attention in the field of industrial chemistry. A variety of solid acid PMO catalysts having sulfonic acid sites have been reported.⁷⁸ Sulfonic acid sites can be typically introduced by i) direct sulfonation of the bridging organic groups in the PMOs and ii) oxidation of thiol-modified PMOs including co-condensation PMOs. The immobilized sulfonic acid sites can be used as a Brønsted acid catalyst for acetalization,⁷⁹ esterification,⁸⁰

⁷⁴ a) Nakai, K.; Oumi, Y.; Horie, H.; Sano, T.; Yoshitake, H. *Microporous Mesoporous Mater.* **2007**, *100*, 328–339; b) Vercaemst, C.; Ide, M.; Wiper, P. V.; Jones, J. T. A.; Khimyak, Y. Z.; Verpoort, F.; Van Der Voort, P. *Chem. Mater.* **2009**, *21*, 5792–5800; c) Xia, Y. D.; Zang, Z. X.; Mokaya, R. *Chem. Mater.* **2006**, *18*, 1141–1148; d) Xia, Y. D.; Mokaya, R. *Microporous Mesoporous Mater.* **2005**, *86*, 231–242; e) Xia, Y. D.; Mokaya, R. *J. Mater. Chem.* **2006**, *16*, 395–400; f) Wang, W. H.; Xie, S. H.; Zhou, W. Z.; Sayari, A. *Chem. Mater.* **2004**, *16*, 1756–1762.

⁷⁵ Sasidharan, M.; Fujita, S.; Ohashi, M.; Goto, Y.; Nakashima, K.; Inagaki, S. *Chem. Commun.* **2011**, *47*, 10422–10424.

⁷⁶ Polarz, S.; Jeremias, F.; Haunz, U. *Adv. Funct. Mater.* **2011**, *21*, 2953–2959.

⁷⁷ a) Nakajima, K.; Tomita, I.; Hara, M.; Hayashi, S.; Domen, K.; Kondo, J. N. *Adv. Mater.* **2005**, *17*, 1839–1842; b) Nakajima, K.; Tomita, I.; Hara, M.; Hayashi, S.; Domen, K.; Kondo, J. N. *Catal. Today* **2006**, *116*, 151–156.

⁷⁸ a) Dhepe, P. L.; Ohashi, M.; Inagaki, S.; Ichikawa, M.; Fukuoka, A. *Catal. Lett.* **2005**, *102*, 163–169; b) Yang, J.; Yang, Q. H.; Wang, C.; Feng, Z. C.; Liu, J. *J. Mol. Catal. A: Chem.* **2006**, *256*, 122–129.

⁷⁹ a) Dube, D.; Rat, M.; Shen, W.; Beland, F.; Kaliaguine, S. *J. Mater. Sci.* **2009**, *44*, 6683–6692; c) Rat, M.; Zahedi-Niaki, M. H.; Kaliaguine, S.; Do, T. O. *Microporous Mesoporous Mater.* **2008**, *112*, 26–31.

⁸⁰ a) Kapoor, M. P.; Fujii, W.; Kasama, Y.; Yanagi, M.; Nanbu, H.; Juneja, L. R. *J. Mater. Chem.* **2008**, *18*, 4683–4691; b) Yang, Q. H.; Kapoor, M. P.; Inagaki, S.; Shirokura, N.; Kondo, J. N.; Domen, K. *J. Mol. Catal. A: Chem.* **2005**, *230*, 85–89; c) Esquivel, D.; De Canck, E.; Jimenez-Sanchidrian, C.; Van Der Voort, P.; Romero-Salguero, F. J. *J. Mater. Chem.* **2011**, *21*, 10990–10998.

etherification,⁸¹ dehydration reaction,⁸² hydrolysis reaction⁸³ and Friedel–Crafts reactions.⁸⁴ In comparison with sulfonic acid immobilized on mesoporous silica, solid acid PMO catalysts show high catalytic activity in acid catalyzed reactions in which water is produced as a by-product.⁸⁵ This increased activity can be explained by increased hydrophobicity of near acid sites thanks to organosilica frameworks, which is helpful for smooth exclusion of water from the acid sites and incorporation of hydrophobic organic substrate into the mesochannels.⁸⁶

A few examples of PMO catalysts having a base site have been also reported. Amino-functionalized crystal-like benzene-PMO can be used as a catalyst for Knoevenagel condensation reaction.⁸⁷ It has also been reported that PMO synthesized from tris(3-(trimethoxysilyl)propyl)amine can be used as a catalyst for Knoevenagel condensation reaction and Henry reaction.⁸⁸

Acid-base bifunctional PMO catalysts, in which acid sites are introduced in to the bridging organic groups and base sites are introduced into the silica layer, have been developed. Thiel and co-workers synthesized acid-base bifunctional PMO catalyst by sulfonation of crystal-like benzene-PMO followed by surface-modification with silane coupling agent bearing amino group (Figure 1.9).⁸⁹ As the combined use of acid and base catalysts is impossible in a homogeneous reaction system, fixation of acid and base sites utilizing the pore surface of PMO is effective and attractive for construction of novel reaction system.⁹⁰ Thiel and co-workers applied to acid-base bifunctional PMO catalyst for acid-base sequential reaction from benzaldehyde dimethyl acetal and

⁸¹ a) Morales, G.; Athens, G.; Chmelka, B. F.; van Grieken, R.; Melero, J. A. *J. Catal.* **2008**, *254*, 205–217; b) Karam, A.; Alonso, J. C.; Gerganova, T. I.; Ferreira, P.; Bion, N.; Barrault, J.; Jerome, F. *Chem. Commun.* **2009**, 7000–7002.

⁸² Liu, J.; Yang, J.; Li, C. M.; Yang, Q. H. *J. Porous Mater.* **2009**, *16*, 273–281; b) Sow, B.; Hamoudi, S.; Zahedi-Niaki, M. H.; Kaliaguine, S. *Microporous Mesoporous Mater.* **2005**, *79*, 129–136.

⁸³ Yang, Q. H.; Kapoor, M. P.; Shirokura, N.; Ohashi, M.; Inagaki, S.; Kondo, J. N.; Domen, K. *J. Mater. Chem.* **2005**, *15*, 666–673.

⁸⁴ a) Kapoor, M. P.; Kasama, Y.; Yanagi, M.; Yokoyama, T.; Inagaki, S.; Shimada, T.; Nanbu, H.; Juneja, L. R. *Microporous Mesoporous Mater.* **2007**, *101*, 231–239; b) Yang, Q. H.; Liu, J.; Yang, J.; Kapoor, M. P.; Inagaki, S.; Li, C. *J. Catal.*, **2004**, *228*, 265–272; c) Rac, B.; Hegyes, P.; Forgo, P.; Molnar, A. *Appl. Catal., A* **2006**, *299*, 193–201.

⁸⁵ Kang, C. M.; Huang, J. L.; He, W. H.; Zhang, F. *J. Organomet. Chem.* **2010**, *695*, 120–127.

⁸⁶ Li, C. M.; Yang, H.; Shi, X.; Liu, R.; Yang, Q. H. *Microporous Mesoporous Mater.* **2007**, *98*, 220–226.

⁸⁷ Kapoor, M. P.; Kasama, Y.; Yokoyama, T.; Yanagi, M.; Inagaki, S.; Hironobu, N.; Juneja, L. R. *J. Mater. Chem.* **2006**, *16*, 4714–4722.

⁸⁸ El Hankari, S.; Motos-Perez, B.; Hesemann, P.; Bouhaouss, A.; Moreau, J. J. E. *J. Mater. Chem.* **2011**, *21*, 6948–6955.

⁸⁹ Shylesh, S.; Wagener, A.; Seifert, A.; Ernst, S.; Thiel, W. R. *Angew. Chem., Int. Ed.* **2010**, *49*, 184–187.

⁹⁰ Alauzun, J.; Mehdi, A.; Reye, C.; Corriu, R. J. P. *J. Am. Chem. Soc.* **2006**, *128*, 8718–8719.

nitromethane into trans- β -nitrostyrene, which involves acid-catalyzed deprotection of the acetal group followed by base-catalyzed Aza-Henry reaction.

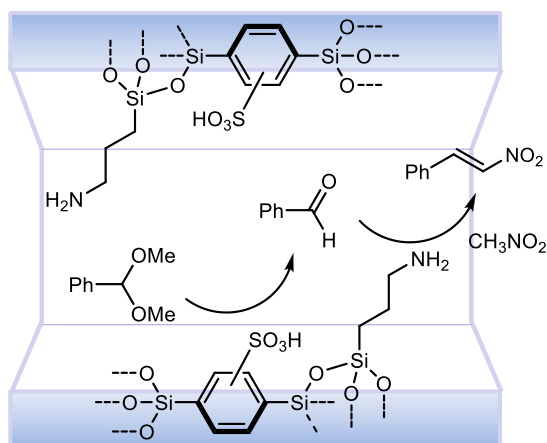


Figure 1.9. Acid-base bifunctional PMO catalyst for acid-base sequential reaction.

Heterogeneous metal complex catalysts

Transition metal complex catalysts have been widely used for industrial production of pharmaceuticals and chemical products.⁹¹ Although homogeneous metal complex catalyst showed excellent activity and selectivity, they are difficult to recover and reuse due to their high solubility in reaction media.⁹² Immobilization of a metal complex onto the solid supports is therefore highly demanded from the viewpoint of the economic efficiency and safety of the catalyst process in addition to environmental issue.⁹³ PMOs have several advantages as a solid support for heterogeneous catalysts as follows: i) well-ordered mesoporous structure, ii) large surface area and pore volume, iii) high mechanical and chemical stabilities of organosilica framework, and iv) direct metal complex formation onto the pore surface of PMOs. This immobilization manner is quite different from conventional approach using a molecular linker to immobilize metal complexes on the conventional solid supports (silica gel, polymers, etc.). In case of PMOs, uniform catalyst

⁹¹ Applied Homogeneous Catalysis with Organometallic Compounds (Eds.: B. Cornils, W. A. Hermann), VCH, Weinheim, 1996.

⁹² Hübner, S.; de Vries, J. G.; Farina, V. *Adv. Synth. Catal.* **2016**, *358*, 3–25.

⁹³ Copéret, C.; Comas-Vives, A.; Conley, M. P.; Estes, D. P.; Fedorov, A.; Mougel, V.; Nagae, H.; Núñez-Zarur, F.; Zhizhko, P. A. *Chem. Rev.* **2016**, *116*, 323–421.

environment can be formed on the pore surface without large reduction of pore size after the immobilization of metal complexes.

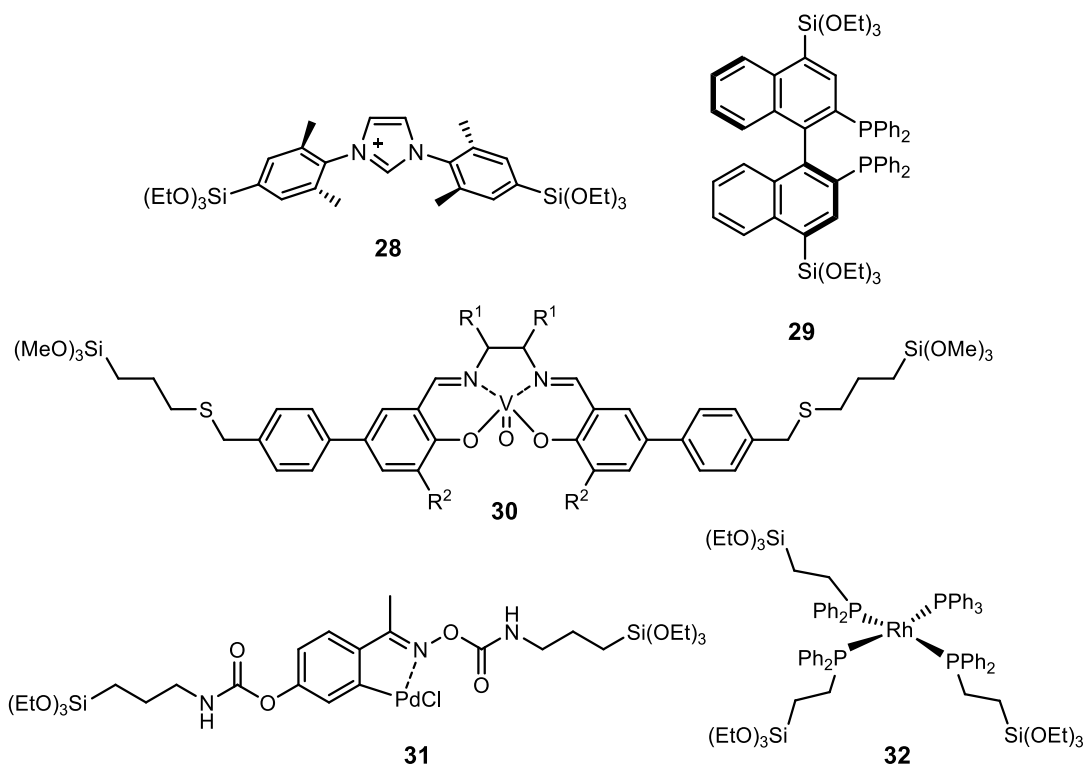


Figure 1.10. Ligand and metal complex precursors used in the synthesis of PMOs.

A variety of PMOs incorporating organic ligands such as NHC (**28**),⁶⁹ phosphine (**29**),⁹⁴ diamine,⁹⁵ porphyrin⁹⁶ and others have been synthesized. Co-condensation between corresponding coordinative organosilane precursor and other silica sources such as tetraalkoxysilanes and organic-bridged alkoxy silanes affords well-ordered mesoporous structure with high hydrothermal and mechanical stability. After the metal complex formation, the obtained PMO catalysts can be used for organic transformations. Yang and co-workers reported Pd-complexed NHC-PMOs showed high catalytic activity and reusability for Suzuki-Miyaura cross-coupling reaction between aryl chlorides and arylboronic acids. Recently, Inagaki and co-workers reported the synthesis of crystal-like PMOs embedded with organic ligands such as divinylpyridine and phenylpyridine

⁹⁴ Seki, T.; McEleney, K.; Crudden, C. M. *Chem. Commun.* **2012**, 48, 6369–6371.

⁹⁵ Jiang, D. M.; Yang, Q. H.; Wang, H.; Zhu, G. R.; Yang, J.; Li, C. *J. Catal.* **2006**, 239, 65–73.

⁹⁶ Jeong, E. Y.; Burri, A.; Lee, S. Y.; Park, S. E. *J. Mater. Chem.* **2010**, 20, 10869–10875.

ligands in the organosilica frameworks. It revealed that these bridging ligands in the pore walls allowed immobilizing metal complexes containing copper (Cu), Ru, and iridium (Ir) with preservation of mesoporous structure and molecular-scale periodicity in the framework. These findings indicate potential application of crystal-like chelating PMOs in the synthesis of novel heterogeneous metal complex catalysts.

A variety of metal complex catalysts can be directly introduced into the framework of PMOs by co-condensation of silylated organometallic precursors and other silane sources. Corma and co-workers reported vanadyl (V)-Schiff base co-condensation PMO catalyst synthesized from silylated organometallic precursor (**30**),^{97,98} which showed good catalytic activity but low enantioselectivity for asymmetric cyanosilylation of aldehydes. They also synthesized co-condensation PMO catalyst starting from silylated carbopalladacycle (**31**), which showed catalytic activity for Pd-catalyzed Suzuki–Miyaura cross-coupling reaction.⁹⁹ Li and co-workers reported that bis- and tris-silylated metal phosphine complexes (**32**) are versatile precursors for co-condensation PMO catalysts aimed for various organic transformations in water.¹⁰⁰ These PMO catalysts exhibited similar catalytic activity to homogeneous catalysts and higher catalytic activity than graft-type solid catalysts. Park and co-workers synthesized co-condensation PMO starting from tetrakis-silylated porphyrin metal complex precursors. Iron (Fe)-porphyrin PMO catalyst showed high catalytic activity for Baeyer-Villiger oxidation reaction of cyclohexanone.¹⁰¹

Heterogeneous organic molecular catalyst

PMOs are utilized not only as solid supports for immobilizing a metal complex catalyst but also as organic molecular catalysts. It has been reported that several examples of heterogeneous organic molecular catalysts based on PMOs. Yang and co-workers reported proline-immobilized hollow PMO catalysts prepared by co-condensation of L-prolineamide organosilane and ethane-bridged

⁹⁷ Baleizao, C.; Gigante, B.; Das, D.; Alvaro, M.; Garcia, H.; Corma, A. *Chem. Commun.* **2003**, 1860–1861

⁹⁸ Baleizao, C.; Gigante, B.; Das, D.; Alvaro, M.; Garcia, H.; Corma, A. *J. Catal.* **2004**, *223*, 106–113.

⁹⁹ Corma, A.; Das, D.; García, H.; Leyva, A. *J. Catal.* **2005**, *229*, 322–311.

¹⁰⁰ a) Zhang, F.; Kang, C. M.; Wei, Y. Y.; Li, H. X. *Adv. Funct. Mater.* **2011**, *21*, 3189–3197; b) Huang, J. L.; Zhu, F. X.; He, W. H.; Zhang, F.; Wang, W.; Li, H. X. *J. Am. Chem. Soc.* **2010**, *132*, 1492–1493; c) Dufaud, V.; Beauchesne, F.; Bonneviot, L. *Angew. Chem., Int. Ed.* **2005**, *44*, 3475–3477; d) Yang, X. S.; Zhu, F. X.; Huang, J. L.; Zhang, F.; Li, H. X. *Chem. Mater.* **2009**, *21*, 4925–4933.

¹⁰¹ Jeong, E.-Y.; Ansari, M. B.; Park, S.-E. *ACS Catal.* **2011**, *1*, 855–863.

precursors.¹⁰² This PMO catalyst showed high product yield and enantioselectivity for asymmetric aldol reactions between nitrobenzaldehyde and cyclohexanone in water. It also revealed that surface hydrophobic treatment improved the catalysis and high reusability of catalyst at least 7 cycles without loss of enantioselectivity. Wang and co-workers immobilized MacMillan catalyst on the pore surface of azido-functionalized hollow benzene-PMO by using click reaction approach (Figure 1.11).¹⁰³ This PMO catalyst showed high catalytic activity and enantioselectivity for asymmetric Diels–Alder reaction between *trans*-cinnamaldehyde and cyclopentadiene in water. This catalyst was easily recovered and reused for next reactions at least 7 cycles. In general, an organic molecular catalyst requires a larger amount of catalyst than a metal complex catalyst in order to facilitate the reaction efficiency. As the PMO solid catalysts show excellent recovery and recyclability, it is expected to overcome problems related to homogeneous organic molecular catalysts.

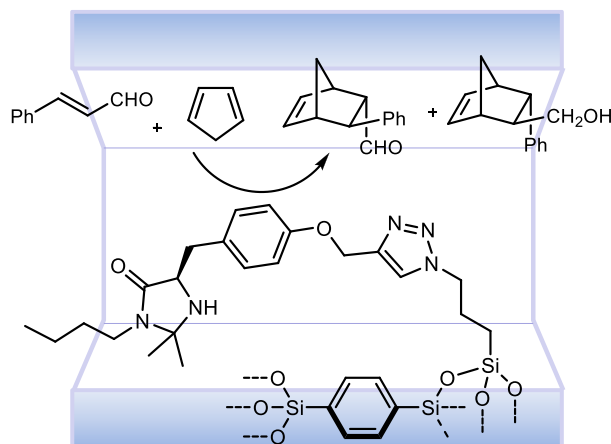


Figure 1.11. Immobilized MacMillan PMO catalyst for asymmetric Diels–Alder reaction.

Light-harvesting system

In natural photosynthesis, a light-harvesting antenna was utilized to concentrate sunlight with low photon density and promote difficult multi electron reaction. Figure 1.12a shows a schematic diagram of a light-harvesting antenna of red photosynthetic bacteria. Numerous chlorophyll molecules were located around the reaction center and form a beautiful double ring structure. These

¹⁰² Gao, J.; Liu, J.; Tang, J.; Jiang, D.; Li, B.; Yang, Q. *Chem.–Eur. J.* **2010**, *16*, 7852–7858.

¹⁰³ Shi, J. Y.; Wang, C. A.; Li, Z. J.; Wang, Q.; Zhang, Y.; Wang, W. *Chem.–Eur. J.* **2011**, *17*, 6206–6213.

chlorophyll molecules absorb sunlight and become excited states. The excited chlorophyll molecules propagate adjacent chlorophyll molecules. Ultimately, excitation energy is concentrated at the reaction center. PMOs with a high density of aromatic groups in the pore framework exhibit excellent light-harvesting effect. In case of PMOs, different chromophores can be introduced into two independent regions. The organic chromophores can be incorporated in the framework, and dyes can be introduced into the mesochannels. This spatial arrangement is similar to the natural light-harvesting system and ideal for efficient excitation energy transfer from the donor in the framework to the acceptor in the mesochannels.

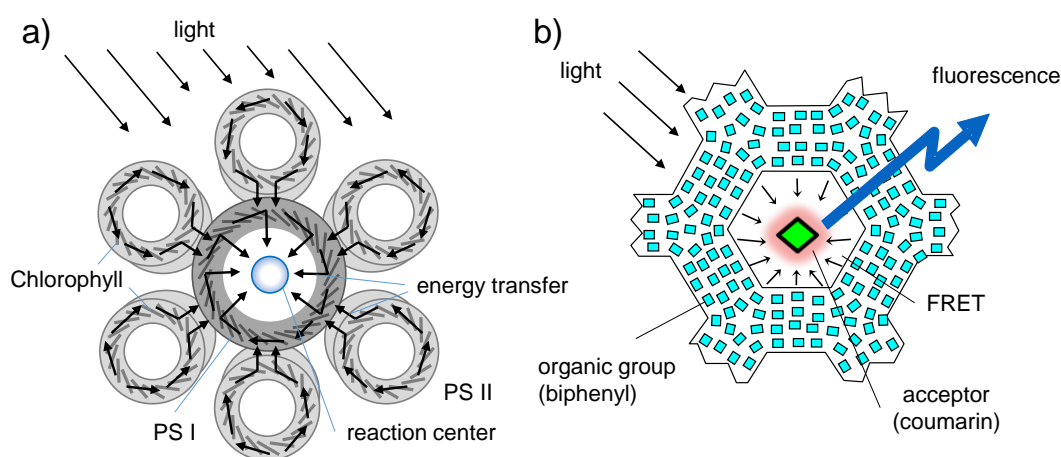


Figure 1.12. Schematic diagram of a light-harvesting antenna of a) red photosynthetic bacteria and b) BPh-PMO/coumarin dye system.

In 2009, Inagaki and co-workers reported efficient light-harvesting system based on crystal-like biphenyl-PMO (BPh-PMO) was reported.^{23a} Figure 1.12b shows a schematic diagram of BPh-PMO/coumarin dye system, where biphenyl groups are embedded in the framework and small amount of coumarin dye is introduced into the mesochannels. The dense biphenyl groups incorporated in the framework absorb UV-light and exhibits strong fluorescence at 380 nm upon irradiation at 270 nm with a fluorescence quantum yield of 0.42. The excitation energy transfer occurs when coumarin dyes are located in the mesochannels. The fluorescence emission of BPh groups was gradually disappeared with increasing the amount of coumarin dyes. In contrast, the fluorescence blue emission of coumarin dye at 440-450 nm was clearly observed. The total fluorescence quantum yield of BPh-PMO/coumarin dye (0.8 mol% coumarin) upon excitation at

270 nm was 0.80. This result indicates energy transfer from BPh groups into the coumarin dye without a radiation-reabsorption process. It revealed that excitation energy absorbed by 125 biphenyl groups was integrated into one coumarin molecule with nearly 100% quantum efficiency. This superior antenna effect is the highest among artificial antenna substances (dendrimers, organic gels etc.) reported so far. The wavelength range of PMOs can be adjusted by selecting the appropriate bridging organic groups. Visible-light absorptive PMOs can be synthesized from π -conjugated organosilane precursors. The combination of visible-light absorptive PMOs and light-harvesting system is attractive for the developing the applications such as efficient photocatalysts and light-emitting devices (see below).

Photocatalysts

Integration of light-harvesting antenna function of PMOs and photoreaction center located in mesopores is attractive approach for construction of efficient solid-state photocatalyst system. As the collected light energy is concentrated into the photoreaction center, it is expected to improve the photocatalysis performance. Recently, photocatalytic carbon dioxide (CO₂) reduction and oxygen evolution systems based on PMOs using light-harvesting antenna effect have been reported.¹⁰⁴

Figure 1.13 is a schematic diagram of a photocatalytic CO₂ reduction system that a Ru-rhenium (Re) supramolecular complex (Ru-Re) is anchored on the pore surface of visible-light absorptive acridone (Acid)-PMO. Here, the Ru complex functions as a photosensitization site and the Re complex functions as a CO₂ reduction catalyst. First, the Acid groups absorb visible light (405 nm), and their excitation energies are concentrated in the Ru unit of Ru-Re. Since the emission spectrum of Acid-PMO is overlapped with the absorption spectrum of Ru complex, efficient energy transfer occurs from Acid groups in the framework to Ru complex on the pore surface. Subsequently, electron transfer occurs from the Ru complex to the Re complex, and the reduction reaction of CO₂ proceeds on Re complex. The catalytic activity of Ru-Re@Acid-PMO system was about ten times higher than that of Ru-Re@mesoporous silica which is anchored on mesoporous silica without antenna function. This is because irradiation light of 405 nm is efficiently absorbed by the Acid-PMO, and its excitation energy is concentrated to Ru-Re with high efficiency.

¹⁰⁴ Ueda, Y.; Takeda, T.; Yui, T.; Koike, K.; Goto, Y.; Inagaki, S.; Ishitani, O. *ChemSusChem* **2015**, *8*, 439–442.

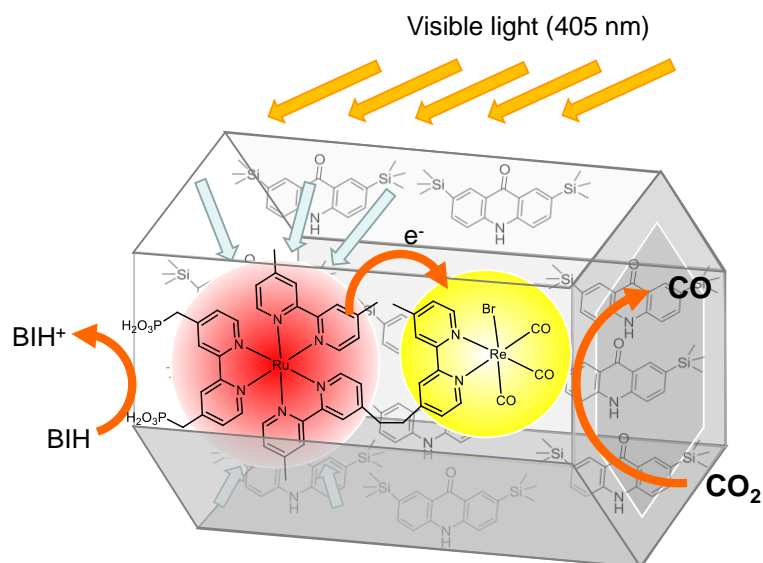


Figure 1.13. Schematic diagrams of a photocatalytic CO₂ reduction system using Ru-Re@Acid-PMO.

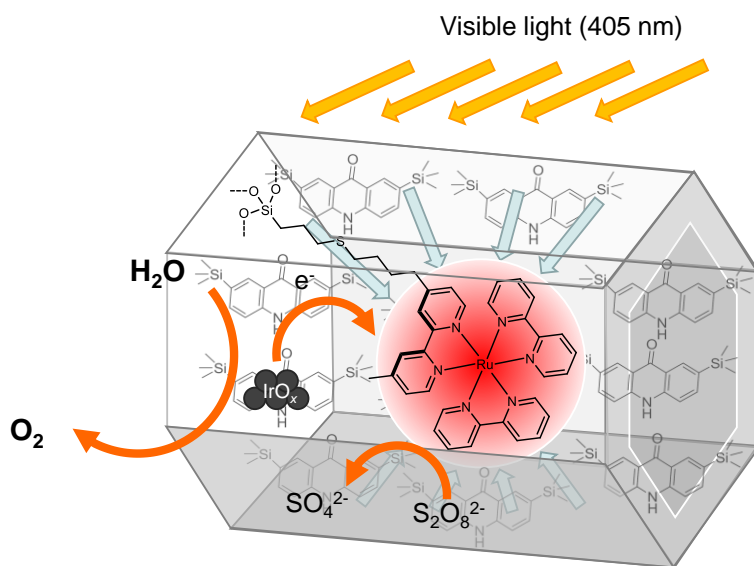


Figure 1.14. Schematic diagrams of photocatalytic oxygen evolution system from water using Ru/IrO_x@Acid-PMO.

Photocatalytic oxidation of water is indispensable for the construction of sacrificial agent free photocatalytic systems. Figure 1.14 is a schematic diagram of a photocatalytic oxygen evolution system from water using Acid-PMO.¹⁰⁵ After the immobilization of Ru complex as a photosensitizer onto the pore surface of Acid-PMO, iridium oxide (IrO_x) nanoparticles were in-situ

¹⁰⁵ Takeda, H.; Ohashi, M.; Goto, Y.; Ohsuna, T.; Tani, T.; Inagaki, S. *Chem.–Eur. J.* **2014**, *20*, 9130–9136.

formed by photoreduction method. When visible light (400 nm) was irradiated in water containing sacrificial reagent ($S_2O_8^{2-}$), oxygen evolution was occurred. The Ru complex excited by energy transfer from Acd-PMO is oxidatively quenched by a sacrificial agent, and then transformed into one electron oxidizing species of Ru complex. Oxidation reaction of water occurs on iridium oxide by the aid of strong oxidizing power of the one electron oxidized Ru complex.

These results indicated that light-harvesting PMOs have significant potential for construction of novel photocatalytic systems because of high designability of organosilica framework and high tunability of the photoreaction center.

Luminescent materials

High luminescent PMO films can be prepared by using the fluorescence organic-bridged alkoxysilane precursors in the presence of surfactant via EISA.¹⁰⁶ It has been reported the synthesis of luminescent PMO films prepared from up to 100% organic-bridged alkoxysilane precursors containing luminescent chromophores such as biphenyl,¹⁰⁷ naphthalene,^{23b} anthracene,⁶⁶ oligo(phenylenevinylene) (OPV),⁶⁷ 1,3,6,8-tetraphenylpyrene (TPPy),¹⁰⁸ and etc. Inagaki and co-workers reported high luminescent mesostructured oligo(phenylenevinylene) (OPV)-films with different lateral substituents such as hexyl and 2-ethylhexyl groups.⁶⁷ Although mesostructured OPV-films without lateral substituent showed low fluorescence quantum yield of 0.25, mesostructured OPV-films with lateral substituent showed high fluorescence quantum yields of 0.61–0.66. The introduction of bulky lateral substitutions was found to be effective for suppression of aggregation of OPV units in the organosilica framework, which inhibits their solid-state quenching.

By controlling energy transfer from bridging organic groups in the organosilica framework to dye molecules located in the mesochannels, multicolor luminescent materials can be prepared. Figure 1.15a shows the emission spectral change when the dye (rubrene) is doped in the hexyloxy-substituted OPV-bridged mesostructured organosilica films and schematic illustration of emission color control by dye doping. The dye undoped mesostructured organosilica films exhibit

¹⁰⁶ Tani, T.; Mizoshita, N.; Inagaki, S. *J. Mater. Chem.* **2009**, *19*, 4451–4456.

¹⁰⁷ Goto, Y.; Mizoshita, N.; Okada, T.; Shimada, T.; Tani, T.; Inagaki, S. *Chem. Mater.* **2008**, *20*, 4495–4498.

¹⁰⁸ Mizoshita, N.; Goto, Y.; Maegawa, Y.; Tani, T.; Inagaki, S. *Chem. Mater.* **2010**, *22*, 2548–2554.

blue light emission with a fluorescence quantum yield of 0.61 (Figure 1.15b, left). On the other hand, when a small amount of rubrene as a yellow fluorescent dye is doped, a part of the excitation energy of OPV groups in the framework is transferred to rubrene located in the mesochannels (Figure 1.15b, center and right). Therefore, rubrene-doped organosilica films exhibit fluorescence emission containing blue emission of OPV and yellow emission of rubrene. When the doping amount of rubrene was gradually increased, the luminescent color of rubrene-doped organosilica films changed continuously from blue to white and yellow. The emission quantum yield of the white light emitter reaches 67%. It is expected to be used as white light emitting films by combining with a near ultraviolet LED light source.

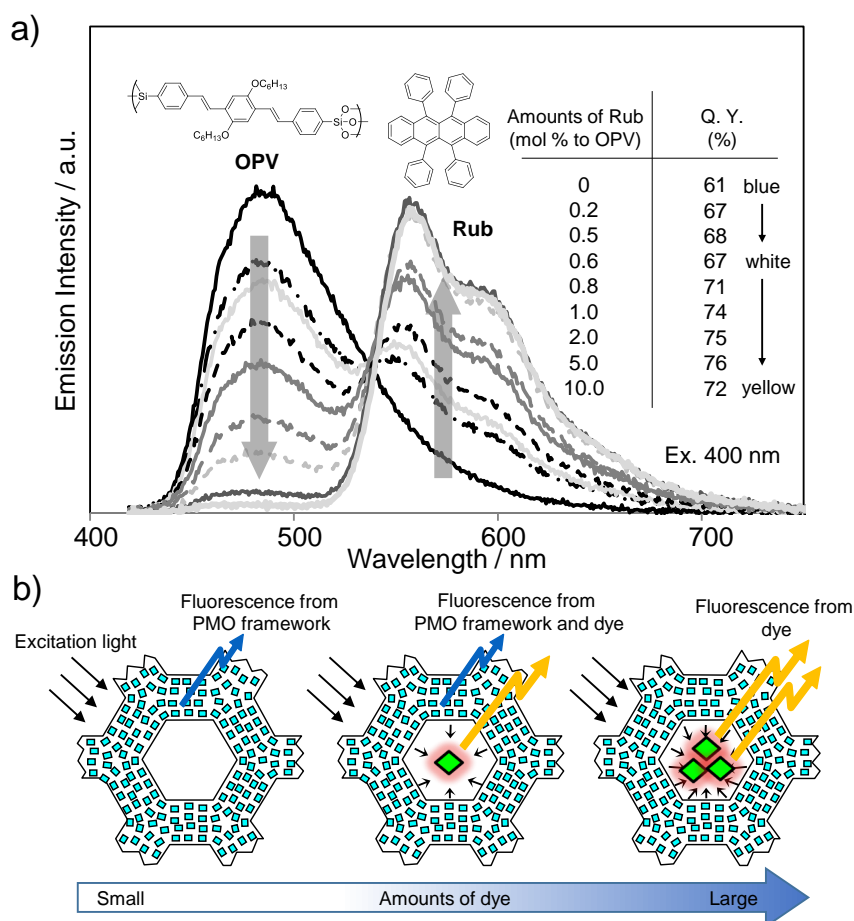


Figure 1.15. a) The emission spectral change of rubrene-doped hexyloxy-substituted OPV-bridged mesostructured organosilica films and b) schematic illustration of emission color control by dye doping.

Tuning of emission color can easily adjust by not only selecting the dye but also designing fluorescence bridging organic groups. A white light emitter was also obtained by doping dye into TPPy-bridged mesostructured organosilica films. Although non-doped mesostructured TPPy-organosilica films showed strong blue emission at 460 nm with quantum yields of over 0.7, 1 mol% doping of rhodamine 6G as a yellow dye into the mesochannels showed white luminescent color with quantum yield of 0.43.¹⁰⁸ These results indicate that doping of fluorescent dyes in the mesochannels of luminescent PMOs allows fine tuning of luminescent color over a wide range of spectrum with high emission quantum yields.

Photovoltaic devices

Introduction of electroactive organic groups into the PMO framework is one of attractive approaches for developing new redox catalysts, optical materials and electronic devices. There has been reported the synthesis of co-condensation PMOs containing electroactive organic groups such as methyl viologen and fullerene.^{109,110} In case of co-condensation PMOs, the electroactive organic groups are diluted with insulating silica moieties in their frameworks, which weakens the electronic coupling between the organic groups.

The dense packing of electroactive organic groups is desirable to achieve efficient charge transfer within the organosilica framework (Figure 1.16). Inagaki and co-workers synthesized hole-transporting mesostructured organosilica films packed with a high density of π -conjugated OPV units.¹¹¹ By using molecularly designed three-armed OPV-bridged alkoxy silane precursor, they achieved the increase of the electronic coupling of the electroactive organic units and the formation of the mesostructure. The hole-mobility of the mesostructured organosilica films was comparable to that of the π -conjugated organic amorphous polymer. Inagaki and co-workers also reported a new class of molecularly ordered PMOs by hydrolysis and polycondensation of perylene bisimide (PBI)-bridged precursor bearing four trialkoxysilyl groups (**34**).¹¹² The pore framework consists of π - π stacking PBI-silica columns, which exhibited unique optical and electronic properties. The strong intermolecular interactions of electroactive organic group have significant

¹⁰⁹ Álvaro, M.; Ferrer, B.; Fornés, V.; García, H. *Chem. Commun.* **2001**, 2546–2547.

¹¹⁰ Whitnall, W.; Cademartiri, L.; Ozin, G. A. *J. Am. Chem. Soc.* **2007**, *129*, 15644–15649.

¹¹¹ Mizoshita, N.; Ikai, M.; Tani, T.; Inagaki, S. *J. Am. Chem. Soc.* **2009**, *131*, 14225–14227.

¹¹² Mizoshita, N.; Tani, T.; Shinokubo, H.; Inagaki, S. *Angew. Chem., Int. Ed.* **2012**, *51*, 1156–1160.

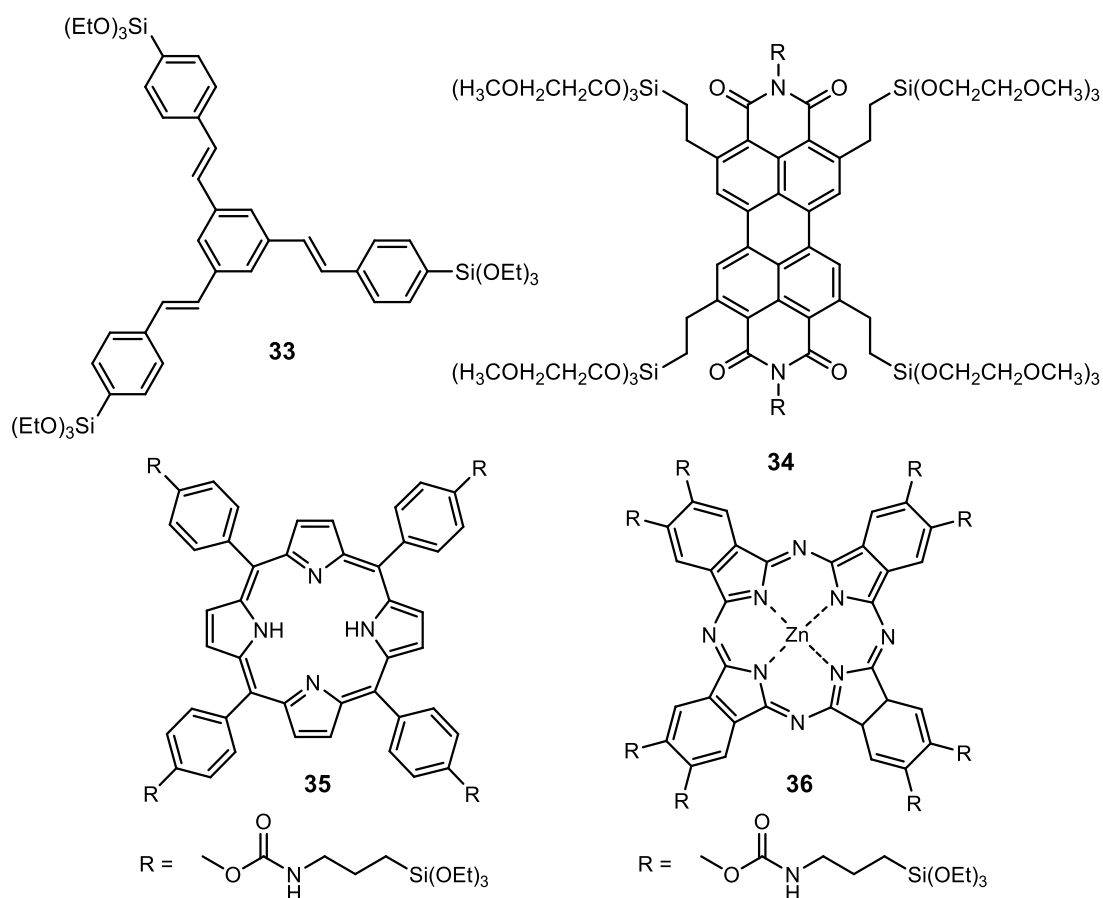


Figure 1.16. Electroactive functional organic-bridged alkoxy silane precursors used in the synthesis of hole-transporting and electroactive PMOs.

potential for the design of high functional organosilica hybrids.

Trauner and Bein groups reported new type of photovoltaic devices having nano-sized controlled p-n heterojunction interfaces by filling the mesopores of the hole-transporting PMOs with the electron-transporting material.^{113,114} They synthesized hole-transporting PMO films, which have a face-centered orthorhombic porous structure with diameters over 10 nm, starting from porphyrin- (**35**) and zinc phthalocyanine-bridged alkoxy silane precursors (**36**). These PMO films offered to infiltrate fullerene derivatives into the pore space and formed interpenetrating donor-acceptor interfaces (Figure 1.17). Optoelectronic measurements demonstrated the

¹¹³ Li, Y.; Auras, F.; Löbermann, F.; Döblinger, M.; Schuster, J.; Peter, L.; Trauner, D.; Bein, T. *J. Am. Chem. Soc.* **2013**, *135*, 18513–18519.

¹¹⁴ Auras, F.; Li, Y.; Löbermann, F.; Döblinger, M.; Schuster, J.; Peter, L. M.; Trauner, D.; Bein, T. *Chem.–Eur. J.* **2014**, *20*, 14971–14975.

light-charge generation and hole-transport ability of these PMO films. The photovoltaic devices based on zinc phthalocyanine-PMO films:[6,6]-phenyl C₇₁ butyric acid methyl ester sandwiched between electrodes showed open-circuit voltage of 905 mV and short-circuit current of 9.8 $\mu\text{A cm}^{-2}$ under simulated AM1.5G solar irradiation. Although the power conversion efficiency of the power conversion efficiency is very low, it is expected that the performance of photovoltaic devices can be improved by expanding the visible-light absorption region of the PMO films, improving the hole-transporting mobility, and controlling the pore structure of the PMO. The ability to easily form p-n heterojunction interfaces on the order of nanometers by utilizing hole-transporting PMOs is attractive for a wide range of optoelectronic applications.

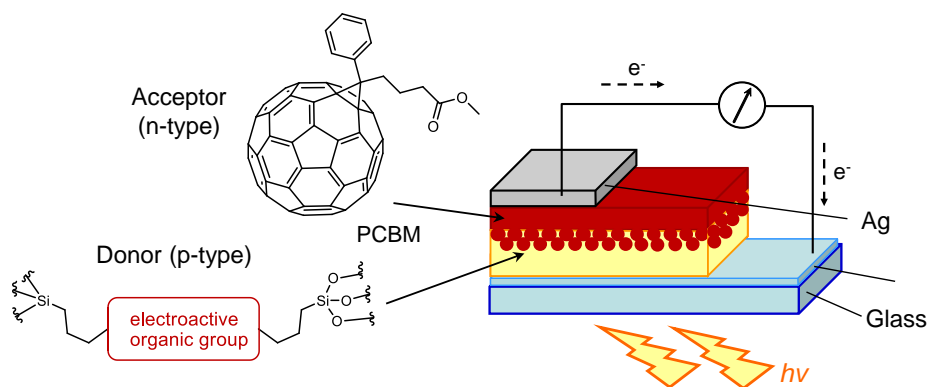


Figure 1.17. Schematic illustration of photovoltaic devices based on hole-transporting PMO films infilling with electron-transporting materials.

1.3 The Aim and Outline of the Thesis

This thesis deals with synthesis of highly-designed functional periodic mesoporous organosilicas (PMOs) and their applications. In this thesis, the author focuses on the development of new synthetic methods of high functional organic-bridged alkoxy silane precursors where functional organic groups were bridged with two or more hydrolyzable silyl groups, which cannot be synthesized by conventional synthetic methods. The author describes the synthesis of high functional PMOs starting from highly-designed functional organic-bridged alkoxy silane precursors, and their applications in optical materials, organic solar cells, and heterogeneous catalysts.

After the discovery of synthetic method of mesoporous silica using structure-directing agents in 1990, organic functionalization of mesoporous silica was extensively conducted by co-condensation of mono-organosilane precursors and silica precursors and/or post-modification of mesoporous silica with silane coupling agents to enhance the organic functionality. In 1999, three research groups, Inagaki, Ozin, and Stein groups, independently reported the synthesis of PMOs by surfactant-directed hydrolysis and polycondensation of organic-bridged alkoxy silane precursors. By using organic-bridged alkoxy silane precursors, the organic groups were uniformly distributed in the organosilica frameworks, which is different structural feature from conventional organic-functionalized mesoporous silicas and polysilsesquioxanes prepared by the sol-gel polymerization of organic-bridged alkoxy silane precursors.

In early stage of the research, a variety of synthetic approaches of PMOs having different pore structures and morphologies extensively were studied by selecting the reaction conditions (e.g. catalyst, temperature), organosilane precursors, and surfactant templates. It therefore became possible to control the hierarchical structure of PMOs from molecular- and meso-scale structures to mesoscopic morphology. In addition to these fundamental researches, a wide variety of functional π -conjugated aromatics and organic groups containing heteroelements (N, S, P, O, etc.) have been introduced to further functionalize their organosilica frameworks. Recent research subject has been gradually shifted to development of high functional PMOs and their applications.

As the organic functional groups in the organosilica frameworks are directly linked to the surface and bulk properties of PMOs, the use of desired functional organic-bridged alkoxy silane

precursors has been indispensable for development of high functional PMOs. However, it is very difficult to synthesize the organic-bridged alkoxy silane precursors having desired functions because a rational synthetic route has not been established. Although the organic-bridged alkoxy silane precursors have been synthesized by several synthetic methods, easily hydrolyzable alkoxy silyl groups not only restrict their applicable synthetic conditions but also make it difficult to purify by silica gel chromatography. These synthetic drawbacks have been limited the synthesis of high functional organic-bridged alkoxy silane precursors.

If it is possible to develop new synthetic methods which allows the synthesis of well-designed functional organic-bridged alkoxy silane precursors, further functionalization of PMOs can be expected, which can be contributed to the development of high functional PMOs aimed for optical materials, electronic devices, adsorbents, drug-delivery systems, and heterogeneous catalysts, etc.

The first subject of this thesis is to establish the synthetic methods of high functional organic-bridged silane precursors aimed for functionalization of PMOs. The second subject is to synthesize high functional PMOs starting from designed functional organic-bridged silane precursors which are synthesized by the author's synthetic methods. The third subject is the applications of high functional PMOs and to demonstrate their utilities for optical material, organic solar cell, and heterogeneous catalysts.

The outline of the thesis is as follow.

In chapter 2, several new synthetic methods for highly functional organic-bridged silane precursors are described. Initially, attention was focused on the direct alkoxy silylation of aryl dihalide with triethoxy silane by Rh catalyst to prepare the functional organic-bridged alkoxy silane precursors, which are most commonly used for synthesizing organosilica hybrid materials including PMOs. In order to overcome the problem of conventional alkoxy silane synthesis, synthetic approach of high functional organic-bridged allyl silane precursors, which are stable for silica gel column purification but act as synthetic equivalents of alkoxy silane precursors, was developed. The synthetic method of highly functional organic-bridged triisopropoxy silane precursors having stability for silica gel column purification and readily hydrolyzable property was also developed. The Pd-catalyzed

cross-coupling reactions using a series of building blocks containing diallylethoxysilyl and triisopropoxysilyl group are reported. In order to densify the organic chromophores into the organosilica frameworks, synthetic approach for organic-bridged alkoxy silane precursor with short molecular linker was developed. Finally, in order to enhance the hydrolysis ability of the allylsilyl group in the organic-bridged allylsilane precursors, deallylation behaviors of the acidic sol-gel polymerization in various organic solvents were investigated.

In chapters 3–5, the synthesis of highly-designed functional PMOs starting from functional organic-bridged silane precursors and their applications were described.

In chapter 3, transparent and visible-light absorptive methylacridone (MeAcrid)-PMO thin films were synthesized from newly designed MeAcrid-bridged triethoxysilane precursors. The optical properties and visible-light harvesting antenna functions were also investigated.

In chapter 4, visible-light absorptive and hole-transporting dithienylbenzothiadiazole (DTBT)-PMO films were synthesized from highly functional DTBT-bridged triisopropoxysilane precursors. The preparation of organic solar cells based on DTBT-PMO thin films and their photovoltaic performances were also investigated

In chapter 5, synthesis of new class of crystal-like bipyridine (BPy)-PMO, in which 2,2'-bipyridine ligands are densely and regularly arranged and exposed on the pore surface, was described. The metal coordination ability of BPy-PMO was examined and a variety of heterogeneous metal complex catalysts were synthesized on the pore surface of BPy-PMO. The catalysis of the immobilized metal complexes was investigated for not only organic transformations such as direct C–H borylation of arenes and heteroarenes, and epoxidation of olefins but also photocatalytic reactions such as hydrogen evolution from water.

In chapter 6, the conclusions and outlook will be described.

Chapter 2

Synthetic Methodologies for Functional Organosilane Precursors

Organic-bridged silane compounds $\{R-[Si(X)_3]_n, n \geq 2, R = \text{organic group}, X = \text{OMe, OEt, } O\text{-}i\text{-Pr, allyl}\}$, are useful synthetic precursor for the preparation of organic–inorganic hybrids such as bridged silsesquioxanes (BSQs) and periodic mesoporous organosilicas (PMOs). However, their synthetic methodologies have been limited due to the high reactivity of alkoxy-silyl groups under organic synthetic conditions. In addition, their purifications are usually difficult due to the low volatility for distillation and hydrolyzability for silica gel chromatography. Here, several synthetic approaches for functional organic-bridged alkoxy- and allyl-silane precursors were described. First, rhodium-catalyzed direct silylation of aryl halide with triethoxysilane was applied to the synthesis of organic-bridged ethoxysilane precursors. This key reaction can be generally utilized for the synthesis of functional organic-bridged ethoxysilane precursors. Next, a variety of molecular building blocks containing both reaction site and hydrolyzable allylsilyl or bulky isopropoxysilyl groups were synthesized. These building blocks enabled us to synthesize a variety of functional organic-bridged allylsilane and isopropoxysilane precursors by palladium-catalyzed cross-coupling reactions. These silyl groups have enough stability under various organic reaction conditions and purification using silica gel chromatography. In addition, a new synthetic procedure for organic-bridged alkoxy-silane precursors with shortest linker between bridged organic group and alkoxy-silyl group was developed. Regioselective hydrosilylation of olefinic substrate allowed the selective synthesis of organic-bridged alkoxy-silane precursors with methylene or propylene linkers. Finally, the reactivity of allylsilyl group under sol–gel conditions was investigated. A systematic study of solvent effect on acid-catalyzed sol–gel polymerization revealed that the use of solvent with low solvent basicity enhanced the deallylation process. This finding can be helpful for the preparation of organic-bridged allylsilane-derived organosilica hybrid materials. These new synthetic procedures and findings would be valuable for synthesis of functional organic-bridged silane precursors that are essential for high functionalization of organosilica hybrid materials.

2.1 Rh-catalyzed Silylation for Functional Organic-bridged Alkoxysilanes

Bis(pyridine)iodonium tetrafluoroborate (IPy₂BF₄) was successfully used as a iodination reagent for carbazole and its derivatives to give 3,6-diiodocarbazoles in excellent yield. Subsequent rhodium-catalyzed disilylation of 3,6-diiodocarbazoles with triethoxysilane gave the corresponding 3,6-bis(triethoxysilyl)carbazoles in good yield. The obtained carbazole-bridged alkoxysilane precursor was utilized for synthesis of periodic mesostructured organosilica hybrid materials in the presence of surfactant template as a structure directing agent under basic and acidic conditions.

2.1.1 Introduction

Organosilanes are useful building blocks for the preparation of organic–inorganic hybrid materials; to date, several types of organosilane precursor have been synthesized,¹ including arylene-bridged organosilanes, which are used in the synthesis of various bridged polysilsesquioxanes.^{1b,c} Inagaki et al. recently reported the synthesis of phenylene- and biphenylene-bridged mesoporous materials with crystal-like pore walls, which offer much potential as framework materials based on their stacking structures.² The incorporation of arylene groups as an integral component of the hybrid network gives rise to a number of promising organic–inorganic hybrid materials; however, it is very difficult to prepare the desired organosilanes in high yield by the conventional method, which involves lithiation of arylene dihalides followed by silylation, due to low solubility and inferior functional-group compatibility in the substrates and the difficulty of purifying the alkoxysilane products. Here, the author discloses a facile preparation of novel carbazole-bridged trialkoxysilane derivatives and synthesis of carbazole-bridged periodic mesostructured organosilica hybrid materials. In order to introduce the triethoxysilyl groups at 3,6-positions of carbazole and its derivatives, highly reactive 3,6-diiodocarbazoles were prepared by electrophilic iodination using

¹ a) Wight, A. P.; Davis, M. E. *Chem. Rev.* **2002**, *102*, 3589–3614, and references cited therein; b) Loy, D. A.; Shea, K. J. *Chem. Rev.* **1995**, *95*, 1431–1442, and references cited therein; c) Cerveau, G.; Chappellet, S.; Corriu, R. J. P.; Dabiens, B. *J. Organomet. Chem.* **2001**, *626*, 92–99.

² a) Inagaki, S.; Guan, S.; Ohsuna, T.; Terasaki, O. *Nature* **2002**, *416*, 304–307; b) Yang, Q.; Kapoor, M. P.; Inagaki, S. *J. Am. Chem. Soc.* **2002**, *124*, 9694–9695; c) Kapoor, M. P.; Yang, Q.; Inagaki, S. *J. Am. Chem. Soc.* **2002**, *124*, 15176–15177; d) Kapoor, M. P.; Yang, Q.; Inagaki, S. *Chem. Mater.* **2004**, *16*, 1209–1213; e) Kapoor, M. P.; Inagaki, S.; Ikeda, S.; Kakiuchi, K.; Suda, M.; Shimada, T. *J. Am. Chem. Soc.* **2005**, *127*, 8174–8178.

bis(pyridine)iodonium tetrafluoroborate (IPy₂BF₄). The author then applied rhodium-catalyzed disilylation of 3,6-diiodocarbazoles with triethoxysilane to give the corresponding carbazole-bridged triethoxysilane precursors. The novel purification method using charcoal was also developed for bridged organoalkoxysilane precursors. The obtained precursor was successfully transformed to carbazole-bridged periodic mesostructured organosilica by hydrolysis and polycondensation under basic and acidic condition in the presence of surfactant.

2.1.2 Experimental

Materials and methods

All reagents and solvents were purchased from Aldrich, Tokyo Chemical Industry, and Wako Pure Chemical Industries and used without further purification. All moisture sensitive manipulations were carried out under a nitrogen atmosphere. Nitrogen gas was dried by passage through P₂O₅. Optical rotations were recorded with a JASCO DIP-370 polarimeter. NMR spectra were recorded on JEOL JNM LA500 spectrometer (270 MHz for ¹H, 67.5 MHz for ¹³C). Chemical shifts are reported in δ ppm referenced to an internal SiMe₄ standard for ¹H NMR, chloroform-*d* (δ 77.0) for ¹³C NMR. The following abbreviations were used to explain the multiplicities: s = singlet, d = doublet, t = triplet, q = quartet, m = multiplet, dd = double doublet. High resolution mass spectra (HRMS) were recorded with JEOL JMS-700 spectrometer. X-ray diffraction (XRD) measurements were performed on a Rigaku RINT-TTR diffractometer with Cu-Kα radiation (50 kV, 300 mA).

General procedure for diiodination of carbazoles

To a solution of IPy₂BF₄ (278 mg, 0.75 mmol) and carbazole (**1a**) (50.0 mg, 0.30 mmol) in dry CH₂Cl₂ (8 mL), was added dropwise trifluoromethanesulfonic acid (TfOH) (26.4 μL, 0.30 mmol) and the mixture was stirred at room temperature for 20 h. The reaction was quenched with saturated Na₂S₂O₃ aqueous solution and the mixture was extracted with CH₂Cl₂. The organic phase was washed with brine and then with water, dried over anhydrous Na₂SO₄, and concentrated. The residue was chromatographed on silica gel (eluent: hexane/EtOAc = 5:1) to give 3,6-diiodocarbazole (**2a**).

3,6-Diiodocarbazole (2a). 96% yield. ^1H NMR (270 MHz, CDCl_3) δ 7.22 (d, $J = 8.4$ Hz, 2H), 7.68 (dd, $J = 8.4$ Hz, 1.9 Hz, 2H), 8.09 (br, 1H), 8.32 (d, $J = 1.9$ Hz, 2H); ^{13}C NMR (67.5 MHz, CDCl_3) δ 82.4, 112.6, 124.4, 129.3, 134.7, 138.4.

3,6-Diiodo-9-methylcarbazole (2b). 93% yield. ^1H NMR (270 MHz, CDCl_3) δ 3.80 (s, 3H), 7.17 (d, $J = 8.6$ Hz, 2H), 7.73 (d, $J = 8.6$ Hz, 1.6 Hz, 2H), 8.32 (d, $J = 1.6$ Hz, 2H); ^{13}C NMR (67.5 MHz, CDCl_3) δ 29.2, 81.7, 110.5, 123.6, 129.0, 134.3, 139.7.

3,6-Diiodo-9-octylcarbazole (2c). 95% yield. ^1H NMR (270 MHz, CDCl_3) δ 0.85 (t, $J = 6.8$ Hz, 3H), 1.21–1.28 (m, 10H), 1.75–1.80 (m, 2H), 4.16 (t, $J = 7.0$ Hz, 2H), 7.12 (d, $J = 8.4$ Hz, 2H), 7.67 (dd, $J = 8.4$ Hz, 1.6 Hz, 2H), 8.27 (d, $J = 1.6$ Hz, 2H); ^{13}C NMR (67.5 MHz, CDCl_3) δ 14.2, 22.7, 27.2, 28.8, 29.2, 29.3, 31.8, 43.2, 81.6, 110.7, 126.7, 129.1, 134.2, 139.2.

3,6-Diiodo-9-phenylcarbazole (2d). 93% yield. ^1H NMR (270 MHz, CDCl_3) δ 7.10 (d, $J = 8.6$ Hz, 2H), 7.41 (d, $J = 8.6$ Hz, 2H), 7.46 (t, $J = 7.0$ Hz, 1H), 7.55 (d, $J = 7.0$ Hz, 2H), 7.63 (dd, $J = 8.6$ Hz, 2.2 Hz, 2H), 8.33 (d, $J = 2.2$ Hz, 2H); ^{13}C NMR (67.5 MHz, CDCl_3) δ 82.9, 111.8, 112.4, 126.7, 127.9, 129.1, 129.9, 134.7, 136.4, 139.8.

Synthesis of carbazole-bridged triethoxysilane precursors

To a mixture of $[\text{Rh}(\text{cod})(\text{CH}_3\text{CN})_2]\text{BF}_4$ (45 mg, 0.12 mmol) and 3,6-diiodocarbazole (**2a**) (1.00 g, 2.39 mmol) was added dry DMF (20 mL) and dry Et_3N (1.99 mL, 27 mmol). The mixture was stirred at room temperature for 30 min, after which triethoxysilane (1.76 mL, 18 mmol) was added dropwise, and stirring was continued at 80 °C for 7 h. The reaction mixture was then concentrated under vacuum to remove DMF. The resulting mixture was treated with Et_2O to obtain a solution of product in Et_2O , which was filtered through a Celite plug, and the filter cake was rinsed with Et_2O . The combined filtrates were concentrated under vacuum and the residue was passed through charcoal to give pure 3,6-bis(triethoxysilyl)carbazole (**4a**).

3,6-Bis(triethoxysilyl)carbazole (4a). 89% yield. ^1H NMR (270 MHz, CDCl_3) δ 1.29 (t, $J = 7.3$ Hz, 18H), 3.93 (q, $J = 7.3$ Hz, 12H), 7.43 (dd, $J = 7.7$ Hz, 0.8 Hz, 2H), 7.72 (dd, $J = 7.8$ Hz, 0.8 Hz, 2H), 8.26 (s, 1H), 8.46 (d, $J = 0.8$ Hz, 2H); ^{13}C NMR (67.5 MHz, CDCl_3) δ 18.3, 58.7, 110.5, 119.8, 122.7, 127.4, 131.8, 140.9; ESI-HRMS m/z calcd for $\text{C}_{24}\text{H}_{37}\text{NO}_6\text{Si}_2$ (M^-): 490.2081; found: 490.2073.

3,6-Bis(triethoxysilyl)-9-methylcarbazole (4b). 75% yield. ^1H NMR (270 MHz, CDCl_3) δ 1.29 (t, $J = 7.1$ Hz, 18H), 3.84 (s, 3H), 3.95 (q, $J = 7.1$ Hz, 12H), 7.43 (d, $J = 8.1$ Hz, 2H), 7.79 (d, $J = 8.1$ Hz, 2H), 8.49 (s, 2H); ^{13}C NMR (67.5 MHz, CDCl_3) δ 18.4, 29.1, 58.7, 108.2, 119.5, 122.5, 127.5, 131.9, 142.3; ESI-HRMS m/z calcd for $\text{C}_{25}\text{H}_{39}\text{NO}_6\text{Si}_2$ ($\text{M}+\text{Na}^+$): 528.2214; found: 528.2211.

3,6-Bis(triethoxysilyl)-9-octylcarbazole (4c). 70% yield. ^1H NMR (270 MHz, CDCl_3) δ 0.86 (t, $J = 7.3$ Hz, 3H), 1.18–1.32 (m, 28H), 1.84–1.89 (m, 2H), 3.94 (q, $J = 7.3$ Hz, 12H), 4.29 (t, $J = 7.3$ Hz, 2H), 7.43 (d, $J = 8.1$ Hz, 2H), 7.77 (d, $J = 8.1$ Hz, 2H), 8.49 (s, 2H); ^{13}C NMR (67.5 MHz, CDCl_3) δ 14.1, 18.4, 22.7, 27.3, 29.0, 29.2, 29.4, 31.8, 43.1, 58.7, 108.4, 119.3, 122.5, 127.5, 131.8, 141.7; ESI-HRMS m/z calcd for $\text{C}_{32}\text{H}_{53}\text{NO}_6\text{Si}_2$ ($\text{M}+\text{Na}^+$): 626.3309; found: 626.3346.

Preparation of carbazole-bridged periodic mesostructured organosilica under basic condition (Cbz-PMO-B)

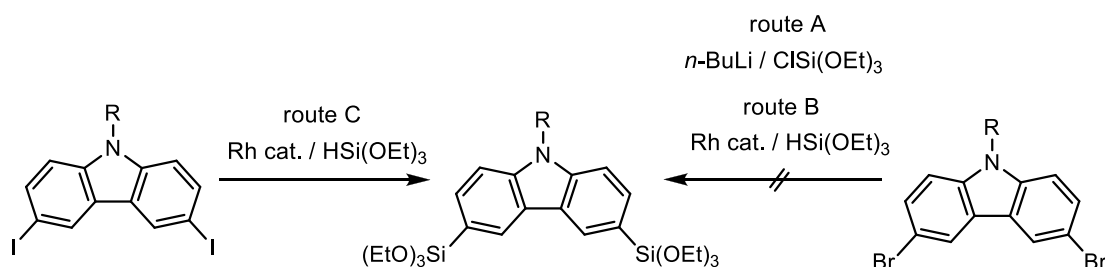
Octadecyltrimethylammonium chloride ($\text{C}_{18}\text{TMACl}$, 87 mg) was dissolved in a mixture of H_2O (6 mL) and 6 M NaOH aqueous solution (0.1 mL). Then **4a** (100 mg) was added to the surfactant solution, and the mixture was stirred at room temperature for 24 h. The solution was kept at 60 °C for 24 h under static conditions. The resulting white precipitate was recovered by filtration to give the desired mesostructured organosilica material.

Preparation of carbazole-bridged periodic mesostructured organosilica under acidic condition (Cbz-PMO-A)

1,12-Dodecanediaminium- N^1, N^1, N^{12}, N^{12} -tetramethyl- N^1, N^{12} -dioctadecyl dibromide ($\text{C}_{18}\text{-C}_{12}\text{-C}_{18}$, 76 mg) was dissolved in a mixture of H_2O (6 mL) and 12 M HCl aqueous solution (0.1 mL). Then **4a** (100 mg) was added to the surfactant solution, and the mixture was stirred at room temperature for 24 h. The solution was kept at 60 °C for 24 h under static conditions. The resulting white precipitate was recovered by filtration to give the desired mesostructured organosilica material.

2.1.3 Results and Discussion

Carbazole derivatives have attracted a great deal of attention due to their potential as components of electroluminescent materials, thin-film transistors,³ photochemical materials,⁴ dendrimers,⁵ nonlinear optical polymers⁶ and active ligands for transition metal-catalyzed reactions.⁷ However, there have been no reports describing the preparation of 3,6-bis(triethoxysilyl)carbazole as a precursor for functional materials.



Scheme 2.1. Synthetic route for carbazole-bridged triethoxysilane precursors starting from 3,6-dibromocarbazoles and 3,6-diiodocarbazoles.

First, the author examined the lithiation of commercially available 3,6-dibromocarbazole with *n*-butyllithium followed by addition of chlorotriethoxysilane (Scheme 2.1, route A). Unfortunately, this reaction gave a mixture of many unidentified products, including trace amounts of the desired 3,6-bis(triethoxysilyl)carbazole. Recently, efficient palladium- and rhodium-catalyzed silylations of aryl halides with triethoxysilane were reported by the Masuda and co-workers^{8a,b} and the DeShong and Manoso,^{8c} respectively. Because aryl bromides have successfully been used as starting materials for rhodium-catalyzed silylation,^{8b} the author attempted to carry out this reaction using

³ a) Yang, Y.; Heeger, A. J. *Nature* **1994**, *372*, 344–346; b) Horowitz, G. *Adv. Mater.* **1998**, *10*, 365–377; c) Dodabalapur, A.; Torsi, L.; Katz, H. E. *Science* **1995**, *268*, 270–271.

⁴ a) Garnier, F. *Acc. Chem. Res.* **1999**, *32*, 209–215; b) Fox, M. A. *Acc. Chem. Res.* **1999**, *32*, 201–207.

⁵ a) Zhu, Z.; Moore, J. S. *Macromolecules* **2000**, *33*, 801–807; b) Kimoto, A.; Cho, J.-S.; Higuchi, M.; Yamamoto, K. *Macromolecules* **2004**, *37*, 5531–5537; c) Loiseau, F.; Campagna, S.; Hameurlaine, A.; Dehaen, W. *J. Am. Chem. Soc.* **2005**, *127*, 11352–11363.

⁶ a) Zhang, Y.; Wada, T.; Sasabe, H. *J. Mater. Chem.* **1998**, *8*, 809–828; b) Zhang, Y.; Wada, T.; Wang, L.; Sasabe, H. *Chem. Mater.* **1997**, *9*, 2798–2804; c) Zhang, Y.; Wang, L.; Wada, T.; Sasabe, H. *Macromol. Chem. Phys.* **1996**, *197*, 1877–1888.

⁷ Inoue, M.; Suzuki, T.; Nakada, M. *J. Am. Chem. Soc.* **2003**, *125*, 1140–1141.

⁸ a) Murata, M.; Suzuki, K.; Watanabe, S.; Masuda, Y. *J. Org. Chem.* **1997**, *62*, 8569–8571; b) Murata, M.; Ishikura, M.; Nagata, M.; Watanabe, S.; Masuda, Y. *Org. Lett.* **2002**, *4*, 1843–1845; c) Manoso, A. S.; DeShong, P. *J. Org. Chem.* **2001**, *66*, 7449–7455.

3,6-dibromocarbazole and triethoxysilane; however, 3,6-dibromocarbazole was recovered unchanged (Scheme 2.1, route B). In general, cross-coupling reactions of aryl bromides often result in the absence of desired products, due to their reactive order toward transition metal-catalyzed reactions ($\text{ArI} > \text{ArOTf} > \text{ArBr} > \text{ArCl}$);⁹ carbazole and its derivatives are not exceptional in this respect. Therefore, the author decided to use 3,6-diiodocarbazole as a starting material for disilylation of carbazoles (Scheme 2.1, route C). Although several monoiodination reactions of carbazole have been reported,¹⁰ there have been few reports of efficient preparation methods for 3,6-diiodocarbazole. Very recently, there have been reports of efficient iodination reactions of *N*-unsubstituted and *N*-substituted carbazoles in the presence of the required reagents.¹¹

In order to introduce diiodo groups at 3,6-positions, the author carried out electrophilic diiodination because carbazole derivatives readily undergo electrophilic addition at the 3- and 6-positions. The author used bis(pyridine)iodonium tetrafluoroborate (IPy_2BF_4) as a iodination reagent.¹² This iodination reagent is highly active for various types of substrate and Shimada et al. reported a facile preparation of 5,5'-diiodo-BINAP derivatives starting from BINAP dioxide and IPy_2BF_4 in the presence of trifluoromethanesulfonic acid (TfOH), which opened the door to preparation of BINAP-based materials.¹³

First, diiodination condition for *N*-unsubstituted carbazole (**1a**) was optimized (Table 2.1). When the iodination of **1a** was performed with 2 equiv of IPy_2BF_4 and 4 equiv of TfOH in CH_2Cl_2 at 25 °C for 20 h, this reaction gave an inseparable mixture of **2a** and **3a** in a 62:38 ratio in 35% yield, along with polyiodinated compounds and several unidentified byproducts (Table 2.1, entry 1). In order to investigate the effect of equivalent of IPy_2BF_4 , the iodination was performed with excess amounts of IPy_2BF_4 (3 equiv) and TfOH (6 equiv) under the identical condition. Unfortunately, this

⁹ Jutland, A.; Mosleh, A. *Organometallics* **1995**, *14*, 1840–1843.

¹⁰ a) Jan, P.; Jan, B. K.; Krakowia, I. P.; Krakow, P. *Rev. Chim.* **1984**, *35*, 988–991; b) Monge, M. E.; Bonesi, S. M.; Erra-Balsells, R. J. *Heterocycl. Chem.* **2002**, *39*, 933–941.

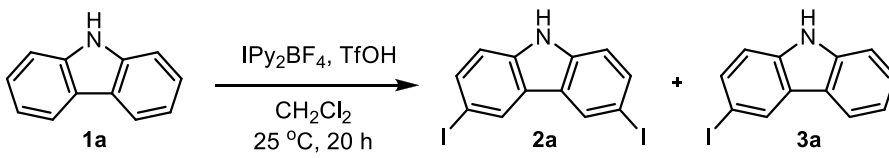
¹¹ a) Filimonov, V. D.; Krasnokutskaya, E. A.; Lesina, Y. A. *Russ. J. Org. Chem.* **2003**, *39*, 875–880; b) Bogdal, D.; Lukasiewicz, M.; Pielichowski, J. *Green Chem.* **2004**, *6*, 110–113; c) Grigalevicius, S.; Blazys, G.; Ostruskaite, J.; Grazulevicius, J. V.; Gaidelis, V.; Jankauskas, V.; Montrmas, E. *Symtetic Metals* **2002**, *128*, 127–131; d) Maruyama, S.; Hokari, H.; Wada, T.; Sasabe, H. *Synthesis* **2001**, 1794–1799.

¹² a) Barluenga, J.; Gonzalez, J. M.; Campos, P. J.; Asensio, G. *Angew. Chem., Int. Ed. Engl.* **1985**, *24*, 319–320; b) Barluenga, J.; Rodriguez, M. A.; Campos, P. J. *J. Org. Chem.* **1990**, *55*, 3104–3106; c) Barluenga, J.; Gonzalez, J. M.; Campos, P. J.; Asensio, G. *J. Chem. Soc., Perkin Trans. 1* **1984**, 2623–2624; d) Barluenga, J.; Gonzalez, J. M.; Martin, M.; Campos, P. J. *Tetrahedron Lett.* **1993**, *24*, 3893–3896; e) Barluenga, J.; Gonzalez, J. M.; Martin, M.; Campos, P. J.; Asensio, G. *J. Org. Chem.* **1993**, *58*, 2058–2060.

¹³ Shimada, T.; Suda, M.; Nagano, T.; Kakiuchi, K. *J. Org. Chem.* **2005**, *70*, 10178–10181.

reaction condition resulted in triiodinated carbazole in 71% isolated yield without formation of **2a** or **3a** (Table 2.1, entry 2). These findings suggest that the use of excess amounts of IPy₂BF₄ is not preferable for selective diiodination. In addition, the author observed the formation of insoluble green precipitates when TfOH was added to the reaction mixture. It is likely to cause the protonation of nitrogen in carbazole skeleton under strong acidic condition. Therefore, the iodination was carried out by using 2.5 equiv of IPy₂BF₄ and 1 equiv of TfOH under identical condition. This reaction system gave the desired product **2a** in 96% yield without formation of byproducts such as monoiodinated and polyiodinated carbazoles (Table 2.1, entry 3).

Table 2.1. Iodination of *N*-unsubstituted carbazole.



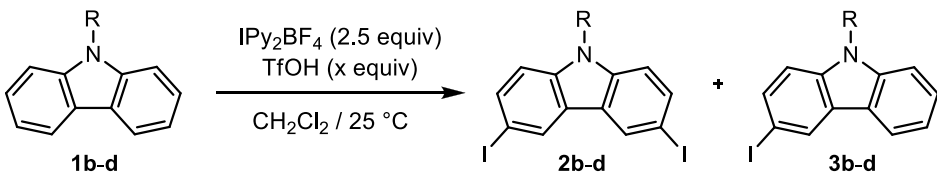
Entry	IPy ₂ BF ₄ / equiv	TfOH / equiv	2a / 3a ^a	Yield / % ^b
1	2	4	62 : 38	35
2 ^c	3	6	—	0
3	2.5	1	100 : 0	96

^a Determined by ¹H NMR analysis. ^b Isolated yield of **2a** + **3a**. ^c 1,3,6-triiodocarbazole was obtained in 71% yield.

Next, the author applied the optimized condition to the reactions of *N*-substituted carbazoles (Table 2.2). The reaction of *N*-methylcarbazole (**1b**) at 25 °C for 40 h gave the corresponding diiodinated product **2b** in 93% yield, but the reaction was not completed within 20 h (Table 2.2, entries 1 and 2). The reaction of *N*-octylcarbazole (**1c**) gave an inseparable mixture of di- and monoiodinated products, and was not completed even with prolonged reaction times (Table 2.2, entry 3). When the reaction was carried out at 40 °C, the starting material was perfectly consumed. However, a ratio of **2c**/**3c** at 40 °C did not change from that at 25 °C. In contrast, when the reaction was carried out at -30 °C, monoiodinated carbazole was selectively obtained (Table 2.2, entry 5), and a ratio of **2c**/**3c** was not changed even prolonged reaction times of 60 h (Table 2.2, entry 6). While seeking the optimal reaction conditions, the author found that the diiodination of **1c** perfectly

proceeds by using 2.5 equiv of IPy₂BF₄ and 2 equiv of TfOH at 25 °C for 60 h, and give the desired product **2c** in excellent yield of 95% (Table 2.2, entry 7). *N*-phenylcarbazole (**1d**) was also diiodinated under optimized general condition but gave a mixture of **2d** and **3d** (Table 2.2, entry 8). Interestingly, **1d** was exclusively diiodinated in the presence of 2.5 equiv of IPy₂BF₄ and TfOH to give **2d** in an isolated yield of 93% (Table 2.2, entry 9). These results indicate that the reactivity of carbazole ring was strongly depended on the substituents at nitrogen atom, and the iodination behaviors could be controlled by amounts of TfOH and reaction temperature.

Table 2.2. Iodination of *N*-substituted carbazoles.



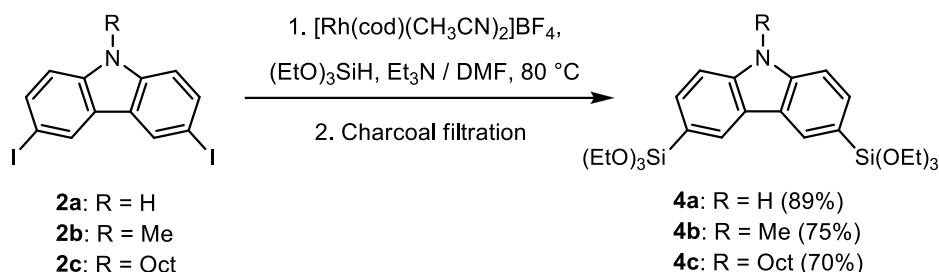
Entry	R	TfOH / equiv	Time / h	2 / 3 ^a	Yield / % ^b
1	Me (1b)	1	20	39 : 61	75
2		1	40	100 : 0	93
3	Oct (1c)	1	120	77 : 23	76
4 ^c		1	60	75 : 25	100
5 ^d		1	20	8 : 92	97
6 ^d		1	60	9 : 91	84
7		2	60	100 : 0	95
8	Ph (1d)	1	20	70 : 30	90
9		2.5	20	100 : 0	93

^a Determined by ¹H NMR analysis. ^b Isolated yield of **2** + **3**. ^c Reaction was performed at 40 °C.

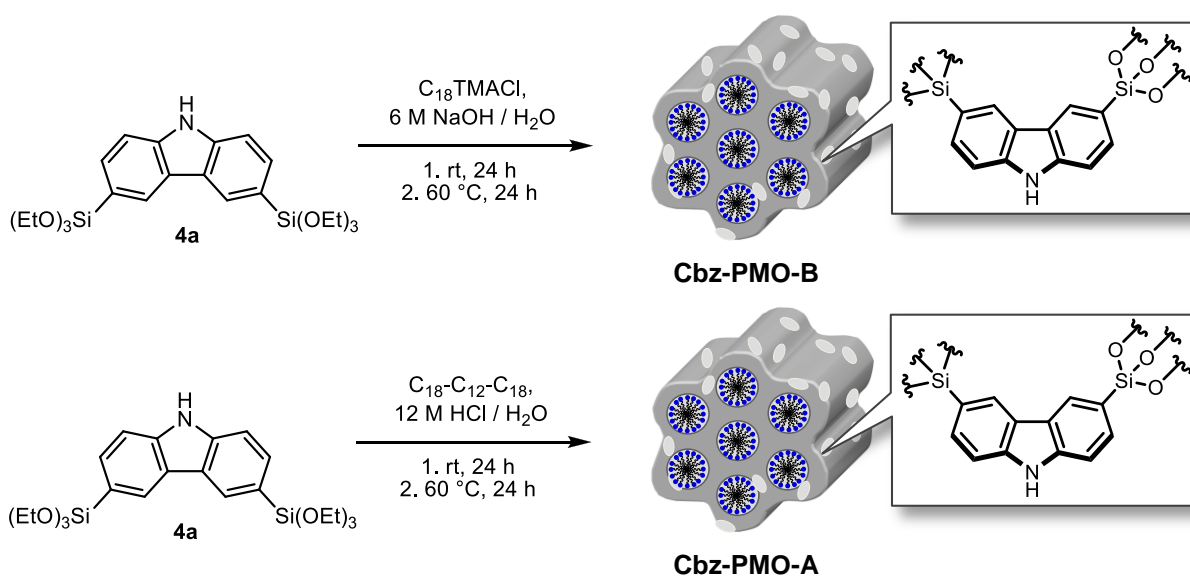
^d Reaction was performed at -30 °C.

The resulting diiodocarbazoles **2a–c** were subjected to rhodium-catalyzed disilylation with triethoxysilane. These reactions proceeded smoothly to give the corresponding 3,6-bis(triethoxysilyl)carbrazoles **4a–c** in 89%, 75% and 70% yields, respectively (Scheme 2.2). In contrast, the use of 3,6-dibromocarbrazole as a starting material resulted in no reaction under identical reaction conditions. In addition, the author developed a purification method using charcoal.

By passing the ethereal solution of the resulting crude products **4a–c** with charcoal filter, the reduction product such as **1a** and monosilylated product could be easily separated.



Scheme 2.2. Rhodium-catalyzed disilylation of 3,6-diiodocarbazole derivatives **2a–c** giving carbazole-bridged triethoxysilane precursors **4a–c**.



Scheme 2.3. Synthesis of carbazole-bridged periodic mesostructured organosilicas (**Cbz-PMO-B** and **Cbz-PMO-A**) starting from carbazole-bridged triethoxysilane precursor **4a** under basic and acidic conditions.

Hydrolysis and polycondensation of the purified **4a** under basic condition in the presence of octadecyltrimethylammonium chloride ($\text{C}_{18}\text{TMACl}$) as a structure directing agent gave carbazole-bridged periodic mesostructured organosilica (**Cbz-PMO-B**) (Scheme 2.3). The periodic mesostructured organosilica (**Cbz-PMO-A**) could be also synthesized under acidic condition in the

presence of 1,12-dodecanediaminium- N^1,N^1,N^{12},N^{12} -tetramethyl- N^1,N^{12} -dioctadecyl dibromide as a gemini surfactant ($C_{18}C_{12}C_{18}$). Figure 2.1 shows the X-ray diffraction (XRD) pattern of **Cbz-PMO-B** and **Cbz-PMO-A**. Both PMOs showed a strong diffraction at $2\theta = 2.49^\circ$ and 2.41° , which corresponds to ordered mesostructures with d -spacings of 3.55 and 3.67 nm, respectively. This novel preparation method for arylene-bridged organosilanes should allow the development of numerous promising precursors for organosilica hybrid materials such as periodic mesoporous organosilicas (PMOs) and bridged silsesquioxanes (BSQs).

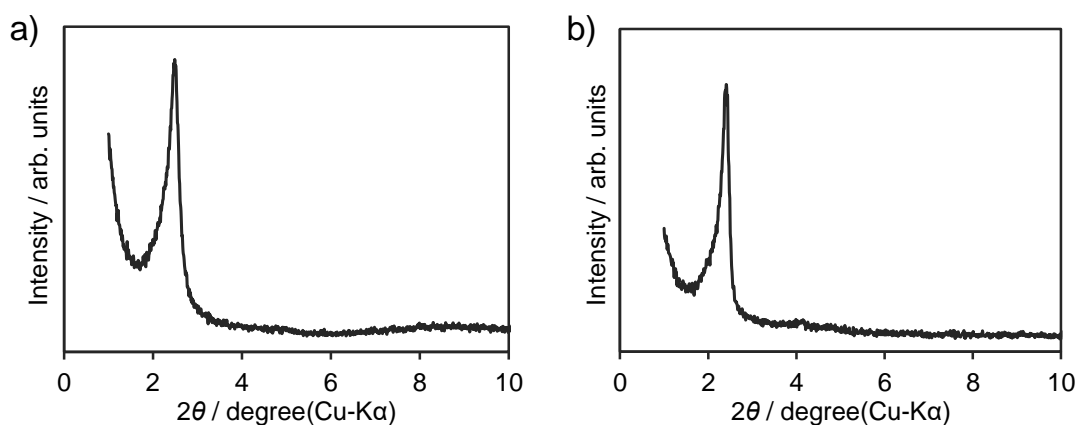


Figure 2.1. XRD patterns of a) **Cbz-PMO-B** and b) **Cbz-PMO-A**.

2.1.4 Conclusions

The author developed a useful method for diiodination of N -unsubstituted, N -methyl and N -octyl, and N -phenylcarbazoles with bis(pyridine)iodonium tetrafluoroborate in the presence of TfOH under mild condition. Rhodium-catalyzed disilylation of 3,6-diiodocarbazoles with triethoxysilane afforded the corresponding 3,6-bis(triethoxysilyl)carbazoles in good yields of 70–89%. Hydrophobic reduced byproducts could be easily removed from the crude mixture by passing through the charcoal filter and purified carbazole-bridged triethoxysilane precursors were obtained. The obtained organosilane precursors could be used for synthesis of carbazole-bridged mesostructured organosilicas under basic and acidic conditions in the presence of surfactant templates.

2.2 Pd-catalyzed Coupling Reactions for Highly Functional Organic-bridged Allylsilanes

A series of molecular building blocks containing allylsilyl groups, which can be incorporated into the appropriate sol-gel precursors as fragments, were prepared. The allylsilyl group is retained unchanged over the course of all reactions giving sol-gel precursors and behave as the synthetic equivalent of alkoxy-silyl groups toward sol-gel polymerization, but are stable enough to allow purification by silica gel chromatography. These allylsilanes were successfully used as building blocks to construct functional sol-gel precursors via palladium-catalyzed coupling reactions.

2.2.1 Introduction

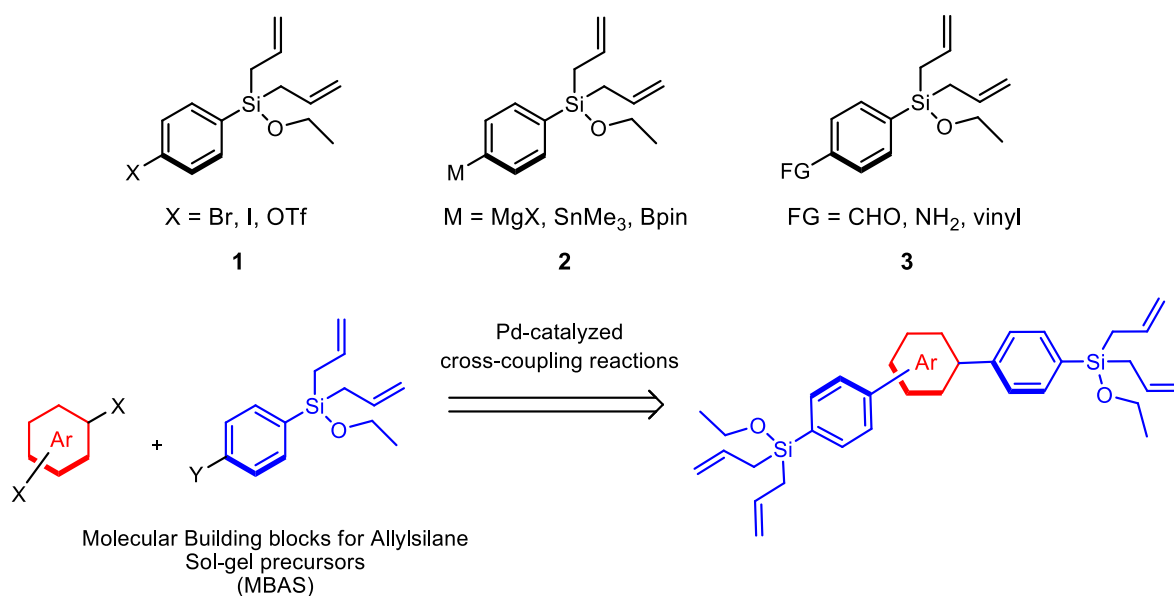
Organic-inorganic hybrid materials integrate the intrinsic characteristics of organic and inorganic materials. The usual method of preparation to date has been polymerization of organotrialkoxysilanes under sol-gel conditions.¹ Materials which incorporate functional organomoieties in a silica matrix have been prepared by Shea and Loy,^{2a-c} Schubert,^{2d} Corriu and Cerveau,^{2e-g} Inagaki,^{2h} Ozin,^{1d} Moreau and Dautel,²ⁱ and Shimada groups.^{2j} In the pioneer work in this area, Shea and Loy reported the preparation and sol-gel polymerization of a variety of bridged trialkoxyarylenesilanes.^{2a} However, the development of appropriate sol-gel precursors for organic-inorganic hybrid materials has been rather slow compared to the progress in the synthesis of

¹ a) Brinker, C. J.; Scherer, G. W. *Sol-Gel Science: The Physics and Chemistry of Sol-Gel Processing*; Academic: San Diego, CA, 1990; b) Loy, D. A.; Shea, K. J. *Chem. Rev.* **1995**, *95*, 1431-1434; c) Cerveau, G.; Corriu, R. J. P.; Dabiens, B.; Le Bideau, J. *Angew. Chem., Int. Ed.* **2000**, *39*, 4533-4537; d) Hunks, W. J.; Ozin, G. A. *Chem. Mater.* **2004**, *16*, 5465-5472; e) Kapoor, M. P.; Inagaki, S. *Bull. Chem. Soc. Jpn.* **2006**, *79*, 1463-1475; f) Hoffmann, F.; Cornelius, M.; Morell, J.; Fröba, M. *Angew. Chem., Int. Ed.* **2006**, *45*, 3216-3251.

² a) Shea, K. J.; Loy, D. A.; Webster, O. W. *Chem. Mater.* **1989**, *1*, 572-574; b) Shea, K. J.; Loy, D. A.; Webster, O. W. *J. Am. Chem. Soc.* **1992**, *114*, 6700-6710; c) Zhao, L.; Loy, D. A.; Shea, K. J. *J. Am. Chem. Soc.* **2006**, *128*, 14250-14251; d) Schubert, U.; Hüsing, N.; Lorenz, A. *Chem. Mater.* **1995**, *7*, 2010-2027; e) Cerveau, G.; Chappellet, S.; Corriu, R. J. P.; Dabiens, B. *J. Organomet. Chem.* **2001**, *626*, 92-99; f) Cerveau, G.; Chappellet, S.; Corriu, R. J. P.; Dabiens, B.; Bideau, J. L. *Organometallics* **2002**, *21*, 1560-1564; g) Nathalie, B.; Frederic, L.; Benoit, P.; Genevieve, C.; Corriu, R. J. P. *Eur. J. Org. Chem.* **2005**, *1*, 136-146; h) Inagaki, S.; Guan, S.; Ohsuna, T.; Terasaki, O. *Nature* **2002**, *416*, 304-307; i) Dautel, O. J.; Wantz, G.; Almairac, R.; Flot, D.; Hirsch, L.; Lere-Porte, J.-P.; Pameix, J.-P.; Serein-Spirau, F.; Vignau, L.; Moreau, J. J. E. *J. Am. Chem. Soc.* **2006**, *128*, 4892-4901; j) Maegawa, Y.; Goto, Y.; Inagaki, S.; Shimada, T. *Tetrahedron Lett.* **2006**, *47*, 6957-6960.

chemicals and medicines, because trialkoxysilyl groups are so reactive toward hydrolysis that their compounds cannot be handled under hydrolytic conditions and cannot be purified by silica gel chromatography.

Shimada et al. recently found that allylsilyl groups behave as the synthetic equivalent of alkoxy-silyl groups, but are stable enough to allow purification by silica gel chromatography.³ For example, the use of 1,4-bis(triallylsilyl)benzene or 1,4-bis(diallylethoxysilyl)benzene in the place of 1,4-bis(triethoxysilyl)benzene gave the same organic–inorganic hybrid materials containing periodic mesostructures with crystal-like pore walls.^{3c} Although these organoallylsilane precursors can be readily prepared from corresponding organoalkoxysilane by addition of allylmagnesium halide or allyllithium, use of high reactive organometallic reagents generally suffers from functional group comparability in the substrates. Therefore, development of rapid and divergent synthetic route for organoallylsilane precursors is valuable for synthesis of highly functional organic–inorganic hybrid materials.



Scheme 2.4. Chemical structures of molecular building blocks for allylsilane sol–gel precursors (MBAS) and their palladium-catalyzed cross-coupling reactions giving sol–gel precursors.

³ a) Shimada, T.; Aoki, K.; Shinoda, Y.; Nakamura, T.; Tokunaga, N.; Inagaki, S.; Hayashi, T. *J. Am. Chem. Soc.* **2003**, *125*, 4688–4689; b) Aoki, K.; Shimada, T.; Hayashi, T. *Tetrahedron: Asymmetry* **2004**, *15*, 1771–1777; c) Kapoor, M. P.; Inagaki, S.; Ikeda, S.; Kakiuchi, K.; Suda, M.; Shimada, T. *J. Am. Chem. Soc.* **2005**, *127*, 8174–8178; d) Kapoor, M. P.; Yanagi, M.; Kasama, Y.; Yokoyama, T.; Inagaki, S.; Shimada, T.; Nanbu, H.; Juneja, L. R. *J. Mater. Chem.* **2006**, *16*, 3305–3311; e) Wang, Y.; Hu, S.; Brittain, W. J. *Macromolecules* **2006**, *39*, 5675–5678.

Herein the author discloses a general synthetic route for functional organoallylsilanes by using molecular building blocks for allylsilane sol-gel precursors (MBAS). A series of molecular building blocks containing both allylsilyl group and halogen, metal, or functional group, were prepared. The allylsilyl group was retained unchanged over the course of all reactions to give a variety of functional organoallylsilane sol-gel precursors via palladium-catalyzed cross-coupling reactions. The allylsilyl groups were stable enough to allow purification by silica gel chromatography to give functional organoallylsilane precursors in pure form (Scheme 2.4).

2.2.2 Experimental

Materials and methods

All reagents and solvents were purchased from Aldrich, Tokyo Chemical Industry, and Wako Pure Chemical Industries and used without further purification. All moisture sensitive manipulations were carried out under a nitrogen atmosphere. Nitrogen gas was dried by passage through P₂O₅. Optical rotations were recorded with a JASCO DIP-370 polarimeter. Nuclear magnetic resonance (NMR) spectra were recorded on JEOL JNM LA500 spectrometer (270 MHz for ¹H, 67.5 MHz for ¹³C, and 109 MHz for ³¹P). Chemical shifts are reported in δ ppm referenced to an internal SiMe₄ standard for ¹H NMR, chloroform-*d* (δ 77.0) for ¹³C NMR, and an external 85% H₃PO₄ standard for ³¹P NMR. The following abbreviations were used to explain the multiplicities: s = singlet, d = doublet, t = triplet, q = quartet, sep = septet, m = multiplet, br = broad, dd = double doublet, dt = double triplet, ddd = doublet of double doublet, ddt = doublet of double triplet. High resolution mass spectra (HRMS) were recorded with JEOL JMS-700 spectrometer.

Preparation of molecular building blocks

1-Bromo-4-(diallylethoxysilyl)benzene (1a). To a solution of 1-bromo-4-iodobenzene (2.60 g, 9.19 mmol), *n*-Bu₄NI (3.39 g, 9.18 mmol), dry Et₃N (2.56 mL, 18.4 mmol), and [Rh(cod)(CH₃CN)₂][BF₄] (105 mg, 0.277 mmol) in dry DMF (26 mL) was added dropwise triethoxysilane (1.87 mL, 10.1 mmol) at 0 °C. The mixture was stirred at 80 °C for 1 h. The mixture was concentrated under reduced pressure, treated with Et₂O, and filtered through a short Celite plug. The crude mixture was purified by bulb-to-bulb distillation under reduced pressure to give

1-bromo-4-(triethoxysilyl)benzene (2.38 g, 81% yield). To the resulting ethoxysilane (4.74 g, 14.8 mmol) was added a solution of allylmagnesium bromide (AllylMgBr) (59.4 mL, 1.0 M in Et₂O, 59.4 mmol). The reaction mixture was stirred at room temperature for 10 h and quenched with 10% hydrochloric acid (HCl). It was then diluted with Et₂O and the organic layer was washed with saturated NaHCO₃ aqueous solution and brine, dried over anhydrous MgSO₄, and evaporated under reduced pressure. The crude mixture was purified by bulb-to-bulb distillation under reduced pressure to give **1a** (4.20 g, 91% yield). ¹H NMR (270 MHz, CDCl₃) δ 1.21 (t, *J* = 6.8 Hz, 3H), 1.91 (ddd, *J* = 7.8 Hz, 1.4 Hz, 1.1 Hz, 4H), 3.76 (q, *J* = 6.8 Hz, 2H), 4.92 (ddt, *J* = 9.7 Hz, 1.6 Hz, 1.1 Hz, 2H), 4.95 (ddt, *J* = 15.7 Hz, 1.6 Hz, 1.4 Hz, 2H), 5.79 (ddt, *J* = 15.7 Hz, 9.7 Hz, 7.8 Hz, 2H), 7.43 (d, *J* = 8.4 Hz, 2H), 7.52 (d, *J* = 8.4 Hz, 2H); ¹³C NMR (67.5 MHz, CDCl₃) δ 18.32, 21.08, 59.27, 114.96, 124.68, 130.90, 132.63, 133.88, 135.50; FAB-HRMS *m/z* calcd for C₁₄H₁₈OBrSi [M-H]⁺: 309.0310; found 309.0321. Anal. Calcd for C₁₄H₁₉OBrSi: C, 54.02; H, 6.15. found: C, 53.93; H, 6.23.

1-Iodo-4-(diallylethoxysilyl)benzene (1b). To a solution of 1,4-diiodobenzene (15 g, 45.6 mmol) in dry THF (114 mL) was added dropwise a solution of isopropylmagnesium chloride (*i*-PrMgCl) (24 mL, 2.0 M in THF, 48 mmol) at -30 °C. The reaction mixture was stirred at -30 °C for 5.5 h to give 4-iodophenylmagnesium chloride solution. The resulting Grignard reagent solution was added dropwise (three drops per second) via cannula at -30 °C to tetraethyl orthosilicate (TEOS) (60.6 mL, 272 mmol) in dry THF (90 mL), which was cooled to -30 °C. The reaction mixture was stirred at -30 °C for 1 h and then at room temperature for 44 h. To the reaction mixture was added Et₂O (100 mL) and then washed with H₂O. The mixture was extracted with Et₂O. The organic layer was washed with brine, dried over anhydrous MgSO₄, and concentrated. The crude mixture was purified by bulb-to-bulb distillation under reduced pressure (1.5 mmHg, 120 °C) to give 1-iodo-4-(triethoxysilyl)benzene (10.2 g, 61% yield). ¹H NMR (270 MHz, CDCl₃) δ 1.24 (t, *J* = 7.3 Hz, 9H), 3.88 (q, *J* = 7.3 Hz, 6H), 7.39 (dd, *J* = 7.8 Hz, 1.4 Hz, 2H), 7.73 (dd, *J* = 7.8 Hz, 1.4 Hz, 2H); ¹³C NMR (67.5 MHz, CDCl₃) δ 18.36, 21.08, 59.35, 97.08, 115.04, 132.69, 134.49, 135.59, 136.87; EI-HRMS *m/z* calcd for C₁₂H₁₉O₃ISi (M⁺): 358.0250; found 358.0243. To the resulting ethoxysilane (9.4 g, 25.7 mmol) was added dropwise a solution of AllylMgBr (77 mL, 1.0 M in Et₂O, 77 mmol) at 0 °C. The reaction mixture was stirred at room temperature for 10 h and quenched with 10% HCl. It was then diluted with Et₂O and the organic layer was washed with

saturated NaHCO₃ aqueous solution and brine, dried over anhydrous MgSO₄, and evaporated under reduced pressure. The residue was chromatographed on silica gel (eluent: hexane/EtOAc = 20:1) to give **1b** (9.0 g, 98% yield): ¹H NMR (270 MHz, CDCl₃) δ 1.20 (t, *J* = 6.8 Hz, 3H), 1.91 (d, *J* = 8.1 Hz, 4H), 3.75 (q, *J* = 6.8 Hz, 2H), 4.89–4.98 (m, 4H), 5.71–5.87 (m, 2H), 7.29 (d, *J* = 8.1 Hz, 2H), 7.72 (d, *J* = 8.1 Hz, 2H); ¹³C NMR (67.5 MHz, CDCl₃) δ 18.34, 21.08, 59.35, 97.08, 115.04, 132.69, 134.49, 135.59, 136.87; EI-HRMS *m/z* calcd for C₁₄H₁₉OISi (M⁺): 358.0250; found 358.0243; Anal. Calcd for C₁₄H₁₉OISi: C, 46.93; H, 5.35. Found: C, 46.80; H, 5.46.

4-(Diallylethoxysilyl)phenyl triflate (1c). To a mixture of 4-iodophenol (6.0 g, 27.3 mmol), [Rh(cod)(CH₃CN)₂]BF₄ (104 mg, 0.27 mmol), and *n*-Bu₄NI (10.0 g, 27.3 mmol) were added dry DMF (180 mL), dry Et₃N (11.4 mL, 81.8 mmol), and triethoxysilane (15.1 mL, 81.8 mmol). The reaction mixture was stirred at 80 °C for 3 h. The mixture was concentrated under reduced pressure, treated with Et₂O, and filtered through a short Celite plug. The filtrates were concentrated under reduced pressure. To the residue was added dropwise a solution of AllylMgBr (1.0 M in Et₂O, 136 mL, 136 mmol) at 0 °C. The reaction mixture was stirred at room temperature for 19 h and quenched with 10% HCl. It was then diluted with Et₂O and the organic layer was washed with saturated NaHCO₃ aqueous solution and brine, dried over anhydrous MgSO₄, and evaporated under reduced pressure. The residue was chromatographed on silica gel (eluent: hexane/EtOAc = 5:1) to give 4-(diallylethoxysilyl)phenol (5.30 g, 78%, in two steps). ¹H NMR (270 MHz, CDCl₃) δ 1.20 (t, *J* = 6.8 Hz, 3H), 1.92 (d, *J* = 7.8 Hz, 4H), 3.75 (q, *J* = 6.8 Hz, 2H), 4.92 (ddt, *J* = 10.3 Hz, 1.4 Hz, 0.8 Hz, 2H), 4.96 (ddt, *J* = 15.9 Hz, 1.4 Hz, 1.1 Hz, 2H), 5.57 (br, 1H), 5.82 (ddt, *J* = 15.9 Hz, 10.3 Hz, 7.8 Hz, 2H), 6.85 (d, *J* = 8.6 Hz, 2H), 7.46 (d, *J* = 8.6 Hz, 2H); ¹³C NMR (67.5 MHz, CDCl₃) δ 18.30, 21.24, 59.29, 114.72, 115.04, 125.85, 133.19, 135.82, 157.18. To a mixture of the resulting allylsilane (197 mg, 0.79 mmol) and 2-[*N,N*-bis(trifluoromethylsulfonyl)amino]-5-chloropyridine (343 mg, 0.87 mmol) were added dry CH₂Cl₂ (5 mL) and dry *i*-Pr₂NEt (553 mL, 3.17 mmol). The reaction mixture was stirred at room temperature for 19 h. The reaction mixture was then concentrated. The residue was chromatographed on silica gel (eluent: hexane/EtOAc = 10:1) to give **1c** (253 mg, 84% yield). ¹H NMR (270 MHz, CDCl₃) δ 1.23 (t, *J* = 7.0 Hz, 3H), 1.93 (d, *J* = 7.8 Hz, 4H), 3.79 (q, *J* = 7.0 Hz, 2H), 4.91–4.99 (m, 4H), 5.79 (ddt, *J* = 16.2 Hz, 10.3 Hz, 7.8 Hz, 2H), 7.28 (d, *J* = 8.1 Hz, 2H), 7.67 (d, *J* = 8.1 Hz, 2H); ¹³C NMR (67.5 MHz, CDCl₃) δ 18.28, 21.13, 59.43, 115.21, 120.55, 132.40, 136.05, 136.46, 150.87; Anal. Calcd for C₁₅H₁₉O₄F₃SSi: C, 47.35; H, 5.03.

Found: C, 47.47; H, 5.05.

4-(Diallylethoxysilyl)phenylmagnesium chloride (2a). To a solution of **1b** (255 mg, 0.71 mmol) in dry THF (2 mL) was added a solution of *i*-PrMgCl (0.71 mL, 2.0 M in THF, 1.42 mmol) at $-30\text{ }^{\circ}\text{C}$. The reaction mixture was stirred at $-30\text{ }^{\circ}\text{C}$ for 1.5 h to give a THF solution of **2a**.

Diallyl[4-(trimethylstannyl)phenyl]ethoxysilane (2b). To a solution of **1b** (2.02 g, 5.64 mmol) in dry THF (15 mL) was added a solution of *i*-PrMgCl (5.9 mL, 2.0 M in THF, 11.8 mmol) at $-30\text{ }^{\circ}\text{C}$. The reaction mixture was stirred at $-30\text{ }^{\circ}\text{C}$ for 4 h to give a THF solution of **2a**. To the resulting solution of **2a** was added a solution of Me_3SnCl (11.2 mL, 1.0 M in THF, 11.2 mmol) at $-30\text{ }^{\circ}\text{C}$. The reaction mixture was stirred at $-30\text{ }^{\circ}\text{C}$ for 1 h, and at room temperature for 19 h. The reaction mixture was then quenched with H_2O and extracted with Et_2O . The organic layer was washed with saturated NaHCO_3 aqueous solution and brine, dried over anhydrous MgSO_4 , and concentrated under reduced pressure. The residue was chromatographed on silica gel (eluent: hexane/ EtOAc = 3:1) to give **2c** (2.20 g, 99% yield). ^1H NMR (270 MHz, CDCl_3) δ 0.29 (t, $J(\text{Sn}-\text{CH}_3) = 54.5$ Hz, 9H), 1.21 (t, $J = 6.8$ Hz, 3H), 1.93 (d, $J = 8.1$ Hz, 4H), 3.76 (q, $J = 6.8$ Hz, 2H), 4.92 (ddt, $J = 16.2$ Hz, 1.6 Hz, 1.1 Hz, 2H), 4.96 (ddt, $J = 10.3$ Hz, 1.6 Hz, 0.5 Hz, 2H), 5.84 (ddt, $J = 16.2$ Hz, 10.3 Hz, 8.1 Hz, 2H), 7.52 (d, $J = 1.62$ Hz, 4H); ^{13}C NMR (67.5 MHz, CDCl_3) δ -9.63 ($J(^{119}\text{Sn}-\text{CH}_3) = 348.6$ Hz, $J(^{117}\text{Sn}-\text{CH}_3) = 333.0$ Hz), 18.40, 21.21, 59.29, 114.72, 133.20, 133.40, 134.76, 135.27, 144.58; FAB-HRMS m/z calcd for $\text{C}_{17}\text{H}_{27}\text{OSiSn}$ ($\text{M}-\text{H}^+$): 395.0853; found 395.0850.

Diallyl[4-(4,4,5,5-tetramethyl-1,3,2-dioxaborolan-2-yl)phenyl]ethoxysilane (2c). To a solution of **1b** (2.02 g, 5.64 mmol) in dry THF (15 mL) was added a solution of *i*-PrMgCl (5.9 mL, 2.0 M in THF, 11.8 mmol) at $-30\text{ }^{\circ}\text{C}$. The reaction mixture was stirred at $-30\text{ }^{\circ}\text{C}$ for 4 h to give a THF solution of **2a**. To the resulting solution of **2a** was added 2-isopropoxy-4,4,5,5-tetramethyl-1,3,2-dioxaborolane (2.3 mL, 11.3 mmol) at $-78\text{ }^{\circ}\text{C}$. The reaction mixture was stirred at $-78\text{ }^{\circ}\text{C}$ for 1 h, and then at room temperature for 19 h. The reaction mixture was quenched with 10% HCl. It was then diluted with Et_2O and the organic layer was washed with saturated NaHCO_3 aqueous solution and brine, dried over anhydrous MgSO_4 , and evaporated under reduced pressure. The residue was chromatographed on silica gel (eluent: hexane/ EtOAc = 3:1) to give **2b** (2.02 g, 100% yield). ^1H NMR (270 MHz, CDCl_3) δ 1.20 (t, $J = 7.0$ Hz, 3H), 1.34 (s, 12H), 1.94 (d, $J = 7.8$ Hz, 4H), 3.75 (q, $J = 7.0$ Hz, 2H), 4.89 (ddt, $J = 10.3$ Hz, 1.6 Hz, 1.1 Hz, 2H), 4.94 (ddt, $J = 15.9$ Hz, 1.6 Hz, 1.4 Hz, 2H), 5.81 (ddt, $J = 15.9$ Hz, 10.3 Hz, 7.8 Hz, 2H), 7.58 (d, $J = 8.4$ Hz, 2H), 7.81 (d, $J = 8.4$ Hz,

2H); ^{13}C NMR (67.5 MHz, CDCl_3) δ 18.33, 21.05, 24.81, 59.28, 83.76, 114.77, 127.74, 132.94, 133.22, 133.80, 138.49; FAB-HRMS m/z calcd for $\text{C}_{20}\text{H}_{30}\text{O}_3\text{BSi}$ ($\text{M}-\text{H}^+$): 357.2057; found 357.2070.

Diallyl(4-aminophenyl)ethoxysilane (3a). To a mixture of 4-iodoaniline (1.32 g, 6.0 mmol), $\text{Pd}_2(\text{dba})_3$ (82.4 mg, 0.090 mmol), and (*o*-biphenyl) $\text{P}(t\text{-Bu})_2$ (JohnPhos) (107.6 mg, 0.36 mmol) were added dry NMP (24 mL), dry *i*- Pr_2NEt (3.13 mL, 18 mmol), and triethoxysilane (1.66 mL, 9.0 mmol). The reaction mixture was stirred at room temperature for 20 h. The reaction mixture was then concentrated to remove excess of amine and triethoxysilane. The residue was diluted with Et_2O , the organic layer was washed with H_2O , dried over anhydrous MgSO_4 , and concentrated. The residue was distilled under reduced pressure (0.1 mmHg, 110 °C) to give 4-(triethoxysilyl)aniline (1.23 g, 80%). To the resulting ethoxysilane (1.15 g, 4.5 mmol) was added dropwise a solution of AllylMgBr (22.5 mL, 1.0 M in Et_2O , 22.5 mmol) at 0 °C. The reaction mixture was stirred at room temperature for 13 h. The reaction was quenched with H_2O and the mixture was extracted with Et_2O . The organic layer was washed with saturated NaHCO_3 aqueous solution and brine, dried over anhydrous MgSO_4 , and concentrated. The residue was chromatographed on silica gel (eluent: hexane/ EtOAc = 3:1) to give **3b** (1.08 g, 96% yield). ^1H NMR (270 MHz, CDCl_3) δ 1.48 (t, J = 7.0 Hz, 3H), 1.90 (d, J = 8.4 Hz, 4H), 3.73 (q, J = 7.0 Hz, 4H containing NH_2), 4.86–4.98 (m, 4H), 5.79 (ddt, J = 16.2 Hz, 9.5 Hz, 8.1 Hz, 2H), 6.68 (d, J = 8.1 Hz, 2H), 7.36 (d, J = 8.1 Hz, 2H); ^{13}C NMR (67.5 MHz, CDCl_3) δ 18.36, 21.36, 59.04, 114.37, 122.82, 133.55, 135.42, 136.00, 147.90; FAB-HRMS m/z calcd for $\text{C}_{14}\text{H}_{22}\text{ONSi}$ ($\text{M}+\text{H}^+$): 248.1471; found 248.1471.

Diallyl(4-formylphenyl)ethoxysilane (3b). To a solution of **1b** (255 mg, 0.71 mmol) in dry THF (2 mL) was added a solution of *i*- PrMgCl (0.71 mL, 2.0 M in THF, 1.42 mmol) at –30 °C. The reaction mixture was stirred at –30 °C for 1.5 h to give a THF solution of **2a**. To the resulting solution of **2a** was added dry DMF (110 μL , 1.42 mmol) at –30 °C. The reaction mixture was stirred at room temperature for 13 h. The reaction mixture was quenched with 10% HCl and extracted with Et_2O . The organic layer was washed with saturated NaHCO_3 aqueous solution and brine, dried over anhydrous MgSO_4 , and concentrated under reduced pressure. The residue was chromatographed on silica gel (eluent: hexane/ EtOAc = 20:1) to give **3a** (158 mg, 85% yield). ^1H NMR (270 MHz, CDCl_3) δ 1.24 (t, J = 6.8 Hz, 3H), 1.96 (ddd, J = 8.1 Hz, 1.4 Hz, 0.8 Hz, 4H), 3.81 (q, J = 6.8 Hz, 2H), 4.91–4.99 (m, 4H), 5.80 (ddt, J = 16.2 Hz, 10.3 Hz, 8.1 Hz, 2H), 7.75 (d, J

= 8.4 Hz, 2H), 7.87 (d, $J = 8.4$ Hz, 2H), 10.0 (s, 1H); ^{13}C NMR (67.5 MHz, CDCl_3) δ 18.35, 21.06, 59.50, 115.24, 128.58, 132.43, 134.53, 137.07, 143.53, 192.55; EI-HRMS m/z calcd for $\text{C}_{15}\text{H}_{20}\text{O}_2\text{Si}$ (M^+): 260.1233; found 260.1236.

Wittig olefination giving 4-(diallylethoxysilyl)styrene (3c). To a mixture of PPh_3MeI (970 mg, 2.4 mmol) and $\text{KO}t\text{-Bu}$ (269 mg, 2.4 mmol) was added dry toluene (15 mL). The reaction mixture was stirred at 80 °C for 2 h. To the reaction mixture was added a solution of **3b** (250 mg, 0.96 mmol) in dry toluene (5 mL) at 50 °C. The reaction mixture was stirred at 50 °C for 12 h. The reaction mixture was then quenched with H_2O and extracted with Et_2O . The organic layer was washed with brine, dried over anhydrous MgSO_4 , and concentrated. The residue was chromatographed on silica gel (eluent: hexane/ $\text{EtOAc} = 3:1$) to give **3c** (233.2 mg, 94% yield). ^1H NMR (270 MHz, CDCl_3) δ 1.20 (t, $J = 7.0$ Hz, 3H), 1.93 (ddd, $J = 8.1$ Hz, 1.4 Hz, 1.1 Hz, 4H), 3.76 (q, $J = 7.0$ Hz, 2H), 4.90 (ddt, $J = 10.3$ Hz, 1.6 Hz, 1.1 Hz, 2H), 4.96 (ddt, $J = 16.2$ Hz, 1.6 Hz, 1.4 Hz, 2H), 5.27 (dd, $J = 11.1$ Hz, 0.8 Hz, 1H), 5.79 (dd, $J = 17.8$ Hz, 0.8 Hz, 1H), 5.82 (ddt, $J = 16.2$ Hz, 10.3 Hz, 8.1 Hz, 2H), 6.73 (dd, $J = 17.8$ Hz, 11.1 Hz, 1H), 7.41 (d, $J = 8.1$ Hz, 2H), 7.54 (d, $J = 8.1$ Hz, 2H); ^{13}C NMR (67.5 MHz, CDCl_3) δ 18.36, 21.21, 59.25, 114.55, 114.75, 125.54, 133.05, 134.27, 134.62, 136.72, 138.81; FAB-HRMS m/z calcd for $\text{C}_{16}\text{H}_{23}\text{OSi}$ ($\text{M}+\text{H}^+$): 259.1518; found 259.1512.

Coupling reaction of molecular building blocks with coupling partners

Sonogashira–Hagihara coupling reaction giving 1-diallylethoxysilyl-4-(trimethylsilylethynyl)-benzene (4a) (Table 2.3, entry 1). To a mixture of $\text{Pd}_2(\text{dba})_3$ (82 mg, 0.14 mmol), PPh_3 (152 mg, 0.58 mmol), and CuI (50 mg, 0.26 mmol) were added a solution of trimethylsilylacetylene (545 mL, 3.86 mmol) and **1a** (1.0 g, 3.21 mmol) in dry Et_3N (50 mL). The reaction mixture was stirred at 75 °C for 24 h. The reaction mixture was then diluted with Et_2O , washed with H_2O and brine, dried over anhydrous MgSO_4 , and concentrated. The residue was chromatographed on silica gel (eluent: hexane/ $\text{EtOAc} = 5:1$) to give **4a** (920 mg, 87% yield). ^1H NMR (270 MHz, CDCl_3) δ 0.249 (s, 9H), 1.20 (t, $J = 6.8$ Hz, 3H), 1.92 (d, $J = 8.1$ Hz, 4H), 3.78 (q, $J = 6.8$ Hz, 2H), 4.88–4.99 (m, 4H), 5.79 (ddt, $J = 16.2$ Hz, 9.5 Hz, 8.1 Hz, 2H), 7.45 (d, $J = 8.1$ Hz, 2H), 7.51 (d, $J = 8.1$ Hz, 2H); ^{13}C NMR (67.5 MHz, CDCl_3) δ -0.074, 18.36, 21.10, 59.34, 95.21, 104.97, 114.92, 124.39, 131.05, 132.81, 133.77, 135.78; FAB-HRMS m/z calcd for $\text{C}_{19}\text{H}_{27}\text{OSi}_2$ ($\text{M}-\text{H}^+$): 327.1600; found 327.1606.

Suzuki–Miyaura coupling reaction giving 4-(diallylethoxysilyl)biphenyl (4b) (Table 2.3, entry 2). To a mixture of **1a** (152 mg, 0.49 mmol), Pd(PPh₃)₄ (16.9 mg, 0.015 mmol), K₂CO₃ (101 mg, 0.73 mmol), and phenylboronic acid (71.4 mg, 0.59 mmol) was added dry toluene (5 mL). The reaction mixture was stirred at 80 °C for 13 h. The reaction mixture was then diluted with Et₂O, which was filtered through a Celite plug, and the filter cake was rinsed with Et₂O. The combined filtrates were concentrated under reduced pressure. The residue was chromatographed on silica gel (eluent: hexane/EtOAc = 10:1) to give **4b** (91.2 mg, 61% yield). ¹H NMR (270 MHz, CDCl₃) δ 1.23 (t, *J* = 6.8 Hz, 3H), 1.97 (d, *J* = 7.8 Hz, 4H), 3.80 (q, *J* = 6.8 Hz, 2H), 4.93 (ddt, *J* = 9.7 Hz, 1.4 Hz, 1.1 Hz, 2H), 4.99 (ddt, *J* = 15.9 Hz, 1.4 Hz, 0.5 Hz, 2H), 5.86 (ddt, *J* = 15.9 Hz, 9.7 Hz, 7.8 Hz, 2H), 7.36 (t, *J* = 7.0 Hz, 1H), 7.45 (t, *J* = 7.0 Hz, 2H), 7.60–7.68 (m, 6H); ¹³C NMR (67.5 MHz, CDCl₃) δ 18.38, 21.24, 59.29, 114.78, 126.46, 127.10, 127.45, 128.73, 133.09, 133.75, 134.49, 140.83, 142.43; FAB-HRMS *m/z* calcd for C₂₀H₂₃OSi (M–H⁺): 307.1518; found 307.1526; Anal. Calcd for C₂₀H₂₄OSi: C, 77.87; H, 7.84. Found: C, 77.62; H, 8.03.

Buchwald–Hartwig amination giving 4-diallylethoxysilyl-*N,N*-diphenylaniline (4c) (Table 2.3, entry 3). To a mixture of **1a** (486 mg, 1.56 mmol), Pd₂(dba)₃ (21.5 mg, 0.023 mmol), JohnPhos (42.0 mg, 0.14 mmol), NaOt-Bu (225 mg, 2.34 mmol), and diphenylamine (317 mg, 1.87 mmol) was added dry toluene (15 mL). The reaction mixture was stirred at 80 °C for 19 h. The reaction mixture was then diluted with Et₂O, which was filtered through a Celite plug, and the filter cake was rinsed with Et₂O. The combined filtrates were concentrated under reduced pressure. The residue was chromatographed on silica gel (eluent: hexane/EtOAc = 5:1) to give **4c** (384 mg, 62% yield). ¹H NMR (270 MHz, CDCl₃) δ 1.20 (t, *J* = 7.0 Hz, 3H), 1.92 (d, *J* = 8.1 Hz, 4H), 3.77 (q, *J* = 7.0 Hz, 2H), 4.90–5.00 (m, 4H), 5.77–5.93 (m, 2H), 7.03 (d, *J* = 8.1 Hz, 2H), 7.02–7.13 (m, 6H), 7.25 (d, *J* = 8.1 Hz, 2H), 7.28 (d, *J* = 8.1 Hz, 2H), 7.41 (d, *J* = 8.1 Hz, 2H); ¹³C NMR (67.5 MHz, CDCl₃) δ 18.40, 21.34, 59.17, 114.58, 121.69, 123.28, 124.95, 127.30, 129.27, 133.37, 134.95, 147.33, 149.19; FAB-HRMS *m/z* calcd for C₂₆H₃₀ONSi (M+H⁺): 400.2097; found 400.2093.

Sonogashira–Hagihara coupling reaction giving 1-diallylethoxysilyl-4-(3-hydroxy-3-methyl-1-butynyl)benzene (4d) (Table 2.3, entry 4). To a mixture of **1b** (130 mg, 0.36 mmol), PdCl₂(PPh₃)₂ (10.2 mg, 0.015 mmol), and CuI (2.8 mg, 0.015 mmol) were added dry THF (3 mL), dry Et₃N (3 mL), and 2-methyl-3-butyn-2-ol (42 mL, 0.43 mmol). The reaction mixture was stirred at 50 °C for 1.5 h. The reaction mixture was then diluted with Et₂O, washed with H₂O and brine, dried over

anhydrous MgSO_4 , and concentrated. The residue was chromatographed on silica gel (eluent: hexane/EtOAc = 5:1) to give **4d** (114 mg, 100% yield). ^1H NMR (270 MHz, CDCl_3) δ 1.20 (t, J = 7.0 Hz, 3H), 1.62 (s, 6H), 1.92 (d, J = 8.1 Hz, 4H), 2.09 (s, 1H), 3.76 (q, J = 7.0 Hz, 2H), 4.89–4.96 (m, 4H), 5.71–5.87 (m, 2H), 7.41 (d, J = 8.1 Hz, 2H), 7.51 (d, J = 8.1 Hz, 2H); ^{13}C NMR (67.5 MHz, CDCl_3) δ 18.33, 21.08, 31.42, 59.32, 65.57, 82.03, 94.71, 114.91, 124.02, 130.74, 132.79, 133.81, 135.44; FAB-HRMS m/z calcd for $\text{C}_{19}\text{H}_{25}\text{O}_2\text{Si}$ ($\text{M}-\text{H}^+$): 313.1624; found 313.1624.

Suzuki–Miyaura coupling reaction giving 4-diallylethoxysilyl-4'-methoxybiphenyl (4e) (Table 2.3, entry 5). To a mixture of **1b** (187 mg, 0.52 mmol), $\text{Pd}(\text{PPh}_3)_4$ (18.1 mg, 0.016 mmol), K_2CO_3 (108 mg, 0.78 mmol), and 4-methoxyphenylboronic acid (95.2 mg, 0.63 mmol) was added dry toluene (5 mL). The reaction mixture was stirred at 80 °C for 13 h. The reaction mixture was then diluted with Et_2O , which was filtered through a Celite plug, and the filter cake was rinsed with Et_2O . The combined filtrates were concentrated under vacuum to give a residue. The residue was chromatographed on silica gel (eluent: hexane/EtOAc = 10:1) to give **4e** (157.3 mg, 89% yield). ^1H NMR (270 MHz, CDCl_3) δ 1.23 (t, J = 6.8 Hz, 3H), 1.97 (d, J = 8.1 Hz, 4H), 3.79 (q, J = 6.8 Hz, 2H), 3.86 (s, 3H), 4.93 (ddt, J = 9.5 Hz, 1.4 Hz, 0.8 Hz, 2H), 4.98 (ddt, J = 17.3 Hz, 1.4 Hz, 1.1 Hz, 2H), 5.86 (ddt, J = 17.3 Hz, 9.5 Hz, 8.1 Hz, 2H), 6.99 (d, J = 8.4 Hz, 2H), 7.55 (d, J = 8.4 Hz, 2H), 7.57 (d, J = 7.6 Hz, 2H), 7.63 (d, J = 7.6 Hz, 2H); ^{13}C NMR (67.5 MHz, CDCl_3) δ 18.38, 21.24, 55.22, 59.25, 114.17, 114.73, 125.98, 128.09, 132.94, 133.14, 133.28, 134.47, 141.99, 159.27; FAB-HRMS m/z calcd for $\text{C}_{21}\text{H}_{26}\text{O}_2\text{Si}$ (M^+): 338.1702; found 338.1707; Anal. Calcd for $\text{C}_{21}\text{H}_{26}\text{O}_2\text{Si}$: C, 74.51; H, 7.74. Found: C, 74.38; H, 7.87.

Suzuki–Miyaura coupling reaction giving 4e (Table 2.3, entry 6). To a mixture of **1c** (150 mg, 0.39 mmol), $\text{Pd}(\text{PPh}_3)_4$ (13.6 mg, 0.012 mmol), K_2CO_3 (81.7 mg, 0.59 mmol), and 4-methoxyphenylboronic acid (71.9 mg, 0.47 mmol) was added dry toluene (5 mL). The reaction mixture was stirred at 80 °C for 16 h. The reaction mixture was then diluted with Et_2O , which was filtered through a Celite plug, and the filter cake was rinsed with Et_2O . The combined filtrates were concentrated under vacuum to give a residue. The residue was chromatographed on silica gel (eluent: hexane/EtOAc = 10:1) to give **4e** (101.7 mg, 76% yield).

Grignard cross-coupling reaction giving 2-[4-(diallylethoxysilyl)phenyl]pyridine (4f) (Table 2.3, entry 7). To a solution of **1b** (240 mg, 0.67 mmol) in dry THF (2 mL) was added a solution of *i*-PrMgCl (0.70 mL, 2.0 M in THF, 1.40 mmol) at –30 °C. The reaction mixture was stirred at

–30 °C for 2 h to give a THF solution of **2a**. To a solution of Pd₂(dba)₃ (25.6 mg, 0.028 mmol), dppf (15.5 mg, 0.028 mmol), and 2-bromopyridine (54.4 mL, 0.56 mmol) in dry THF (3 mL) was added a THF solution of **2a** at –30 °C. The reaction mixture was stirred at –30 °C for 17 h. The reaction mixture was then quenched with saturated NH₄Cl aqueous solution and extracted with Et₂O. The organic layer was dried over anhydrous MgSO₄ and concentrated. The residue was chromatographed on silica gel (eluent: hexane/EtOAc = 3:1) to give **4f** (158 mg, 91% yield). ¹H NMR (270 MHz, CDCl₃) δ 1.22 (t, *J* = 7.0 Hz, 3H), 1.97 (d, *J* = 8.4 Hz, 4H), 3.79 (q, *J* = 7.0 Hz, 2H), 4.92 (ddt, *J* = 10.0 Hz, 1.9 Hz, 0.8 Hz, 2H), 4.98 (ddt, *J* = 16.2 Hz, 1.9 Hz, 1.4 Hz, 2H), 5.84 (ddt, *J* = 16.2 Hz, 10.0 Hz, 8.4 Hz, 2H), 7.33 (dt, *J* = 5.1 Hz, 0.5 Hz, 1H), 7.69 (d, *J* = 8.4 Hz, 2H), 7.73–7.80 (m, 2H), 8.00 (d, *J* = 8.4 Hz, 2H), 8.71 (dt, *J* = 5.1 Hz, 0.8 Hz, 1H); ¹³C NMR (67.5 MHz, CDCl₃) δ 18.35, 21.16, 59.30, 114.95, 120.62, 122.25, 126.00, 132.96, 134.55, 135.82, 136.69, 140.55, 149.68, 157.20; FAB-HRMS *m/z* calcd for C₁₉H₂₄ONSi (M+H⁺): 310.1627; found 310.1635; Anal. Calcd for C₁₉H₂₃ONSi: C, 73.74; H, 7.49; N, 4.53. Found: C, 74.19; H, 7.84; N, 4.02.

Migita–Kosugi–Stille coupling reaction giving 4f (Table 2.3, entry 8). To a mixture of 2-bromopyridine (74.8 mg, 0.473 mmol), **2c** (205 mg, 0.521 mmol), Pd(PPh₃)₄ (31.9 mg, 0.0276 mmol), and LiCl (64.6 mg, 1.52 mmol) was added dry toluene (3 mL). The reaction mixture was refluxed for 1 h, diluted with Et₂O, and treated successively with water. The reaction mixture was extracted with Et₂O, washed with water, saturated NaHCO₃ aqueous solution, and brine. The organic layer was dried over anhydrous MgSO₄ and concentrated. The residue was chromatographed on silica gel (eluent: hexane/EtOAc = 3:1) to give the desired **4f** (73.5 mg, 50% yield) with (diallylethoxysilyl)benzene (7.9 mg, 7%) and 4,4'-bis(diallylethoxysilyl)-1,1'-biphenyl (10.9 mg, 1%) as byproducts.

Suzuki–Miyaura coupling reaction giving 4e (Table 2.3, entry 9). To a mixture of **2b** (200 mg, 0.558 mmol), 4-iodoanisole (109 mg, 0.465 mmol), silver carbonate (154 mg, 0.558 mmol), and Pd(PPh₃)₄ (16.0 mg, 0.014 mmol) was added dry THF (5 mL). The reaction mixture was stirred at 60 °C for 24 h, diluted with ether, and filtered through a Celite plug. The filter cake was rinsed with ether. The combined filtrates were concentrated in vacuo and the residue was chromatographed on silica gel (eluent: hexane/EtOAc = 3:1) to give **4e** (134 mg, 89% yield).

Buchwald–Hartwig amination giving *N*-[4-(diallylethoxysilyl)phenyl](4-methylphenyl)-

amine (4g) (Table 2.3, entry 10). To a mixture of **3b** (254 mg, 1.0 mmol), Pd₂(dba)₃ (4.3 mg, 4.7 μmol), 4-iodotoluene (204 mg, 0.94 mmol), JohnPhos (8.4 mg, 28 μmol), and NaOt-Bu (135 mg, 1.4 mmol) was added dry toluene (7 mL). The reaction mixture was stirred at room temperature for 18 h. The reaction mixture was diluted with Et₂O, which was filtered through a Celite plug, and the filter cake was rinsed with Et₂O. The combined filtrates were concentrated under vacuum to give a residue. The residue was chromatographed on silica gel (eluent: hexane/EtOAc = 3:1) to give **4g** (242 mg, 77% yield). ¹H NMR (270 MHz, CDCl₃) δ 1.20 (t, *J* = 6.8 Hz, 3H), 1.91 (d, *J* = 8.1 Hz, 4H), 2.32 (s, 3H), 3.95 (q, *J* = 6.8 Hz, 2H), 4.90 (dd, *J* = 10.0 Hz, 1.1 Hz, 2H), 4.96 (dd, *J* = 16.5 Hz, 1.1 Hz, 2H), 5.70 (br, 1H), 5.85 (ddt, *J* = 16.5 Hz, 10.0 Hz, 8.1 Hz, 2H), 6.98 (d, *J* = 8.4 Hz, 2H), 7.04 (d, *J* = 8.6 Hz, 2H), 7.11 (d, *J* = 8.6 Hz, 2H), 7.43 (d, *J* = 8.4 Hz, 2H); ¹³C NMR (67.5 MHz, CDCl₃) δ 18.40, 20.72, 21.37, 59.11, 114.47, 115.13, 119.95, 124.58, 129.85, 131.71, 133.50, 135.37, 139.21, 145.68; EI-HRMS *m/z* calcd for C₂₁H₂₇ONSi (M⁺): 337.1862; found 337.1863.

Preparation of functional sol–gel precursors with molecular building blocks

Sonogashira–Hagihara coupling reaction giving (S)-5,5'-bis[4-(diallylethoxysilyl)phenylethynyl]-2,2'-bis(diphenylphosphinyl)-1,1'-binaphthyl (5a). To a solution of (S)-5,5'-bis(trimethylsilylethynyl)-2,2'-bis(diphenylphosphinyl)-1,1'-binaphthyl (301 mg, 0.355 mmol) in dry CH₂Cl₂ (12 mL) was added a solution of TBAF (0.78 mL, 1.0 M in CH₂Cl₂, 0.781 mmol) and the mixture was stirred at room temperature for 2 h. Solvent was removed under reduced pressure and the residue was chromatographed on silica gel (eluent: hexane/EtOAc = 1:3) to give (S)-5,5'-diethynyl-2,2'-bis(diphenylphosphinyl)-1,1'-binaphthyl (218.4 mg, 88%). ¹H NMR (270 MHz, CDCl₃) δ 3.46 (s, 2H), 6.66–6.74 (m, 4H), 7.21–7.43 (m, 16H), 7.49–7.60 (m, 4H), 7.66–7.74 (m, 4H), 8.39–8.43 (dd, *J* = 8.6 Hz, 2.4 Hz, 2H); ³¹P NMR (CDCl₃, 109 Hz) δ 28.48. To a solution of resulting acetylene (166.8 mg, 0.237 mmol) in dry benzene (8 mL) was added a solution of **1b** (211.1 mg, 0.589 mmol), PdCl₂(PPh₃)₂ (17.5 mg, 0.025 mmol), and CuI (4.8 mg, 0.025 mmol) in dry benzene (1 mL). The reaction mixture was stirred at 50 °C for 23 h. Solvent was removed under reduced pressure and the residue was chromatographed on silica gel (eluent: hexane/EtOAc = 1:1) to give **5a** (201.2 mg, 71% yield). [α]_D²⁰ -225 (*c* 0.60, CHCl₃); ¹H NMR (270 MHz, CDCl₃) δ 1.24 (t, *J* = 6.8 Hz, 6H), 1.97 (d, *J* = 8.1 Hz, 8H), 3.80 (q, *J* = 6.8 Hz, 4H), 4.93–5.01 (m, 8H), 5.76–5.89 (m, 4H), 6.73 (d, *J* = 4.3 Hz, 4H), 7.25–7.45 (m, 16H), 7.52–7.62 (m,

12H), 7.70–7.78 (m, 4H), 8.49–8.53 (dd, $J = 8.6, 2.4$ Hz, 2H); ^{13}C NMR (67.5 MHz, CDCl_3) δ 18.38, 21.11, 59.37, 88.25, 94.57; ^{31}P NMR (109 MHz, CDCl_3) δ 28.68; FAB-HRMS m/z calcd for $\text{C}_{76}\text{H}_{69}\text{O}_4\text{Si}_2\text{P}_2$ ($\text{M}+\text{H}^+$): 1163.4210; found 1163.4209.

Sonogashira–Hagihara coupling reaction giving bis[4-[4-(diallylethoxysilyl)phenylethynyl]phenyl]acetylene (5b). To a mixture of **1b** (75.7 mg, 0.21 mmol), $\text{PdCl}_2(\text{PPh}_3)_2$ (2.97 mg, 4.2 μmol), CuI (0.8 mg, 4.2 μmol), and 4,4'-(diethynylphenyl)acetylene (34.5 mg, 0.15 mmol) was added dry THF (5 mL) and dry Et_3N (1 mL). The reaction mixture was stirred at 50 °C for 15 h. The reaction mixture was diluted with Et_2O and then the organic layer was washed with brine, dried over anhydrous MgSO_4 , and concentrated under reduced pressure. The residue was chromatographed on silica gel (eluent: hexane/ $\text{EtOAc} = 10:1$) to give **5b** (68.1 mg, 94% yield). ^1H NMR (270 MHz, CDCl_3) δ 1.23 (t, $J = 7.0$ Hz, 6H), 1.95 (d, $J = 8.1$ Hz, 8H), 3.79 (q, $J = 7.0$ Hz, 4H), 4.91–4.99 (m, 8H), 5.82 (ddt, $J = 16.2$ Hz, 9.7 Hz, 8.1 Hz, 4H), 7.52 (s, 8H), 7.53 (d, $J = 8.1$ Hz, 4H), 7.58 (d, $J = 8.1$ Hz, 4H); ^{13}C NMR (67.5 MHz, CDCl_3) δ 18.38, 21.11, 59.37, 89.96, 90.98, 91.33, 114.96, 122.89, 123.19, 124.27, 130.72, 131.54, 131.59, 132.81, 133.94, 135.85; FAB-HRMS m/z calcd for $\text{C}_{46}\text{H}_{47}\text{O}_2\text{Si}_2$ ($\text{M}+\text{H}^+$): 687.3115; found 687.3105; Anal. Calcd for $\text{C}_{46}\text{H}_{46}\text{O}_2\text{Si}_2$: C, 80.42; H, 6.75. Found: C, 80.02; H, 6.31.

Buchwald–Hartwig amination giving N,N' -bis[4-(diallylethoxysilyl)phenyl]benzidine (5c). To a mixture of **3a** (505 mg, 2.0 mmol) and 4,4'-diiodobiphenyl (378 mg, 0.94 mmol), $\text{Pd}_2(\text{dba})_3$ (25 mg, 0.027 mmol), JohnPhos (49.5 mg, 0.17 mmol), and NaOt-Bu (267 mg, 2.8 mmol) was added dry toluene (7 mL). The reaction mixture was stirred at room temperature for 18 h. The reaction mixture was diluted with Et_2O , which was filtered through a Celite plug, and the filter cake was rinsed with Et_2O . The combined filtrates were concentrated under reduced pressure. The residue was chromatographed on silica gel (eluent: hexane/ $\text{EtOAc} = 3:1$) to give **5c** (430 mg, 72%): ^1H NMR (270 MHz, CDCl_3) δ 1.21 (t, $J = 7.0$ Hz, 6H), 1.93 (d, $J = 8.1$ Hz, 8H), 3.76 (q, $J = 7.0$ Hz, 4H), 4.89–5.00 (m, 8H), 5.78–5.94 (m, 6H), 7.08 (d, $J = 8.6$ Hz, 4H), 7.17 (d, $J = 8.6$ Hz, 4H), 7.48 (d, $J = 8.6$ Hz, 4H), 7.50 (d, $J = 8.6$ Hz, 4H); ^{13}C NMR (67.5 MHz, CDCl_3) δ 18.41, 21.37, 59.17, 114.57, 116.0, 119.11, 125.54, 127.38, 133.43, 134.16, 135.42, 140.93, 144.77; FAB-HRMS m/z calcd for $\text{C}_{40}\text{H}_{48}\text{O}_2\text{N}_2\text{Si}_2$ (M^+): 644.3254; found 644.3246.

2.2.3 Results and Discussion

Preparation of molecular building blocks for allylsilane sol–gel precursors

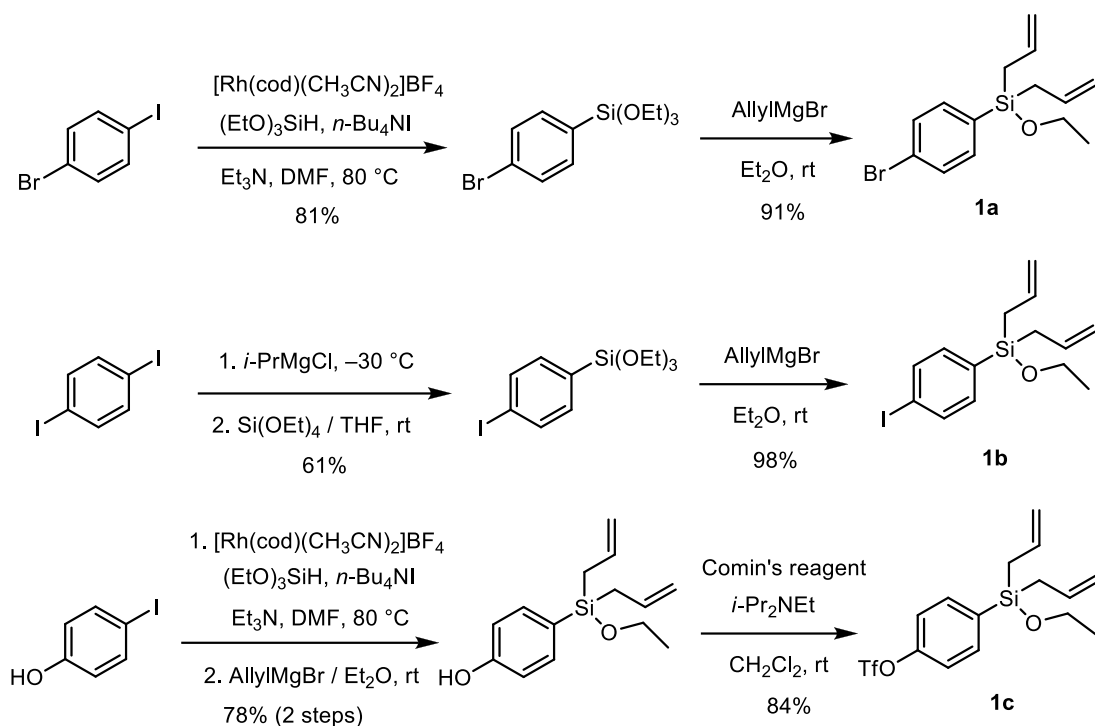
The use of a diallylethoxysilyl group as a polymerizable moiety in allylsilyl sol–gel precursors is not only more effective for sol–gel polymerization, but also confers stability under general hydrolysis conditions. The author focused on diallylethoxysilyl sol–gel precursors as promising precursors of organic–inorganic hybrid materials. MBAS **1**, **2**, and **3** contain both a diallylethoxysilyl group to form Si–O–Si bonds by polymerization under sol–gel conditions, and a halogen, metal, or functional group which is active toward cross-coupling reactions to give the desired sol–gel precursors (Scheme 2.4).

Halogen building blocks **1** were synthesized by trialkoxysilylation of aryl halides followed by the addition of allylmagnesium bromide (AllylMgBr) to transform the alkoxy group into the diallylethoxysilyl group (Scheme 2.5). Rhodium-catalyzed triethoxysilylation⁴ of 1-bromo-4-iodobenzene with triethoxysilane gave selectively 1-bromo-4-(triethoxysilyl)benzene in 81% yield. The triethoxysilyl group was transformed into diallylethoxysilyl group by the addition of AllylMgBr to afford bromide building block **1a** in 91% yield. It is noteworthy that the allylation of the triethoxysilyl group is completely converted to the diallylethoxysilyl group even using excess amounts of AllylMgBr. Grignard-exchange reaction of 1,4-diiodobenzene with isopropylmagnesium chloride (*i*-PrMgCl)⁵ followed by the addition of tetraethyl orthosilicate (TEOS) gave 1-iodo-4-(triethoxysilyl)benzene in 61% yield. Subsequent treatment with AllylMgBr afforded iodide building block **1b** in 98% yield. The iodide group was perfectly remained unchanged during the allylation. Triflate building block **1c** was prepared by rhodium-catalyzed triethoxysilylation of 4-iodophenol with triethoxysilane followed by the addition of AllylMgBr and trifluoromethanesulfonylation using Comins' reagent⁶ in total yield of 66% yield.

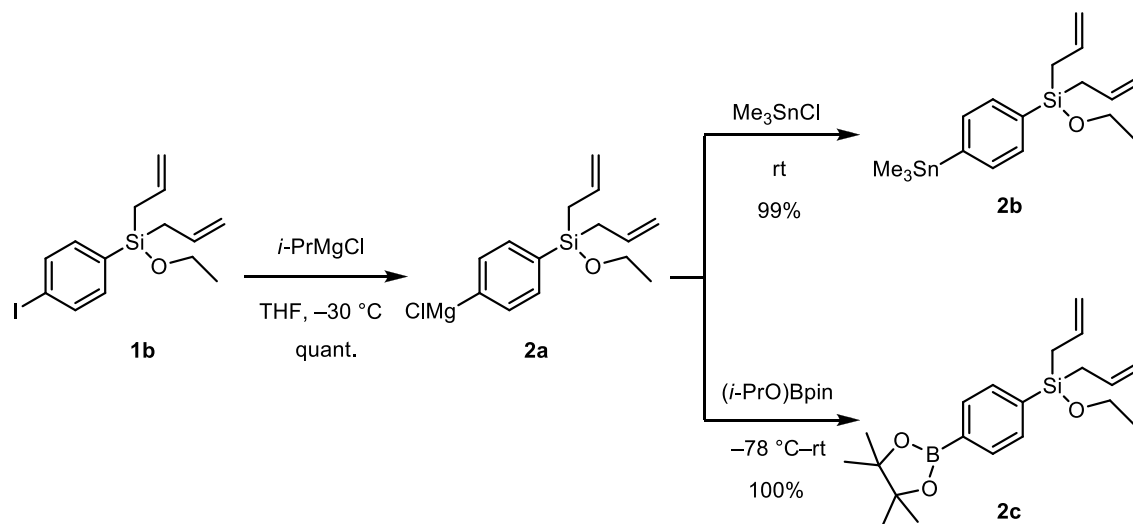
⁴ Murata, M.; Ishikura, M.; Nagata, M.; Watanabe, S.; Masuda, Y. *Org. Lett.* **2002**, *4*, 1843–1845.

⁵ Knochel, P.; Dohle, W.; Gommermann, N.; Kneisel, F. F.; Kopp, F.; Korn, T.; Sapountzis, I.; Vu, V. A. *Angew. Chem., Int. Ed.* **2003**, *42*, 4302–4320.

⁶ Comins, D. L.; Dehghani, A. D.; Foti, C. J.; Joseph, S. P. *Org. Synth.* **1997**, *74*, 77–80.



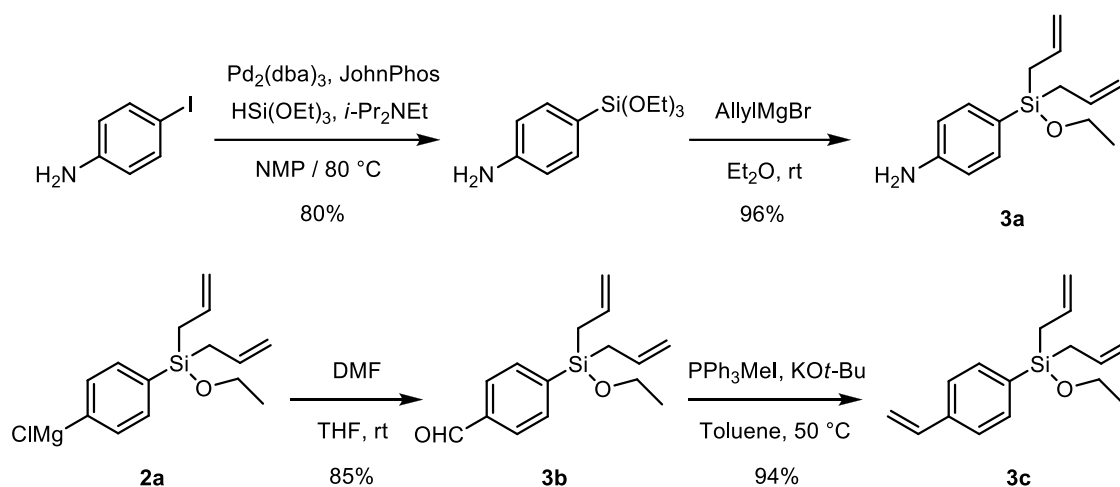
Scheme 2.5. Preparation of molecular building blocks containing bromide (**1a**), iodide (**1b**), and triflate group (**1c**).



Scheme 2.6. Preparation of molecular building blocks containing magnesium (**2a**), stannyl (**2b**), and boryl group (**2c**).

Preparation of metal building blocks **2** starting from halogen building blocks **1a** and **1b** via lithiation with n -butyllithium and Grignard reagent formation using magnesium metal were unsuccessful. These reactions resulted in formation of n -butyl adducts and complex mixture.

However, a Grignard-exchange reaction of **1b** with *i*-PrMgCl was successfully gave magnesium building block **2a** (Scheme 2.6). Surprisingly, diallylethoxysilyl group is compatible with the use of *i*-PrMgCl and the coexistence of Grignard reagent moiety in **2a**. The treatment of magnesium building block **2a** with trimethyltin chloride (Me₃SnCl) and 2-isopropoxy-4,4,5,5-tetramethyl-1,3,2-dioxaborolane ((*i*-PrO)Bpin)⁷ afforded stannyl building block **2c** and boryl building block **2b** in 99% and 100% yields for two steps, respectively (Scheme 2.6). It is noteworthy that a variety of aryl halides can be used for coupling partners of **2** in palladium-catalyzed cross-coupling reactions.



Scheme 2.7. Preparation of molecular building blocks containing amino (**3a**), formyl (**3b**), and vinyl groups (**3c**).

Functional building blocks **3** were synthesized according to Scheme 2.7. Palladium-catalyzed triethoxysilylation⁸ of 4-iodoaniline with triethoxysilane in the presence of Pd₂(dba)₃ and (*o*-biphenyl)P(*t*-Bu)₂ (JohnPhos) gave 4-(triethoxysilyl)aniline in 80% yield. The triethoxysilyl group was transformed into diallylethoxysilyl group by using excess amount of AllylMgBr to avoid the quenching by reactive amino group, affording amino building block **3a** in 96% yield. A nucleophilic addition of magnesium building block **2a** to DMF gave formyl building block **3b** in 85% yield. The obtained **3b** was further transformed into vinyl building block **3c** by Wittig olefination with methyltriphenylphosphonium iodide in 94% yield,⁹ which can be useful for the

⁷ Suginome, M.; Matsuda, T.; Ito, Y. *Organometallics* **2000**, *19*, 4647–4649.

⁸ Manoso, A. S.; DeShong, P. *J. Org. Chem.* **2001**, *66*, 7449–7455.

⁹ Wittig, G.; Schöllkopf, U. *Chem. Ber.* **1954**, *87*, 1318–1330.

Mizoroki–Heck reaction.¹⁰

Cross-coupling reactions of molecular building blocks with various coupling partners

Palladium-catalyzed cross-coupling reactions between MBAS and various coupling partners were carried out, and the results are summarized in Table 2.3. The diallylethoxysilyl group was retained unchanged over the course of all reactions. Sonogashira–Hagihara coupling reaction¹¹ between

Table 2.3. Palladium-catalyzed cross-coupling reactions between MBAS and coupling partners.

Building block
Coupling partner
Product

Entry	Building block	Coupling partner	Product	Yield / % ^b
1	 1a		 4a	87
2	 1a		 4b	61
3	 1a		 4c	62
4	 1b		 4d	100

^a Isolated yield.

¹⁰ a) Mizoroki, T.; Mori, K.; Ozaki, A. *Bull. Chem. Soc. Jap.* **1971**, *44*, 581–581; b) Heck, R. F.; Nolley, J. P. *J. Org. Chem.* **1972**, *37*, 2320–2322.

¹¹ a) Sonogashira, K.; Tohda, Y.; Hagihara, N. *Tetrahedron Lett.* **1975**, *50*, 4467–4470.; b) Chanteau, S. H.; Tour, J. M. *J. Org. Chem.* **2003**, *68*, 8750–8766.

Table 2.3. Continued.

Pd-catalyzed cross-coupling reactions

Entry	Building block	Coupling partner	Product	Yield / % ^b
5	1b		4e	89
6	1c		4e	76
7	2a		4f	91
8	2c		4f	50
9	2b		4e	89
10	3a		4g	77

^a Isolated yield.

bromide **1a** and trimethylsilylacetylene proceeded in the presence of Pd₂(dba)₃, PPh₃, and CuI in triethylamine at 75 °C for 24 h to give product **4a** in 87% yield (Table 2.3, entry 1). Bromide **1a** could also be used for Suzuki–Miyaura coupling reaction¹² with phenylboronic acid and Buchwald–Hartwig amination¹³ with diphenylamine and the corresponding coupling products **4b**

¹² Miyaura, N.; Suzuki, A. *Chem. Rev.* **1995**, *95*, 2457–2483.¹³ Wolfe, J. P.; Tomori, H.; Sadighi, J. P.; Yin, J.; Buchwald, S. L. *J. Org. Chem.* **2000**, *65*, 1158–1174.

and **4c** were obtained in 61% and 62% yield, respectively (Table 2.3, entries 2 and 3). Iodide **1b** is reactive building block for Sonogashira–Hagihara coupling reaction with 2-methyl-3-butyn-2-ol and Suzuki–Miyaura coupling reaction with 4-methoxyphenylboronic acid in the presence of palladium catalyst to give the corresponding coupling products **4d** and **4e** in high yields (Table 2.3, entries 4 and 5). Triflate **1c** can also be used for Suzuki–Miyaura coupling reaction with 4-methoxyphenylboronic acid to afford product **4e** in 76% yield (Table 2.3, entry 6).

The molecular building blocks containing magnesium chloride (**2a**) smoothly underwent palladium-catalyzed Grignard cross-coupling¹⁴ between 2-bromopyridine in the presence of Pd₂(dba)₃ and dppf at –30 °C to give 2-phenylpyridine derivative containing a diallylethoxysilyl group (**4f**) in 91% yield (Table 2.3, entry 7). Allylsilane precursor **4f** can also be prepared by Migita–Kosugi–Stille coupling reaction¹⁵ between stannyl **2b** and 2-bromopyridine in 50% yield along with formation of (diallylethoxysilyl)benzene (7%) and 4,4'-bis(diallylethoxysilyl)-1,1'-biphenyl (1%) as byproduct (Table 2.3, entry 8). Suzuki–Miyaura coupling between boryl ester **2c** and 4-iodoanisole proceeded efficiently in the presence of Pd(PPh₃)₄ and silver carbonate in THF to give product **4e** in 89% yield (Table 2.3, entry 9). Amine building block **3a** can be used for Buchwald–Hartwig amination with 4-iodotoluene and the corresponding coupling product **4g** was obtained in 77% yield (Table 2.3, entry 10).

Palladium-catalyzed cross-coupling reactions between MBAS and coupling partners bearing two functional groups could be utilized for broadly applicable synthesis for bridged sol–gel precursors. Chiral BINAP-bridged sol–gel precursor **5a** was synthesized by Sonogashira–Hagihara coupling between iodide **1b** and 5,5'-diethynyl-BINAP dioxide¹⁶ in 71% yield (Scheme 2.8). Oligo(phenyleneethynylene)-bridged sol–gel precursor **5b** was also obtained by Sonogashira–Hagihara coupling between iodide **1b** and 4,4'-diethynyltolan¹⁷ in 94% yield (Scheme 2.9). Buchwald–Hartwig amination between **3a** and 4,4'-diiodobiphenyl gave benzidine derivative **5c** in 72% yield (Scheme 2.10). The author convinced that a synthetic method using MBAS would, in addition to its wide application to easy preparation of functionally bridged sol–gel precursors, open

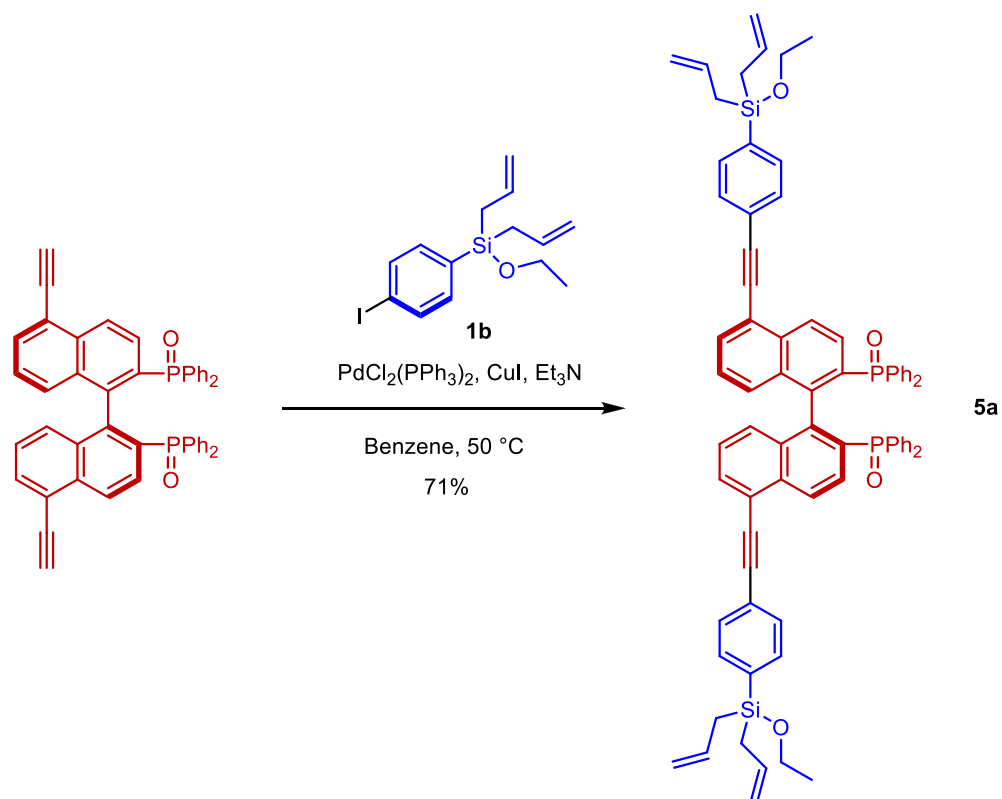
¹⁴ Bonnet, V.; Mongin, F.; Trecourt, F.; Queguiner, G.; Knochel, P. *Tetrahedron Lett.* **2001**, *42*, 5717–5719.

¹⁵ Schwab, P. F. H.; Fleischer, F.; Michl, J. *J. Org. Chem.* **2002**, *67*, 443–449.

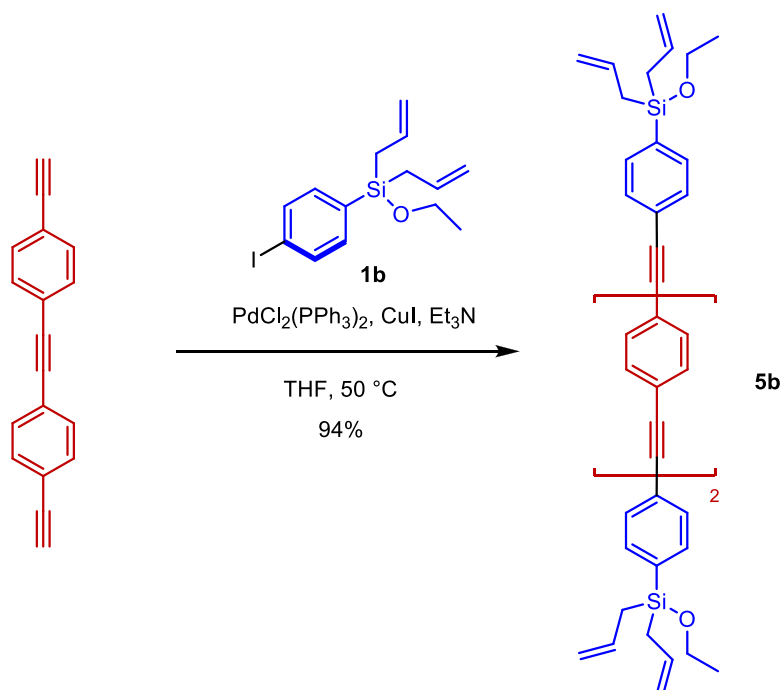
¹⁶ Shimada, T.; Suda, M.; Nagano, T.; Kakiuchi, K. *J. Org. Chem.* **2005**, *70*, 10178–10181.

¹⁷ Simpson, C. D.; Brand, J. D.; Berresheim, A. J.; Przybilla, L.; Räder, H. J.; Müllen, K. *Chem.–Eur. J.* **2002**, *8*, 1424–1429.

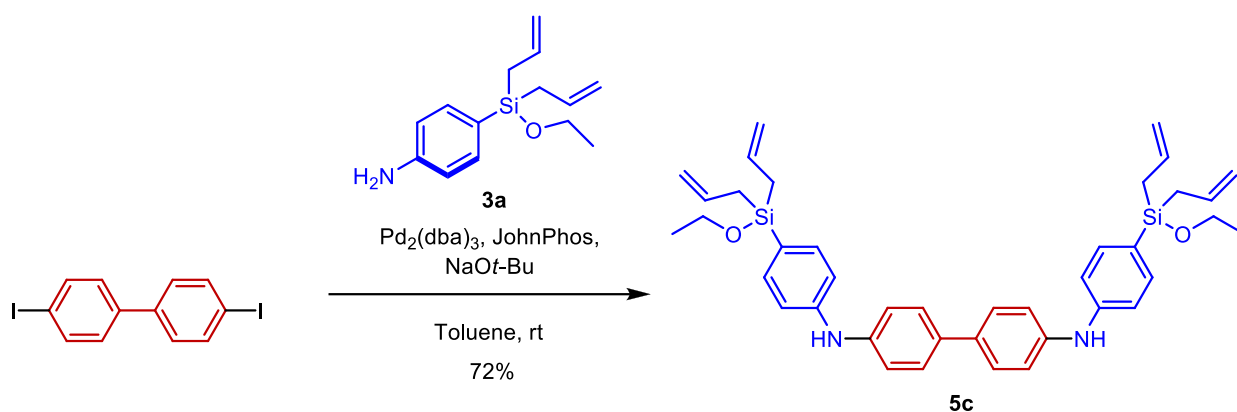
the door to a new branch of materials chemistry.



Scheme 2.8. Synthesis of chiral BINAP-bridged sol-gel precursor **5a**.



Scheme 2.9. Synthesis of oligophenylene-ethynylene-bridged sol-gel precursor **5b**.



Scheme 2.10. Synthesis of benzidine-bridged sol-gel precursor **5c**.

2.2.4 Conclusions

A variety type of molecular building blocks for allylsilyl sol-gel precursors (MBAS) was successfully synthesized. Palladium-catalyzed cross-coupling reactions between MBAS and coupling partners gave a various type of sol-gel precursors including bridged-type organoallylsilanes. This approach overcomes the limitations and problems associated with the use of conventional alkoxy-silyl groups, and thus can be applied as a general synthetic method for high functional sol-gel precursors toward functionalization of organic-inorganic hybrid materials.

2.3 Pd-catalyzed Coupling Reactions for Highly Functional Organic-bridged Alkoxysilanes

The author reports an efficient synthetic approach for well-designed organic-bridged alkoxysilanes, which allow the formation of highly functional organosilica hybrids under mild sol–gel conditions. A series of molecular building blocks containing a triisopropoxysilyl group were synthesized and used in cross-coupling reactions. The triisopropoxysilyl group showed a good tolerance for various organic transformations. 1,4-Diketo-3,6-dithienylpyrrolo[3,4-*c*]pyrrole-bridged triisopropoxysilane was successfully prepared, allowing rapid formation of organosilica hybrid without loss of functionality under mildly acidic conditions.

2.3.1 Introduction

Organosilica hybrid materials, such as periodic mesoporous organosilicas (PMOs)^{1,2} and bridged silsesquioxanes (BSQs)^{3,4} have received considerable attention in the fields of catalyst,⁵ adsorbents,⁶ and optical devices.⁷ These materials are typically prepared by acid- or base-catalyzed hydrolysis and polycondensation (sol–gel polymerization) of organic-bridged alkoxysilanes ($R[\text{Si}(\text{OR}')_3]_n$, $n \geq 2$, R: organic group, R': Me, Et). The hydrolyzable trimethoxysilyl ((MeO)₃Si) and triethoxysilyl ((EtO)₃Si) groups are most frequently used for alkoxysilane precursors because they are readily hydrolyzed and condensed under mildly acidic or basic conditions to form stable siloxane networks. However, the high reactivity of these alkoxysilyl groups has limited the design and synthesis of alkoxysilane precursors with highly functional organic groups (R) and caused formidable problems during work-up and purification using silica gel chromatography.⁸ Shimada et al. found that allylsilyl ($R[\text{Si}(\text{CH}_2\text{CH}=\text{CH}_2)_m(\text{OEt})_{3-m}]_n$; $m = 1-$

¹ Hoffmann, F.; Cornelius, M.; Morell, J.; Fröba, M. *Angew. Chem., Int. Ed.* **2006**, *45*, 3216–3251.

² Mizoshita, N.; Tani, T.; Inagaki, S. *Chem. Soc. Rev.* **2011**, *40*, 789–800.

³ Loy, D. A.; Shea, K. J. *Chem. Rev.* **1995**, *95*, 1431–1442.

⁴ Baney, R. H.; Itoh, M.; Sakakibara, A.; Suzuki, T. *Chem. Rev.* **1995**, *95*, 1409–1430.

⁵ Wight, A. P.; Davis, M. E. *Chem. Rev.* **2002**, *102*, 3589–3614.

⁶ Stein, A.; Melde, B. J.; Schrodin, R. C. *Adv. Mater.* **2000**, *12*, 1403–1419.

⁷ Sanchez, C.; Lebeau, B.; Chaput, F.; Boilot, J. P. *Adv. Mater.* **2003**, *15*, 1969–1994.

⁸ a) Murata, M.; Ishikura, M.; Nagata, M.; Watanabe, S.; Masuda, Y. *Org. Lett.* **2002**, *4*, 1843–1845; b) Marciniak, B. *Comprehensive Handbook on Hydrosilylation*; Pergamon: Oxford, United Kingdom, 1992; c)

3) groups behaved as the synthetic equivalent of alkoxy-silyl groups, and were stable enough to allow purification using silica gel chromatography.^{9,10} A series of molecular building blocks containing allylsilyl groups has been reported for synthesis of sol-gel precursors with highly functional organic groups via palladium-catalyzed coupling reactions.¹¹ However, the allylsilyl groups were hydrolyzed and condensed under harsher conditions, such as high temperatures or high concentrations of acid or base,^{12,13} or in the presence of expensive Lewis acids,¹⁴ which sometimes damaged the functional organic groups and/or caused undesired Si-C bond cleavage in the organosilane.¹⁵

Organosilanes with bulky alkoxy-silyl groups, such as isopropoxy-silyl have been used only to a limited extent to date, but have potential as ideal sol-gel precursors because of their medium stability and reactivity due to the steric bulk of the alkoxy group on the silicon atom.¹⁶ However, synthetic methodologies have been limited to alkoxy exchange reactions of unstable chlorosilanes and/or less bulky alkoxy-silanes.¹⁷ Here, the author reports the preparation of a series of molecular building blocks containing triisopropoxy-silyl ((*i*-PrO)₃Si) groups and the synthesis of highly functional organosilane precursors via cross-coupling reaction of the building blocks (Scheme 2.11). The triisopropoxy-silyl group was found to show a good tolerance for various organic transformations. The resulting organosilane precursor was successfully hydrolyzed and condensed to form an organosilica hybrid without loss of functionality under mildly acidic conditions.

Brethon, A.; Hesemann, P.; Rejaud, L.; Moreau, J. J. E.; Wong Chi Man, M. *J. Organomet. Chem.* **2001**, *627*, 239–248.

⁹ Shimada, T.; Aoki, K.; Shinoda, Y.; Nakamura, T.; Tokunaga, N.; Inagaki, S.; Hayashi, T. *J. Am. Chem. Soc.* **2003**, *125*, 4688–4689.

¹⁰ Kapoor, M. P.; Inagaki, S.; Ikeda, S.; Kakiuchi, K.; Suda, M.; Shimada, T. *J. Am. Chem. Soc.* **2005**, *127*, 8174–8178.

¹¹ Maegawa, Y.; Nagano, T.; Yabuno, T.; Nakagawa, H.; Shimada, T. *Tetrahedron* **2007**, *63*, 11467–11474.

¹² Waki, M.; Mizoshita, N.; Maegawa, Y.; Hasegawa, T.; Tani, T.; Shimada, T.; Inagaki, S. *Chem.–Eur. J.* **2012**, *18*, 1992–1998.

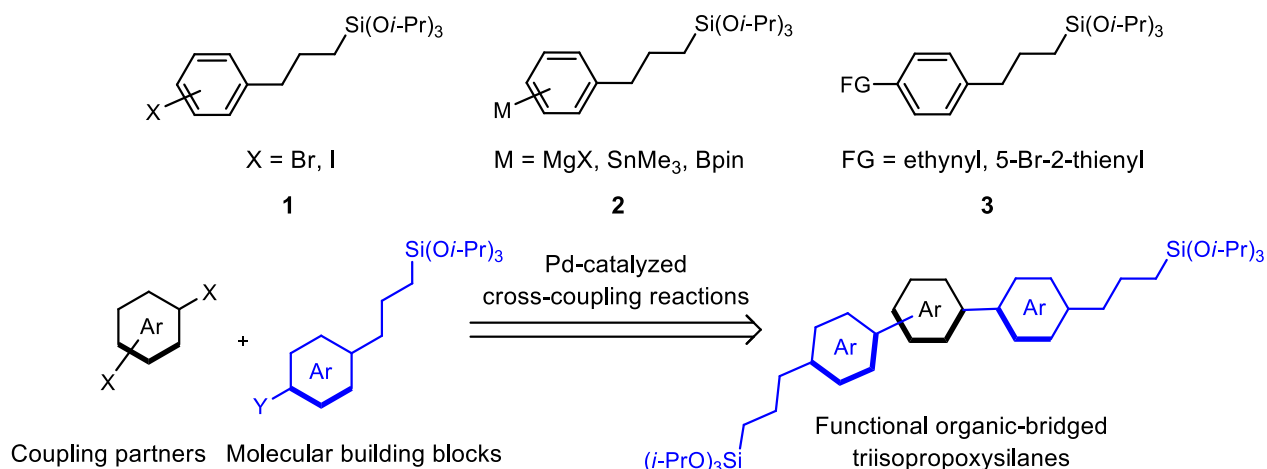
¹³ a) Tanaka, N.; Mizoshita, N.; Maegawa, Y.; Tani, T.; Inagaki, S.; Jorapur, Y. R.; Shimada, T. *Chem. Commun.* **2011**, 5025–5027; b) Maegawa, Y.; Mizoshita, N.; Tani, T.; Shimada, T.; Inagaki, S. *J. Mater. Chem.* **2011**, *21*, 14020–14024.

¹⁴ Yeon, Y.-R.; Park, Y. J.; Lee, J.-S.; Park, J.-W.; Kang, S.-G.; Jun, C.-H. *Angew. Chem., Int. Ed.* **2007**, *47*, 109–112.

¹⁵ Shirai, S.; Goto, Y.; Mizoshita, N.; Ohashi, M.; Tani, T.; Shimada, T.; Hyodo, S.; Inagaki, S. *J. Phys. Chem. A* **2010**, *114*, 6047–6054.

¹⁶ a) Brondani, D. J.; Corriu, R. J. P.; Ayoubi, S. E.; Moreau, J. J. E.; Wong Chi Man, M. *J. Organomet. Chem.* **1993**, *451*, C1–C3; b) Kuschel, A.; Polarz, S. *Adv. Funct. Mater.* **2008**, *18*, 1272–1280; c) Mizoshita, N.; Tani, T.; Shinokubo, H.; Inagaki, S. *Angew. Chem., Int. Ed.* **2012**, *51*, 1156–1160.

¹⁷ Cerveau, G.; Chappellet, S.; Corriu, R. J. P.; Dabiens, B. *J. Organomet. Chem.* **2001**, *626*, 92–99.



Scheme 2.11. Synthetic method for functional organic-bridged triisopropoxysilanes using molecular building blocks.

2.3.2 Experimental

Materials and methods

Unless otherwise noted, all materials, including dry solvents, were purchased from commercial suppliers (Sigma-Aldrich, Tokyo Chemical Industry Co., Ltd., and Wako Pure Chemical Industries Ltd.) and used without further purification. All reactions were carried out under argon using standard high vacuum and Schlenk-line techniques. Nuclear magnetic resonance (NMR) spectra were recorded on a Jeol JNM-EXC400P spectrometer (400 MHz for ^1H and 100 MHz for ^{13}C). Chemical shifts are reported in δ parts per million referenced to an internal SiMe_4 standard (δ 0.00) for ^1H NMR and chloroform-*d* (δ 77.0) for ^{13}C NMR, respectively. The following abbreviations were used to explain the multiplicities: s = singlet, d = doublet, t = triplet, q = quartet, sep = septet, m = multiplet, br = broad, dd = double doublet, dt = double triplet, ddd = doublet of double doublet, ddt = doublet of double triplet. Mass spectra were recorded on a Micromass GCT Premier mass spectrometer (FI: field ionization) and Micromass Q-TOF mass spectrometer (ESI: electrospray ionization). Ultraviolet-visible (UV-vis) absorption spectra were measured using a Jasco V-670 spectrometer.

Synthesis of allylhalobenzene derivatives

1-Allyl-4-bromobenzene. A 200 mL three-neck round bottom flask connected to a dropping funnel and dry argon flow was charged with a stir bar, 1,4-dibromobenzene (15.0 g, 63.6 mmol), and dry cyclopentyl methyl ether (CPME) (35 mL). The mixture was cooled to $-5\text{ }^{\circ}\text{C}$, and a solution of isopropylmagnesium chloride (*i*-PrMgCl) (12.7 mL, 2.0 M in THF, 25.4 mmol) and a solution of *n*-butyllithium (*n*-BuLi) (31.8 mL, 1.6 M in hexane, 50.9 mmol) were added dropwise over a period of 30 min, respectively. The reaction mixture was stirred for 4 h at $-5\text{ }^{\circ}\text{C}$. CuCN (285 mg, 3.18 mmol, 5 mol% Cu) was added at once, and the reaction mixture was stirred for 5 min at $-5\text{ }^{\circ}\text{C}$. Allyl bromide (10.8 mL, 127.7 mmol) was then added dropwise over a period of 30 min at $-5\text{ }^{\circ}\text{C}$. It was then allowed to reach room temperature and stirred for 15 h. The precipitated magnesium salt was filtered off and the resulting organic phase was extracted with Et₂O and washed with saturated NH₄Cl aqueous solution and brine and dried over anhydrous MgSO₄, filtered, and concentrated under reduced pressure. The resulting crude residue was purified by bulb-to-bulb distillation (150 Pa, 50 $^{\circ}\text{C}$) affording title compound as a transparent colorless liquid (12.2 g, 97% yield). ¹H NMR (400 MHz, CDCl₃) δ 3.33 (d, *J* = 6.8 Hz, 2H), 5.03–5.09 (m, 2H), 5.87–5.97 (m, 1H), 7.05 (d, *J* = 8.4 Hz, 2H), 7.40 (t, *J* = 8.4 Hz, 2H). The same procedure was followed for the synthesis of 1-allyl-3-bromobenzene as described below.

1-Allyl-3-bromobenzene. Transparent colorless liquid. Yield: 93%. Bp: 150 Pa, 50 $^{\circ}\text{C}$. ¹H NMR (400 MHz, CDCl₃) δ 3.35 (d, *J* = 6.8 Hz, 2H), 5.06–5.11 (m, 2H), 5.87–5.97 (m, 1H), 7.10–7.17 (m, 2H), 7.31–7.34 (m, 2H); ¹³C NMR (100 MHz, CDCl₃) δ 39.7, 116.5, 122.4, 127.2, 129.1, 129.9, 131.6, 136.4, 142.3.

1-Allyl-3,5-dibromobenzene. A 500 mL three-neck round-bottom flask connected to a dropping funnel and dry argon flow was charged with a stir bar, 1,3,5-tribromobenzene (25.4 g, 80.7 mmol), and dry CPME (120 mL). The mixture was cooled to $-5\text{ }^{\circ}\text{C}$, and a solution of *i*-PrMgCl (16.2 mL, 2.0 M in THF, 32.4 mmol) and a solution of *n*-BuLi (25.8 mL, 2.5 M in hexane, 64.5 mmol) were added dropwise over a period of 30 min, respectively. The reaction mixture was stirred for 8 h at $-5\text{ }^{\circ}\text{C}$. CuCN (723 mg, 8.0 mmol, 10 mol% Cu) was added at once, and the reaction mixture was stirred for 5 min at $-5\text{ }^{\circ}\text{C}$. Allyl bromide (10.2 mL, 120.6 mmol) was then added dropwise over a period of 30 min at $-5\text{ }^{\circ}\text{C}$. It was then allowed to reach room temperature and stirred for 15 h. The precipitated magnesium salt was filtered off and the resulting organic phase was extracted with

Et₂O and washed with saturated NH₄Cl aqueous solution and brine and dried over anhydrous MgSO₄, filtered, and concentrated under reduced pressure affording title compound as a transparent light brown liquid (21.4 g, 96% yield), which was used without further purification. ¹H NMR (400 MHz, CDCl₃) δ 3.33 (d, *J* = 6.8 Hz, 2H), 5.08–5.15 (m, 2H), 5.83–5.94 (m, 1H), 7.27 (d, *J* = 1.6 Hz, 2H), 7.50 (t, *J* = 1.6 Hz, 1H).

1-Bromo-3,5-diallylbenzene. A 500 mL three-neck round-bottom flask connected to a dropping funnel and dry argon flow was charged with a stir bar and 1-allyl-3,5-dibromobenzene (21.4 g, 77.5 mmol), dry CPME (100 mL). The mixture was cooled to –5 °C, and a solution of *i*-PrMgCl (16.2 mL, 2.0 M in THF, 32.5 mmol) and a solution of *n*-BuLi (25.8 mL, 2.5 M in hexane, 64.5 mmol) were added dropwise over a period of 30 min, respectively. The reaction mixture was stirred for 8 h at –5 °C. CuCN (705 mg, 7.8 mmol, 10 mol% Cu) was added at once, and the reaction mixture was stirred for 5 min at –5 °C. Allyl bromide (10.2 mL, 120.6 mmol) was then added dropwise over a period of 30 min at –5 °C. It was then allowed to reach room temperature and stirred for 15 h. The precipitated magnesium salt was filtered off and the resulting organic phase was extracted with Et₂O and washed with saturated NH₄Cl aqueous solution and brine and dried over anhydrous MgSO₄, filtered, and concentrated under reduced pressure. The resulting crude residue was purified by bulb-to-bulb distillation (150 Pa, 100 °C) affording title compound as a transparent colorless liquid (17.5 g, 96% yield). ¹H NMR (400 MHz, CDCl₃) δ 3.33 (d, *J* = 6.8 Hz, 4H), 5.05–5.11 (m, 4H), 5.86–5.96 (m, 2H), 6.92 (s, 1H), 7.25 (s, 2H); ¹³C NMR (100 MHz, CDCl₃) δ 39.8, 116.5, 122.4, 127.7, 129.3, 136.5, 142.3; FI-HRMS *m/z* calcd for C₁₂H₁₃Br (M⁺): 236.0201; found: 236.0204.

1-Allyl-4-iodobenzene. A 200 mL three-neck round-bottom flask connected to a dropping funnel and dry argon flow was charged with a stir bar, 1-allyl-4-bromobenzene (12.0 g, 60.9 mmol), and dry CPME (30 mL). The mixture was cooled to –5 °C, and a solution of *i*-PrMgCl (15.2 mL, 2.0 M in THF, 30.4 mmol) and a solution of *n*-BuLi (24.4 mL, 2.5 M in hexane, 61.0 mmol) were added dropwise over a period of 30 min, respectively. The reaction mixture was stirred for 6 h at –5 °C. The resulting reaction mixture was then added dropwise to a solution of iodine (23.2 g, 91.4 mmol) in THF (100 mL) at –78 °C. It was then allowed to reach room temperature and stirred for 18 h. The resulting mixture was quenched with saturated NH₄Cl aqueous solution at 0 °C, and organic phase was extracted with Et₂O and washed with brine and dried over anhydrous MgSO₄, filtered,

and concentrated under reduced pressure. The resulting crude residue was purified by bulb-to-bulb distillation (150 Pa, 70 °C) affording title compound as a transparent colorless liquid (13.4 g, 90% yield). ^1H NMR (400 MHz, CDCl_3) δ 3.33 (d, $J = 6.6$ Hz, 2H), 5.04–5.10 (m, 2H), 5.86–5.97 (m, 1H), 6.94 (d, $J = 8.3$ Hz, 2H), 7.61 (d, $J = 8.3$ Hz, 2H). The same procedure was followed for the synthesis of 1-allyl-3-iodobenzene and 1,3-diallyl-5-iodobenzene as described below.

1-Allyl-3-iodobenzene. Transparent colorless liquid. Yield: 87%. Bp: 150 Pa, 100 °C. ^1H NMR (400 MHz, CDCl_3) δ 3.33 (d, $J = 6.4$ Hz, 2H), 5.06–5.11 (m, 2H), 5.86–5.97 (m, 1H), 7.02 (t, $J = 8.0$ Hz, 1H), 7.15 (d, $J = 8.0$ Hz, 1H), 7.53 (d, $J = 8.0$ Hz, 1H), 7.54 (s, 1H); ^{13}C NMR (100 MHz, CDCl_3) δ 39.7, 94.5, 116.5, 127.9, 130.1, 135.1, 136.5, 137.5, 142.4.

1,3-Diallyl-5-iodobenzene. Transparent colorless liquid. Yield: 77%. Bp: 200 Pa, 110 °C. ^1H NMR (400 MHz, CDCl_3) δ 3.30 (d, $J = 6.8$ Hz, 4H), 5.05–5.11 (m, 4H), 5.85–5.95 (m, 2H), 6.96 (s, 1H), 7.38 (d, $J = 1.2$ Hz, 2H); ^{13}C NMR (100 MHz, CDCl_3) δ 39.6, 94.6, 116.4, 128.3, 135.3, 136.5, 142.4. FI-HRMS m/z calcd for $\text{C}_{12}\text{H}_{13}\text{I}$ (M^+): 284.0062; found: 284.0051.

Synthesis of molecular building blocks containing bulky alkoxysilyl group

1-Bromo-4-(3-(triisopropoxysilyl)propyl)benzene (1a). A 500 mL three-neck round-bottom flask connected to a condenser and dry argon flow was charged with a stir bar, 1-allyl-4-bromobenzene (12.0 g, 60.9 mmol), and $[\text{PtCl}_2(\text{C}_2\text{H}_4)]_2$ (4.0 mg, 6.8 mmol, 0.25 mol% Pt). The mixture was cooled to 0 °C, and trichlorosilane (20.0 mL, 198 mmol) was then added dropwise over a period of 15 min at 0 °C. After complete addition of the trichlorosilane, the temperature was progressively raised to room temperature. The mixture was stirred for 18 h at room temperature. The reaction mixture was concentrated under reduced pressure and the residue was dissolved in dry CH_2Cl_2 (50 mL). The resulting solution was then carefully added dropwise to a mixed solution of dry *i*-PrOH (21.0 mL, 274 mmol) and dry pyridine (22.2 mL, 274 mmol) in dry CH_2Cl_2 (200 mL) over a period of 30 min at 0 °C, and the resulting mixture was stirred for 6 h at room temperature. The reaction mixture was then concentrated under reduced pressure. The precipitated pyridinium salt was filtered off, and residue was extracted with hexane (300 mL). The combined organic phase was concentrated under reduced pressure, and the resulting crude residue was purified by silica gel chromatography (eluent: hexane/EtOAc = 10:1) affording **1a** as a transparent colorless liquid (21.2 g, 86% yield). ^1H NMR (400 MHz, CDCl_3) δ 0.57–0.61 (m, 2H), 1.17 (d, $J = 6.4$ Hz, 18H), 1.67–

1.71 (m, 2H), 2.58 (t, $J = 7.2$ Hz, 2H), 4.18 (sept, $J = 6.4$ Hz, 3H), 7.04 (d, $J = 8.8$ Hz, 2H), 7.37 (d, $J = 8.8$ Hz, 2H); ^{13}C NMR (100 MHz, CDCl_3) δ 11.6, 25.0, 25.6, 38.6, 64.9, 119.3, 130.3, 131.2, 141.5; FI-HRMS m/z calcd for $\text{C}_{18}\text{H}_{31}\text{BrO}_3\text{Si}$ (M^+): 402.1226; found: 402.1224. The same procedure was followed for the synthesis of compounds **1b**, **1d**, and **1e** as described below.

1-Bromo-3-(3-(triisopropoxysilyl)propyl)benzene (1b). Transparent colorless liquid. Yield: 85%. ^1H NMR (400 MHz, CDCl_3) δ 0.58–0.62 (m, 2H), 1.18 (d, $J = 6.4$ Hz, 18H), 1.67–1.75 (m, 2H), 2.60 (t, $J = 7.6$ Hz, 2H), 4.19 (sept, $J = 6.4$ Hz, 3H), 7.08–7.15 (m, 2H), 7.28–7.32 (m, 2H); ^{13}C NMR (100 MHz, CDCl_3) δ 11.9, 25.2, 25.9, 39.1, 65.2, 122.6, 127.5, 129.0, 130.0, 131.9, 145.2; FI-HRMS m/z calcd for $\text{C}_{18}\text{H}_{31}\text{BrO}_3\text{Si}$ (M^+): 402.1226; found: 402.1211.

1-Iodo-4-(3-(triisopropoxysilyl)propyl)benzene (1d). Transparent colorless liquid. Yield: 86%. ^1H NMR (400 MHz, CDCl_3) δ 0.57–0.61 (m, 2H), 1.17 (d, $J = 6.4$ Hz, 18H), 1.57–1.73 (m, 2H), 2.57 (t, $J = 7.6$ Hz, 2H), 4.18 (sept, $J = 6.4$ Hz, 3H), 6.92 (d, $J = 8.4$ Hz, 2H), 7.57 (d, $J = 8.4$ Hz, 2H); ^{13}C NMR (100 MHz, CDCl_3) δ 11.6, 24.9, 25.6, 38.7, 64.9, 90.5, 130.7, 137.2, 142.2; FI-HRMS m/z calcd for $\text{C}_{18}\text{H}_{31}\text{IO}_3\text{Si}$ (M^+): 450.1087; found: 450.1065.

1-Iodo-3-(3-(triisopropoxysilyl)propyl)benzene (1e). Transparent colorless liquid. Yield: 85%. ^1H NMR (400 MHz, CDCl_3) δ 0.57–0.61 (m, 2H), 1.18 (d, $J = 6.0$ Hz, 18H), 1.66–1.74 (m, 2H), 2.57 (t, $J = 7.6$ Hz, 2H), 4.19 (sept, $J = 6.0$ Hz, 3H), 6.99 (d, $J = 8.0$ Hz, 1H), 7.12 (d, $J = 8.0$ Hz, 1H), 7.50 (d, $J = 8.0$ Hz, 1H), 7.53 (s, 1H); ^{13}C NMR (100 MHz, CDCl_3) δ 11.6, 24.9, 25.6, 38.7, 64.9, 94.4, 127.8, 129.9, 134.6, 137.5, 145.0; FI-HRMS m/z calcd for $\text{C}_{18}\text{H}_{31}\text{IO}_3\text{Si}$ (M^+): 450.1087; found: 450.1091.

1,3-Bis(3-(triisopropoxysilyl)propyl)-5-bromobenzene (1c). A 300 mL three-neck round-bottom flask connected to a condenser and dry argon flow was charged with a stir bar, 1-bromo-3,5-diallylbenzene (4.50 g, 19.0 mmol), dry Et_2O (12 mL), and dry CH_2Cl_2 (15 mL). After the addition of a solution of $(\text{Bu}_4\text{N})_2\text{PtCl}_6$ (17.0 mg, 19.0 mmol, 0.1 mol% Pt) in dry CH_2Cl_2 (3 mL), trichlorosilane (7.50 mL, 74.3 mmol) was then added dropwise over a period of 15 min at 0 °C. After complete addition of the trichlorosilane, the temperature was progressively raised to room temperature. The mixture was stirred overnight at room temperature. The reaction mixture was concentrated under reduced pressure and the residue was dissolved in dry CH_2Cl_2 (75 mL). The resulting solution was then carefully added dropwise to a mixed solution of dry *i*-PrOH (13.0 mL, 170 mmol) and dry pyridine (14.0 mL, 170 mmol) in dry CH_2Cl_2 (100 mL) over a period of 30 min

at 0 °C, and the resulting mixture was stirred for 3 h at room temperature. The reaction mixture was then concentrated under reduced pressure. The precipitated pyridinium salt was filtered off and residue was extracted with hexane (300 mL). The combined organic phase was concentrated under reduced pressure, and the resulting crude residue was purified by silica gel chromatography (eluent: hexane/EtOAc = 10:1) affording **1c** as a transparent colorless liquid (10.2 g, 83% yield). ¹H NMR (400 MHz, CDCl₃) δ 0.58–0.62 (m, 4H), 1.18 (d, *J* = 6.4 Hz, 36H), 1.65–1.73 (m, 4H), 2.56 (t, *J* = 8.0 Hz, 4H), 4.19 (sept, *J* = 6.4 Hz, 6H), 6.88 (s, 1H), 7.12 (d, *J* = 1.4 Hz, 2H); ¹³C NMR (100 MHz, CDCl₃) δ 11.7, 24.9, 25.6, 38.9, 64.9, 122.0, 127.6, 128.8, 144.6; FD-HRMS *m/z* calcd for C₃₀H₅₇BrO₆Si₂ (M⁺): 648.2877; found: 648.2869. The same procedure was followed for the synthesis of compound **1f** as described below.

1,3-Bis(3-(triisopropoxysilyl)propyl)-5-iodobenzene (1f). Transparent colorless liquid. Yield: 84%. ¹H NMR (400 MHz, CDCl₃) δ 0.57–0.62 (m, 4H), 1.18 (d, *J* = 6.0 Hz, 36H), 1.64–1.72 (m, 4H), 2.53 (t, *J* = 7.6 Hz, 4H), 4.19 (sept, *J* = 6.0 Hz, 6H), 6.92 (s, 1H), 7.33 (s, 2H); ¹³C NMR (100 MHz, CDCl₃) δ 11.7, 24.9, 25.6, 38.8, 64.9, 94.3, 128.3, 134.8, 144.7; ESI-HRMS *m/z* calcd for C₃₀H₅₇INaO₆Si₂ (M+Na⁺): 719.2623; found: 719.2668.

4-(3-(Triisopropoxysilyl)propyl)phenylmagnesium chloride (2a). A 20 mL Schlenk flask connected to dry argon flow was charged with a stir bar, **1d** (247 mg, 0.55 mmol), and dry THF (5 mL). The mixture was cooled to –40 °C, and a solution of isopropylmagnesium chloride lithium chloride complex (*i*-PrMgCl•LiCl) (0.85 mL, 1.3 M in THF, 1.10 mmol) and dry 1,4-dioxane (0.50 mL) were added dropwise over a period of 5 min, respectively. The reaction mixture was stirred for 4 h at –40 °C. Conversion of starting material was checked by ¹H NMR after the quenching water. The same procedure was followed for the preparation of compound **2b** and **2c**.

4-(3-(Triisopropoxysilyl)propyl)-1-(trimethylstannyl)benzene (2d). A 100 mL two-neck round-bottom flask connected to dry argon flow was charged with a stir bar and **2a** (3.33 mmol) in dry THF/dry 1,4-dioxane (10:1 = v/v, 38 mL). The mixture was cooled to –40 °C, trimethyltin chloride (1.33 g, 6.67 mmol) was added one-portion. It was then allowed to reach room temperature and stirred for 18 h. The resulting mixture was quenched with saturated NH₄Cl aqueous solution at 0 °C, and organic phase was extracted with Et₂O and washed with brine and dried over anhydrous MgSO₄, filtered, and concentrated under reduced pressure affording **2d** as a transparent colorless liquid (1.41 g, 87% yield). Compound **2d** was used without further purification. ¹H NMR (400

MHz, CDCl₃) δ 0.27 (t, J = 27.6 Hz, 9H), 0.62–0.66 (m, 2H), 1.18 (d, J = 6.4 Hz, 18H), 1.69–1.76 (m, 2H), 2.61 (t, J = 8.0 Hz, 2H), 4.19 (sept, J = 6.4 Hz, 3H), 7.17 (d, J = 7.6 Hz, 2H), 7.40 (d, J = 7.6 Hz, 2H); ¹³C NMR (100 MHz, CDCl₃) δ -9.6, 11.9, 25.1, 25.6, 39.4, 64.8, 128.4, 135.7, 138.6, 142.7; ESI-HRMS m/z calcd for C₂₁H₄₀NaO₃SiSn (M+Na⁺): 511.1666; found: 511.1679.

4-(4,4,5,5-Tetramethyl-1,3,2-dioxaborolan-2-yl)-1-(3-(triisopropoxysilyl)propyl)benzene (2e).

A 20 mL Schlenk flask connected to dry argon flow was charged with a stir bar and **2a** (0.55 mmol) in dry THF/dry 1,4-dioxane (10:1 = v/v, 6.35 mL). The mixture was cooled to -40 °C, 2-isopropoxy-4,4,5,5-tetramethyl-1,3,2-dioxaborolane (225 μ L, 1.10 mmol) was added one-portion. It was then allowed to reach room temperature and stirred for 18 h. The resulting mixture was quenched with saturated NH₄Cl aqueous solution at 0 °C, and organic phase was extracted with Et₂O and washed with brine and dried over anhydrous MgSO₄, filtered, and concentrated under reduced pressure affording **2e** as a transparent colorless liquid (230 mg, 93% yield). ¹H NMR (400 MHz, CDCl₃) δ 0.59–0.63 (m, 2H), 1.17 (d, J = 6.0 Hz, 18H), 1.33 (s, 12H), 1.69–1.76 (m, 2H), 2.64 (t, J = 7.6 Hz, 2H), 4.18 (sept, J = 6.0 Hz, 3H), 7.18 (d, J = 8.0 Hz, 2H), 7.71 (d, J = 8.0 Hz, 2H); ¹³C NMR (100 MHz, CDCl₃) δ 11.7, 24.5, 24.8, 25.5, 39.5, 64.8, 83.6, 128.0, 133.8, 134.7, 146.0; FI-HRMS m/z calcd for C₂₄H₄₃BO₅Si (M⁺): 450.2973; found: 450.2978.

4-(Thiophen-2-yl)-1-(3-(triisopropoxysilyl)propyl)benzene (2f). A 500 mL three-neck round-bottom flask connected to a condenser and dry argon flow was charged with a stir bar, **1d** (6.60 g, 14.7 mmol), 2-thiopheneboronic acid (2.82 g, 22.0 mmol), NaHCO₃ (2.46 g, 29.3 mmol), dry 1,4-dioxane (220 mL), and degassed distilled water (22 mL). After the mixture was stirred for 10 min at room temperature, Pd(PPh₃)₄ (400 mg, 0.35 mmol, 2.4 mol% Pd) was added one-portion under argon flow. The temperature was progressively raised to 85 °C and then the reaction mixture was stirred for 24 h. The reaction mixture was then concentrated under reduced pressure and the resulting crude residue was purified by silica gel chromatography (eluent: hexane/CHCl₃ = 1:1) affording **2f** as a transparent light-yellow liquid (4.24 g, 71% yield). ¹H NMR (400 MHz, CDCl₃) δ 0.61–0.66 (m, 2H), 1.18 (d, J = 6.4 Hz, 18H), 1.70–1.78 (m, 2H), 2.64 (t, J = 7.6 Hz, 2H), 4.19 (sept, J = 6.4 Hz, 3H), 7.06 (dd, J = 5.2 Hz, 3.6 Hz, 1H), 7.18 (d, J = 8.0 Hz, 2H), 7.23 (dd, J = 5.2 Hz, 1.2 Hz, 1H), 7.26 (dd, J = 3.6 Hz, 0.8 Hz, 1H), 7.51 (d, J = 8.0 Hz, 2H); ¹³C NMR (100 MHz, CDCl₃) δ 11.7, 25.0, 25.5, 38.9, 64.8, 122.5, 124.2, 125.8, 127.8, 129.0, 131.8, 142.0, 144.5; FI-HRMS m/z calcd for C₂₂H₃₄O₃SSi (M⁺): 406.1988; found: 406.1977.

4-(5-Bromothiophen-2-yl)-1-(3-(triisopropoxysilyl)propyl)benzene (2g). A 100 mL two-neck round-bottom flask connected to dry argon flow was charged with a stir bar, **2f** (1.05 g, 2.58 mmol), and dry DMF (30 mL). After the mixture was stirred for 10 min at 0 °C, *N*-bromosuccinimide (636 mg, 3.57 mmol) was added one-portion under argon flow. The reaction mixture was stirred for 2 h at room temperature. The organic phase was extracted with hexane and concentrated under reduced pressure. The resulting crude residue was purified by silica gel chromatography (eluent: hexane/EtOAc = 10:1) affording **2g** as a transparent light-yellow liquid (1.01 g, 81% yield). ¹H NMR (400 MHz, CDCl₃) δ 0.61–0.65 (m, 2H), 1.18 (d, *J* = 6.4 Hz, 18H), 1.69–1.77 (m, 2H), 2.63 (t, *J* = 7.6 Hz, 2H), 4.19 (sept, *J* = 6.4 Hz, 3H), 6.99 (s, 2H), 7.17 (d, *J* = 8.4 Hz, 2H), 7.40 (d, *J* = 8.4 Hz, 2H); ¹³C NMR (100 MHz, CDCl₃) δ 11.7, 25.0, 25.6, 38.9, 64.8, 110.7, 122.6, 125.5, 129.1, 130.7, 131.1, 142.6, 146.1; FI-HRMS *m/z* calcd for C₂₂H₃₃BrO₃SSi (M⁺): 484.1103; found: 484.1096.

1-(3-Hydroxy-3-methyl-1-butyryl)-4-(3-(triisopropoxysilyl)propyl)benzene (2h). A 500 mL three-neck round-bottom flask connected to a condenser and dry argon flow was charged with a stir bar, **1a** (7.13 g, 17.6 mmol), PdCl₂(PPh₃)₂ (495 mg, 0.71 mmol), CuI (135 mg, 0.70 mmol), and dry Et₃N (70 mL). After the mixture was stirred for 1 min at room temperature, 2-methyl-3-butyryl-2-ol (2.10 mL, 21.5 mmol) was added. The temperature was progressively raised to 80 °C and then the reaction mixture was stirred for 20 h. The reaction mixture was then concentrated under reduced pressure and the resulting crude residue was purified by silica gel chromatography (eluent: hexane/EtOAc = 10:1) affording **2h** as a transparent light-yellow liquid (6.21 g, 86% yield). ¹H NMR (400 MHz, CDCl₃) δ 0.57–0.61 (m, 2H), 1.17 (d, *J* = 6.4 Hz, 18H), 1.61 (s, 6H), 1.66–1.74 (m, 2H), 2.62 (t, *J* = 7.6 Hz, 2H), 4.18 (sept, *J* = 6.4 Hz, 3H), 7.10 (d, *J* = 8.4 Hz, 2H), 7.31 (d, *J* = 8.4 Hz, 2H); ¹³C NMR (100 MHz, CDCl₃) δ 11.6, 24.8, 25.5, 31.5, 39.0, 64.8, 65.6, 82.3, 93.0, 119.8, 128.5, 131.5, 143.0; FI-HRMS *m/z* calcd for C₂₃H₃₈O₄Si (M⁺): 406.2539; found: 406.2545.

1-Ethynyl-4-(3-(triisopropoxysilyl)propyl)benzene (2i). A 300 mL three-neck round-bottom flask connected to a condenser and dry argon flow was charged with a stir bar, **2h** (10.0 g, 24.6 mmol), and dry toluene (150 mL). After the mixture was stirred for 5 min at room temperature, NaH (60%, dispersion in paraffin liquid, 195 mg, 4.88 mmol) was added. The temperature was progressively raised to 115 °C and then the reaction mixture was stirred for 1 h. The reaction mixture was then concentrated under reduced pressure and the resulting crude residue was purified by silica gel

chromatography (eluent: hexane/CHCl₃ = 2:1) affording **2i** as a transparent light-yellow liquid (6.08 g, 71% yield). ¹H NMR (400 MHz, CDCl₃) δ 0.57–0.62 (m, 2H), 1.17 (d, *J* = 6.0 Hz, 18H), 1.69–1.73 (m, 2H), 2.63 (t, *J* = 8.0 Hz, 2H), 3.03 (s, 1H), 4.18 (sept, *J* = 6.0 Hz, 3H), 7.12 (d, *J* = 8.4 Hz, 2H), 7.39 (d, *J* = 8.4 Hz, 2H); ¹³C NMR (100 MHz, CDCl₃) δ 11.6, 24.8, 25.6, 39.1, 64.9, 76.4, 83.9, 119.2, 128.5, 132.0, 143.6; FI-HRMS *m/z* calcd for C₂₀H₃₂O₃Si (M⁺): 348.2121; found: 348.2129.

Synthesis of molecular building blocks containing triallylsilyl group

1-Iodo-4-(3-(triallylsilyl)propyl)benzene. A 300 mL three-neck round-bottom flask connected to a condenser and dry argon flow was charged with a stir bar, 1-allyl-4-iodobenzene (6.0 g, 24.6 mmol), and [PtCl₂(C₂H₄)₂] (7.25 mg, 12.3 mmol, 0.1 mol% Pt). The mixture was cooled to 0 °C, and trichlorosilane (15.0 mL, 149 mmol) was then added dropwise over a period of 15 min at 0 °C. After complete addition of the trichlorosilane, the temperature was progressively raised to room temperature. The mixture was stirred for 15 h at room temperature. The reaction mixture was concentrated under reduced pressure and the residue was dissolved in dry Et₂O (10 mL). The mixture was cooled to 0 °C, and a solution of allylmagnesium bromide (98.0 mL, 1.0 M in Et₂O, 98.0 mmol) was added dropwise over a period of 30 min. The reaction mixture was stirred for 20 h at room temperature. The resulting mixture was quenched with saturated NH₄Cl aqueous solution at 0 °C, and organic phase was extracted with Et₂O and washed with brine and dried over anhydrous MgSO₄, filtered, and concentrated under reduced pressure. The resulting crude residue was purified by bulb-to-bulb distillation (130 Pa, 90 °C) affording title compound as a transparent colorless liquid (5.73 g, 59% yield). ¹H NMR (400 MHz, CDCl₃) δ 0.60–0.63 (m, 2H), 1.58 (d, *J* = 8.0 Hz, 6H), 1.56–1.66 (m, 2H), 2.55 (t, *J* = 8.0 Hz, 2H), 4.84–4.89 (m, 6H), 5.70–5.81 (m, 3H), 6.91 (d, *J* = 8.0 Hz, 2H), 7.59 (d, *J* = 8.0 Hz, 2H); FI-HRMS *m/z* calcd for C₁₈H₂₅ISi (M⁺): 396.0770; found: 396.0766.

4-(3-(Triallylsilyl)propyl)-1-(trimethylstannyl)benzene (3). A 100 mL two-neck round-bottom flask connected to dry argon flow was charged with a stir bar, 1-iodo-4-(3-(triallylsilyl)propyl)benzene (2.32 g, 5.85 mmol), and dry THF (16 mL). The mixture was cooled to 0 °C, and a solution of *i*-PrMgCl (6.0 mL, 2.0 M in THF, 12.0 mmol) was added dropwise over a period of 5 min. The reaction mixture was stirred for 8 h at 0 °C. Then, trimethyltin

chloride (2.40 g, 12.0 mmol) was added one-portion. It was then allowed to reach room temperature and stirred for 15 h. The resulting mixture was quenched with saturated NH₄Cl aqueous solution at 0 °C, and organic phase was extracted with Et₂O and washed with brine and dried over anhydrous MgSO₄, filtered, and concentrated under reduced pressure affording **3** as a transparent colorless liquid (2.50 g, 99% yield). Compound **3** was used without further purification. ¹H NMR (400 MHz, CDCl₃) δ 0.28 (t, *J* = 24.8 Hz, 9H), 0.64–0.68 (m, 2H), 1.58 (d, *J* = 8.4 Hz, 6H), 1.62–1.68 (m, 2H), 2.59 (t, *J* = 7.6 Hz, 2H), 4.83–4.89 (m, 6H), 5.71–5.81 (m, 3H), 7.15 (d, *J* = 8.0 Hz, 2H), 7.41 (d, *J* = 8.0 Hz, 2H); ¹³C NMR (100 MHz, CDCl₃) δ -9.6, 11.5, 19.5, 25.7, 39.9, 113.5, 128.2, 134.3, 135.8, 138.8, 142.4; FI-HRMS *m/z* calcd for C₂₁H₃₄SiSn (M⁺): 434.1452; found: 434.1446.

Synthesis of DPP-bridged organosilane

3,6-Bis(5-(4-(triisopropoxysilyl)propyl)phenylthiophen-2-yl)-2,5-bis(2-ethylhexyl)pyrrolo[3,4-*c*]pyrrole-1,4-dione (4a). A 100 mL two-neck round-bottom flask connected to a condenser and dry argon flow was charged with a stir bar, **2e** (420 mg, 0.86 mmol), 3,6-di(2-bromothiophen-5-yl)-2,5-bis(2-ethylhexyl)pyrrolo[3,4-*c*]pyrrole-1,4-dione (198 mg, 0.29 mmol), Pd₂(dba)₃ (13.3 mg, 0.015 mmol, 10 mol% Pd), tri(2-furyl)phosphine (14.6 mg, 0.058 mmol, 20 mol%), and dry THF (30 mL). The temperature was progressively raised to 70 °C and then the reaction mixture was stirred for 20 h. The reaction mixture was then concentrated under reduced pressure and the resulting crude residue was purified by flash chromatography (eluent: hexane/EtOAc = 40:1) affording **4a** as a dark blue tacky solid (289 mg, 85% yield). ¹H NMR (400 MHz, CDCl₃) δ 0.62–0.66 (m, 4H), 0.87 (t, *J* = 6.8 Hz, 6H), 0.91 (t, *J* = 7.2 Hz, 6H), 1.19 (d, *J* = 6.4 Hz, 36H), 1.24–1.42 (m, 16H), 1.72–1.80 (m, 4H), 1.90–2.00 (m, 2H), 2.67 (t, *J* = 7.6 Hz, 4H), 4.03–4.13 (m, 4H), 4.20 (sept, *J* = 6.4 Hz, 6H), 7.23 (d, *J* = 8.4 Hz, 4H), 7.42 (d, *J* = 4.0 Hz, 2H), 7.58 (d, *J* = 8.4 Hz, 4H), 8.96 (d, *J* = 4.0 Hz, 2H); ¹³C NMR (100 MHz, CDCl₃) δ 10.6, 11.8, 14.1, 23.1, 23.7, 25.0, 25.6, 28.6, 30.4, 39.0, 39.2, 46.0, 64.9, 108.0, 124.0, 126.0, 128.3, 129.3, 130.7, 136.8, 139.8, 143.8, 150.0, 161.7; ESI-HRMS *m/z* calcd for C₆₆H₁₀₀N₂NaO₈S₂Si₂ (M+Na⁺): 1191.6357; found: 1191.6323. The same procedure was followed for the synthesis of DPP-bridged triallylsilane (**4b**) as described below.

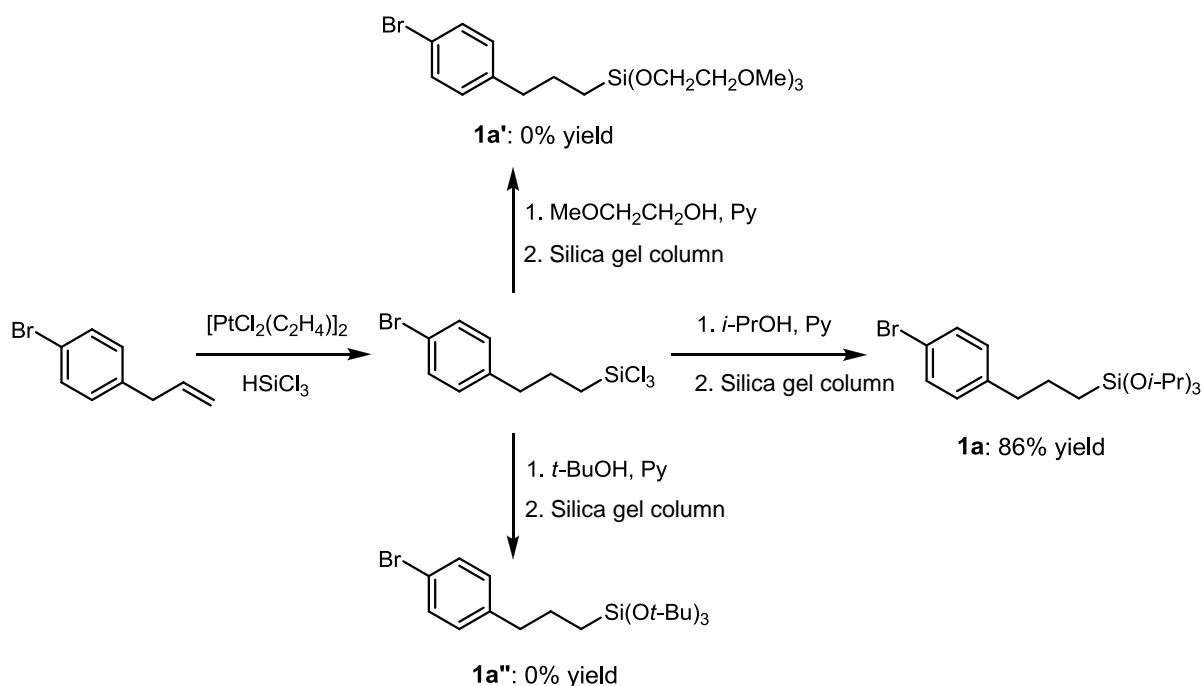
3,6-Bis(5-(4-(triallylsilyl)propyl)phenylthiophen-2-yl)-2,5-bis(2-ethylhexyl)pyrrolo[3,4-c]pyrrole-1,4-dione (4b). Dark blue tacky solid. Yield: 57%. ¹H NMR (400 MHz, CDCl₃) δ 0.64–0.68 (m, 4H), 0.87 (t, *J* = 7.2 Hz, 6H), 0.92 (t, *J* = 7.2 Hz, 6H), 1.23–1.44 (m, 16H), 1.59 (d, *J* = 8.4 Hz, 12H), 1.64–1.72 (m, 4H), 1.91–1.98 (m, 2H), 2.65 (t, *J* = 7.6 Hz, 4H), 4.03–4.11 (m, 4H), 4.84–4.91 (m, 12H), 5.71–5.82 (m, 6H), 7.22 (d, *J* = 8.0 Hz, 4H), 7.44 (d, *J* = 4.0 Hz, 2H), 7.59 (d, *J* = 8.0 Hz, 4H), 8.96 (d, *J* = 4.0 Hz, 2H); ¹³C NMR (100 MHz, CDCl₃) δ 10.6, 11.3, 14.1, 19.5, 23.1, 23.6, 25.5, 28.5, 30.3, 39.2, 39.6, 45.9, 108.0, 113.6, 124.0, 126.0, 128.3, 129.2, 130.7, 134.2, 136.8, 139.7, 143.4, 149.8, 161.6; ESI-HRMS *m/z* calcd for C₆₆H₈₈N₂NaO₂S₂Si₂ (M+Na⁺): 1083.5724; found: 1083.5712.

Preparation of DPP-bridged organosilica film

DPP-bridged organosilane **4a** (12.4 mg, 10.6 mmol) was dissolved in THF (3.4 mL) and then 2 M hydrochloric acid (HCl) aqueous solution (8.5 μL) was added to the solution (5 mM HCl in THF). The mixture was stirred at room temperature for 45 min. The sol solution was coated on a quartz glass plate by spin-coating (1000 rpm, 30 sec) and dried under reduced pressure to give an organosilica film.

2.3.3 Results and Discussion

First, the author sought a suitable bulky trialkoxysilyl group for the building blocks. The tris(2-methoxyethoxy)silyl- and tri(*tert*-butoxy)silyl-groups, in addition to the triisopropoxysilyl group, were introduced by hydrosilylation of allylbromobenzene with trichlorosilane in the presence of $[\text{PtCl}_2(\text{C}_2\text{H}_4)]_2$, followed by alkoxylation using appropriate alcohols in the presence of pyridine in CH_2Cl_2 (Scheme 2.12).¹⁸ The triisopropoxysilyl group was efficiently introduced and showed sufficient stability during general work-up and silica gel chromatography. The bulkier linear tris(2-methoxyethoxy)silyl group was not retained during the reaction and purification, giving a complex mixture that contained none of the target compound. The introduction of the bulkier branched tri(*tert*-butoxy)silyl group failed due to steric hindrance during the alkoxylation reaction.



Scheme 2.12. Synthesis of bromobenzene-based molecular building blocks containing various bulky trialkoxysilyl groups.

¹⁸ Maegawa, Y.; Mizoshita, N.; Tani, T.; Inagaki, S. *Chem. Lett.* **2012**, *41*, 316–318.

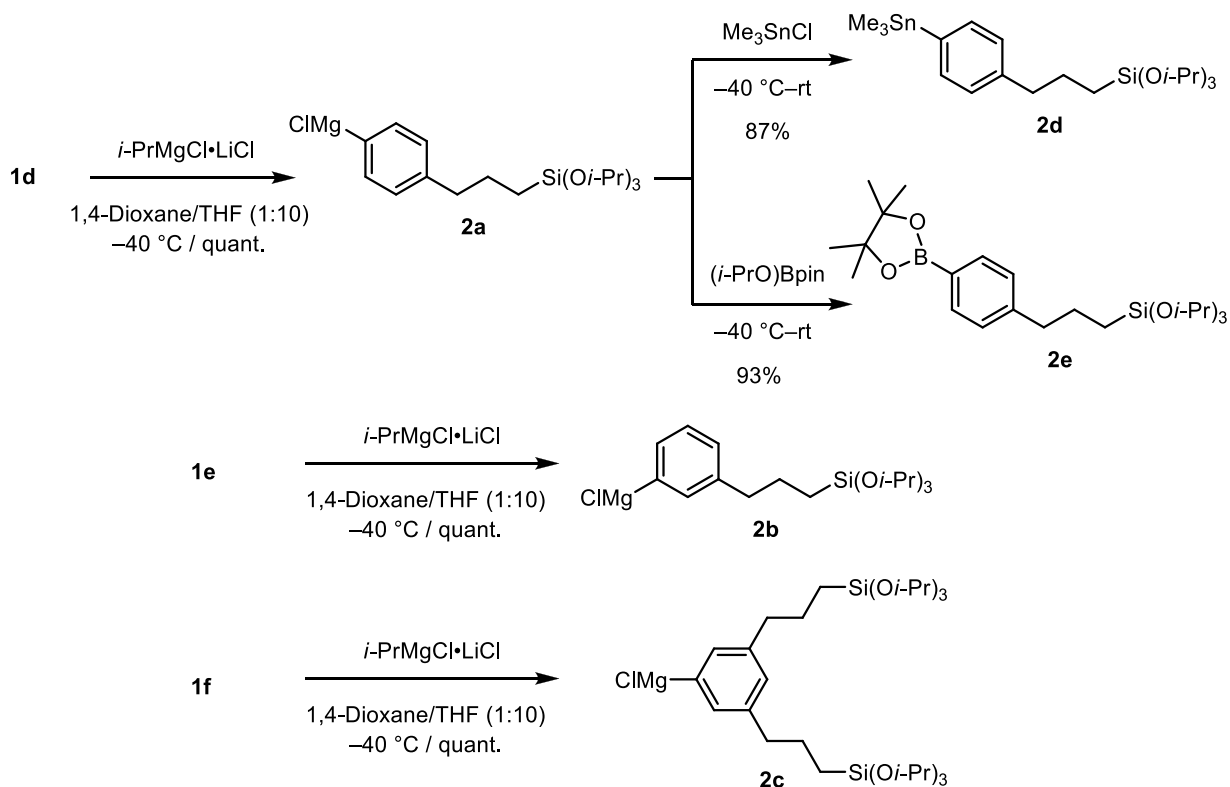
Table 2.4. Synthesis of halogen-substituted molecular building blocks containing one or two triisopropoxysilyl groups^a

Entry	Pt catalyst	Allylhalobenzene	Product	Yield / % ^b
1	[PtCl ₂ (C ₂ H ₄) ₂]		 1a	86
2	[PtCl ₂ (C ₂ H ₄) ₂]		 1b	85
3	[(Bu ₄ N) ₂ PtCl ₆]		 1c	83
4	[PtCl ₂ (C ₂ H ₄) ₂]		 1d	86
5	[PtCl ₂ (C ₂ H ₄) ₂]		 1e	85
6	[(Bu ₄ N) ₂ PtCl ₆]		 1f	84

^a Reagents and conditions: 1. allylhalobenzene (1 equiv), HSiCl₃ (3.3 equiv), Pt catalyst (0.25 mol% Pt), rt, overnight, 2. *i*-PrOH (4.5 equiv), Pyridine (4.5 equiv), CH₂Cl₂, 0 °C-rt, 6 h. ^b 0.1 mol% Pt, ^c Isolated yield.

The author then synthesized a variety of halogenated benzene-based building blocks with triisopropoxysilyl groups attached, as shown in Table 2.4. During this study, the author found that

allylhalobenzene was readily prepared by halogen–magnesium exchange reaction of bromobenzene derivatives with a mixture of isopropylmagnesium chloride (*i*-PrMgCl) and *n*-butyllithium (*n*-BuLi) in cyclopentyl methyl ether (CPME) followed by allylation with allyl bromide in the presence of CuCN.¹⁹ Both hydrosilylation and isopropoxylation of *p*- and *m*-allylbromobenzene proceeded successfully to give the corresponding building blocks **1a** and **1b** in high yields of 86% and 85%, respectively (Table 2.4, entries 1 and 2). The bis-silylated building block **1c** could be synthesized from 1-bromo-3,5-diallylbenzene (Table 2.4, entry 3). In this case, hydrosilylation proceeded effectively in the presence of (Bu₄N)₂PtCl₆ as a catalyst.²⁰ A series of iodobenzene building blocks, **1d–1f**, were also obtained under same reaction conditions (Table 2.4, entries 4–6).

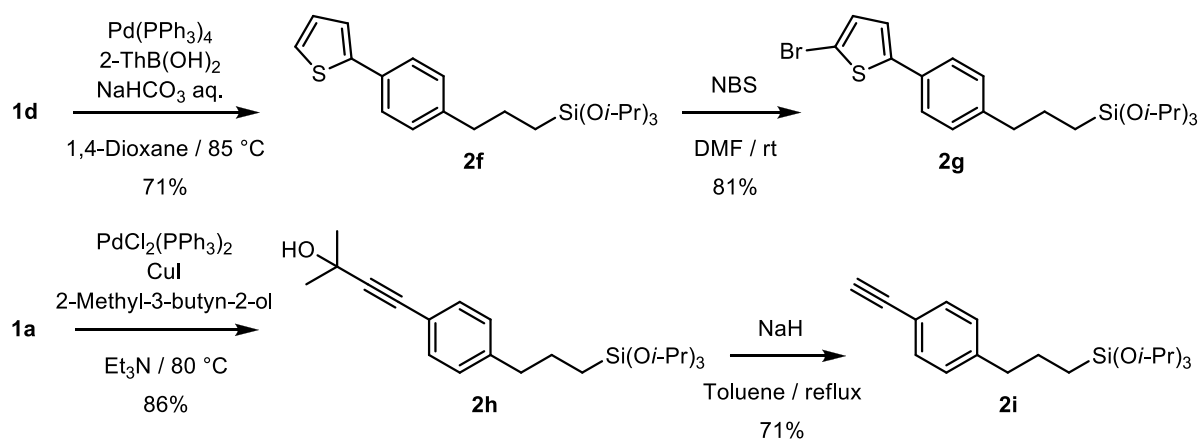


Scheme 2.13. Synthesis of magnesium-containing building blocks **2a–2c** and borylated- **2d** and stannylated building blocks **2e**.

¹⁹ Gallou, F.; Haenggi, R.; Hirt, H.; Marterer, W.; Schaefer, F.; Seeger-Weibel, M. *Tetrahedron Lett.* **2008**, *49*, 5024–5027.

²⁰ van Heerbeek, R.; Kamer, P. C. J.; van Leeuwen, P. N. M. W.; Reek, J. N. H. *Org. Biomol. Chem.* **2006**, *4*, 211–223.

Magnesium-containing building blocks were obtained from the iodobenzene-based building blocks (Scheme 2.13). A Grignard exchange reaction of **1d** with isopropylmagnesium chloride lithium chloride complex (*i*-PrMgCl•LiCl) in a mixture of 1,4-dioxane/THF (1:10 v/v) proceeded effectively at $-40\text{ }^{\circ}\text{C}$ for 4 h and gave the magnesium-containing building block **2a** quantitatively. It is notable that the triisopropoxysilyl group was stable towards *i*-PrMgCl•LiCl and the resulting magnesium reagent, owing to its bulky structure. Interestingly, no reaction occurred in the absence of 1,4-dioxane, and unreacted **1d** was recovered. This may be attributed to the formation of a magnesium complex between *i*-PrMgCl and the triisopropoxysilyl group. Indeed, the use of excess *i*-PrMgCl in THF gave the corresponding **2a**. The addition of 1,4-dioxane affects the dissociation of the magnesium complex, as reported by Knochel's group.²¹ *m*-Silylated (**2b**) and bis-silylated (**2c**) Grignard reagents were also successfully obtained from corresponding iodo-building blocks **1e** and **1f** under the same reaction conditions (Scheme 2.13). The magnesium-containing building blocks successfully underwent transmetallation upon treatment with other metal reagents (Scheme 2.13). The transmetallation of **2a** with trimethyltin chloride in a mixture of 1,4-dioxane/THF (1:10 v/v) afforded the trimethylstannylated building block **2d** in a high yield of 87%. The reaction of **2a** with 2-isopropoxy-4,4,5,5-tetramethyl-1,3,2-dioxaborolane ((*i*-PrO)Bpin) gave the borylated building block **2e** in 93% yield.



Scheme 2.14. Synthesis of functional molecular building blocks by cross-coupling reactions.

²¹ Krasovskiy, A.; Straub, B. F.; Knochel, P. *Angew. Chem., Int. Ed.* **2006**, *45*, 159–162.

With key building blocks in hand, the author then examined the utility of the molecular building blocks as cross-coupling partners (Scheme 2.14). The halogen-substituted building blocks can be used as coupling reagents for Suzuki–Miyaura²² and Sonogashira–Hagihara cross-coupling reactions.²³ Suzuki–Miyaura coupling between **1d** and 2-thiophenboronic acid in the presence of Pd(PPh₃)₄ and NaHCO₃ gave the thiophene-substituted building block **2f** in 71% yield. Notably, in the reaction, the use of a basic aqueous solution did not affect the hydrolysis of the triisopropoxysilyl group. The α -proton on thiophene ring in **2f** was readily brominated using *N*-bromosuccinimide (NBS) to afford the bromothiophene building block **2g** in 81% yield. The resulting **2g** is a useful coupling partner for the construction of π -conjugated thiophene bridging groups. Sonogashira–Hagihara coupling between **1a** and 2-methyl-3-butyn-2-ol in the presence of PdCl₂(PPh₃)₂ and CuI as a catalyst gave the ethynylated compound **2h** in 86% yield. The resulting **2h** can easily be deprotected using NaH to afford the terminal ethyne-substituted building block **2i** in 71% yield without decomposition of the triisopropoxysilyl group. The obtained **2i** can then be used as a coupling partner for Sonogashira–Hagihara coupling and/or click reactions with azide compounds.²⁴

Materials based on 1,4-diketo-3,6-dithienylpyrrolo[3,4-*c*]pyrrole (DPP) have attracted tremendous attention in the fields of solar cells and field effect transistors because of their promising optical and electrical properties.^{25,26} DPP-bridged triisopropoxysilane precursor was synthesized by cross-coupling reaction using building block **2d** as shown in Scheme 2.15. Migita–Kosugi–Stille cross-coupling between **2e** and dibrominated DPP gave the desired DPP-bridged triisopropoxysilane **4a** in high yield (85%).^{27,28} The corresponding DPP-bridged triallylsilane **4b** also synthesized using triallylsilane building block **3**. Both functional precursors were purified by silica gel chromatography and isolated in pure form.

An organosilica hybrid film was readily obtained from the DPP-bridged triisopropoxysilane **4a** by sol–gel polymerization under mildly acidic conditions. A purple solution of the precursor **4a**

²² Miyaura, N.; Suzuki, A. *Chem. Rev.* **1995**, *95*, 2457–2483.

²³ Sonogashira, K.; Tohda, Y.; Hagihara, N. *Tetrahedron Lett.* **1975**, *50*, 4467–4469.

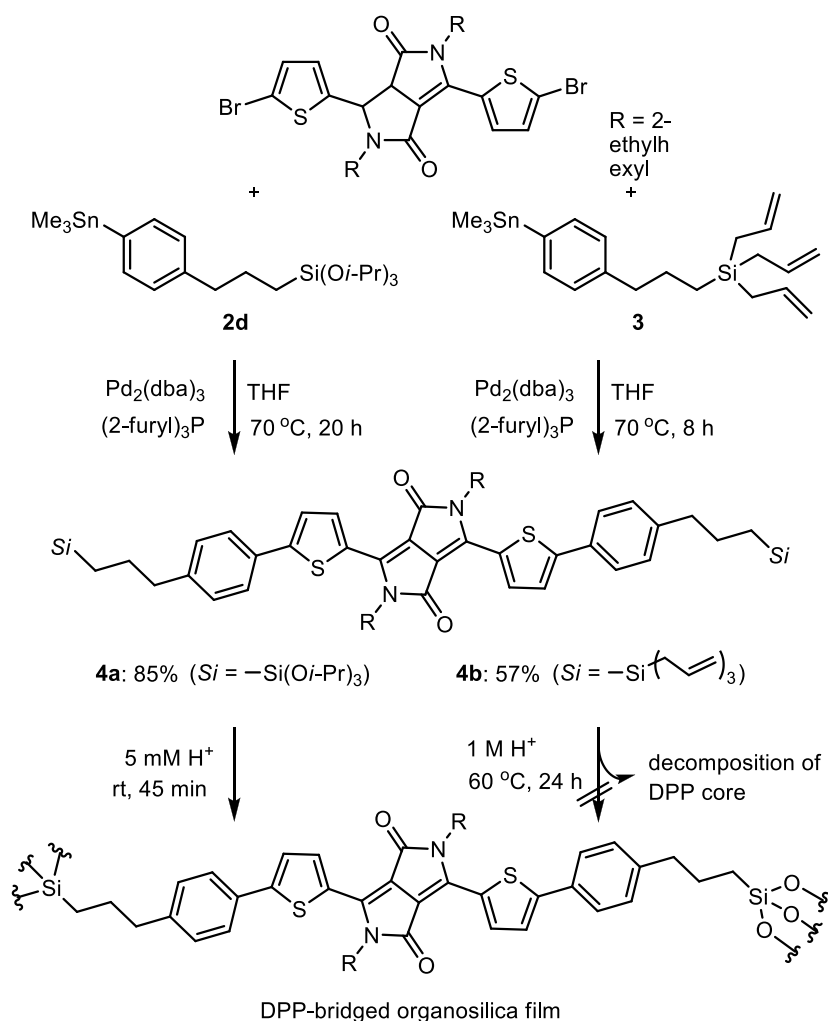
²⁴ Moitra, N.; Moreau, J. J. E.; Cattoën, X.; Wong Chi Man, M. *Chem. Commun.* **2010**, 8416–8418.

²⁵ Walker, B.; Tamayo, A. B.; Dang, X.-D.; Zalar, P.; Seo, J. H.; Garcia, A.; Tantiwiwat, M.; Nguyen, T.-Q. *Adv. Funct. Mater.* **2009**, *19*, 3063–3069.

²⁶ Sonar, P.; Singh, S. P.; Li, Y.; Soh, M. S.; Dodabalapur, A. *Adv. Mater.* **2010**, *22*, 5409–5413.

²⁷ Kosugi, M.; Sasazawa, K.; Shimizu, Y.; Migita, T. *Chem. Lett.* **1977**, 301–302.

²⁸ Stille, J. K. *Angew. Chem., Int. Ed. Engl.* **1986**, *25*, 508–524.



Scheme 2.15. Synthesis of DPP-bridged triisopropoxysilane **4a** and triallylsilane **4b** by Migita–Kosugi–Stille cross-coupling reaction between dibrominated DPP and building blocks, and preparation of organosilica films under acidic condition.

containing aqueous hydrochloric acid (HCl) (5 mM HCl in THF) was smoothly converted to a dark blue sol by stirring for only 45 min (Figure 2.2a). The color change indicated the formation of a soluble siloxane oligomer in the sol. The obtained sol formed an insoluble solid organosilica film by spin-coating and drying under reduced pressure. The resulting organosilica film showed absorption maxima at 564 nm and 609 nm, attributed to an intramolecular charge transfer transition in the DPP unit, which indicated that the optical properties of the DPP unit remained after formation of the organosilica film (Figure 2.2b). However, the corresponding DPP-bridged triallylsilane **4b** did not form an insoluble organosilica film under same sol–gel conditions. Unfortunately, the color

of the sol faded under highly acidic conditions (1 M HCl in THF, Figure 2.2a), and an insoluble organosilica film did not form. This indicates decomposition of the donor–acceptor–donor structure in the DPP skeleton during preparation of the sol (Figure 2.2b). The triisopropoxysilyl group proved to be useful in the synthesis of functional organosilica hybrids without loss of organic group functionality.

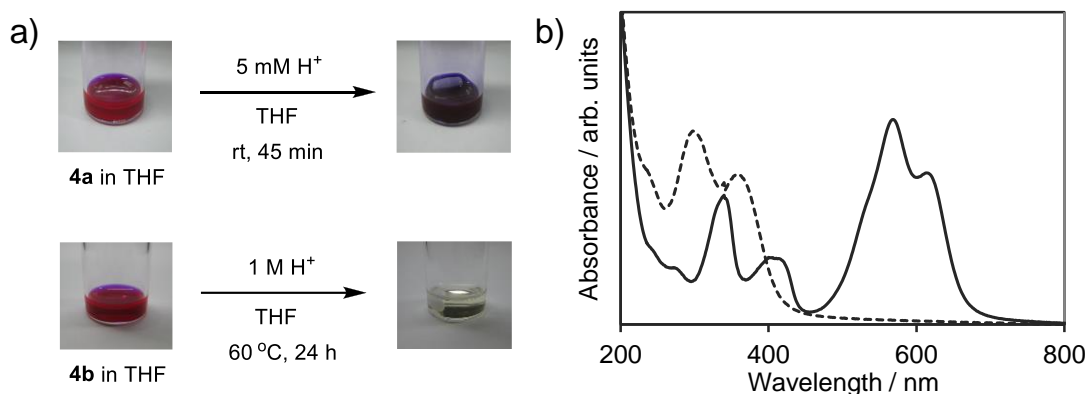


Figure 2.2. a) Color change of sol–solution containing DPP-bridged triisopropoxysilane **4a** and triallylsilane **4b** before and after the hydrolysis in THF in the presence of HCl. b) UV-vis absorption spectra of organosilica films prepared from DPP-bridged silane precursors **4a** (solid line) and **4b** (broken line).

2.3.4 Conclusions

The author developed a novel synthetic route for π -conjugated organosilica precursors by using molecular building blocks containing one or two triisopropoxysilyl groups. The synthesized molecular building blocks could be used as coupling partners for various palladium-catalyzed cross-coupling reactions. Indeed, opto and electroactive organosilanes were successfully synthesized and isolated in pure form. Furthermore, one organosilane was readily hydrolyzed and condensed to give an organosilica hybrid without loss of functionality. This innovative approach is expected to extend and complement the conventional approach using allylsilane-based molecular building blocks and will lead to significant development of organosilica hybrids.

2.4 Synthetic Route to Functional Organic-bridged Alkoxysilanes with Short Linker

Tetraphenylpyrene (TPPy)-bridged alkoxysilane precursors with short linkers were synthesized by development of a facile synthetic route, and sol-gel polymerized to transparent organosilica films which showed higher absorption coefficient than the conventional route owing to dense accumulation of TPPy units in the films.

2.4.1 Introduction

Organosilica hybrids, synthesized by sol-gel polymerization of organic-bridged alkoxysilane precursors ($R[Si(OR')_3]_n$, $n \geq 2$, R: functional organic group, R': Me, Et), are a new class of functional organic-inorganic hybrid materials in which organic groups are covalently and homogeneously embedded in the robust silica networks.^{1,2} Recently, these materials have received considerable attention in various areas such as optical materials,³ photocatalyst,⁴ and electronic devices due to their organic functionalities and high stability.⁵ For the development of these applications, efficient light absorption and/or strong intermolecular interaction are essential factors. Consequently, the high-density accumulation of organic chromophores in the organosilica hybrids has become a currently interesting work in this field.

The density of chromophores in organosilica hybrids should strongly depend on the molecular architecture of the alkoxysilane precursor. Thus, precursors with chromophores directly attached

¹ Loy, D. A.; Shea, K. J. *Chem. Rev.* **1995**, *95*, 1431–1442.

² a) Shea, K. J.; Loy, D. A.; Webster, O. *J. Am. Chem. Soc.* **1992**, *114*, 6700–6710; b) Corriu, R. J. P.; Hesemann, P.; Lanneau, G. F. *Chem. Commun.* **1996**, 1845–1846; c) Sanchez, C.; Julián, B.; Belleville, P.; Popall, M. *J. Mater. Chem.* **2005**, *15*, 3559–3592.

³ Sanchez, C.; Lebeau, B.; Chaput, F.; Boilot, J.-P. *Adv. Mater.* **2003**, *15*, 1969–1994.

⁴ a) Ohashi, M.; Aoki, M.; Yamanaka, K.-i.; Nakajima, K.; Ohsuna, T.; Tani, T.; Inagaki, S. *Chem.–Eur. J.* **2009**, *15*, 13041–13046; b) Takeda, H.; Ohashi, M.; Tani, T.; Ishitani, O.; Inagaki, S. *Inorg. Chem.* **2010**, *49*, 4554–4559.

⁵ a) Dautel, O. J.; Wantz, G.; Almairac, R.; Flot, D.; Hirsch, L.; Lere-Porte, J.-P.; Parneix, J.-P.; Serein-Spirau, F.; Vignau, L.; Moreau, J. J. E. *J. Am. Chem. Soc.* **2006**, *128*, 4892–4901; b) Lin, C.-L.; Yeh, M.-Y.; Chen, C.-H.; Sudhakar, S.; Luo, S.-J.; Hsu, Y.-C.; Huang, C.-Y.; Ho, K.-C.; Luh, T.-Y. *Chem. Mater.* **2006**, *18*, 4157–4162; c) Mizoshita, N.; Ikai, M.; Tani, T.; Inagaki, S. *J. Am. Chem. Soc.* **2009**, *131*, 14225–14227; d) Lim, Y.; Park, Y.-S.; Kang, Y.; Jang, D. Y.; Kim, J. H.; Kim, J.-J.; Sellinger, A.; Yoon, D. Y. *J. Am. Chem. Soc.* **2011**, *133*, 1375–1382.

with silyl groups, which are typically prepared by halogen-lithium and magnesium exchange reactions^{2a} or rhodium-catalyzed silylation of aryl halides,⁶ are the most desirable for dense accumulation. However, the synthesis of desired functional alkoxy silane precursor is generally difficult, because the high reactivity of trialkoxysilyl groups is likely to cause side reactions such as polymerization and decomposition during these silylation reactions and purification. Furthermore, conventional routes are often limited in terms of difficulties in the preparation of halogenated substrate and functional tolerance in their reaction conditions. In addition, the Si–C bonds of this type of precursors sometimes cleave during the acidic or basic sol–gel polymerization.⁷

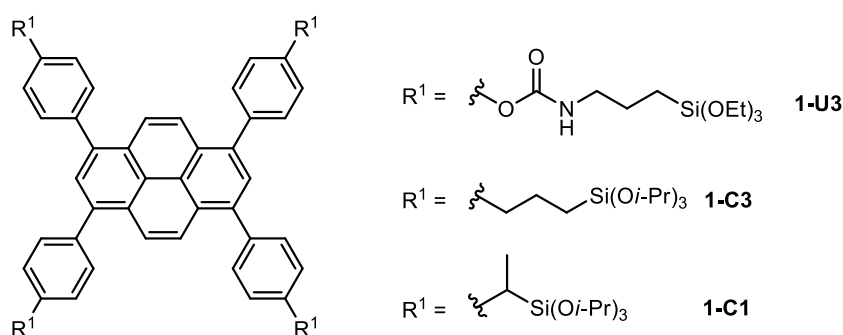


Figure 2.3. TPPy-bridged alkoxy silane precursors **1-U3**, **1-C3**, and **1-C1**.

The coupling reaction of hydroxy- or amino-substituted substrate with silane coupling agents has been widely used for the synthesis of functional organosilane precursors due to easiness in the preparation of substrates and mild reaction conditions.⁸ Mizoshita et al. recently reported the synthesis of 1,3,6,8-tetraphenylpyrene (TPPy)-bridged alkoxy silane precursor **1-U3** by coupling reaction of tetrahydroxy-substituted TPPy with 3-(triethoxysilyl)propyl isocyanate and its conversion to the transparent periodic mesostructured organosilica film with efficient blue fluorescence emissions (Figure 2.3).⁹ However, the long linkers in **1-U3** were also found to limit

⁶ a) Murata, M.; Ishikura, M.; Nagata, M.; Watanabe, S.; Masuda, Y. *Org. Lett.* **2002**, *4*, 1843–1845; b) Maegawa, Y.; Goto, Y.; Inagaki, S.; Shimada, T. *Tetrahedron Lett.* **2006**, *47*, 6957–6960; c) Mizoshita, N.; Goto, Y.; Tani, T.; Inagaki, S. *Adv. Funct. Mater.* **2008**, *18*, 3699; d) Maegawa, Y.; Mizoshita, N.; Tani, T.; Inagaki, S. *J. Mater. Chem.* **2010**, *20*, 4399–4403.

⁷ Shirai, S.; Goto, Y.; Mizoshita, N.; Ohashi, O.; Tani, T.; Shimada, T.; Hyodo, S.-a.; Inagaki, S. *J. Phys. Chem. A* **2010**, *114*, 6047–6054.

⁸ a) Lerouge, F.; Cerveau, G.; Corriu, R. J. P. *New J. Chem.* **2006**, *30*, 1364–1376; b) Kishida, T.; Fujita, N.; Sada, K.; Shinkai, S. *Chem. Lett.* **2004**, *33*, 1002–1004.

⁹ Mizoshita, N.; Goto, Y.; Maegawa, Y.; Tani, T.; Inagaki, S. *Chem. Mater.* **2010**, *22*, 2548–2554.

light absorption efficiency of the hybrid films. It is required to establish silylation routes other than direct silylation for dense accumulation of the organic-bridging groups (e.g., TPPy in **1-U3**). There have been few reports, however, on successful synthesis of high functional organosilane precursors with short linker.¹⁰ Herein, the author reports facile synthetic routes of aromatic-bridged alkoxyxilanes with short linkers, their sol-gel conversions to organosilica films, and optical properties of the films.

2.4.2 Experimental

Materials and methods

Unless otherwise noted, all materials including dry solvents were purchased from commercial suppliers, Sigma-Aldrich, Tokyo Chemical Industry and Wako Pure Chemical Industries, and were used without further purification. 1,3,6,8-Tetrabromopyrene,¹ **1-U3**,² and *rac*-2-diphenylphosphino-1,1'-binaphthyl (*rac*-H-MOP)^{3,4} were prepared according to methods given in the literature. All reactions were carried out under argon using standard high vacuum and Schlenk techniques. Nuclear magnetic resonance (NMR) spectra were recorded on a Jeol JNM-EXC400P spectrometer (400 MHz for ¹H and 100 MHz for ¹³C). Chemical shifts are reported in δ ppm with reference to an internal SiMe₄ standard for ¹H NMR and chloroform-*d* (δ 77.0) for ¹³C NMR. The following abbreviations were used to explain the multiplicities: s = singlet, d = doublet, t = triplet, q = quartet, m = multiplet, dd = double doublet. Infrared (IR) absorption measurements were conducted on a Thermo Nicolet Avatar 360 FT-IR spectrometer using an attenuated total reflection (ATR) attachment. Mass spectra were recorded on a Bruker Daltonics Autoflex mass spectrometer (MALDI: matrix-assisted laser desorption/ionization) or a Micromass Q-TOF mass spectrometer (ESI: electrospray ionization). The thickness of the films was measured using an Ulvac Dektak^{3ST} surface profiler. Optical microscopy observations were performed using an Olympus BX51 microscope. Ultraviolet-visible (UV-vis) absorption spectra were measured using a Jasco V-670 spectrometer. Fluorescence emission spectra were obtained using a Jasco

¹⁰ a) Huang, Q.; Evmenenko, G. A.; Dutta, P.; Lee, P.; Armstrong, N. R.; Marks, T. J. *J. Am. Chem. Soc.* **2005**, *127*, 10227–10242; b) Inagaki, S.; Guan, S.; Yang, Q.; Kapoor, M. P.; Shimada, T. *Chem. Commun.* **2008**, 202–204.

FP-6500 spectrometer.

Synthesis of precursors

1-Allyl-4-iodobenzene. To a solution of 1,4-diiodobenzene (20.0 g, 60.6 mmol) in dry THF (200 mL) was added dropwise a solution of isopropylmagnesium chloride (*i*-PrMgCl) (32.0 mL, 2.0 M in THF, 64 mmol) at $-30\text{ }^{\circ}\text{C}$. The reaction mixture was stirred at $-30\text{ }^{\circ}\text{C}$ for 8 h to give 4-iodophenylmagnesium chloride. To this Grignard reagent solution was added allyl bromide (5.26 mL, 60.8 mmol) at $-30\text{ }^{\circ}\text{C}$ in one portion, and then stirred at room temperature for 18 h. The reaction mixture was quenched with saturated NH_4Cl aqueous solution and extracted with Et_2O . The combined organic layers were washed with brine and dried over anhydrous MgSO_4 , filtered and concentrated under reduced pressure. The crude residue was purified by bulb-to-bulb distillation (1 mmHg, $70\text{ }^{\circ}\text{C}$) affording the title compound as a colorless oil (10.4 g, 70%). ^1H NMR (400 MHz, CDCl_3) δ 3.33 (t, $J = 6.6$ Hz, 2H), 5.04–5.10 (m, 2H), 5.86–5.97 (m, 2H), 6.94 (d, $J = 8.3$ Hz, 2H), 7.61 (d, $J = 8.3$ Hz, 2H); ^{13}C NMR (100 MHz, CDCl_3) δ 39.7, 91.2, 116.3, 130.7, 136.7, 137.4, 139.6.

4-Allylphenylboronic acid. To a solution of 1-allyl-4-iodobenzene (9.0 g, 36.9 mmol) in dry THF (90 mL) was added dropwise a solution of *i*-PrMgCl (24.0 mL, 2.0 M in THF, 48 mmol) at $0\text{ }^{\circ}\text{C}$. The reaction mixture was stirred at $0\text{ }^{\circ}\text{C}$ for 8 h to give 4-allylphenylmagnesium chloride. To this Grignard reagent solution was added trimethylborate (5.40 mL, 48.4 mmol) at $0\text{ }^{\circ}\text{C}$, and then stirred at room temperature for 15 h. The reaction mixture was quenched with 2 M HCl solution (60 mL) and extracted with Et_2O . The combined organic layers were washed with brine and dried over anhydrous MgSO_4 , filtered and concentrated under reduced pressure. The crude residue was washed with hexane affording the title compound with a small amount of its anhydrides as a white powder (5.97 g, 100%). ^1H NMR (400 MHz, CDCl_3) δ 3.48 (t, $J = 6.8$ Hz, 2H), 5.06–5.15 (m, 2H), 5.91–5.15 (m, 2H), 7.33 (d, $J = 8.1$ Hz, 2H), 8.16 (d, $J = 8.1$ Hz, 2H); ^{13}C NMR (100 MHz, CDCl_3) δ 40.5, 116.2, 128.3, 133.7, 135.8, 136.9, 144.9; ESI-HRMS m/z calcd for $\text{C}_9\text{H}_{11}\text{BO}_2$ (M^-): 161.0774; found: 161.0771; ν_{max} (neat) 3236 (O-H), 3080, 2935, 1637 (C=C), 1405, 1380, 1330, 1178 cm^{-1} .

1,3,6,8-Tetrakis(4-allylphenyl)pyrene (2a). To a suspension of 1,3,6,8-tetrabromopyrene (3.90 g, 7.53 mmol), 4-allylphenylboronic acid (6.24 g, 38.5 mmol), K_2CO_3 (5.00 g, 36.2 mmol) in dry

1,4-dioxane (330 mL) and degassed H₂O (33 mL) was added Pd(PPh₃)₄ (1.04 g, 0.90 mmol, 12 mol%) in one portion. The reaction mixture was stirred at 90 °C for 3 days. After cooling, the reaction mixture was quenched with water and extracted with CHCl₃. The combined organic layers were washed with brine and dried over anhydrous MgSO₄, filtered and concentrated under reduced pressure. The crude residue was purified by silica gel chromatography (eluent: hexane/CHCl₃=5:1) affording the title compound as a light yellow powder (4.75 g, 95%). ¹H NMR (400 MHz, CDCl₃) δ 3.52 (t, *J* = 6.8 Hz, 8H), 5.12–5.21 (m, 8H), 6.02–6.13 (m, 4H), 7.36 (d, *J* = 8.0 Hz, 8H), 7.60 (d, *J* = 8.0 Hz, 8H), 7.99 (s, 2H), 8.11 (s, 4H); ¹³C NMR (100 MHz, CDCl₃) δ 40.0, 46.9, 116.0, 125.2, 128.1, 128.6, 129.5, 130.7, 137.0, 137.4, 138.9, 139.1; MALDI-HRMS *m/z* calcd for C₅₂H₄₂ (M⁺): 666.3285; found: 666.3287; *v*_{max} (neat) 3074, 3056, 3047, 3023, 1801, 1637 (C=C), 1606, 1494 cm⁻¹.

1,3,6,8-Tetrakis(4-vinylphenyl)pyrene (2b). To a suspension of 1,3,6,8-tetrabromopyrene (500 mg, 0.97 mmol), 4-vinylphenylboronic acid (855 mg, 5.78 mmol), tripotassium phosphate (5.00 g, 36.2 mmol) in dry 1,4-dioxane (50 mL) and degassed H₂O (5 mL) was added Pd(PPh₃)₄ (135 mg, 0.12 mmol, 12 mol%) in one portion. The reaction mixture was stirred at 80 °C for 4 h. After cooling, the reaction mixture was quenched with water and extracted with CHCl₃. The combined organic layers were washed with brine and dried over anhydrous MgSO₄, filtered and concentrated under reduced pressure. The crude residue was purified by silica gel chromatography (eluent: hexane/EtOAc = 10:1) affording the title compound as a yellow powder (550 mg, 93%). ¹H NMR (400 MHz, CDCl₃) δ 5.34 (dd, *J* = 10.8 Hz, 0.8 Hz, 4H), 5.87 (dd, *J* = 17.6 Hz, 0.8 Hz, 4H), 6.84 (dd, *J* = 17.6 Hz, 10.8 Hz, 4H), 7.59 (d, *J* = 8.4 Hz, 8H), 7.64 (d, *J* = 8.4 Hz, 8H), 8.00 (s, 2H), 8.19 (s, 4H); ¹³C NMR (100 MHz, CDCl₃) δ 114.2, 125.3, 126.0, 126.2, 128.1, 129.3, 130.8, 136.5, 136.6, 136.9, 140.5; MALDI-HRMS *m/z* calcd for C₄₈H₃₄ (M⁺): 610.2661; found: 610.2670; *v*_{max} (neat) 3079, 3058, 3031, 3002, 1801, 1627 (C=C), 1604, 1494 cm⁻¹.

1,3,6,8-Tetrakis{4-[3-triisopropoxysilyl]propyl}phenyl}pyrene (1-C3). To a solution of **2a** (424 mg, 0.64 mmol) and a catalytic amount of H₂PtCl₆•6H₂O (Speier's catalyst) in dry benzene (15 mL) was added dropwise trichlorosilane (5.0 mL, 49.5 μmol) at 0 °C. The reaction mixture was stirred at 40 °C for 3 h in darkness. The reaction mixture was concentrated under reduced pressure and the residue was re-dissolved in dry CH₂Cl₂ (20 mL). The resultant solution was then carefully added to a solution of dry *i*-PrOH (876 μL, 11.4 mmol) and dry pyridine (926 μL, 11.4 mmol) in dry CH₂Cl₂

(60 mL) at 0 °C. The reaction mixture was stirred at room temperature for 3 h and then evaporated. The crude residue was purified by silica gel chromatography (eluent: hexane/EtOAc = 5:1) affording the title compound as a yellow powder (625 mg, 66%). ¹H NMR (400 MHz, CDCl₃) δ 0.69–0.74 (m, 8H), 1.21 (t, *J* = 8.0 Hz, 72H), 1.79–1.87 (m, 8H), 2.76 (t, *J* = 8.0 Hz, 8H), 4.20–4.26 (m, 12H), 7.34 (d, *J* = 8.0 Hz, 8H), 7.57 (d, *J* = 8.0 Hz, 8H), 7.99 (s, 2H), 8.17 (s, 4H); ¹³C NMR (100 MHz, CDCl₃) δ 12.0, 25.2, 25.6, 39.1, 64.9, 125.2, 128.0, 128.5, 130.5, 134.1, 137.2, 138.5, 141.5, 141.7; MALDI-HRMS *m/z* calcd for C₈₈H₁₃₀O₁₂Si₄ (M⁺): 1490.8639; found: 1490.8657; ν_{\max} (neat) 2968, 2929, 2873, 1496, 1461, 1407, 1378, 1368, 1170, 1116, 1025 (Si-O) cm⁻¹; $\lambda_{\text{abs}}(i\text{-PrOH})/\text{nm}$ 299 ($\epsilon/\text{dm}^3 \text{ mol}^{-1} \text{ cm}^{-1}$ 57700), 385 (41800).

1,3,6,8-Tetrakis{4-[1-(triisopropoxysilyl)ethyl]phenyl}pyrene (1-C1). To a solution of **2b** (75 mg, 0.12 mmol), [PdCl(π -C₃H₅)₂] (0.45 mg, 1.2 μmL , 2 mol%Pd) and *rac*-H-MOP (2.15 mg, 4.9 μmol , 4 mol%L) in dry benzene (5 mL) was added dropwise trichlorosilane (0.50 mL, 4.95 mmol) at 0 °C. The reaction mixture was stirred at 40 °C for 16 h in darkness. The reaction mixture was concentrated under reduced pressure and the residue was re-dissolved in dry CH₂Cl₂ (10 mL). The resultant solution was then carefully added to a solution of dry *i*-PrOH (169 μL , 2.21 mmol) and dry pyridine (174 μL , 2.21 mmol) in dry CH₂Cl₂ (10 mL) at 0 °C. The reaction mixture was stirred at room temperature for 3 h and then evaporated. The crude residue was purified by silica gel chromatography (eluent: hexane/EtOAc = 5:1) affording the title compound as a mixture of diastereomers (155 mg, 88%) as a greenish yellow powder. ¹H NMR (400 MHz, CDCl₃) δ 1.17 (dd, *J* = 6.4 Hz, 3.2 Hz, 72H), 1.50 (d, *J* = 7.6 Hz, 12H), 2.36 (q, *J* = 7.6 Hz, 4H), 4.17–4.25 (m, 12H), 7.41 (d, *J* = 8.4 Hz, 8H), 7.53 (d, *J* = 8.4 Hz, 8H), 7.96 (s, 2H), 8.12 (s, 4H); ¹³C NMR (100 MHz, CDCl₃) δ 16.0, 25.5, 27.0, 65.4, 125.0, 126.1, 128.1, 129.6, 130.2, 137.3, 137.5, 143.8; MALDI-HRMS *m/z* calcd for C₈₄H₁₂₂O₁₂Si₄ (M⁺): 1434.8014; found: 1434.8025; ν_{\max} (neat) 2969, 2929, 2871, 1381, 1367, 1170, 1114, 1027 (Si-O) cm⁻¹; $\lambda_{\text{abs}}(i\text{-PrOH})/\text{nm}$ 300 ($\epsilon/\text{dm}^3 \text{ mol}^{-1} \text{ cm}^{-1}$ 52500), 385 (39600).

Preparation of organosilica films

TPPy-bridged organosilane precursors (**1-U3**, **1-C3** or **1-C1**, 10 mg) were dissolved in propylene glycol propyl ether (0.5 g). A 2 M hydrochloric acid (HCl) aqueous solution (15 μL) was then added to the precursor solutions and the mixtures were stirred at room temperature for 12 h to

obtain sol solutions for the preparation of **1-C3-F** and **1-C1-F**. The concentration of the HCl aqueous solution and the stirring time were changed to 0.67 M and 4 h, respectively, for the preparation of **1-U3-F**, due to higher reactivity for hydrolysis of the triethoxysilyl group than that of the triisopropoxysilyl group. The prepared sol solutions were cast on a quartz glass plate and dried under reduced pressure in the dark to give the organosilica films.

2.4.3 Results and Discussion

The author synthesized novel TPPy-bridged alkoxy silane precursors with short linkers, **1-C3** and **1-C1** (Figure 2.3). To develop the synthetic route of these precursors, the author employed two main reactions, the Suzuki–Miyaura coupling and regioselective hydrosilylation. The efficient synthetic route of olefinic aromatics has been limited to the allylation of unstable metalated species and/or vinylation of aldehydes (Figure 2.4, methods a and b).^{10a,11} Although these methods have been applied to the synthesis of various olefinic aromatics, the reaction requires moisture-free and cryogenic conditions and often results in low yields or undesired product. Furthermore, these routes are required additional steps to prepare the corresponding substrates such as aryl dihalides and aryl dialdehydes and therefore are usually time-consuming process. To overcome these limitations and

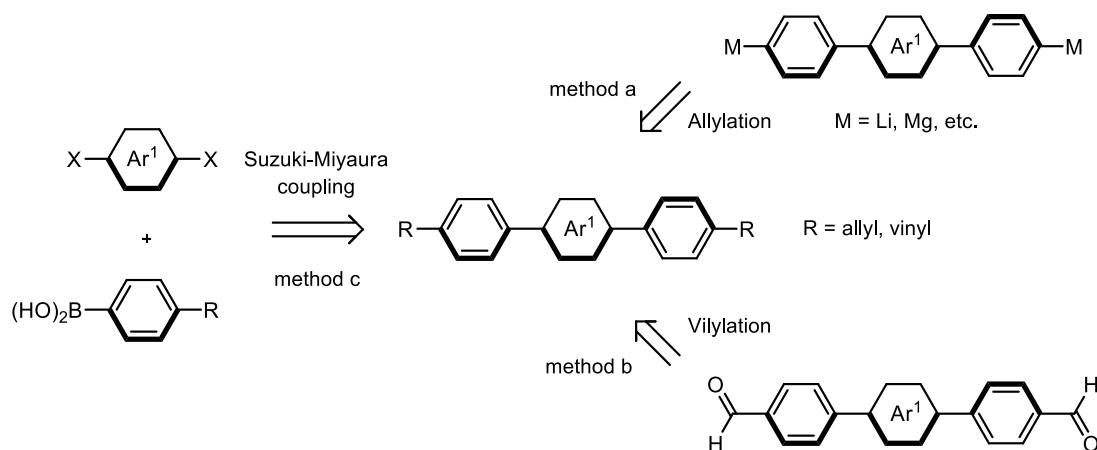


Figure 2.4. Synthetic routes for olefinic aromatics by allylation of metalated aromatic compounds (method a), vinylation of aromatic dialdehydes (method b), and Suzuki–Miyaura coupling between aryl dihalides and olefin-substituted phenylboronic acid (method c).

¹¹ Wittig, C.; Schöllkopf, U. *Chem. Ber.* **1954**, *87*, 1318–1330.

difficulties, the author employed a useful approach, the Suzuki–Miyaura coupling of aryl halide with olefin-substituted phenylboronic acid (Figure 2.4, method c).¹²

To introduce the hydrolyzable alkoxy-silyl groups, the author carried out regioselective hydrosilylation with trichlorosilane followed by alkoxylation with *i*-PrOH. It is well-known that the platinum-catalyzed hydrosilylation of allyl-substituted compound gives the γ -silylated (linear) product (Figure 2.5a).¹³ On the other hand, palladium-catalyzed hydrosilylation of vinyl-substituted compound furnishes the α -silylated (branched) product (Figure 2.5b).¹⁴ Therefore, organosilane precursors with short linkers could be prepared from olefinic aromatics by regioselective hydrosilylation.¹⁵

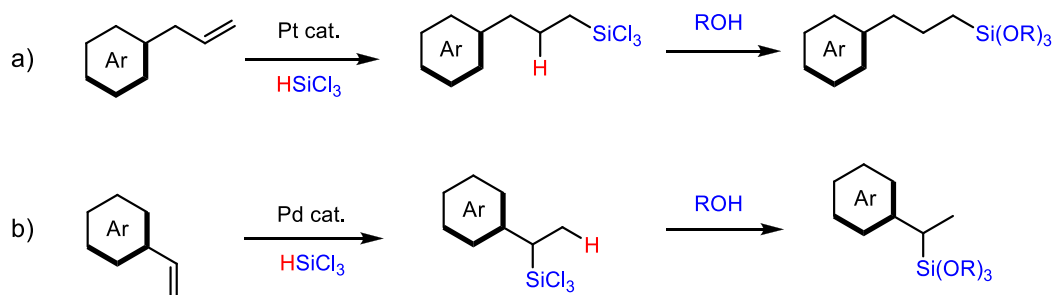


Figure 2.5. Regioselective hydrosilylation of olefinic aromatics catalyzed by a) platinum- or b) palladium-catalyst followed by alkoxylation with alcohol.

The olefinic TPPy derivatives **2a** and **2b** were synthesized by the palladium-catalyzed Suzuki–Miyaura coupling of 1,3,6,8-tetrabromopyrene with 4-allylphenylboronic acid or 4-vinylphenylboronic acid, respectively (Scheme 2.16). Each reaction successfully proceeded in the presence of Pd(PPh₃)₄ (12 mol%) as catalyst and gave the desired product **2a** and **2b** in 95% and 93% yield, respectively. Fortunately, undesired side reactions such as isomerization and polymerization of olefinic moiety were not observed. The obtained **2a** and **2b** were then regioselectively hydrosilylated with trichlorosilane in the presence of platinum or palladium

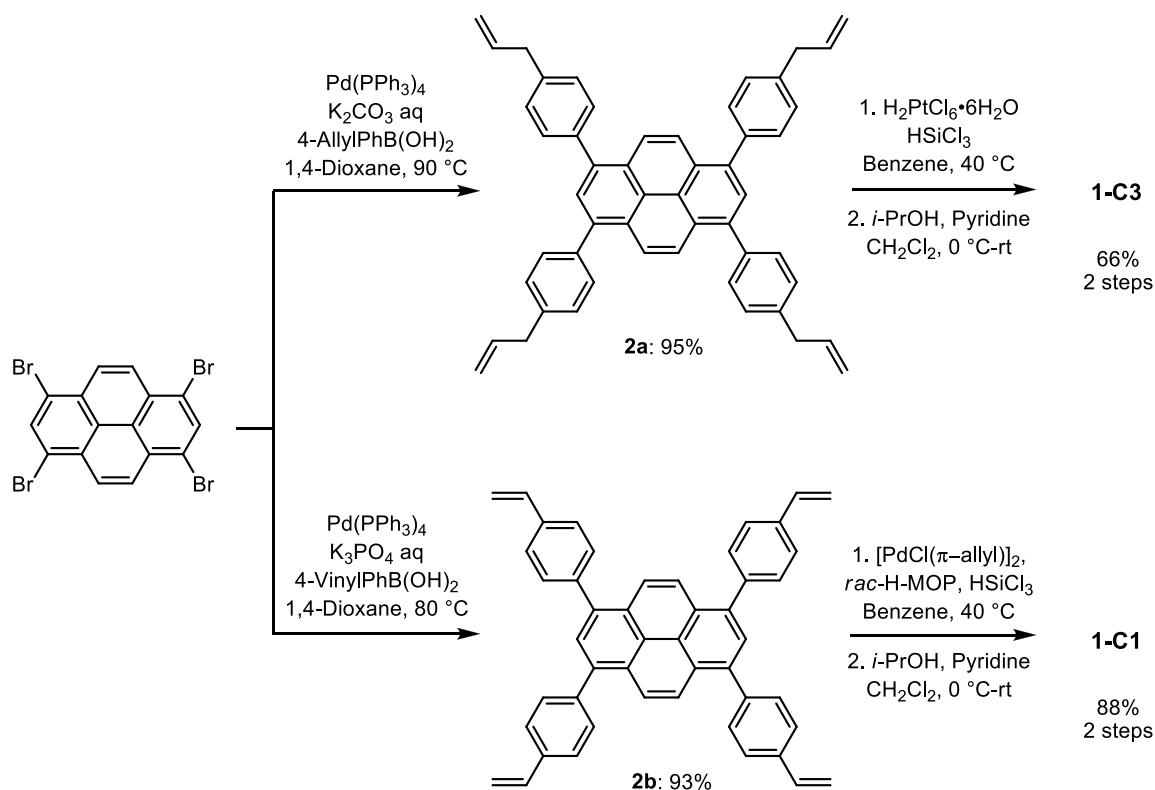
¹² Miyaura, N.; Suzuki, A. *Chem. Rev.* **1995**, *95*, 2457–2483.

¹³ Speier, J. L.; Webster, J. A.; Barnes, G. H. *J. Am. Chem. Soc.* **1957**, *79*, 974–979.

¹⁴ Hayashi, T. *Acc. Chem. Res.* **2000**, *33*, 354–362.

¹⁵ a) Kato, S.; Moriyama, H.; Takahashi, K.; Pac, C. *J. Mater. Chem.* **2009**, *19*, 8403–8410; b) Huang, Q.; Evmenenko, G.; Dutta, P.; Marks, T. J. *J. Am. Chem. Soc.* **2003**, *125*, 14704–14705; c) Hains, A. W.; Ramanan, C.; Irwin, M. D.; Liu, J.; Wasielewski, M. R.; Marks, T. J. *ACS Appl. Mater. Interfaces* **2010**, *2*, 175–185.

catalyst, respectively. The use of $\text{H}_2\text{PtCl}_6 \cdot 6\text{H}_2\text{O}$ (Speier's catalyst)¹³ was found to be effective for **2a**. The hydrosilylation proceeded regioselectively at γ -position of four allyl groups and gave the TPPy-bridged trichlorosilane in almost quantitative yield. The 4-fold hydrosilylation of **2b** was carried out in the presence of $\text{PdCl}(\pi\text{-C}_3\text{H}_5)_2$ and *rac*-H-MOP.¹⁴ As expected, the reaction regioselectively proceeded at α -positions of four vinyl groups and furnished the desired TPPy-bridged trichlorosilane quantitatively. However, the obtained chlorosilanes were too moisture-sensitive to handle as a precursor for the organosilica hybrids. Thus, these trichlorosilyl groups were transformed into relatively stable triisopropoxysilyl groups by quenching with 2-propanol in the presence of pyridine as a base, which afforded desired TPPy-bridged alkoxy silane precursors with short linkers **1-C3** and **1-C1** in 66% and 88% yield, respectively.¹⁶



Scheme 2.16. Synthetic routes to newly designed TPPy-bridged alkoxy silane precursors **1-C3** and **1-C1**.

¹⁶ Triethoxysilylation of TPPy-bridged trichlorosilanes with ethanol in the presence of pyridine were failed because side reaction (e.g., hydrolysis and polycondensation) occurred during the triethoxysilylation and purification with silica gel chromatography due to high reactivity of triethoxysilyl group.

From TPPy-bridged organosilanes **1-U3**, **1-C3**, and **1-C1**, organosilica hybrid films could be obtained by sol-gel polymerization in the presence of HCl and water in propylene glycol propyl ether. Transparent yellow films without cracks and inclusions were successfully obtained from all the precursors (Figure 2.6). The use of the high boiling point solvent facilitates the formation of uniform thickness of film due to the suppression of heterogeneous shrinkage during solvent evaporation.¹⁷ The thicknesses of **1-U3-F**, **1-C3-F**, and **1-C1-F** were 1450 ± 50 , 455 ± 30 , and 235 ± 30 nm, respectively. The change in the thickness can be attributed to the difference in the viscosity of the sol solutions.



Figure 2.6. Optical micrographs of a) **1-U3-F**, b) **1-C3-F** and c) **1-C1-F** (scale bar represents 20 μm).

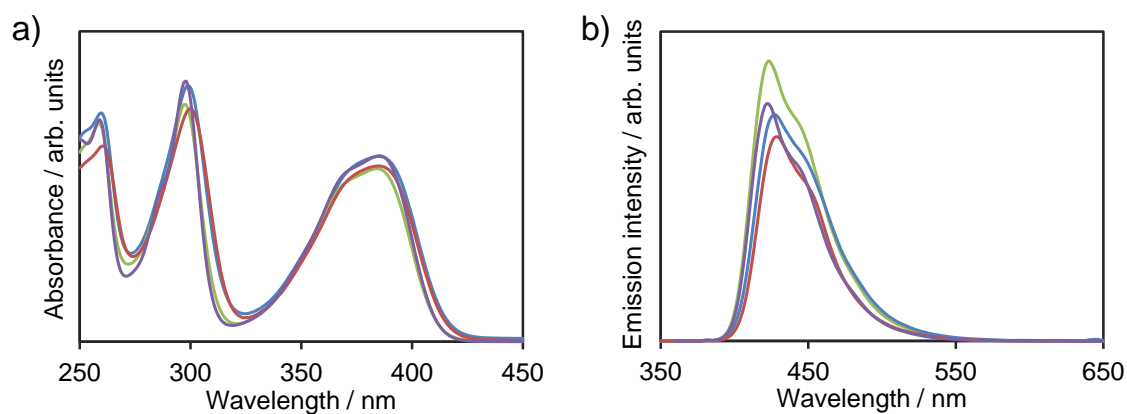


Figure 2.7. a) UV-vis absorption spectra and b) fluorescence emission spectra of **1-U3** (green line), **1-C3** (blue line), and **1-C1** (red line) in *i*-PrOH (1.0×10^{-5} M). The spectra for TPPy (purple line) in CH_2Cl_2 (1.0×10^{-5} M) are also presented for comparison.

The author evaluated the optical properties of TPPy-bridged alkoxy silane precursors and derived organosilica films to elucidate the effects of the linker length on accumulation state of

¹⁷ Brinker, C. J. *J. Non-Cryst. Solids* **1988**, *100*, 31–50.

TPPy moieties in these silica hybrids. The novel TPPy precursors **1-C3** and **1-C1** in diluted solution showed primary similar absorption and fluorescence properties compared with those of conventional precursor **1-U3** and their parent TPPy molecule (Figure 2.7). This suggests that the present linkers hardly influenced the electronic ground and excited state of these precursors in diluted condition.

Optical properties of derived organosilica films were quite different from one another. Figure 2.8 shows the wavelength dependence of the absorption coefficients (absorbance normalized by the film thickness) for organosilica and TPPy molecular films (**TPPy-F**). The absorption coefficient was significantly increased in the order of **1-U3-F** (17000 cm^{-1}) < **1-C3-F** (29400 cm^{-1}) < **1-C1-F** (39900 cm^{-1}) < **TPPy-F** (59800 cm^{-1}). It is quite reasonable to observe the difference in absorption coefficients because the ratios of TPPy moiety to whole molecules are completely different in their precursors. The maximum wavelengths of absorption spectra (λ_{max}) slightly red-shifted with respect to that for corresponding precursor solutions due to intermolecular interaction between TPPy moieties at the ground state. However, the observed red shift in the films is very small and shift values do not depend on the linker length. This may be attributed to the bulky structure of TPPy which inhibits dense packing of TPPy moiety in organosilica hybrids.

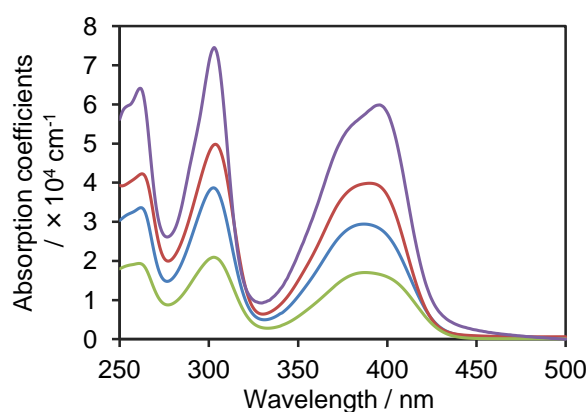


Figure 2.8. Dependence of the absorption coefficients for **1-U3-F** (green line), **1-C3-F** (blue line), **1-C1-F** (red line), and **TPPy-F** (purple line) on the wavelength. The absorption coefficients were obtained by normalizing the absorbance of the films at every wavelength according to the film thicknesses.

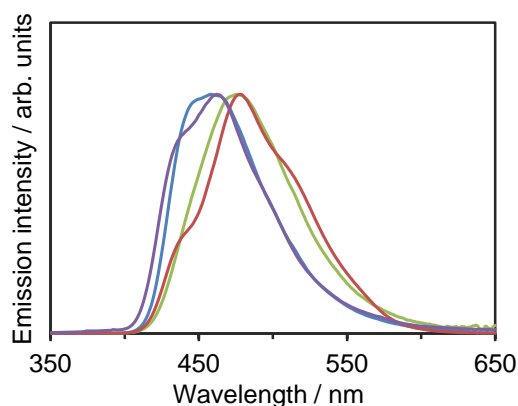


Figure 2.9. Normalized fluorescence emission spectra of **1-U3-F** (green line), **1-C3-F** (blue line), **1-C1-F** (red line), and **TPPy-F** (purple line). The excitation wavelength was 380 nm for all samples.

Figure 2.9 shows normalized fluorescence emission spectra for the organosilica and TPPy molecular films. The organosilica film **1-U3-F** showed broad emission bands at 450 and 470 nm which are assignable to monomer-like and excimer emissions, respectively.⁹ The existence of the strong monomer-like band and the relatively small red shift of the excimer band suggest relatively weak intermolecular interaction between the TPPy moieties in the excited state due to the long linker length in **1-U3**. In contrast, organosilica films **1-C3-F** and **1-C1-F** mainly showed the excimer emission band at 478 nm, which is red-shifted from that of **1-U3-F**, together with a weak monomer-like emission at 440 nm. In addition, **1-C1-F** showed a shoulder possibly due to the emission from TPPy dimer at 510 nm.¹⁸ These results strongly suggest that the shortening of the linker effectively enhanced intermolecular interaction between the TPPy moieties in the excited state. On the other hand, **TPPy-F** showed a fluorescence spectrum similar to that of **1-U3-F** despite the densest packing of the TPPy moieties possibly due to their different molecular arrangement from those of the organosilica films in which the TPPy moieties are fixed in the silica network.

¹⁸ Adachi et al. reported that TPPy molecule shows unusual photoluminescence characteristics in the solid-state morphologies. They demonstrated that TPPy exhibits blue fluorescence with a peak of $\lambda_{\text{max}} = 451\text{nm}$ and green fluorescence with a peak of $\lambda_{\text{max}} = 510\text{nm}$ by controlling their aggregate morphologies. Oyamada, T.; Akiyama, S.; Yahiro, M.; Saigou, M.; Shiro, M.; Sasabe, H.; Adachi, C. *Chem. Phys. Lett.* **2006**, *421*, 295–299.

2.4.4 Conclusions

The author demonstrated the facile synthetic route of functional organic-bridged alkoxy silane with short linker by regioselective hydrosilylation. Novel TPPy-bridged alkoxy silane precursors with short linker were successfully synthesized using the present procedure with aim to increase the absorption coefficient of TPPy-bridged organosilica film. A significant improvement of the absorption coefficient of the film was observed by shortening of linker length due to the high density of TPPy moieties in the film.

2.5 Sol–gel Polymerization Behavior of Organoallylsilanes

The author investigated solvent effects on the acid-catalyzed deallylation of organoallylsilane precursors to identify mild sol–gel polymerization conditions. Organoallylsilanes are expected to be alternative precursors for preparation of functionalized organosilica hybrids but they undergo sol–gel polymerization with difficulty due to their low reactivity towards hydrolysis. Sol–gel polymerization of model organoallylsilane precursors was conducted in various organic solvents and deallylation was monitored by ^1H NMR spectroscopy. The nature of the solvent was found to strongly influence the deallylation rate and a significant correlation was observed between reaction rate and solvent basicity, which suggests that proton activity is a key factor in enhancing the reaction rate. In particular, acetonitrile was found to most effectively enhance the rate, and it accelerated the formation of a spirobifluorene-bridged organosilica hybrid film from its allylsilane precursor under a mild acidic condition. This key finding can be generally utilized for the preparation of organoallylsilane-derived highly functionalized organosilica hybrids.

2.5.1 Introduction

Organosilica hybrid materials have received considerable attention in various research areas for their potential application in catalysts¹, adsorbents² and optical devices.³ These materials are readily prepared through sol–gel polymerization (hydrolysis and polycondensation) of organosilane precursors with hydrolyzable silyl groups ($\text{R}_n\text{SiX}_{4-n}$: R: organic group, X : OR', halide, OCOR', NR'₂, etc.)^{4,5} A broad spectrum of functional organic groups has been incorporated into amorphous and ordered silicate frameworks alike.^{1–3,6} Recent demands for the development of highly functionalized organosilica hybrids necessitate the use of organosilane precursors having significant

¹ Wight, A. P.; Davis, M. E. *Chem. Rev.* **2002**, *102*, 3589–3614.

² Stein, A.; Melde, B. J.; Schroden, R. C. *Adv. Mater.* **2000**, *12*, 1403–1419.

³ Sanchez, C.; Lebeau, B.; Chaput, F.; Boilot, J. P. *Adv. Mater.* **2003**, *15*, 1969–1994.

⁴ Loy, D. A.; Shea, K. J. *Chem. Rev.* **1995**, *95*, 1431–1442.

⁵ Vansant, E. F.; Van Der Voort, P.; Vrancken, C. in *Studies in Surface Science and Catalysis*, ed. B. Delmon and T. Yates, Elsevier, Amsterdam, 1995, vol. 93, part II.

⁶ a) Hoffmann, F.; Cornelius, M.; Morell, J.; Fröba, M. *Angew. Chem., Int. Ed.* **2006**, *45*, 3216–3251 b) Mizoshita, N.; Tani, T.; Inagaki, S. *Chem. Soc. Rev.* **2011**, *40*, 789–800; c) Wang, W.; Lofgreen, J. E.; Ozin, G. A. *Small* **2010**, *6*, 2634–2642.

optical, chemical or electrical functionalities. However, synthesis of the desired precursors is often difficult, because the high reactivity of conventional silyl groups causes side reactions such as polymerization and decomposition during the silylation reaction and purification. In particular, a serious problem is that silica gel chromatography cannot be utilized for purification of conventional organosilane precursors, unlike for general organic compounds.

Recently, allylsilyl groups ($\text{Si}-\text{CH}_2\text{CH}=\text{CH}_2$) have been found to behave as a synthetic equivalent to conventional silyl groups.^{7,8} Allylsilyl groups can be hydrolyzed and condensed under acidic hydrolytic conditions through the elimination of propene (deallylation) (Scheme 2.17).^{7a,9} They have a good tolerance for cross-coupling reaction conditions and silica gel chromatography,¹⁰ and thus are expected to be an alternative source of hydrolyzable silyl groups for synthesis of complex organosilane precursors.¹⁰ Recently, Tanaka et al. also reported on a new organoallylsilane precursor containing spirobifluorene as a bridging group, which underwent acidic sol-gel polymerization to form a periodic mesoporous organosilica (PMO) film.¹¹ However, allylsilyl groups are generally less reactive to hydrolysis than conventional silyl groups, and thus high acid concentrations (e.g. 0.2 M hydrochloric acid (HCl) in THF) and high temperatures (e.g. 60 °C) are usually required for hydrolysis in organic solvents compared to those for organoalkoxysilanes (e.g. 0.01M HCl at rt).^{7d} This is likely to cause decomposition of bridging organic groups and/or undesired Si-C bond cleavage between the silyl group and the bridging-organic group.^{12,13} Thus it is of great importance to identify mild conditions for sol-gel

⁷ a) Shimada, T.; Aoki, K.; Shinoda, Y.; Nakamura, T.; Tokunaga, N.; Inagaki, S.; Hayashi, T. *J. Am. Chem. Soc.* **2003**, *125*, 4688–4689; b) Aoki, K.; Shimada, T.; Hayashi, T. *Tetrahedron: Asymmetry* **2004**, *15*, 1771–1777; c) Kapoor, M. P.; Inagaki, S.; Ikeda, S.; Kakiuchi, K.; Suda, M.; Shimada, T. *J. Am. Chem. Soc.* **2005**, *127*, 8174–8178; d) Kapoor, M. P.; Yanagi, M.; Kasama, Y.; Yokoyama, T.; Inagaki, S.; Shimada, T.; Nanbu, H.; Juneja, L. R. *J. Mater. Chem.* **2006**, *16*, 3305–3311.

⁸ a) Yeon, Y.-R.; Park, Y. J.; Lee, J.-S.; Park, J.-W.; Kang, S.-G.; Jun, C.-H. *Angew. Chem., Int. Ed.* **2008**, *47*, 109–112; b) Zhang, Y.; Zhao, L.; Lee, S. S.; Ying, J. Y. *Adv. Synth. Catal.* **2006**, *348*, 2027–2032; c) Wang, Y.; Hu, S.; Brittain, W. J. *Macromolecules* **2006**, *39*, 5675–5678.

⁹ a) Sommer, L. H.; Tyler, L. J.; Whitmore, F. C. *J. Am. Chem. Soc.* **1948**, *70*, 2872–2874; b) Chan, T. H.; Fleming, I. *Synthesis* **1979**, 761–786; c) Morita, T.; Okamoto, Y.; Sakurai, H. *Tetrahedron Lett.* **1980**, *21*, 835–838.

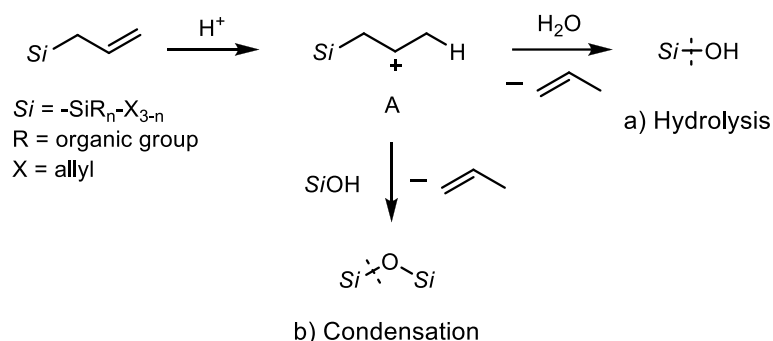
¹⁰ Maegawa, Y.; Nagano, T.; Yabuno, T.; Nakagawa, H.; Shimada, T. *Tetrahedron* **2007**, *63*, 11467–11474.

¹¹ Tanaka, N.; Mizoshita, N.; Maegawa, Y.; Tani, T.; Inagaki, S.; Jorapur, Y. R.; Shimada, T. *Chem. Commun.* **2011**, *47*, 5025–5027.

¹² Yoshina-Ishii, C.; Asefa, T.; Coombs, N.; MacLachlan, M. J.; Ozin, G. A. *Chem. Commun.* **1999**, 2539–2540.

¹³ Shirai, S.; Goto, Y.; Mizoshita, N.; Ohashi, M.; Tani, T.; Shimada, T.; Hyodo, S.; Inagaki, S. *J. Phys. Chem. A* **2010**, *114*, 6047–6054.

polymerization of organoallylsilane precursors.



Scheme 2.17. Presumed deallylation mechanism of an allylsilyl group during acid-catalyzed a) hydrolysis and b) condensation.

In this paper, the author investigated the effects of solvents on the acid-catalyzed deallylation of organoallylsilane precursors to identify mild conditions for sol–gel polymerization. Hydrolysis and polycondensation of model precursors were conducted in various organic solvents and the deallylation behaviors were monitored by ^1H NMR spectroscopy. The nature of the solvent strongly influenced the reaction rate and the observed solvent effect was well explained in terms of the solvent basicity parameter (solvent basicity: SB), which suggests that the proton activity is a key factor in enhancing the reaction rate. The use of a solvent with low SB was confirmed to accelerate the formation of a functional organosilica hybrid film from its allylsilane precursor under a mild acidic condition.

2.5.2 Experimental

Materials and methods

Unless otherwise noted, all materials, including dry solvents, were purchased from commercial suppliers (Sigma-Aldrich, Tokyo Chemical Industry, Wako Pure Chemical Industries and AZmax Co., Ltd) and used without further purification. **SBF-Si** was prepared according to a literature method.¹⁴ All reactions were carried out under argon using standard high vacuum and Schlenk

¹⁴ Tanaka, T.; Mizoshita, N.; Maegawa, Y.; Tani, T.; Inagaki, S.; Jorapur, Y. R.; Shimada, T. *Chem. Commun.* **2011**, 47, 5025-5027

techniques. Nuclear magnetic resonance (NMR) spectra were recorded on a Jeol JNM-EXC400P spectrometer (400 MHz for ^1H and 100 MHz for ^{13}C). Chemical shifts are reported in δ ppm referenced to an internal SiMe_4 standard for ^1H NMR and chloroform-*d* (δ 77.0) for ^{13}C NMR, respectively. The following abbreviations were used to explain the multiplicities: s = singlet, d = doublet, t = triplet, q = quartet, ddd = doublet of double doublet, ddt = doublet of double triplet, ddq = doublet of double quartet. Mass spectra were recorded on a Waters GCT Premiermass spectrometer (FI: field ionization). Ultraviolet-visible (UV-vis) absorption spectra were measured using a Jasco V-670 spectrometer. Fluorescence emission spectra were obtained using a Jasco FP-6500 spectrometer. Fluorescence quantum yields were determined using a photoluminescence quantum yield measurement system equipped with a calibrated integrating sphere (Hamamatsu Photonics, C9920-02).

Synthesis of organoallylsilane precursors

Diallyl(ethoxy)(*p*-tolyl)silane (1a). To a solution of triethoxy(*p*-tolyl)silane (12.0 g, 47.2 mmol) in dry Et_2O (20 mL) was added dropwise a solution of allylmagnesium bromide (AllylMgBr) (142 mL, 1.0 M in Et_2O , 142 mmol) at 0 °C. The reaction mixture was stirred at room temperature for 24 h and quenched with saturated NH_4Cl aqueous solution and extracted with Et_2O . The combined organic layers were dried over anhydrous MgSO_4 , filtered and concentrated under reduced pressure. The crude residue was purified by silica gel chromatography (eluent: hexane) affording the title compound as a colorless oil (9.94 g, 86%). ^1H NMR (400 MHz, CDCl_3) δ 1.20 (t, J = 6.8 Hz, 3H), 1.93 (ddd, J = 8.0 Hz, 1.2 Hz, 0.8 Hz, 4H), (s, 3H), 3.75 (q, J = 6.8 Hz, 2H), 4.90 (ddt, J = 10.0 Hz, 1.4 Hz, 0.8 Hz, 2H), 4.95 (ddt, J = 16.0 Hz, 1.4 Hz, 1.2 Hz, 2H), 5.82 (ddt, J = 16.0 Hz, 10.0 Hz, 8.0 Hz, 2H), 7.20 (d, J = 7.8 Hz, 2H), 7.47 (d, J = 7.6 Hz, 2H); ^{13}C NMR (100 MHz, CDCl_3) δ 18.4, 21.3, 21.5, 59.2, 114.6, 128.6, 131.4, 133.3, 134.1, 139.8; FI-HRMS m/z calcd for $\text{C}_{15}\text{H}_{22}\text{OSi}$ (M^+): 246.1440; found: 246.1430.

Triallyl(*p*-tolyl)silane (1b). To a solution of (*p*-tolyl)trichlorosilane (2.40 g, 10.6 mmol) in dry Et_2O (30 mL) was added dropwise a solution of AllylMgBr (40 mL, 1.0 M in Et_2O , 40 mmol) at 0 °C. The reaction mixture was refluxed for 16 h, quenched with saturated NH_4Cl aqueous solution and extracted with Et_2O . The combined organic layers were dried over anhydrous MgSO_4 , filtered

and concentrated under reduced pressure. The crude residue was purified by silica gel chromatography (eluent: hexane) affording the title compound as a colorless oil (2.46 g, 95%). ^1H NMR (400 MHz, CDCl_3) δ 1.85 (ddd, $J = 8.2$ Hz, 1.2 Hz, 0.8 Hz, 6H), 2.35 (s, 3H), 4.88 (ddt, $J = 10.4$ Hz, 1.6 Hz, 0.8 Hz, 3H), 4.91 (ddt, $J = 16.0$ Hz, 1.6 Hz, 1.2 Hz, 3H), 5.79 (ddt, $J = 16.0$ Hz, 10.4 Hz, 8.2 Hz, 3H), 7.18 (d, $J = 8.0$ Hz, 2H), 7.41 (d, $J = 8.0$ Hz, 2H); ^{13}C NMR (100 MHz, CDCl_3) δ 19.6, 21.5, 114.2, 128.6, 131.5, 134.0, 134.3, 139.3; FI-HRMS m/z calcd for $\text{C}_{16}\text{H}_{22}\text{Si}$ (M^+): 242.1491; found: 242.1493.

Observation of sol–gel polymerization of model organoallylsilane precursors by ^1H NMR measurements

Precursor **1a** (25 mg, 0.10 mmol) was dissolved in $\text{MeOH-}d_4$, $\text{THF-}d_8$, $\text{DMSO-}d_6$, $\text{acetone-}d_6$ or $\text{MeCN-}d_3$ (0.25 mL), respectively. Precursor **1b** (25 mg, 0.10 mmol) was dissolved in $\text{acetone-}d_6$ or $\text{MeCN-}d_3$ (0.25 mL), respectively. As an internal standard, a small amount of 1,4-dichlorobenzene or naphthalene was added to the precursor solution. To calculate the initial concentration of the allyl group relative to the internal standard, a reaction aliquot was measured by ^1H NMR spectroscopy before the reaction. Then 2 M HCl aqueous solution was added (2.5–25 μL , 5.0–50 μmol , 0.02–0.2 M in reaction solvent), and the reaction mixture stirred at 60 °C. The sol solution was cast on a glass plate to determine whether a solid organosilica film could be obtained. The reaction aliquot (25 μL) was also rapidly diluted with the same deuterated solvent and quickly measured by ^1H NMR spectroscopy. Conversion of the allyl and ethoxy groups was determined by integrating the selected resonance peaks for the allyl and ethoxy groups, respectively, relative to that of the internal standard.

Identification of the generated gas during sol–gel polymerization of 1a and 1b

The generated gas during acid-catalyzed sol–gel polymerization of **1a** and **1b** was identified by ^1H NMR spectroscopy. A 50 mL, one-necked, round-bottomed flask equipped with a magnetic stirring bar was sequentially charged with **1a** or **1b** (250 mg, 1.0 mmol) and MeCN (2.50 mL). After addition of a 2 M HCl aqueous solution (0.25 mL, 0.50 mmol), the flask was capped with a septum and stirred at 60 °C for 1 h (*Caution!:* the increased inner pressure may blow out the septum). The gas phase in the flask was collected with a syringe and passed through MeCN- d_3 . The solution was

immediately characterized by ^1H NMR spectroscopy. The generated gas was identified as propene. ^1H NMR (400 MHz, $\text{MeCN-}d_3$) δ 1.70 (ddd, $J = 6.4$ Hz, 1.7 Hz, 1.4 Hz, 3H), 4.93 (ddq, $J = 10.1$ Hz, 2.2 Hz, 1.4 Hz, 1H), 5.04 (ddq, $J = 16.6$ Hz, 2.2 Hz, 1.7 Hz, 1H), 5.85 (ddq, $J = 16.6$ Hz, 10.1 Hz, 6.4 Hz, 1H).

Preparation of spirobifluorene-bridged organosilica film

Spirobifluorene-bridged allylsilane precursor **SBF-Si** (10 mg, 7.5 μmol) was dissolved in THF/MeCN (2 : 1 = v/v, 0.40 mL) and then 2 M HCl aqueous solution (4.0 μL , 8.0 μmol , 0.02 M in reaction solvent) was added to the solution. The mixture was stirred at 60 $^\circ\text{C}$ for 3 h. The sol solution was diluted with THF (1.20 mL), coated on a quartz glass plate by spin-coating (4000 rpm, 30 s) and dried under reduced pressure to give an organosilica film.

2.5.3 Results and Discussion

Sol-gel polymerization behavior of model organoallylsilane precursors by ^1H NMR spectroscopy

The behavior of organoallylsilanes under acid-catalyzed hydrolysis and polycondensation was examined in various organic solvents containing HCl (0.2 M in the solutions). Organoallylsilanes **1a** and **1b** (Figure 2.10) were used as model precursors because both diallylethoxy- and triallyl-silyl groups have been utilized as precursors for PMO synthesis.^{7d,11} Water-soluble polar solvents, methanol (MeOH), tetrahydrofuran (THF), dimethyl sulfoxide (DMSO), acetone and acetonitrile (MeCN) were chosen because they were appropriate for preparing a homogeneous solution containing the organoallylsilane, HCl and water. Solutions of **1a** and **1b** were stirred at 60 $^\circ\text{C}$ for 3–48 h and subjected to hydrolysis and polycondensation to obtain sol solutions. The sol solutions were cast on a glass substrate in order to check whether a solid film was obtained.

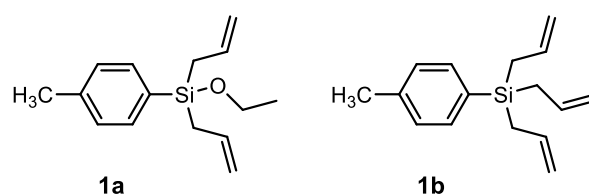
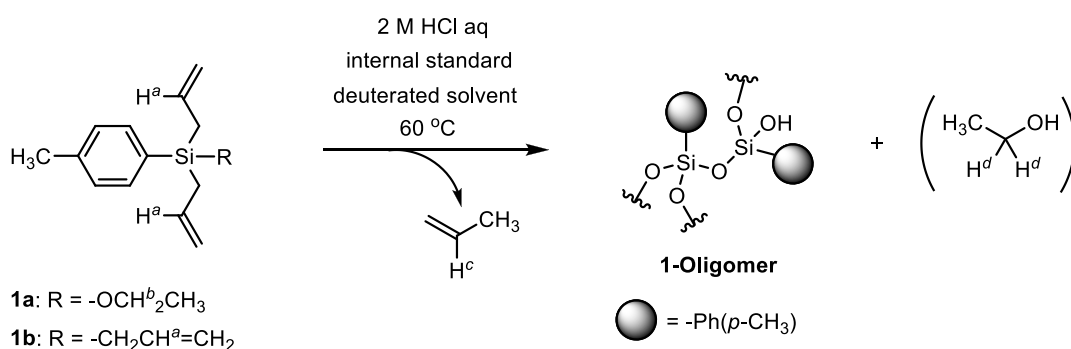


Figure 2.10. Chemical structures of model organoallylsilane precursors **1a** and **1b**.



Scheme 2.18. Acid-catalyzed sol-gel polymerization of **1a** and **1b**. The protons H^a , H^b , H^c and H^d were monitored by ^1H NMR spectroscopy.

Table 2.5 Acidic sol-gel polymerization of model organoallylsilane precursors **1a** and **1b** in various organic solvents^a

1. 2 M HCl aq / Solvent
60 °C, 3-48 h
2. Cast on glass plates

1a: R = OEt, 1b: R = allyl

1-Film
● = $-\text{Ph}(p\text{-CH}_3)$

Entry	Precursor	Solvent	$\nu_0^b / \text{M s}^{-1}$	Solid film formation
1	1a	MeOH	2.40×10^{-5}	No
2	1a	THF	2.14×10^{-5}	No
3	1a	DMSO	0.90×10^{-5}	No
4	1a	Acetone	8.64×10^{-5}	Yes (24 h) ^c
5	1a	MeCN	45.3×10^{-5}	Yes (3 h) ^c
6	1b	Acetone	1.23×10^{-5}	No
7	1b	MeCN	3.88×10^{-5}	Yes (4 h) ^c

^a Reactions of the allylsilane precursors **1a** and **1b** (0.10 mmol) were carried out at 60 °C for 3-48 h in the solvents (0.25 mL) in the presence of HCl (0.2 M). ^b The deallylation rate at the initial 0.5 h. ^c The reaction time required for the formation of a solid organosilica film from the sol-solution.

Conversion of the allyl groups in the organoallylsilane precursors during the reactions was monitored by ^1H NMR spectroscopy (signals from the β -hydrogens of the allylsilyl groups, Figures 2.11–2.16) in deuterated solvents. The measurements were carried out for their sol-solutions containing internal standards (1,4-dichlorobenzene: DCB or naphthalene: Nap). Figures 2.11-2.16

show the ^1H NMR spectra of **1a** or **1b** in various deuterated solvents at 0 min, 10 min and 4 h after the addition of HCl. In these figures, the letters (*a*, *b*, *c*, and *d*) indicate the signals corresponding to the protons shown in Scheme 2.18.

For **1a**, the signals corresponding to the proton *b* completely disappeared along with the appearance of the signals corresponding to the proton *d* within 10 min for all the solvents (Figures 2.11–2.15), which indicates that the ethoxy group in **1a** is immediately hydrolyzed to ethanol regardless of the nature of solvents. This surely indicates that hydrolysis of the ethoxysilyl group is very fast compared to that of the allylsilyl group and deallylation determines the overall sol–gel polymerization rate of **1a**. The nature of solvents strongly affected the deallylation rate of **1a**. After 4 h, intensities of the signals corresponding to the proton *a* decreased by 100% for MeCN (Figure 2.11), 76% for acetone (Figure 2.12) and less than 30% for MeOH, THF, and less than 10% for DMSO (Figures 2.13–2.15). MeCN was also effective for deallylation of **1b** and the signals corresponding to the proton *a* completely disappeared within 4 h (Figure 2.16a). Meanwhile, 80% of the allyl groups remained after 4 h for acetone (Figure 2.16b).

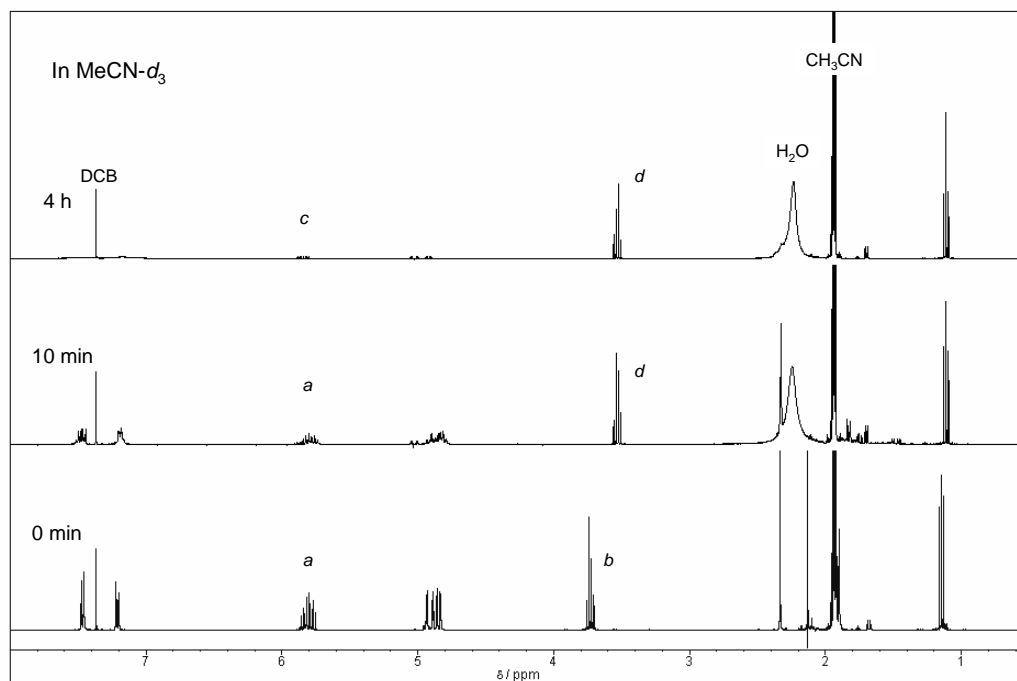


Figure 2.11. Changes in the ^1H NMR spectra of the sol–solution of **1a** in $\text{MeCN-}d_3$ at 0 min, 10 min and 4 h after the addition of HCl.

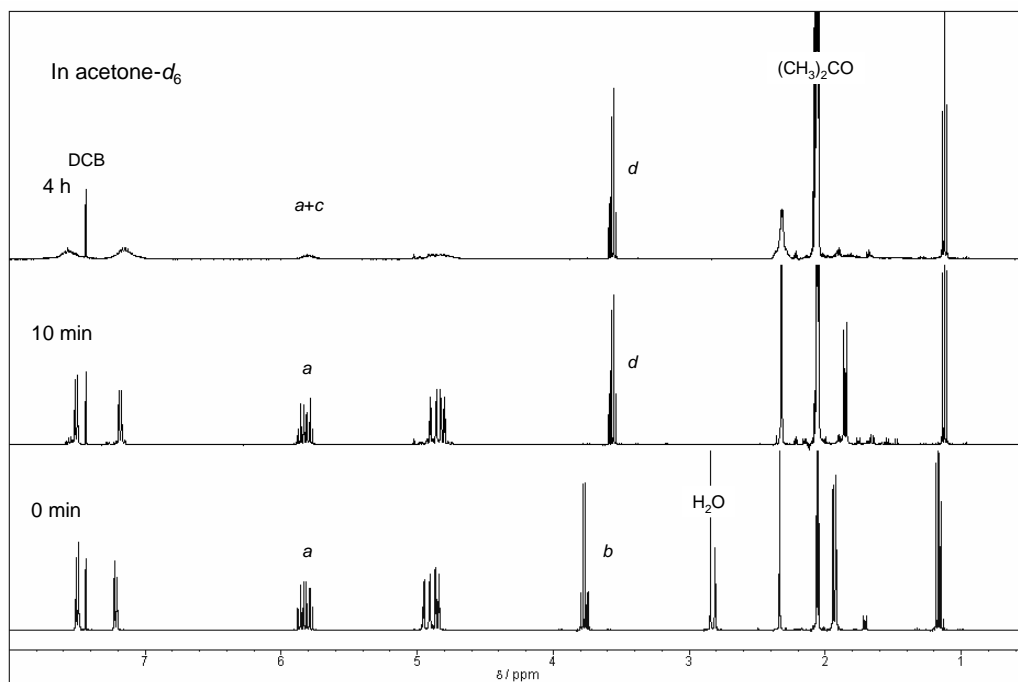


Figure 2.12. Changes in the ¹H NMR spectra of the sol–solution of **1a** in acetone-*d*₆ at 0 min, 10 min and 4 h after the addition of HCl.

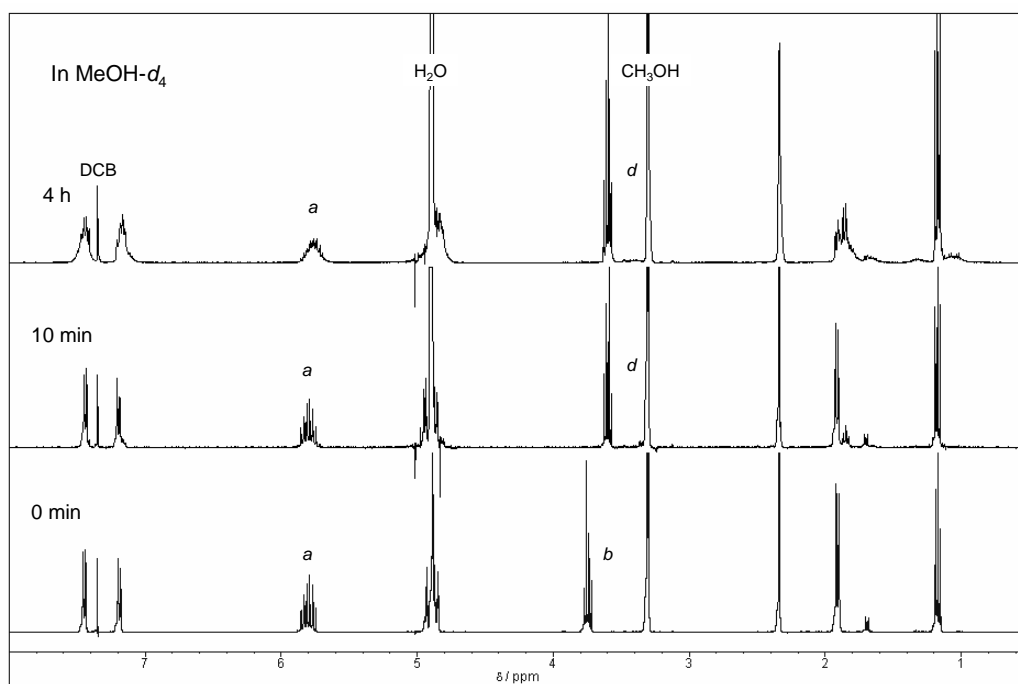


Figure 2.13. Changes in the ¹H NMR spectra of the sol–solution of **1a** in MeOH-*d*₄ at 0 min, 10 min and 4 h after the addition of HCl.

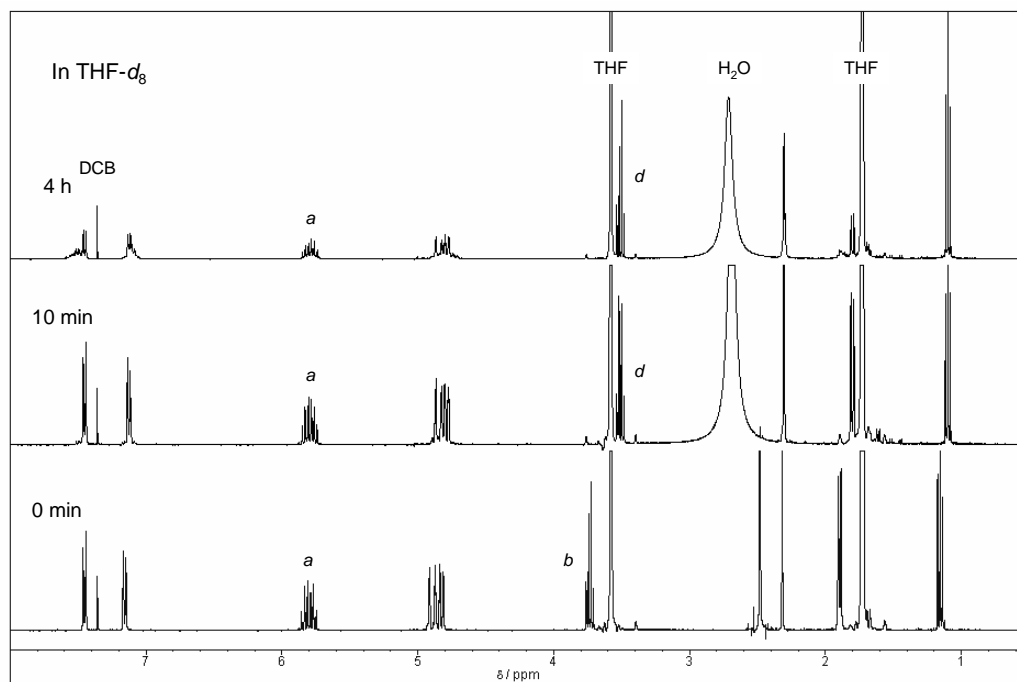


Figure 2.14. Changes in the ¹H NMR spectra of the sol–solution of **1a** in THF-*d*₈ at 0 min, 10 min and 4 h after the addition of HCl.

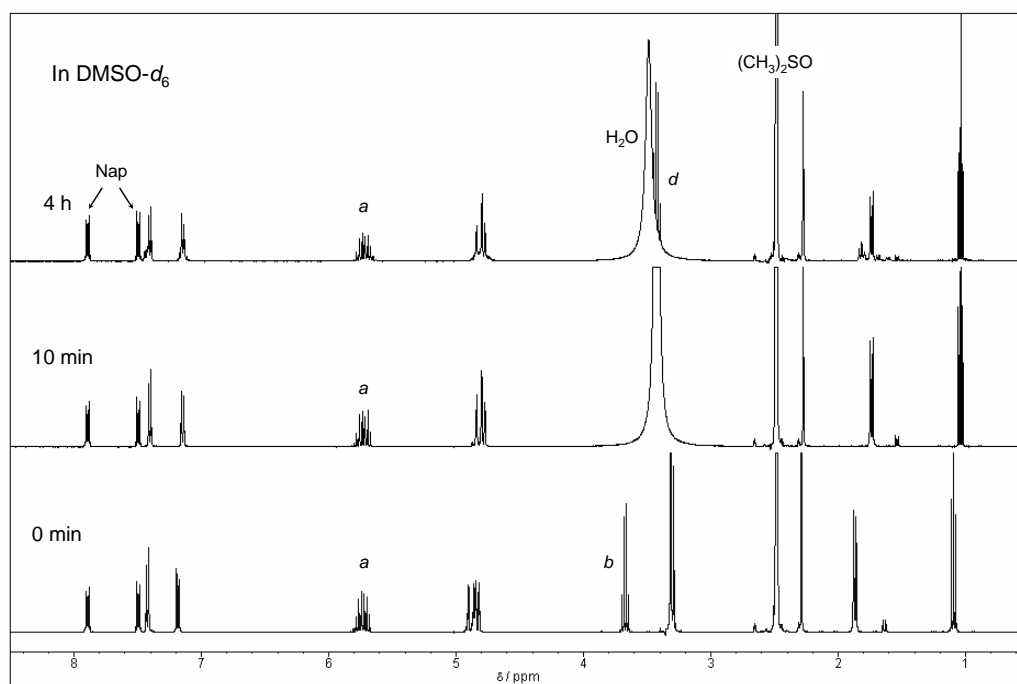


Figure 2.15. Changes in the ¹H NMR spectra of the sol–solution of **1a** in DMSO-*d*₆ at 0 min, 10 min and 4 h after the addition of HCl.

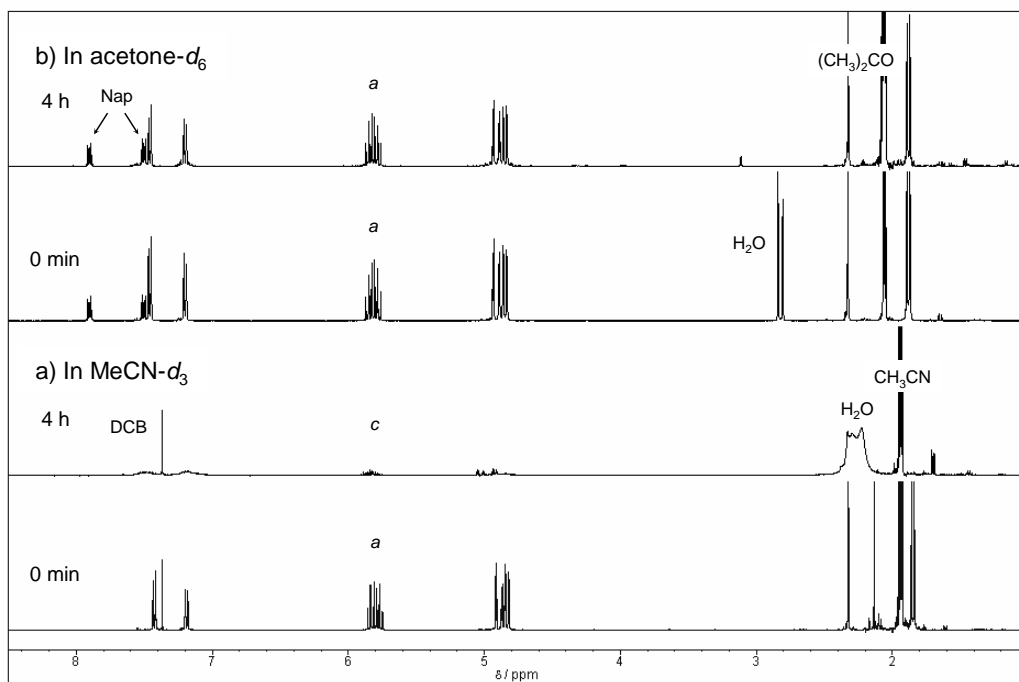


Figure 2.16. Changes in the ^1H NMR spectra of the sol-solutions of **1b** in a) $\text{MeCN-}d_3$ and b) $\text{acetone-}d_6$ at 0 min and 4 h after the addition of HCl.

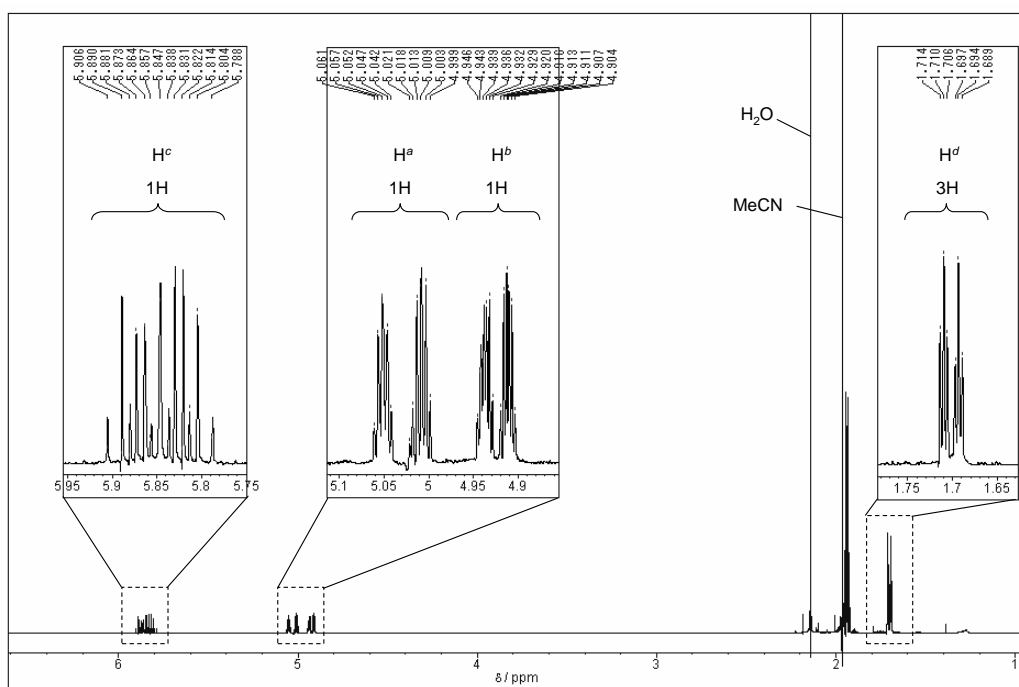


Figure 2.17. ^1H NMR spectrum of the generated gas dissolved in $\text{MeCN-}d_3$.

Figure 2.18a plots the conversion of allyl groups in **1a** in various solvents after the addition of HCl, and Table 2.5 gives the deallylation rates (v_0) at the initial 0.5 h.¹⁵ The v_0 was strongly influenced by the solvent. The highest v_0 of $45.3 \times 10^{-5} \text{ M s}^{-1}$ was obtained with MeCN, which gave complete deallylation within 3 h (Figure 2.11). The second highest v_0 of $8.64 \times 10^{-5} \text{ M s}^{-1}$ was obtained with acetone, which gave 76% deallylation after 4 h (Figure 2.12). These solutions (MeCN and acetone) released considerable amounts of a gas during the reaction, which was identified as propene by ^1H NMR spectroscopy (Figure 2.17). Solid films were formed from the sol solutions after stirring in MeCN and acetone for 3 h and 24 h, respectively, to allow evaporation of the solvents (Table 2.5, entries 4 and 5). In MeCN, a solid film was also obtained even at a HCl concentration ten-fold lower (0.02 M) than that used for the other solvents after 30 h. These results indicate that the polycondensation reaction was significantly promoted in MeCN. In contrast, the use of MeOH, THF and DMSO resulted in relatively low v_0 of $2.40 \times 10^{-5} \text{ M s}^{-1}$, $2.14 \times 10^{-5} \text{ M s}^{-1}$ and $0.90 \times 10^{-5} \text{ M s}^{-1}$, respectively (Table 2.5, entries 1–3). For example, more than 90% of the allyl groups remained after 4 h in DMSO (Figure 2.15). For these solvents, the sol solutions formed soluble gel-like films even after stirring for 120 h.

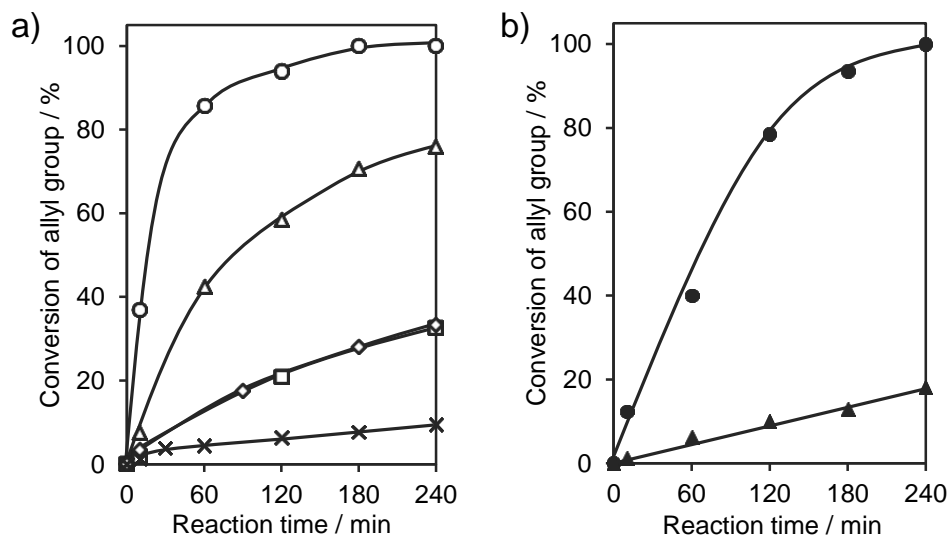


Figure 2.18. Conversion of allyl groups in a) **1a** and b) **1b** with the reaction time for the sol solutions using various deuterated solvents. Solvents are labelled as follows: MeCN (○); acetone (△); MeOH (◇); THF (□); and DMSO (×) for **1a**, MeCN (●); acetone (▲) for **1b**.

¹⁵ The deallylation rate v_0 was estimated from the linear interpolation of the data, corresponding to decay of allyl group at the initial 0.5 h.

Figure 2.18b plots the conversion of allyl groups in **1b** in MeCN and acetone. The v_0 of **1b** is higher for MeCN ($3.88 \times 10^{-5} \text{ M s}^{-1}$) than acetone ($1.23 \times 10^{-5} \text{ M s}^{-1}$), which was a similar result to that observed for **1a**. On the other hand, the deallylation rates of **1b** were smaller than those of **1a** due to the lower reactivity of the triallylsilyl group (Table 2.5, entries 6 and 7). However, despite the low reactivity, the sol–solution of **1b** in MeCN formed a solid film after stirring for 4 h.

Mechanism of solvent effect on sol–gel polymerization of organoallylsilane precursors

In the following the author outlined the origin of the observed solvent effect based on the underlying reaction mechanism. Hydrolysis and condensation of the allylsilyl groups are considered to proceed as follows: (i) electrophilic addition of a proton to the allyl group forms a β -silyl cation intermediate **A** and (ii) subsequent nucleophilic attack of water to **A** forms a silanol species along with the generation of propene (Scheme 2.17a). The silanol species then further reacts with **A** (or another silanol species) to form a siloxane bond, allowing condensation to progress (Scheme 2.17b). According to this scheme, the deallylation reaction can be influenced by three factors: (i) proton activity, (ii) stability of the β -silyl cation intermediate and (iii) nucleophilicity of the water (or silanol species). These factors are closely related to the Catalan solvent basicity (SB),¹⁶ dielectric constant (D_C)¹⁷ and Gutmann's acceptor number (AN),¹⁸ respectively. Here, the SB is an index for hydrogen-bond acceptor basicity and a low SB leads to a high proton activity, accelerating electrophilic addition of the proton to the allyl group. D_C is an index for solvent polarity and a high D_C leads to high stability of the cationic intermediate **A**, decreasing the activation barriers of both steps. AN is an index for the strength of the solvent as a Lewis acid and a low AN leads to high nucleophilicity of the oxygen atoms in water (or the silanol species), accelerating the nucleophilic attack step. Figures 2.19a–c show the relationship between the initial deallylation rate v_0 of **1a** and SB, D_C , and AN, respectively, for various solvents. A correlation was apparent for v_0 vs SB, but not for v_0 vs D_C or v_0 vs AN.

¹⁶ Catalan, J.; Palomar, J.; Diaz, C.; de Paz, J. L. G. *J. Phys. Chem. A* **1997**, *101*, 5183–5189.

¹⁷ Lide, D. R. in *CRC Handbook of Chemistry and Physics: A Ready-Reference Book of Chemical and Physical Data*, CRC Press, 85th edn, 2004, section 8, p. 141.

¹⁸ Gutmann, V. *Coord. Chem. Rev.* **1976**, *18*, 225–255.

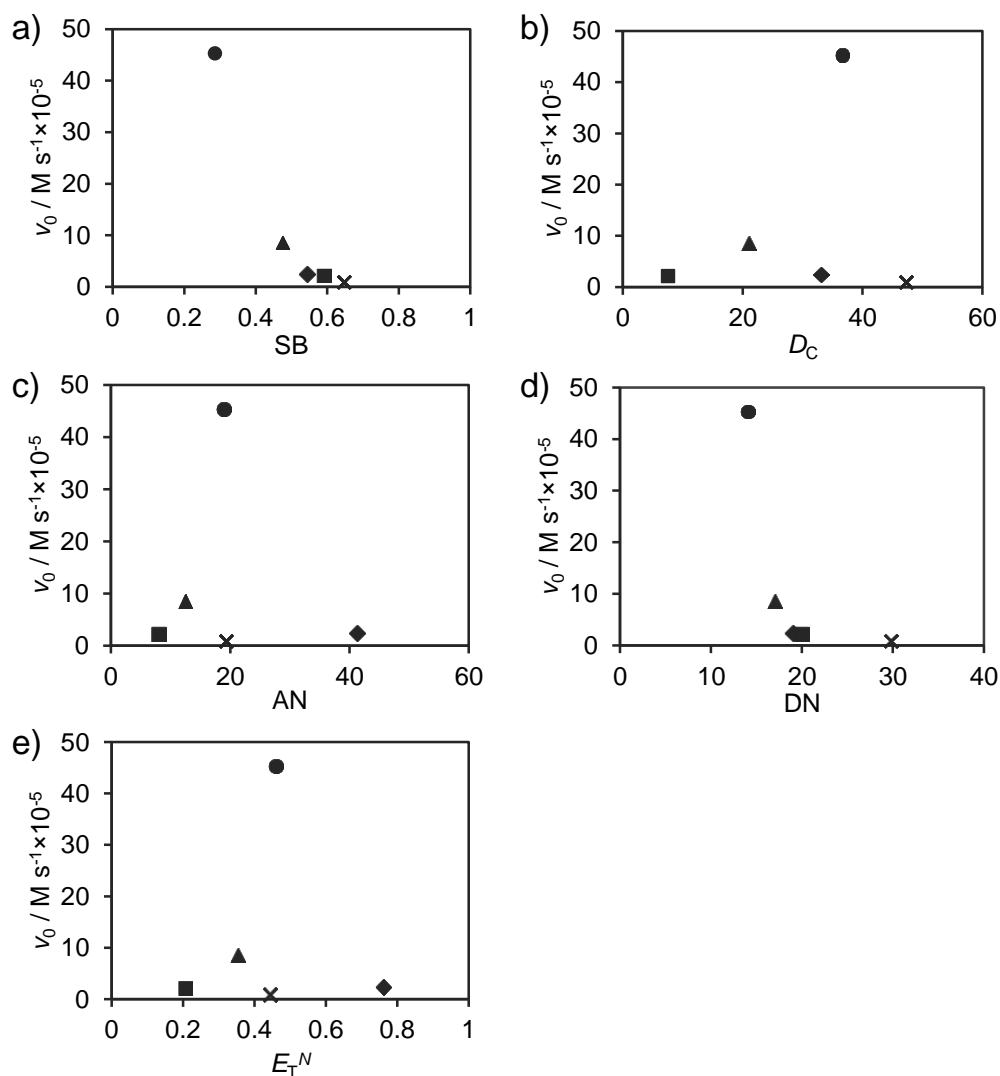


Figure 2.19. Relationship between the initial deallylation rate (v_0) of **1a** and a) solvent basicity (SB), b) dielectric constant (D_C), c) acceptor number (AN), d) Gutmann's donor number (DN) or e) Dimroth-Reichardt's E_T^N for various solvents. Solvents are labelled as follows: MeCN (●); acetone (▲); MeOH (◆); THF (■); and DMSO (×).

The strong SB-dependence of v_0 was further supported by additional experiments. The author investigated the sol-gel polymerization behaviors of **1a** in other organic solvents to further confirm that SB rather than D_C or AN is the key factor of the reaction. *N,N*-dimethylformamide (DMF; SB: 0.614, D_C : 35.9, AN: 16.0) and a mixed solvent of 2,2,2-trifluoroethanol (TFE; SB: 0.107, D_C : 26.7, AN: 53.3)/THF (10:1) were newly selected and the sol-gel polymerization were carried out under 0.2 M HCl concentration for this purpose. The use of DMF did not form a solid organosilica film

from the sol solution of **1a** even after stirring for 24 h. In contrast, the use of TFE/THF formed a solid organosilica film after stirring for only 1 h. These experimental results and relationship between the SB and D_C or AN value were plotted, respectively (Figure 2.20). As shown in Figure 2.20, the use of low SB solvents was found to be effective for the reaction regardless of D_C and AN values (MeCN vs DMF or THF, and TFE/THF vs MeCN). In addition, it should be noted that the use of high SB solvents is ineffective for the reaction regardless of D_C and AN values (DMF, MeOH and THF). These results clearly indicate that that SB is the key factor of the reaction rather than D_C or AN. The author also investigated the relationships between initial deallylation rate v_0 of **1a** and other solvent parameters. The initial deallylation rate v_0 of **1a** was plotted against Gutmann's donor number (an index of Lewis basicity) but not to Dimroth–Reichardt's E_T^N value¹⁹ (an index of solvent polarity), which indicate that apparent correlation was observed for v_0 vs DN, but not for v_0 vs E_T^N value (Figures 2.19d and 2.19e). These results suggest that the present strong solvent effect results from differences in the proton activities in the solvents. This may also suggest that electrophilic addition of a proton is the rate-determining step in the deallylation reaction, which is reasonable since this step was found to be slow in other electrophilic substitution reactions of allylic silanes.^{9b}

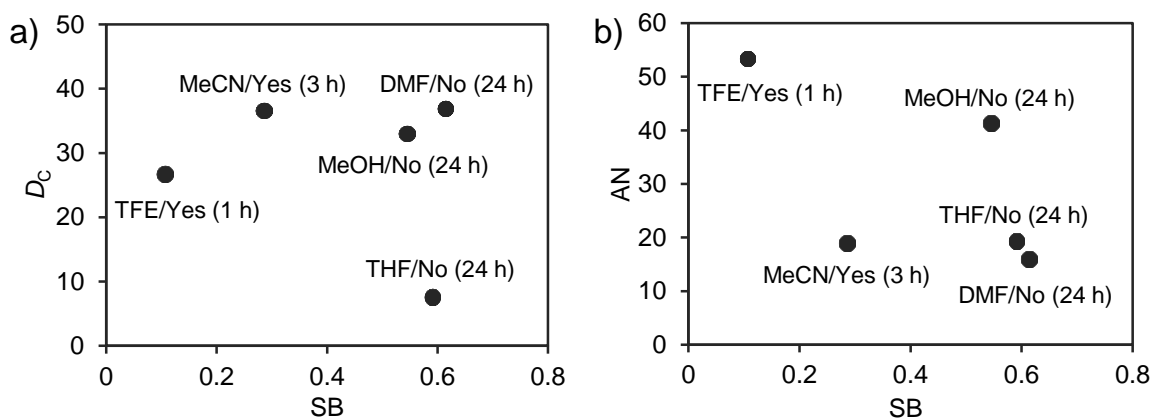


Figure 2.20. Plots of a) D_C and b) AN vs. SB for DMF, TFE, MeCN, MeOH and THF. “Yes (X h)” and “No (X h)” denotes whether a solid organosilica film was formed or not from the sol solutions of **1a** using the corresponding solvents after stirring for X h.

¹⁹ Reichardt, C. *Chem. Rev.* **1994**, *94*, 2319–2358.

Preparation of spirobifluorene-bridged organosilica film under a mild sol–gel polymerization condition

The solvent effect was also confirmed for highly functional spirobifluorene-bridged allylsilane precursor **SBF-Si** (Figure 2.21). In a previous report, **SBF-Si** underwent hydrolysis and polycondensation in the presence of a surfactant under a highly acidic condition (e.g. 0.2 M HCl in THF) to yield a highly emissive PMO film.¹⁴ Here, the author carried out sol–gel polymerization of **SBF-Si** in a mixed solvent of THF/MeCN (2 : 1) and in pure THF at an acid concentration ten-fold lower (0.02 M HCl) without a surfactant. The sol solution of THF/MeCN formed a solid film after stirring for 3 h, whereas the sol solution of pure THF did not form a solid film even after stirring for 24 h.

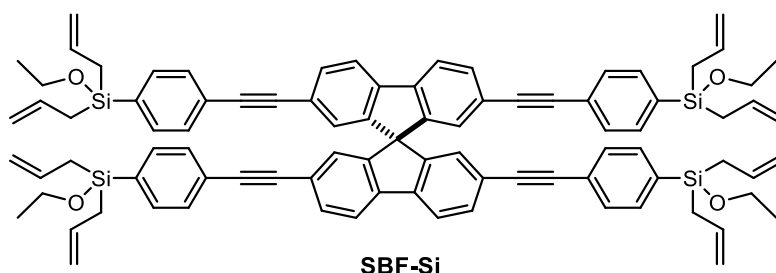


Figure 2.21. Chemical structure of spirobifluorene-bridged allylsilane precursor **SBF-Si**.

Figure 2.22 shows UV-vis absorption and fluorescence emission spectra of the obtained spirobifluorene-silica hybrid film. The film shows absorption bands at 364 and 378 nm and exhibits strong blue emission bands at 448 and 470 nm with a total fluorescence quantum yield of 0.50 (excited at 360 nm). These optical properties were largely similar to those of a previously reported PMO film prepared under a strong acidic condition.¹⁴ These results suggest that the solvent effect can be generally applied to the preparation of highly functional organosilica hybrid materials from a variety of functional and stable organoallylsilane precursors.

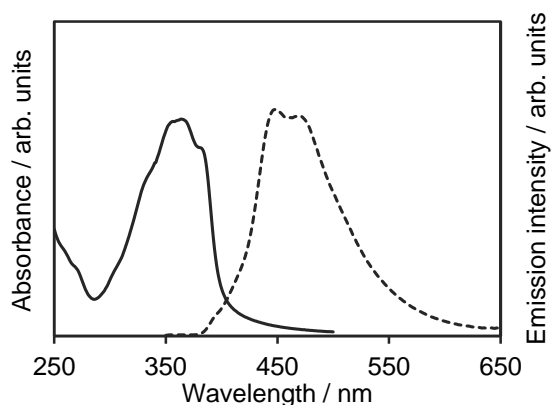


Figure 2.22. UV-vis absorption (solid line) and fluorescence emission (broken line, excited at 360 nm) spectra of the spirobifluorene-bridged organosilica film.

2.5.4 Conclusions

The author identified a significant solvent effect on the acid-catalyzed deallylation of organoallylsilane precursors and in mild sol-gel polymerization conditions. The observed solvent effect was well explained in terms of SB but not the D_C or AN of the solvent. These results suggest that proton activity is a key factor in enhancing the reaction rate. In particular, MeCN was found to most effectively enhance the rate, and accelerated sol-gel polymerization of highly functional spirobifluorene-bridged allylsilane precursor to form a highly emissive organosilica hybrid film under a mild acidic condition. This key finding can be generally utilized for the preparation of a variety of organoallylsilane-derived highly functionalized organosilica hybrids.

Chapter 3

Transparent and Visible-Light Harvesting PMO Films

Transparent and visible-light harvesting acridone-bridged periodic mesoporous organosilica (PMO) films were prepared by acidic sol-gel polycondensation of non-methylated acridone (Acd) and *N*-methylated acridone (MeAcd)-bridged triethoxysilane precursors in the presence of a template surfactant via evaporation-induced self-assembly (EISA). A muddy film containing small aggregates was obtained from the nonmethylated precursor. The aggregate was formed by strong intermolecular hydrogen bonds between N-H and C=O of the Acd groups during EISA. However, a transparent PMO film was successfully formed from the *N*-methylated precursor. Capping of the amine group hindered the intermolecular hydrogen bonds and effectively suppressed aggregate formation. The obtained MeAcd-bridged PMO film showed a visible light absorption band with an edge at 430 nm and fluorescence emission centered at 500 nm. Furthermore, doping of a fluorescent dye into the mesochannels of the MeAcd-PMO film promoted efficient energy funneling from the framework MeAcd groups into the dye, resulting in a strong fluorescence emission centered at 600 nm from the dye.

3.1 Introduction

Periodic mesoporous organosilicas (PMOs),^{1,2} synthesized from up to 100% organic-bridged alkoxy silane precursors $[(R'O)_3Si-R-Si(OR')]_3$, R = organic group, R' = Me, Et] by surfactant-templated supramolecular assembly, are a new class of functional hybrid materials in which the organic groups are densely and covalently embedded within the silica framework forming ordered mesochannels. A broad spectrum of functionalities can be introduced into the frameworks by the design of organosilane precursors with specific functional organic groups (R). A large number of PMOs bearing various bridging organic groups have been reported.³ Some PMOs with interactive bridging organic groups, such as benzene,⁴ biphenyl,⁵ naphthalene,⁶ and divinylbenzene,⁷ have been found to exhibit crystal-like molecular-scale periodicity of the organic groups in the frameworks. As a result of these unique features, PMOs have attracted much attention for use in various applications such as catalysts,⁸ adsorbents,⁹ and optical devices.¹⁰

Inagaki and co-workers have found unique optical functionalities of biphenyl (BPh)-bridged PMO, such as efficient fluorescence emission¹¹ and light harvesting antenna properties, that is, the

¹ a) Hunks, W. A.; Ozin, G. A. *J. Mater. Chem.* **2005**, *15*, 3716–3724; b) Hoffmann, F.; Cornelius, M.; Morell, J.; Fröba, M. *Angew. Chem., Int. Ed.* **2006**, *45*, 3216–3251; c) Fujita, S.; Inagaki, S. *Chem. Mater.* **2008**, *20*, 891–908; d) Nicole, L.; Boissiere, C.; Grosso, D.; Quach, A.; Sanchez, C. *J. Mater. Chem.* **2005**, *15*, 3598–3627; e) Van Der Voort, P.; Vercaemst, C.; Schaubroeck, D.; Verpoort, F. *Phys. Chem. Chem. Phys.* **2008**, *10*, 347–360.

² a) Inagaki, S.; Guan, S.; Fukushima, Y.; Ohsuna, T.; Terasaki, O. *J. Am. Chem. Soc.* **1999**, *121*, 9611–9614; b) Melde, B. J.; Holland, B. T.; Blanford, C. F.; Stein, A. *Chem. Mater.* **1999**, *11*, 3302–3308; c) Asefa, T.; MacLachlan, M. J.; Coombs, N.; Ozin, G. A. *Nature* **1999**, *402*, 867–871.

³ a) Minoofar, P. N.; Dunn, B. S.; Zink, J. I. *J. Am. Chem. Soc.* **2005**, *127*, 2656–2665; b) Johansson, E.; Zink, J. I. *J. Am. Chem. Soc.* **2007**, *129*, 14437–14443; c) Maegawa, Y.; Goto, Y.; Inagaki, S.; Shimada, T. *Tetrahedron Lett.* **2006**, *47*, 6957–6960; d) Whitnall, W.; Cademartiri, L.; Ozin, G. A. *J. Am. Chem. Soc.* **2007**, *129*, 15644–15649; e) Nguyen, T. P.; Hesemann, P.; Gaveau, P.; Moreau, J. J. E. *J. Mater. Chem.* **2009**, *19*, 4164–4171; f) Tani, T.; Mizoshita, N.; Inagaki, S. *J. Mater. Chem.* **2009**, *19*, 4451–4456; g) Mizoshita, N.; Ikai, M.; Tani, T.; Inagaki, S. *J. Am. Chem. Soc.* **2009**, *131*, 14225–14427.

⁴ Inagaki, S.; Guan, S.; Ohsuna, T.; Terasaki, O. *Nature* **2002**, *416*, 304–307.

⁵ Kapoor, M. P.; Yang, Q.; Inagaki, S. *J. Am. Chem. Soc.* **2002**, *124*, 15176–15177.

⁶ Mizoshita, N.; Goto, Y.; Kapoor, M. P.; Shimada, T.; Tani, T.; Inagaki, S. *Chem.–Eur. J.* **2009**, *15*, 219–226.

⁷ a) Sayari, A.; Wang, W. *J. Am. Chem. Soc.*, **2005**, *127*, 12194–12195; b) Cornelius, M.; Hoffmann, F.; Fröba, M. *Chem. Mater.* **2005**, *17*, 6674–6678.

⁸ Yang, Q.; Liu, J.; Yang, J.; Kapoor, M. P.; Inagaki, S.; Li, C. *J. Catal.* **2004**, *228*, 265–272.

⁹ Rebbin, V.; Schmidt, R.; Fröba, M. *Angew. Chem., Int. Ed.* **2006**, *45*, 5210–5214.

¹⁰ Minoofar, P. N.; Hernandez, R.; Chia, S.; Dunn, B.; Zink, J. I.; Franville, A.-C. *J. Am. Chem. Soc.* **2002**, *124*, 14388–14396.

¹¹ Goto, Y.; Mizoshita, N.; Ohtani, O.; Okada, T.; Shimada, T.; Tani, T.; Inagaki, S. *Chem. Mater.* **2008**, *20*, 4495–4498.

acridone-bridged PMO film via evaporation-induced self-assembly (EISA). Using the conventional Acridone-bridged triethoxysilane precursor **1** (Figure 3.1) resulted in the formation of a muddy film containing aggregates. These aggregates were generated by intermolecular hydrogen bonds between N–H and C=O of the Acridone groups during EISA. For the suppression of aggregate formation, the author designed a new precursor **2** (Figure 3.1) in which the nitrogen atom is capped with a methyl substituent. The capping hindered intermolecular hydrogen bonding, and this allowed the successful formation of a transparent methylacridone (MeAcridone)-bridged PMO film. The obtained film exhibited visible light absorption and efficient light harvesting antenna properties.

3.2 Experimental

Materials and methods

All reagents and solvents were purchased from Sigma-Aldrich, Tokyo Chemical Industry, Wako Pure Chemical Industries, and Nacalai Tesque and used without further purification. A poly(ethylene oxide)-block-poly(propylene oxide)-block-poly(ethylene oxide) triblock copolymer (EO₂₀-PO₇₀-EO₂₀, P123) (Aldrich) was used as a nonionic template surfactant. Precursor **1** was synthesized according to the literature.¹⁸ Nuclear magnetic resonance (NMR) spectra were recorded on a Jeol JNM-EXC400P spectrometer (400 MHz for ¹H and 100 MHz for ¹³C). Chemical shifts are reported in δ ppm referenced to an internal SiMe₄ standard for ¹H NMR and chloroform-*d* (δ 77.0) for ¹³C NMR. The following abbreviations were used to explain the multiplicities: s = singlet, d = doublet, t = triplet, q = quartet, dd = double doublet, dt = double triplet. Infrared (IR) absorption measurements were conducted on a Thermo Nicolet Avatar 360 FT-IR spectrometer using an attenuated total reflection (ATR) attachment. Mass spectra were recorded on a Bruker Daltonics Autoflex mass spectrometer (MALDI: matrix-assisted laser desorption ionization). Optical microscopy observations were performed using an Olympus BX51 microscope. X-ray diffraction (XRD) measurements were performed on a Rigaku RINT-TTR diffractometer with Cu-K α radiation (50 kV, 300 mA). Ultraviolet-visible (UV-vis) absorption spectra were measured using a Jasco V-670 spectrometer. Fluorescence emission spectra were obtained using a Jasco FP-6500 spectrometer. Fluorescence quantum yields were determined using a photoluminescence quantum yield measurement system equipped with a calibrated integrating sphere (Hamamatsu Photonics,

C9920-02). Optical measurements were carried out for the films without extraction of the surfactant to suppress fluorescence quenching by oxygen¹¹ and aggregation of dye molecules in the mesochannels.¹⁷

Synthesis of organosilane precursor

9-Methylacridone. To a mixture of 9(10*H*)-acridone (6.00 g, 30.7 mmol) in dry DMF (240 mL) was added NaH (3.07 g, 60% oil dispersion, 76.7 mmol) at 0 °C. The reaction mixture was stirred at 60 °C for 30 min, then iodomethane (4.80 mL, 77.0 mmol) was added, and stirring was continued at 60 °C for 18 h. The reaction mixture was quenched with H₂O. The resulting solid was collected by filtration and thoroughly washed with EtOH to give title compound as light-yellow solid (4.77 g, 74%). The filtrated water phase was extracted with CHCl₃, then washed with brine, dried over anhydrous MgSO₄, and concentrated to give the title compound (1.31 g, total yield is 95%). ¹H NMR (400 MHz, CDCl₃) δ 3.89 (s, 3H), 7.29 (dt, *J* = 7.3 Hz, 1.3 Hz, 2H), 7.51 (d, *J* = 7.7 Hz, 2H), 7.72 (dt, *J* = 7.3 Hz, 1.8 Hz, 2H), 8.56 (dd, *J* = 7.7 Hz, 1.8 Hz, 2H).

2,7-Dibromo-9-methylacridone. To a mixture of 9-methylacridone (6.00 g, 28.7 mmol) in dry DMF (280 mL) was added dropwise a solution of *N*-bromosuccinimide (10.8 g, 60.7 mmol) in dry DMF (80 mL) at 0 °C. The reaction mixture was stirred at 80 °C for 18 h, and quenched with H₂O. The resulting solid was collected by filtration and thoroughly washed with hexane to give the title compound as yellow solid (6.57 g, 62%). The filtrated water phase was extracted with CHCl₃, then washed with brine, dried over anhydrous Na₂SO₄, and concentrated. The residue was washed with hexane to give the title compound (3.80 g, total yield is 98%). ¹H NMR (400 MHz, CDCl₃) δ 3.87 (s, 3H), 7.41 (d, *J* = 9.2 Hz, 2H), 7.79 (dd, *J* = 9.2 Hz, 2.6 Hz, 2H), 8.62 (d, *J* = 2.6 Hz, 2H).

2,7-Bis(triethoxysilyl)-9-methylacridone (2). To a mixture of [Rh(cod)(CH₃CN)₂]BF₄ (74.4 mg, 0.20 mmol), 2,7-dibromo-9-methylacridone (1.20 g, 3.27 mmol), and *n*-Bu₄NI (2.41 g, 6.52 mmol) were added dry DMF (48 mL) and dry Et₃N (2.74 mL, 19.7 mmol). After addition of triethoxysilane (2.41 mL, 13.1 mmol), the reaction mixture was stirred at 80 °C for 2 h, then concentrated under vacuum to remove DMF. The resulting mixture was treated with dry Et₂O to give a solution of the title compound in dry Et₂O, which was filtered through a Celite plug and charcoal, and the filter cake was rinsed with dry Et₂O. The combined filtrates were concentrated under vacuum to give the title compound as yellow crystalline solid (1.72 g, 99%). ¹H NMR (400

MHz, CDCl₃) δ 1.28 (t, $J = 7.2$ Hz, 18H), 3.92 (s, 3H), 3.93 (q, $J = 7.2$ Hz, 12H), 7.55 (d, $J = 8.7$ Hz, 2H), 8.02 (dd, $J = 8.7$ Hz, 1.4 Hz, 2H), 8.91 (d, $J = 1.4$ Hz, 2H); ¹³C NMR (100 MHz, CDCl₃) δ 18.3, 33.6, 58.9, 114.3, 122.3, 123.4, 135.5, 139.7, 143.9, 178.0 (C=O); ν_{\max} (neat) 2971, 2925, 2887, 1641(C=O), 1599, 1479, 1176, 958 cm⁻¹; ESI-HRMS m/z calcd for C₂₆H₃₉NO₇Si₂ (M⁺): 533.2265; found: 533.2250; λ_{\max} (*i*-PrOH)/nm 314 ($\epsilon/\text{dm}^3 \text{ mol}^{-1} \text{ cm}^{-1}$ 10800), 381 (6400), 398 (7600).

Preparation of organosilica films

The Acd- or MeAcd-bridged triethoxysilane precursors (**1** or **2**, 60 mg) and P123 (60 mg) were dissolved in EtOH (2.0 g), and then deionized water (12.0 μL) and 2 M hydrochloric acid (HCl) aqueous solution (4.0 μL) were added to the solution. The mixture was stirred at room temperature for 3 h (for **1**) or 24 h (for **2**) to form the sol solution. After passing through a membrane filter (0.20 μm), the sol solution was coated on a quartz glass plate by spin-coating (4000 rpm, 30 s) and dried under reduced pressure to give an organosilica film. In case of the dye doping, a solution of DCM dye (4-(dicyanomethylene)-2-methyl-6-(*p*-dimethyl-aminostyryl)-4*H*-pyran) in EtOH was added to the sol solution (the molar DCM/**2** ratios of 0.5–5 mol%) and then stirred for a few minutes at room temperature just prior to spin-coating.

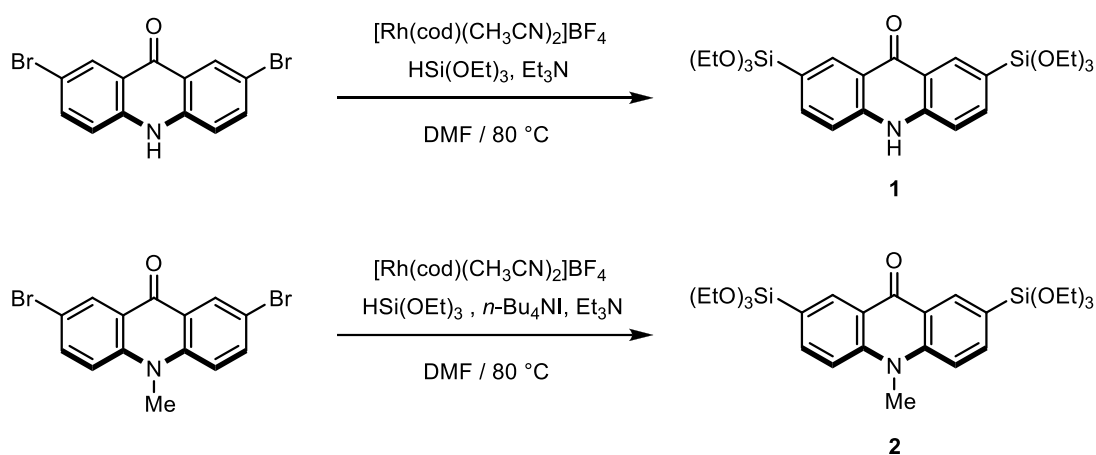
Removal of the template surfactant from organosilica films

In order to remove the template surfactant, the organosilica films were exposed to the vapor of a 28% NH₃ aqueous solution at 60 °C for 12 h, and then immersed in EtOH for 12 h at 60 °C to provide a surfactant-free sample. Complete removal of the surfactant was confirmed by IR measurements.

3.3 Results and Discussion

Synthesis of organosilane precursors

Two types of acridone-bridged triethoxysilane precursors, 2,7-bis(triethoxysilyl)acridone **1**¹⁸ and 2,7-bis(triethoxysilyl)-9-methylacridone **2** (with nitrogen atom capped by a methyl substituent), were synthesized by rhodium-catalyzed triethoxysilylation²¹ of the corresponding 2,7-dibrominated acridone derivatives in 60% and 99% yield, respectively (Scheme 3.1).



Scheme 3.1. Synthetic illustration of Acrid- and MeAcrid-bridged triethoxysilane precursors **1** and **2**.

The infrared absorption (IR) spectrum of **1** showed absorption bands at 3260 and 1621 cm^{-1} corresponding to the stretching mode of hydrogen-bonded N–H and C=O groups, respectively (Figure 3.2). Precursor **1** showed relatively low solubility in EtOH and THF, which are typically used as solvents for acidic sol–gel polycondensation, due to strong interaction between the Acrid groups by hydrogen bonding. In contrast, precursor **2** was quite soluble, due to the hindering of intermolecular hydrogen bonds by capping of the nitrogen atom.

²¹ Murata, M.; Ishikura, M.; Nagata, M.; Watanabe, S.; Masuda, Y. *Org. Lett.* **2002**, *4*, 1843–1845.

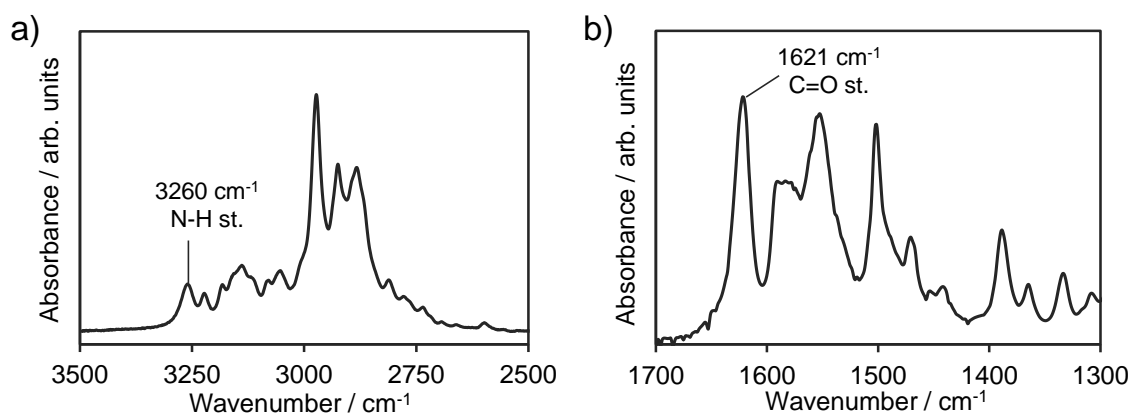


Figure 3.2. IR absorption spectra of the precursor **1** at a) 2500–3500 cm⁻¹ and b) 1300–1700 cm⁻¹.

Preparation of mesoporous organosilica films

Acid- and MeAcid-PMO films were prepared by spin-coating of sol solutions containing precursors **1** or **2**, a template surfactant P123, HCl, and water in EtOH. While the sol solution of **1** formed a small amount of precipitates within 3 h, possibly due to low solubility of the oligomers of **1**, the sol solution of **2** did not form any precipitates for at least 3 days, and a transparent sol solution containing the oligomers of **2** was obtained. These sol solutions were filtered using a membrane filter (0.20 μm) prior to spin-coating to remove the precipitates. The ultraviolet-visible (UV-vis) absorption measurement of the sol solution of **1** showed that > 93% of **1** was still remained after filtration (Figure 3.3).

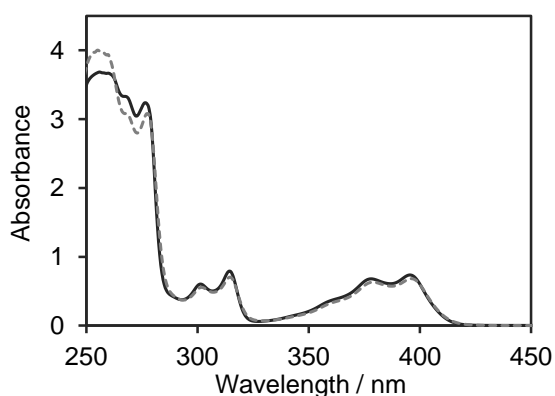


Figure 3.3. UV-vis absorption spectra of the sol solution of **1** before (solid line) and after (broken line) the filtration.

Figure 3.4 shows a photograph and optical micrographs of the spin-coated films prepared from

the filtered sol solutions of **1** and **2** (denoted as **F-1** and **F-2**, respectively). **F-1** was muddy yellow and contained small aggregates of approximately 1 μm in size (Figures 3.4a and 3.4b). The transmittance of **F-1** was 96% at 500 nm due to light scattering by the aggregates. These aggregates were formed during EISA, because $> 0.20 \mu\text{m}$ particles were removed by filtration prior to spin-coating. In contrast, **F-2** was obtained as a transparent yellow film without aggregates (Figure 3.4c) that exhibited high transmittance of $> 99\%$ at 500 nm, due to the lack of light scattering loss. **F-2** was stable without cracking in air and its transparency was mostly retained even after extraction of the surfactant (Figure 3.4d).

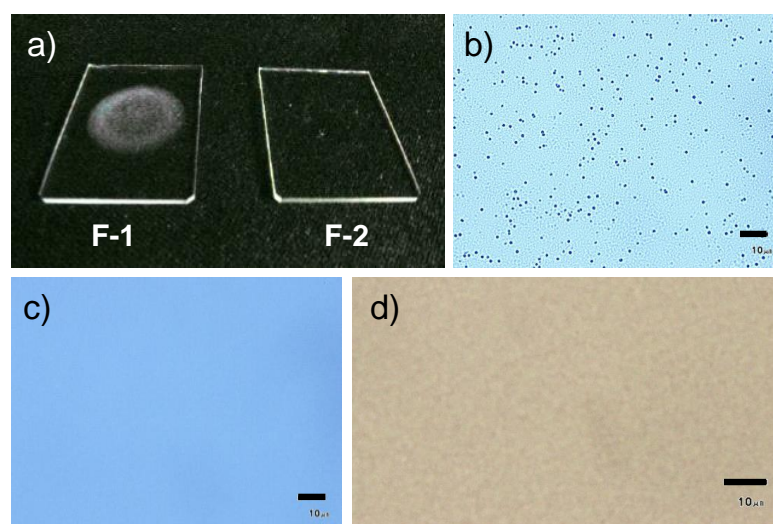


Figure 3.4. a) Photograph of **F-1** (left) and **F-2** (right), and optical micrographs of b) **F-1** and c) **F-2** (scale bar represents 10 μm). d) optical micrograph of **F-2** after removal of surfactant template (scale bar represents 10 μm).

Figure 3.5 shows X-ray diffraction (XRD) patterns of **F-1** and **F-2** before and after extraction of the template surfactant. Complete removal of the surfactant was confirmed by IR measurements. **F-1** and **F-2** show diffraction peaks with d -spacings of 8.83 and 10.0 nm, respectively, which indicates the formation of periodic mesostructures before extraction of the surfactant. For **F-1**, the diffraction peak was significantly broadened after the extraction, which suggests partial collapse of the periodic mesostructure, even after treatment with ammonia vapor for reinforcing of the framework structure. The collapse may be attributed to a low degree of condensation in the organosilica framework, which could possibly be due to a small fraction of the oligomers in the sol

solution and preferential aggregate formation by strong intermolecular hydrogen bonding. In contrast, **F-2** shows an intense diffraction peak (8.83 nm) after the surfactant extraction, which suggests formation of the periodic mesoporous structure with shrinkage (from 10.0 to 8.83 nm), but without collapse. This result indicates that the framework structure of **F-2** is well-condensed, due to hindering of the intermolecular hydrogen bonds. Both films showed no peaks at $2\theta > 4.4^\circ$ (d -spacing < 2 nm), which indicates no molecular-scale periodicity of the acridone groups in the frameworks.

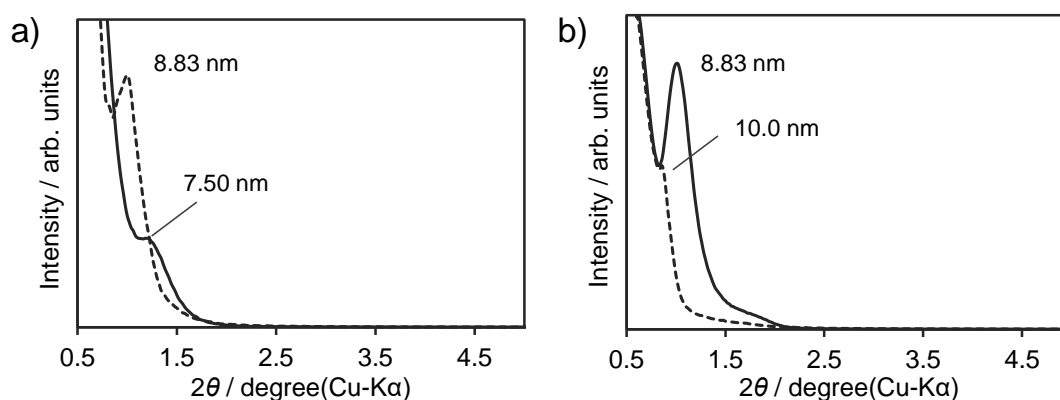


Figure 3.5. XRD patterns of a) **F-1** and b) **F-2** before (broken lines) and after (solid lines) the extraction of surfactant.

Optical properties of mesoporous organosilica films

UV-vis absorption and fluorescence emission measurements were carried out to characterize the optical properties of the obtained films **F-1** and **F-2**, and to elucidate details of the aggregates in **F-1**. Figure 3.6 depicts UV-vis absorption and fluorescence emission spectra of **F-2** and *i*-PrOH solution of the corresponding precursor **2**. **F-2** showed absorption bands at 385 and 399 nm (Figure 3.6a). The absorption spectrum was primarily similar to that for the **2** solution, which has been typically observed in PMO films¹¹ and suggests weak interaction between the MeAcid groups in the ground state. However, **F-1** showed a strong absorption band at 416 nm and a weak absorption band at 392 nm (Figure 3.7a). The absorption spectrum was quite different from that of the **1** solution, but was similar to that of the aggregates of precursor **1** prepared by spin-coating an EtOH solution (Figure 3.7a). This suggests that the conformation of most of the Acid groups in **F-1** is similar to that of the aggregates of precursor **1**.

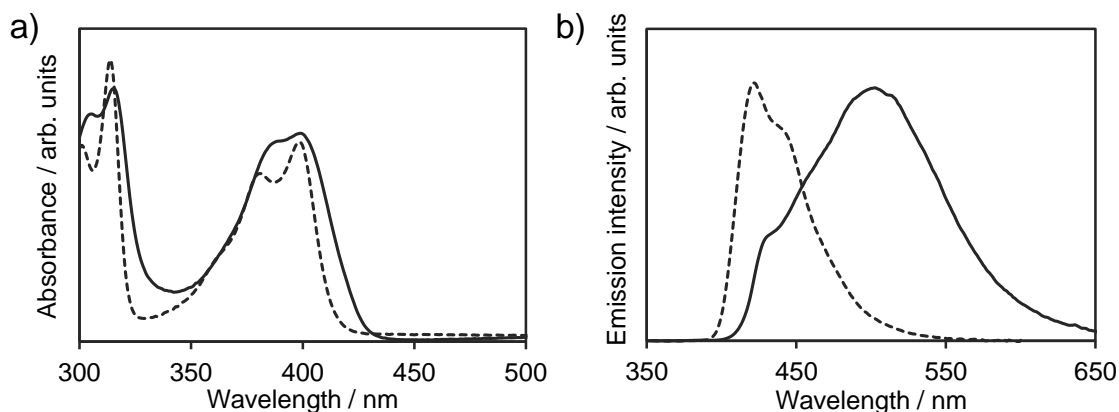


Figure 3.6. a) UV-vis absorption and b) fluorescence emission spectra of mesostructured organosilica film **F-2** (solid lines) and *i*-PrOH solutions of MeAcid-bridged precursor **2** (broken lines). The excitation wavelength was 380 nm for all samples.

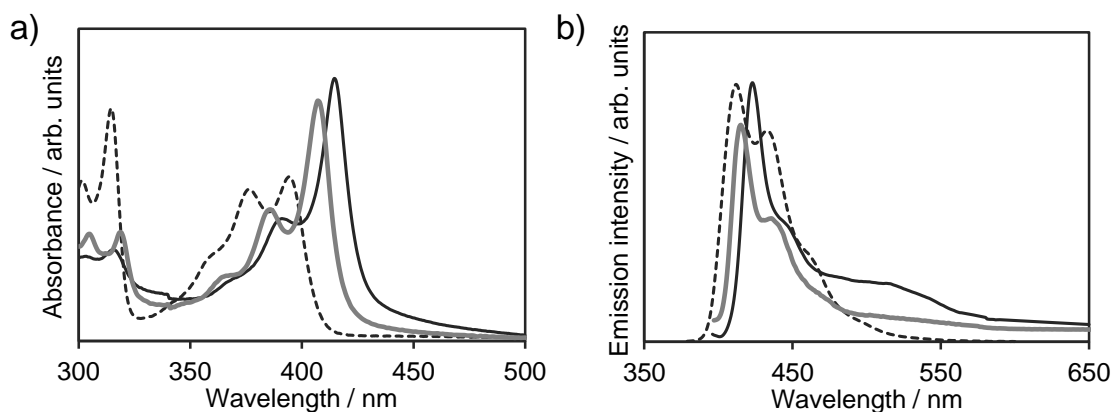


Figure 3.7. a) UV-vis absorption and b) fluorescence emission spectra of mesostructured organosilica film **F-1** (solid lines), *i*-PrOH solutions of Acid-bridged precursor **1** (broken lines), and aggregates of the precursor **1** (bold gray lines). The excitation wavelength was 380 nm for all samples.

The fluorescence band of **F-2** was red-shifted and broadened from that of the **2** solution, due to formation of the excimer, which suggests strong interaction between the acridone groups in the excited state, as typically observed in PMO films (Figure 3.6b).¹¹ In addition, the excitation spectrum at the band maximum (500 nm) was primarily identical to the UV-vis absorption spectrum, which indicates that the fluorescence emission is originated from one component, which indicates the formation of a homogeneous film of **F-2** (Figure 3.8a). In contrast, **F-1** showed

fluorescence emissions from at least two components, with a sharp emission band at 422 nm and two broad emission bands at 450 and 520 nm (Figure 3.7b). The two former bands could result from emission of the aggregates in the film, because the band positions are similar to those for the aggregates of precursor **1** (Figure 3.7b, bold gray line) and the excitation spectrum at 450 nm showed a sharp peak attributable to the aggregates at 416 nm as shown in Figure 3.8b.²² The latter band at 520 nm is attributed to the excimer emission from the homogeneous organosilica phase, due to the similar band position and excitation spectrum (520 nm: Figure 3.8b) to those of **F-2** (Figure 3.8a). The fluorescence quantum yields were 0.03 and 0.06 for **F-1** and **F-2**, respectively. Both films showed a significant decrease in their fluorescence quantum yields from the corresponding precursor solutions (**1**: 0.75, **2**: 0.60), possibly due to solid state quenching.

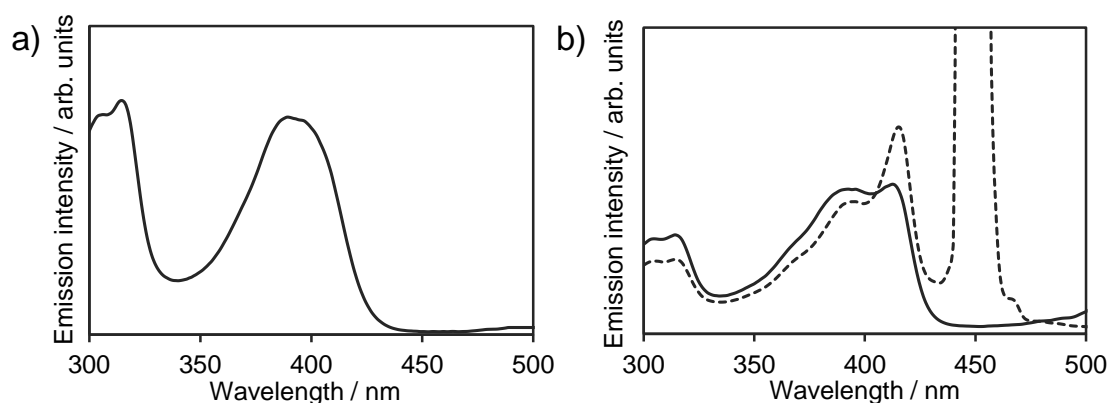


Figure 3.8. Excitation spectra of a) **F-2** at 500 nm and b) **F-1** at 450 nm (broken line) and at 520 nm (solid line).

Finally, the light harvesting antenna properties of the transparent MeAc-d-PMO film (**F-2**) were investigated. The DCM dye was chosen as an energy acceptor, due to good overlap of its absorption band and the emission band of **F-2** (Figure 3.9a), which would promote efficient excitation energy transfer. The UV-vis absorption spectrum of the dye-doped **F-2** (1 mol%) showed a weak band at 478 nm, due to the dye in the mesochannels, in addition to a strong band at 399 nm due to the MeAc groups (Figure 3.9b). The band position of the dye in **F-2** was similar to that in

²² Excitation spectrum of **F-1** at 422 nm could not be measured due to overlap of the excitation light and the excitation spectrum.

polar solvents such as dimethyl sulfoxide (DMSO),²³ which suggests that the dye molecules are likely to be present at the hydrophilic interface of the surfactant micelles and the framework, rather than at the hydrophobic cores. Figure 3.9c shows fluorescence emission spectra for dye-doped **F-2** at various dye concentrations (0, 0.5, 1 and 5 mol%) upon excitation at 380 nm. 0.5 mol% dye-doping significantly quenched the emission from the MeAc groups, while promoting a strong emission from the dye at 600 nm. 1 mol% dye-doping further decreased and increased the emission from the acridone groups and the dye, respectively, and the fluorescence quantum yield reached 0.36. This value is much higher than that of non-doped **F-2** (0.06), which suggests that the emission from the dye results not from a radiation–reabsorption process, but from direct excitation energy

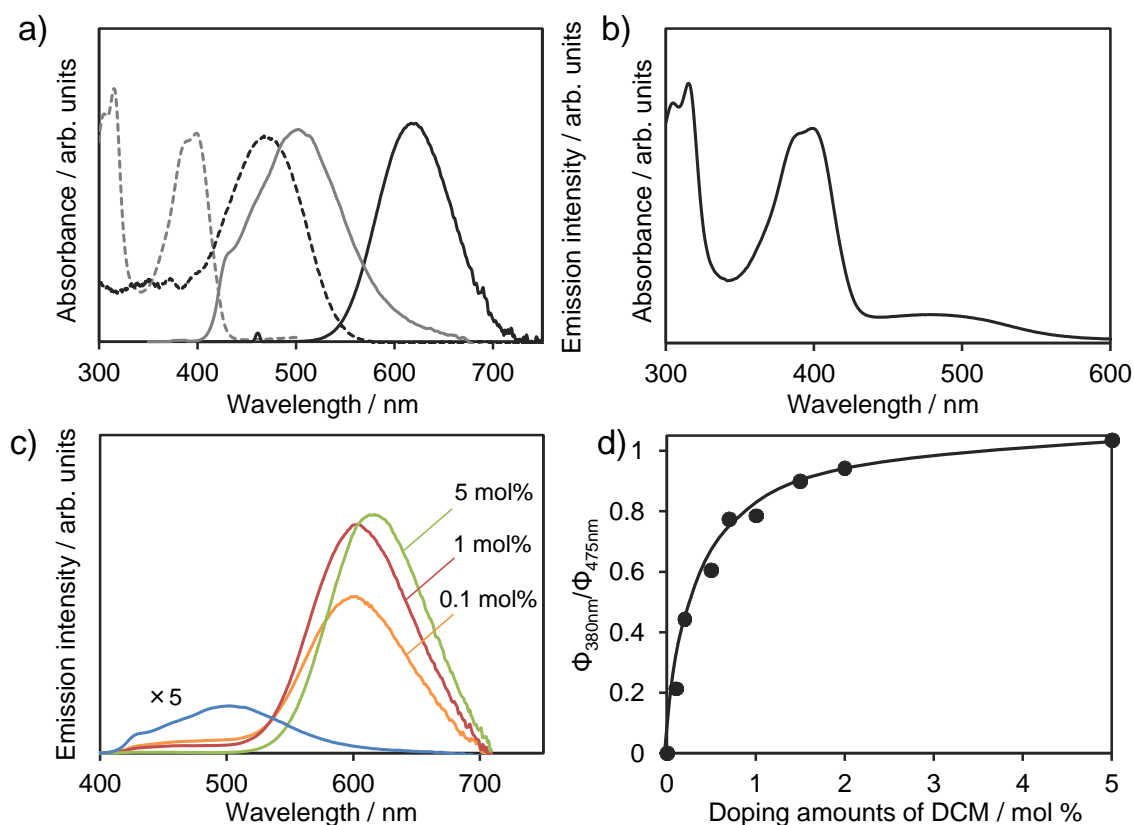


Figure 3.9. a) UV-vis absorption (broken lines) and fluorescence emission spectra (solid lines) of **F-2** (gray) and DCM (10^{-5} M in *i*-PrOH). b) UV-vis absorption spectrum of 1 mol% DCM doped **F-2**. c) fluorescence emission spectra of 0 (blue line), 0.5 (orange line), 1 (red line), and 5 mol% (green line) DCM-doped **F-2**. The excitation wavelength was 380 nm for all samples. d) excitation energy transfer efficiency of **F-2**.

²³ Boldrini, B.; Cavalli, E.; Painelli, A.; Terenziani, F. *J. Phys. Chem. A* **2002**, *106*, 6286–6294.

Table 3.1. Fluorescence quantum yields measured at excitation wavelengths of 380 nm and 475 nm for **F-2** with different dye-doping.

Doping / mol%	Host excitation $\Phi_{\text{ex380nm}} (\Phi_{\text{guest}} : \Phi_{\text{host}})$	Guest excitation Φ_{ex475nm}
0	0.063	—
0.1	0.116 (0.085 : 0.031)	0.397
0.2	0.213 (0.193 : 0.020)	0.434
0.5	0.269 (0.256 : 0.013)	0.422
0.7	0.363 (0.353 : 0.010)	0.456
1	0.361 (0.354 : 0.007)	0.450
1.5	0.410 (0.406 : 0.004)	0.451
2	0.415 (0.412 : 0.003)	0.437
5	0.372 (0.371 : 0.001)	0.358

transfer from the MeAcid groups to the dye, as also observed in the Acid-PMO powder.¹⁸ On the other hand, 5 mol% dye-doping resulted in a slight red-shift of the dye emission band, due to aggregation of the dye.

Table 3.1 shows the fluorescence quantum yields measured at excitation wavelengths of 380 and 475 nm for **F-2** with different dye-doping. The fluorescence quantum yield upon host excitation was divided into the fluorescence quantum yield from the host (MeAcid-PMO film) and the guest (DCM dye). The fluorescence quantum yield of dye-doped **F-2** showed an average of 0.37 (0.5–2 mol%). The > 2 mol% dye-doping minimized the difference in fluorescence quantum yields upon host excitation and guest excitation, and the fluorescence quantum yield from the host decreased to < 0.003, suggesting almost complete excitation energy transfer.

The excitation energy transfer efficiency (η_{ET}) was calculated from the following equation:

$$\eta_{\text{ET}} = \frac{\Phi_{\text{ex380nm}}}{\Phi_{\text{ex475nm}}}$$

where Φ_{ex380nm} is the fluorescence quantum yield of dye-doped **F-2** upon host excitation, and Φ_{ex475nm} is the fluorescence quantum yield of dye-doped **F-2** upon guest excitation. The relationship between the excitation energy transfer efficiency and the dye doping amount was investigated (Figure 3.9d). When > 2 mol% dye-doping caused excitation energy transfer efficiency of > 94%.

In the case of the previously reported BPh-PMO/coumarin 1 system,¹² addition of > 2 mol% dye-doping was necessary to achieve complete excitation energy transfer. MeAc-d-PMO films showed the same level of excitation energy transfer characteristics as BPh-PMO in spite of non-luminescent character. Therefore, it can be expected as an excellent visible-light harvesting scaffold for optical devices and photocatalysts.

3.4 Conclusions

A transparent and visible-light absorptive acridone-bridged PMO film was successfully prepared from the newly designed *N*-methylated acridone-bridged triethoxysilane precursor **2**. Compared with the conventional precursor **1**, capping of the nitrogen atom with a methyl substituent improved the solubility of the precursor and its oligomers, due to the hindering of intermolecular hydrogen bonds, which suppressed the formation of precipitates in the sol solution and aggregates during EISA, allowing successful formation of a transparent PMO film. The film exhibited monomeric absorption and an excimer fluorescence emission, which is a typical behavior for PMO films. Dye-doping of the film resulted in quenching of the emission from the framework, while strong emission from the dye was promoted, which confirmed visible-light harvesting antenna properties.

Chapter 4

Visible-Light-Absorptive and Hole-Transporting PMO Films for Organic Solar Cells

Periodic mesoporous organosilica (PMO) thin films that possess both visible-light absorption and hole-transporting properties were synthesized from a newly designed 4,7-dithienyl-2,1,3-benzothiadiazole (DTBT)-bridged organosilane precursor using polystyrene-*block*-poly(ethylene oxide) (PS-*b*-PEO) as a template. DTBT-based PMO films were successfully obtained from the 100% organosilane precursor without the addition of other alkoxy silanes such as tetraethoxysilane and by control of the THF–EtOH solvent ratio and the PS/PEO group ratio in the block copolymer. The PMO films possess connected cage-like mesopores with diameters of ca. 15–20 nm, which could be derived from templating with spherical micelles. The PMO films exhibited absorption in the visible range between 400 and 650 nm and hole-transport mobility in the order of $10^{-5} \text{ cm}^2 \text{ V}^{-1} \text{ s}^{-1}$. The author demonstrates that the PMO thin film functions as a p-type layer for organic solar cells by filling an n-type [6,6]-phenyl C₆₁ butyric acid methyl ester into the mesopores.

4.1 Introduction

Periodic mesoporous organosilicas (PMOs), synthesized by surfactant-directed polycondensation of organic-bridged alkoxy silane precursors ($R[\text{Si}(\text{OR}')_3]_n$, where R = organic group and R' = Me, Et, *i*-Pr, etc., $n \geq 2$), are a new class of organic–inorganic hybrid materials with well-defined nanopores (2–30 nm) and high functionality attributed to the organic groups (R) fixed within the silicate frameworks.^{1,2} Desired framework functionalities can be constructed by molecular design of the organosilane precursors.² A number of PMOs with aromatic and π -conjugated bridging groups have been reported to have useful optical and electrical properties,³ such as strong fluorescence,⁴ light harvesting capability⁵ and photocatalytic activity.⁶

Mizoshita et al. recently reported a hole-transporting PMO thin film synthesized from a three-armed organosilane precursor with an electroactive π -conjugated 1,3,5-tris(styryl)benzene.⁷ Hole-transporting PMOs have the potential to be utilized in optoelectronic devices due to their high surface area and well-controlled nanoporous structures. In particular, they have potential for

¹ a) Inagaki, S.; Guan, S.; Fukushima, Y.; Ohsuna, T.; Terasaki, O. *J. Am. Chem. Soc.* **1999**, *121*, 9611–9614; b) Melde, B. J.; Holland, B. T.; Blanford, C. F.; Stein, A. *Chem. Mater.* **1999**, *11*, 3302–3308; c) Asefa, T.; MacLachlan, M. J.; Coombs, N.; Ozin, G. A. *Nature* **1999**, *402*, 867–871.

² a) Hoffmann, F.; Cornelius, M.; Morell, J.; Fröba, M. *Angew. Chem., Int. Ed.* **2006**, *45*, 3216–3251; b) Wang, W.; Lofgreen, J. E.; Ozin, G. A. *Small* **2010**, *6*, 2634–2642; c) Mizoshita, N.; Tani, T.; Inagaki, S. *Chem. Soc. Rev.* **2011**, *40*, 789–800.

³ a) Yoshina-Ishii, C.; Asefa, T.; Coombs, N.; MacLachlan, M. J.; Ozin, G. A. *Chem. Commun.* **1999**, 2539–2540; b) Inagaki, S.; Guan, S.; Ohsuna, T.; Terasaki, O. *Nature* **2002**, *416*, 304–307; c) Minoofar, P. N.; Dunn, B. S.; Zink, J. I. *J. Am. Chem. Soc.* **2005**, *127*, 2656–2665; d) Johansson, E.; Zink, J. I. *J. Am. Chem. Soc.* **2007**, *129*, 14437–14443; e) Whitnall, W.; Cademartiri, L.; Ozin, G. A. *J. Am. Chem. Soc.* **2007**, *129*, 15644–15649; f) Wahab, M. A.; Sudhakar, S.; Yeo, E.; Sellinger, A. *Chem. Mater.* **2008**, *20*, 1855–1861; g) Cornelius, M.; Hoffmann, F.; Ufer, B.; Behrens, P.; Fröba, M. *J. Mater. Chem.* **2008**, *18*, 2587–2592; h) Mizoshita, N.; Tani, T.; Shinokubo, H.; Inagaki, S. *Angew. Chem., Int. Ed.* **2012**, *51*, 1156–1160.

⁴ a) Goto, Y.; Mizoshita, N.; Ohtani, O.; Okada, T.; Shimada, T.; Tani, T.; Inagaki, S. *Chem. Mater.* **2008**, *20*, 4495–4498; b) Mizoshita, N.; Goto, Y.; Tani, T.; Inagaki, S. *Adv. Funct. Mater.* **2008**, *18*, 3699–3705; c) Mizoshita, N.; Goto, Y.; Kapoor, M. P.; Shimada, T.; Tani, T.; Inagaki, S. *Chem.–Eur. J.* **2009**, *15*, 219–226; d) Tani, T.; Mizoshita, N.; Inagaki, S. *J. Mater. Chem.* **2009**, *19*, 4451–4456, and references therein; e) Mizoshita, N.; Goto, Y.; Maegawa, Y.; Tani, T.; Inagaki, S. *Chem. Mater.* **2010**, *22*, 2548–2554.

⁵ a) Inagaki, S.; Ohtani, O.; Goto, Y.; Okamoto, K.; Ikai, M.; Yamanaka, K.; Tani, T.; Okada, T. *Angew. Chem., Int. Ed.* **2009**, *48*, 4042–4046; b) Takeda, H.; Goto, Y.; Maegawa, Y.; Ohsuna, T.; Tani, T.; Matsumoto, K.; Shimada, T.; Inagaki, S. *Chem. Commun.* **2009**, 6032–6034; c) Maegawa, Y.; Mizoshita, N.; Tani, T.; Inagaki, S. *J. Mater. Chem.* **2010**, *20*, 4399–4403.

⁶ a) Ohashi, M.; Aoki, M.; Yamanaka, K.; Nakajima, K.; Ohsuna, T.; Tani, T.; Inagaki, S. *Chem.–Eur. J.* **2009**, *15*, 13041–13046; b) Takeda, H.; Ohashi, M.; Tani, T.; Ishitani, O.; Inagaki, S. *Inorg. Chem.* **2010**, *49*, 4554–4559.

⁷ Mizoshita, N.; Ikai, M.; Tani, T.; Inagaki, S. *J. Am. Chem. Soc.* **2009**, *131*, 14225–14227.

application as the p-type layer in organic solar cells (OSCs)⁸ because well-defined interpenetrating p–n heterojunction structures can be constructed by filling the mesopores with an n-type material such as [6,6]-phenyl C₆₁ butyric acid methyl ester (PCBM).⁹

Very recently, Trauner and Bein first reported photovoltaic devices based on a porphyrin-based PMO and PCBM.¹⁰ Photovoltaic devices using photoactive covalent organic frameworks were also reported.¹¹ These reports revealed the potential application of organic-based nanoporous materials as the active layer of OSCs. However, the external quantum efficiency (EQE) of the porphyrin-PMO:PCBM device was limited to 0.035% or less with simulated solar irradiation. The nonlinear dependence of the steady-state current on the irradiation density revealed a transport-limit of the porphyrin-PMO devices, which resulted in non-geminate recombination at high light intensities and indicated very low hole mobility for the porphyrin-PMO film.

The author has envisaged a strategy toward improvement of the PMO-based solar cell performance. The author's approach is based on (i) the introduction of bridging organic groups which have high hole-transporting properties in the PMO framework, and (ii) the construction of large mesopores with diameters of ca. 15–20 nm to enable efficient infiltration of n-type materials into the mesopores. Toward this goal, the author focused on 4,7-dithienyl-2,1,3-benzothiadiazole (DTBT) as a bridging organic group because the DTBT unit has attracted much attention recently for use in both polymer- and molecular-based OSCs due to its high hole mobility and wide range of visible-light absorption from the unique donor–acceptor–donor molecular structure.¹² In this study, two- and four-armed organosilane precursors were designed for preparation of the PMO films from the precursors without the addition of any pure silica precursors such as tetraethyl orthosilicate

⁸ a) Yu, G.; Gao, J.; Hummelen, J. C.; Wudl, F.; Heeger, A. J. *Science* **1995**, *270*, 1789–1791; b) Peet, J.; Heeger, A. J.; Bazan, G. C. *Acc. Chem. Res.* **2009**, *42*, 1700–1708, and references therein; c) Brabec, C. J.; Dyakonov, V.; Scherf, U. in *Organic Photovoltaics: Materials, Device Physics, and Manufacturing Technologies*, John Wiley & Sons, 2008.

⁹ Ikai, M.; Maegawa, Y.; Mizoshita, N.; Tani, T.; Inagaki, S. Solar cell and method for manufacturing the same., Japanese Patent, JP 5110399, 2012.

¹⁰ Li, Y.; Auras, F.; Löbermann, F.; Döblinger, M.; Schuster, J.; Peter, L.; Trauner, D.; Bein, T. *J. Am. Chem. Soc.* **2013**, *135*, 18513–18519.

¹¹ a) Dogru, M.; Handloser, M.; Auras, F.; Kunz, T.; Medina, D.; Hartschuh, A.; Knochel, P.; Bein, T. *Angew. Chem., Int. Ed.* **2013**, *52*, 2920–2924; b) Guo, J.; Xu, Y.; Jin, S.; Chen, L.; Kaji, T.; Honsho, Y.; Addicoat, M. A.; Kim, J.; Saeki, A.; Ihee, H.; Seki, S.; Irle, S.; Hiramoto, M.; Gao, J.; Jiang, D. *Nat. Commun.* **2013**, *4*, 2736.

¹² a) Chen, J. W.; Cao, Y. *Acc. Chem. Res.* **2009**, *42*, 1709–1718, and references therein; b) Wu, X.; Fan, B.; Xue, F.; Adachi, C.; Ouyang, J. *Sol. Energy Mater. Sol. Cells* **2010**, *94*, 2230–2237.

(TEOS). For the synthesis of DTBT-PMO films with large mesopores, block copolymer (polystyrene-*block*-poly(ethylene oxide) (PS-*b*-PEO)) was used as a template in place of typical template surfactants such as alkyltrimethylammonium salts and tri- or di-block copolymers.

Here the author reports the successful synthesis of novel visible-light-absorptive and hole-transporting DTBT-bridged PMO films that possess connected cage-like mesopores with diameters of ca. 15–20 nm. The DTBT-PMO films exhibit a strong visible light absorption band with an edge at 650 nm and high hole-transportation. The OSC devices were fabricated by filling n-type PCBM into the large mesopores of the p-type DTBT-PMO films. DTBT-PMO:PCBM devices exhibited photovoltaic performance under visible light irradiation with a maximum EQE of 18%, which was more than 500 times higher than that for the previously reported porphyrin-PMO:PCBM device.

4.2 Experimental

Materials and methods

Unless otherwise noted, all chemicals, including dry solvents, were purchased from commercial suppliers (Sigma-Aldrich, Tokyo Chemical Industry Co., Ltd., and Wako Pure Chemical Industries Ltd.) and used without further purification. Compounds **3** and **4** were prepared according to the literature procedures.¹³ Block copolymers **P1** ($M_n = 20\text{-}b\text{-}14 \text{ kg mol}^{-1}$, polydispersity index (PDI) = 1.08), **P2** ($M_n = 20\text{-}b\text{-}6.5 \text{ kg mol}^{-1}$, PDI = 1.06), and **P3** ($M_n = 58.6\text{-}b\text{-}71.0 \text{ kg mol}^{-1}$, PDI = 1.03) were purchased from Polymer Source, Inc. PCBM (nanom spectra E100H, purity > 99.5%) was purchased from Frontier Carbon. PEDOT:PSS (Clevios P) was purchased from H. C. Starck and passed through a 0.45 μm filter before spin-coating. High-purity (6N grade) MoO₃ was purchased from Mitsuwa Chemicals. All reactions for organic synthesis were carried out under argon using standard high vacuum and Schlenk-line techniques. Nuclear magnetic resonance (NMR) spectra were recorded on a Jeol JNM-EXC400P spectrometer (400 MHz for ¹H and 100 MHz for ¹³C). Chemical shifts are reported in δ ppm referenced to an internal SiMe₄ standard (δ 0.00) for ¹H NMR and chloroform-*d* (δ 77.0) for ¹³C NMR, respectively. The following abbreviations were used to explain the multiplicities: s = singlet, d = doublet, t = triplet, sept = septet, m = multiplet, br =

¹³ Maegawa, Y.; Waki, M.; Umemoto, A.; Shimada, T.; Inagaki, S. *Tetrahedron* **2013**, *69*, 5312–5318.

broad, dd = double doublet. Mass spectra were recorded on a Micromass GCT Premier mass spectrometer (FI: field ionization and FD: field desorption). UV-vis absorption spectra were measured using a Jasco V-670 spectrometer. SEM images were obtained using a Hitachi S-5500 with an accelerating voltage of 2 or 10 kV. Krypton adsorption/desorption isotherms were measured using a Quantachrome Autosorb-1 at 87 K. Prior to measurements, all samples were outgassed at 80 °C for over 1 h in vacuum. Brunauer–Emmett–Teller (BET) surface areas were calculated from the linear section of the BET plot ($P/P_0 = 0.1\text{--}0.2$). For analyzing pore size distribution for mesopores in top-view SEM images of PMO films, the author used image analysis software. Thicknesses of organosilica films for hole-only devices were measured by using a Dektak^{3ST} surface profilometer. Ionization potentials were measured by using a photo-electron spectrometer (AC-2, Riken Keiki). J – V characteristics for the hole-only devices were measured by using a Keithley 2636A System SourceMeter. Both EQE and J – V characteristics of solar cells were measured by using CEP-2000 (Bunkoukeiki). The J – V characteristics were obtained under dark and white light illumination (simulated solar light, air mass (AM) 1.5G, 100 mW cm⁻²).

Synthetic procedures and characterization

4,7-Bis(5-(4-(3-(triisopropoxysilyl)propyl)phenyl)thiophene-2-yl)-2,1,3-benzothiadiazole (1). A 100 mL three-neck round bottom flask connected to a condenser and dry argon flow was charged with a stir bar, compound **3** (378 mg, 0.77 mmol), 4,7-bis(4,4,5,5-tetramethyl-1,3,2-dioxaborolan-2-yl)-2,1,3-benzothiadiazole (143 mg, 0.37 mmol), potassium triphosphate (328 mg, 1.54 mmol), dry 1,4-dioxane (15 mL), and degassed distilled water (1.5 mL). After the mixture was stirred for 10 min at room temperature, Pd(PPh₃)₄ (44.5 mg, 38.5 μmol, 10 mol% Pd) was added one-portion under argon flow. The temperature was progressively raised to 80 °C and then the reaction mixture was stirred for 20 h. The reaction mixture was then concentrated under reduced pressure and the resulting crude residue was purified by flash silica gel chromatography (eluent: hexane/THF = 40:1) affording **1** as a red tacky solid (246 mg, 71% yield). ¹H NMR (400 MHz, CDCl₃) δ 0.64–0.68 (m, 4H), 1.20 (d, $J = 6.4$ Hz, 36H), 1.72–1.80 (m, 4H), 2.67 (br, 4H), 4.21 (sept, $J = 6.4$ Hz, 6H), 7.21 (d, $J = 8.4$ Hz, 4H), 7.35 (d, $J = 4.0$ Hz, 2H), 7.60 (s, $J = 8.4$ Hz, 4H), 7.80 (s, 2H), 8.05 (d, $J = 4.0$ Hz, 2H); ¹³C NMR (100 MHz, CDCl₃) δ 11.7, 25.0, 25.6, 39.0, 64.9, 123.5, 125.2, 125.7, 128.5, 129.1, 131.5, 138.1, 142.5, 145.74, 145.78, 152.5; FD-HRMS m/z calcd for C₅₀H₆₈N₂O₆S₃Si₂

(M⁺): 944.3778; found: 944.3802; λ_{\max} (CHCl₃)/nm 349 ($\epsilon/\text{dm}^3 \text{ mol}^{-1} \text{ cm}^{-1}$ 38800), 499 (28400).

1,3-Bis(3-(triisopropoxysilyl)propyl)-5-(thiophene-2-yl)benzene (5). A 500 mL three-neck round-bottom flask connected to a condenser and dry argon flow was charged with a stir bar, compound **4** (4.85 g, 7.46 mmol), 2-thiopheneboronic acid (1.91 g, 14.9 mmol), NaHCO₃ (1.88 g, 22.4 mmol), dry 1,4-dioxane (100 mL), and degassed distilled water (10 mL). After the mixture was stirred for 10 min at room temperature, Pd(PPh₃)₄ (260 mg, 0.22 mmol, 3 mol% Pd) was added one portion under argon flow. The temperature was progressively raised to 85 °C and then the reaction mixture was stirred for 24 h. The reaction mixture was then concentrated under reduced pressure and the resulting crude residue was purified by silica gel chromatography (eluent: hexane/CH₂Cl₂ = 1:2) affording **5** as a transparent light-yellow liquid (4.10 g, 84% yield). ¹H NMR (400 MHz, CDCl₃) δ 0.63–0.68 (m, 4H), 1.18 (d, J = 6.4 Hz, 36H), 1.71–1.79 (m, 4H), 2.64 (t, J = 7.6 Hz, 4H), 4.20 (sept, J = 6.4 Hz, 6H), 6.92 (s, 1H), 7.05 (dd, J = 4.8 Hz, 3.6 Hz, 1H), 7.23 (d, J = 4.8 Hz, 1H), 7.24 (s, 2H), 7.26 (d, J = 3.6 Hz, 1H); ¹³C NMR (100 MHz, CDCl₃) δ 11.8, 25.1, 25.6, 39.3, 64.8, 122.7, 123.6, 124.3, 127.8, 128.1, 134.0, 143.1, 145.0; FD-HRMS m/z calcd for C₃₄H₆₀O₆SSi₂ (M⁺): 652.3649; found: 652.3662.

1,3-Bis(3-(triisopropoxysilyl)propyl)-5-(-5-bromothiophene-2-yl)benzene (6). A 100 mL two-neck round-bottom flask connected to dry argon flow was charged with a stir bar, the compound **5** (837 mg, 1.28 mmol), and dry THF (50 mL). After the mixture was stirred for 10 min at 0 °C, *N*-bromosuccinimide (320 mg, 1.80 mmol) was added one-portion under argon flow. The reaction mixture was stirred for 2 h at room temperature. The organic phase was washed with saturated NaHCO₃ aqueous solution and dried over anhydrous MgSO₄, filtered and concentrated under reduced pressure. The resulting crude residue was purified by silica gel chromatography (eluent: hexane/EtOAc = 10:1) affording **6** as a transparent light-yellow liquid (915 mg, 98% yield). ¹H NMR (400 MHz, CDCl₃) δ 0.62–0.66 (m, 4H), 1.18 (d, J = 6.4 Hz, 36H), 1.69–1.78 (m, 4H), 2.62 (t, J = 7.6 Hz, 4H), 4.19 (sept, J = 6.4 Hz, 6H), 6.93 (s, 1H), 7.00 (s, 2H), 7.13 (d, J = 1.6 Hz, 2H); ¹³C NMR (100 MHz, CDCl₃) δ 11.8, 25.1, 25.6, 39.2, 64.9, 110.8, 122.9, 123.3, 128.6, 130.6, 133.3, 143.3, 146.5; FD-HRMS m/z calcd for C₃₄H₅₉BrO₆SSi₂ (M⁺): 730.2754; found: 730.2733.

4,7-Bis(5-(3,5-bis(3-(triisopropoxysilyl)propyl)phenyl)thiophene-2-yl)-2,1,3-benzothiadiazole (2). A 100 mL three-neck round-bottom flask connected to a condenser and dry argon flow was charged with a stir bar, compound **6** (418 mg, 0.57 mmol), 4,7-bis(4,4,5,5-tetramethyl-1,3,2-

dioxaborolan-2-yl)-2,1,3-benzothiadiazole (100 mg, 0.26 mmol), potassium triphosphate (120 mg, 0.57 mmol), dry 1,4-dioxane (20 mL), and degassed distilled water (2.0 mL). After the mixture was stirred for 10 min at room temperature, Pd(PPh₃)₄ (26.3 mg, 22.8 mmol, 4.0 mol% Pd) was added one-portion under argon flow. The temperature was progressively raised to 80 °C and then the reaction mixture was stirred for 30 min. Then, 4,7-bis(4,4,5,5-tetramethyl-1,3,2-dioxaborolan-2-yl)-2,1,3-benzothiadiazole (50 mg, 0.13 mmol) was added and the reaction mixture was stirred for 3 h. The reaction mixture was then concentrated under reduced pressure and the resulting crude residue was purified by flash silica gel chromatography (eluent: hexane/THF = 40:1) affording **2** as a red tacky solid (166 mg, 40% yield). ¹H NMR (400 MHz, CDCl₃) δ 0.66–0.70 (m, 8H), 1.20 (d, *J* = 6.4 Hz, 72H), 1.75–1.83 (m, 8H), 2.67 (t, *J* = 7.6 Hz, 4H), 4.21 (sept, *J* = 6.4 Hz, 12H), 6.96 (s, 2H), 7.35 (d, *J* = 1.6 Hz, 4H), 7.39 (d, *J* = 4.0 Hz, 2H), 7.89 (s, 2H), 8.11 (d, *J* = 4.0 Hz, 2H); ¹³C NMR (100 MHz, CDCl₃) δ 11.9, 25.1, 26.0, 39.3, 64.8, 123.6, 123.8, 125.2, 125.8, 128.5, 128.6, 133.8, 138.2, 143.2, 146.3, 152.6; FD-HRMS *m/z* calcd for C₇₄H₁₂₀N₂O₁₂S₃Si₄ (M⁺): 1436.7081; found: 1436.7035; λ_{max}(CHCl₃)/nm 347 (ε/dm³ mol⁻¹ cm⁻¹ 38600), 497 (29100).

Preparation of sol mixtures and films

Unless otherwise specified, the sol mixtures described below were stirred (500 rpm) at 17–25 °C for 1 h. All of the sol mixtures described below was passed through 0.2 μm filter before casting on the substrates. Unless otherwise described, the sol mixtures were spin-coated onto each substrate at 4000 rpm for 30 s. Vapor treatments were conducted by storing the samples in a covered shallow plastic container where EtOH is placed.

Sol mixtures for entry 1–6 in Table 4.1. Precursor **1** or **2** (5.0 mg) and the template block copolymer **P1** or **P2** (7.5 mg) or **P3** (5.0 mg) were dissolved in a mixture of THF and EtOH ((487.5 mg, entries 1–4, 7/1, 3/1, 2/1 or 3/1 (w/w), respectively) or (490 mg, entries 5–6, 3/1, or 2/1 (w/w), respectively)). After adding 4 M hydrochloric acid (HCl) aqueous solution (2.0 μL), the sol mixtures were stirred and then spin-coated onto each PEDOT:PSS/ITO substrate.

Sol A for 1-NP-F, sol B for 2-NP-F. Precursor **1** or **2** (5.0 mg) was dissolved in a mixture of THF and EtOH (495 mg, sol A (3/1 (w/w)), sol B (2/1 (w/w))). After adding 4 M HCl aqueous solution (2.0 μL), the sol mixture was stirred.

Sol A' for a buffer layer (10-NP-F). Precursor **1** (5.0 mg) was dissolved in THF (495 mg). After

adding 12 M HCl aqueous solution (0.5 μL), the sol mixture was stirred. The obtained sol was diluted by adding THF and resulting in 0.125 wt% of sol mixture was prepared.

Sol C for 1-PMO-F, sol D for 2-PMO-F. Precursor **1** or **2** (5.0 mg) and the template block copolymer **P3** (5.0 mg) were dissolved in a mixture of THF and EtOH (490 mg, sol C (3/1 (w/w)), sol D (2/1 (w/w))). After adding 4 M HCl aqueous solution (2.0 μL), the sol mixture was stirred.

1-NP-F or 2-NP-F on Si(100) for ionization potential measurements. The film was formed on Si(100) substrate by spin-coating sol A or B at 3000 rpm for 30 s.

Fabrication methods of hole-only devices and the SCLC measurements

Hole-only devices were fabricated by using thermal evaporation onto cleaned glass substrates precoated with conductive, transparent ITO under high-vacuum conditions (the background pressure of the vacuum chamber was 5×10^{-7} Torr for MoO_3 and 1×10^{-7} Torr for electrode materials.). The glass substrates precoated with ITO (Sanyo Vacuum, thickness: 150 nm, sheet resistance: $10 \Omega \text{ square}^{-1}$) were cleaned ultrasonically in acetone and *i*-PrOH. Prior to the MoO_3 deposition, the substrates were treated with UV-ozone, and immediately transferred into an evaporation chamber. A 10 nm-thick- MoO_3 was deposited on the substrates at a rate of 0.5 \AA s^{-1} . After the evaporation of MoO_3 , Sol A or sol B was spin-coated onto the MoO_3 film to form DTBT-silica films (**1-NP-F** or **2-NP-F** (at 2000 rpm for 30 s)). After evaporating Au cathodes on the DTBT-silica films under high vacuum conditions, the hole-only devices were encapsulated using a UV-epoxy resin and a glass plate under a nitrogen atmosphere.

The author obtained the J - V characteristics for the hole-only devices. The hole mobilities are determined by fitting the J - V curves into Mott-Gurney's square law:

$$J = \frac{9}{8} \varepsilon_0 \varepsilon_r \mu \frac{V^2}{L^3}$$

where ε_0 is the permittivity of free space, ε_r is the relative permittivity of the materials (assuming $\varepsilon_r = 3.5$ for DTBT silica films), μ is the hole mobility, V is the voltage drop across the device, and L is the thickness of the organosilica layer.

Fabrication methods of PMO-based solar cells

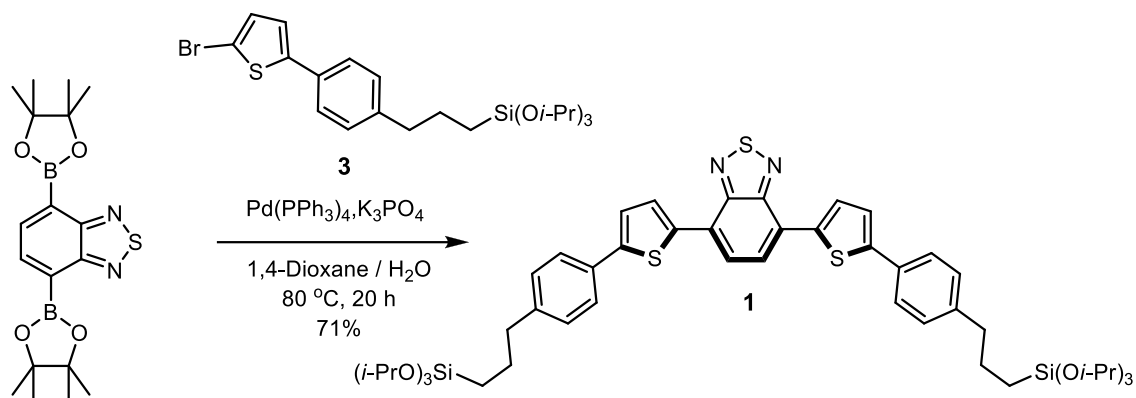
Device structures (device A or device B): Al (100 nm)/LiF (0.5 nm)/PCBM/(**1-PMO-F** or **2-PMO-F**) (ca. 50 nm)/**1'-NP-F**/PEDOT:PSS (50 nm)/ITO (150 nm)/glass. A PEDOT:PSS was spin-coated onto the ITO substrates after passing through 0.45 μm filter. The samples were annealed on a hot plate at 140 $^{\circ}\text{C}$ for 90 min. Then the author formed a thin layer (**1'-NP-F**) as a buffer layer by casting 200 μL of sol A' on the PEDOT:PSS/ITO substrates and spinning the samples. The samples were stored in shallow plastic containers with a cover over night and dried in air to facilitate condensation of the buffer layers. Then the author constructed a thin film as an active layer by casting 100 μL of sol C or D on the **1'-NP-F** layers and spinning the samples. After drying the samples in air by storing in the container with a cover over night, the author formed PMO films by extracting the block copolymer **P3** twice in a heated toluene at 105 $^{\circ}\text{C}$ in an oven for 24 h. After the preparation of **1-PMO-F** or **2-PMO-F** on **1'-NP-F**/PEDOT:PSS/ITO substrates, the samples were heated at 50 $^{\circ}\text{C}$ for 5 min. Then, a 2 wt% chlorobenzene solution of PCBM (400 μL) at 50 $^{\circ}\text{C}$ was cast on top of the PMO films, and left for a few minutes to infiltrate the PCBM solution into the mesopores. The excess solution was then removed by spinning the substrate (at 1500 rpm, 30 s). Through a shadow mask, LiF (0.5 nm) and Al (150 nm) were then deposited onto the PCBM layer as an electron extraction layer and a cathode, respectively. The active area of the solar cells was 9 mm^2 . The solar cells were encapsulated using a UV-epoxy resin and a glass plate under a nitrogen atmosphere.

4.3 Results and Discussion

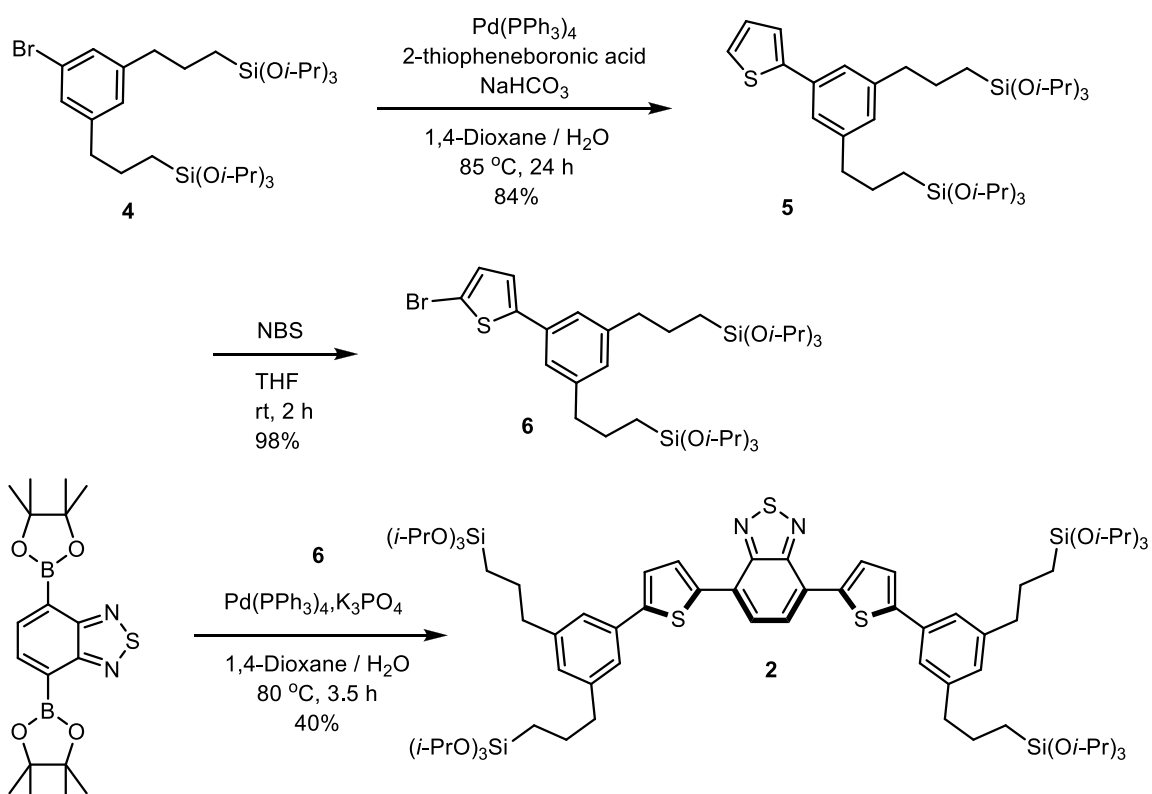
Synthesis of organosilane precursors

The DTBT-bridged alkoxy silane precursors **1** and **2** with two or four alkoxy silyl groups were synthesized as shown in Schemes 4.1 and 4.2. Synthesis of the precursors using a conventional synthetic approach was not easily accomplished, because the typical trimethoxysilyl ((MeO)₃Si) and triethoxysilyl ((EtO)₃Si) groups were difficult to attach to the DTBT unit due to their high reactivity during the synthesis and purification steps. Therefore, the triisopropoxysilyl ((*i*-PrO)₃Si) group was employed as a silyl group rather than conventional silyl groups because it has sufficient stability for the cross-coupling reaction and purification using silica gel chromatography.¹³

Suzuki–Miyaura cross-coupling between molecular building blocks **3** or **6** and 2,1,3-benzothiadiazole-4,7-diboronic acid bis(pinacol) ester followed by purification with silica gel chromatography successfully afforded the precursors **1** or **2** in pure form (Schemes 4.1 and 4.2).



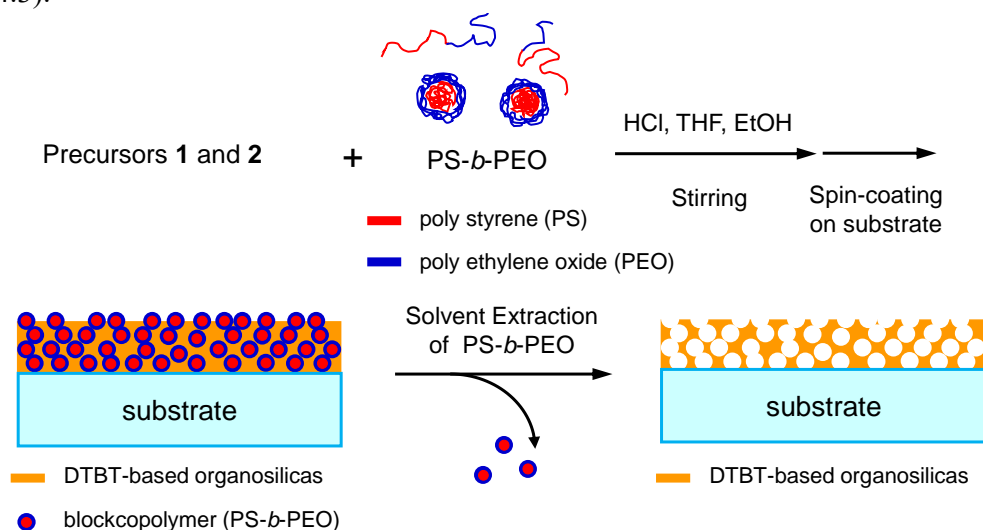
Scheme 4.1. Synthesis route for two-armed DTBT-bridged organosilane precursor **1**.



Scheme 4.2. Synthesis route for four-armed DTBT-bridged organosilane precursor **2**.

Preparation of PMO thin films

DTBT-PMO films were then synthesized by acidic sol–gel polymerization of the organosilane precursors in the presence of a block copolymer via evaporation-induced self-assembly (EISA) (Scheme 4.3).



Scheme 4.3. Synthesis route for DTBT-based PMO films.

Table 4.1. Optimization of reaction conditions for the formation of well-defined PMO films

Entry	Precursor	Block copolymer (M_n : PS- <i>b</i> -PEO/kg mol ⁻¹)	THF/EtOH (w/w)	PMO structure
1	1	P1 (20- <i>b</i> -14)	7/1	No formation
2	1	P1	3/1	Defined
3	1	P1	2/1	Disordered
4	1	P2 (20- <i>b</i> -6.5)	3/1	Disordered
5	1	P3 (58.6- <i>b</i> -71.0)	3/1	Well-defined
6	2	P3	2/1	Well-defined

The reaction conditions and preparation procedure were carefully examined to obtain the desired PMO films because it was assumed that the bulky DTBT unit can weaken the interaction between the hydrolyzed silyl group and surfactant micelles to form a well-ordered mesostructure (Table 4.1). Sol mixtures containing precursor **1**, block copolymers **P1–P3**, and HCl in a reaction organic solvent were spin-coated on poly(3,4-ethylenedioxythiophene):poly(styrene sulfonic acid) (PEDOT:PSS)/indium tin oxide (ITO)/glass substrates (Scheme 4.3). After removal of the template,

cross-sectional scanning electron microscopy (SEM) observations of the PMO films were conducted (Figure 4.1).

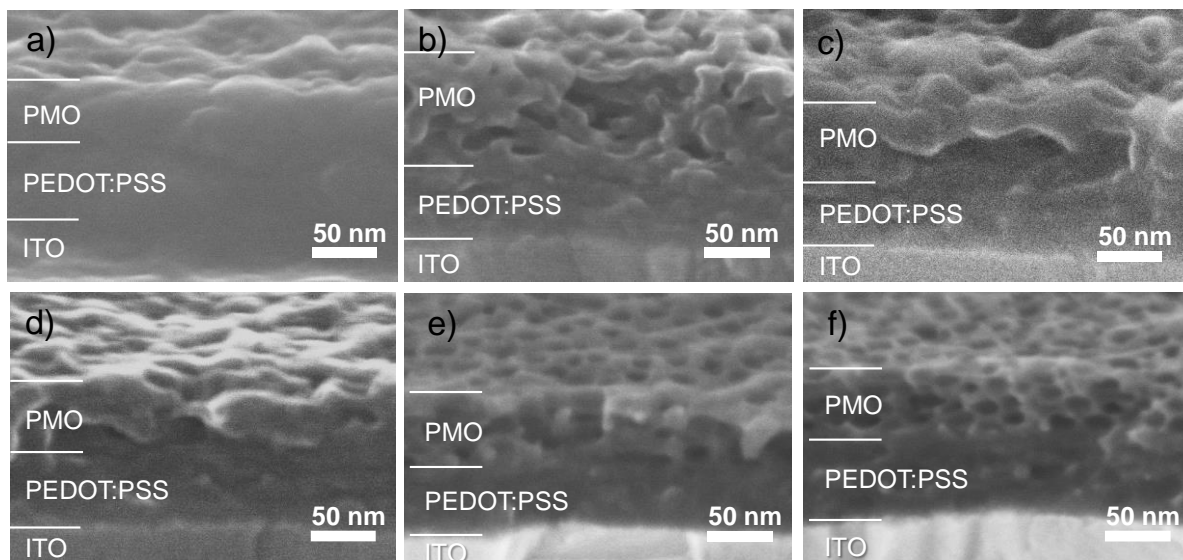


Figure 4.1. Cross-sectional SEM images of PMO films. a)–f) correspond to entries 1 to 6 in Table 4.1.

Using **P1** ($M_n = 20\text{-}b\text{-}14 \text{ kg mol}^{-1}$) as a template, the solvent effect on the formation of well-ordered PMO structures was examined initially. The use of THF/EtOH = 7/1, w/w mixed solvent had no effect on the formation of a well-ordered PMO film (Table 4.1, entry 1, Figure 4.1a). However, the PMO structures did become easier to form with an increase in the ratio of EtOH to THF. For example, a defined structure was observed when the solvent ratio of THF/EtOH was 3/1 (Table 4.1, entry 2, Figure 4.1b). The pore sizes were estimated to be 15–20 nm, which is consistent with the shape of the spherical micelles of **P1**. This behavior can be explained by the stabilizing effect of the PS blocks in the presence of poor solvents such as EtOH and water.¹⁴ However, when the THF/EtOH solvent ratio was 2/1, vacant mesopores became unclear (Table 4.1, entry 3, Figure 4.1c). Increasing the ratio of EtOH further (THF/EtOH = 1/2) induced the precipitation of organosilica during preparation of the sol. This is considered to be caused by a weakening of the

¹⁴ a) Yu, K.; Eisenberg, A. *Macromolecules* **1996**, *29*, 6359; b) Cheng, Y.-J.; Gutmann, J. S. *J. Am. Chem. Soc.* **2006**, *128*, 4658–4674; c) Chandra, D.; Ohji, T.; Kato, K.; Kimura, T. *Phys. Chem. Chem. Phys.* **2011**, *13*, 12529–12535; d) Barton, A. F. M. *CRC Handbook of Polymer-Liquid Interaction Parameters and Solubility Parameters*, CRC Press, Boca Raton, 1990.

interactions between micelles and hydrolyzed precursors due to a decrease in silanol groups and/or unwanted consumption of precursors.

The influence of the size and ratio of PS and PEO groups in the block copolymers was investigated next. When the films were prepared from **P2** ($M_n = 20\text{-}b\text{-}6.5 \text{ kg mol}^{-1}$), it was very difficult to obtain spherical pore structures (Table 4.1, entry 4, Figure 4.1d). This could be explained by the instability of the spherical micelles structures caused by the short hydrophilic PEO moiety.^{14a} In contrast, the use of **P3** ($M_n = 58.6\text{-}b\text{-}71.0 \text{ kg mol}^{-1}$) was effective for the formation of well-defined PMO films (denoted as **1-PMO-F**) (Table 4.1, entry 5, Figure 4.1e). It is noteworthy that well-defined PMO films are obtained even if a two-armed organosilane precursor is used without the addition of any pure silica precursors. This is because stable micelles are formed during the EISA due to the long PEO moiety in **P3**. In the case of precursor **2**, well-defined PMO films (denoted as **2-PMO-F**) were easily obtained from the sol using the THF/EtOH mixed solvent with a ratio of 2/1 (Table 4.1, entry 6, Figure 4.1f). Compared with **1-PMO-F**, the surface structure appears more isotropic, and well-ordered mesopores were formed. The ease of formation of the PMO structure can be attributed to the increased amount of silanol groups in the precursor.

Structural analysis of PMO thin films

Krypton adsorption, which is much more sensitive than nitrogen adsorption,¹⁵ was applied to assess surface area of **1-PMO-F** because the sample amount was too small to measure nitrogen adsorption due to very thin layer of PMO ($\sim 50 \text{ nm}$). The Brunauer–Emmett–Teller (BET) surface area of **1-PMO-F** calculated from the krypton adsorption isotherm was $285 \text{ m}^2 \text{ g}^{-1}$ (Figure 4.2). From SEM images of **1-PMO-F**, the author estimated the number of mesopores with a diameter of 15 nm to be 18 in a unit cell of $(50 \times 50 \times 50) \text{ nm}^3$. Using this information and the weight of **1-PMO-F** measured (0.31 mg), the author estimated that the surface area is $225 \text{ m}^2 \text{ g}^{-1}$. There is no large difference between the value obtained from the experiment and the estimated value. Unfortunately, the pore size distribution in the pore diameter range over $\sim 9 \text{ nm}$ cannot be determined from a krypton adsorption isotherm because pore condensation of krypton cannot be observed for pore diameters larger than 10 nm.¹⁵

Instead, the pore size distribution was obtained from top view SEM images of **1-PMO-F** using

¹⁵ Thommes, M.; Nishiyama, N.; Tanaka, S. *Stud. Surf. Sci. Catal.* **2007**, *165*, 551–554.

an image analysis software. Figure 4.3 shows pore size distribution of mesopores. Three different SEM images (samples: a–c) were used (analyzed area: $1.1 \mu\text{m}^2$). The pores were distributed in a narrow range with an average pore diameter of 15 nm and a standard deviation of 4 nm. The coefficient of variation (standard deviation/average pore diameter) is about 0.28. The value is similar to that (0.22) of a conventional PMO film which was estimated by the pore size distribution curve derived from nitrogen adsorption.¹⁶ 2D-grazing incidence small-angle X-ray scattering (GI-SAXS) for **1-PMO-F** did not give helpful information on periodicity probably because the PMO layer is too thin to detect enough diffraction intensity.

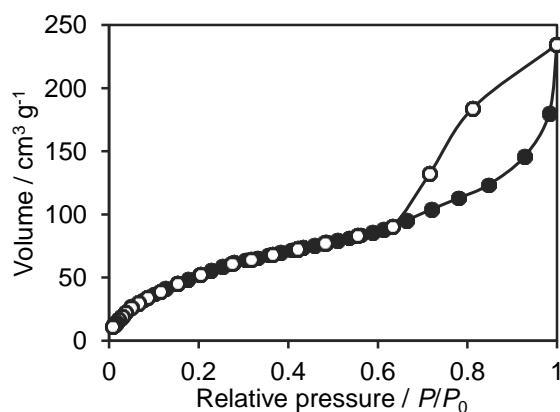


Figure 4.2. Krypton adsorption–desorption isotherm of **1-PMO-F**. Closed circles: adsorption, open circles: desorption.

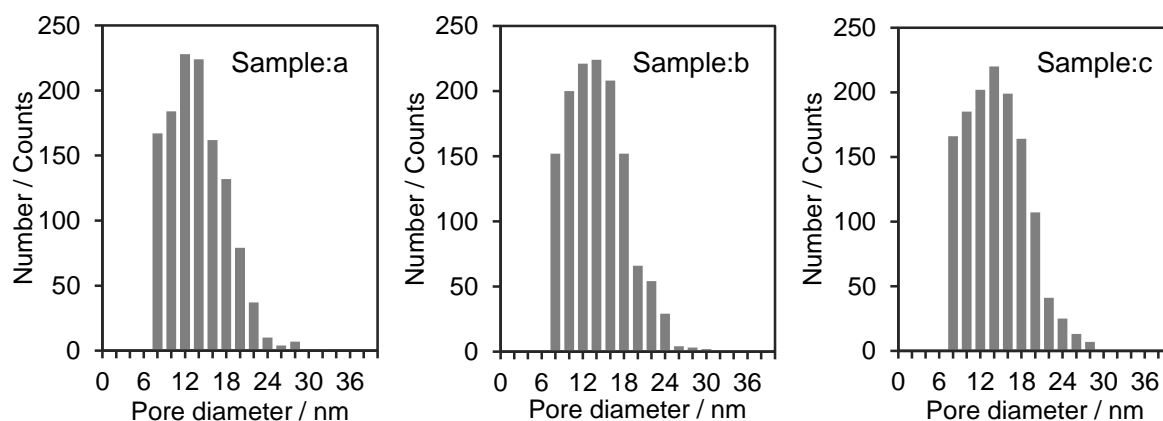


Figure 4.3. Pore size distribution of mesopores for **1-PMO-F** obtained from their top view SEM images (Samples a–c) using an image analysis software.

¹⁶ Mizoshita, N.; Yamanaka, K.; Shimada, T.; Tani, T.; Inagaki, S. *Chem. Commun.* **2010**, 46, 9235–9237

UV-vis absorption properties

Figure 4.4 shows normalized UV-vis absorption spectra for DTBT-PMO films and their organosilane precursors (CHCl_3 solution). Both of the PMO films and their precursor solutions exhibited absorption over a wide range from 300 to 650 nm. The absorption peaks at around 350 and 500 nm can be assigned to the $\pi-\pi^*$ transition of the DTBT units and the intramolecular charge transfer between electron-rich thiophene and electron deficient benzothiadiazole units, respectively.^{12b,17} These results support the successful incorporation of DTBT units into the PMO frameworks without loss of the absorption properties. The absorption bands for the PMO films at around 500 nm are broader than those for the precursor solutions, which suggest there are molecular interactions between DTBT units in the organosilica framework. In the case of **1-PMO-F**, the maximum wavelengths (λ_{max}) of absorption spectra was blue shifted with respect to that for corresponding precursor solutions, which could indicate the H aggregation of DTBT units within the organosilica framework (Figure 4.4a). In contrast, λ_{max} for **2-PMO-F** was primarily similar to that of the precursor solution, which suggests weak interaction between the DTBT groups in the ground state (Figure 4.4b).

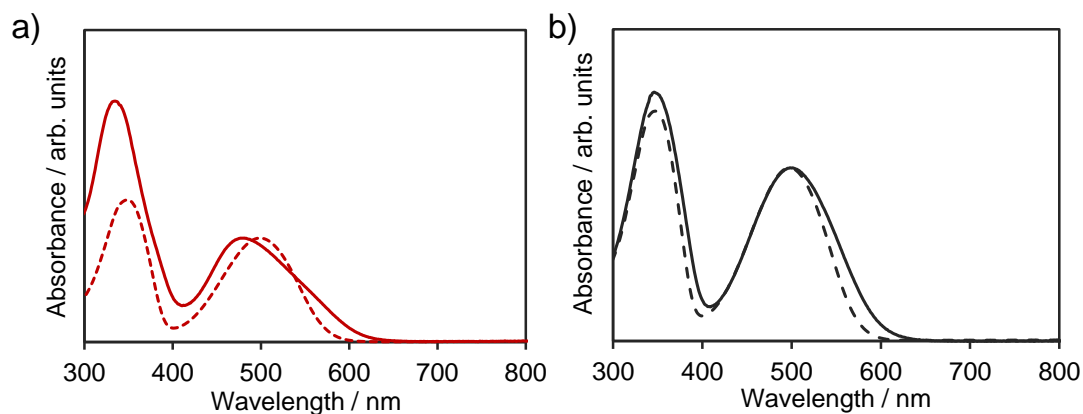


Figure 4.4. Normalized UV-vis absorption spectra of a) **1-PMO-F** (red solid line) and precursor **1** (red dashed line), b) **2-PMO-F** (black solid line) and precursor **2** (black dashed line). The concentration of the CHCl_3 solutions for precursors **1** and **2** was 10^{-5} M.

¹⁷ a) Jespersen, K. G.; Beenken, W. J. D.; Zaushitsyn, Y.; Yartsev, A.; Andersson, M.; Pullerits, T.; Sundström, V. J. *Chem. Phys.* **2004**, *121*, 12613–12617; b) Roquet, S.; Cravino, A.; Leriche, P.; Alèvêque, O.; Frère, P.; Roncali, J. *J. Am. Chem. Soc.* **2006**, *128*, 3459–3466.

Hole mobilities

Space-charge-limited current (SCLC) method was employed for measurement of the hole mobilities. Hole-only devices were fabricated by spin-coating of DTBT-silica films onto MoO₃-coated ITO/glass substrate and evaporation of an Au cathode onto the DTBT-silica films. Nonporous DTBT-silica films (**1-NP-F** and **2-NP-F**), which were prepared by spin-coating of a DTBT-sol mixture without template, were measured instead of the PMO films (**1-PMO-F** and **2-PMO-F**) because the Au cathode could not be uniformly deposited onto the PMO films due to the highly porous structures. Very similar absorption spectra between the nonporous DTBT-silica films and the PMO films suggest similar optical and electrical properties for both films (Figure 4.5).

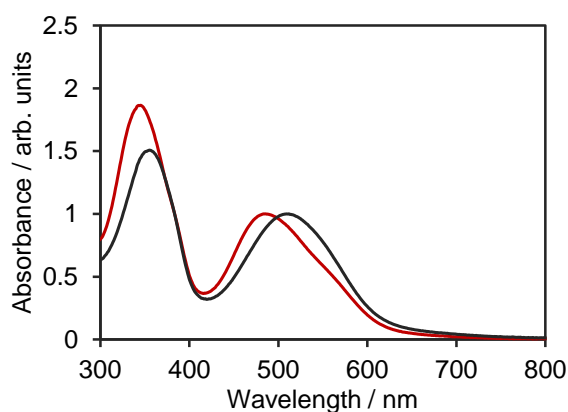


Figure 4.5. Normalized absorbance of both **1-NP-F** (red) and **2-NP-F** (black) films.

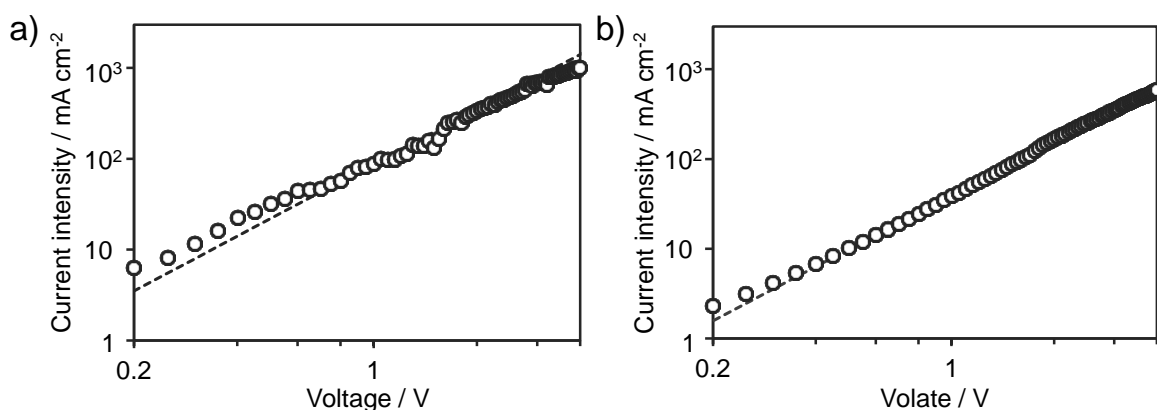
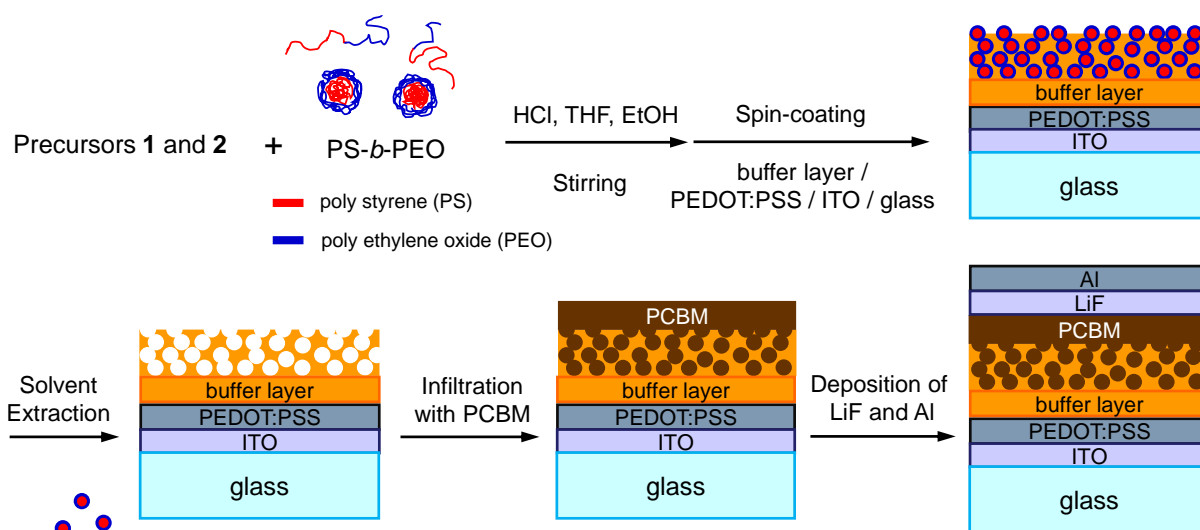


Figure 4.6. J - V characteristics for hole-only devices with a) **1-NP-F** (film thickness: 62 nm, open circles) and b) **2-NP-F** (film thickness: 51 nm, open squares) films under the dark conditions. The dashed lines represent the prediction obtained using the SCLC model.

Figure 4.6 shows the current density-voltage ($J-V$) characteristics of hole-only devices consisting of Au/**1-NP-F**/MoO₃/ITO/glass and Au/**2-NP-F**/MoO₃/ITO/glass. The hole mobilities for **1-NP-F** and **2-NP-F** were estimated to be 6×10^{-5} and 1.5×10^{-5} cm² V⁻¹ s⁻¹, respectively. The hole mobilities for the PMO films are comparable with that for a DTBT-based molecular film without silica (ca. 10^{-5} cm² V⁻¹ s⁻¹).^{12b} The higher mobility of **1-NP-F** than **2-NP-F** can be attributed to the lower content of insulating silica and alkylene moieties and/or stronger interaction between DTBT units (H aggregation), as suggested from the UV-vis spectra for **1-NP-F**.

Photovoltaic performance of PMO-based OSCs

DTBT-PMO films were applied as a p-type active layer for the construction of OSCs. Scheme 4.4 shows a schematic illustration of the fabrication steps for the DTBT-PMO-based OSCs. A buffer layer of nonporous two-armed DTBT-silica thin film (**1'-NP-F**) was inserted between the PMO film and PEDOT:PSS layers to prevent direct contact between PCBM filled in the mesopores and the PEDOT:PSS/ITO anode. After preparation of the PMO films (ca. 50 nm thickness) onto a buffer layer coated PEDOT:PSS/ITO substrate, a chlorobenzene solution of PCBM was cast on top of the film and kept for a few minutes to infiltrate the PCBM solution into the mesopores. The excess solution was then removed by spinning the substrate.



Scheme 4.4. Schematic illustration of the fabrication steps for the OSC using p-type PMO film (orange) and PCBM (dark brown).

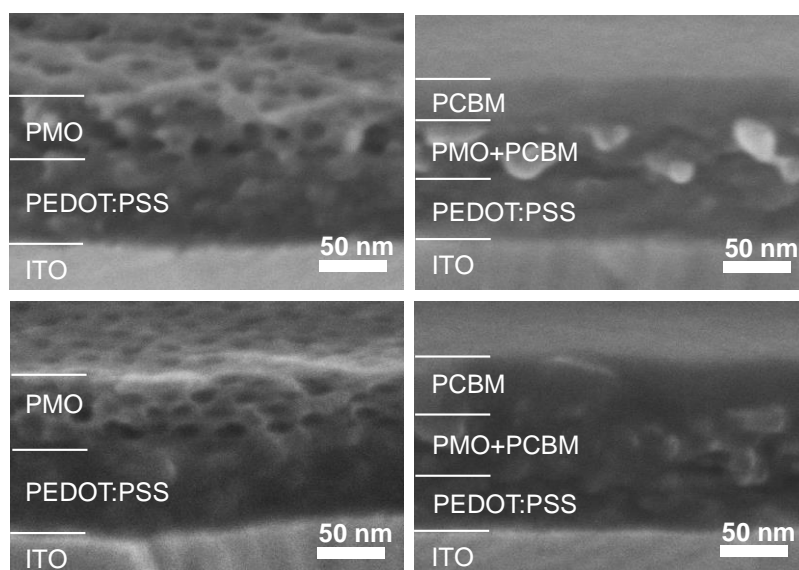


Figure 4.7. Cross-sectional SEM images of **1-PMO-F** (top) and **2-PMO-F** (bottom) on PEDOT:PSS/ITO before (left) and after (right) infiltration with PCBM.

Figure 4.7 shows cross-sectional SEM images of the films before and after the infiltration of PCBM into the mesopores (top: **1-PMO-F**, bottom: **2-PMO-F**). The contrast attributable to vacant mesopores disappeared, which suggests that the mesopores are sufficiently filled with PCBM. LiF and Al were then deposited onto the PCBM layer as an electron extraction layer and cathode, respectively. The EQE and $J-V$ characteristics of the devices were evaluated under 1 sun (AM 1.5G) simulated irradiation.

Figure 4.8a shows the EQE spectra for devices based on **1-PMO-F**:PCBM (device A) and **2-PMO-F**:PCBM (device B). Both devices exhibited EQE spectra over a wide range of 300–650 nm with two peaks at around 340 and 480 nm. A comparison of the EQE spectrum with the UV-vis absorption spectra for DTBT-PMO and PCBM films (Figure 4.9) suggests that the carriers are generated from excitons both in PMO films and PCBM. The carriers generated from excitons at around 480 nm are mainly due to absorption by the DTBT-PMOs. These results indicate that the PMO film can function as a p-type active layer for OSCs by filling the mesopores with an n-type material. The EQEs for device A reached 18% in the region of both wavelengths, while device B based on **2-PMO-F**:PCBM had EQE values of 5.5% at 340 nm and 4.3% at 480 nm. Notably, the EQEs of device A are more than 500 times higher than that of a conventional porphyrin-PMO:

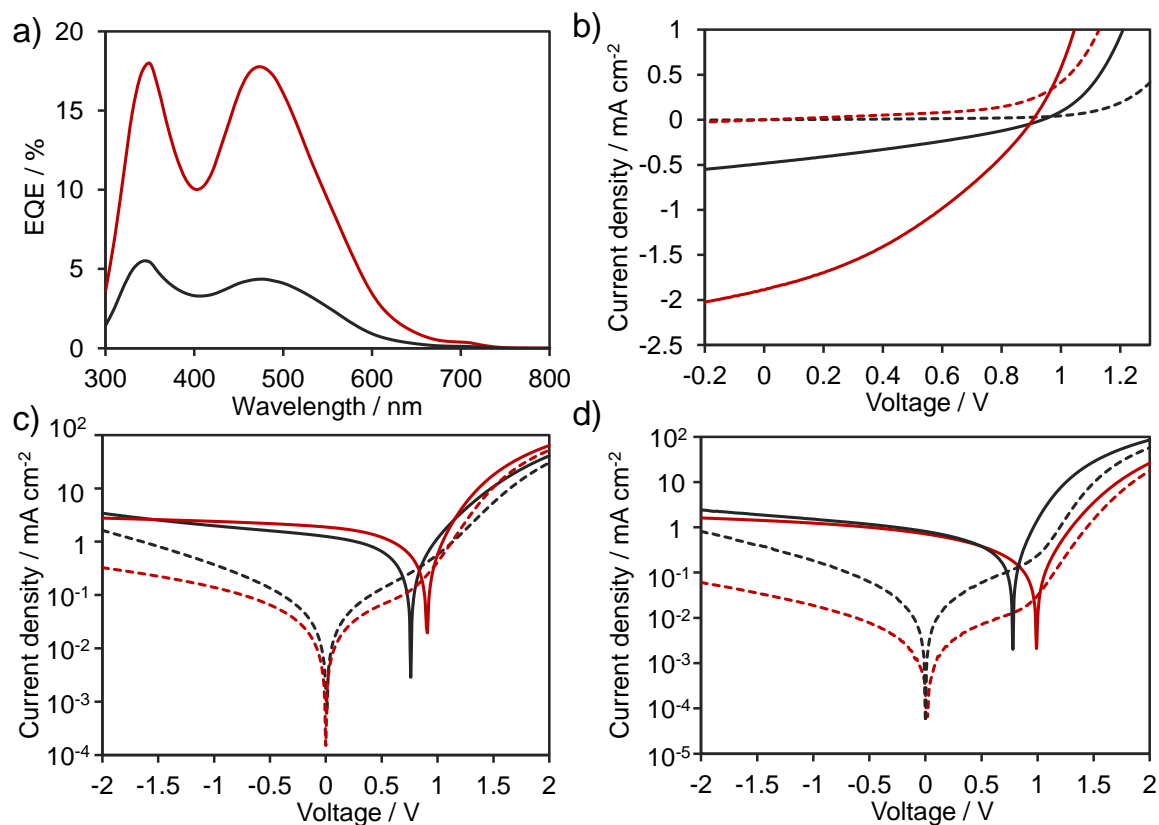


Figure 4.8. a) External quantum efficiency (EQE) and b) J - V characteristics of the PMO-based OSCs (red: device A, black: device B) under 1 sun (AM 1.5G) simulated irradiation (solid lines) and in the dark (dashed lines). J - V characteristics of c) device A or d) device B without a buffer layer (black lines) and with **1'-NP-F** buffer layer (red lines) in the dark (broken lines) and under 1 sun, AM1.5G illumination (solid lines).

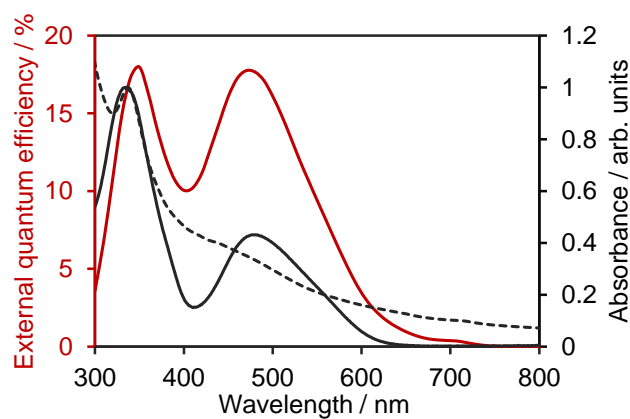


Figure 4.9. EQE of the **1-PMO-F** based solar cell (red, solid), and normalized absorbance of both **1-PMO-F** (black, solid) and PCBM (black, dashed) films.

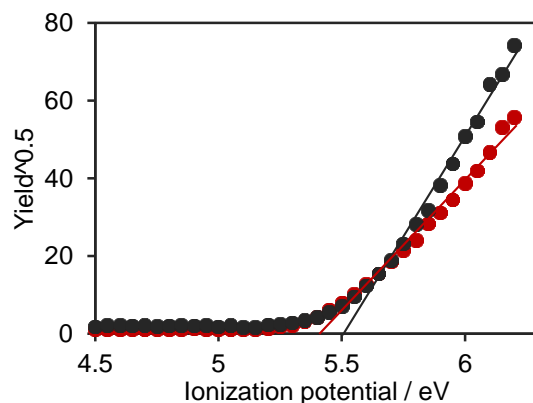


Figure 4.10. Ionization potentials of **1-NP-F** and **2-NP-F** measured by using AC-2.

PCBM device.¹⁰ This large difference of EQE between these devices is possibly related to the high hole mobility of the DTBT-PMO films.

Figure 4.8b shows the J - V characteristics for the DTBT-PMO-based OSCs. The open circuit voltages (V_{OC}) for device A and device B were 0.91 V and 0.94 V, respectively. The large V_{OC} values are attributable to the large ionization potential of the DTBT-PMO films (Figure 4.10). It should be noted that V_{OC} was significantly reduced when no buffer layer was inserted between the active layer and PEDOT:PSS (Figures 4.8c and 4.8d). This is probably caused by leakage current due to the direct contacts between PEDOT:PSS/ITO anode and the PCBM filled in the mesopores.¹⁸ At negative voltages, the dark current for the device without a buffer layer was approximately an order of magnitude larger than that with a buffer layer (Figures 4.8c and 4.8d), which indicates that the mesopores are filled with PCBM down to the interface between PEDOT:PSS and DTBT-PMO (**1-PMO-F** or **2-PMO-F**). The short circuit current density (J_{SC}) and fill factor (FF) values for device A were 1.89 mA cm^{-2} and 0.36, respectively. Thus, the power conversion efficiency (PCE) reached 0.61%. In contrast, the PCE for device B was only 0.14%, due to the low values of J_{SC} (0.48 mA cm^{-2}) and FF (0.32). The lowered J_{SC} and FF can be explained mainly by the low hole mobility of **2-PMO-F** compared with **1-PMO-F**. It is considered that the molecular design of the organosilane precursor and the packing control of the electroactive organic units in the PMO

¹⁸ a) Hains, A. W.; Marks, T. J. *Appl. Phys. Lett.* **2008**, *92*, 023504–023509; b) Li, N.; Lassiter, B. E.; Lunt, R. R.; Wei, G.; Forrest, S. R. *Appl. Phys. Lett.* **2009**, *94*, 023307–023500; c) Perez, M. D.; Borek, C.; Forrest, S. R.; Thompson, M. E. *J. Am. Chem. Soc.* **2009**, *131*, 9281–9286.

framework should increase the hole mobility of the PMO active layer to achieve further improvement of the device performance. Thus, the design and synthesis of novel organosilane precursors and their PMO films are under further investigation by the author's group.

4.4 Conclusions

Visible-light-absorptive and hole-transporting PMO films with large pore size were successfully synthesized from newly designed organosilane precursors containing DTBT units and block copolymers as a template. The DTBT-PMO films were obtained from 100% DTBT-based organosilane precursors without the addition of another alkoxy silane such as TEOS by optimization of the reaction conditions. Well-defined and pore size-controlled p–n heterojunction structures were constructed by filling the mesopores with an n-type material such as PCBM. DTBT-PMO-based OSCs were fabricated and showed a PCE of 0.61%, which demonstrates the DTBT-PMO films can function as a p-type active layer for OSCs.

Chapter 5

Solid Chelating PMO for Heterogeneous Metal Complex Catalysts

The immobilization of homogeneous transition-metal complexes onto solid supports has attracted much attention in the fields of industrial chemical processes because heterogeneous catalysts have crucial advantages such as easy handling, separation, and reusability. However, conventional immobilization approaches decrease the catalytic activity and selectivity of the original homogeneous metal complex catalyst due to the loss of the metal coordination structure of the active centers. To construct a well-defined metal coordination structure on the support surface, the author synthesized a crystal-like bipyridine-bridged periodic mesoporous organosilica (BPy-PMO) where 2,2'-bipyridine groups were densely and regularly arranged on the pore surface as a chelating ligand. BPy-PMO could be synthesized by hydrolysis and polycondensation of 5,5'-bis(triisopropoxysilyl)-2,2'-bipyridine without addition of pure silica source under basic condition in the presence of cationic surfactant as a structural directing agent. BPy-PMO showed high metal coordination ability to construct a well-defined metal complex structure on the pore surface. A variety of metal-bipyridine complexes based on iridium (Ir), ruthenium (Ru), rhenium (Re), and palladium (Pd) were formed on the pore surface without loss of metal coordination structure of the corresponding molecular metal complexes. The author succeeded in the development of i) highly active heterogeneous Ir-bipyridine complex catalysts for direct C–H borylation of arenes and heteroarenes with bis(pinacolate)diboron or pinacolborane, ii) heterogeneous photocatalytic hydrogen evolution system from water by integration of Ru(bpy)₃²⁺ as a photosensitizer and platinum nanoparticle as a catalyst on the pore surface, and iii) highly active heterogeneous molybdenum (Mo)-bipyridine catalyst for epoxidation of olefins with *tert*-butyl hydroperoxide. These heterogeneous metal complex catalysts showed high catalytic performance without loss of the original activity of the corresponding homogeneous catalysts.

5.1 Synthesis of Crystal-like Bipyridine-bridged PMO and Its Metalation Ability

Synthesis of a solid chelating ligand for the formation of efficient heterogeneous catalysts is highly desired in the fields of organic transformation and solar energy conversion. Here, the author reports the surfactant-directed self-assembly of a novel periodic mesoporous organosilica (PMO) containing 2,2'-bipyridine (bpy) ligands within the framework (BPy-PMO) from a newly synthesized organosilane precursor $[(i\text{-PrO})_3\text{Si}-\text{C}_{10}\text{H}_6\text{N}_2-\text{Si}(\text{O}i\text{-Pr})_3]$ without addition of any other silane precursors. BPy-PMO had a unique pore wall structure in which bipyridine groups were densely and regularly packed and exposed on the surface. The high coordination ability to metals was also preserved. Various bipyridine-based metal complexes were prepared using BPy-PMO and BPy-PMO end-capped with trimethylsilyl (TMS) groups (BPy-PMO-TMS) as a solid chelating ligand such as $\text{Ru}(\text{bpy})_2(\text{BPy-PMO})$, $\text{Ir}(\text{ppy})_2(\text{BPy-PMO})$ (ppy = 2-phenylpyridine), $\text{Ir}(\text{cod})(\text{OMe})(\text{BPy-PMO-TMS})$ (cod = 1,5-cyclooctadiene), $\text{Re}(\text{CO})_3\text{Cl}(\text{BPy-PMO})$, and $\text{Pd}(\text{OAc})_2(\text{BPy-PMO})$. BPy-PMO showed excellent ligand properties for heterogeneous Ir-catalyzed direct C–H borylation of arenes, resulting in superior activity, durability, and recyclability to the homogeneous analogous Ir catalyst. An efficient photocatalytic hydrogen evolution system was also constructed by integration of a Ru-complex as a photosensitizer and platinum as a catalyst on the pore surface of BPy-PMO without any electron relay molecules. These results demonstrate the great potential of BPy-PMO as a solid chelating ligand and a useful integration platform for construction of efficient molecular-based heterogeneous catalysis systems.

5.1.1 Introduction

A variety of functional systems based on metal complexes with chelating ligands have been constructed for applications such as catalysts for organic synthesis¹ and photosensitizers for photoreaction systems.² For practical applications, immobilization of metal complexes on solid

¹ Noyori, R. *Asymmetric Catalysis in Organic Synthesis*; John Wiley & Sons Ltd: New York, 1994; pp16–94.

² a) Amouyal, E. In *Homogeneous Photocatalysis*; Chanon, E., Ed.; John Wiley & Sons Ltd: New York, 1997; pp263–307; b) Nicewicz, D. A.; MacMillan, D. W. C. *Science* **2008**, 322, 77–80.

supports is important for easy recovery and recycle uses and allows easy integration of different components for constructing highly functional systems.³ There are some successful examples for heterogenized metal complex showing comparable or superior catalytic performance to the homogeneous analogue.⁴ However, immobilization on conventional supports such as silica gel has often resulted in decreases in the performances of metal complexes, such as catalytic activity and selectivity, because the uniform environment of the homogeneous metal complexes is disturbed by unfavorable interactions with the solid surface and nonuniform fixation on the surface.⁵ Moreover, the diffusion limitation of substrate and product molecules has been a problem for porous supports due to a decrease in reaction efficiency in their narrow channels. Thus, the development of a new support preserving the inherent functions of metal complexes is still a challenge for realizing their practical applications.

Ordered mesoporous materials, synthesized by a surfactant-directed self-assembly approach, are ideal supports due to their high surface areas and uniform mesopores for facile diffusion of molecules and ions. Periodic mesoporous organosilicas (PMOs), synthesized from organic-bridged silane precursors $\{R-[Si(X)_3]_n, n \geq 2, R = \text{organic group, } X = \text{OMe, OEt, Oi-Pr, allyl}\}$, are especially promising because functional organic groups can be incorporated into the framework without plugging the mesopore space, in contrast to mesoporous silicas functionalized with organic groups grafted on the pore surface.⁶ PMOs with a variety of organic groups in the frameworks have already been synthesized, including organic groups having metal ligand abilities.^{7,8} Recently, Waki

³ a) Huang, J.; Zhu, F.; He, W.; Zhang, F.; Wang, W.; Li, H. *J. Am. Chem. Soc.* **2010**, *132*, 1492–1493; b) Raja, R.; Thomas, J. M.; Jones, M. D.; Johnson, B. F. G.; Vaughan, D. E. W. *J. Am. Chem. Soc.* **2003**, *125*, 14982–14983; c) Karamé, I.; Boualleg, M.; Camus, J.-M.; Maishal, T. K.; Alauzun, J.; Basset, J.-M.; Copéret, C.; Corriu, R. J. P.; Jeanneau, E.; Mehdi, A.; Reyé, C.; Veyre, L.; Thieuleux, C. *Chem.–Eur. J.* **2009**, *15*, 11820–11823.

⁴ a) Benyahya, S.; Monnier, F.; Taillefer, M.; Man, M. W. C.; Beid, C.; Ouazzani, F. *Adv. Synth. Catal.* **2008**, *350*, 2205–2208; b) Nobre, S.; Cattoën, X.; Ferreira, R. A. S.; Man, M. W. C.; Carlos, L. D. *Phys. Status Solidi RRL* **2010**, *4*, 55–57.

⁵ a) Li, C. *Catal. Rev.* **2004**, *46*, 419–492; b) Maschmeyer, T.; Rey, F.; Sankar, G.; Thomas, J. M. *Nature* **1995**, *378*, 159–162; c) Li, H.; Yin, H.; Zhang, F.; Li, H.; Huo, Y.; Lu, Y. *Environ. Sci. Technol.* **2009**, *43*, 188–194.

⁶ a) Inagaki, S.; Guan, S.; Fukushima, Y.; Ohsuna, T.; Terasaki, O. *J. Am. Chem. Soc.* **1999**, *121*, 9611–9614; b) Asefa, T.; MacLachlan, M. J.; Coombs, N.; Ozin, G. A. *Nature* **1999**, *402*, 867–871; c) Melde, B. J.; Holland, B. T.; Blanford, C. F.; Stein, A. *Chem. Mater.* **1999**, *11*, 3302–3308.

⁷ a) Hunks, W. J.; Ozin, G. A. *J. Mater. Chem.* **2005**, *15*, 3716–3724; b) Hoffmann, F.; Cornelius, M.; Morell, J.; Fröba, M. *Angew. Chem.* **2006**, *118*, 3290–3328; c) Fujita, S.; Inagaki, S. *Chem. Mater.* **2008**, *20*, 891–908.

⁸ a) Wang, W.; Lofgreen, J. E.; Ozin, G. A. *Small* **2010**, *6*, 2634–2642; b) Mizoshita, N.; Tani, T.; Inagaki, S.

et al. reported the synthesis of crystal-like PMOs containing divinylpyridine⁹ and phenylpyridine (PPy) groups¹⁰ in the frameworks from 100% organosilane precursors of $(\text{EtO})_3\text{Si}-\text{CH}=\text{CH}-\text{C}_5\text{H}_3\text{N}-\text{CH}=\text{CH}-\text{Si}(\text{OEt})_3$ and $(\text{EtO})_3\text{Si}-\text{C}_6\text{H}_4-\text{C}_5\text{H}_3\text{N}-\text{Si}(\text{OEt})_3$, respectively. These pyridine-based PMOs have a crystal-like pore wall structure in which the pyridine moieties are densely and regularly arranged in the pore walls to form well-defined pore surface structures. PPy-PMO was successfully utilized as a solid chelating ligand for the formation of metal complexes such as ruthenium (Ru) and iridium (Ir) on the pore surface by postsynthetic cyclometalation.^{10,11}

2,2'-Bipyridine is the most widely used chelating ligand for forming metal complexes in coordination and supramolecular chemistry.^{12,13} Although there have been several reports on the synthesis of mesoporous silicas¹⁴ or PMOs¹⁵ containing 2,2'-bipyridine ligands, they possessed a nonuniform pore surface structure due to the amorphous pore walls in which 2,2'-bipyridine groups were randomly distributed on the pore surface or in the walls. The amorphous pore walls resulted from the use of 2,2'-bipyridine precursors attached by one or two trialkoxysilyl groups via linkers such as alkyl chains, amides, or thioethers. Thus, the formation of crystal-like pore wall structures has been limited to PMOs synthesized from rigid bridging organics such as benzene,¹⁶ biphenyl,¹⁷ naphthalene,¹⁸ divinylbenzene,¹⁹ divinylpyridine,⁹ and phenylpyridine¹⁰ attached to two silyl groups but no linkers. The author envisaged that a new precursor with a 2,2'-bipyridine directly

Chem. Soc. Rev. **2011**, *40*, 789–800.

⁹ Waki, M.; Mizoshita, N.; Tani, T.; Inagaki, S. *Chem. Commun.* **2010**, *46*, 8163–8165.

¹⁰ Waki, M.; Mizoshita, N.; Tani, T.; Inagaki, S. *Angew. Chem., Int. Ed.* **2011**, *50*, 11667–11671.

¹¹ Grüning, W. R.; Rossini, A. J.; Zagdoun, A.; Gajan, D.; Lesage, A.; Emsley, L.; Copéret, C. *Phys. Chem. Chem. Phys.* **2013**, *15*, 13270–13274.

¹² Gispert, J. R. *Coordination Chemistry*; Wiley-VCH Verlag: Weinheim, 2008.

¹³ Lehn, J.-M. *Supramolecular Chemistry*; VCH: Weinheim, 1995.

¹⁴ a) Nunes, C. D.; Valente, A. A.; Pillinger, M.; Fernandes, A. C.; Romão, C. C.; Rocha, J.; Conçalves, I. S. *J. Mater. Chem.* **2002**, *12*, 1735–1742; b) Nguyen, J. V.; Jones, C. W. *Macromolecules* **2004**, *37*, 1190–1203.

¹⁵ a) Minoofar, P. N.; Hernandez, R.; Chia, S.; Dunn, B.; Zink, J. I.; Franville, A.-C. *J. Am. Chem. Soc.* **2002**, *124*, 14388–14396; b) Kumar, R.; Chen, H.-T.; Escoto, J. L. V.; Lin, V. S.-Y.; Pruski, M. *Chem. Mater.* **2006**, *18*, 4319–4327; c) Font, J.; March, P. d.; Busqué, F.; Casas, E.; Benitez, M.; Teruel, L.; García, H. *J. Mater. Chem.* **2007**, *17*, 2336–2343; d) Sun, L.; Mai, W.; Dang, S.; Qiu, Y.; Deng, Y.; Shi, L.; Yana, W.; Zhang, H. *J. Mater. Chem.* **2012**, *22*, 5121–5127.

¹⁶ Inagaki, S.; Guan, S.; Ohsuna, T.; Terasaki, O. *Nature* **2002**, *416*, 304–307.

¹⁷ Kapoor, M. P.; Yang, Q.; Inagaki, S. *J. Am. Chem. Soc.* **2002**, *124*, 15176–15177.

¹⁸ Mizoshita, N.; Goto, Y.; Kapoor, M. P.; Shimada, T.; Tani, T.; Inagaki, S. *Chem.–Eur. J.* **2009**, *15*, 219–226.

¹⁹ a) Sayari, A.; Wang, W. *J. Am. Chem. Soc.* **2005**, *127*, 12194–12195; b) Cornelius, M.; Hoffmann, F.; Fröba, M. *Chem. Mater.* **2005**, *17*, 6674–6678.

attached to two silyl groups would be essential for the synthesis of crystal-like bipyridine-PMO (BPy-PMO).

Here, the author reports the successful synthesis of the crystal-like BPy-PMO from 100% organosilane precursor [(*i*-PrO)₃Si-C₁₀H₆N₂-Si(O*i*-Pr)₃]. BPy-PMO had a well-defined pore surface structure where 2,2'-bipyridines were densely and regularly arranged and preserved the high coordination ability to metals. A variety of bipyridine-based metal complexes including Ir, Ru, rhenium (Re), and palladium (Pd) were easily formed on the pore surface. Furthermore, the author discovered the excellent ligand properties of BPy-PMO in heterogeneous Ir-catalyzed direct C-H borylation of arenes with bis(pinacolato)diboron²⁰ and in heterogeneous photocatalytic hydrogen evolution from water using a Ru-complex photosensitizer and platinum nanoparticles integrated on the pore surface.

5.1.2 Experimental

Materials and methods

Unless otherwise noted, all chemicals, including dry solvents, were purchased from commercial suppliers (Sigma-Aldrich, Tokyo Chemical Industry Co., Ltd., and Wako Pure Chemical Industries Ltd.) and used without further purification. All reactions for organic synthesis were carried out under argon using standard high-vacuum and Schlenk-line techniques. Nuclear magnetic resonance (NMR) spectra were recorded on a Jeol JNM-EXC400P spectrometer (400 MHz for ¹H, 100 MHz for ¹³C, and 376 MHz for ¹⁹F). Chemical shifts are reported in δ parts per million referenced to SiMe₄ or residual protonated solvent as an internal standard. The following abbreviations were used to explain the multiplicities: s = singlet, d = doublet, sept = septet, dd = double doublet. Mass spectra were recorded on a Micromass GCT Premier mass spectrometer (FI: field ionization) and Micromass Q-TOF mass spectrometer (ESI: electrospray ionization). ²⁹Si dipolar decoupling (DD) and ¹³C cross-polarization (CP) MAS (magic-angle spinning) NMR measurements were respectively performed at 79.49 and 100.6 MHz at a sample spinning frequency of 4 or 6 kHz using a Bruker Avance 400 spectrometer with a 7 mm zirconia rotor. For the ²⁹Si DD MAS NMR measurements, the repetition delay was 60 s, and the pulse width was 4.5 μs. For the ¹³C CP MAS

²⁰ Maegawa, Y.; Inagaki, S. *Solid catalyst*, Japanese Patent, JP 2013-39764, 2013.

NMR measurements, the repetition delay was 5 s, the contact time was 1.75 ms, and the pulse width was 4.5 μ s (^1H 90° pulse). Chemical shifts were referenced to SiMe_4 and glycine for ^{29}Si and ^{13}C NMR, respectively. X-ray diffraction (XRD) profiles were recorded on a Rigaku RINT-TTR diffractometer using $\text{Cu-K}\alpha$ radiation (50 kV, 300 mA). Nitrogen adsorption/desorption isotherms were measured using a Quantachrome Nova3000e sorptometer. Brunauer-Emmett-Teller surface areas (S_{BET}) were calculated from the linear sections of BET plots ($P/P_0 = 0.1\text{--}0.2$). Pore-size distributions were calculated using the DFT method (DFT kernel: N_2 at 77 K on silica, cylindrical pores, nonlinear density functional theory (NLDFE) equilibrium model). The density functional theory pore diameters (d_{DFT}) were estimated from the desorption isotherm. Pore volumes ($V_{t\text{-plot}}$) were estimated by the t -plot method. Scanning electron microscopy (SEM) and Transmission electron microscopy (TEM) observations were performed using a Hitachi S-3600N and a Jeol JEM-EX2000 operating at 5 kV and 200 kV, respectively. Infrared (IR) spectra were collected on a Thermo Fisher Scientific Nicolet Avatar-360 FT-IR spectrometer using an attenuated total reflection (ATR) attachment. Ultraviolet-visible (UV-vis) absorption and fluorescence emission spectra were obtained using Jasco V-670 and FP-6500 spectrometers, respectively. X-ray photoelectron spectroscopy (XPS) was recorded with an ULVAC Quantera SXM using $\text{Al-K}\alpha$ as the X-ray source. The charge neutralization function was employed to compensate for the charge built up on solid samples by X-ray irradiation. Binding energies were referenced to In_{3d5} at 444.4 eV from indium oxide (In_2O_3). X-ray absorption fine structure (XAFS) measurements at Ru K -edge and Re L_{III} -edge were conducted by a quick XAFS (QXAFS) method in transmission mode at BL01B1 of SPring-8. X-rays stemming from synchrotron were monochromatized by $\text{Si}(311)$ at Ru or $\text{Si}(111)$ Re double-crystal monochromator, and the monochromator was quickly rotated within ~ 6 min for the measurement of a QXAFS spectrum. XAFS measurements at Ir L_{III} -edge were conducted at 30 K by a step scan method in transmission mode at BL-12C of KEK-PF using $\text{Si}(111)$ double-crystal monochromator. An ion chamber was used to detect I_0 (intensity of incident X-rays), and another one placed behind the samples was used to detect I (intensity of transmitted X-rays). Background subtraction was performed with Autobk and Spline smoothing algorithm.²¹ The k^3 -weighted extended X-ray absorption fine structure (EXAFS) oscillations were Fourier transformed into R -space. Inductively coupled plasma-atomic emission spectrometry (ICP-AES)

²¹ Ravel, B.; Newville, M. *J. Synchrotron Radiat.* **2005**, *12*, 537–541.

spectroscopy measurements and CHN elemental analyses of PMO materials were performed in Toray Research Center, Inc..

Synthesis of organosilane precursors

2-Bromo-5-(triisopropoxysilyl)pyridine (2). A 500 mL three-neck flask connected to a condenser was charged with a stir bar, 2-bromo-5-iodopyridine (**1**) (8.0 g, 28.2 mmol), [Rh(cod)(CH₃CN)₂]BF₄ (0.11 g, 0.28 mmol), and *n*-Bu₄NI (12.5 g, 33.8 mmol). Dry DMF (150 mL), dry Et₃N (24 mL), and triisopropoxysilane (8.7 g, 42.3 mmol) were added. The reaction mixture was stirred at 100 °C for 24 h. After cooling to room temperature, the reaction mixture was evaporated, extracted with Et₂O, and filtered, and then the solvent was completely evaporated. The residue was purified by silica gel chromatography (eluent: hexane/CH₂Cl₂ = 1:1 to 1:4) to give **2** (7.0 g, 69%) as a light-yellow oil. ¹H NMR (400 MHz, CDCl₃) δ 1.18 (d, *J* = 6.2 Hz, 18H), 4.25 (sept, *J* = 6.2 Hz, 3H), 7.44 (d, *J* = 7.8 Hz, 1H), 7.74 (dd, *J* = 1.8, 7.8 Hz, 1H), 8.53 (d, *J* = 1.8 Hz, 1H); ¹³C NMR (100 MHz, CDCl₃) δ 25.4, 65.9, 127.5, 127.6, 144.3, 144.7, 155.7; *v*_{max} (neat) 2974, 2933, 2895, 1562, 1539, 1446, 1383, 1371, 1286, 1174, 1117, 1074, 1043, 1016, 891, 872, 827, 762 cm⁻¹; FI-HRMS *m/z* calcd for C₁₄H₂₄BrNO₃Si (M⁺): 361.0709; found: 361.0710.

5,5'-Bis(triisopropoxysilyl)-2,2'-bipyridine (3). A 1 L three-neck flask connected to a condenser was charged with a stir bar, **2** (10.0 g, 27.6 mmol), bis(tributyltin) (8.0 g, 13.8 mmol), and dry *m*-xylene (200 mL). Pd(PPh₃)₄ (0.5 g, 0.45 mmol) was added, and reaction mixture was stirred at 130 °C for 40 h. The resulting mixture was cooled down to room temperature and evaporated to remove solvent. The residue was purified by silica gel chromatography (eluent: CH₂Cl₂ to EtOAc/hexane = 1:10). The obtained orange-yellow solid (5.0 g) was dissolved in CH₃CN (50 mL) and extracted with hexane (500 mL). The hexane solution was treated with activated carbon (3.0 g) for 10 min, filtered, and evaporated to give **3** (4.56 g, 59%) as a light-yellow solid. ¹H NMR (400 MHz, CDCl₃) δ 1.24 (d, *J* = 6.0 Hz, 6H), 4.31 (sept, *J* = 6.2 Hz, 1H), 8.09 (dd, *J* = 1.6, 8.0 Hz, 2H), 8.40 (d, *J* = 7.3 Hz, 2H), 8.92 (s, 2H); ¹³C NMR (100 MHz, CDCl₃) δ 25.5, 65.8, 120.4, 128.6, 143.7, 1548, 157.0; *v*_{max} (neat) 2972, 2929, 2885, 1579, 1524, 1454, 1381, 1369, 1352, 1286, 1223, 1173, 1113, 1028, 1016, 889, 872, 843, 756, 737 cm⁻¹; FI-HRMS *m/z* calcd for C₂₈H₄₈N₂O₆Si₂ (M⁺): 564.3051; found: 564.3041.

Synthesis of BPy-PMO

A 300 mL one-neck flask was charged with a stir bar, octadecyltrimethylammonium chloride (C₁₈TMACl: 2.43 g, 6.98 mmol), 6 M NaOH aqueous solution (0.77 mL, 4.62 mmol), and distilled water (132 mL). The mixture was heated at 50 °C. A solution of precursor **3** (2.97 g, 5.26 mmol) in EtOH (5 mL) was directly added to the surfactant solution through the pipet at a constant speed (2.0 mL h⁻¹ for initial 1 h, then 2.5–3.0 mL h⁻¹) using a syringe-pump system under vigorous stirring at 50 °C. The white suspension was then sonicated for 2 h with stirring condition at 50 °C. The mixture was stirred for another 3 days and continued heating at 50 °C for 3 days under static conditions. Then, the resulted precipitation was filtered and washed with distilled water, affording as-made bipyridine-bridged PMO. The as-made sample (2.39 g) was added into the distilled water (433 mL) in the presence of C₁₈TMACl (8.70 g) again to increase condensation degree of organosilica framework. The mixture was heated at 95 °C for 24 h under static conditions. After filtration, as-made sample (1.56 g) with thermal treatment was extracted with acidic EtOH solution prepared from 2 M hydrochloric acid (HCl) aqueous solution (7.2 mL) and EtOH (260 mL) at room temperature for 12 h to give BPy-PMO as a white powder (1.39 g, 3.18 mmol BPy g⁻¹).

Synthesis of BPy-PMO-TMS

A 50 mL two-neck flask connected to a condenser was charged with a stir bar and BPy-PMO (500 mg). *N*-trimethylsilylimidazole (2 mL) was added and the reaction mixture was stirred at 60 °C for 12 h under argon atmosphere. After dilution with toluene (10 mL), the suspension was filtered and washed with toluene and methanol, respectively. The material was dried over under reduced pressure to give end-capped BPy-PMO (denoted as BPy-PMO-TMS) as a white powder (2.92 mmol BPy g⁻¹).

Synthesis of metal-complexed BPy-PMO

Ru(bpy)₂(BPy-PMO). A 200 mL three-neck flask connected to a condenser was charged with a stir bar, BPy-PMO (300 mg), and Ru(bpy)₂Cl₂•2H₂O (300 mg, 0.57 mmol). After addition of dry EtOH (60 mL), the reaction mixture was stirred at 90 °C for 24 h. The resulting precipitate was filtered and washed with CH₂Cl₂ to give Ru(bpy)₂(BPy-PMO) as an orange powder (319.9 mg, Ru content: 0.20 mmol g⁻¹).

Ir(ppy)₂(BPy-PMO). A 50 mL two-neck flask connected to a condenser was charged with a stir bar, BPy-PMO (100 mg), and [Ir(ppy)₂Cl]₂ (176 mg, 1.88 mmol). After addition of dry CH₂Cl₂ (33 mL), the reaction mixture was stirred at 45 °C for 15 h. The resulting precipitate was filtered and washed with CH₂Cl₂ to give Ir(ppy)₂(BPy-PMO) as a light-orange powder (122.5 mg, Ir content: 0.26 mmol g⁻¹).

Ir(OMe)(cod)(BPy-PMO-TMS). A 50 mL Schlenk-tube was charged with a stir bar and BPy-PMO-TMS (77.5 mg, 0.226 mmol). A solution of [Ir(OMe)(cod)]₂ (5.0 mg, 0.015 mmol Ir) in dry benzene (20 mL) was added at room temperature. The reaction mixture was stirred at room temperature for 12 h. The resulting suspension was filtered and then washed with dry benzene. The material was dried over under reduced pressure to give Ir(OMe)(cod)(BPy-PMO-TMS) as a light-gray powder (80 mg, Ir content: 0.156 mmol g⁻¹).

Re(CO)₃Cl(BPy-PMO). A 100 mL two-neck flask connected to a condenser was charged with a stir bar, BPy-PMO (100 mg), and Re(CO)₅Cl (137 mg, 0.38 mmol). After addition of dry toluene (50 mL), the reaction mixture was stirred at 110 °C for 24 h. The resulting precipitate was filtered and washed with toluene to give Re(CO)₃Cl(BPy-PMO) as a yellow-orange powder (149.1 mg, Re content: 1.12 mmol g⁻¹).

Pd(OAc)₂(BPy-PMO). A 20 mL Schlenk-tube was charged with a stir bar, BPy-PMO (100 mg), and Pd(OAc)₂ (21 mg, 0.08 mmol). After addition of dry THF (10 mL), the suspension was stirred at room temperature for 24 h. The resulting precipitate was filtered and washed with THF to give Pd(OAc)₂(BPy-PMO) as a yellow powder (117.5 mg, Pd content: 0.74 mmol g⁻¹).

Pt@Ru(bpy)₂(BPy-PMO). A 50 mL Schlenk-tube was charged with a stir bar and K₂PtCl₄ (64 mg, 0.15 mmol). After addition of degassed distilled water (24 mL), Ru(bpy)₂(BPy-PMO) (100 mg) was added to this solution under argon flow. The suspension was stirred at 80 °C for 24 h. The resulting precipitate was filtered and washed with EtOH to remove any unreacted platinum precursor, affording Pt@Ru(bpy)₂(BPy-PMO) as a dark-brown powder (123.5 mg, Pt content: 0.10 mmol g⁻¹).

$S_{\text{BET}} = 570 \text{ m}^2 \text{ g}^{-1}$, $V_{t\text{-plot}} = 0.19 \text{ cm}^3 \text{ g}^{-1}$, $d_{\text{DFT}} = 2.7 \text{ nm}$.

Synthesis of BPy-grafted mesoporous silica and silica gel

4-methyl-4'-(4-(triisopropoxysilyl)butyl)-2,2'-bipyridine. A 200 mL three-neck flask charged with a stir bar, 4,4'-dimethyl-2,2'-bipyridine (2.0 g, 10.9 mmol), and Dry THF (75 mL). After

cooling at 0 °C, lithium diisopropylamide (9.87 mL, 1.1 M in hexane/ethylbenzene, 10.9 mmol) was added dropwise over a period of 30 min. The resulting solution was stirred for 30 min at 0 °C, then (3-bromopropyl)triisopropoxysilane (4.27 g, 13.0 mmol) was added. The resulting reaction mixture was stirred at 0 °C for 2 h and room temperature for 4 h. Then, the reaction mixture was added *i*-PrOH (50 mL) and washed with water. The water layer was extracted with Et₂O. The combined organic layer was dried with anhydrous MgSO₄ and the solvent was removed under reduced pressure. The resulting crude product was purified by silica gel chromatography (eluent: hexane = 100 to hexane/EtOAc = 5:1 to hexane/EtOAc/*i*-PrOH = 5:1:0.5) to yield 4-methyl-4'-(4-(triisopropoxysilyl)butyl)-2,2'-bipyridine (3.80 g, 81%) as a colorless liquid. ¹H NMR (400 MHz, CDCl₃) δ 0.60–0.64 (m, 2H), 1.17 (d, *J* = 6.0 Hz, 18H), 1.46–1.50 (m, 2H), 1.67–1.74 (m, 2H), 2.43 (s, 3H), 2.69 (t, *J* = 8.0 Hz, 2H), 4.16–4.21 (m, 3H), 7.12 (d, *J* = 2.4 Hz, 2H), 8.21 (br, 2H), 8.53 (br, 2H); ¹³C NMR (100 MHz, CDCl₃) δ 11.8, 21.2, 22.8, 25.5, 33.8, 35.1, 64.8, 121.3, 121.9, 123.9, 124.6, 148.0, 148.9, 152.8, 156.0, 156.1; ESI-HRMS *m/z* calcd for C₂₄H₃₈N₂NaO₃Si (M+Na⁺): 453.2549; found: 453.2552.

L1 and **L2**. An 100 mL two-neck flask connected to a condenser was charged with a stir bar and 4-methyl-4'-(4-(triisopropoxysilyl)butyl)-2,2'-bipyridine (500 mg, 1.16 mmol). Dry toluene (60 mL) and silica gel (spherical, 60 Å) or FSM-16 (2.0 g) were added. Trifluoroacetic acid (1 drop) was then added and the suspension was refluxed for 24 h. After cooling, the suspension was filtered and washed with toluene, MeOH, and acetone to remove unreacted precursor in the material. The resulting material was extracted with toluene and MeOH for 24 h by Soxhlet extraction, respectively. The obtained white powder was suspended in dry toluene (5 mL) and treated with *N*-trimethylsilylimidazole (5 mL) at 60 °C for 12 h under argon atmosphere. After dilution with toluene (30 mL), the suspension was filtered and washed with toluene and MeOH. The material was dried over under reduced pressure to give bipyridine-immobilized silica gel (**L1**) or FSM-16 (**L2**) as a white powder. **L1**: 0.47 mmol BPy g⁻¹; ¹³C CP MAS NMR δ 3.46, 14.5, 20.1, 26.0, 36.3, 41.9, 122.3 (overlapped), 124.4 (overlapped), 147.6, 149.8, 150.9, 158.0 (Figure 5.1a); ²⁹Si DD MAS NMR δ -111.2, -67.0, -58.5, 12.5; *S*_{BET} = 443 m² g⁻¹, *V*_{*t*-plot} = ND, *d*_{DFT} = 6.3 nm (Figure 5.1c). **L2**: 0.44 mmol BPy g⁻¹; ¹³C CP MAS NMR δ 2.84, 14.1, 20.0, 25.3, 36.3, 42.1, 122.3 (overlapped), 124.3 (overlapped), 147.6, 149.8, 152.5, 158.1 (Figure 5.1b); ²⁹Si DD MAS NMR δ -111.5, -66.8, -57.5, 13.6; *S*_{BET} = 720 m² g⁻¹, *V*_{*t*-plot} = 0.28 cm³ g⁻¹, *d*_{DFT} = 3.2 nm (Figure 5.1d).

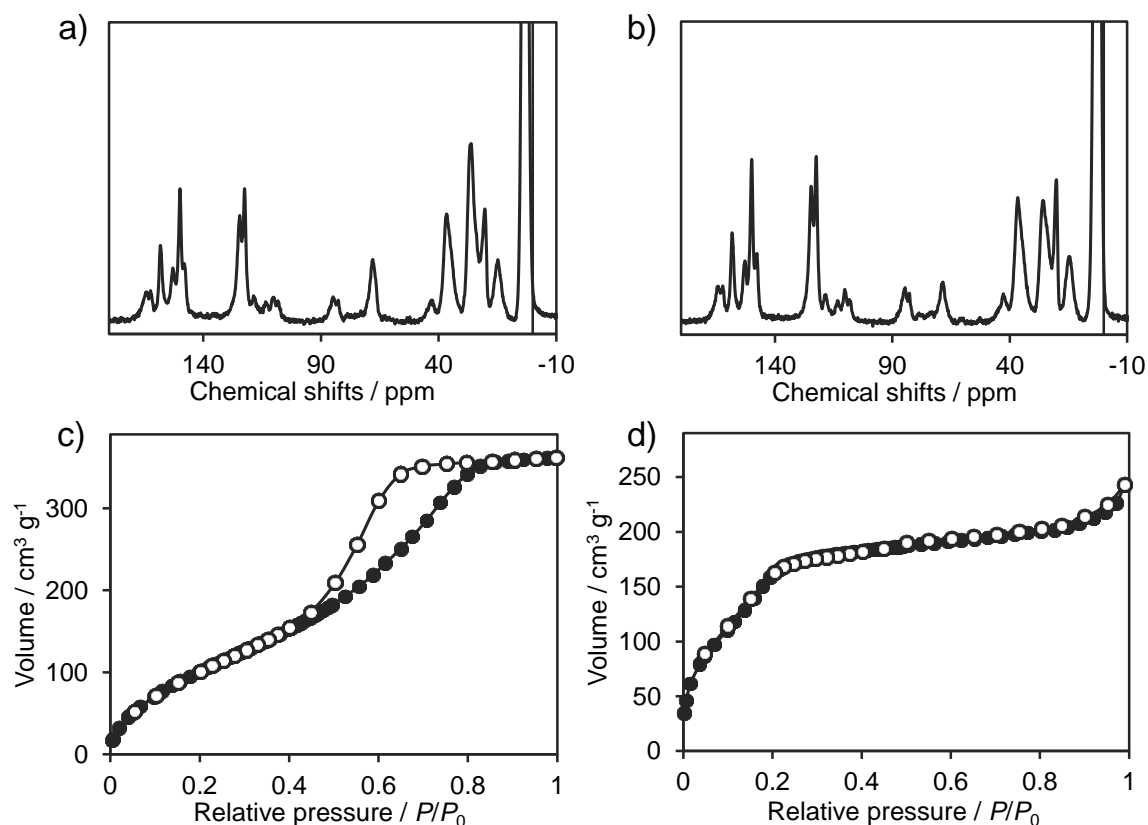


Figure 5.1. ^{13}C CP MAS NMR spectra of a) L1 and b) L2. Nitrogen adsorption/desorption isotherms of c) L1 and d) L2. Closed circle: adsorption, open circle: desorption.

Synthesis of homogeneous Ir complex catalyst

A 20 mL Schlenk-tube assembled a stir bar and a septum inlet was charged with $[\text{Ir}(\text{OMe})(\text{cod})]_2$ (75 mg, 0.113 mmol) and 2,2'-bipyridine (35.3 mg, 0.226 mmol). After addition of dry THF (10 mL), the reaction mixture was allowed to stir at room temperature for 3 h. The resulting precipitation was filtered and washed with dry hexane, and then dried over under reduced pressure to give $\text{Ir}(\text{OMe})(\text{cod})(\text{bpy})$ as a brown solid (30 mg) containing a small amount of 2,2'-bipyridine. ^1H NMR (400 MHz, $\text{DMSO}-d_6$) δ 1.80–1.84 (m, 4H), 2.31–2.33 (m, 4H), 3.91 (brs, 4H), 7.77 (t, $J = 6.4$ Hz, 2H), 8.33 (t, $J = 7.6$ Hz, 2H), 8.43 (d, $J = 5.6$ Hz, 2H), 8.72 (d, $J = 7.6$ Hz, 2H); ^{13}C NMR (100 MHz, $\text{DMSO}-d_6$) δ 31.4, 63.5, 124.0, 127.9, 139.4, 148.7, 156.2; ESI-HRMS m/z calcd for $\text{C}_{18}\text{H}_{20}\text{N}_2\text{Ir}$ (M^+): 457.1256; found: 471.1051.

General procedure for the direct C–H borylation of arenes catalyzed by Ir(OMe)(cod)(BPy-PMO-TMS)

A 20 mL Schlenk-tube assembled a stir bar and a septum inlet was charged with Ir(OMe)(cod)(BPy-PMO-TMS) (0.156 mmol Ir g⁻¹, 32.0 mg, 0.005 mmol Ir) and bis(pinacolato)diboron (B₂pin₂) (84.6 mg, 0.33 mmol) and then flushed with argon. An arene (20 mmol) was added, and the mixture was stirred at 80 °C for 12 h. The mixture was diluted with Et₂O (5 mL) and filtered through a membrane filter (0.20 μm). Solvent was removed under reduced pressure. The crude product was purified by flash silica gel chromatography (eluent: hexane/EtOAc = 100:0 to 70:30) provided analytically pure samples. The recovered catalyst was used for next reaction in the presence of B₂pin₂ and dry benzene under same reaction condition.

(4,4,5,5-Tetramethyl-1,3,2-dioxaborolan-2-yl)benzene (4a). Yield: 94%. ¹H NMR (400 MHz, CDCl₃) δ 1.35 (s, 12H), 7.37 (t, *J* = 7.4 Hz, 2H), 7.46 (t, *J* = 7.3 Hz, 1H), 7.81 (d, *J* = 7.3 Hz, 2H); ¹³C NMR (100 MHz, CDCl₃) δ 24.87, 83.75, 127.69, 131.23, 134.72; ESI-HRMS *m/z* calcd for C₁₂H₂₁BNO₂ (M+NH₄⁺): 222.1662; found: 222.1664.

(4,4,5,5-Tetramethyl-1,3,2-dioxaborolan-2-yl)toluene (4b). Yield: 85% (*m*-isomer:*p*-isomer = 63:37). ¹H NMR (400 MHz, CDCl₃) δ (*m*-isomer) 1.34 (s, 12H), 2.35 (s, 3H), 7.25–7.27 (m, 2H), 7.60 (t, *J* = 4.4 Hz, 1H), 7.63 (s, 1 H), (*p*-isomer) 1.34 (s, 12H), 2.36 (s, 3H), 7.18 (d, *J* = 7.6 Hz, 2H), 7.70 (d, *J* = 7.6 Hz, 2H); ¹³C NMR (100 MHz, CDCl₃) δ (*m*-isomer) 21.27, 24.85, 83.71, 127.66, 131.73, 132.01, 135.29, 137.10, (*p*-isomer) 21.73, 24.85, 83.60, 128.49, 134.76, 141.37; ESI-HRMS *m/z* calcd for C₁₃H₂₃BNO₂ (M+NH₄⁺): 236.1819; found: 236.1819.

(4,4,5,5-Tetramethyl-1,3,2-dioxaborolan-2-yl)anisole (4c). Yield: 88% (*m*-isomer:*p*-isomer = 63:37). ¹H NMR (400 MHz, CDCl₃) δ (*m*-isomer) 1.34 (s, 12H), 3.83 (s, 3H), 7.00 (dd, *J* = 2.8, 8.4 Hz, 1H), 7.29 (t, *J* = 8.0 Hz, 1H), 7.32 (d, *J* = 2.8 Hz, 1H), 7.40 (d, *J* = 7.2 Hz, 1H), (*p*-isomer) 1.33 (s, 12H), 3.83 (s, 3H), 6.88 (d, *J* = 8.4 Hz, 2H), 7.75 (d, *J* = 8.4 Hz, 2H); ¹³C NMR (100 MHz, CDCl₃) δ (*m*-isomer) 24.85, 55.23, 83.80, 117.90, 118.61, 127.14, 128.91, 158.97, (*p*-isomer) 24.85, 55.08, 83.53, 113.27, 136.47, 162.08; ESI-HRMS *m/z* calcd for C₁₃H₂₃BNO₃ (M+NH₄⁺): 252.1768; found: 252.1768.

Methyl (4,4,5,5-tetramethyl-1,3,2-dioxaborolan-2-yl)-benzoate (4d). Yield: 88% (*m*-isomer:*p*-isomer = 56:44). ¹H NMR (400 MHz, CDCl₃) δ (*m*-isomer) 1.36 (s, 12H), 3.91 (s, 3H), 7.44 (t, *J* = 8.0 Hz, 1H), 7.98 (d, *J* = 7.6 Hz, 1H), 8.12 (d, *J* = 8.0 Hz, 1H), 8.46 (s, 1H), (*p*-isomer)

1.36 (s, 12H), 3.92 (s, 3H), 7.86 (d, $J = 8.4$ Hz, 2H), 8.02 (d, $J = 8.4$ Hz, 2H); ^{13}C NMR (100 MHz, CDCl_3) δ (*p*-isomer) 24.83, 52.10, 84.15, 128.52, 132.23, 134.59, 167.10, (*m*-isomer) 24.83, 52.00, 84.06, 127.74, 129.47, 135.76, 139.09, 167.07; ESI-HRMS m/z calcd for $\text{C}_{14}\text{H}_{23}\text{BNO}_4$ ($\text{M}+\text{NH}_4^+$): 280.1717; found: 280.1719.

4-(4,4,5,5-Tetramethyl-1,3,2-dioxaborolan-2-yl)-*o*-xylene (4e). Yield: 60%. ^1H NMR (400 MHz, CDCl_3) δ 1.34 (s, 12H), 2.27 (s, 3H), 2.28 (s, 3H), 7.14 (d, $J = 7.6$ Hz, 1H), 7.54 (d, $J = 7.6$ Hz, 1H), 7.58 (s, 1H); ^{13}C NMR (100 MHz, CDCl_3) δ 19.47, 20.00, 24.83, 83.56, 129.13, 132.36, 135.88, 140.12; ESI-HRMS m/z calcd for $\text{C}_{14}\text{H}_{25}\text{BNO}_2$ ($\text{M}+\text{NH}_4^+$): 250.1975; found: 250.1975.

1,2-Dichloro-4-(4,4,5,5-tetramethyl-1,3,2-dioxaborolan-2-yl)benzene (4f). Yield: 92%. ^1H NMR (400 MHz, CDCl_3) δ 1.33 (s, 12H), 7.43 (d, $J = 8.0$ Hz, 1H), 7.59 (dd, $J = 1.2$ Hz, 8.0 Hz, 1H), 7.86 (d, $J = 1.6$ Hz, 1H); ^{13}C NMR (100 MHz, CDCl_3) δ 25.15, 84.64, 130.29, 132.53, 134.04, 135.77, 136.83; ESI-HRMS m/z calcd for $\text{C}_{12}\text{H}_{19}\text{BNCl}_2\text{O}_2$ ($\text{M}+\text{NH}_4^+$): 290.0883; found: 290.0882.

1,3-Dichloro-4-(4,4,5,5-tetramethyl-1,3,2-dioxaborolan-2-yl)benzene (4g). Yield: 81%. ^1H NMR (400 MHz, CDCl_3) δ 1.34 (s, 12H), 7.42 (t, $J = 2.0$ Hz, 1H), 7.64 (d, $J = 2.0$ Hz, 2H); ^{13}C NMR (100 MHz, CDCl_3) δ 24.83, 84.48, 129.34, 131.04, 132.66, 134.68; ESI-HRMS m/z calcd for $\text{C}_{12}\text{H}_{19}\text{BNCl}_2\text{O}_2$ ($\text{M}+\text{NH}_4^+$): 290.0883; found: 290.0884.

1,3-Bis(trifluoromethyl)-5-(4,4,5,5-tetramethyl-1,3,2-dioxaborolan-2-yl)benzene (4h). Yield: 47%. ^1H NMR (400 MHz, CDCl_3) δ 1.37 (s, 12H), 7.94 (s, 1 H), 8.23 (s, 2H); ^{13}C NMR (100 MHz, CDCl_3) δ 24.86, 84.83, 122.09, 124.66, 124.69, 130.68, 131.02, 134.61; ^{19}F NMR (376 MHz, CDCl_3) δ -62.76; ESI-HRMS m/z calcd for $\text{C}_{14}\text{H}_{19}\text{BNF}_6\text{O}_2$ ($\text{M}+\text{NH}_4^+$): 358.1410; found: 358.1408.

Kinetic study of direct C–H borylation of benzene

A 20 mL Schlenk-tube assembled a stir bar and a septum inlet was charged with B_2pin_2 (84.6 mg, 0.33 mmol) and $\text{Ir}(\text{OMe})(\text{cod})(\text{BPy-PMO})$ (32.0 mg, 0.005 mmol Ir) or $\text{Ir}(\text{OMe})(\text{cod})(\text{bpy})$ (2.43 mg, 0.005 mmol Ir), or $[\text{Ir}(\text{OMe})(\text{cod})]_2$ (1.68 mg, 0.005 mmol Ir) and solid ligands **L1–L3** (0.050 mmol BPy). The mixture was flushed with argon. After the addition of dry benzene (20 mmol), the mixture was stirred at 80 °C. At suitable time intervals, portions of solution were removed by syringe and filtered by membrane filter (0.20 μm) and diluted with chloroform-*d* containing internal standard (SiMe_4). The yield of phenylboronate pinacol ester was analyzed by ^1H NMR spectroscopy.

Evaluation of photocatalytic hydrogen evolution

The photocatalysis test was carried out using a glass-enclosed gas circulation and gas-evacuation system. The vessel was loaded with Pt@Ru(bpy)₂(BPy-PMO) (10 mg, 110 μmol Pt, 1.63 μmol Ru) suspended in acetate buffer solution (25 mM, pH 4.2, 40 mL) containing EDTA (1.0 mM), followed by irradiation of visible light (> 385 nm) from above using high-power xenon lamp. Producing hydrogen was detected by gas chromatography. Amount of hydrogen was plotted against irradiation time.

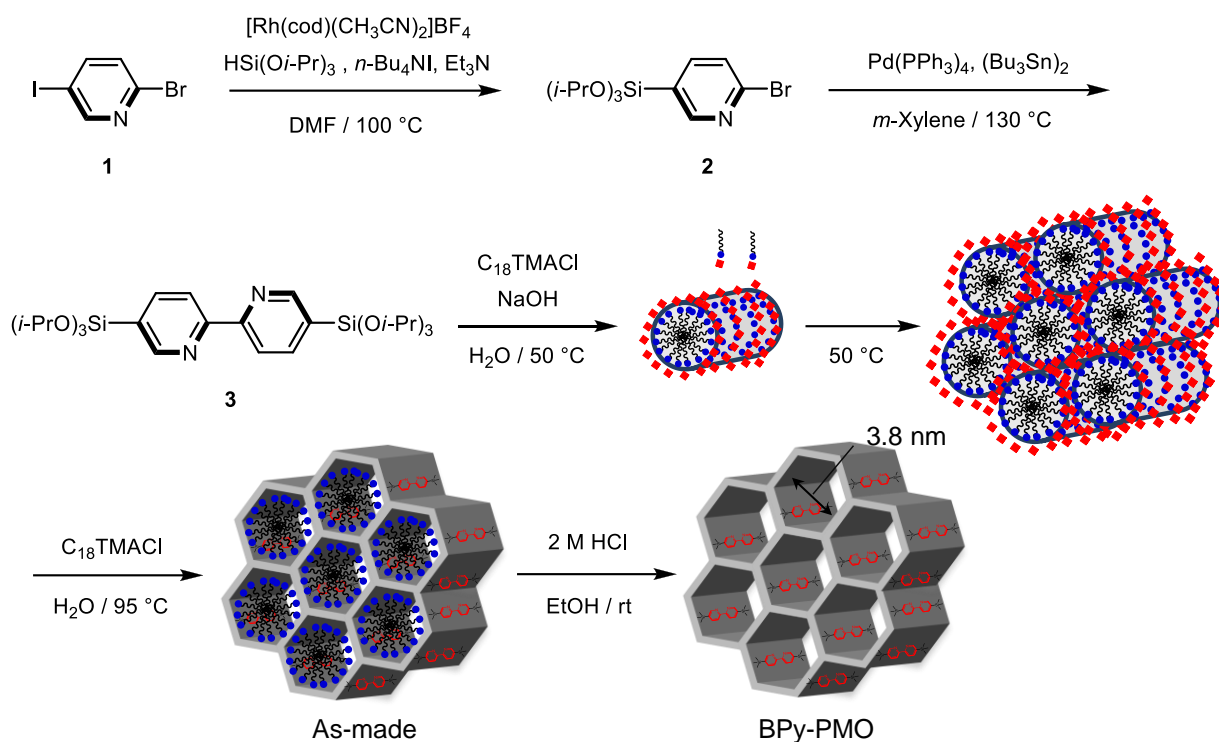
5.1.3 Results and Discussion

Synthesis of crystal-like BPy-PMO from 100% organosilane precursor

The bipyridine precursor was prepared in two steps from a commercially available reagent. As shown in Scheme 5.1, 2-bromo-5-iodopyridine (**1**) was silylated with triisopropoxysilane in the presence of [Rh(cod)(CH₃CN)₂]⁺BF₄⁻ to give 2-bromo-5-(triisopropoxysilyl)pyridine (**2**), followed by Stille coupling of **2** with bis(tributyltin) in the presence of Pd(PPh₃)₄ to successfully afford 5,5'-bis(triisopropoxysilyl)-2,2'-bipyridine (**3**). Although methoxysilyl or ethoxysilyl groups have been widely employed as organosilane precursors for the synthesis of PMOs and silica-based sol-gel materials, they have low tolerance for many organic reactions and are difficult to purify due to their high reactivity. In contrast, the isopropoxysilyl group was stable enough to allow several reactions using organometallic reagents and purification by silica gel chromatography.²² The use of the isopropoxysilyl group led to easy synthesis of the bipyridine precursor **3** which is directly attached to two alkoxysilyl groups at 5,5'-positions.

BPy-PMO was prepared by hydrolysis and polycondensation from precursor **3** under basic conditions in the presence of octadecyltrimethylammonium chloride (C₁₈TMACl) surfactant as a structure directing agent, followed by extraction of the surfactant with an acidic EtOH solution (Scheme 5.1). During optimization of the synthetic conditions, slow addition of the precursor solution was found to be crucial to prepare well-ordered BPy-PMO. Thus, the precursor solution

²² a) Bezombes, J.-P.; Chuit, C.; Corriu, R. J. P.; Rey , C. *J. Mater. Chem.* **1998**, *8*, 1749–1759; b) Kuschel, A.; Polarz, S. *Adv. Funct. Mater.* **2008**, *18*, 1272–1280; c) Maegawa, Y.; Waki, M.; Umamoto, A.; Shimada, T.; Inagaki, S. *Tetrahedron* **2013**, *69*, 5312–5318.



Scheme 5.1. Synthesis of 5,5'-bis(triisopropoxysilyl)-2,2'-bipyridine precursor **3** and schematic illustration of synthesis of BPy-PMO from precursor **3** by surfactant-templated supramolecular assembly.

was slowly added over a period of 3 h at a constant speed using a syringe pump. Fast addition of the precursor caused the aggregation of precursor molecules in aqueous reaction media due to the slow hydrolysis rate of isopropoxysilyl groups, which resulted in the formation of disordered material. Strongly basic conditions (0.25 M) with aging at 95 °C caused cleavage of the Si–C bond in the bipyridine precursor (Figure 5.2a). The Si–C bond cleavage was very sensitive to basicity and temperature due to the localization of electrons at the nitrogen atoms and the resulting deficiency of electrons in the pyridine rings, which was predicted from theoretical studies on Si–C cleavage in organosilane precursors during the condensation process.²³ However, at weak basicity (0.005 M) and room temperature, the hydrolysis of the isopropoxysilyl groups was found to be slow, which was attributed to the low nucleophilicity of hydroxide for attacking the bulky isopropoxy group. Consequently, the synthesis was carried out under moderately basic conditions of 0.035 M

²³ Shirai, S.; Goto, Y.; Mizoshita, N.; Ohashi, M.; Tani, T.; Shimada, T.; Hyodo, S.; Inagaki, S. *J. Phys. Chem. A* **2010**, *114*, 6047–6054.

and 50 °C with a long aging time (6 days), which successfully afforded highly ordered BPy-PMO powder after the removal of surfactant using acidic EtOH solution. The ^{29}Si DD MAS NMR, ^{13}C CP MAS MAS NMR, and FT-IR spectra confirmed the preservation of both the bipyridine moieties

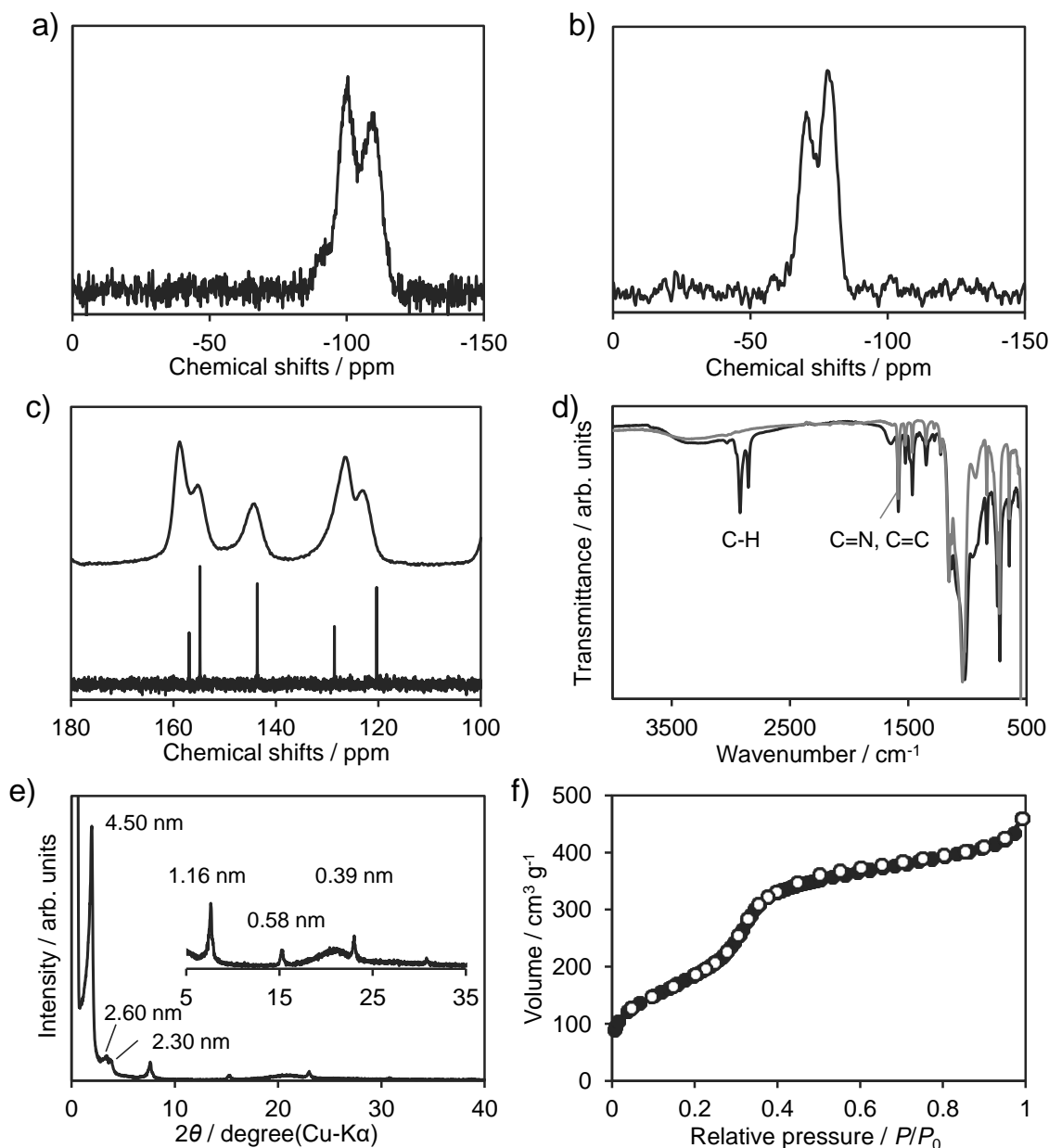


Figure 5.2. ^{29}Si DD MAS NMR spectra of BPy-PMO synthesized under a) 0.25 M OH^- , and b) 0.035 M OH^- conditions. c) ^{13}C CP MAS NMR spectrum of BPy-PMO (above) and ^{13}C NMR spectrum of precursor **3** (below). d) FT-IR spectrum of BPy-PMO before (black) and after (gray) the removal of surfactant. e) XRD patterns, and f) nitrogen adsorption/desorption isotherms (closed circles: adsorption, open circles: desorption) for BPy-PMO.

and Si–C bonds during the synthesis and extraction processes. The ^{29}Si DD MAS NMR spectrum showed T^2 [$\text{SiC}(\text{OSi})_2(\text{OH})$] and T^3 [$\text{SiC}(\text{OSi})_3$] signals, but almost no Q^n [$\text{Si}(\text{OSi})_n(\text{OH})_{4-n}$, $n = 2-4$] signals between -90 and -120 ppm, indicating almost complete preservation of Si–C bonds (Figure 5.2b). The presence of T^2 signal also shows that a considerable amount of silanol groups exist in BPy-PMO. The ^{13}C CP MAS NMR spectrum revealed the five aromatic resonances at 158.7, 155.1, 144.3, 126.2, and 123.0 ppm, which can be assigned to carbons on the pyridine ring (Figure 5.2c, above). These chemical shift values were almost similar to those of ^{13}C NMR spectrum of precursor **3** (Figure 5.2c, below). FT-IR spectrum showed a sharp bands at 1583 and 1463 cm^{-1} characteristic of C=N and C=H group of pyridine rings (Figure 5.2d). After the extraction of surfactant, the obtained material showed the disappearance of the C–H bands of surfactant at 2921 and 2850 cm^{-1} , indicating the perfect extraction of surfactant by acidic EtOH extraction.

The XRD patterns of surfactant-free BPy-PMO showed low angle reflections at $2\theta = 1.96^\circ$, 3.40° , and 3.84° (d spacings of 4.50, 2.60, and 2.30 nm, respectively) corresponding to a two-dimensional hexagonal lattice ($a_0 = 5.2$ nm), and four other peaks at a medium scattering angle of $7^\circ-23^\circ$ (d spacings of 1.16, 0.58, and 0.39 nm), corresponding to a lamellar structure with a molecular-scale periodicity of bipyridine and silica moieties in the pore walls (Figure 5.2e). The broad peak at $2\theta = 18^\circ-25^\circ$ was due to disordered arrangement of atoms in the regions or contamination of amorphous materials. The nitrogen adsorption/desorption isotherms showed a type-IV isotherm, typical of ordered mesoporous materials (Figure 5.2f). The d_{DFT} , S_{BET} , and $V_{t\text{-plot}}$ were 3.8 nm, 739 $\text{m}^2 \text{g}^{-1}$, and 0.41 $\text{cm}^3 \text{g}^{-1}$, respectively. The pore wall thickness was estimated to be 1.4 nm ($a_0 - d_{\text{DFT}}$), corresponding to three layers of the bipyridine moieties in the pore walls.

Figure 5.3a–d shows SEM and TEM images of BPy-PMO. The SEM image showed particle morphology with diameters of 200–500 nm (Figure 5.3a). The TEM images showed one-dimensional channels going through the particles, indicating that the particles have a single crystal-like structure (Figure 5.3b). The enlarged TEM images showed a hexagonal arrangement of uniform pores (Figure 5.3c) and many lattice fringes with a basal spacing of ca. 1.2 nm in the perpendicular direction to the mesochannels (Figure 5.3d), which was in good agreement with the result obtained by XRD. Figure 5.3e shows a structural model of BPy-PMO. The bipyridine and silica belt-like layers in the walls are arranged alternatively with a periodicity of 1.16 nm in the

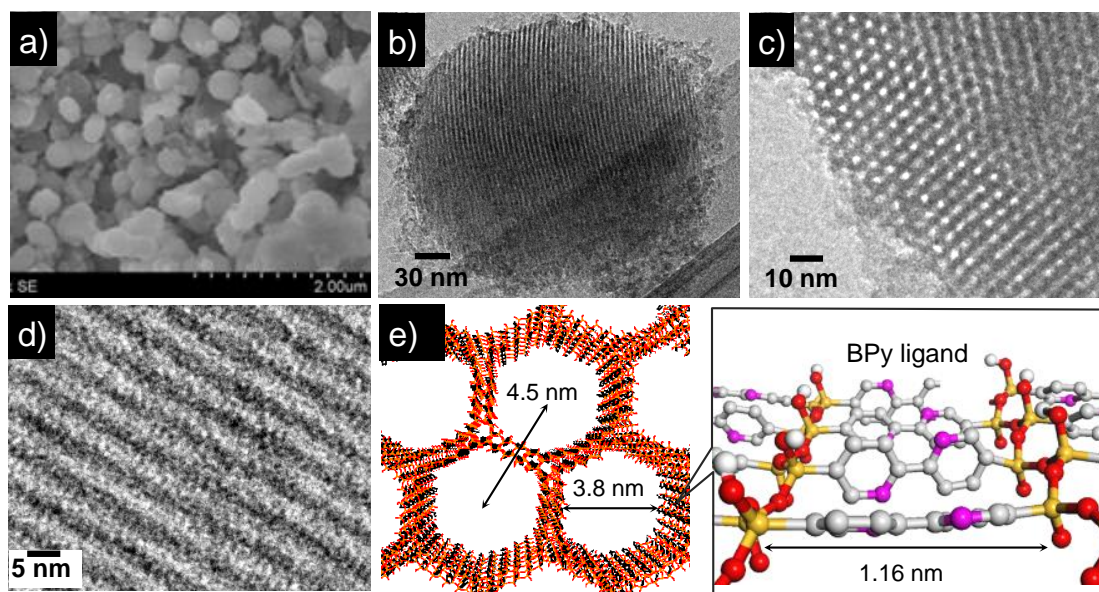


Figure 5.3. a) SEM and b–d) TEM images and e) structural model of BPy-PMO. Silicon, yellow; oxygen, red; carbon, gray; nitrogen, blue; hydrogen, white.

channel direction whose periodicity was clearly observed by XRD and TEM (Figures 5.2e and 5.3d). A molecular mechanics simulation showed that the neighboring bipyridine–bipyridine distance is approximately 0.44 nm, which is larger than the usual π – π stacking distance of aromatic compounds, although the molecular arrangement and intermolecular distance can fluctuate due to the flexibility of the silica framework. The loosely packed bipyridine groups could have a high degree of freedom to rotate about the Si–C axis because rotary motion of the bridging organic groups in crystal-like benzene- and biphenyl-PMOs with similar packing structures has been demonstrated by NMR spectroscopy.²⁴ It is suggested that the framework bipyridine groups preserved their coordination ability for metal complex formation.

Elemental analysis of carbon and nitrogen in BPy-PMO gave a carbon/nitrogen ratio of 4.5, which is consistent with that expected from the chemical formula ($C_{10}H_6N_2$) of the bipyridine bridges. The amount of bipyridine moieties in BPy-PMO was estimated from the nitrogen content as 3.18 mmol g^{-1} . Thermogravimetric analysis showed that weight loss due to decomposition of the

²⁴ a) Bracco, S.; Comotti, A.; Valsesia, P.; Chmelka, B. F.; Sozzania, P. *Chem. Commun.* **2008**, 4798–4800; b) Comotti, A.; Bracco, S.; Valsesia, P.; Beretta, M.; Sozzani, P. *Angew. Chem., Int. Ed.* **2010**, *49*, 1760–1764.

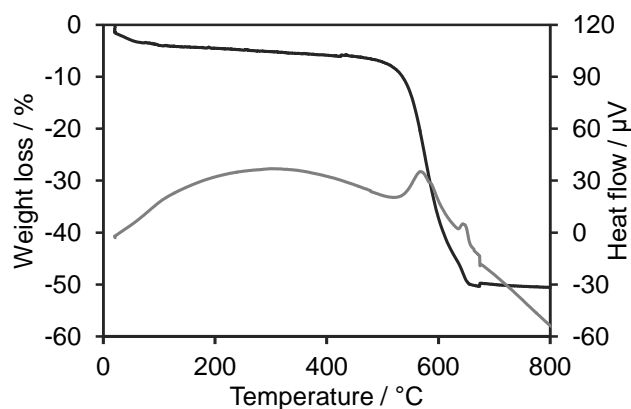


Figure 5.4. Thermogravimetry (TG) (black) and differential thermal analysis (DTA) curves (gray line) of BPy-PMO in air stream.

BPy moieties occurred in the temperature range of 500–600 °C with a maximum at 570 °C, showing high thermal stability up to 500 °C due to the robust siloxane bond network (Figure 5.4).

The residual silanol groups in the BPy-PMO can be almost perfectly end-capped with trimethylsilyl (TMS) groups through the trimethylsilylation with *N*-trimethylsilylimidazole. FT-IR spectra of BPy-PMO-TMS showed the disappearance of silanol groups at 3270 cm^{-1} and appearance of C–H bonds of TMS groups at 2960 cm^{-1} , respectively (Figure 5.5).

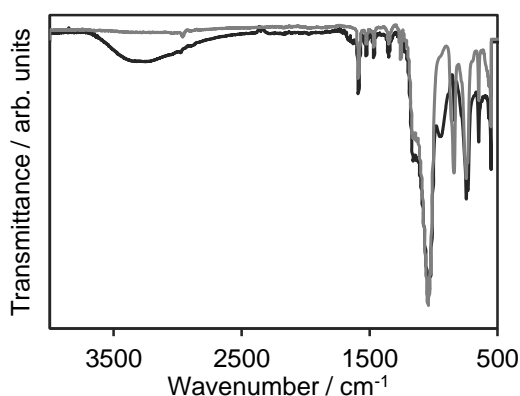


Figure 5.5. FT-IR absorption spectra of BPy-PMO (black line) and BPy-PMO-TMS (gray line).

The XRD profile and nitrogen adsorption/desorption isotherms revealed the preservation of ordered and uniformed mesoporous structure and crystal-like pore wall structure (Figures 5.6a and

5.6b). The values for S_{BET} , $V_{t\text{-plot}}$, and d_{DFT} were $540 \text{ m}^2 \text{ g}^{-1}$, $0.27 \text{ cm}^3 \text{ g}^{-1}$, and 3.7 nm , which are slightly reduced compared with those of BPy-PMO due to the end-capping of silanols on the inner pore surface with TMS groups. The ^{13}C CP MAS NMR and ^{29}Si DD MAS NMR spectra showed characteristic resonances of TMS groups at 1.5 and 12.3 ppm, respectively, indicating the passivation of surface silanols through the covalent siloxane bond (Figures 5.6c and 5.6d).

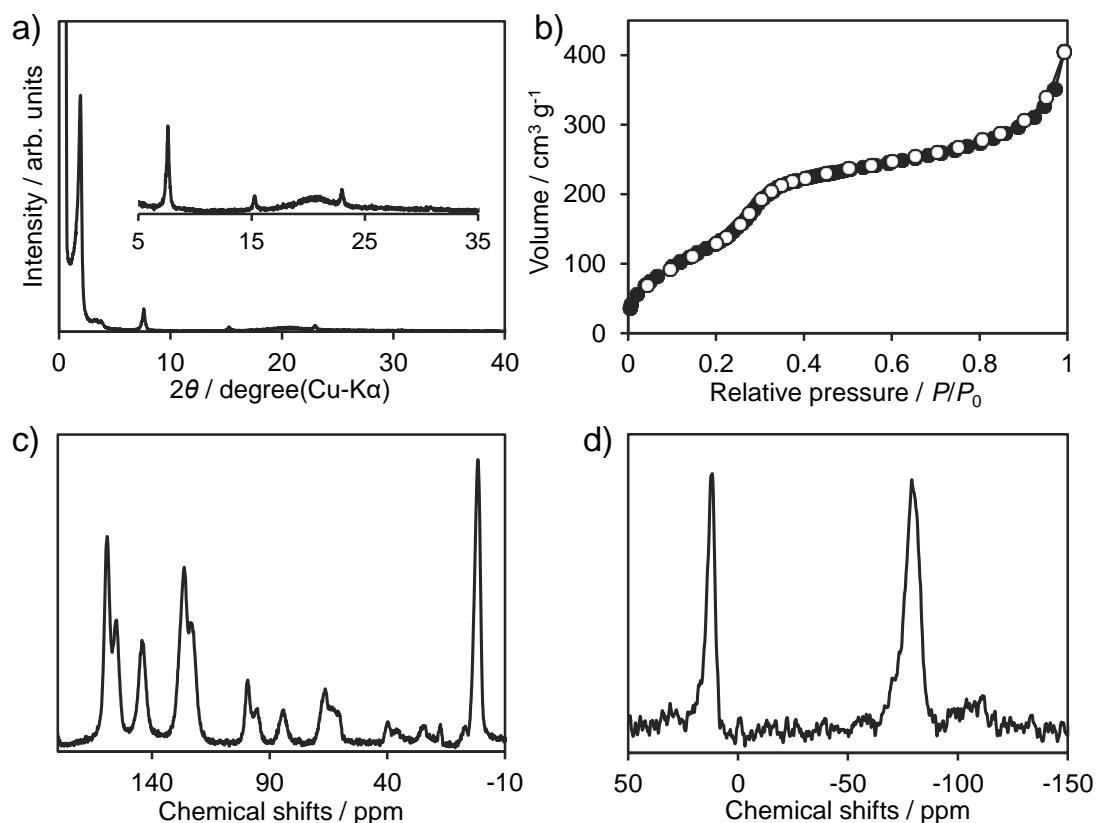


Figure 5.6. a) XRD patterns, b) nitrogen adsorption/desorption isotherms (closed circles: adsorption, open circles: desorption), c) ^{13}C CP MAS NMR, d) ^{29}Si DD MAS NMR spectra of BPy-PMO-TMS.

Metal complex formations using BPy-PMO as a ligand

A variety of bipyridine-based metal complexes can be readily formed on the pore surface of BPy-PMO by simple stirring of the BPy-PMO powder in a solution containing a metal precursor (Figure 5.7). The chemical structures of representative metal complexes immobilized on BPy-PMO or BPy-PMO-TMS as a solid chelating ligand were shown in Figure 5.8.

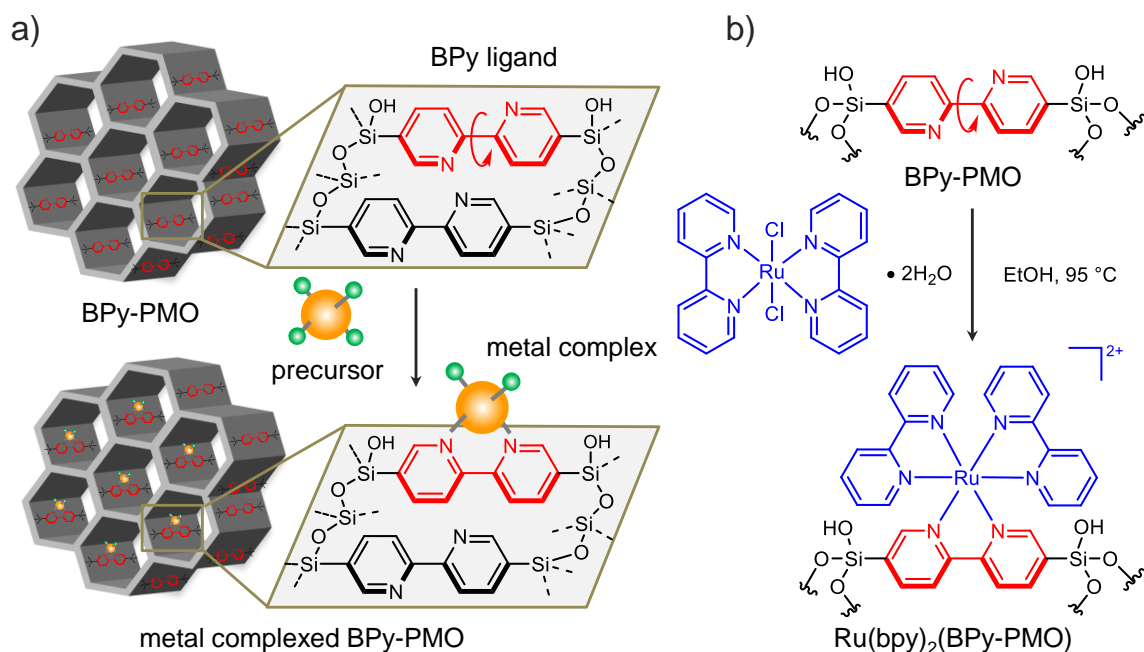


Figure 5.7. a) Schematic illustration of direct metal complex formation of the pore surface of BPy-PMO. b) Synthesis of Ru(bpy)₂(BPy-PMO) starting from BPy-PMO and ruthenium precursor Ru(bpy)₂Cl₂•2H₂O.

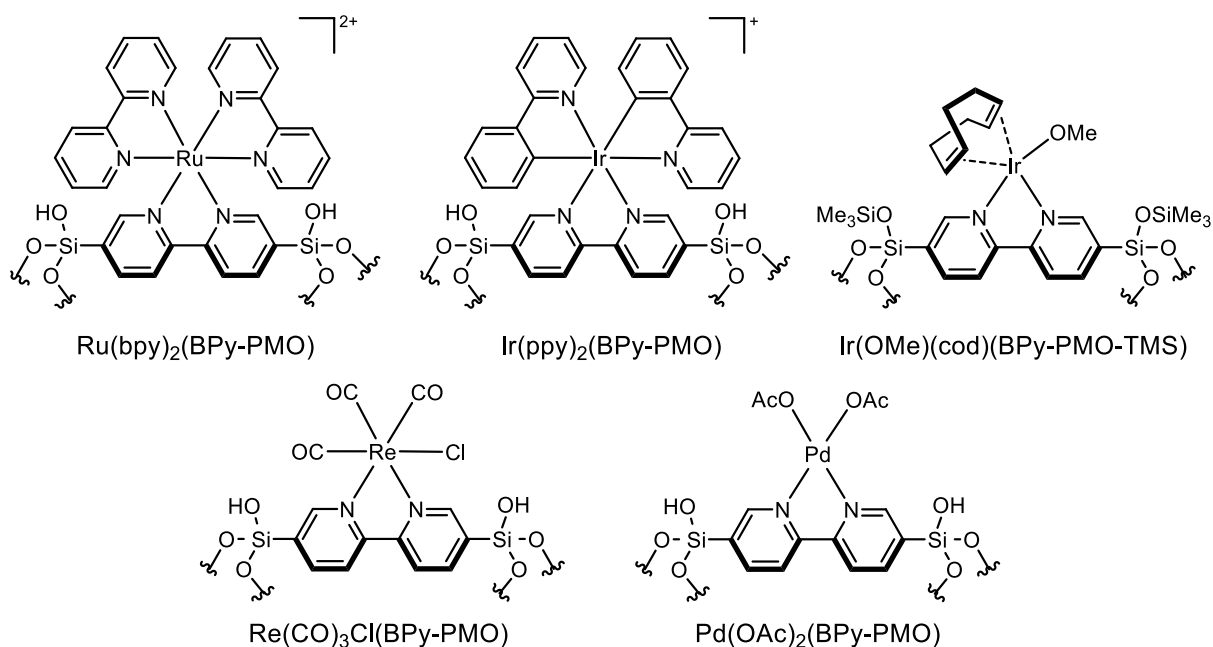


Figure 5.8. Chemical structures of representative metal complexes immobilized on BPy-PMO as a solid chelating ligand.

$\text{Ru}(\text{bpy})_2(\text{BPy-PMO})$ was formed by dispersion of BPy-PMO powder in EtOH solution containing $\text{Ru}(\text{bpy})_2\text{Cl}_2 \cdot 2\text{H}_2\text{O}$ precursor (Figure 5.7b).²⁵ The UV-vis diffuse reflectance spectrum of the obtained powder showed a broad band at around 450 nm due to metal-to-ligand charge transfer (MLCT) and an intense peak at around 300 nm due to $\pi-\pi^*$ transition of ligands, which was very similar to the absorption spectrum of a homogeneous solution of $\text{Ru}(\text{bpy})_3\text{Cl}_2$ except for peak broadening (Figure 5.9a).²⁶ The peak broadening suggests a slight difference in the electronic state of $\text{Ru}(\text{bpy})_2(\text{BPy-PMO})$ from its homogeneous analogue because one of the bipyridine atoms at the 5,5'-positions.²⁷ This was also suggested by the slightly different emission band from that of the homogeneous one (Figure 5.9b). A detailed investigation on this difference is currently underway in the author's laboratory.

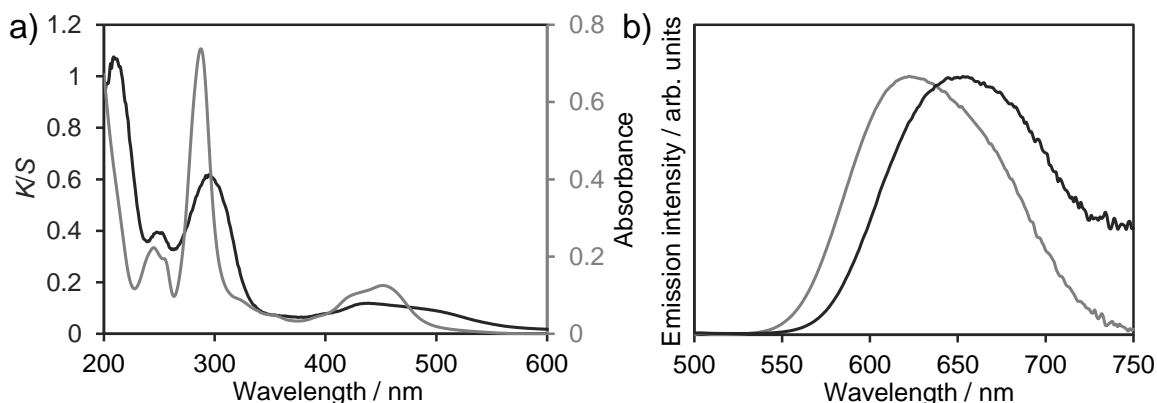


Figure 5.9. a) UV-vis diffuse reflectance spectrum of $\text{Ru}(\text{bpy})_2(\text{BPy-PMO})$ (black line) and UV-vis absorption spectrum of $\text{Ru}(\text{bpy})_3\text{Cl}_2$ in CH_3CN (gray line), b) photoluminescence spectra of $\text{Ru}(\text{bpy})_2(\text{BPy-PMO})$ (black line) and $\text{Ru}(\text{bpy})_3\text{Cl}_2$ in CH_3CN (gray line).

XAFS measurement was also carried out to elucidate the structure of the Ru center in the pore walls (Figure 5.10). The X-ray absorption near edge spectroscopy (XANES) spectrum and EXAFS Fourier transform at Ru *K*-edge showed spectral characteristics corresponding to those of homogeneous $\text{Ru}(\text{bpy})_3\text{Cl}_2$, suggesting successful formation of $[\text{Ru}(\text{bpy})_3]^{2+}$ complex on the pore surface of BPy-PMO.

²⁵ Palmer, R. A.; Piper, T. S. *Inorg. Chem.* **1966**, *5*, 864–878.

²⁶ Juris, A.; Balzani, V.; Barigelletti, F.; Campagna, S.; Belser, P.; von Zelewsky, A. *Coord. Chem. Rev.* **1988**, *84*, 85–277.

²⁷ Stange, A. F.; Tokura, S.; Kira, M. *J. Organomet. Chem.* **2000**, *612*, 117–124.

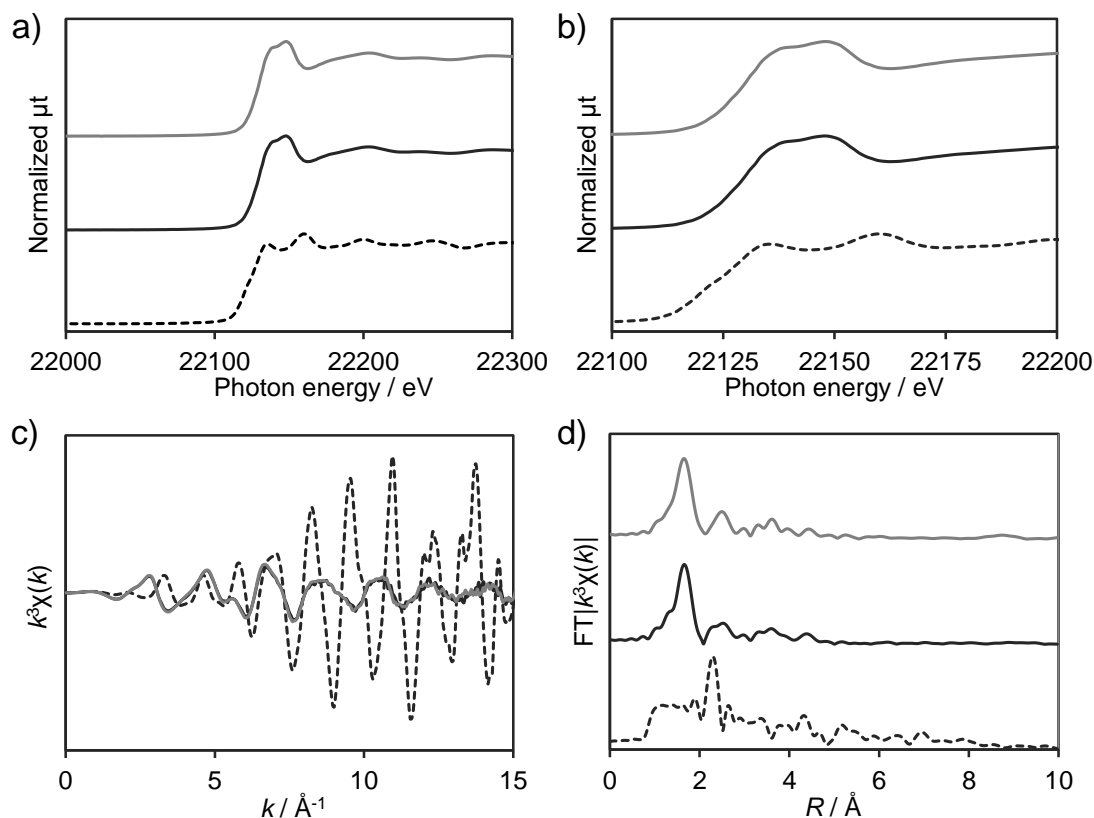


Figure 5.10. Ru *K*-edge a, b) XANES spectra, c) EXAFS oscillations, and d) EXAFS Fourier transform ($k = 3\text{--}14 \text{ \AA}^{-1}$) of $\text{Ru}(\text{bpy})_2(\text{BPy-PMO})$ (black solid lines), $\text{Ru}(\text{bpy})_3\text{Cl}_2$ (gray solid lines), and Ru powder (black broken lines).

$\text{Ir}(\text{ppy})_2(\text{BPy-PMO})$ was prepared by reaction with $[\text{Ir}(\text{ppy})_2\text{Cl}]_2$ in CH_2Cl_2 .²⁸ The UV-vis diffuse reflectance spectrum showed an absorption band of MLCT at 378 nm with a long tail above 450 nm (Figure 5.11, black line). The tail was attributed to a direct spin-forbidden absorption from the singlet ground state to triplet excited state as observed for $[\text{Ir}(\text{C}^{\wedge}\text{N})_2(\text{N}^{\wedge}\text{N})]^+$, where (C \wedge N) and (N \wedge N) indicate a cyclometalating ligand such as 2-phenylpyridine and a neutral ligand such as 2,2'-bipyridine.²⁷ The emission of $\text{Ir}(\text{ppy})_2(\text{BPy-PMO})$ was also observed at a similar wavelength for the homogeneous analogue (Figure 5.11, gray line).^{27b}

²⁸ a) Lowry, M. S.; Goldsmith, J. I.; Slinker, J. D.; Rohl, R.; Pascal, R. A., Jr.; Malliaras, G. G.; Bernhard, S. *Chem. Mater.* **2005**, *17*, 5712–5719; b) Costa, R. D.; Monti, F.; Accorsi, G.; Barbieri, A.; Bolink, H. J.; Ortí, E.; Armaroli, N. *Inorg. Chem.* **2011**, *50*, 7229–7238; c) Goldsmith, J. I.; Hudson, W. R.; Lowry, M. S.; Anderson, T. H.; Bernhard, S. *J. Am. Chem. Soc.* **2005**, *127*, 7502.

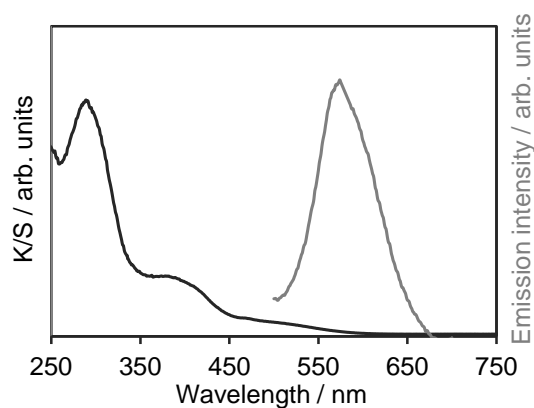


Figure 5.11. UV-vis diffuse reflectance spectrum (black line) and photoluminescence spectrum of Ir(ppy)₂(BPy-PMO) excited at 385nm (gray line).

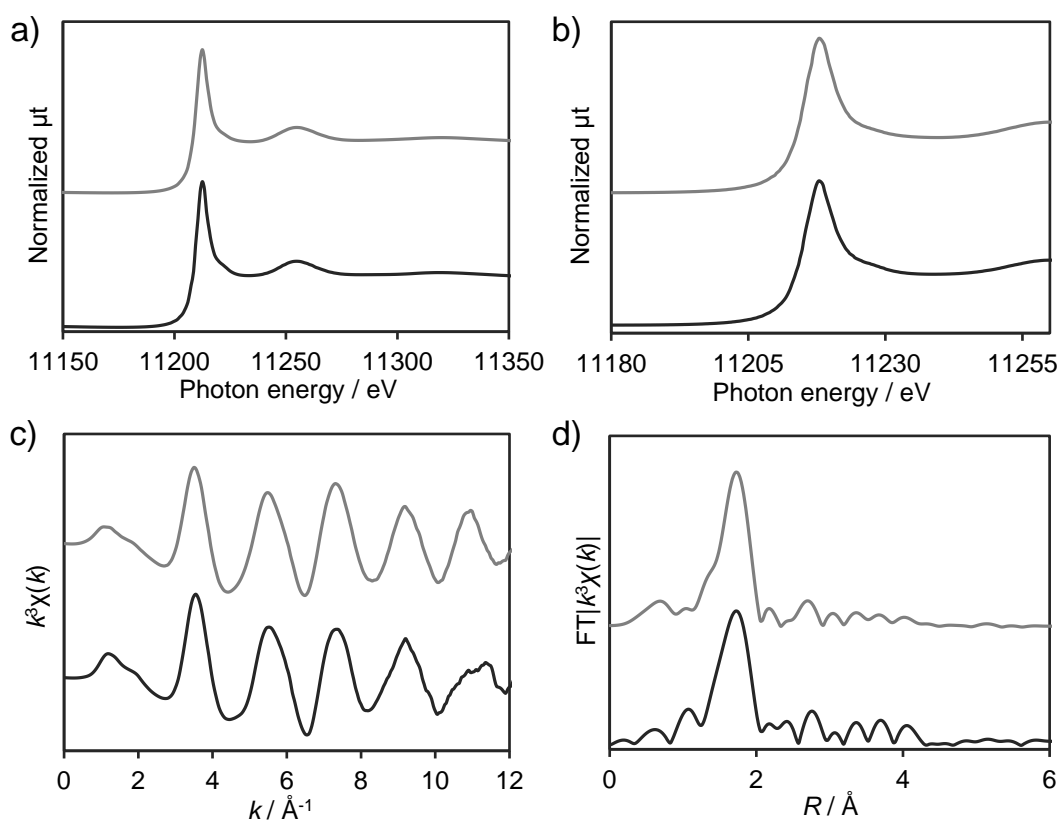


Figure 5.12. Ir L_{III} -edge a, b) XANES spectra, c) EXAFS oscillations, and d) EXAFS Fourier transform of Ir(OMe)(cod)(BPy-PMO-TMS) (black lines) and Ir(OMe)(cod)(bpy) (gray lines).

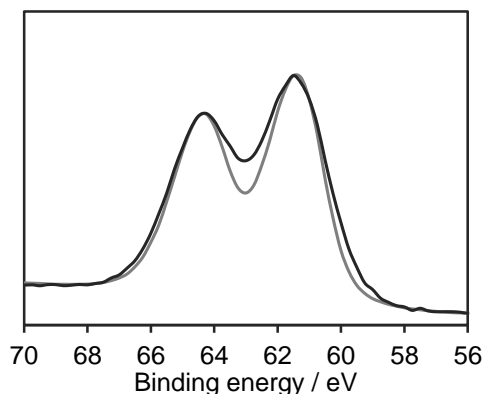


Figure 5.13. XPS spectra of Ir(OMe)(cod)(BPy-PMO-TMS) (black line) and [Ir(OMe)(cod)(bpy)] (gray line).

Ir(cod)(OMe)(BPy-PMO-TMS) was synthesized by treating an BPy-PMO-TMS with [Ir(OMe)(cod)]₂ precursor in benzene. XANES spectrum and EXAFS Fourier transform at Ir *L*_{III}-edge of the PMO were in good agreement with those of the homogeneous complex [Ir(OMe)(cod)(bpy)] (Figure 5.12). The XPS spectra of Ir(cod)(OMe)(BPy-PMO-TMS) displayed almost the same binding energies of 61.3 eV for Ir 4f_{7/2} and 64.5 eV for Ir 4f_{5/2} as the homogeneous analogue (Figure 5.13). These results suggest successful formation of Ir(cod)(OMe)(BPy-PMO).

Re(CO)₃Cl(BPy-PMO) was prepared by treatment with Re(CO)₅Cl in toluene.²⁹ The UV-vis diffuse reflectance spectrum of Re(CO)₃Cl(BPy-PMO) showed an MLCT absorption band (around 390 nm) assignable to the coordination of Re to bpy ligand (Figure 5.14a).²⁶ In the FT-IR spectrum of the Re complex, three characteristic CO stretching bands were observed at 1893, 1920, and 2023 cm⁻¹, which is in good agreement with those of Re(bpy)(CO)₃Cl (Figure 5.14b).³⁰ The XAFS measurement also suggested the formation of the desired Re complex in the PMO material (Figure 5.15).

²⁹ a) Hawecker, J.; Lehn, J.-M.; Ziessel, R. *J. Chem. Soc., Chem. Commun.* **1983**, 536–538; b) Hawecker, J.; Lehn, J.-M.; Ziessel, R. *Helv. Chim. Acta* **1986**, *69*, 1990–2012; c) Takeda, H.; Koike, K.; Inoue, H.; Ishitani, O. *J. Am. Chem. Soc.* **2008**, *130*, 2023–2031.

³⁰ Worl, L. A.; Duesing, R.; Chen, P.; Ciana, L. D.; Meyer, T. *J. Chem. Soc., Dalton Trans.* **1991**, 849–858.

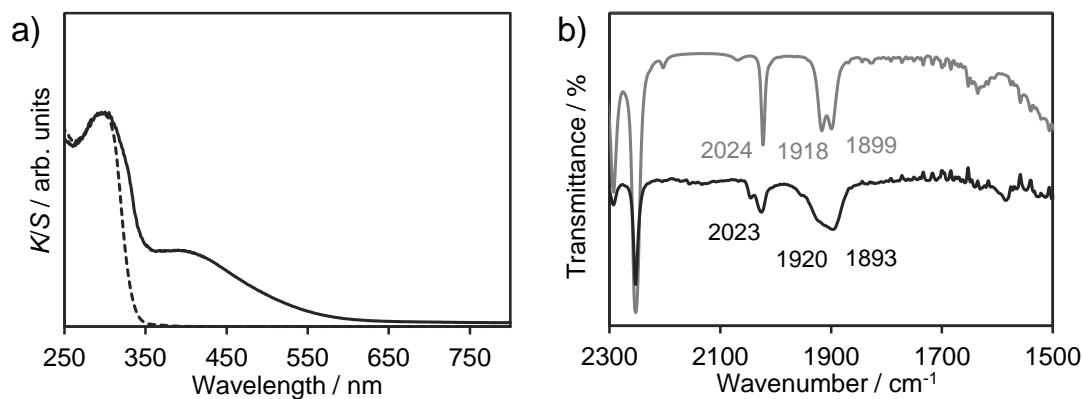


Figure 5.14. a) UV-vis diffuse reflectance spectra of $\text{Re}(\text{CO})_3(\text{BPy-PMO})$ (solid line) and BPy-PMO (broken line), b) FT-IR absorption spectrum of $\text{Re}(\text{CO})_3\text{Cl}(\text{BPy-PMO})$ dispersed in CH_3CN (black line) and $\text{Re}(\text{bpy})(\text{CO})_3\text{Cl}$ in CH_3CN solution (gray line).

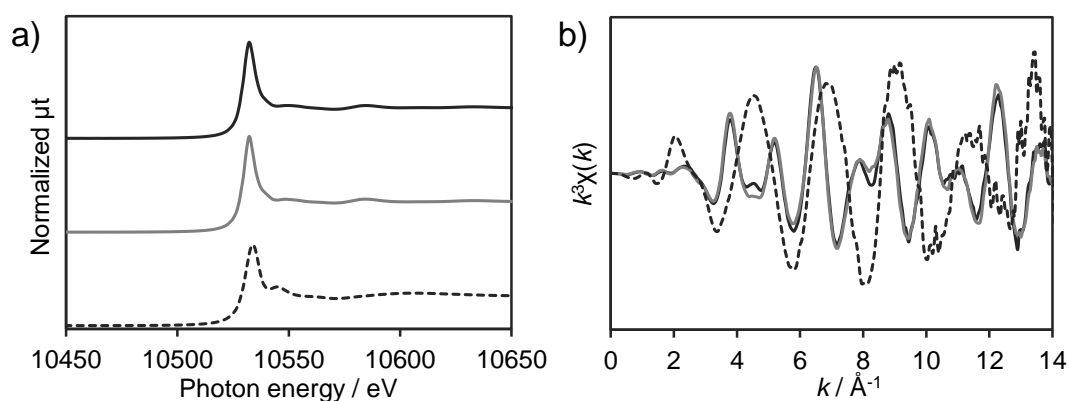


Figure 5.15. Re L_{III} -edge a) XANES spectra and b) EXAFS oscillations of $\text{Re}(\text{CO})_3\text{Cl}(\text{BPy-PMO})$ (black solid lines), $\text{Re}(\text{bpy})(\text{CO})_3\text{Cl}$ (gray solid lines), and $(\text{NH}_4)\text{ReO}_4$ (black broken lines).

$\text{Pd}(\text{OAc})_2(\text{BPy-PMO})$ was obtained by reaction with $\text{Pd}(\text{OAc})_2$ in THF.³¹ The UV-vis diffuse reflectance spectrum of $\text{Pd}(\text{OAc})_2(\text{BPy-PMO})$ showed the appearance of a shoulder band around 370 nm, suggesting that $\text{Pd}(\text{II})$ directly interacts with BPy groups in the PMO framework without formation of Pd black (Figure 5.16a). The formation of $\text{Pd}(\text{OAc})_2(\text{BPy-PMO})$ was also confirmed

³¹ a) Lu, X.; Lin, S. *J. Org. Chem.* **2005**, *70*, 9651–9653; b) Kirchberg, S.; Tani, S.; Ueda, K.; Yamaguchi, J.; Studer, A.; Itami, K. *Angew. Chem., Int. Ed.* **2011**, *50*, 2387–2391; c) Uehara, T. N.; Yamaguchi, J.; Itami, K. *Asian J. Org. Chem.* **2013**, *2*, 938–942.

by XPS investigation. As shown in Figure 5.16b, the binding energy of Pd 3d_{5/2} in the PMO is 337.0 eV, indicating the strong coordination of BPy groups in PMO to Pd(II) species. The observed binding energy is lower than that of 337.5 eV for free Pd(OAc)₂, suggesting that the electron-donating character of BPy induced a negative shift in binding energy for the Pd species.³²

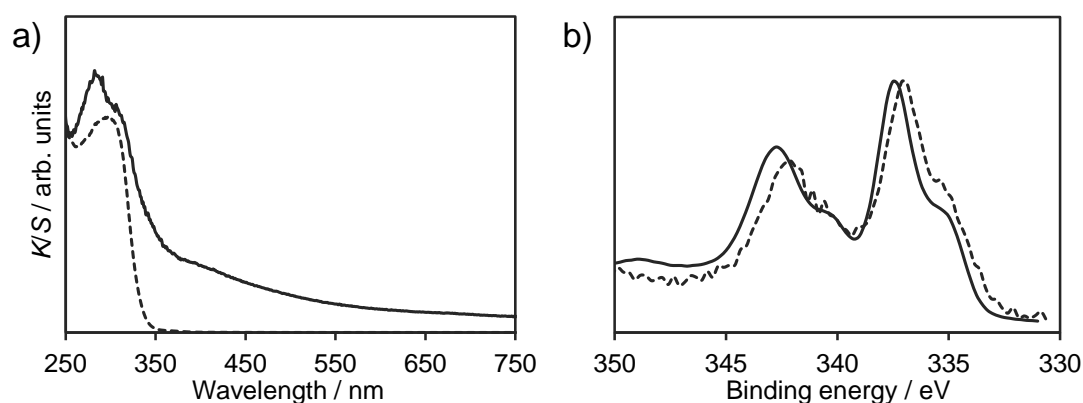


Figure 5.16. a) UV-vis diffuse reflectance spectra of Pd(OAc)₂(BPy-PMO) (solid line) and BPy-PMO (broken line), b) XPS spectra of Pd(OAc)₂(BPy-PMO) (solid line) and Pd(OAc)₂ (broken line) for Pd_{3d5}.

The loading amounts of metals on BPy-PMO were determined by inductively coupled plasma (ICP)-atomic emission spectrometry (AES) and are listed in Table 5.1. The amounts of metals were 0.16–1.12 mmol g⁻¹, which indicated that 8–53% of surface bipyridine groups in BPy-PMO were coordinated to metals. The large differences in the loading amounts of metals may be explained by the bulkiness of free ligands or the reactivity of BPy-PMO with each metal complex precursor. However, the loading amounts can be controlled to some extent by conditions such as concentration of metal precursors in the treated solution. The XRD patterns and nitrogen adsorption/desorption isotherms for BPy-PMOs after the formation of metal complexes showed almost complete preservation of the ordered mesoporous structure and molecular scale periodicity, indicating high chemical stability of BPy-PMO (Figures 5.17 and 5.18). In addition, the metal-BPy-PMOs still have large mesopores of 3.1–3.8 nm and high surface areas of 500–740 m² g⁻¹ (Table 5.1).

³² Ding, S.-Y.; Gao, J.; Wang, Q.; Zhang, Y.; Song, W.-G.; Su, C.-Y.; Wang, W. *J. Am. Chem. Soc.* **2011**, *133*, 19816–19822.

Table 5.1. Physical parameters of metal complexes prepared using BPy-PMO

Metal-BPy-PMO	Metal loading / mmol g ⁻¹	Metal/BPy _{surf}	S _{BET} / m ² g ⁻¹	d _{DFT} / nm
Ru(bpy) ₂ (BPy-PMO)	0.20	0.094	530	3.2
Ir(ppy) ₂ (BPy-PMO)	0.26	0.12	700	3.1
Ir(OMe)(cod)(BPy-PMO-TMS)	0.16	0.082	520	3.5
Re(CO) ₃ Cl(BPy-PMO)	1.12	0.53	500	3.2
Pd(OAc) ₂ (BPy-PMO)	0.74	0.35	580	3.4
BPy-PMO	—	—	740	3.8
BPy-PMO-TMS	—	—	540	3.7

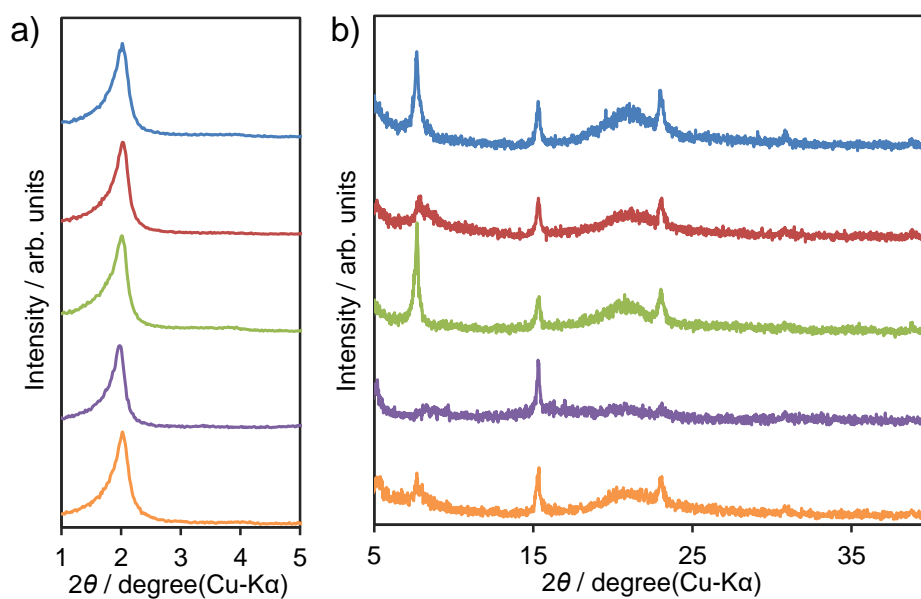


Figure 5.17. a) Low-angle and b) high-angle XRD patterns for Ru(bpy)₂(BPy-PMO) (blue lines), Ir(ppy)₂(BPy-PMO) (red lines), Ir(OMe)(cod)(BPy-PMO-TMS) (green lines), Re(CO)₃Cl(BPy-PMO) (purple lines), and Pd(OAc)₂(BPy-PMO) (orange lines).

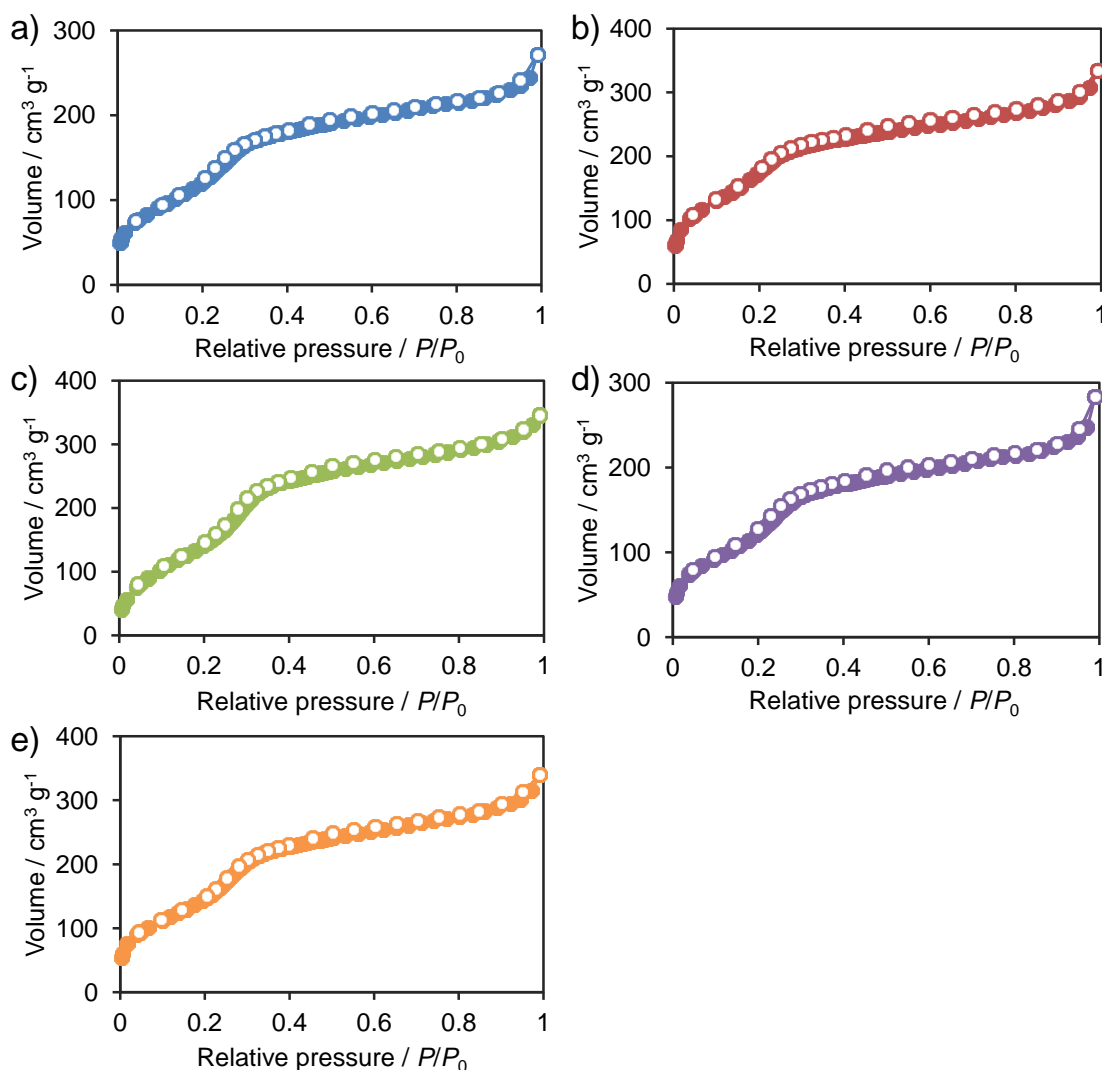


Figure 5.18. Nitrogen adsorption/desorption isotherms of a) $\text{Ru}(\text{bpy})_2(\text{BPy-PMO})$, b) $\text{Ir}(\text{ppy})_2(\text{BPy-PMO})$, c) $\text{Ir}(\text{OMe})(\text{cod})(\text{BPy-PMO-TMS})$, d) $\text{Re}(\text{CO})_3\text{Cl}(\text{BPy-PMO})$, and e) $\text{Pd}(\text{OAc})_2(\text{BPy-PMO})$. Closed circle: adsorption, open circle: desorption.

^{13}C CP MAS NMR spectra of metalated BPy-PMOs showed mainly no major change compared with that of parent BPy-PMO (Figure 5.19a). However, peak broadening or new characteristic resonances attributable to ligand on the metal complexes were observed for metalated BPy-PMOs with relatively high loading amount of metal complexes on the pore surface such as $\text{Re}(\text{CO})_3(\text{BPy-PMO})$. The ^{13}C CP MAS NMR spectra of $\text{Ir}(\text{ppy})_2(\text{BPy-PMO})$ showed new resonance at 169 ppm, which is characteristic for the α -carbons in the 2-phenylpyridines. ^{29}Si DD MAS NMR spectra of metalated BPy-PMOs showed no Q sites, indicating that metal complex

formation does not affect the Si–C bond cleavage in the siloxane bonding network of pore walls (Figure 5.19b).

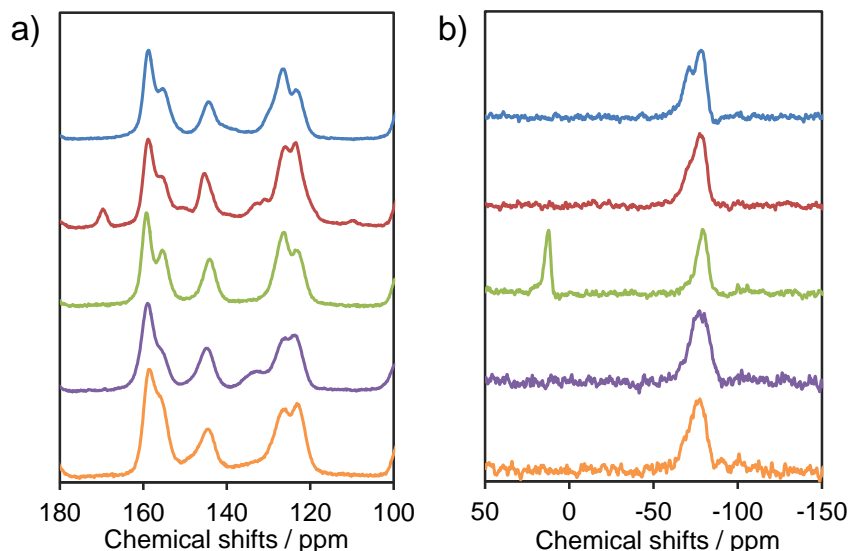


Figure 5.19. a) ^{13}C CP MAS NMR spectra and b) ^{29}Si DD MAS NMR spectra of $\text{Ru}(\text{bpy})_2(\text{BPy-PMO})$ (blue lines), $\text{Ir}(\text{ppy})_2(\text{BPy-PMO})$ (red lines), $\text{Ir}(\text{OMe})(\text{cod})(\text{BPy-PMO-TMS})$ (green lines), $\text{Re}(\text{CO})_3\text{Cl}(\text{BPy-PMO})$ (purple lines), and $\text{Pd}(\text{OAc})_2(\text{BPy-PMO})$ (orange lines).

The above results clearly indicate the great potential of BPy-PMO as a chelating ligand for the formation of a variety of solid-state bipyridine-based metal complexes with high surface areas. The metal complex-BPy-PMOs have the potential to show good catalytic performance similar to their homogeneous analogues because of the well-defined catalytic centers on the surface and efficient mass transportation due to the large mesopores. Furthermore, the high stability of BPy-PMO could allow easy separation and recycle use of the heterogeneous metal catalysts.

Solid ligand properties for direct C–H borylation of arenes

Construction of isolated and well-defined catalytic active centers onto solid supports is a subject of central importance in the development of efficient heterogeneous molecular catalysts.³³ In homogeneous catalysis, the Ir-bipyridine complex was found to show both high catalytic activity and functional tolerance for direct C–H borylation of arenes, one of the most important

³³ Maishal, T. K.; Alauzun, J.; Basset, J.-M.; Copéret, C.; Corriu, R. J. P.; Jeanneau, E.; Mehdi, A.; Reyé, C.; Veyre, L.; Thieuleux, C. *Angew. Chem., Int. Ed.* **2008**, *47*, 8654–8656.

transformations for preparing useful aryl boryl ester intermediates.³⁴ To date, heterogeneous molecular catalysts for C–H borylation have been limited to the Ir-silica-supported phosphine complex³⁵ and polymeric Ir-bipyridine complex catalysts.³⁶ Herein, BPy-PMO-TMS was used as a solid chelating ligand for the heterogeneous Ir-bipyridine catalyst for direct C–H borylation of arenes.

Direct C–H borylation was carried out in the presence of Ir(OMe)(cod)(BPy-PMO-TMS) (denoted as Ir@BPy-PMO-TMS in this section, 0.75 mol % Ir) and bis(pinacolato)diboron (B₂pin₂) (0.33 mmol) in arenes (20 mmol) at 80 °C for 12 h (Table 5.2). The catalytic activity was compared to those of a homogeneous iridium catalyst with a molecular bipyridine ligand and heterogeneous iridium catalysts with bipyridine ligands grafted on silica gel (**L1**), mesoporous silica (**L2**), and polystyrene (**L3**) (Figure 5.20). Ir@BPy-PMO-TMS catalyzed the direct C–H borylation of benzene and gave the desired product in high yield of 94% (Table 5.2, entry 1), which was higher than those obtained with a homogeneous catalyst (Table 5.2, entry 2, 80%) and grafted catalysts on silica gel (Table 5.2, entry 3, 33%) and mesoporous silica (Table 5.2, entry 4, 63%). The grafted catalyst on polystyrene showed no catalytic activity (Table 5.2, entry 5, 0%).

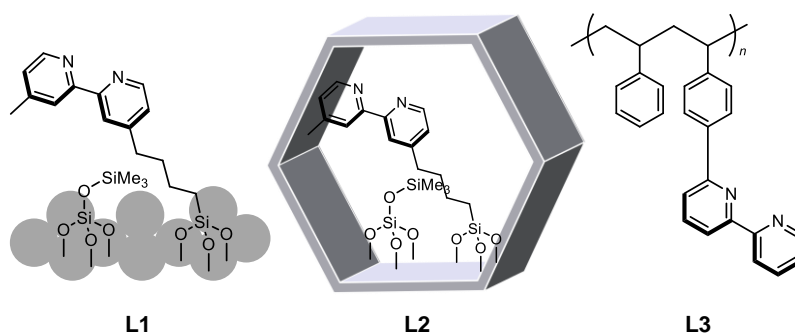
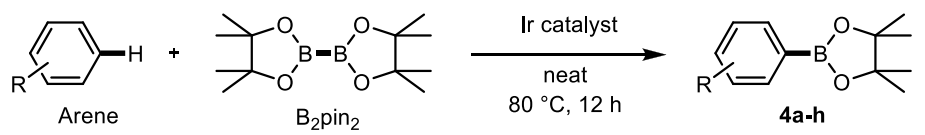


Figure 5.20. Chemical structure of solid bipyridine ligands **L1**, **L2**, and **L3**.

³⁴ a) Ishiyama, T.; Takagi, J.; Ishida, K.; Miyaura, N.; Anastasi, N. R.; Hartwig, J. F. *J. Am. Chem. Soc.* **2002**, *124*, 390–391; b) Ishiyama, T.; Takagi, J.; Hartwig, J. F.; Miyaura, N. *Angew. Chem., Int. Ed.* **2002**, *41*, 3056–3058; c) Mkhaliid, I. A. I.; Barnard, J. H.; Marder, T. B.; Murphy, J. M.; Hartwig, J. F. *Chem. Rev.* **2010**, *110*, 890–931.

³⁵ Kawamorita, S.; Ohmiya, H.; Hara, K.; Fukuoka, A.; Sawamura, M. *J. Am. Chem. Soc.* **2009**, *131*, 5058–5059.

³⁶ Tagata, T.; Nishida, M.; Nishida, A. *Tetrahedron Lett.* **2009**, *50*, 6176–6179.

Table 5.2. Ligand effects in Ir-catalyzed direct C–H borylation of arenes with B₂pin₂.


Entry	Ir catalyst	R	Yield / % ^b
1	Ir@BPy-PMO-TMS	H (4a)	94
2	Ir(OMe)(cod)(bpy)	4a	80
3 ^c	[Ir(OMe)(cod)] ₂ / L1	4a	33
4 ^c	[Ir(OMe)(cod)] ₂ / L2	4a	63
5 ^c	[Ir(OMe)(cod)] ₂ / L3	4a	0
6	Ir@BPy-PMO-TMS	CH ₃ (4b)	85 ^d
7	Ir@BPy-PMO-TMS	OMe (4c)	88 ^e
8	Ir@BPy-PMO-TMS	CO ₂ Me (4d)	88 ^f
9	Ir@BPy-PMO-TMS	1,2-(CH ₃) ₂ (4e)	60
10	Ir@BPy-PMO-TMS	1,2-Cl ₂ (4f)	92
11	Ir@BPy-PMO-TMS	1,3-Cl ₂ (4g)	81
12	Ir@BPy-PMO-TMS	1,3-(CF ₃) ₂ (4h)	47

^a Reaction conditions: Ir catalyst (0.75 mol% Ir), arene (20 mmol), B₂pin₂ (0.33 mmol) at 80 °C, 12 h. ^b Isolated yield of **4** based on boron atom in B₂pin₂. ^c Ir catalyst was in-situ prepared from [Ir(OMe)(cod)]₂ and solid bipyridine ligand. ^d *m* : *p* = 63 : 37. ^e *m* : *p* = 63 : 37. ^f *m* : *p* = 56 : 44.

In order to elucidate the catalytic behavior, the reaction kinetics were studied as shown in Figure 5.21a. The PMO catalyst retained its activity until the end of the reaction, while the reaction rates of homogeneous and grafted iridium complexes decreased within 2 h. The decreased reaction rates indicate deactivation of the active center possibly due to aggregation of the iridium species and/or undesired interaction between the active center and solid surface. These results suggest that BPy-PMO is an effective solid ligand for suppression of aggregation and undesired interactions of the metal center due to the isolate binding of metals on the well-defined surface. It is noteworthy that the initial reaction rate for Ir@BPy-PMO-TMS is almost the same as that of the homogeneous

catalyst with the same amount of Ir (Figure 5.21a, red and blue lines). This result suggests a very small diffusion limitation of molecules (B_2pin_2 , products, etc.) in the mesochannels due to the large pore size. The grafted mesoporous silica showed a slightly lower initial reaction rate than Ir@BPy-PMO-TMS, possibly due to the effect of the protruded iridium complexes into the mesochannels (Figure 5.21a, green line). The grafted silica gel showed an initial reaction rate similar to that of Ir@BPy-PMO-TMS because of the large mean pore diameter (6.3 nm) of the silica gel (Figure 5.21a, purple line).

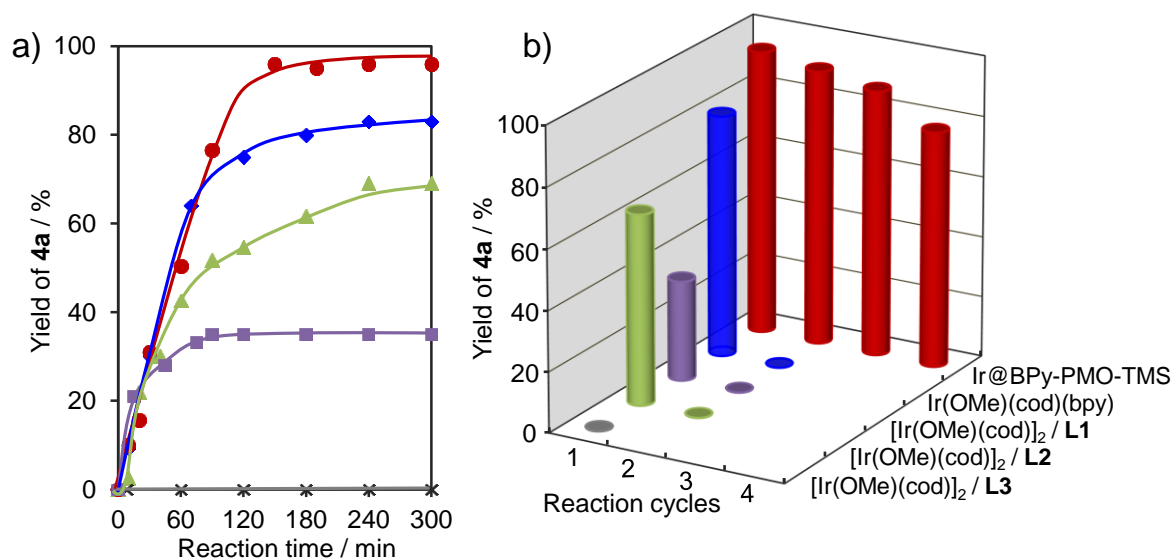


Figure 5.21. a) Reaction kinetic curves of C–H borylation of benzene catalyzed by iridium catalysts based on BPy-PMO (red line), 2,2'-bipyridine (blue line), L1 (purple line), L2 (green line), and L3 (gray line). b) Reusability of Ir@BPy-PMO-TMS catalyst, first cycle (original: 94%), second cycle (91%), third cycle (88%), and fourth cycle (78%), and other heterogeneous and homogeneous catalysts.

The scope of this system was then examined using various types of substrates (Table 5.2, entries 6–12). Ir@BPy-PMO-TMS catalyzed C–H borylation of both electron-rich and -poor substituted arenes. In the case of monosubstituted arenes, the reaction gave regioisomeric mixtures of the *m*- and *p*-borylation products (Table 5.2, entries 6–8). In contrast, regioselective borylation was observed for disubstituted arenes. Both 1,2- and 1,3-disubstituted arenes yielded the corresponding boronate esters as single regioisomers due to steric hindrance of the substituents (Table 5.2, entries 9–12). Similar behaviors were observed for the homogeneous system.³²

The Ir@BPy-PMO-TMS was easily recovered by simple filtration and was available for recycle use (Figure 5.21b). The recovered Ir@BPy-PMO-TMS retained good catalytic activity with slight loss of product yield for at least three cycles. In contrast, the homogeneous and the grafted catalysts showed almost no catalytic activity for recycle use, indicating almost complete deactivation during the first reaction cycle. These results indicate good recyclability of Ir@BPy-PMO-TMS.

A hot-filtration experiment was conducted to check the catalytic activity of leached Ir species. After the reaction had proceeded for 1 h with a yield of 54%, Ir@BPy-PMO-TMS was filtered by using a membrane filter (0.20 μm) under argon, and the resulting transparent solution was allowed to react under identical conditions for another 23 h (Figure 5.22a). No significant change in the product yield was observed, indicating that the reaction completely stopped. Figures 5.22b and 5.22c show the photographs of reaction mixture containing homogeneous catalyst (left) and Ir@BPy-PMO-TMS (right) before (Ir content was 835 ppm) and after the filtration. ICP analysis showed that the concentration of Ir species in the filtrate of Ir@BPy-PMO-TMS system was under the detection limit (< 1 ppm) (Figure 5.22c, right). In contrast, the concentration of Ir species in the filtrate of homogeneous system was 130 ppm (Figure 5.22c, left). These results clearly indicate that the catalytic reaction occurred by the iridium complex fixed on BPy-PMO without leaching of Ir species.

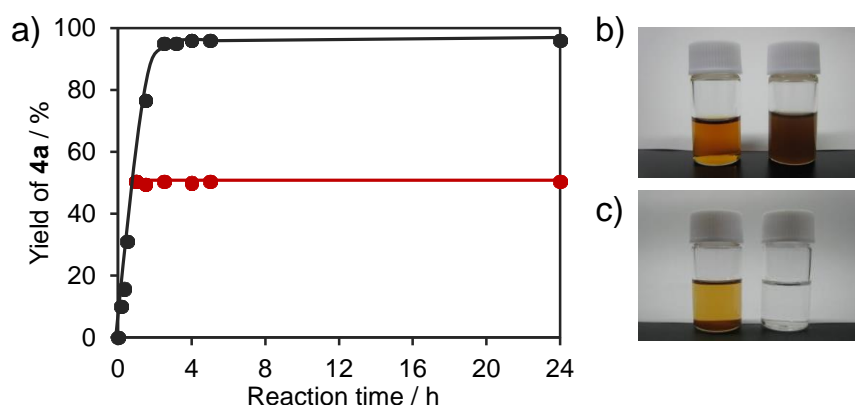


Figure 5.22. a) Reaction kinetic curves of direct C–H borylation of benzene with B_2pin_2 catalyzed by Ir(OMe)(cod)(BPy-PMO) and after the removal of Ir(OMe)(cod)(BPy-PMO) (red line). Photographs of reaction mixture b) before (Ir content was 835 ppm) and c) after the removal of homogeneous catalyst (left) and Ir@BPy-PMO-TMS (right) catalysts by filtration.

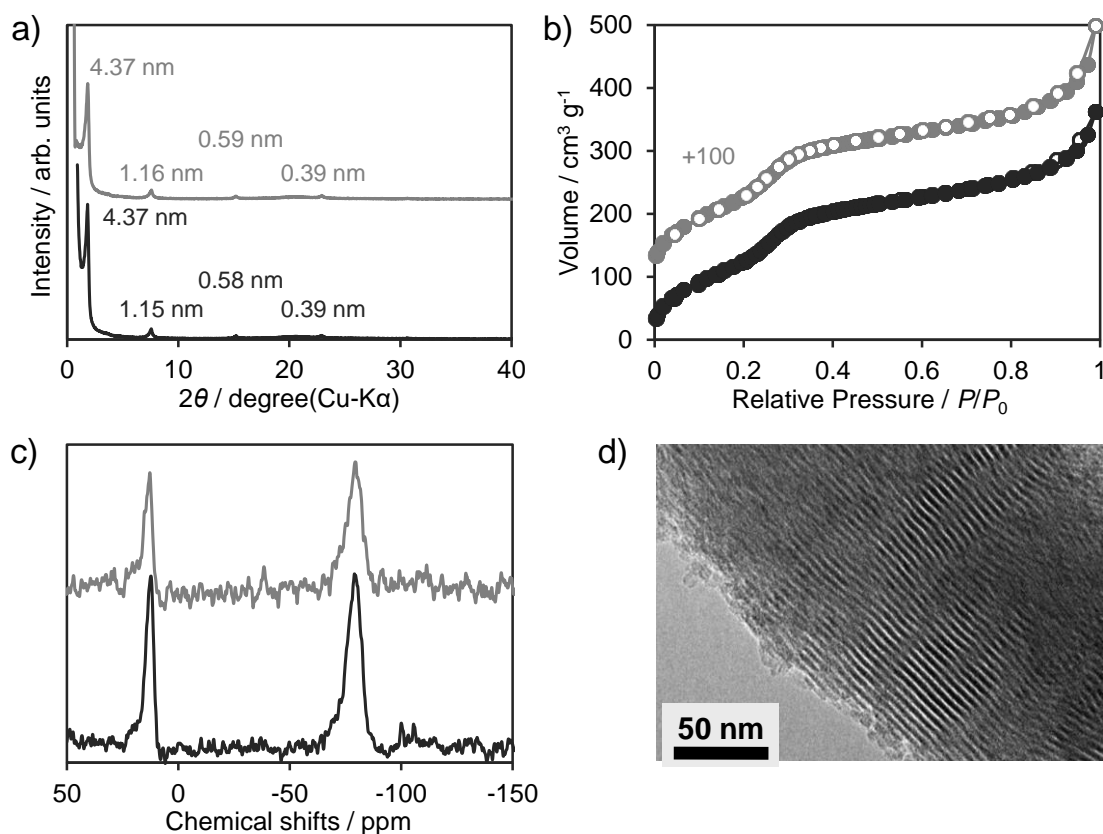


Figure 5.23. a) XRD profiles, b) nitrogen adsorption/desorption isotherms (closed circles: adsorption, open circles: desorption), and (c) ^{29}Si DD MAS NMR spectra of Ir@BPy-PMO-TMS before (black lines) and after (gray lines) the reactions. d) TEM image of recovered Ir@BPy-PMO-TMS.

In order to investigate the structural and textural properties of recovered Ir@BPy-PMO-TMS catalyst, the XRD profile, nitrogen adsorption/desorption isotherms, ^{29}Si DD MAS NMR spectrum measurements and TEM observation were carried out. The XRD patterns were almost identical to fresh catalyst and the textural properties such as S_{BET} , $V_{t\text{-plot}}$, and d_{DFT} were almost preserved even after the reaction (Figures 5.23a and 5.23b). ^{29}Si DD MAS NMR spectrum remained unchanged and showed no Q sites, indicating the C–H borylation does not lead to any modification of the pore framework (Figure 5.23c). The TEM image clearly showed the presence of well-ordered mesoporous structure and crystal-like pore wall structure (Figure 5.23d). It is noted that no aggregation of Ir species were observed. These structural features were homogeneously distributed through the PMO particles, indicating that Ir complexes were well-isolated and strongly

immobilized on the pore surface even after the reaction.

A platform for integrated heterogeneous photocatalytic hydrogen evolution system

BPy-PMO is also expected to be a useful platform with which to integrate different functional components for construction of efficient solar energy conversion systems. $[\text{Ru}(\text{bpy})_3]^{2+}$ is a typical photosensitizer which has been widely applied to homogeneous and heterogeneous photocatalysis systems such as photocatalytic hydrogen evolution from water in the presence of platinum (as a catalyst), methylviologen (as an electron mediator), and EDTA as a sacrificial reducing agent.³⁷ In this work, the author constructed a heterogeneous photocatalytic hydrogen evolution assembly of BPy-PMO integrated with a $[\text{Ru}(\text{bpy})_3]^{2+}$ photosensitizer and platinum catalyst on the pore surface without any electron mediators such as methylviologen as shown in Figure 5.24.

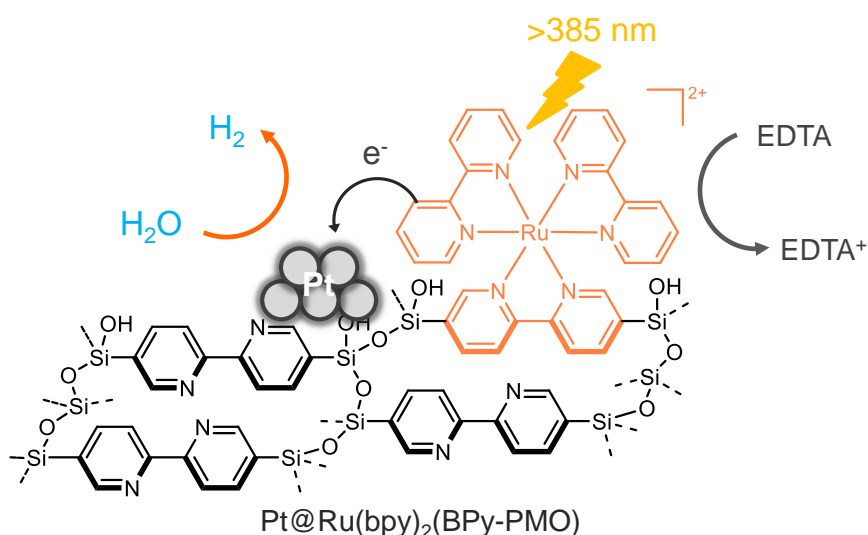


Figure 5.24. Schematic illustration of a hydrogen evolution system based on Pt@Ru-BPy-PMO.

$\text{Ru}(\text{bpy})_2(\text{BPy-PMO})$ (denoted as Ru-BPy-PMO in this section) was loaded with Pt by stirring in an aqueous Pt(II) salt solution at 80 °C to afford Pt@Ru-BPy-PMO. The color of Ru-BPy-PMO was changed from orange to dark brown possibly due to the formation of Pt nanoparticles and/or Pt complexes on the free bipyridine ligand on the pore surface. UV-vis diffuse reflectance spectra of Ru-BPy-PMO after the loading of Pt species was broadened and showed absorption bands in wide range of 250-600 nm (Figure 5.25a). The ¹³C CP MAS NMR spectra showed spectral shape

³⁷ Kiwi, J.; Grätzel, M. *Nature* **1979**, *281*, 657–658.

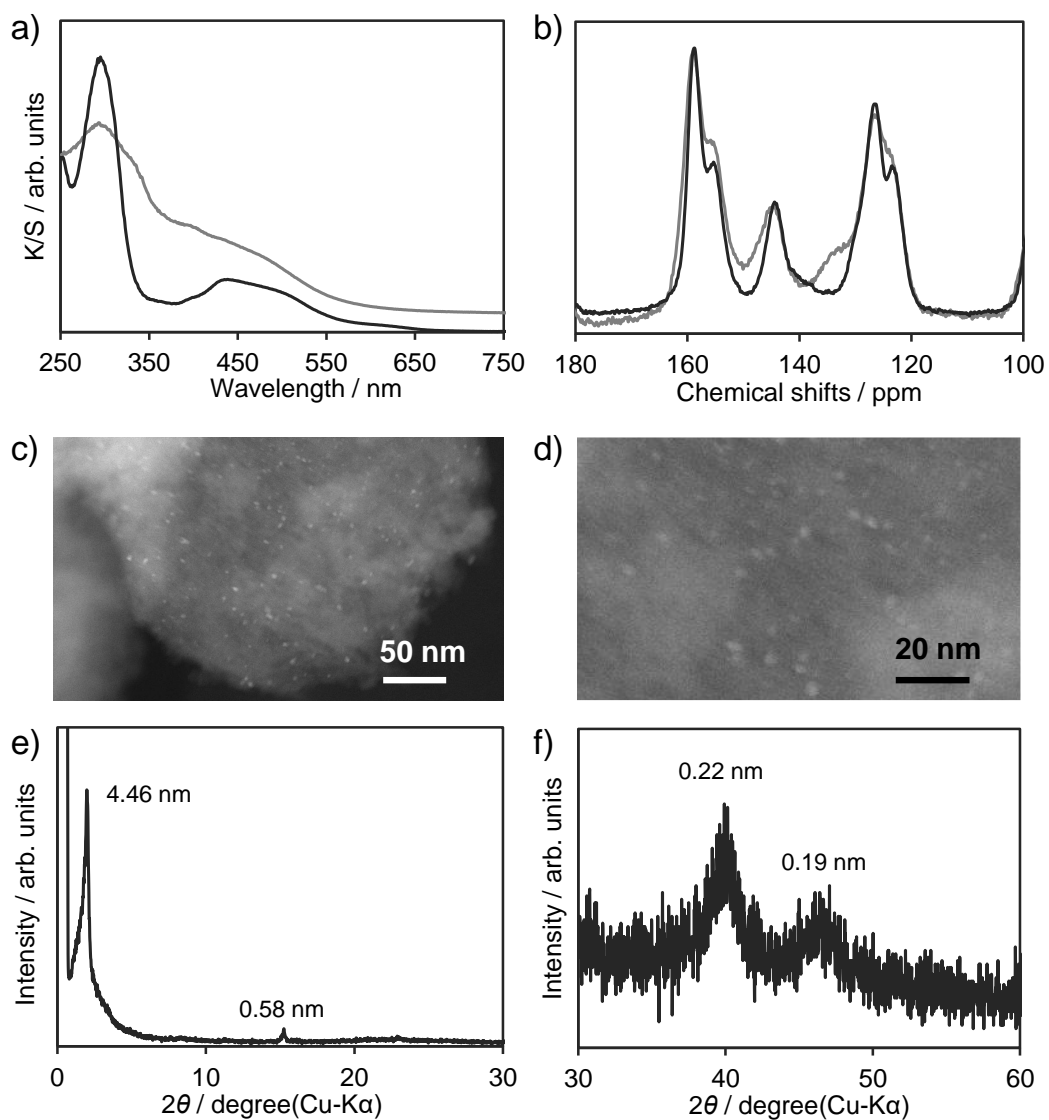


Figure 5.25. a) UV-vis diffuse reflectance spectra and b) ^{13}C CP MAS NMR spectra of Pt@Ru-BPy-PMO (gray lines) and Ru(bpy) $_2$ (BPy-PMO) (black lines). c, d) TEM images and e, f) XRD patterns of Pt@Ru-BPy-PMO.

changes and new signals after the loading of Pt species, which suggests the formation of Pt-bipyridine complex in partially (Figure 5.25b). The loading amount of Pt was 1.10 mmol g^{-1} , which was determined by ICP-AES analysis. TEM revealed the formation of many small nanoparticles with diameters of 2–3 nm in the PMO particles (Figures 5.25c and 5.25d). The XRD pattern exhibited strong diffraction peak at $2\theta = 1.98^\circ$ (d spacing of 4.46 nm) corresponding to ordered mesoporous structure and very broad peaks at $2\theta = 31.9^\circ$ and 46.4° (d spacings of 0.22 and

0.19 nm) corresponding to (111) and (200) faces of the Pt crystal (Figures 5.25e and 5.25f).³⁸ These results indicate that Pt nanoparticles were supported on Ru-BPy-PMO, including inside the mesochannels, owing to the small sizes of the Pt nanoparticles.

Although nitrogen adsorption/desorption isotherms of Pt@Ru-BPy-PMO showed slightly reduced adsorption property compared with that of Ru-BPy-PMO due to the immobilization of Pt nanoparticles inside the mesochannels, Pt@Ru-BPy-PMO still have mesopores of 2.7 nm and high surface area of 570 m² g⁻¹ (Figure 5.26a). In addition, ²⁹Si DD MAS NMR spectra revealed no cleavage of Si-C bond during the immobilization of Pt species (Figure 5.26b).

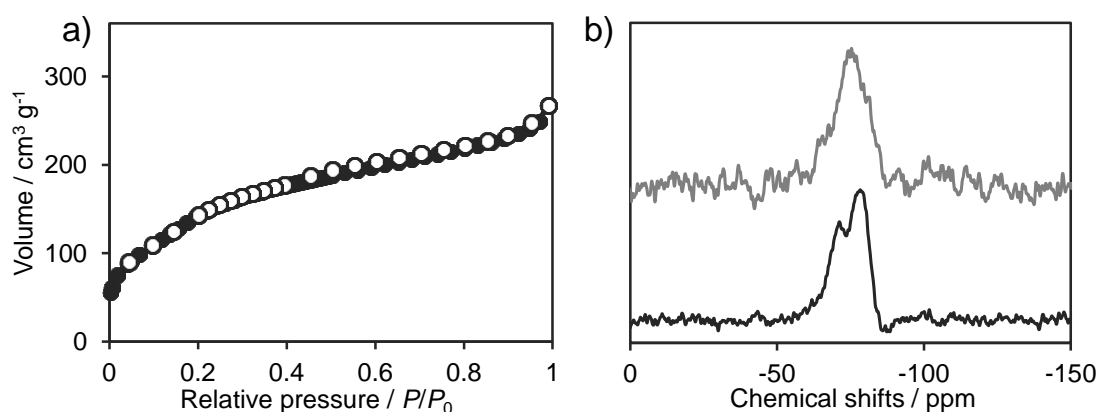


Figure 5.26. a) Nitrogen adsorption/desorption isotherms of Pt@Ru-BPy-PMO. Closed circle: adsorption, open circle: desorption. b) ²⁹Si MAS NMR spectra of Pt@Ru-BPy-PMO (gray lines) and Ru-BPy-PMO (black lines).

The photocatalytic reaction was carried out using a Pyrex reaction vessel connected to a glass-enclosed gas circulation and evacuation system. Pt@Ru-BPy-PMO was suspended in an acetate buffer solution containing EDTA as a sacrificial reducing agent in the vessel. Hydrogen was evolved continuously and steadily under irradiation of visible light (> 385 nm) (Figure 5.27, closed circles). The amount of produced hydrogen reached 300 μmol after 24 h, corresponding to a Ru-based turnover number of 184. This indicates that Ru-BPy-PMO can act as a photosensitizer for hydrogen evolution in combination with Pt nanoparticles without any electron mediators. Direct electron transfer from Ru complexes to Pt nanoparticles occurred in this system because both components were fixed on the pore surface and were in constant contact with each other. As a

³⁸ Huang, S.; Hara, K.; Fukuoka, A. *Chem.–Eur. J.* **2012**, *18*, 4738–4747.

control experiment, homogeneous $\text{Ru}(\text{bpy})_3\text{Cl}_2$ and colloidal platinum particles were used instead of Pt@Ru-BPy-PMO with the same Ru and Pt contents. The homogeneous system showed almost no hydrogen evolution (Figure 5.27, open circles). However, the addition of methylviologen to the homogeneous system brought about evolution of a considerable amount of hydrogen. These results suggest that BPy-PMO acts a useful platform to integrate $[\text{Ru}(\text{bpy})_3]^{2+}$ and Pt on the pore surface and promotes efficient photoinduced electron transfer from the photosensitizer to the catalyst without any electron relay molecules.

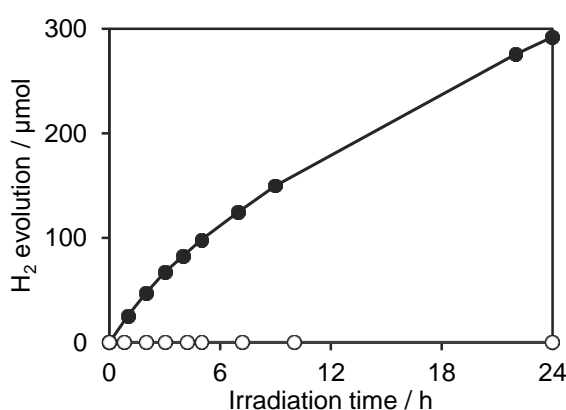


Figure 5.27. Time-dependent hydrogen evolution curves of Pt@Ru-BPy-PMO (closed circles) and homogeneous $\text{Ru}(\text{bpy})_3\text{Cl}_2$ and colloidal platinum particles system (open circles) under irradiation of visible light ($> 385 \text{ nm}$).

5.1.4 Conclusions

A novel crystal-like PMO with a high density of bipyridine groups in the framework was successfully synthesized from a bipyridine-bridged organosilane precursor. BPy-PMO was demonstrated to act as a versatile chelating ligand for the formation of various bipyridine-based metal complexes on the pore surface due to the high coordination ability of the framework bipyridine ligands. BPy-PMO end-capped with trimethylsilyl (TMS) groups (BPy-PMO-TMS) was successfully used in the heterogeneous Ir-catalyzed direct C–H borylation of arenes, which showed high activity similar to the corresponding homogeneous Ir-bipyridine complex and high durability due to the suppression of Ir-complex aggregation on the pore surface. Ir-complexed BPy-PMO-TMS allowed for easy recovery and recycle use and very low contamination of Ir in the

final product. BPy-PMO was also a useful platform for construction of a heterogeneous molecular photocatalyst system. The integration of $\text{Ru}(\text{bpy})_3^{2+}$ photosensitizer and Pt catalyst on the pore surface exhibited catalytic hydrogen evolution from water without any electron mediators. These results demonstrate the great potential of BPy-PMO as a solid chelating ligand and an integration platform for a variety of molecular-based heterogeneous metal complex catalyst systems such as organic transformations and solar energy conversion.

5.2 Direct C–H Borylation of Arenes and Heteroarenes by Ir-immobilized BPy-PMO Catalyst

Heterogeneous catalysis for direct C–H borylation of arenes and heteroarenes in the combination of iridium (Ir) complex fixed on periodic mesoporous organosilica containing bipyridine ligands within the framework (denoted as Ir-BPy-PMO) and pinacolborane (HBpin) is reported. Ir-BPy-PMO showed higher catalytic activity toward the borylation of benzene with inexpensive HBpin compared to expensive bis(pinacolato)diboron (B_2pin_2). The precatalyst could be handled without the use of a glove box. The catalyst was easily recovered from reaction mixtures by simple filtration under air. The recovered catalyst still showed good catalytic activity for at least three more times for the borylation of benzene. A variety of arenes and heteroarenes were successfully borylated with high boron efficiency by Ir-BPy-PMO using HBpin, whereas almost no activity was observed for borylation of some heteroarenes with B_2pin_2 . The system using Ir-BPy-PMO and HBpin was also utilized in syntheses of multi-boronated thiophene-based building blocks containing ladder-, acenefused-, and fused-thiophene skeletons. The combination of a stable and reusable solid catalyst and inexpensive HBpin is expected to be superior to conventional approaches for the development of industrial applications.

5.2.1 Introduction

Transition-metal catalyzed direct C–H borylation has been developed as an efficient and straightforward synthetic strategy for aryl/heteroarylboronate esters,¹ which are valuable intermediates in organic synthesis.^{2,3} In particular, the combination of an iridium(Ir)–bipyridine complex and bis(pinacolato)diboron (B_2pin_2 , pin = $O_2C_2Me_4$) or pinacolborane (HBpin) has been established as one of the most reliable catalytic systems in terms of catalytic activity, boron

¹ For selected reviews on borylation of aromatic C–H bonds, see: a) Ishiyama, T.; Miyaura, N. *J. Organomet. Chem.* **2003**, *680*, 3–11; b) Mkhalid, I. A. I.; Barnard, J. H.; Marder, T. B.; Murphy, J. M.; Hartwig, J. F. *Chem. Rev.* **2010**, *110*, 890–931; c) Hartwig, J. F. *Acc. Chem. Res.* **2011**, *45*, 864–873.

² Hall, D. G. *Boronic Acids: Preparation and Applications in Organic Synthesis and Medicine*, Wiley-VCH Verlag GmbH & Co. KGaA, 2005, pp. 1–99.

³ Miyaura, N.; Suzuki, A. *Chem. Rev.* **1995**, *95*, 2457–2483.

efficiency, and functional group tolerance.^{4,5} Unfortunately, this method still suffers from problems related to homogeneous systems such as fast deactivation of the catalyst and difficult separation and recycling of residual catalyst from the reaction mixture. Thus, the development of a synthetic approach to aryl/heteroarylboronate esters using a heterogeneous transition-metal catalyst is a subject of paramount importance for sustainable organic synthesis.

Recently, the author reported a unique solid chelating ligand, periodic mesoporous organosilica containing 2,2'-bipyridine groups within the framework (BPy-PMO). As the 2,2'-bipyridine ligands in BPy-PMO are regularly arranged and exposed on the pore surface, various metal complexes can be directly formed on the pore surface using the framework bipyridine as one of the ligands (Figure 5.28).⁶ Iridium (Ir)-bipyridine complex formed on the pore surface of BPy-PMO end-capped with trimethylsilyl (TMS) groups showed high catalytic activity and durability for direct C-H borylation of arenes because of suppression of undesired interactions and aggregation of the metal centers due to the isolated binding of metals on the well-defined surface. The recovered Ir-BPy-PMO was available for recycle use. Independently, Copéret et al. reported a similar strategy to prepare a well-isolated catalytic active center on the pore surface of PMO where bipyridine groups were diluted with biphenylene units (Ir-bpy^{1/10}-PMO, Figure 5.28).⁷ More recently, mesoporous silica and a metal-organic framework-supported Ir-bipyridine heterogeneous catalyst (bpy-SBA-15-Ir, bpy-UiO-Ir, Figure 5.28) have also been reported.^{8,9} These findings indicate that ordered nanoporous materials containing bipyridine ligands in their framework have

⁴ a) Ishiyama, T.; Takagi, J.; Ishida, K.; Miyaura, N.; Anastasi, N. R.; Hartwig, J. F. *J. Am. Chem. Soc.* **2002**, *124*, 390–391; b) Ishiyama, T.; Takagi, J.; Hartwig, J. F.; Miyaura, N. *Angew. Chem., Int. Ed.* **2002**, *41*, 3056–3058; c) Ishiyama, T.; Miyaura, N. *Pure Appl. Chem.* **2006**, *78*, 1369–1375.

⁵ a) Ishiyama, T.; Takagi, J.; Yonekawa, Y.; Hartwig, J. F.; Miyaura, N. *Adv. Synth. Catal.* **2003**, *345*, 1103–1106; b) Takagi, J.; Sato, K.; Hartwig, J. F.; Ishiyama, T.; Miyaura, N. *Tetrahedron Lett.* **2002**, *43*, 5649–5651; c) Mkhaliid, I. A. I.; Coventry, D. N.; Albesa-Jove, D.; Batsanov, A. S.; Howard, J. A. K.; Marder, T. B.; Perutz, R. N. *Angew. Chem., Int. Ed.* **2006**, *45*, 489–491; d) Chotana, G. A.; Kallepalli, V. A.; Maleczka, Jr. R. E.; Smith, III, M. R. *Tetrahedron* **2008**, *64*, 6103–6114; e) Paul, S.; Chotana, G. A.; Holmes, D.; Reichle, R. C.; Maleczka, Jr. R. E.; Smith, III, M. R. *J. Am. Chem. Soc.* **2006**, *128*, 15552–15553; f) Lo, W. F.; Kaiser, H. M.; Spannenberg, A.; Beller, M.; Tse, M. K. *Tetrahedron Lett.* **2007**, *48*, 371–375; g) Coventry, D. N.; Batsanov, A. S.; Goeta, A. E.; Howard, J. A. K.; Marder, T. B.; Perutz, R. N. *Chem. Commun.* **2005**, 2172–2174; h) Kimoto, T.; Tanaka, K.; Sakai, Y.; Ohno, A.; Yoza, K.; Kobayashi, K. *Org. Lett.* **2009**, *11*, 3658–3661; i) Hata, H.; Shinokubo, H.; Osuka, A. *J. Am. Chem. Soc.* **2005**, *127*, 8264–8265.

⁶ Waki, M.; Maegawa, Y.; Hara, K.; Goto, Y.; Shirai, S.; Yamada, Y.; Mizoshita, N.; Tani, T.; Chun, W.-J.; Muratsugu, S.; Tada, M.; Fukuoka, A.; Inagaki, S. *J. Am. Chem. Soc.* **2014**, *136*, 4003–4011.

⁷ Grüning, W. R.; Siddiqi, G.; Safonova, O. V.; Copéret, C. *Adv. Synth. Catal.* **2014**, *356*, 673–679.

⁸ Wu, F.; Feng, Y.; Jones, C. W. *ACS Catal.* **2014**, *4*, 1365–1375.

⁹ Manna, K.; Zhang, T.; Lin, W. *J. Am. Chem. Soc.* **2014**, *136*, 6566–6569.

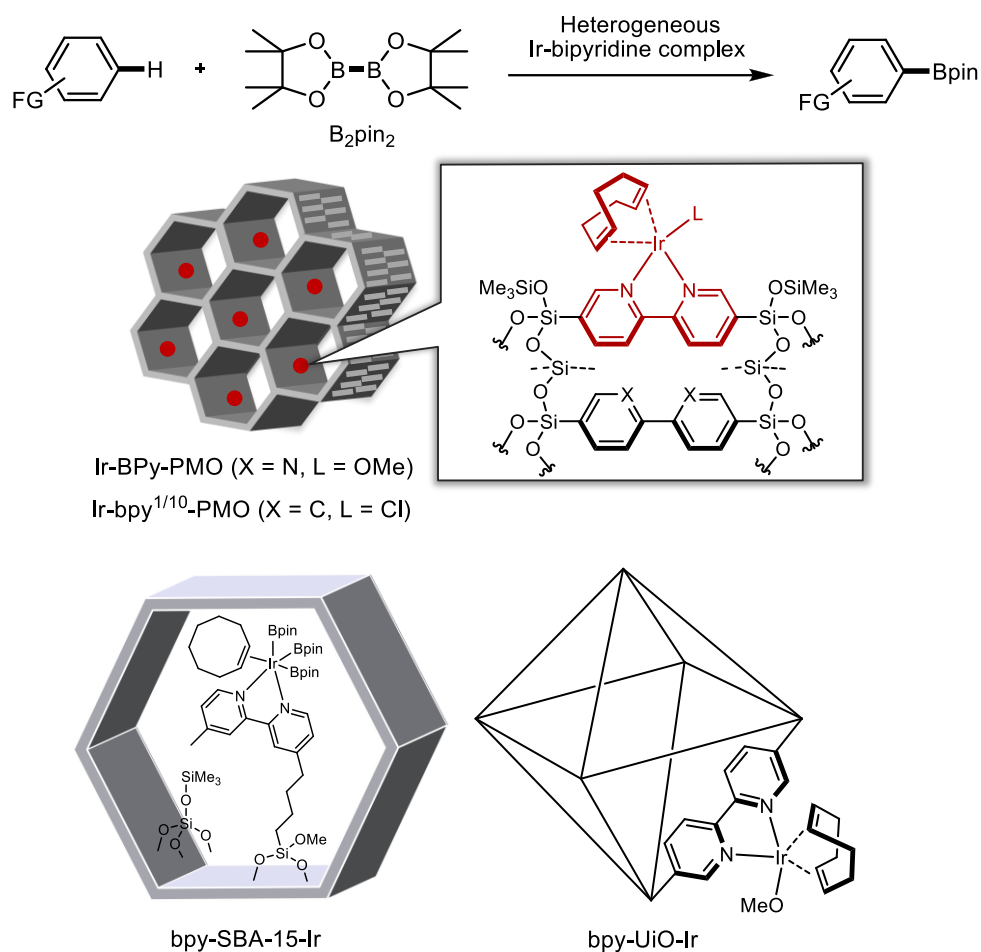


Figure 5.28. Representative heterogeneous Ir–bipyridine complex catalysts based on well-defined bipyridine solid chelating ligands for direct C–H borylation of arenes with bis(pinacolato)diboron.

great potential for heterogenization of homogeneous Ir–bipyridine catalyst without loss of activity.

In the preliminary results, the author only showed the Ir-BPy-PMO catalyzed borylation of arenes in combination with B_2pin_2 under neat conditions.⁶ It should be required to evaluate the borylation reactions in combination with Ir-BPy-PMO and HBpin, a cheaper boron source than B_2pin_2 , as well as a wide range of substrate scope in order to develop further potential of Ir-BPy-PMO for industrial applications.

Here, the author reports Ir-BPy-PMO catalyzed borylation using an inexpensive HBpin for a wide range of arenes and heteroarenes. It was revealed that Ir-BPy-PMO showed higher catalytic activity for direct C–H borylation of a wide range of arenes and heteroarenes in combination with HBpin rather than B_2pin_2 . The combination with HBpin allowed multiple borylation of

π -conjugated and/or fused-thiophene derivatives with high yields of 95–99% while almost no reaction was observed in the combination with B_2pin_2 . The combination of Ir-BPy-PMO and HBpin has great potential for industrial applications affording useful molecular building blocks for the synthesis of functional π -conjugated materials using Suzuki–Miyaura coupling reaction.

5.2.2 Experimental

Materials and methods

Unless otherwise noted, all chemicals, including dry solvents, were purchased from commercial suppliers (Sigma-Aldrich, Tokyo Chemical Industry Co., Ltd, and Wako Pure Chemical Industries Ltd) and used without further purification. BPy-PMO and end-capped BPy-PMO were prepared according to the literature.⁶ All reactions were carried out under argon using standard high-vacuum and Schlenk-line techniques. Nuclear magnetic resonance (NMR) spectra were recorded on a Jeol JNM-EXC400P spectrometer (400 MHz for 1H , 100 MHz for ^{13}C , and 376 MHz for ^{19}F). Chemical shifts are reported in δ parts per million referenced to $SiMe_4$ or residual protonated solvent as an internal standard. The following abbreviations were used to explain the multiplicities: s = singlet, d = doublet, t = triplet, m = multiplet, br = broad, dd = double doublet. Mass spectra were recorded on a Micromass GCT Premier mass spectrometer (FI: field ionization) and Micromass Q-TOF mass spectrometer (ESI: electrospray ionization). GC mass analyses were performed on an Agilent 7890A GC instrument equipped with a capillary column (HP-5MS, 0.25 mm \times 30 m) and a flame ionization detector. IR spectra were collected on a Thermo Fisher Scientific Nicolet Avatar-360 FT-IR spectrometer using an attenuated total reflection (ATR) attachment. XRD profiles were recorded on a Rigaku RINT-TTR diffractometer using Cu-K α radiation (50 kV, 300 mA). Nitrogen adsorption/desorption isotherms were measured using a Quantachrome Nova3000e sorptometer. BET surface areas were calculated from the linear sections of BET plots ($P/P_0 = 0.1$ – 0.2). Pore-size distributions were calculated using the DFT method (DFT kernel: N_2 at 77 K on silica, cylindrical pores, nonlinear density functional theory (NLDFT) equilibrium model). Pore volumes were estimated by the t -plot method.

Preparation of Ir-BPy-PMO

A 50 mL Schlenk-tube was equipped with a stir bar and end-capped BPy-PMO (77.5 mg, 0.226 mmol) and dry hexane (10 mL). A solution of [Ir(OMe)(cod)]₂ (5.0 mg, 0.015 mmol Ir) in dry hexane (20 mL) was added at room temperature. The reaction mixture was stirred at room temperature for 3–6 h. The resulting suspension was filtered and then washed with dry hexane. The material was dried under reduced pressure to give Ir-BPy-PMO as a light grey powder (75 mg, Ir content: 0.15–0.16 mmol g⁻¹).

General procedure for direct C–H borylation of arenes and heteroarenes

A 20 mL Schlenk-tube equipped with a stir bar and a septum inlet was charged with Ir-BPy-PMO (32.0 mg, 0.005 mmol Ir) and arenes or heteroarenes (1.33 mmol) then flushed with argon. Dry cyclohexane (2.0 mL) and HBpin (95 μL, 0.66 mmol) were added, and the mixture was stirred at 80 °C for 12 h. The mixture was diluted with Et₂O (5 mL) and filtered through a membrane filter (0.20 μm). Solvent was removed under reduced pressure. The crude product was purified using flash silica gel chromatography (eluent: hexane/EtOAc = 100/0 to 70/30) which provided analytically pure samples. The recovered catalyst was used for next reaction in the presence of HBpin and dry benzene under same reaction conditions.

(4,4,5,5-Tetramethyl-1,3,2-dioxaborolan-2-yl)benzene (2a). Yield: 94%. ¹H NMR (400 MHz, CDCl₃) δ 1.35 (s, 12H), 7.37 (t, *J* = 7.4 Hz, 2H), 7.46 (t, *J* = 7.3 Hz, 1H), 7.81 (d, *J* = 7.3 Hz, 2H); ¹³C NMR (100 MHz, CDCl₃): δ 24.87, 83.75, 127.69, 131.23, 134.72; ν_{max} (neat) 2983, 1604, 1437, 1350, 1137, 1092, 857, 705, 657 cm⁻¹; ESI-HRMS *m/z* calcd for C₁₂H₂₁BNO₂ (M+NH₄⁺): 222.1662; found: 222.1664.

Methyl (4,4,5,5-tetramethyl-1,3,2-dioxaborolan-2-yl)-benzoate(2b). Yield: 86% (*p*-isomer:*m*-isomer = 53:47). ¹H NMR (400 MHz, CDCl₃) δ (*m*-isomer) 1.36 (s, 12H), 3.91 (s, 3H), 7.44 (t, *J* = 8.0 Hz, 1H), 7.98 (d, *J* = 7.6 Hz, 1H), 8.12 (d, *J* = 8.0 Hz, 1H), 8.46 (s, 1H), (*p*-isomer) 1.36 (s, 12H), 3.92 (s, 3H), 7.86 (d, *J* = 8.4 Hz, 2H), 8.02 (d, *J* = 8.4 Hz, 2H); ¹³C NMR (100 MHz, CDCl₃) δ (*p*-isomer) 24.83, 52.10, 84.15, 128.52, 132.23, 134.59, 167.10, (*m*-isomer) 24.83, 52.00, 84.06, 127.74, 129.47, 135.76, 139.09, 167.07; ν_{max} (neat) 2952, 1726, 1461, 1362, 906 cm⁻¹; ESI-HRMS *m/z* calcd for C₁₄H₂₃BNO₄ (M+NH₄⁺): 280.1717; found: 280.1719.

(4,4,5,5-Tetramethyl-1,3,2-dioxaborolan-2-yl)(trifluoromethyl)benzene (2c). Yield: 91%

(*p*-isomer:*m*-isomer = 31:69). ^1H NMR (400 MHz, CDCl_3) δ (*m*-isomer) 1.36 (s, 12H), 7.48 (t, $J = 7.6$ Hz, 1H), 7.70 (d, $J = 7.8$ Hz, 1H), 7.97 (d, $J = 7.6$ Hz, 1H), 8.06 (s, 1H), (*p*-isomer) 1.36 (s, 12H), 7.61 (d, $J = 8.1$ Hz, 2H), 7.91 (d, $J = 7.8$ Hz, 2H); ^{13}C NMR (100 MHz, CDCl_3) δ (*m*-isomer) 24.85, 84.26, 124.29, 127.60, 127.99, 131.32, 137.96, (*p*-isomer) 24.53, 84.26, 124.15, 124.29, 132.30, 134.96; ^{19}F NMR (376 MHz, CDCl_3) δ (*m*-isomer) -62.93 , (*p*-isomer) -62.51 ; ν_{max} (neat) 2976, 1584, 1552, 1334, 1144, 966 cm^{-1} ; ESI-HRMS m/z calcd for $\text{C}_{13}\text{H}_{20}\text{BF}_3\text{NO}_2$ ($\text{M}+\text{NH}_4^+$): 250.1539; found: 250.1539.

(4,4,5,5-Tetramethyl-1,3,2-dioxaborolan-2-yl)toluene (2d). Yield: 92% (*p*-isomer:*m*-isomer = 40:60). ^1H NMR (400 MHz, CDCl_3) δ (*m*-isomer) 1.34 (s, 12H), 2.35 (s, 3H), 7.25–7.27 (m, 2H), 7.60 (t, $J = 4.4$ Hz, 1H), 7.63 (s, 1H), (*p*-isomer) 1.34 (s, 12H), 2.36 (s, 3H), 7.18 (d, $J = 7.6$ Hz, 2H), 7.70 (d, $J = 7.6$ Hz, 2H); ^{13}C NMR (100 MHz, CDCl_3) δ (*m*-isomer) 21.27, 24.85, 83.71, 127.66, 131.73, 132.01, 135.29, 137.10, (*p*-isomer) 21.73, 24.85, 83.60, 128.49, 134.76, 141.37; ν_{max} (neat) 2960, 1611, 1461, 1358, 1089 cm^{-1} ; ESI-HRMS m/z calcd for $\text{C}_{13}\text{H}_{23}\text{BNO}_2$ ($\text{M}+\text{NH}_4^+$): 236.1819; found: 236.1819.

(4,4,5,5-Tetramethyl-1,3,2-dioxaborolan-2-yl)anisole (2e). Yield: 87% (*p*-isomer:*m*-isomer = 49:51). ^1H NMR (400 MHz, CDCl_3) δ (*m*-isomer) 1.34 (s, 12H), 3.83 (s, 3H), 7.00 (dd, $J = 8.4$ Hz, 2.8 Hz, 1H), 7.29 (t, $J = 8.0$ Hz, 1H), 7.32 (d, $J = 2.8$ Hz, 1H), 7.40 (d, $J = 7.2$ Hz, 1H), (*p*-isomer) 1.33 (s, 12H), 3.83 (s, 3H), 6.88 (d, $J = 8.4$ Hz, 2H), 7.75 (d, $J = 8.4$ Hz, 2H); ^{13}C NMR (100 MHz, CDCl_3) δ (*m*-isomer) 24.85, 55.23, 83.80, 117.90, 118.61, 127.14, 128.91, 158.97, (*p*-isomer) 24.85, 55.08, 83.53, 113.27, 136.47, 162.08; ν_{max} (neat) 2952, 1603, 1461, 1382, 1354, 1093 cm^{-1} ; ESI-HRMS m/z calcd for $\text{C}_{13}\text{H}_{23}\text{BNO}_3$ ($\text{M}+\text{NH}_4^+$): 252.1768; found: 252.1768.

4-(4,4,5,5-Tetramethyl-1,3,2-dioxaborolan-2-yl)-*o*-xylene (2f). Yield: 60%. ^1H NMR (400 MHz, CDCl_3) δ 1.34 (s, 12H), 2.27 (s, 3H), 2.28 (s, 3H), 7.14 (d, $J = 7.6$ Hz, 1H), 7.54 (d, $J = 7.6$ Hz, 1H), 7.58 (s, 1H); ^{13}C NMR (100 MHz, CDCl_3) δ 19.47, 20.00, 24.83, 83.56, 129.13, 132.36, 135.88, 140.12; ν_{max} (neat) 2952, 1611, 1465, 1374, 1350, 1093 cm^{-1} ; ESI-HRMS m/z calcd for $\text{C}_{14}\text{H}_{25}\text{BNO}_2$ ($\text{M}+\text{NH}_4^+$): 250.1975; found: 250.1975.

1,2-Dichloro-4-(4,4,5,5-tetramethyl-1,3,2-dioxaborolan-2-yl)-benzene (2g). Yield: 95%. ^1H NMR (400 MHz, CDCl_3) δ 1.33 (s, 12H), 7.43 (d, $J = 8.0$ Hz, 1H), 7.59 (dd, $J = 8.0$ Hz, 1.2 Hz, 1H), 7.86 (d, $J = 1.6$ Hz, 1H); ^{13}C NMR (100 MHz, CDCl_3) δ 25.15, 84.64, 130.29, 132.53, 134.04, 135.77, 136.83; ν_{max} (neat) 2976, 1588, 1477, 1382, 1342, 1144, 1085, 1040, 960 cm^{-1} ; ESI-HRMS

m/z calcd for $C_{12}H_{19}BNCl_2O_2$ ($M+NH_4^+$): 290.0883; found: 290.0882.

1,3-Dichloro-4-(4,4,5,5-tetramethyl-1,3,2-dioxaborolan-2-yl)-benzene (2h). Yield: 94%. 1H NMR (400 MHz, $CDCl_3$) δ 1.34 (s, 12H), 7.42 (t, $J = 2.0$ Hz, 1H), 7.64 (d, $J = 2.0$ Hz, 2H); ^{13}C NMR (100 MHz, $CDCl_3$) δ 24.83, 84.48, 129.34, 131.04, 132.66, 134.68; ν_{max} (neat) 2976, 1584, 1552, 1440, 1334, 1144, 966 cm^{-1} ; ESI-HRMS m/z calcd for $C_{12}H_{19}BNCl_2O_2$ ($M+NH_4^+$): 290.0883; found: 290.0884.

1,3-Bis(trifluoromethyl)-5-(4,4,5,5-tetramethyl-1,3,2-dioxaborolan-2-yl)benzene (2i). Yield: 91%. 1H NMR (400 MHz, $CDCl_3$) δ 1.37 (s, 12H), 7.94 (s, 1 H), 8.23 (s, 2H); ^{13}C NMR (100 MHz, $CDCl_3$) δ 24.86, 84.83, 122.09, 124.66, 124.69, 130.68, 131.02, 134.61; ^{19}F NMR (376 MHz, $CDCl_3$) δ -62.76; ν_{max} (neat) 2983, 1618, 1279, 1123, 849, 677 cm^{-1} ; ESI-HRMS m/z calcd for $C_{14}H_{19}BNF_6O_2$ ($M+NH_4^+$): 358.1410; found: 358.1408.

2-(4,4,5,5-Tetramethyl-1,3,2-dioxaborolan-2-yl)thiophene (2j). Yield: 92%. 1H NMR (400 MHz, $CDCl_3$) δ 1.35 (s, 12H), 7.19 (dd, $J = 4.4$ Hz, 3.6 Hz, 1H), 7.63 (d, $J = 4.8$ Hz, 1H), 7.64 (d, $J = 3.6$ Hz, 1H); ^{13}C NMR (100 MHz, $CDCl_3$) δ 24.76, 84.07, 128.20, 132.34, 137.13; ν_{max} (neat) 2966, 1519, 1423, 1358, 1132, 846 cm^{-1} ; ESI-HRMS m/z calcd for $C_{10}H_{19}BNO_2S$ ($M+NH_4^+$): 228.1224; found: 228.1224.

5-(4,4,5,5-Tetramethyl-1,3,2-dioxaborolan-2-yl)-2-furancarboxylic acid methyl ester (2k). Yield: 93% (2-isomer:3-isomer = 86:14). 1H NMR (400 MHz, $CDCl_3$) δ (2-isomer) 1.35 (s, 12H), 3.89 (s, 3H), 7.07 (d, $J = 3.6$ Hz, 1H), 7.19 (d, $J = 3.6$ Hz, 1H), (3-isomer) 1.32 (s, 12H), 3.89 (s, 3H), 7.37 (s, 1H), 7.87 (s, 1H); ^{13}C NMR (100 MHz, $CDCl_3$) δ (2-isomer) 24.70, 51.93, 84.70, 117.86, 124.00, 148.29, 159.03, (3-isomer) 24.75, 51, 95, 83.91, 121.80, 123.9, 154.01, 159.07; ν_{max} (neat) 3112, 2977, 1714, 1575, 1527, 1437, 1358, 1324, 1284, 1103, 780 cm^{-1} ; ESI-HRMS m/z calcd for $C_{12}H_{21}BNO_5$ ($M+NH_4^+$): 270.1507; found: 270.1508.

2-(4,4,5,5-Tetramethyl-1,3,2-dioxaborolan-2-yl)benzo[b]thiophene (2l). Yield: 90%. 1H NMR (400 MHz, $CDCl_3$) δ 1.38 (s, 12H), 7.32–7.39 (m, 2H), 7.83–7.86 (m, 1H), 7.88 (s, 1H), 7.89–7.91 (m, 1H); ^{13}C NMR (100 MHz, $CDCl_3$) δ 24.81, 84.42, 122.49, 124.07, 124.34, 125.27, 134.46, 140.39, 143.66; ν_{max} (neat) 2977, 1595, 1553, 1522, 135, 1120, 849, 753, 662 cm^{-1} ; ESI-HRMS m/z calcd for $C_{14}H_{21}BNO_2S$ ($M+NH_4^+$): 278.1381; found: 278.1382.

2-(4,4,5,5-Tetramethyl-1,3,2-dioxaborolan-2-yl)benzofuran (2m). Yield: 92% (2-isomer:3-isomer = 80:20). 1H NMR (400 MHz, $CDCl_3$) δ (2-isomer) 1.39 (s, 12H), 7.22 (t, $J =$

7.2 Hz, 1H), 7.33 (dt, $J = 7.2$ Hz, 1.2 Hz, 1H), 7.40 (s, 1H), 7.56 (d, $J = 8.4$ Hz, 1H), 7.62 (d, $J = 8.0$ Hz, 1H), (3-isomer) 1.37 (s, 12H), 7.26–7.29 (m, 2H), 7.91–7.93 (m, 2H), 7.95 (s, 1H); ^{13}C NMR (100 MHz, CDCl_3) δ (2-isomer) 24.77, 84.66, 111.93, 119.51, 121.85, 122.70, 125.90, 127.44, 157.46, (3-isomer) 24.87, 83.48, 111.0, 122, 84, 122.92, 124.19, 153.5; ν_{max} (neat) 2971, 1612, 1561, 1471, 1321, 1132, 1069, 750 cm^{-1} ; ESI-HRMS m/z calcd for $\text{C}_{14}\text{H}_{21}\text{BNO}_3$ ($\text{M}+\text{NH}_4^+$): 262.1609; found: 272.1612.

2-(4,4,5,5-Tetramethyl-1,3,2-dioxaborolan-2-yl)indole (2n). Yield: 93%. ^1H NMR (400 MHz, CDCl_3) δ 1.37 (s, 12H), 7.09 (t, $J = 8.0$ Hz, 1H), 7.11 (s, 1H), 7.22 (t, $J = 8.0$ Hz, 1H), 7.38 (d, $J = 8.4$ Hz, 1H), 7.66 (d, $J = 8.4$ Hz, 1H), 8.55 (br, 1H); ^{13}C NMR (100 MHz, CDCl_3) δ 24.83, 84.13, 111.24, 113.82, 119.76, 121.58, 123.60, 128.24, 138.17; ν_{max} (neat) 3333, 2977, 1615, 1581, 1539, 1372, 1313, 1137, 968, 852, 696 cm^{-1} ; ESI-HRMS m/z calcd for $\text{C}_{14}\text{H}_{19}\text{BNO}_2$ ($\text{M}+\text{NH}_4^+$): 244.1503; found: 244.1507.

2,6-Dichloro-4-(4,4,5,5-tetramethyl-1,3,2-dioxaborolan-2-yl)-pyridine (2o). Yield: 92%. ^1H NMR (400 MHz, CDCl_3) δ 1.35 (s, 12H), 7.58 (s, 2H); ^{13}C NMR (100 MHz, CDCl_3) δ 24.82, 85.19, 127.75, 150.37; ν_{max} (neat) 3007, 2983, 1516, 1369, 1341, 1163, 1137, 965, 807 cm^{-1} ; ESI-HRMS m/z calcd for $\text{C}_{11}\text{H}_{15}\text{BCl}_2\text{NO}_2$ ($\text{M}+\text{NH}_4^+$): 274.0567; found: 274.0569.

General procedure for multiple-direct C–H borylation of thiophene derivatives

A 20 mL Schlenk-tube equipped with a stir bar and a septum inlet was charged with Ir-BPy-PMO (32.0 mg, 0.005 mmol Ir) and thiophene derivatives (0.22 mmol) and then flushed with argon. Dry cyclohexane (2.0 mL) and HBpin (95 μL , 0.66 mmol) were added, and the mixture was stirred at 80 $^\circ\text{C}$ for 12 h. The mixture was diluted with CHCl_3 (5 mL) and filtered through a membrane filter (0.20 μm). Solvent was removed under reduced pressure. The crude product was washed with cold hexane (1 mL) to afford analytically pure samples.

2,5-Bis(4,4,5,5-tetramethyl-1,3,2-dioxaborolan-2-yl)thiophene (3a). Yield: 99%. ^1H NMR (400 MHz, CDCl_3) δ 1.34 (s, 24H), 7.66 (s, 2H); ^{13}C NMR (100 MHz, CDCl_3) δ 24.76, 84.11, 137.64; ν_{max} (neat) 2971, 1522, 1318, 1260, 1134, 1038, 855, 671 cm^{-1} ; ESI-HRMS m/z calcd for $\text{C}_{16}\text{H}_{27}\text{B}_2\text{O}_4\text{S}$ (M^+): 337.1811; found: 337.1718.

5,5'-Bis(4,4,5,5-tetramethyl-1,3,2-dioxaborolan-2-yl)-2,2'-bithiophene (3b). Yield: 99%. ^1H NMR (400 MHz, CDCl_3) δ 1.35 (s, 24H), 7.28 (d, $J = 8.4$ Hz, 2H), 7.52 (d, $J = 8.4$ Hz, 2H); ^{13}C

NMR (100 MHz, CDCl₃) δ 24.76, 84.21, 125.60, 137.95, 143.83; ν_{\max} (neat) 2983, 1513, 1434, 1327, 1253, 1134, 1069, 852, 654 cm⁻¹; ESI-HRMS m/z calcd for C₂₀H₂₉B₂O₄S₂ (M⁺): 419.1688; found: 419.1698.

5,5''-Bis(4,4,5,5-tetramethyl-1,3,2-dioxaborolan-2-yl)-2,2':5',2''-terthiophene (3c). Yield: 99%. ¹H NMR (400 MHz, CDCl₃) δ 1.35 (s, 24H), 7.14 (s, 2H), 7.23 (d, J = 3.6 Hz, 2H), 7.52 (d, J = 3.6 Hz, 2H); ¹³C NMR (100 MHz, CDCl₃) δ 24.77, 84.22, 124.97, 125.11, 136.63, 137.95, 143.61; ν_{\max} (neat) 3056, 2977, 1510, 1448, 1349, 1321, 1137, 1067, 849, 660 cm⁻¹; FI-HRMS m/z calcd for C₂₄H₃₁B₂O₄S₃ (M⁺): 501.1565; found: 501.1577.

2,6-Bis(4,4,5,5-tetramethyl-1,3,2-dioxaborolan-2-yl)benzo[1,2-*b*:4,5-*b'*]dithiophene (3d). Yield: 99%. ¹H NMR (400 MHz, CDCl₃) δ 1.39 (s, 24H), 7.90 (s, 2H); 8.36 (s, 2H); ¹³C NMR (100 MHz, CDCl₃) δ 24.83, 84.54, 117.52, 133.59, 139.31, 140.56; ν_{\max} (neat) 2983, 1539, 1443, 1395, 1298, 1137, 852, 660 cm⁻¹; ESI-HRMS m/z calcd for C₂₂H₂₉B₂O₄S₂ (M⁺): 443.1688; found: 443.1696.

2,6-Bis(4,4,5,5-tetramethyl-1,3,2-dioxaborolan-2-yl)-4,8-dihexyloxybenzo[1,2-*b*:4,5-*b'*]dithiophene (3e). Yield: 92%. ¹H NMR (400 MHz, CDCl₃) δ 0.93 (t, J = 6.8 Hz, 6H), 1.36–1.38 (m, 12H), 1.38 (s, 24H), 1.50–1.55 (m, 4H), 1.84–1.91 (m, 4H), 4.30 (t, J = 6.8 Hz, 4H), 8.01 (s, 2H); ¹³C NMR (100 MHz, CDCl₃) δ 14.10, 22.65, 24.71, 24.81, 25.66, 30.53, 31.70, 73.94, 84.55, 130.82, 132.98, 133.77, 144.82; ν_{\max} (neat) 2981, 2926, 2853, 1553, 1448, 1348, 1307, 1129, 846, 665 cm⁻¹; ESI-HRMS m/z calcd for C₃₄H₅₃B₂O₆S₂ (M⁺): 643.3464; found: 643.3472.

2,5-Bis(4,4,5,5-tetramethyl-1,3,2-dioxaborolan-2-yl)thieno-[3,2-*b*]thiophene (3f). Yield: 99%. ¹H NMR (400 MHz, CDCl₃) δ 1.36 (s, 24H), 7.75 (s, 2H); ¹³C NMR (100 MHz, CDCl₃) δ 24.79, 84.35, 128.87, 146.61; ν_{\max} (neat) 2983, 1485, 1338, 1259, 1134, 1030, 950, 849, 665 cm⁻¹; ESI-HRMS m/z calcd for C₁₈H₂₇B₂O₄S₂ (M⁺): 393.1531; found: 393.1539.

2,6-Bis(4,4,5,5-tetramethyl-1,3,2-dioxaborolan-2-yl)dithieno-[3,2-*b*:2',3'-*d*]thiophene (3g). Yield: 89%. ¹H NMR (400 MHz, CDCl₃) δ 1.36 (s, 24H), 7.76 (s, 2H); ¹³C NMR (100 MHz, CDCl₃) δ 24.78, 84.40, 130.27, 144.74; ν_{\max} (neat) 2977, 1499, 1383, 1250, 1132, 1020, 950, 849, 660 cm⁻¹; ESI-HRMS m/z calcd for C₂₀H₂₇B₂O₄S₃ (M⁺): 449.1252; found: 449.1259.

Synthesis of triarylamine derivative

A 20 mL Schlenk-tube equipped with a stir bar and a septum inlet was charged with Ir-BPy-PMO (32.0 mg, 0.005 mmol Ir) and tris(4-(2-thienyl)phenyl)amine **4** (72 mg, 0.15 mmol) and then

flushed with argon. Dry cyclohexane (2.0 mL) and HBpin (95 μL , 0.66 mmol) were added, and the mixture was stirred at 80 °C for 12 h. The mixture was diluted with CHCl_3 (5 mL) and filtered through a membrane filter (0.20 μm). The solvent was removed under reduced pressure. The crude product was washed with cold hexane (1 mL) to afford analytically pure triborylated amine **4'**. Yield: 98%. ^1H NMR (400 MHz, CDCl_3) δ 1.36 (s, 36H), 7.13 (d, $J = 8.8$ Hz, 6H), 7.32 (d, $J = 3.6$ Hz, 3H), 7.55 (d, $J = 8.8$ Hz, 6H), 7.58 (d, $J = 3.6$ Hz, 3H); ^{13}C NMR (100 MHz, CDCl_3) δ 24.79, 84.11, 123.85, 124.42, 127.10, 129.13, 138.23, 146.73, 150.92; ν_{max} (neat) 2977 1601, 1530, 1451, 1318, 1140, 1070, 950, 850, 804, 665 cm^{-1} ; ESI-HRMS m/z calcd for $\text{C}_{48}\text{H}_{55}\text{B}_3\text{NO}_6\text{S}_3$ (M^+): 870.3465; found: 870.3484. A 50 mL two-neck flask connected to a condenser was charged with a stir bar, triborylated amine **4'** (100 mg, 0.11 mmol), tripotassium phosphate (146 mg, 0.69 mmol), and $\text{Pd}(\text{PPh}_3)_4$ (12 mg, 10.3 μmol). Dry 1,4-dioxane (7.5 mL), degassed distilled water (0.75 mL), and bromobenzene (108 mg, 0.69 mmol) were added. The reaction mixture was stirred at 80 °C for 20 h. After cooling to room temperature, the reaction mixture was diluted with water and extracted with CH_2Cl_2 . The combined organic layers were dried over anhydrous MgSO_4 , filtered, and then the solvent was completely evaporated. The residue was purified using silica gel chromatography (eluent: hexane/ $\text{CH}_2\text{Cl}_2 = 10 : 1$) to yield **5** (77 mg, 92%) as a yellow powder. ^1H NMR (400 MHz, $\text{THF}-d_8$) δ 7.15 (d, $J = 8.8$ Hz, 6H), 7.23 (t, $J = 8.0$ Hz, 3H), 7.32 (d, $J = 3.6$ Hz, 3H), 7.36 (d, $J = 8.0$ Hz, 6H), 7.37 (d, $J = 3.6$ Hz, 3H), 7.68 (d, $J = 8.8$ Hz, 6H), 7.64 (d, $J = 8.4$ Hz, 6H); ^{13}C NMR (100 MHz, $\text{THF}-d_8$) δ 124.44, 125.00, 125.31, 126.05, 127.22, 128.12, 129.67, 130.27, 135.28, 143.67, 143.96, 147.51; ν_{max} (neat) 3016, 2909, 1595, 1482, 1315, 1265, 798, 750, 690 cm^{-1} ; ESI-HRMS m/z calcd for $\text{C}_{48}\text{H}_{34}\text{NS}_3$ ($\text{M}+\text{H}^+$): 720.1848; found: 720.1842.

GC–MS analyses of side products after the reaction of Ir-BPy-PMO with boron reagent

A 20 mL Schlenk-tube equipped with a stir bar and a septum inlet was charged with Ir-BPy-PMO (173 mg, 27 μmol Ir) and then flushed with argon. Then, dry cyclohexane (3.0 mL) and HBpin (58 μL , 0.40 mmol) were added, and the mixture was stirred at 80 °C for 3 h. In the case of B_2pin_2 , B_2pin_2 (51 mg, 0.20 mmol) was directly charged with Ir-BPy-PMO in the Schlenk-tube. The mixture was filtered through a membrane filter (0.20 μm). The obtained reaction solution was analyzed using GC mass spectroscopy. The amount of side product was determined using the calibration curve obtained from known standard chemicals. In the case of HBpin system,

cyclooctane (7.5 μmol), *cis*-cyclooctene (0.03 μmol) and MeOBpin (1.8 μmol) were obtained. In the case of B₂pin₂ system, cyclooctane (0.94 μmol), *cis*-cyclooctene (0.19 μmol), cyclooctadiene (0.008 μmol), and MeOBpin (1.35 μmol) were obtained.

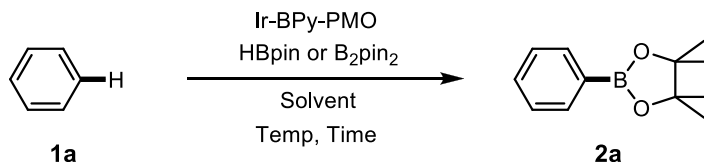
5.2.3 Results and Discussion

Direct C–H borylation of benzene

The heterogeneous Ir-BPy-PMO was prepared according to the literature with a slight modification. The Ir–bipyridine complex was formed on the pore surface of BPy-PMO end-capped with TMS groups without the loss of parent mesoporous structure. The density functional theory pore diameter (d_{DFT}), Brunauer–Emmett–Teller surface area (S_{BET}) and pore volume ($V_{t\text{-plot}}$) were 3.5 nm, 519 m² g⁻¹, and 0.23 cm³ g⁻¹, respectively. The amount of Ir was 0.15–0.16 mmol g⁻¹ which indicated that about 8 mol% of surface bipyridine groups in the BPy-PMO coordinated with Ir.

The benchmark reactions between benzene and HBpin or B₂pin₂ (**1a**, 30 equiv relative to boron atom in the boron reagent) were investigated using the heterogeneous Ir-BPy-PMO catalyst (0.75 mol% Ir relative to boron atom in the boron reagent) under various conditions (Table 5.3). Unlike the homogeneous Ir–bipyridine system,^{4b} the reaction with HBpin did not occur at room temperature even after a prolonged reaction time (Table 5.3, entry 1). However, increasing the reaction temperature gradually promoted the reaction with HBpin and produced the desired phenylboronate ester (**2a**) as the sole product (Table 5.3, entries 2–4). At 80 °C, product **2a** was obtained in an excellent yield of 94% (Table 5.3, entry 4). These results suggest that heating is required for Ir-BPy-PMO, possibly due to the higher activation energy owing to lower flexible environment around the Ir catalytic centers and/or lower diffusion efficiency of the molecules around the catalyst compared to the homogeneous catalytic system. The loading amount of catalyst could be reduced to 0.125 mol% Ir without significant loss of product yield, which resulted in an increase in turnover number (TON) calculated as moles of product/moles of iridium in Ir-BPy-PMO to 728 (Table 5.3, entry 5). This value is higher than those for previously reported heterogeneous metal complex catalysts, such as BPDCA-cat (TON of 55)¹⁰ and silica-SMAP-Ir (TON of 204)¹¹

¹⁰ a) Tagata, T.; Nishida, M.; Nishida, A. *Tetrahedron Lett.* **2009**, *50*, 6176–6179; b) Tagata, T.; Nishida, M.; Nishida, A. *Adv. Synth. Catal.* **2010**, *352*, 1662–1666; c) Nishida, M.; Tagata, T. *J. Synth. Org. Chem., Jpn.*

Table 5.3. Catalytic activities of Ir-BPy-PMO catalyst in direct C–H borylation of benzene with HBpin and B₂pin₂^a

Entry	Boron reagent	Solvent	<i>T</i> / °C	Time / °C	Yield / % ^b	TON ^c
1	HBpin	Neat	25	24	0	0
2		Neat	40	12	16	17
3		Neat	60	12	66	88
4		Neat	80	3	94	125
5		Neat	80	24	91	728
6 ^d	B ₂ pin ₂	CyH	80	12	91	121
7		Neat	25	24	0	0
8		Neat	40	12	0	0
9		Neat	60	12	28	38
10		Neat	80	4	94	125
11 ^d		CyH	80	12	26	34

^a The reactions were conducted with benzene (**1a**, 30 equiv relative to boron atom in boron reagents) and HBpin (1 equiv) or B₂pin₂ (0.5 equiv) in the presence of Ir-BPy-PMO (0.125–0.75 mol% Ir). ^b Isolated yields based on boron atom in boron reagents. ^c TON was calculated as moles of product/moles of iridium in Ir-BPy-PMO. ^d The reaction was conducted with **1a** (2 equiv) in CyH (cyclohexane).

for the direct C–H borylation of benzene under almost the same reaction conditions. Although a high TON of 640 was reported for Ir-bpy^{1/10}-PMO,⁷ it was based on conversion of moles of diboron/moles of iridium in the catalyst. Furthermore, the amount of benzene relative to HBpin could be reduced to 2 equiv with sufficient product yield (Table 5.3, entry 6).

The reaction efficiency of benzene with HBpin was higher than that with B₂pin₂. The maximum conversion of B₂pin₂ below 60 °C was 28%, which is less than half the performance of the HBpin system under the same conditions (Table 5.3, entries 7–9 vs. entry 3). At temperatures

2011, 69, 1212–1220.

¹¹ Kawamorita, S.; Ohmiya, H.; Hara, K.; Fukuoka, A.; Sawamura, M. *J. Am. Chem. Soc.* **2009**, *131*, 5058–5059.

higher than 80 °C, the product yield increased up to 94% similar to the HBpin system (Table 5.3, entry 10). However, the reaction conducted with cyclohexane as the solvent at 80 °C gave **2a** in only 26% yield (Table 5.3, entry 11).

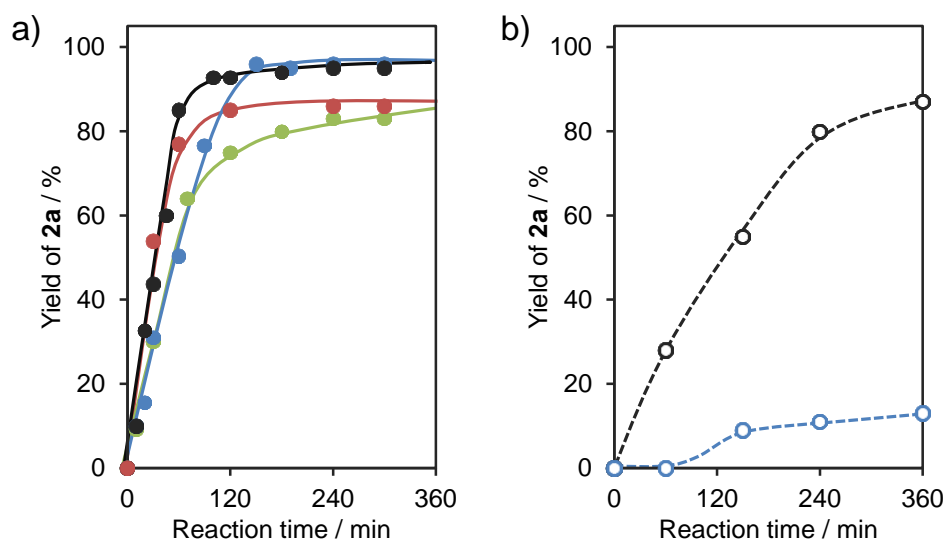


Figure 5.29. Reaction kinetic curves of C–H borylation of benzene catalyzed by a) Ir-BPy-PMO with HBpin (black line) or B₂pin₂ (blue line) and [Ir(bpy)(OMe)(cod)] with HBpin (red line) or B₂pin₂ (green line) under neat benzene conditions and b) Ir-BPy-PMO with HBpin (black broken line) or B₂pin₂ (blue broken line) under diluted conditions with cyclohexane. These reactions were conducted with benzene (**1a**, 30 equiv relative to boron atom in boron reagents) or benzene (**1a**, 2 equiv) in cyclohexane (2 mL) and HBpin (1 equiv) or B₂pin₂ (0.5 equiv) in the presence of Ir-BPy-PMO or [Ir(bpy)(OMe)(cod)] (0.75 mol% Ir).

The reaction kinetics were compared for HBpin and B₂pin₂ as the boron source for Ir-BPy-PMO catalyzed C–H borylation of benzene under neat conditions and diluted conditions with cyclohexane as shown in Figure 5.29. Under neat conditions, both reactions proceeded efficiently without an induction period. The initial rate for the HBpin system was faster than that for the B₂pin₂ system. The TOF at initial 1 h for the HBpin system reached 113 h⁻¹, which is 1.7 times higher than that for the B₂pin₂ system (67 h⁻¹) (Figure 5.29a). A similar trend was observed in the homogeneous catalytic system. This trend was also observed in the reaction conducted with cyclohexane as the solvent. The reaction with B₂pin₂ proceeded after an induction period of 1 h and

the TOF was 8 h^{-1} . On the other hand, the reaction with HBpin proceeded without an induction period and the TOF for the HBpin system was 37 h^{-1} , which is 4.6 times higher than that for the B_2pin_2 system (Figure 5.29b).

In the homogeneous system, borylation was demonstrated to proceed through an Ir–boryl complex as an active intermediate. The Ir–boryl intermediate was generated by elimination of methoxy and cod ligands and formed more easily from HBpin than B_2pin_2 .¹² The author observed side products by GC–MS analysis, such as 2-methoxy-4,4,5,5-tetramethyl-1,3,2-dioxaborolane (MeOBpin) and cyclooctane from the eliminated methoxy and cod ligands in the filtrate after the reaction (see the Experimental section). The amount of side products was larger for the reaction system using HBpin than B_2pin_2 in cyclohexane, indicating higher reactivity of HBpin with Ir-BPy-PMO similar to the homogeneous system. These studies clearly indicate that the use of HBpin is effective for formation of an Ir–boryl complex on the pore surface of the Ir-BPy-PMO precatalyst.

During the course of this study, the author found that the Ir-BPy-PMO precatalyst could be weighed under air. The recovery and reusability of Ir-BPy-PMO were also examined. After the reaction, the solid catalyst could be easily removed from the reaction mixture by simple filtration using a membrane filter ($0.20 \mu\text{m}$) without iridium contamination ($< 1.0 \text{ ppm}$) in the filtrate. The author observed no elution of bipyridine ligand in the filtrate by GC–MS analyses. These results indicate that the ratio of Ir/bipyridine was unchanged after the reaction. The X-ray diffraction patterns and the nitrogen adsorption/desorption isotherms showed that the mesoporous structure of Ir-BPy-PMO almost completely remained (Figure 5.30). The author also found that the recovered Ir-BPy-PMO, which was quickly filtered under air, still showed high catalytic activity in the C–H borylation of benzene with HBpin. Successive recycle reactions could be performed under similar reaction conditions at least three times, although the reaction rate and product yield were gradually decreased (1st recycle: 88% after 5 h, 2nd recycle: 85% after 5 h, 3rd recycle: 69% after 8 h). The lowered catalytic performance might be due to partial deactivation of the active site during the recovery operation and/or recycle reaction.

¹² a) Boller, T. M.; Murphy, J. M.; Hapke, M.; Ishiyama, T.; Miyaura, N.; Hartwig, J. F. *J. Am. Chem. Soc.* **2005**, *127*, 14263–14278; b) Tamura, H.; Yamazaki, H.; Sato, H.; Sakaki, S. *J. Am. Chem. Soc.* **2003**, *125*, 16114–16126.

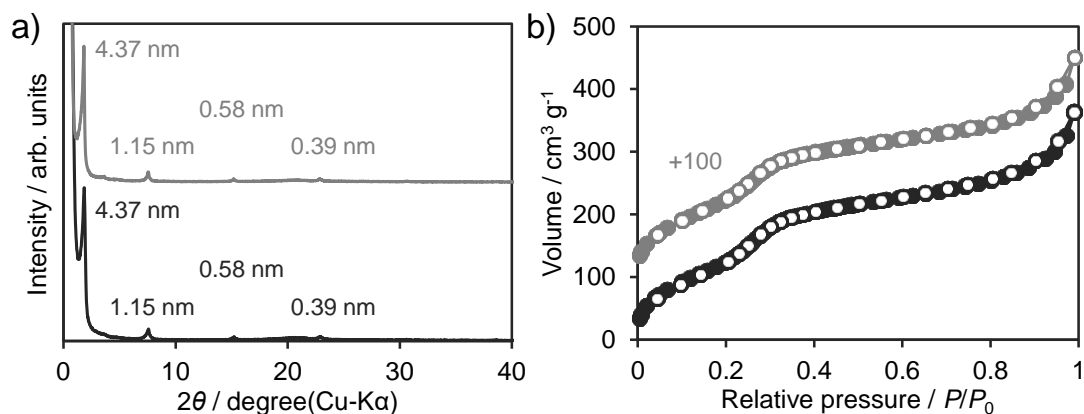


Figure 5.30. Structural properties of Ir-BPy-PMO before (black line) and after 3rd reactions (gray line). a) XRD profiles and b) nitrogen adsorption/desorption isotherms (closed circle: adsorption, open circle: desorption).

Direct C–H borylation of substituted arenes and heteroarenes

The scope and limitations of Ir-BPy-PMO catalyzed direct C–H borylation were then examined with various types of arenes and heteroarenes with HBpin and B₂pin₂ under optimized conditions (Table 5.4). For electron-poor arenes such as methyl benzoate (**1b**) and benzotrifluoride (**1c**), the reactions proceeded effectively with HBpin even under dilute conditions in cyclohexane, providing the arylboronates **2b** and **2c** in 86% and 91% yield, respectively (Table 5.4, entries 1 and 2). In contrast, the reactions by B₂pin₂ provided the products in low yield, possibly due to the inefficient formation of active intermediates as observed for benzene. For electron-rich monosubstituted arenes such as toluene (**1d**) and anisole (**1e**), the reactions with HBpin and B₂pin₂ did not efficiently occur under dilution conditions, and resulted in formation of arylboronates **2d** and **2e** in low yield, respectively (Table 5.4, entries 3 and 5). This result can be explained by the fact that reactivities of electron-rich arenes are usually lower than those of electron-poor arenes for direct C–H borylation. A similar trend has been observed for other homogeneous catalytic systems.¹³ In order to investigate the reaction behaviors, kinetic study was carried out for direct C–H borylation of benzene vs. 1,3-dichlorobenzene (Figure 5.31). The reaction of benzene and 1,3-dichlorobenzene between HBpin in cyclohexane finished within 8 h and 2 h, respectively. Although the molecular size of 1,3-dichlorobenzene is larger than that of benzene, the TOF at initial 60 min for

¹³ Iverson, C. N.; Smith, III, M. R. *J. Am. Chem. Soc.* **1999**, *121*, 7696–7697.

1,3-dichlorobenzene reached 121 h^{-1} , which is about 3.3 times higher than that for benzene (37 h^{-1}). This suggests that reaction kinetics mainly affected by electronic structure and density of substrates

Table 5.4. Direct C–H borylation of arenes and heteroarenes with HBpin catalyzed by Ir-BPy-PMO^a

Entry	Arylboronate	Yield / % ^b	Entry	Arylboronate	Yield / % ^b
1		86 ^d (7)	10		91 (47)
2		91 ^e (52)	11		92 (0)
3		23 (23)	12		93 ^j (0)
4 ^d		92 ^d (85) ^g	13		90 (0)
5		17 (3)	14		92 ^k (0)
6 ^d		86 ^h (88) ⁱ	15		93 (79)
7 ^c		68 (60)	16		92 (0)
8		95 (85)			
9		94 (81)			

^a The reactions were conducted with arenes **1** (2 equiv), HBpin (1 equiv) or B₂pin₂ (0.5 equiv), and Ir-BPy-PMO (0.75 mol% Ir) in CyH. ^b Isolated yields based on HBpin. Isolated yields based on boron atom in B₂pin₂ are given in parentheses. ^c The reactions were carried out under neat conditions. ^d *m*: *p* = 53 : 47. ^e *m*: *p* = 69 : 31. ^f *m*: *p* = 60 : 40. ^g *m*: *p* = 63 : 37. ^h *m*: *p* = 51 : 49. ⁱ *m*: *p* = 63 : 37. ^j 2-isomer : 3-isomer = 86 : 14. ^k 2-isomer : 3-isomer = 80 : 20.

rather than the size of substrate. However, the neat reaction conditions allowed for the borylations of **1d** and **1e** with HBpin or B₂pin₂ to give **2d** and **2e** in high yields of 85–92% (Table 5.4, entries 4 and 6).

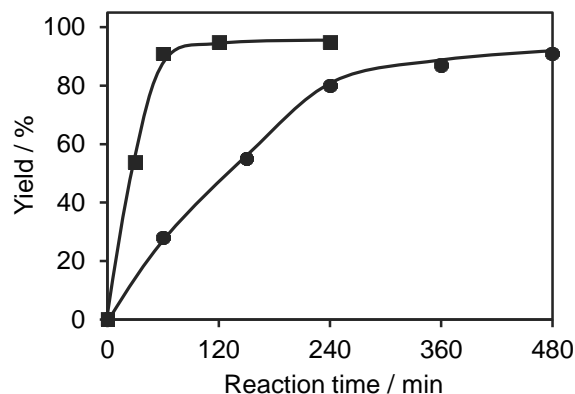


Figure 5.31. Reaction kinetic curves of direct C–H borylation of benzene (●), 1,3-dichlorobenzene (■) catalyzed by Ir-BPy-PMO with HBpin under dilute condition in cyclohexane.

In the cases of mono-substituted arenes, the arylboronates were obtained as a mixture of regioisomers. Although the ratio of regioisomers was dependent on the substrates, the *m*-isomer was preferentially obtained, whereas the *o*-isomer did not form, possibly due to the steric hindrance of the substituents. This regioselectivity was commonly observed for the typical homogeneous catalytic system.⁴ This suggests that the chemical environment of the active site is not strongly affected by the solid bipyridine ligand and the molecular nature of the active site is retained in the pore walls. For 1,2- and 1,3-disubstituted arenes, regioselective borylation occurred to afford a single regioisomer of the product in yields of 68–95% (Table 5.4, entries 7–10). The high regioselectivity can be explained by steric hindrance of the two substituents on the benzene ring.⁴ Electron-poor arenes such as **1g–1h** could be easily transformed into the corresponding arylboronates, whereas electron-rich arene **1f** showed sluggish reactivity even under neat conditions.

A variety of heteroarenes such as thiophene, furan, benzo[*b*]thiophene, benzofuran, indole, and pyridine were also transformed into the corresponding heteroarylboronates by a combination of Ir-BPy-PMO and HBpin in cyclohexane (Table 5.4, entries 11–16). Thiophene, benzo[*b*]thiophene, and indole exclusively formed the corresponding α -substituted heteroarylboronate esters **2j**, **2l**, and

2n, respectively, in yields of 90–93%. This is due to the high acidity of the α -positions from the electronegative heteroatom in the five-membered rings.¹⁴ Furan derivatives **1k** and **1m** selectively gave the 2-isomer of boronate esters in addition to a small amount of the 3-isomer. The reaction of 2,6-dichloropyridine (**1o**) occurred only at the 4-position, due to the substituents blocking the 2,6-positions to yield a pure regioisomer **2o**. It should be noted that the catalytic performance of Ir-BPy-PMO using HBpin is almost comparable with those of homogeneous Ir–bipyridine systems. However, almost no activity of Ir-BPy-PMO was observed for the reactions between B₂pin₂ and some kinds of heteroarenes containing thiophene, furan, and pyridine. The reason is not clear at this moment. A detailed investigation on these behaviors and the reaction mechanism are currently underway in the author's laboratory.

Multiple C–H borylation of thiophene derivatives

The development of an efficient synthetic method for arylene and heteroarylene-bridged boronate esters has been of interest in fundamental organic chemistry. In particular, recent advances in polymer chemistry have focused on thiophenes containing donor–acceptor molecular structures suitable for producing photoluminescence and energy-harvesting materials.¹⁵ The author utilized Ir-BPy-PMO catalytic systems using HBpin and B₂pin₂ as a synthetic approach for multiboronated building blocks (Table 5.5).

For HBpin system, thiophene could be easily diborylated at the α -positions as well as the ladder-type derivatives such as 2,2'-bithiophene and 2,2':5',2''-terthiophene to afford the desired diboronates **3a–3c**, respectively. The product yields were much higher than that of boronate syntheses via conventional magnesium or lithium intermediates.¹⁶ The kinetic studies on direct C–H borylation of the thiophene derivatives revealed that double C–H borylation proceeded efficiently within 1 h even large size of 2,2':5',2''-terthiophene. These results clearly indicate that high activity of α -positions of thiophene ring compared with aromatic ring such as benzene (Figure 5.32).

¹⁴ Ishiyama, T.; Nobuta, Y.; Hartwig, J. F.; Miyaura, N. *Chem. Commun.* **2003**, 2924–2925.

¹⁵ Perepichka, I. F.; Perepichka, D. F. *Handbook of Thiophene-Based Materials: Applications in Organic Electronics and Photonics*, John Wiley & Sons, Ltd, 2009, pp. 1–155.

¹⁶ a) Usta, H.; Lu, G.; Facchetti, A.; Marks, T. J. *J. Am. Chem. Soc.* **2006**, *128*, 9034–9035; b) Hellberg, J.; Remonen, T.; Allared, F.; Slatt, J.; Svensson, M. *Synthesis* **2003**, 2199–2205.

Table 5.5. Multiple borylation of heteroarenes with HBpin catalyzed by Ir-BPy-PMO^a

Reaction scheme: A heteroarene with two C-H bonds reacts with HBpin or B₂pin₂ in the presence of Ir-BPy-PMO and CyH at 80 °C for 12 h to yield a bis-borylated product (3a-g).

Entry	Heteroarene	Heteroarylboronate	Yield / % ^b
1			99 (0)
2			99 (0)
3			99 (0)
4			99 (0)
5			95 (0)
6			99 (0)
7			89 (0)

^a All reactions were conducted with heteroarenes (1 equiv) and HBpin (3.0 equiv) in the presence of Ir-BPy-PMO (1.1 mol% Ir per C-H bond in heteroarene). ^b Isolated yields. Isolated yields based on boron atom in B₂pin₂ are given in parentheses.

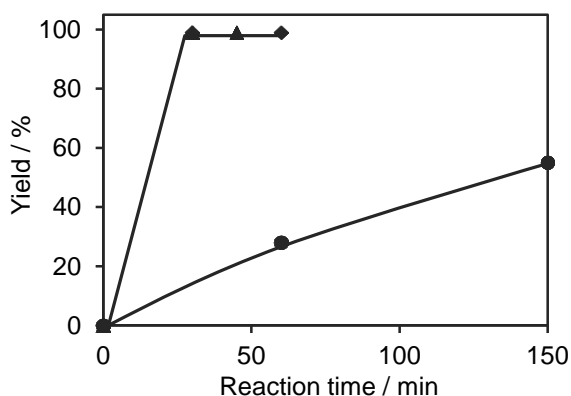


Figure 5.32. Reaction kinetic curves of direct C–H borylation of thiophene (▲), 2,2':5',2''-terthiophene (■), and benzene (●) catalyzed by Ir-BPy-PMO with HBpin under dilute condition in cyclohexane.

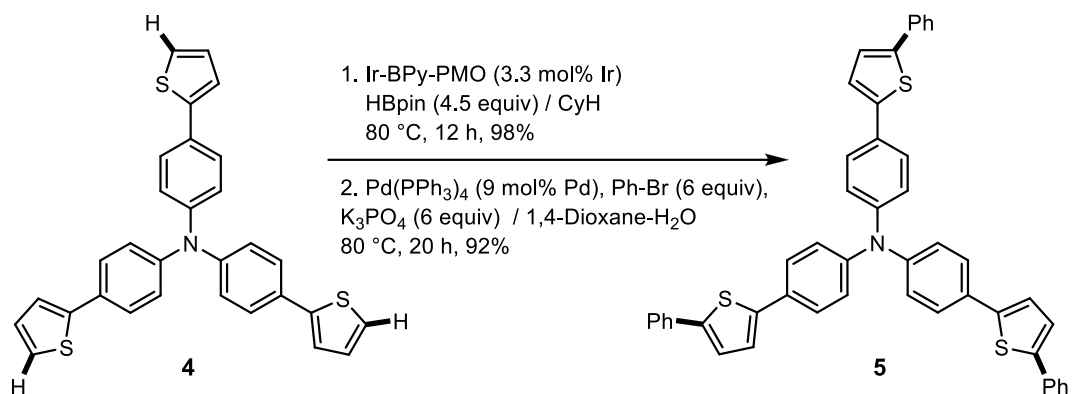
Benzo[1,2-*b*:4,5-*b'*]dithiophene could also be transformed into the diboronated building block **3d**. The introduction of alkoxy groups on the benzo[1,2-*b*:4,5-*b'*]dithiophene skeleton did not significantly affect the yield of product **3e** and regioselectivity. Moreover, diboronated fused-thiophene derivatives containing thieno[3,2-*b*]thiophene and dithieno[3,2-*b*:2',3'-*d*]thiophene were also borylated regioselectively to afford **3f** and **3g**. Notably, all reactions successfully occurred with complete conversion of substrates and excellent yields of 89–99%. The products could be easily isolated after evaporation of the reaction solvents and extraction with cold hexane to remove the excess HBpin. These diboronated products can be used as useful building blocks for π -conjugated functional materials.¹⁷ However, almost no activity was observed for borylation of all thiophene derivatives with B₂pin₂.

Starting from tris[4-(2-thienyl)phenyl]amine **4**,¹⁸ high hole-transporting triarylamine derivative **5** could be readily obtained by direct C–H borylation followed by Suzuki–Miyaura coupling reaction to afford a 90% yield over two steps (Scheme 5.2). Unlike conventional

¹⁷ a) Cheng, Y.-J.; Yang, S.-H.; Hsu, C.-S. *Chem. Rev.* **2009**, *109*, 5868–5923; b) Ong, B. S.; Wu, Y.; Liu, P.; Gardner, S. *J. Am. Chem. Soc.* **2004**, *126*, 3378–3379; c) Pan, H.; Li, Y.; Wu, Y.; Liu, P.; Ong, B. S.; Zhu, S.; Xu, G. *J. Am. Chem. Soc.* **2007**, *129*, 4112–4113; d) McCulloch, I.; Heeney, M.; Bailey, C.; Genevicius, K.; MacDonald, I.; Shkunov, M.; Sparrowe, D.; Tierney, S.; Wagner, R.; Zhang, W.; Chabinyc, M. L.; Kline, R. J.; McGehee, M. D.; Toney, M. F. *Nat. Mater.* **2006**, *5*, 328–333; e) Jung, J. W.; Liu, F.; Russell, T. P.; Jo, W. H. *Energy Environ. Sci.* **2012**, *5*, 6857–6861.

¹⁸ Ohishi, H.; Tanaka, M.; Kageyama, H.; Shirota, Y. *Chem. Lett.* **2004**, *33*, 1266–1267.

approaches using the Grignard coupling reaction (9% yield), a remarkable improvement in product yield was achieved by adopting this approach.¹⁹ This result demonstrated that thiophene-based boronated building blocks are effective and useful in the synthesis of functional organic materials.



Scheme 5.2. Synthesis of hole-transporting triarylamine derivative **5** by direct C–H borylation of **4** followed by Suzuki–Miyaura coupling reaction.

5.2.4 Conclusions

The author developed an efficient heterogeneous Ir-bipyridine-PMO catalyst using inexpensive pinacolborane as a boron source for direct C–H borylation. A wide range of arenes and heteroarenes were successfully borylated with high boron efficiency. The Ir-BPy-PMO catalyst could be weighed in the absence of an inert atmosphere outside a glove box. The PMO catalyst after reaction could be easily recovered from the reaction mixture by filtration under air. The recovered PMO catalyst still showed good catalytic activity. The combination of Ir-BPy-PMO and pinacolborane could be applied to the synthesis of multi-boronated thiophene-based building blocks containing ladder-, acenefused-, and fused-thiophene skeletons. The author demonstrated that one synthetic building block was readily utilized to give a functional hole-transporting organic material in high yield. The uses of the solid catalyst and inexpensive pinacolborane are expected to be superior to conventional approaches in the development of industrial applications.

¹⁹ a) Kageyama, H.; Ohishi, H.; Tanaka, M.; Ohmori, Y.; Shirota, Y. *Adv. Funct. Mater.* **2009**, *19*, 3948–3955; b) Kageyama, H.; Ohishi, H.; Tanaka, M.; Ohmori, Y.; Shirota, Y. *Appl. Phys. Lett.* **2009**, *94*, 063304.

5.3 Epoxidation of Olefins by Mo-immobilized BPy-PMO Catalyst

The dichlorodioxomolybdenum(VI) complex (MoO_2Cl_2) is an efficient and low-cost homogeneous catalyst for a variety of organic reactions, but its activity usually decreases after immobilization on a solid support. This report describes the synthesis of heterogeneous Mo complex catalysts using a bipyridine-periodic mesoporous organosilica (BPy-PMO) as a solid chelating ligand and MoO_2Cl_2 as a precursor, and their catalysis in the epoxidation of olefins with *tert*-butyl hydroperoxide (TBHP). The $\text{MoO}_2\text{Cl}(\text{OH})$ complex could be immobilized on trimethylsilylated BPy-PMO (BPy-PMO-TMS), which was confirmed by Fourier-transform infrared spectroscopy, Raman spectroscopy, and X-ray absorption fine structure analysis. The Mo complex immobilized on BPy-PMO-TMS exhibited greater catalytic activity for the epoxidation of *cis*-cyclooctene compared with conventional heterogeneous Mo complex catalysts using mesoporous silica, polystyrene, and naked BPy-PMO as supports. A large amount (up to 0.72 mmol g^{-1}) of the Mo complex could be loaded on BPy-PMO-TMS, which resulted in 37% of the exposed bipyridine ligands on the surface forming Mo complexes. The turnover frequency relative to Mo was nearly constant, even with a high density of Mo complex on the pore surface. The Mo-BPy-PMO-TMS catalyst exhibited a solvent effect on the catalysis, and the presence of water in the reaction medium was detrimental for the catalysis. Under anhydrous conditions, Mo-BPy-PMO-TMS showed good catalytic activity for at least three reuse cycles in the epoxidation of *cis*-cyclooctene. A variety of olefins including aliphatic and aromatic olefins were successfully oxidized by Mo-BPy-PMO-TMS to give the desired epoxides in high yield.

5.3.1 Introduction

The use of recoverable and reusable heterogeneous metal complex catalysts, instead of homogeneous catalysts, for batch and flow-through systems is of interest in the development of environmentally friendly chemical processes.^{1,2} Flow-through reactions require highly active catalysts because the contact time for column reactors is generally shorter than that for batch

¹ Kobayashi, S.; Akiyama, R. *Chem. Commun.* **2003**, 449–460.

² De Vos, D. E.; Dams, M.; Sels, B. F.; Jacobs, P. A. *Chem. Rev.* **2002**, *102*, 3615–3640.

systems.³ Therefore, a large amount of active metal complex must be immobilized on a solid support to prevent a loss of activity. However, the intrinsic catalytic activity of metal complexes usually decreases after immobilization on conventional solid supports due to unfavorable interactions between the active sites and the heterogeneous solid surface.^{1,4} In addition, high-density immobilization usually causes aggregation of the metal complex on the support, thus decreasing activity.⁵

Recently, the synthesis of a new periodic mesoporous organosilica (PMO) containing 2,2'-bipyridine (BPy) ligands within the framework (BPy-PMO) has been reported.⁶ The BPy-PMO had a molecularly well-defined pore surface structure in which bipyridine ligands were regularly and densely arranged in the siloxane network. The neighboring BPy-BPy distance was approximately 0.44 nm, estimated by a molecular mechanics simulation, which indicated that an extremely high density of BPy ligands existed within the pore walls (elemental analysis indicated that the total amount of BPy ligand in BPy-PMO was 3.18 mmol g⁻¹). Furthermore, BPy-PMO had a large specific surface area (> 600 m² g⁻¹) and large pore size (3.8 nm in diameter), which allowed the smooth diffusion of reactant and product molecules in the mesochannels. Therefore, BPy-PMO was expected to function as a unique solid support that could immobilize a large amount of metal complexes without a loss of activity. Heterogeneous catalysis has been reported for precious metal complexes formed on BPy-PMO such as Ir(OMe)(cod)(BPy-PMO),^{6,7} Ru(bpy)₂(BPy-PMO),⁶ RuCl₂(CO)₂(BPy-PMO),⁸ and Cp*IrCl(BPy-PMO).⁹ However, no report has described the formation of base metal complexes, such as a Mo complex, on BPy-PMO.

Dichlorodioxomolybdenum(VI) complexes, such as [MoO₂Cl₂(L)_n] (L: neutral ligand), have attracted attention as efficient and low-cost homogeneous catalysts for a variety of organic reactions including epoxidation,¹⁰ acylation,¹¹ hydrosilylation,¹² reduction,¹³ and oxidation.¹⁴ Due to their

³ Tsubogo, T.; Oyamada, H.; Kobayashi, S. *Nature* **2015**, *520*, 329–332.

⁴ Hübner, S.; de Vries, J. G.; Farina, V. *Adv. Synth. Catal.* **2016**, *358*, 3–25.

⁵ Copéret, C.; Comas-Vives, A.; Conley, M. P.; Estes, D. P.; Fedorov, A.; Mougél, V.; Nagae, H.; Núñez-Zarur, F.; Zhizhko, P. A. *Chem. Rev.* **2016**, *116*, 323–421.

⁶ Waki, M.; Maegawa, Y.; Hara, K.; Goto, Y.; Shirai, S.; Yamada, Y.; Mizoshita, N.; Tani, T.; Chun, W. J.; Muratsugu, S.; Tada, M.; Fukuoka, A.; Inagaki, S. *J. Am. Chem. Soc.* **2014**, *136*, 4003–4011.

⁷ Maegawa, Y.; Inagaki, S. *Dalton Trans.* **2015**, *44*, 13007–13016.

⁸ Ishito, N.; Kobayashi, H.; Nakajima, K.; Maegawa, Y.; Inagaki, S.; Hara, K.; Fukuoka, A. *Chem.–Eur. J.* **2015**, *21*, 15564–15569.

⁹ Liu, X.; Maegawa, Y.; Goto, Y.; Hara, K.; Inagaki, S. *Angew. Chem., Int. Ed.* **2016**, *55*, 7943–7947.

¹⁰ Kühn, F. E.; Groarke, M.; Bencze, É.; Herdtweck, E.; Prazeres, A.; Santos, A. M.; Calhorda, M. J.; Romão,

attractive catalytic properties and the potential for environmentally friendly (“green”) chemistry, attempts have been made to heterogenize $\text{MoO}_2\text{Cl}_2(\text{L})_n$ using solid supports such as mesoporous silica,¹⁵ metal–organic frameworks (MOF),¹⁶ and hydrotalcite (Figure 5.33).¹⁷ However, in most cases, the catalytic activity of $\text{MoO}_2\text{Cl}_2(\text{L})_n$ decreased significantly after immobilization.

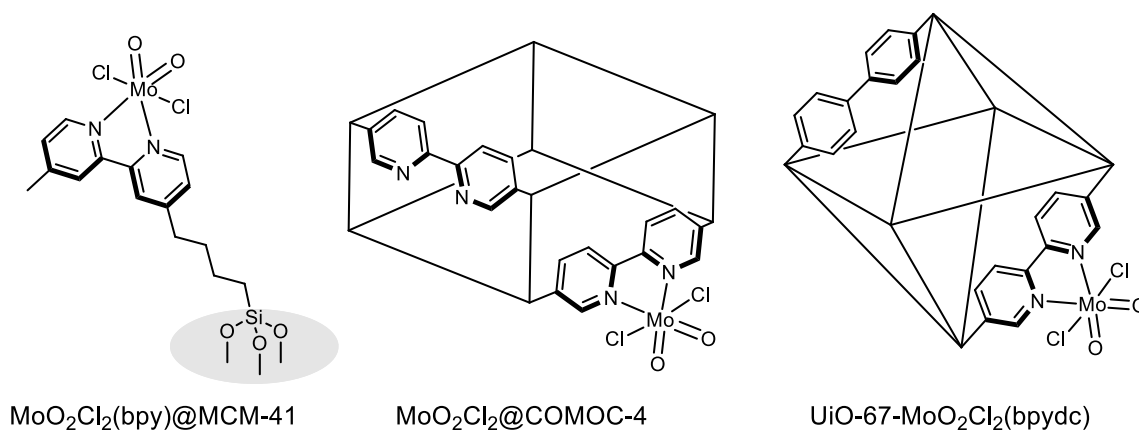


Figure 5.33. Heterogeneous $\text{MoO}_2\text{Cl}_2(\text{bpy})$ -based catalyst for epoxidation of olefins.

The present report describes the immobilization of MoO_2Cl_2 on BPy-PMO, and its catalysis for the epoxidation of olefins using *tert*-butyl hydroperoxide (TBHP). The Mo-immobilized BPy-PMO complexes were formed successfully using BPy-PMO end-capped with trimethylsilyl (TMS) groups on the silanol groups, without changing the ordered mesoporous and pore wall structures. The obtained Mo-BPy-PMO-TMS exhibited catalytic activity for the epoxidation of *cis*-cyclooctene, which was significantly greater than the activity of heterogeneous $\text{MoO}_2\text{Cl}_2(\text{bpy})$

C. C.; Gonçalves, I. S.; Lopes, A. D.; Pillinger, M. *Chem.–Eur. J.* **2002**, *8*, 2370–2383.

¹¹ Chen, C. T.; Kuo, J. H.; Pawar, V. D.; Munot, Y. S.; Weng, S. S.; Ku, C. H.; Liu, C. Y. *J. Org. Chem.* **2005**, *70*, 1188–1197.

¹² Sousa, S. C.; Cabrita, I.; Fernandes, A. C. *Chem. Soc. Rev.* **2012**, *41*, 5641–5653.

¹³ a) Fernandes, A. C.; Romão, C. C. *Tetrahedron Lett.* **2007**, *48*, 9176–9179; b) Fernandes, A. C.; Romão, C. C. *Tetrahedron* **2006**, *62*, 9650–9654; c) Fernandes, A. C.; Romão, C. C. *J. Mol. Catal. A: Chem.* **2006**, *253*, 96–98.

¹⁴ a) Jeyakumar, K.; Chand, D. *J. Chem. Sci.* **2009**, *121*, 111–123; b) de Noronha, R. G.; Fernandes, A. C. *Curr. Org. Chem.* **2012**, *16*, 33–64.

¹⁵ a) Nunes, C. D.; Valente, A. A.; Pillinger, M.; Fernandes, A. C.; Romão, C. C.; Rocha, J.; Gonçalves, I. S. *J. Mater. Chem.* **2002**, *12*, 1735–1742; b) Nunes, C. D.; Valente, A. A.; Pillinger, M.; Rocha, J.; Gonçalves, I. S. *Chem.–Eur. J.* **2003**, *9*, 4380–4390.

¹⁶ a) Leus, K.; Liu, Y. Y.; Meledina, M.; Turner, S.; Van Tendeloo, G.; Van Der Voort, P. A. *J. Catal.* **2014**, *316*, 201–209; b) Neves, P.; Gomes, A. C.; Amarante, T. R.; Paz, F. A. A.; Pillinger, M.; Gonçalves, I. S.; Valente, A. A. *Microporous Mesoporous Mater.* **2015**, *202*, 106–114.

¹⁷ Gago, S.; Pillinger, M.; Valente, A. A.; Santos, T. M.; Rocha, J.; Gonçalves, I. S. *Inorg. Chem.* **2004**, *43*, 5422–5431.

catalysts prepared by a conventional immobilization approach using bipyridine-grafted mesoporous silica, polystyrene, or nontrimethylsilylated (naked) BPy-PMO as solid supports. The relationship between the loading amount and catalytic activity, which has not been well studied for BPy-PMO,⁶⁻⁸ was also investigated. The Mo complexes could be formed on up to 37% of the BPy ligands exposed on the pore surface without a loss of catalytic activity. A hot-filtration experiment clearly indicated that the catalytic reaction proceeded without leaching of Mo species from BPy-PMO. Mo-BPy-PMO-TMS showed good recyclability for the epoxidation of *cis*-cyclooctene for at least three times and could be used for the epoxidation of a variety of olefins such as cyclic, terminal and internal aliphatic olefins, and aromatic olefins.

5.3.2 Experimental

Materials and methods

All chemicals were purchased from commercial suppliers (Sigma-Aldrich, Tokyo Chemical Industry Co., Ltd., and Wako Pure Chemical Industries, Ltd.) and used without further purification. The BPy-PMO and BPy-PMO end-capped with trimethylsilyl groups (BPy-PMO-TMS) were prepared according to a previously reported procedure.⁴ Gas chromatography (GC) mass analyses were performed using an Agilent 6890GC/5973MSD instrument equipped with a capillary column (HP-5MS, 0.25 mm × 30 m) and a flame ionization detector. ¹H NMR spectra were obtained using a Jeol ECX-400 spectrometer operating at 400 MHz. For the NMR experiments, the product yield was determined using the integral value of internal standards such as mesitylene or 1,4-dioxane. X-ray diffraction (XRD) profiles were recorded by a Rigaku RINT-TTR diffractometer using Cu-K α radiation (50 kV, 300 mA). Nitrogen adsorption/desorption isotherms were obtained using a Quantachrome Nova3000e sorptometer at liquid nitrogen temperature (-196 °C). Brunauer–Emmett–Teller (BET) surface areas were calculated from the linear sections of BET plots ($P/P_0 = 0.1-0.25$). Pore-size distributions were calculated using the DFT method (DFT kernel: N₂ at -196 °C on silica, cylindrical pores, nonlinear density functional theory (NLDFT) equilibrium model). Pore volumes were estimated using the *t*-plot method. Scanning electron microscopy (SEM) and energy dispersive X-ray spectrometry (EDX) were performed using a Hitachi S-3600N instrument. Fourier-transform infrared spectroscopy (FT-IR) was performed using a Thermo Fisher

Scientific Nicolet Avatar-360 FT-IR with an attenuated total reflection attachment (ATR). Raman analysis was conducted on a Jasco NRS-3300 instrument using an Ar laser (532 nm). X-ray absorption fine structure (XAFS) measurements at the Mo *K*-edge were conducted using a quick XAFS (QXAFS) method in transmission mode at BL14B2 of SPring-8. X-rays from the synchrotron were monochromatized using a Si(311) double-crystal monochromator. An ion chamber was used to detect I_0 (intensity of incident X-rays), and another placed behind the samples was used to detect I (intensity of transmitted X-rays). Background subtraction was performed with an Autobk and Spline smoothing algorithm.¹⁸ The extended X-ray absorption fine structure (EXAFS) was analyzed with Athena and Artemis using IFEFFIT. The k^3 -weighted Mo *K*-edge EXAFS oscillations (2–13 Å⁻¹) were Fourier transformed into *R*-space and curve fitting was carried out in *R*-space. The fitting parameters were the coordination number (CN), interatomic distance (*R*), Debye–Waller factor (σ^2), and correction-of-edge energy (ΔE_0). The phase shift and backscattering amplitudes were calculated using the FEFF6 code.

Immobilization of dichlorodioxomolybdenum(VI) complex

For preparation of Mo-BPy-PMO-TMS, reagent grade CH₃CN (> 99.5%, undried) was used. First, a 10 mM MoO₂Cl₂ solution was prepared using CH₃CN as the solvent (Caution! MoO₂Cl₂ is hygroscopic and highly reactive with metals to form insoluble materials. The author rapidly weighed MoO₂Cl₂ by using a PTFE spatula). Next, 1, 2, 4, or 6 mL of MoO₂Cl₂ solution were added to a solution containing BPy-PMO-TMS (68.5 mg, 0.20 mmol) dispersed in 9, 8, 6, or 4 mL, respectively, of CH₃CN. The solution obtained was stirred at room temperature for 24 h. After filtration and washing with CH₃CN, the obtained powder was dried under reduced pressure to give *x*% Mo-BPy-PMO-TMS, where *x* represents the molar ratio of Mo against the bipyridine in BPy-PMO-TMS, and was determined by ICP analysis (*x* = 5, 10, 20, 23). The MoO₂Cl₂ was immobilized over bipyridine-grafted mesoporous silica, polystyrene, and nontrimethylsilylated BPy-PMO using the same procedures.

Epoxidation of cis-cyclooctene under undried conditions

These reactions were performed using reagent-grade solvent and TBHP solution in decane

¹⁸ Ravel, B.; Newville, M. *J. Synchrotron Radiat.* **2005**, *12*, 537–541.

(undried). A 20 mL two-necked flask, with a stir bar and septum, was charged with a reaction solution of **1a** (0.65 mL, 5.0 mmol, substrate), 5–6 M TBHP solution in decane (0.96 mL, 5 mmol, oxidant), toluene (3.19 mL, 30 mmol, internal standard, > 99.5%), and decane (5.20 mL, solvent, > 99.0%). The heterogeneous catalyst (20 mg) or MoO₂Cl₂(bpy) (2.1 mg, 5.8 μmol Mo) was added to the reaction solution, and the flask was placed in an oil bath heated to 45–90 °C. The reaction time was measured from the time the flask was placed in the oil bath. Samples of the reaction solution were collected at regular intervals and centrifuged to separate the solid catalyst. After centrifugation, the reaction solution was analyzed by GC using a Shimadzu GC-8A equipped with a capillary column (HP-5, 0.53 mm × 30 m) and FID. After the reaction was completed, the catalyst was filtered and washed with hexane before drying under reduced pressure. The used catalyst was subjected to another reaction under the same reaction conditions.

Epoxidation of cis-cyclooctene under anhydrous conditions

These reactions were performed using anhydrous solvent and TBHP solution in decane dried over molecular sieves 4A. A 20 mL test tube, with a stir bar, was equipped with a two-neck gas adaptor. The side neck was connected to a vacuum/argon manifold. The main neck was capped with a rubber septum. The test tube was charged with 10% Mo-BPy-PMO-TMS (20 mg, 5.8 μmol Mo), then evacuated and backfilled with argon three times. To the test tube were added **1a** (0.65 mL, 5 mmol), dry mesitylene (1 mmol, internal standard), dry solvent (9.0 mL), and dry 5–6 M TBHP solution in decane (0.96 mL, 5 mmol). The test tube was placed in an aluminum block preheated to 75 °C. The reaction time was measured from the time the test tube was placed in the aluminum block. Samples of the reaction solution were collected at regular intervals and diluted with CDCl₃. The sample solution was passed through a membrane filter (0.20 μm) to separate the solid catalyst. The obtained sample solution was analyzed by ¹H NMR spectroscopy. After the reaction was completed, the catalyst was filtered and washed with Et₂O (30 mL) before drying under reduced pressure. The used catalyst was subjected to another reaction under the same reaction conditions. For the recharging system, **1a** (0.65 mL, 5 mmol) and dry 5–6 M TBHP solution in decane (0.96 mL, 5 mmol) were added to the reaction test tube, and another reaction was carried out at the same reaction temperature.

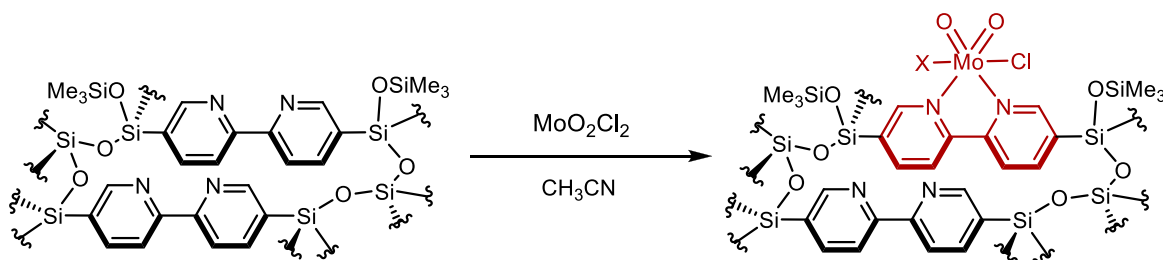
General procedure for epoxidation of olefins

These reactions were performed using anhydrous solvent and TBHP solution in decane dried over molecular sieves 4A. A 20 mL test tube, with a stir bar, was equipped with a two-neck gas adaptor. The side neck was connected to a vacuum/argon manifold. The main neck was capped with a rubber septum. The test tube was charged with 10% Mo-BPy-PMO-TMS (35 mg, 10 μ mol Mo), then evacuated and backfilled with argon three times. To the test tube were added olefin (**1**, 2.5 mmol), dry mesitylene or dry 1,4-dioxane (1 mmol, internal standard), dry 1,2-dichloroethane (1,2-DCE, 4.3 mL), and dry 5–6 M TBHP solution in decane (0.72 mL, 3.75 mmol). The test tube was placed in an aluminum block preheated to 75 °C. The reaction time was measured from the time the test tube was placed in the aluminum block. Samples of the reaction solution were collected at regular intervals and diluted with CDCl₃. The sample solution was passed through a membrane filter (0.20 μ m) to separate the solid catalyst. The obtained sample solution was analyzed by ¹H NMR spectroscopy.

5.3.3 Results and Discussion

Synthesis and characterization

To immobilize the dioxomolybdenum-bipyridine complex over the pore surface of BPy-PMO-TMS, commercially available MoO₂Cl₂ was used as a precursor. A MoO₂Cl₂ solution in CH₃CN was added to a suspension of BPy-PMO-TMS in CH₃CN and stirred at room temperature for 24 h. After filtration and washing with CH₃CN followed by drying under reduced pressure, Mo-BPy-PMO-TMS was obtained in quantitative yield as a white powder (Scheme 5.3).



Scheme 5.3. Schematic illustration for *x*% Mo-BPy-PMO-TMS.

Table 5.6. Physicochemical properties of $x\%$ Mo-BPy-PMO-TMS^a

Sample	Mo amount / mmol g ⁻¹		$S_{\text{BET}} / \text{m}^2 \text{g}^{-1}$	$V_{t\text{-plot}} / \text{cm}^3 \text{g}^{-1}$	$d_{\text{DFT}} / \text{nm}$
	Preparative	ICP			
BPy-PMO-TMS	—	—	654	0.41	3.8
5% Mo	0.14	0.15	657	0.41	3.8
10% Mo	0.29	0.30	647	0.39	3.8
20% Mo	0.58	0.58	608	0.37	3.8
23% Mo	0.87	0.67	585	0.36	3.8

^a Determined from nitrogen adsorption/desorption isotherms at liquid-nitrogen temperature and calculated using the BET method (S_{BET}), t -plot method ($V_{t\text{-plot}}$), or density functional theory (d_{DFT}).

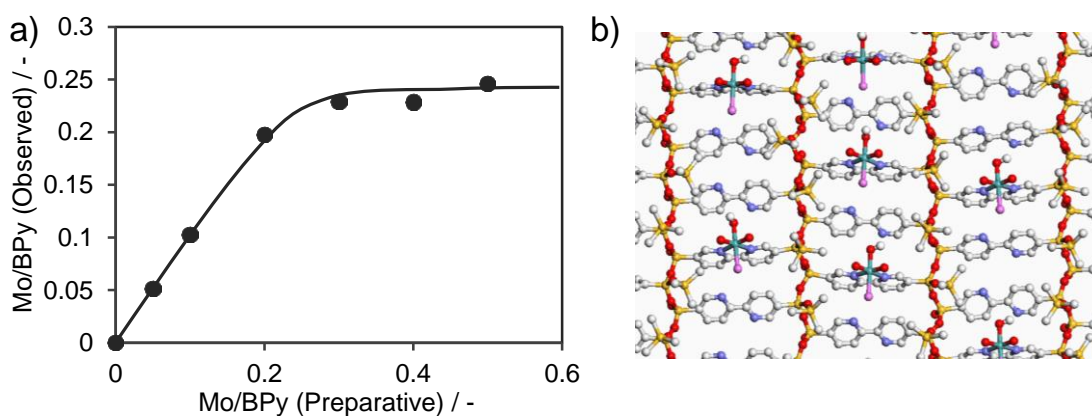


Figure 5.34. a) Relationship between preparative and observed Mo/BPy ratios determined by ICP analysis. b) CG image of pore surface of Mo-BPy-PMO-TMS with Mo/BPy molar ratio of approximately 23% ($\text{Mo}/\text{BPy}_{\text{surf}} = \text{approximately } 35\%$). Mo: sky blue; Cl: pink; O: red; Si: orange; C: light gray; N: purple; H: omitted except for hydrogen atoms of OH ligands in Mo complexes.

The loading amount of the Mo complex on BPy-PMO-TMS could be controlled simply by varying the concentration of the MoO_2Cl_2 solution. Figure 5.34a shows the relationship between preparative Mo/BPy molar ratios in the reaction mixtures and the observed Mo/BPy molar ratios in BPy-PMO-TMS. The Mo/BPy molar ratios in BPy-PMO-TMS were determined from the Mo/Si ratios measured by ICP analysis, with the assumption that the ratio of Si/BPy was 10/3 because the pore walls were composed of three layers of $\text{O}_{1.5}\text{Si-BPy-SiO}_{1.5}$ units, and the silanol groups

(Si–OH) at the inner and outer pore surface (2/3 of the total Si) were almost completely trimethylsilylated.⁶ Preparative Mo/BPy ratios less than 0.20 agreed well with observed Mo/BPy molar ratios, but Mo amounts greater than 0.20 resulted in saturation. The maximum Mo/BPy ratio of 0.246, corresponding to 0.72 mmol Mo g⁻¹, was achieved when the total amount of BPy ligand in BPy-PMO-TMS was 2.92 mmol g⁻¹ by elemental analysis.⁶ This indicates that 37% of the surface BPy ligands (BPy_{surf}) were coordinated with Mo in three layers of pore walls and that a high density of Mo complex could be loaded on BPy-PMO-TMS.

Figure 5.34b shows a CG image of the pore surface of Mo-BPy-PMO-TMS with a Mo/BPy_{surf} molar ratio of 35%, showing that BPy-PMO-TMS enables high-density immobilization of a Mo complex on the pore surface. Four Mo-loaded BPy-PMO-TMS with Mo/BPy ratios of 0.05, 0.10, 0.20, and 0.23 were used to evaluate catalysis (denoted x% Mo-BPy-PMO-TMS, where x = 5, 10, 20, and 23). The Cl/Mo ratios of Mo-BPy-PMO-TMS were 1.2–1.5, which were less than that of the MoO₂Cl₂ precursor (Cl/Mo = 2), indicating that some Cl was released from MoO₂Cl₂ during the immobilization process. This is not surprising because Cl in MoO₂Cl₂ undergoes easy substitution with polar anion species such as ethoxide.¹⁹ The acetonitrile solvent or a small amount of water contaminating the solvent may have promoted the replacement of the chloride ligand from MoO₂Cl₂ on BPy-PMO-TMS.

The mesoporous and pore wall structures of Mo-BPy-PMO-TMS were investigated by XRD and nitrogen adsorption/desorption analyses (Figures 5.35 and 5.36). The XRD diffraction patterns for Mo-BPy-PMO-TMS showed a peak at $2\theta = 1.78^\circ$, attributed to the periodicity of the mesoporous structure. Peaks at $2\theta = 7.54^\circ$, 15.2° , 22.9° , and 30.8° were attributed to the molecular-scale periodicity of bipyridine ligands in the pore walls, similar to that of the parent BPy-PMO-TMS.⁶ No additional peaks corresponding to impurities, such as inorganic salts of MoO₂Cl₂, were observed. These results indicate that the ordered structure of the parent BPy-PMO-TMS was maintained after immobilization of the Mo complex on the pore surface. The nitrogen adsorption/desorption isotherms for Mo-BPy-PMO-TMS were type-IV isotherms, similar to those for the parent BPy-PMO-TMS, which indicates preservation of uniform mesoporosity. The

¹⁹ Gomes, A. C.; Neves, P.; Cunha-Silva, L.; Valente, A. A.; Gonçalves, I. S.; Pillinger, M. *Catal. Sci. Technol.* **2016**, *6*, 5207–5218.

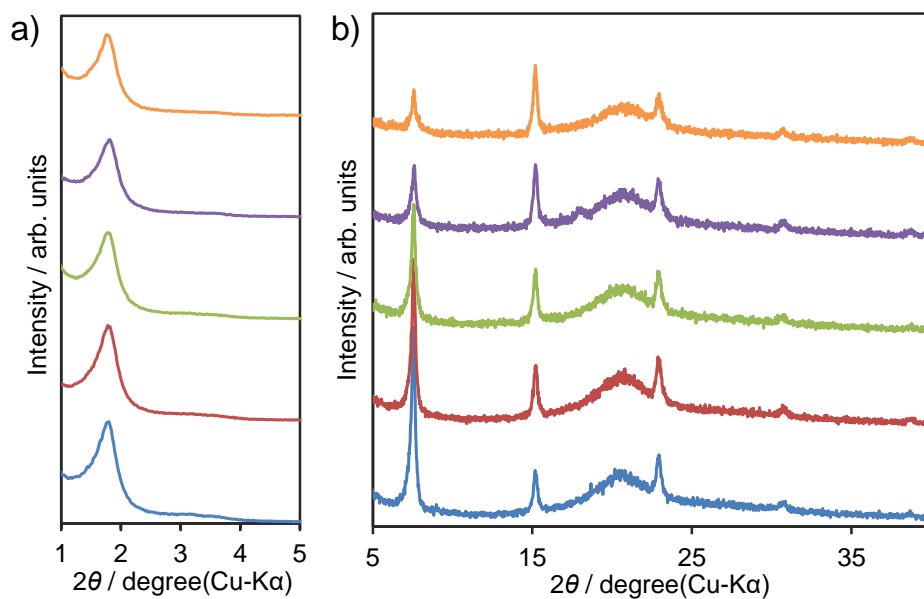


Figure 5.35. a) Low-angle and b) high-angle XRD patterns for BPy-PMO-TMS (blue lines) and $x\%$ Mo-BPy-PMO-TMS ($x = 5$, red lines; 10, green lines; 20, purple lines; 23, orange lines).

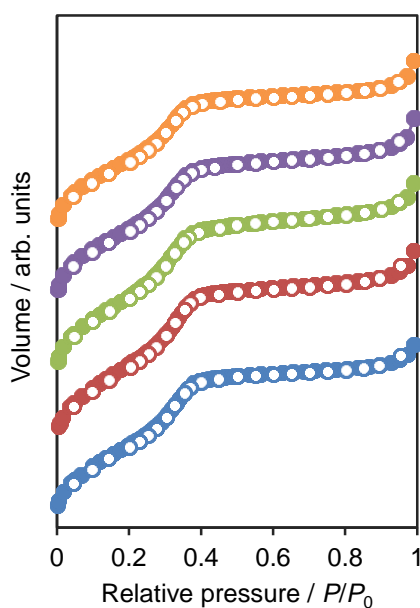


Figure 5.36. Nitrogen adsorption/desorption isotherms for BPy-PMO-TMS (blue lines) and $x\%$ Mo-BPy-PMO-TMS ($x = 5$, red lines; 10, green lines; 20, purple lines; 23, orange lines). Closed symbols: adsorption; open symbols: desorption.

Brunauer–Emmett–Teller surface area (S_{BET}), mesopore volume ($V_{t\text{-plot}}$), and density functional

theory pore diameter (d_{DFT}) are listed in Table 5.6. The S_{BET} and $V_{t\text{-plot}}$ values decreased gradually with increasing Mo complex loading amount due to the increase in sample weight. No change in d_{DFT} was found after immobilization of the Mo complex on the pore surface.

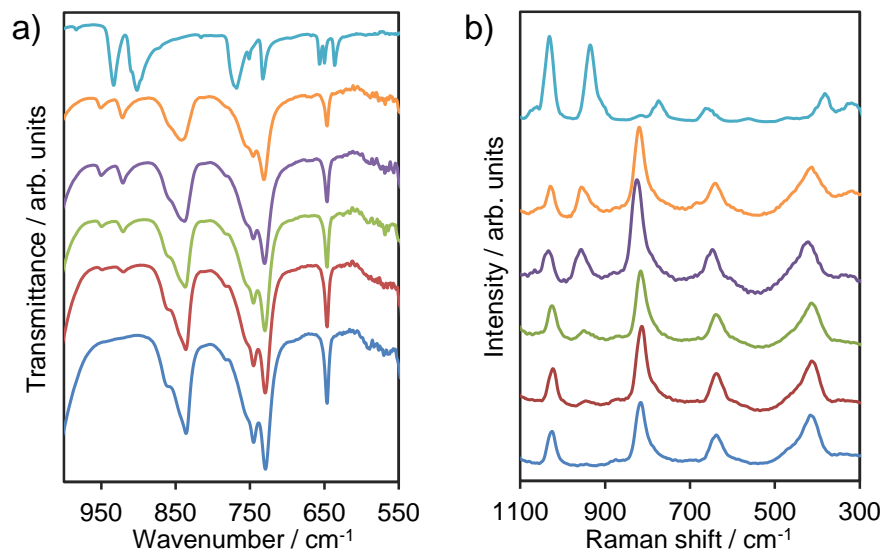


Figure 5.37. a) FT-IR and b) Raman spectra of BPy-PMO-TMS (blue lines), $x\%$ Mo-BPy-PMO-TMS ($x = 5$, red lines; 10, green lines; 20, purple lines; 23, orange lines), and $\text{MoO}_2\text{Cl}_2(\text{bpy})$ (sky blue lines).

The molecular structures of the Mo complexes formed on BPy-PMO-TMS were characterized by FT-IR spectroscopy (Figure 5.37a), Raman spectroscopy (Figure 5.37b), and XAFS analysis. The $x\%$ Mo-BPy-PMO-TMS showed an additional three bands at 945 and 917 cm^{-1} in the IR spectrum and at 953 cm^{-1} in the Raman spectrum, compared with the parent BPy-PMO-TMS. Band intensities increased with the loading amount of Mo. $\text{MoO}_2\text{Cl}_2(\text{bpy})$, which was prepared as a model complex, showed Mo=O symmetric stretching at 932 cm^{-1} in the IR spectrum and 935 cm^{-1} in the Raman spectrum, and a Mo=O asymmetric stretching band at 902 cm^{-1} in the IR.^{10,20} Thus, the additional bands observed in $x\%$ Mo-BPy-PMO-TMS were assigned to symmetric and asymmetric Mo=O stretching in the $\text{MoO}_2\text{Cl}_2(\text{bpy})$ complex. However, the wavenumbers of these bands were blue-shifted compared with those of the model complex $\text{MoO}_2\text{Cl}_2(\text{bpy})$. Kühn et al.

²⁰ Abrantes, M.; Amarante, T. R.; Antunes, M. M.; Gago, S.; Almeida Paz, F. A.; Margiolaki, I.; Rodrigues, A. E.; Pillinger, M.; Valente, A. A.; Gonçalves, I. S. *Inorg. Chem.* **2010**, *49*, 6865–6873.

reported that an electron-deficient Mo center due to coordination of the electron-withdrawing bipyridine ligand increased the Mo=O bond strength.^{10,19} Therefore, the silicon attached to the bipyridine ligand ($O_{1.5}Si-BPy-SiO_{1.5}$) could promote greater electron withdrawal than the bpy ligand alone. The FT-IR spectra of $x\%$ Mo-BPy-PMO-TMS also showed absorption bands derived from TMS groups and no absorption bands related to silanol groups, indicating that TMS was strongly attached during the MoO_2Cl_2 immobilization process (Figure 5.38).

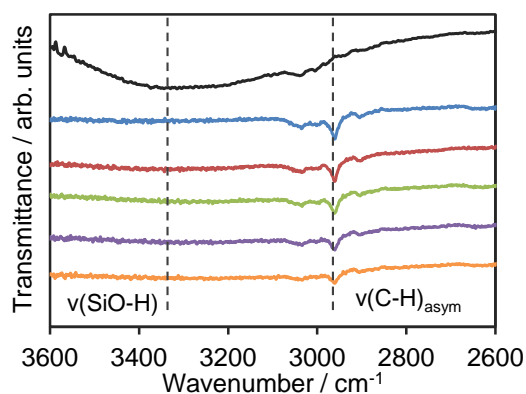


Figure 5.38. FT-IR spectra of BPy-PMO (black line), BPy-PMO-TMS (blue line) and $x\%$ Mo-BPy-PMO-TMS ($x = 5$, red line; 10, green line; 20, purple line; 23, orange line).

The XAFS measurements revealed the electronic state and local structure of the Mo center in $x\%$ Mo-BPy-PMO-TMS. The X-ray absorption near edge structure (XANES) spectra of 10% Mo-BPy-PMO-TMS showed a characteristic shoulder at 20004 eV, which is typically observed for hexavalent Mo compounds such as $MoO_2Cl_2(bpy)$, MoO_2Cl_2 , and MoO_3 (Figures 5.39a and 5.39b). The spectral shape for 10% Mo-BPy-PMO-TMS was slightly different to that for model complex $MoO_2Cl_2(bpy)$. In order to elucidate the local structure of the Mo complex in 10% Mo-BPy-PMO-TMS, an EXAFS analysis was carried out. Figure 5.39c and 5.39d show Mo K -edge EXAFS oscillations and their Fourier transforms with MoO_2Cl_2 and MoO_3 as references. The radial structure functions for 10% Mo-BPy-PMO-TMS were different from those for $MoO_2Cl_2(bpy)$. This presumably stems from elimination of the chloride ligand from the Mo complex in 10% Mo-BPy-PMO-TMS as observed by EDX analysis. Thus, the EXAFS curve fitting of 10% Mo-BPy-PMO-TMS was carried out using $MoO_2Cl(OEt)(bpy)$ as a model complex where one chloride ligand in $MoO_2Cl_2(bpy)$ was replaced with ethoxide (Figures 5.40a and 5.40b). The fitted

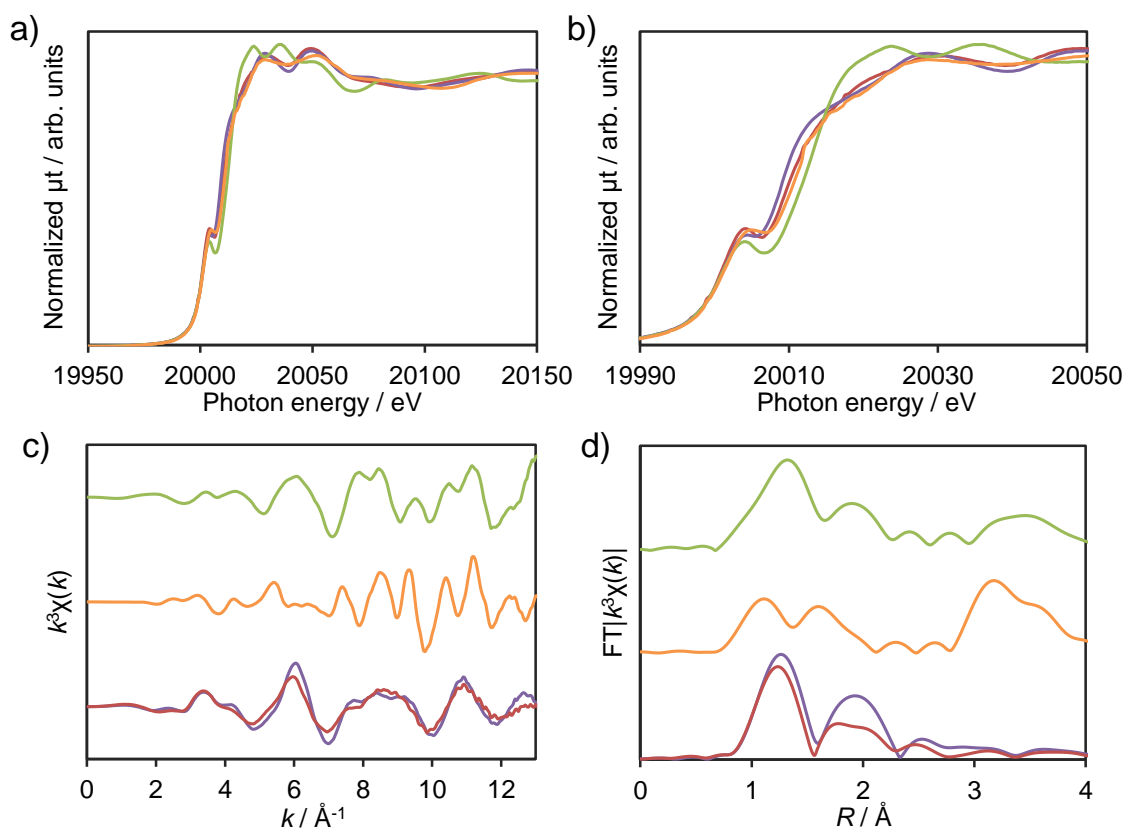


Figure 5.39. a, b) Mo *K*-edge XANES spectra, c) EXAFS oscillations, and d) EXAFS Fourier transforms ($k = 2\text{--}13 \text{ \AA}^{-1}$) of 10% Mo-BPy-PMO-TMS (red lines), $\text{MoO}_2\text{Cl}_2(\text{bpy})$ (purple lines), MoO_2Cl_2 (orange lines), and MoO_3 (green lines).

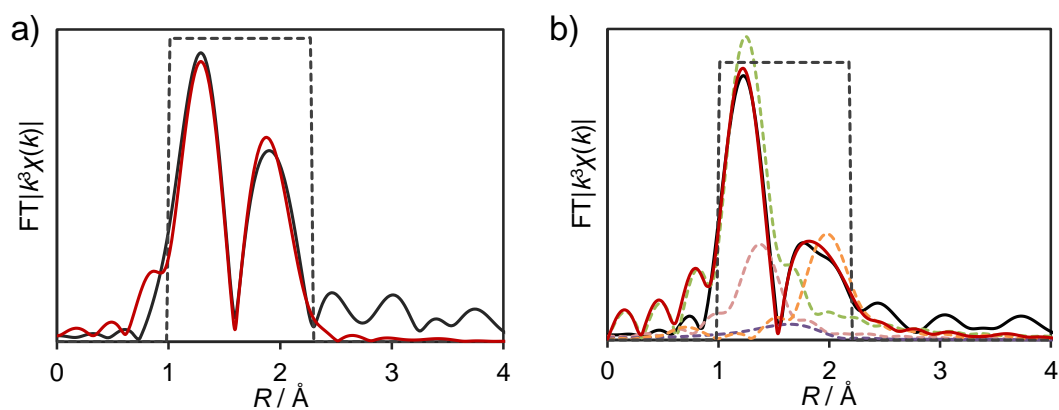


Figure 5.40. Curve fitting of Mo *K*-edge EXAFS Fourier transform for a) $\text{MoO}_2\text{Cl}_2(\text{bpy})$ using the crystal data of $\text{MoO}_2\text{Cl}_2(\text{bpy})$ and b) Mo-BPy-PMO-TMS using the crystal data of $\text{MoO}_2\text{Cl}(\text{OEt})(\text{bpy})$.

curve was consistent with Mo coordinated to two oxygen centers at 1.68 Å (Mo=O), an oxygen center at 1.83 Å (Mo–O), a bipyridine unit by two nitrogen centers at 2.23 Å (Mo–N), and a chloride center at 2.43 Å (Mo–Cl) (Table 5.7). These results strongly suggest the formation of a MoO₂Cl(OR)(bpy) complex. Since the preparation solvent contained a small amount of water, the MoO₂Cl(OH)(bpy) complex would be formed on the surface of the BPy-PMO-TMS.

Table 5.7. Curve-fitting parameters of Mo *K*-edge EXAFS Fourier transforms for MoO₂Cl₂(bpy) and 10% Mo-BPy-PMO-TMS.

Shell	CN	<i>R</i> / Å	ΔE_0 / eV	σ^2 / Å ²
MoO ₂ Cl ₂ (bpy)				
Mo=O	2 (fix)	1.70 ± 0.01	−1.0 ± 4.4	0.0012 ± 0.0001
Mo-N	2 (fix)	2.29 ± 0.08	−1.0 ± 4.4	0.0083 ± 0.0180
Mo-Cl	2 (fix)	2.40 ± 0.01	−1.0 ± 4.4	0.0040 ± 0.0025

10% Mo-BPy-PMO-TMS				
Mo=O	2 (fix)	1.68 ± 0.11	−1.6 ± 35.2	0.0003 ± 0.0062
Mo-O	1 (fix)	1.83 ± 0.27	−1.6 ± 35.2	0.0019 ± 0.0123
Mo-N	2 (fix)	2.23 ± 0.69	−1.6 ± 35.2	0.0199 ± 0.1211
Mo-Cl	1 (fix)	2.43 ± 0.14	−1.6 ± 35.2	0.0023 ± 0.0092

XAFS measurements were also carried out for other compositions of *x*% Mo-BPy-PMO-TMS (*x* = 5, 20, and 23). The Mo *K*-edge XANES, EXAFS oscillations, and EXAFS Fourier transforms for *x*% Mo-BPy-PMO-TMS (*x* = 5, 20, and 23) were similar to those for 10% Mo-BPy-PMO-TMS (Figure 5.41), suggesting the same electronic state and local structure for the Mo complexes even at low and high packing densities.

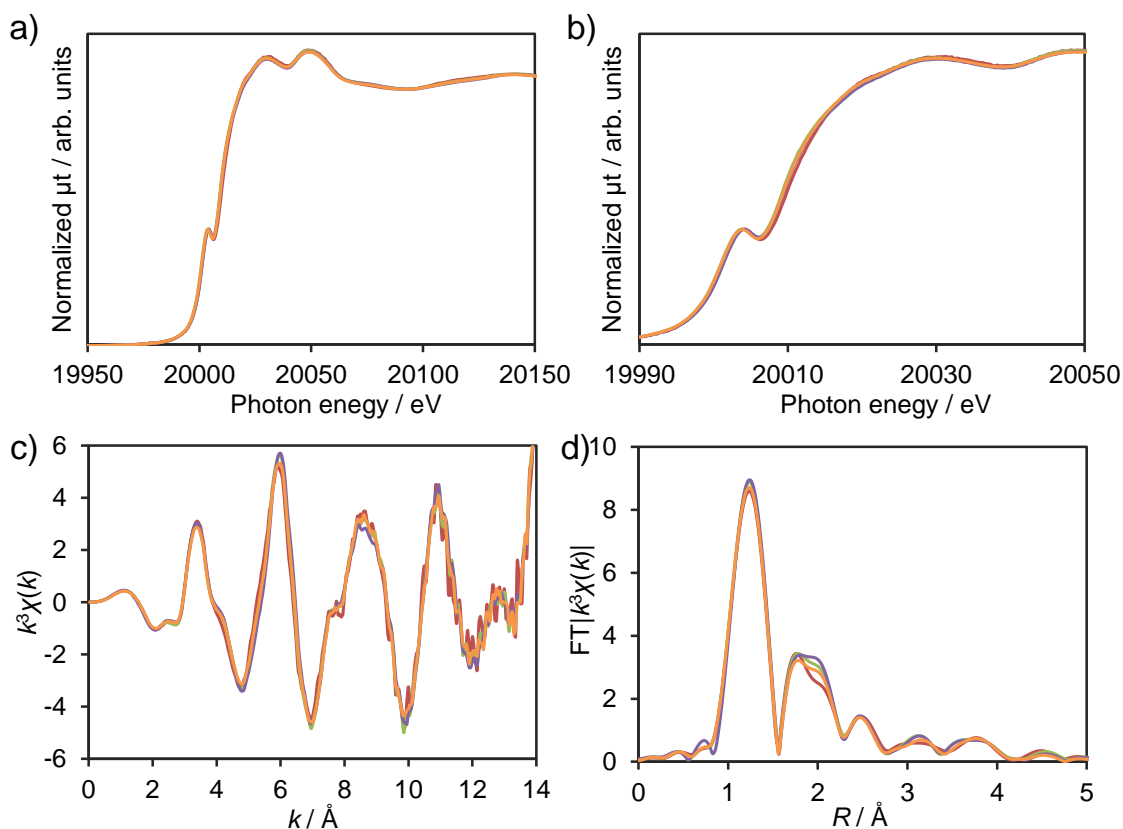


Figure 5.41. Mo *K*-edge a, b) XANES spectra, c) EXAFS oscillations and d) EXAFS Fourier transforms ($k = 2\text{--}13 \text{ \AA}^{-1}$) of $x\%$ Mo-BPy-PMO-TMS ($x = 5$, red lines; 10, green lines; 20, purple lines; 23, orange lines).

Catalytic activity in epoxidation of *cis*-cyclooctene under undried conditions

Epoxidation reactions of *cis*-cyclooctene (**1a**, 5 mmol) were conducted using TBHP (5 mmol) in a solvent of undried decane. Figure 5.42 shows the yield of 1,2-epoxycyclooctane (**2a**) as a function of reaction time over 10% Mo-BPy-PMO-TMS, homogeneous $\text{MoO}_2\text{Cl}_2(\text{bpy})$, and Mo-bipyridine complexes supported on various supports at 75 °C. The turnover number (TON) values were calculated as moles of product (**2a**)/moles of Mo in the catalysts. Initial turnover frequencies (TOFs, h^{-1}) based on the amounts of **2a** per unit of Mo for the first 30 min were calculated and are listed in Table 5.8 along with yields of **2a** after 7–8 h.

The 10% Mo-BPy-PMO-TMS showed high catalytic activity with a **2a** yield of 67% and TON of 609 at 75 °C, while homogeneous $\text{MoO}_2\text{Cl}_2(\text{bpy})$ showed greater activity with a **2a** yield of 90% and TON of 819 under identical conditions (Table 5.8, entries 1 and 2). BPy-PMO-TMS without a

Mo complex was used as a blank reaction. The experiment showed negligible conversion of **1a** (< 1%) after 24 h at 75 °C.

Table 5.8. Catalytic activity of heterogeneous and homogeneous Mo-bipyridine catalysts for epoxidation of *cis*-cyclooctene (**1a**) with TBHP^a

Entry	Mo catalyst	Mo loading (mmol Mo g ⁻¹)	T / °C	Yield / % ^b	TON ^c	TOF / h ⁻¹ ^d
1	MoO ₂ Cl ₂ (bpy)	—	75	90	819	881
2	10% Mo-BPy-PMO-TMS	0.30	75	67	609	382
3 ^e	10% Mo-BPy-PMO-TMS	0.30	90	84	797	1155
4	10% Mo-BPy-PMO-TMS	0.30	60	51	485	175
5 ^f	Mo-BPy-FSM-TMS	0.30	75	48	409	141
6 ^g	Mo-PS-BPy	0.13	75	22	275	96
7	11% Mo-BPy-PMO	0.35	75	12	75	43

^a Reactions were conducted with *cis*-cyclooctene (**1a**, 5 mmol), TBHP (5 mmol), and toluene (30 mmol, internal standard) in the presence of heterogeneous (2.6-5.8 μmol Mo) or homogeneous Mo-bipyridine catalysts (5.8 μmol Mo) in decane (total volume: 10 mL) for 8 h. ^b GC yields based on internal standard. ^c TON was calculated as moles of product/mol of Mo in the Mo-bipyridine catalyst. ^d TOF was calculated as moles of product within the first 30 min/mol of Mo in Mo-bipyridine catalysts. ^e Reaction time was 7 h. ^f Mo/BPy ratio was 0.08. ^g Mo/BPy ratio was 0.64.

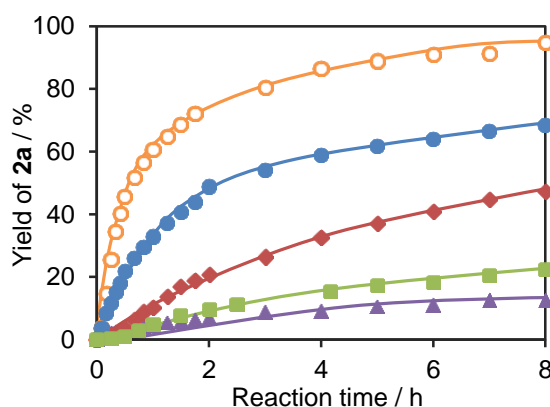


Figure 5.42. Epoxidation of *cis*-cyclooctene (**1a**) with TBHP under undried conditions catalyzed by various Mo-bipyridine complex catalysts at 75 °C. MoO₂Cl₂(bpy) (orange, ○), 10% Mo-BPy-PMO-TMS (blue, ●), Mo-BPy-FSM-TMS (red, ◆), Mo-PS-BPy (green, ■), 11% Mo-BPy-PMO (purple, ▲).

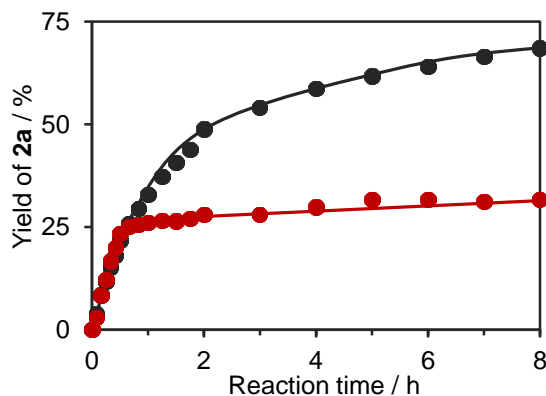


Figure 5.43. Hot filtration experiment for epoxidation of *cis*-cyclooctene (**1a**) with TBHP catalyzed by 10% Mo-BPy-PMO-TMS. Catalyst was not removed (black line). Catalyst was filtrated when reaction time reached 30 min and the reaction was continued without the catalyst (red line).

In order to confirm whether leaching of Mo species from 10% Mo-BPy-PMO-TMS occurred during the reaction, a hot filtration experiment was conducted. The PMO catalyst was removed by filtration after 30 min of reaction, and the resulting clear solution was allowed to react under identical conditions for another 7.5 h (Figure 5.43). No significant change in product yield was observed, which clearly indicated that the reaction was catalyzed by the Mo complex fixed on BPy-PMO, and not leached Mo.

An increase in reaction temperature to 90 °C improved the **2a** yield to 84% and the TON to 797 for 10% Mo-BPy-PMO-TMS (Table 5.8, entry 3), values comparable to those for homogeneous MoO₂Cl₂(bpy) at 75 °C. However, a decrease in reaction temperature to 60 °C reduced the **2a** yield to 51% and the TON to 485 (Table 5.8, entry 4). For comparison, conventional catalyst supports, a mesoporous silica (FSM) grafted with bipyridine ligands using a molecular linker followed by trimethylsilylation (denoted as BPy-FSM-TMS) and polystyrene grafted with bipyridine ligands (denoted as PS-BPy), were used for immobilization of the Mo complex (Figure 5.44). Mo-BPy-FSM-TMS produced a lower product yield of 48% and a TON of 409 compared with 10% Mo-BPy-PMO-TMS at 75 °C even with the same Mo amount (Table 5.8, entry 5), perhaps due to undesirable interactions between the Mo active center and the pore surface of FSM in the presence of a flexible linker. The Mo-PS-BPy produced a much lower product yield of 22% and a TON of 275 (Table 5.8, entry 6), due to the flexible nature of the polymer matrix.

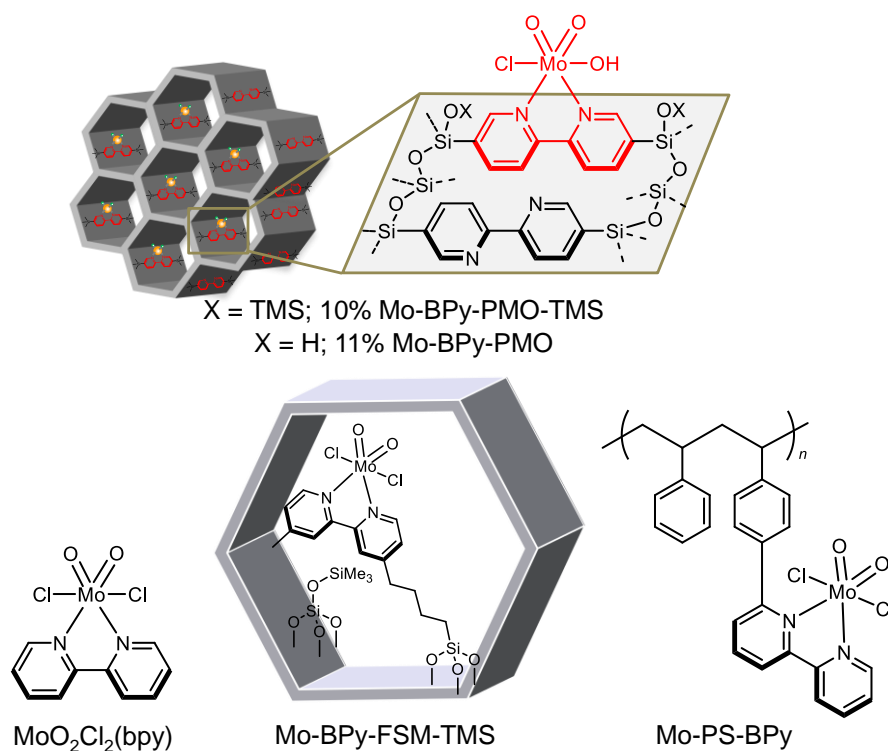


Figure 5.44. Schematic representations of 10% Mo-BPy-PMO-TMS, 11% Mo-BPy-PMO, Mo-BPy-FSM-TMS, and Mo-PS-BPy.

Interestingly, 11% Mo-BPy-PMO without trimethylsilylation possessed very low catalytic activity (TOF of 43 h⁻¹ at ~75 °C, Table 5.8, entry 7). Silanol groups inside the mesopores interact with oxygenated compounds, such as TBHP and epoxide, due to their hydrophilic nature, and prevent smooth diffusion of these compounds inside the mesopores.²¹ Therefore, the treatment of silanol groups with hydrophobic TMS groups is sometimes effective for catalysis, and has been reported for mesoporous silica-based oxidation catalysis.^{20,22} Thus, BPy-PMO-TMS is a very good support for immobilization of Mo complexes, and minimizes the loss of the original activity of the homogeneous MoO₂Cl₂(bpy) catalyst.

In order to compare the catalytic activity to previously reported Mo-bipyridine-based heterogeneous catalysts, the epoxidations of **1a** with TBHP were conducted under the same

²¹ a) Corma, A.; Domine, M.; Gaona, J. A.; Jordá, J. L.; Navarro, M. T.; Rey, F.; Perez-Pariente, J. P.; Tsuji, J.; McCulloch, B. M.; Nemeth, L. T. *Chem. Commun.* **1998**, 2211–2212; b) Jia, M.; Seifert, A.; Thiel, W. R. *Chem. Mater.* **2003**, *15*, 2174–2180.

²² a) Nakatsuka, K.; Mori, K.; Okada, S.; Ikurumi, S.; Kamegawa, T.; Yamashita, H. *Chem.–Eur. J.* **2014**, *20*, 8348–8354; b) Kamegawa, T.; Mizuno, A.; Yamashita, H. *Catal. Today* **2015**, *243*, 153–157.

conditions as the reported ones. We adopted reaction conditions of the Mo-immobilized bipyridine-grafted mesoporous silica (Mo-BPy-MCM-41) catalyst.¹⁵ Mo-BPy-MCM-41 shows an initial TOF of 16 h^{-1} and a TON of 36 at $55 \text{ }^\circ\text{C}$ under neat conditions after 24 h at a molar ratio of $\mathbf{1a}/\text{TBHP}/\text{Mo} = 48:72:1$. In contrast, 10% Mo-BPy-PMO-TMS showed a higher TOF of 5200 h^{-1} and a TON of 1850 after 3 h, although the amount of PMO catalyst was reduced to 40 times that for Mo-BPy-MCM-41 due to difficulty in stirring the reaction mixture. The activity of 10% Mo-BPy-PMO-TMS was also compared to Mo-immobilized bipyridine MOF ($\text{MoO}_2\text{Cl}_2@\text{COMOC-4}$),¹⁶ where the reaction was conducted at $50 \text{ }^\circ\text{C}$ with a molar ratio of $\mathbf{1a}/\text{TBHP}/\text{Mo} = 140:280:1$. 10% Mo-BPy-PMO-TMS showed an initial TOF of 170 h^{-1} and a TON of 90 after 45 min, while the MOF catalyst showed an initial TOF of 12 h^{-1} and a TON of 82 after 24 h. The higher catalytic activity of 10% Mo-BPy-PMO-TMS compared with $\text{MoO}_2\text{Cl}_2@\text{COMOC-4}$ can be ascribed to the smooth diffusion of substrate/product molecules owing to the larger pore diameter (ca. 3.8 nm for BPy-PMO and $> 1 \text{ nm}$ for COMOC-4). These results indicate that the catalytic activity of 10% Mo-BPy-PMO-TMS is greater than those of previously reported Mo-bipyridine-based heterogeneous catalysts.

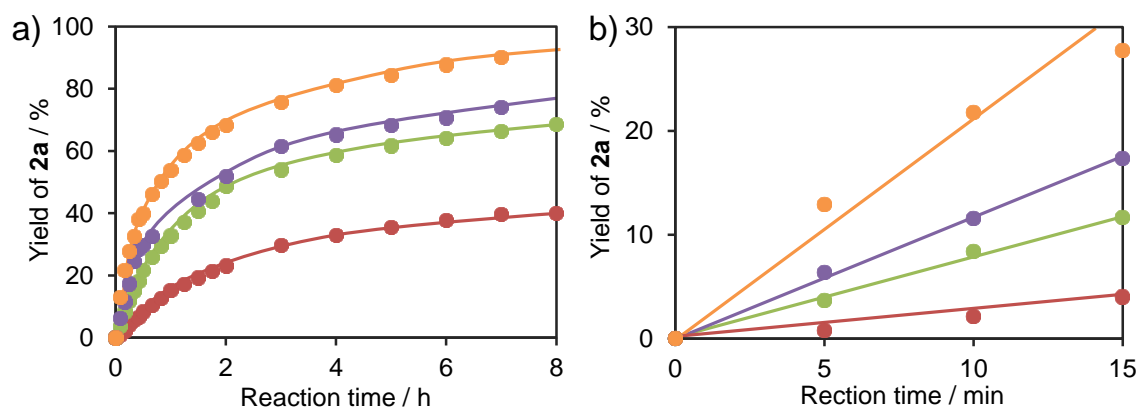


Figure 5.45. a) Epoxidation of *cis*-cyclooctene (**1a**) with TBHP at $75 \text{ }^\circ\text{C}$ catalyzed by $x\%$ Mo-BPy-PMO-TMS ($x = 5$, red lines; 10, green lines; 20, purple lines; 23, orange lines). b) Yield changes of **2a** up to 15 min from the start of the reaction.

Next, the effect of Mo loading amount (5, 10, 20, or 23%) for Mo-BPy-PMO-TMS on catalysis was examined. As the loading amount increased, the reaction rate within the first 15 min

also increased (Figure 5.45). Figure 5.46 shows TOF values in $x\%$ Mo-BPy-PMO-TMS as a function of Mo loading. The TOF value relative to Mo loading in $x\%$ Mo-BPy-PMO-TMS remained nearly constant between 300 and 400 h^{-1} . Catalytic activity was almost completely preserved, indicating that the Mo complex acts as a single-site catalyst for the epoxidation even with a high density of Mo complex on BPy-PMO-TMS.

For comparison, the effect of Mo loading amount of Mo-PS-BPy was examined because it had the greatest bipyridine loading amount (up to 2.0 mmol BPy g^{-1}) among commercially available solid supports. However, immobilization of MoO_2Cl_2 over PS-BPy was difficult when the loading amount of Mo exceeded 0.2 mmol Mo g^{-1} , indicating low coordination ability. The four Mo-PS-BPy catalysts obtained were then evaluated in the epoxidation of **1a**. The TOF values for Mo-PS-BPy decreased as the Mo amount increased perhaps due to an increase of undesirable interactions among Mo complex centers in the polymer matrix upon an increase in loading amount of MoO_2Cl_2 (Figure 5.46b). These results indicate that BPy-PMO-TMS is a unique chelating support that can accept a high density of Mo-bipyridine complex (up to 0.67 mmol g^{-1}) on the pore surface without a loss of activity for the epoxidation of **1a**. From a practical viewpoint, this is an attractive feature for flow-through systems because the same catalysis can be achieved using a much lower amount of catalyst, meaning that the column reactor size can be minimized.

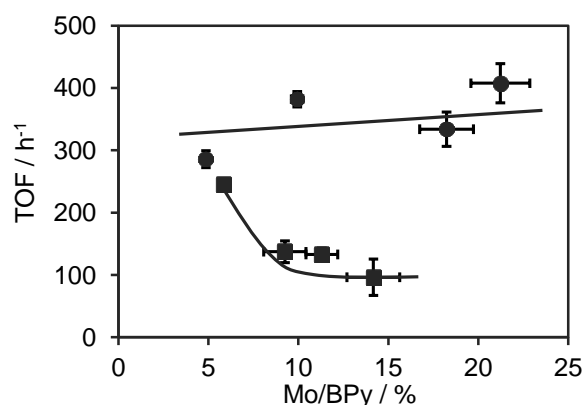


Figure 5.46. TOF value per Mo in Mo-BPy-PMO-TMS (●) and Mo-BPy-Polymer (■). Immobilized Mo amounts were determined by ICP analysis.

Catalytic activity in epoxidation of *cis*-cyclooctene under anhydrous condition.

The author investigated the catalytic reactions in different solvents under anhydrous conditions (Figure 5.47). Gonçalves et al. previously reported enhanced catalysis by a solvent effect on the epoxidation of **1a** catalyzed by Mo(CO)₃-immobilized phenylene-bridged PMO (Mo(CO)₃@Ph-PMO).²² The report also demonstrated that the presence of water was detrimental to the reaction rate, possibly due to undesired coordination to the active Mo complex center. When the epoxidation of **1a** was carried out using anhydrous TBHP dried over molecular sieves 4A in dry decane, the initial TOF for 10% Mo-BPy-PMO-TMS was dramatically improved to 2030 h⁻¹ at 75 °C, and the yield of **2a** was 89% after 3 h. This indicates that a small amount of water in the reaction solvent and/or reagent is very detrimental to the catalysis with the Mo complex. In fact, addition of a small amount of water (5 mmol) to the reaction media severely suppressed the catalysis.

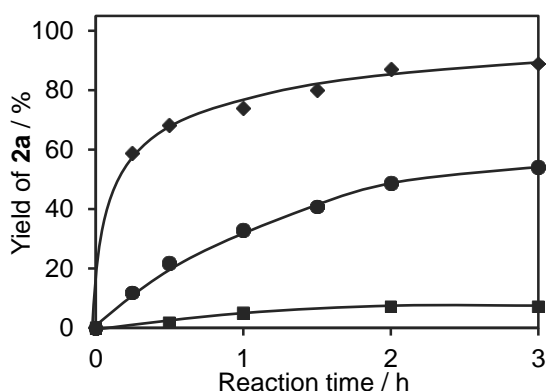


Figure 5.47. Effect of water on epoxidation of *cis*-cyclooctene (**1a**) with TBHP at 75 °C in decane. Dry decane (♦), undried decane (●), and decane containing water (5 mmol) (■).

Under anhydrous conditions, the author examined the influence of solvent polarity on the epoxidation of **1a** with anhydrous TBHP at 75 °C (Figure 5.48). The reactions were performed in dry 1,2-DCE, dry CH₃CN, dry toluene, and dry EtOH. The initial TOF values (h⁻¹) followed the order of CH₃CN (2760) > 1,2-DCE (2480) ≈ toluene (2440) > decane (2030) >> EtOH (520), indicating no clear relationship between the dielectric properties and initial TOF values. The use of 1,2-DCE completed the reaction within 1.5 h to afford **2a** quantitatively. Although the use of CH₃CN and toluene also achieved high TOF, slightly prolonged reaction times were required for

completing the reaction. These solvents showing high TOF likely stabilized the Mo-active intermediate and also promoted diffusion of the substrate/product molecules in the mesopores. The lowered reaction rate observed for EtOH may be due to the coordination of EtOH to the Mo-active intermediate. A similar detrimental effect of EtOH was observed for the catalytic system using $\text{Mo}(\text{CO})_3@ \text{Ph-PMO}$.²³

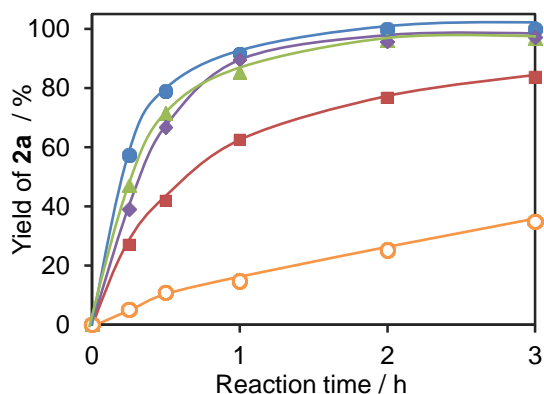


Figure 5.48. Solvent effect on epoxidation of *cis*-cyclooctene (**1a**) with TBHP at 75 °C in dry 1,2-DCE (blue, ●), dry CH_3CN (green, ▲), dry toluene (purple, ◆), dry decane (red, ■), dry EtOH (orange, ○).

Scope and Limitations of Mo-BPy-PMO-TMS for epoxidation of olefins

The scope and limitations of 10% Mo-BPy-PMO-TMS were evaluated in the epoxidation of a variety of olefins **1a–1j**. The reactions were carried out in the presence of olefin (2.5 mmol), anhydrous TBHP solution in decane (3.75 mmol), and 10% Mo-BPy-PMO-TMS (0.4 mol% Mo relative to olefin) in dry 1,2-DCE at 75 °C, and the results are summarized in Table 5.9.

The epoxidation of cycloolefins such as **1a** and cyclohexene (**1b**) proceeded efficiently and gave **2a** and 1,2-epoxycyclohexane (**2b**) quantitatively after 3 h (Table 5.9, entries 1 and 2). The epoxidation of internal aliphatic olefins such as *cis*-2-octene (**1c**) and *trans*-2-octene (**1d**) occurred stereoselectively to afford desired epoxides **2c** and **2d** quantitatively, respectively (Table 5.9, entries 3 and 4). In contrast, the reaction of terminal aliphatic olefin 1-octene (**1e**) showed moderate conversion to give 1,2-epoxyoctane (**2e**) in 61% yield (Table 5.9, entry 5). When limonene (**1f**) was

²³ Coelho, A. C.; Balula, S. S.; Bruno, S. M.; Alonso, J. C.; Bion, N.; Ferreira, P.; Pillinger, M.; Valente, A. A.; Rocha, J.; Goncalves, I. S. *Adv. Synth. Catal.* **2010**, *352*, 1759–1769.

used as a substrate, regioselective oxidation was observed at the endocyclic double bond to give 1,2-epoxy-*p*-menth-8-ene (limonene oxide, **2f**) in 87% yield after full conversion of **1f** (Table 5.9, entry 6). Small amounts of side products such as diepoxide and carveol were detected by GC–MS analysis, suggesting that the epoxidation of the terminal double bond and overoxidation occurred. Mo-BPy-PMO-TMS also catalyzed the epoxidation of styrene (**1g**), giving styrene oxide (**2g**) as the main product in 78% yield along with unidentified side products (Table 5.9, entry 7). The author also examined the epoxidation of the double bonds of *cis*-stilbene (**1h**) and *trans*-stilbene (**1i**). The *cis*-isomer was perfectly consumed after 24 h and transformed into *cis*-stilbene oxide (**2h**) in 96% yield (Table 5.9, entry 8). On the other hand, the *trans*-isomer showed a lower conversion after 24 h

Table 5.9. Epoxidation of olefins with TBHP catalyzed by 10% Mo-BPy-PMO-TMS^a

Entry	Epoxides	Yield / % ^c	Entry	Epoxides	Yield / % ^c
1		100 (100)	6 ^b		78 (48)
2		100 (100)	7		87 (69)
3		100 (100)	8		96 (98)
4		99 (99)	9		82 (84)
5		61 (71)			

^a All reactions were conducted with olefins (**1**, 2.5 mmol), anhydrous TBHP (3.75 mmol), and dry mesitylene or dry 1,4-dioxane (1.0 mmol, internal standard) in the presence of 10% Mo-BPy-PMO-TMS (35 mg, 10 μmol Mo, 0.40 mol% Mo) or MoO₂Cl₂(bpy) (3.6 mg, 10 μmol Mo, 0.40 mol% Mo) in dry 1,2-DCE (4.3 mL) at 75 °C. ^b The reaction was carried out at 50 °C. ^c ¹H NMR yields based on internal standard. ¹H NMR yields for homogeneous catalytic system using MoO₂Cl₂(bpy) are given in parentheses.

to give *trans*-stilbene oxide (**2i**) in 82% yield (Table 5.9, entry 9). This may be due to the steric hindrance of the diphenyl groups of the *trans*-isomer against the immobilized Mo complex on the pore surface. In order to compare the catalytic activity of 10% Mo-BPy-PMO-TMS and homogeneous MoO₂Cl₂(bpy), epoxidation of olefins **1a–1i** was performed using the homogeneous catalyst under the same conditions, and these results are also summarized in Table 5.9. The product yields for the 10% Mo-BPy-PMO-TMS system were comparable with those for homogeneous systems. These results indicated that 10% Mo-BPy-PMO-TMS is a good heterogeneous catalyst for the epoxidation of olefins.

Reusability of Mo-BPy-PMO-TMS.

To investigate the reusability of 10% Mo-BPy-PMO-TMS for the epoxidation of **1a**, the recovered catalyst was reused in a recycling experiment (Figure 5.49). Under undried conditions, the catalytic activity gradually decreased after repeated reactions. The TOF of 382 h⁻¹ for fresh catalyst decreased to 73 and 26 h⁻¹ for the first and second reuse cycles. The yields of **2a** for the first and second reuse cycles after 8 h were 35% and 18%, respectively (Figure 5.49a). However, under anhydrous conditions, the recovered 10% Mo-BPy-PMO-TMS still maintained good catalytic

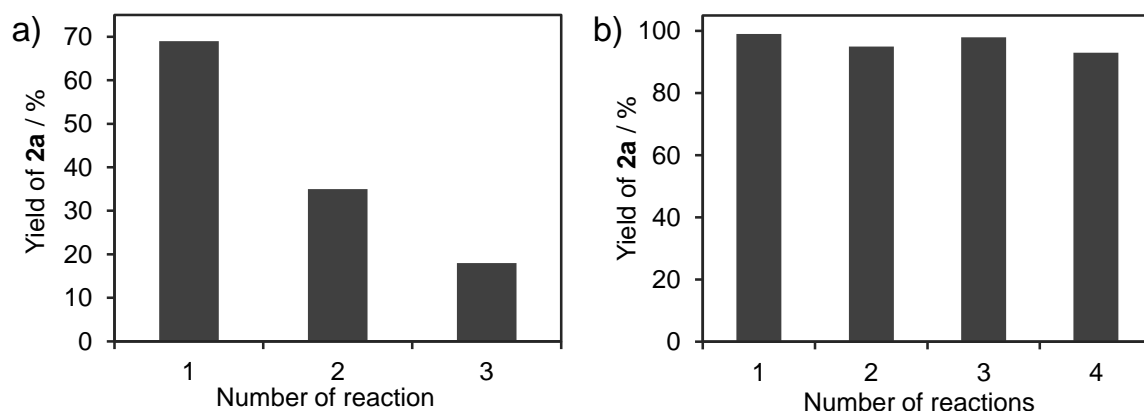


Figure 5.49. Reusability of 10% Mo-BPy-PMO-TMS for epoxidation of *cis*-cyclooctene (**1a**) at 75 °C a) under undried conditions and b) under anhydrous conditions. For a), the recovered catalyst was reused for the recycle reaction under the same conditions. The reaction times were 8 h. For b), after the reaction, **1a** and anhydrous TBHP were recharged. The reaction times were 1.5 h (1st), 1.5 h (2nd), 3 h (3rd), and 3.5 h (4th).

activity at least three more times in the epoxidation of **1a**, although the reaction rate and product yield were gradually decreased (first recycle: 90% after 1.5 h; second recycle: 84% after 3 h; third recycle: 94% after 8 h). The decrease in activity was attributed to a change in the coordination structure of the Mo complex fixed on BPy-PMO-TMS. The change in the Cl/Mo ratio of 10% Mo-BPy-PMO-TMS was measured by EDX after the first reaction. Under undried conditions, the Cl/Mo ratio decreased from 1.5 to 0.33 after 2 h, suggesting a change in the coordination structure of Mo. However, the Cl/Mo ratio was only slightly reduced from 1.5 to 1.1 under anhydrous conditions, indicating that chloride elimination was effectively suppressed. These results suggest that elimination of the chloride ligand may occur as a side reaction with residual water in solvent and/or *t*-BuOH formed in situ. The decomposition of the Mo–Cl complex would be accelerated by the filtration process since it removed liberated chloride ion from the reaction media. Thus, in order to prevent loss of chloride ion from the reaction media, **1a** and anhydrous TBHP were recharged in the reaction test tube after the reaction. In this system, > 95% yield of **2a** was obtained within 4 h for at least three reuse cycles (Figure 5.49b). This result confirms that preservation of the Mo–Cl complex is essential to maintaining the catalytic activity.

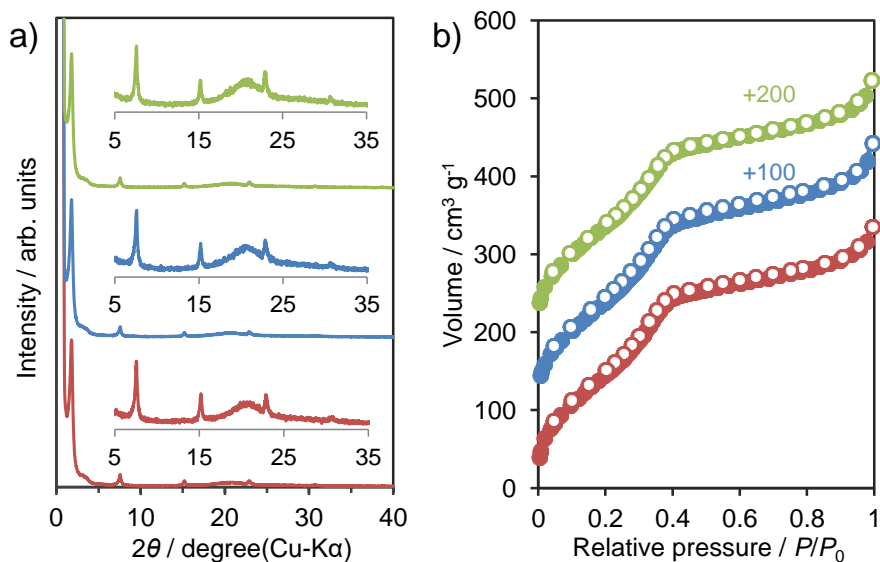


Figure 5.50. a) XRD patterns and b) nitrogen adsorption (closed circle)/desorption (open circle) isotherms of 10% Mo-BPy-PMO-TMS before the reaction (red line), after the 1st reaction run (blue line), after the 4th reaction run (green line).

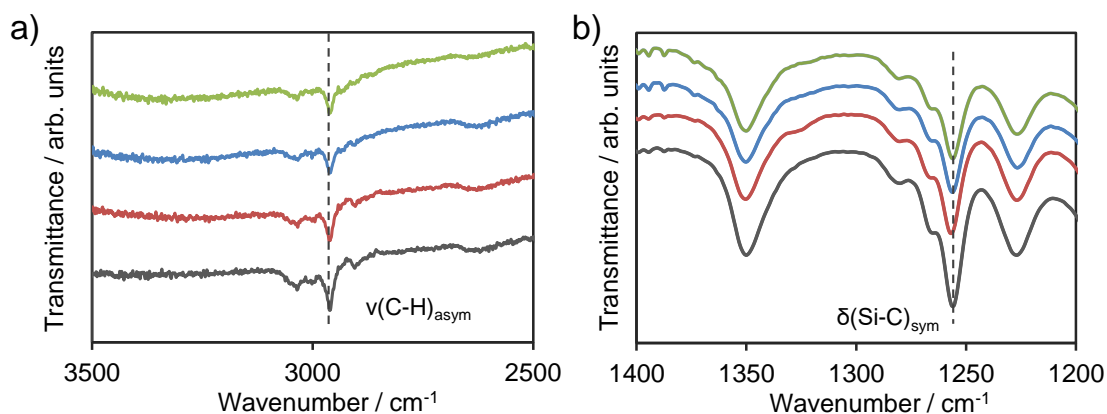


Figure 5.51. IR spectra at (a) 2500–3500 cm⁻¹ and (b) 1200–1400 cm⁻¹ of BPy-PMO-TMS (gray line), 10% Mo-BPy-PMO-TMS before the reaction (red line), after the 1st reaction run (blue line), after the 2nd reaction run (green line).

In order to evaluate the mesoporous structure, the recovered 10% Mo-BPy-PMO-TMS under undried conditions was analyzed by XRD and nitrogen adsorption/desorption isotherm measurements. The XRD pattern for 10% Mo-BPy-PMO-TMS changed little after the reaction, suggesting the preservation of periodic mesoporous and pore wall structures due to the strong covalent siloxane networks (Figure 5.50a). The BET surface area and pore volume remained nearly unchanged after the fourth reaction, clearly indicating robust mesoporous structures (Figure 5.50b). Preservation of TMS groups on the pore surface was also confirmed by IR analysis, which showed that the TMS groups on BPy-PMO-TMS were not eliminated (Figure 5.51).

5.3.4 Conclusions

Heterogeneous Mo complex catalysts were prepared using BPy-PMO-TMS as a solid support and MoO₂Cl₂ as a precursor, and they were evaluated for their ability to catalyze the epoxidation of a variety of olefins by TBHP. The formation of MoO₂Cl(OH) complexes on BPy-PMO-TMS was confirmed by FT-IR spectra, Raman spectra, and XAFS analysis. A high density of Mo complex could be loaded on BPy-PMO-TMS, in which 37% of the surface BPy ligands formed Mo complexes. The Mo-BPy-PMO-TMS exhibited greater catalytic activity for epoxidation compared to the activity of heterogeneous Mo complex catalysts supported on bipyridine-supported

mesoporous silica or polystyrene (PS-BPy). The trimethylsilylation of the surface silanol groups of BPy-PMO was very effective at improving the catalytic activity, perhaps due to the smooth diffusion of oxygenated compounds, such as TBHP and epoxide products, in the mesochannels. The TOF for Mo-BPy-PMO-TMS was nearly constant up to high loading amounts of Mo complex, while the TOF decreased for Mo-PS-BPy. A significant solvent effect was observed for epoxidation of *cis*-cyclooctene catalyzed by Mo-BPy-PMO-TMS. The presence of water in the reaction medium was found to strongly influence the catalysis. Mo-BPy-PMO-TMS was found to catalyze a variety of aliphatic and aromatic olefins and showed good recyclability for at least three reuse cycles in the epoxidation of *cis*-cyclooctene. The high loading and good recyclability indicate that this supported catalyst has the potential for application to a flow-through reactor that requires a solid catalyst containing a large number of active centers and a small loss of activity.

Chapter 6

Conclusions and Outlook

Conclusions

Highly-designed functional PMOs focused on in this study are expected to be practical porous materials because they show various organic functions thanks to the bridged functional organic groups in the pore framework. In this study, the author established various synthetic methods for synthesis of highly-designed functional organosilane precursors, which had been a bottleneck toward the functionalization of PMOs. The new synthetic methodologies enabled to advance the applications of PMOs possessing various functions (light-harvesting antenna effect, charge transportation, fluorescence, metal adsorption/coordination, and catalysis). Indeed, in this study, the author demonstrated that novel light energy conversion systems (visible light-harvesting antenna and organic solar cell) based on functional PMOs can be developed by integrating the organic functions of the PMO frameworks with the well-ordered mesoporous structures. Therefore, the author believes that this study will contribute to enhance the value of PMOs as functional materials for efficient light energy conversion systems. Furthermore, the author demonstrated the synthesis of well-defined heterogeneous metal complex catalysts with excellent catalytic activity by using crystal-like PMO with metal coordination ability. The author believes that this study can be contributed to a paradigm shift of catalytic processes from liquid phase reactions based on homogeneous metal complex catalyst to liquid and gaseous phase reactions using heterogeneous metal complex catalyst aimed for industrial and practical applications. This can significantly change the industrial manufacturing process for chemicals and pharmaceuticals.

The author thinks that highly-designed functional PMOs are considered to be new class of organic-inorganic hybrid materials that exists at the border between organic chemistry, inorganic chemistry, photochemistry and catalytic chemistry. The knowledge obtained in this study will be the basic technology for enhancing the functions of PMOs. By deepening these technologies and developing new technologies, highly-designed functional PMOs will bring forth the development of science and technology that will be useful to humanity in the future.

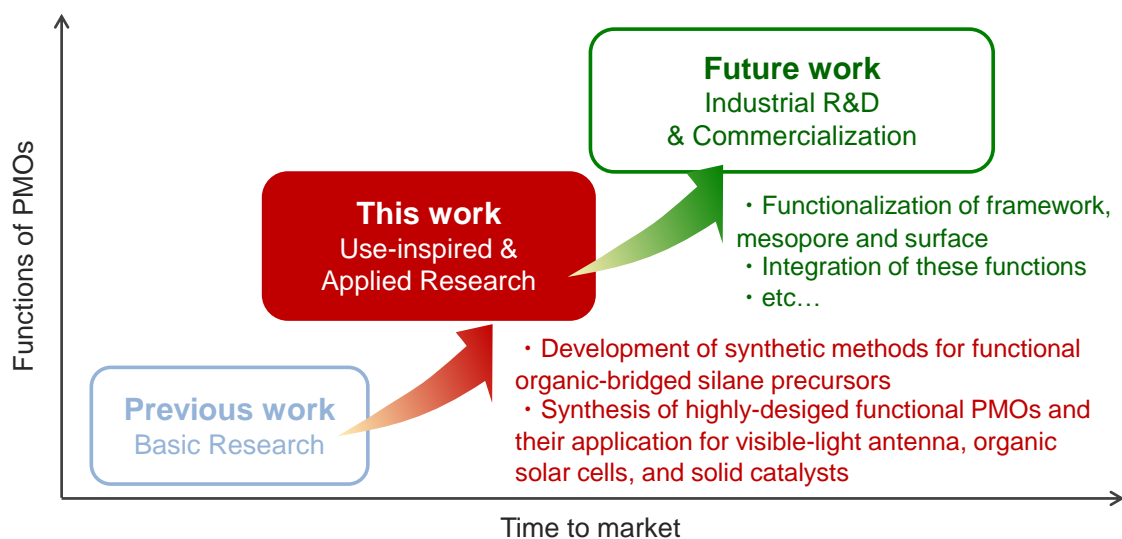


Figure 6.1. Schematic illustration of roadmap from previous work (basic research) and this work (use-inspired & applied research) to future work toward industrial R&D and commercialization of highly-designed functional PMOs.

In this doctoral thesis, the author described the development of rational synthetic methods for functional organic-bridged silane precursors and applications of high functional PMOs synthesized from the newly-designed functional organic-bridged silane precursors aimed for optical materials, photovoltaic devices, and heterogeneous catalysts as use-inspired and applied research (Figure 6.1).

The studies on development of rational synthetic methods for functional organic-bridged silane precursors have revealed the following:

i) Rhodium-catalyzed direct disilylation of aryl dihalide with triethoxysilane enabled us to synthesize the organosilane precursors bridged with high functional groups, which cannot be synthesized by conventional synthetic methods. Direct disilylation of 3,6-diiodocarbazole and its derivatives with triethoxysilane was demonstrated to give the corresponding carbazole-bridged triethoxysilane precursors in high yields of 70–89%. The obtained one alkoxy silane precursor was utilized in synthesis of periodic mesostructured organosilicas in the presence of cationic surfactant under basic and acidic conditions.

ii) A new synthetic method of high functional organic-bridged allylsilane precursors, which are stable during silica gel chromatography but are utilized for synthetic equivalents of alkoxy silane precursors for PMO synthesis, was developed. By using building blocks possessing both diallylethoxysilyl group and reactive site such as halogen, metal, and functional groups, high functional organic-bridged allylsilane precursors were synthesized by palladium-catalyzed cross-coupling reactions. Hydrolysis and condensation behaviors of organoallylsilane in various reaction solvents were also investigated under acidic sol-gel polymerization conditions. It revealed that low hydrolyzability of allylsilyl groups was improved by appropriate selecting the reaction solvent and deallylation rate was closely correlated with solvent basicity of reaction solvent.

iii) A synthetic method for high functional organic-bridged alkoxy silane precursors having column stability and easy hydrolyzability was developed. A variety of building blocks having both triisopropoxysilyl group and functional moiety such as halogen and metal groups were synthesized. By applying these building blocks to the palladium-catalyzed coupling reactions, electroactive diketopyrrolopyrrole (DPP)-bridged isopropoxysilane precursor was successfully prepared. This precursor was readily hydrolyzed and condensed to give visible-light absorptive organosilica film under mild acidic condition. In contrast, corresponding DPP-bridged allylsilane precursor was decomposed under strong acidic conditions and did not form solid organosilica films. This synthetic method based on building blocks having triisopropoxysilyl group is expected to extend and complement the synthetic approach based on building blocks having allylsilyl group.

iv) Dense packing of the organic chromophore into the organosilica frameworks was achieved by molecular design of organosilane precursors. Regioselective hydrosilylation was applied to synthesize 1,3,6,8-tetraphenylpyrene (TPPy)-bridged alkoxy silane precursors bearing shortest molecular linkers between the TPPy unit and alkoxy silyl groups. A newly designed TPPy-bridged alkoxy silane precursor was transformed to organosilica hybrid films under acidic sol-gel polymerization conditions. The obtained organosilica hybrid films showed higher absorption coefficient than organosilica hybrid films prepared from conventional precursors due to dense accumulation of TPPy units in the organosilica frameworks owing the shortest molecular linkers.

The results of studies on synthesis and applications of high functional PMOs have revealed the following:

v) Transparent and visible-light absorptive methylacridone (MeAcid)-PMO films were successfully prepared from newly designed 2,7-bis(triethoxysilyl)-9-methylacridone using P123 as a template. The methyl capping of N-H group of acridone unit was found to be necessary for preparation of stable sol-solution and transparent PMO films. These results can be explained by the improvement of solubility of precursor and suppression of aggregation of acridone units during the preparation of sol-solution and formation of films by evaporation-induced self-assembly. The obtained MeAcid-PMO films showed visible-light harvesting effect thereby efficient excitation energy transfer from MeAcid units to dye molecules located in the mesochannels was observed.

vi) Visible-light absorptive and hole-transporting dithienylbenzothiadiazole (DTBT)-PMO films were also prepared from newly designed isopropoxysilane precursors using polystyrene-*block*-poly(ethylene oxide) (PS-*b*-PEO) as a template. The DTBT-PMO films were successfully obtained from 100% DTBT-bridged isopropoxysilane precursors. It revealed that DTBT-PMO films show visible-light absorption up to 650 nm and hole-transport mobility of 10^{-5} $\text{cm}^2 \text{V}^{-1} \text{s}^{-1}$. Photovoltaic devices based on DTBT-PMO films infiltrated with fullerene derivative as an electron-acceptor showed a high open-circuit voltage of 0.91 V and photocurrent density of 1.89 mA cm^{-2} with fill factor of 0.36 under simulated AM1.5G solar irradiation. The power conversion efficiency reached 0.61%. These results indicate that hole-transport PMO films can be utilized as p-type material for organic solar cells because well-defined and pore size-controlled p-n heterojunction structures can be obtained by filling the mesopores with n-type materials.

vii) A novel crystal-like PMO, BPy-PMO, were synthesized from newly designed 5,5'-bis(triisopropoxysilyl)-2,2'-bipyridine in the presence of cationic surfactant under basic condition. The unique crystal-like organosilica framework, in which 2,2'-bipyridine (BPy) groups were densely and regularly arranged and exposed on the pore surface with a molecular-scale periodicity along with direction of mesochannels, which allowed us to immobilize a variety of well-defined metal complexes on the pore surface. It revealed that BPy-PMO was found to be

versatile solid chelating ligands for formation of metal complexes containing ruthenium (Ru), iridium (Ir), rhenium (Re), and palladium (Pd) as a metal center. The local structure and electronic state of the metal center were characterized by a variety of physicochemical analyses and were revealed almost identical to corresponding homogeneous metal complex catalysts.

viii) The immobilized metal complex catalysts on BPy-PMO showed excellent catalytic activity for organic transformations. Ir@BPy-PMO-TMS, which was prepared from $[\text{Ir}(\text{OMe})(\text{cod})]_2$ and trimethylsilylated BPy-PMO (BPy-PMO-TMS), showed higher catalytic activity for direct C–H borylation of benzene with bis(pinacolate)diboron compared with those of corresponding homogeneous catalyst and heterogeneous Ir-bipyridine complex catalysts immobilized on silica gel, mesoporous silica, and polystyrene. Ir@BPy-PMO-TMS allowed for easy recovery and several reuse of catalyst and almost no leaching of Ir species during the reaction. By using the pinacolborane as a boron source, the catalytic activity was further improved. A variety of arenes and heteroarenes were successfully transformed into corresponding aryl and heteroarylboronate esters in high yields. Multi-borylated ladder-, acenefused-, and fused-thiophene-based building blocks were also obtained and one building block was successfully utilized for synthesis of triarylamine-based hole-transporting organic material.

ix) Immobilization of base-metal bipyridine complex over BPy-PMO was also achieved. High-valent molybdenum (Mo) complex was successfully immobilized on BPy-PMO-TMS by using MoO_2Cl_2 as a precursor. Physicochemical analyses revealed the formation of $\text{MoO}_2\text{Cl}(\text{OH})$ complex on the pore surface. By using crystal-like organosilica framework, high-density immobilization of Mo complex was achieved, in which 37% of the surface BPy ligands formed Mo complexes without change of their electric state and local structure. The obtained Mo-BPy-PMO-TMS showed excellent catalytic activity for epoxidation of *cis*-cyclooctene with *tert*-butyl hydroperoxide (TBHP) compared with heterogeneous Mo-bipyridine catalysts based on mesoporous silica, polystyrene, and naked BPy-PMO, and exhibited good reusability for at least three times. It also revealed that Mo-BPy-PMO-TMS showed high catalytic activity for epoxidation of aliphatic and aromatic olefins. The TOF values for Mo-BPy-PMO-TMS were nearly constant regardless of Mo loading amounts, which indicates that immobilized Mo complex acts as single-site

catalyst. This is attractive catalysis aimed for application to a flow-through reactor because it requires high active solid catalyst containing a large number of active centers to complete the reaction in limited time and space in bed reactor.

x) BPy-PMO was a useful platform for construction of heterogeneous molecular photocatalyst systems. The use of densely and regularly arranged and exposed BPy ligands allowed us to immobilize two or more kinds of metal complex or metal nanoparticles on the pore surface. Co-immobilization of $\text{Ru}(\text{bpy})_3^{2+}$ as a photosensitizer and Pt nanoparticles as a catalyst on the pore surface achieved catalytic hydrogen evolution from water without any electron mediators, possibly due to the efficient electron transfer from $\text{Ru}(\text{bpy})_3^{2+}$ to Pt nanoparticles. These results demonstrate the great potential of BPy-PMO as an integration platform for a variety of molecular-based heterogeneous photocatalyst systems.

Outlook

The results of this study are suggesting that high functional PMOs have infinite possibilities in various research fields. The synthetic strategy for functional organic-bridged silane precursors established in this study has potential to synthesize new class of high functional PMOs. These PMOs have potential applications in optical materials, electronic devices, photocatalysts, and heterogeneous catalysts as demonstrated in this study.

In order to make these material more functional and practical materials, further studies on the rational design and synthesis of the organic-bridged silane precursors are necessary. For example, toward optical and electronic applications of PMOs, further π -conjugated electroactive organic groups should be introduced into the organosilica frameworks. However, the Si–C bonds between silyl groups and electroactive organic unit in organosilane precursor is often cleaved during PMO synthesis. In order to ensure the introduction of desired electroactive organic unit, the alkyl spacer should be incorporated between the Si–C bonds. Unfortunately, these organosilane precursors having a complicated chemical structure are not commercially available and usually synthesized by several steps on lab-scale. If it is possible to establish direct silylation starting from functional organic compounds via C–H functionalization, miscellaneous synthetic steps can be omitted, which can be reduced the manufacturing costs.

A new methodology, which can reliably form the ordered mesoporous structure from various types of organosilane precursors, would be required. Usually, the enlargement of the bridging organic units and introduction of alkyl linker between Si–C bonds of precursors make ordered mesoporous structure more difficult because the interaction between the hydrolyzed organosilane and the surfactant is weakened and inefficient. Therefore, development of synthetic approach using new template would be necessary. This is also attractive for industrial scale synthesis of PMOs because the use of surfactants increases the manufacturing cost and environmental impact.

A well-defined control of bridging organic groups in the organosilica framework would be important subject for functionalization of PMOs. Especially, crystal-like PMOs having metal

coordination ability or electroactive property, in which bridged-organic groups are regularly arranged with a molecular-scale periodicity, have great potential application in not only solid support for heterogeneous catalysts but also electronic devices. In terms of heterogeneous catalysts, a well-defined surface structure is ideal platform to immobilize metal complex catalyst without change of original coordination environment. If a variety of asymmetric ligands can be regularly arranged with a molecular-scale periodicity into organosilica frameworks, novel asymmetric heterogeneous metal complex catalysts might be developed. The use of crystal-like PMO-based heterogeneous catalysts showing excellent catalytic activity would shift the industrial process from batch reaction system to flow reaction system.

The periphery of metal complex center immobilized on the pore surface can be chemically modified by post-synthetic modification. This post-synthetic modification approach can be precisely controlled the steric hindrance and adjusted the hydrophobicity and hydrophilicity near the active sites. It is expected to form specific reaction field such as enzyme for highly efficient and selective chemical transformation, which cannot be constructed in homogeneous system. It would be possible to construct the active site for activation of small molecules by using the chemically modified PMO-based heterogeneous catalysts.

So far, extensive studies on synthesis and application of PMOs have been conducted to realize their industrial applications in the fields of optical materials, electronic devices, and heterogeneous catalysts including photocatalysts. The author hopes that PMOs open the avenues to interesting applications in various fields and contribute to the development of science and technology in the near future.

List of publications

1. Original papers corresponding to this thesis

-Chapter 2-

1) A useful procedure for diiodination of carbazoles and subsequent efficient transformation to novel 3,6-bis(triethoxysilyl)carbazoles giving mesoporous materials

Maegawa, Y.; Goto, Y.; Inagaki, S.; Shimada, T.

Tetrahedron Lett. **2006**, 47, 6957–6960.

2) Preparation of functionalized aryl(diallyl)ethoxysilanes and their palladium-catalyzed coupling reactions giving sol–gel precursors

Maegawa, Y.; Nagano, T.; Yabuno, T.; Nakagawa, H.; Shimada, T.

Tetrahedron **2007**, 63, 11467–11474.

3) A new synthetic approach for functional triisopropoxyorganosilanes using molecular building blocks

Maegawa, Y.; Waki, M.; Umemoto, A.; Shimada, T.; Inagaki, S.

Tetrahedron **2013**, 69, 5312–5318.

4) Facile Synthesis of Functional Alkoxysilane Precursor with Short Linkers toward Organosilica Hybrids with a High Density of Chromophores

Maegawa, Y.; Mizoshita, N.; Tani, T.; Inagaki, S.

Chem. Lett. **2012**, 41, 316–318.

5) Enhanced sol–gel polymerization of organoallylsilanes by solvent effect

Maegawa, Y.; Mizoshita, N.; Tani, T.; Shimada, T.; Inagaki, S.

J. Mater. Chem. **2011**, 21, 14020–14024.

-Chapter 3-

6) Transparent and visible-light harvesting acridone-bridged mesostructured organosilica film

Maegawa, Y.; Mizoshita, N.; Tani, T.; Inagaki, S.

J. Mater. Chem. **2010**, 20, 4399–4403.

-Chapter 4-

7) Synthesis of visible-light-absorptive and hole-transporting periodic mesoporous organosilica thin films for organic solar cells

Ikai, M.*; Maegawa, Y.*; Goto, Y.; Tani, T.; Inagaki, S.

J. Mater. Chem. A. **2014**, 2, 11857–11865 (*equal contribution).

-Chapter 5-

8) A Solid Chelating Ligand: Periodic Mesoporous Organosilica Containing 2,2'-Bipyridine within the Pore Walls

Waki, M.*; Maegawa, Y.*; Hara, K.; Goto, Y.; Shirai, S.; Yamada, Y.; Mizoshita, N.; Tani, T.; Chun, W. J.; Muratsugu, S.; Tada, M.; Fukuoka, A.; Inagaki, S.

J. Am. Chem. Soc. **2014**, 136, 4003–4011 (*equal contribution).

9) Iridium-bipyridine periodic mesoporous organosilica catalyzed direct C–H borylation using a pinacolborane

Maegawa, Y.; Inagaki, S.

Dalton. Trans. **2015**, 44, 13007–13016.

10) Immobilization of a Molybdenum Complex on Bipyridine-Based Periodic Mesoporous Organosilica and Its Catalytic Activity for Epoxidation of Olefins

Ishikawa, S.*; Maegawa, Y.*; Waki, M.; Inagaki, S.

ACS Catal. **2018**, 8, 4160–4169 (*equal contribution).

2. Related papers

1) Visible-light-harvesting periodic mesoporous organosilica

Takeda, H.; Goto, Y.; Maegawa, Y.; Ohsuna, T.; Tani, T.; Matsumoto, K.; Shimada, T.; Inagaki, S.

Chem. Commun. **2009**, 40, 6032–6034.

2) Tetraphenylpyrene-Bridged Periodic Mesostructured Organosilica Films with Efficient Visible-Light Emission

Mizoshita, N.; Goto, Y.; Maegawa, Y.; Tani, T.; Inagaki, S.

Chem. Mater. **2010**, 22, 2548–2554.

-
- 3) Synthesis of a spirobifluorene-bridged allylsilane precursor for periodic mesoporous organosilica
Tanaka, N.; Mizoshita, N.; Maegawa, Y.; Tani, T.; Inagaki, S.; Jorapur, Y.; Shimada, T.
Chem. Commun. **2011**, 47, 5025–5027.
- 4) Enhanced Fluorescence Detection of Metal Ions using Light-Harvesting Mesoporous Organosilica
Waki, M.; Mizoshita, N.; Maegawa, Y.; Hasegawa, T.; Tani, T.; Shimada, T.; Inagaki, S.
Chem. Eur. J. **2012**, 18, 1992–1998.
- 5) A Novel Sol-Gel Approach to Highly Condensed Silicas at Low Temperature
Jorapur, Y. R.; Mizoshita, N.; Maegawa, Y.; Nakagawa, H.; Hasegawa, T.; Tani, T.; Inagaki, S.; Shimada, T.
Chem. Lett. **2012**, 41, 280–281.
- 6) Ab Initio Molecular Orbital Study on the Excited States of [2.2]-, [3.3]-, and Siloxane-Bridged Paracyclophanes
Shirai, S.; Iwata, S.; Maegawa, Y.; Tani, T.; Inagaki, S.
J. Phys. Chem. A. **2012**, 116, 10194–10202.
- 7) Mesoporous organosilica nanotubes containing a chelating ligand in their walls
Liu, X.; Goto, Y.; Maegawa, Y.; Ohsuna, T.; Inagaki, S.
APL Mater. **2014**, 2, 113308.
- 8) Ruthenium-Immobilized Periodic Mesoporous Organosilica: Synthesis, Characterization, and Catalytic Application for Selective Oxidation of Alkanes
Ishito, N.; Kobayashi, H.; Nakajima, K.; Maegawa, Y.; Inagaki, S.; Hara, K.; Fukuoka, A.
Chem. Eur. J. **2015**, 21, 15564–15569.
- 9) Heterogeneous Catalysis for Water Oxidation by an Iridium Complex Immobilized on Bipyridine-Periodic Mesoporous Organosilica
Liu, X.; Maegawa, Y.; Goto, Y.; Hara, K.; Inagaki, S.
Angew. Chem. Int. Ed. **2016**, 55, 7943–7947.
- 10) Synthesis of 9,9'-spirobifluorene-based conjugated microporous polymers by FeCl₃-mediated polymerization
Modak, A.; Maegawa, Y.; Goto, Y.; Inagaki, S.
Polym. Chem. **2016**, 7, 1290–1296.

11) Photocatalytic CO₂ Reduction by Periodic Mesoporous Organosilica (PMO) Containing Two Different Ruthenium Complexes as Photosensitizing and Catalytic Sites

Kuramochi, Y.; Sekine, M.; Kitamura, K.; Maegawa, Y.; Goto, Y.; Shirai, S.; Inagaki, S.; Ishida, H. *Chem. Eur. J.* **2017**, *23*, 10301–10309.

12) Immobilization of luminescent platinum(II) complexes on periodic mesoporous organosilica and their water reduction photocatalysis

Yoshida, M.; Saito, K.; Matsukawa, H.; Yanagida, S.; Ebina, M.; Maegawa, Y.; Inagaki, S.; Kobayashi, A.; Kato, M.

J. Photochem. Photobiol. A: Chem. **2018**, *358*, 334–344.

13) Facile formation of gold nanoparticles on periodic mesoporous bipyridine-silica

Ishito, N.; Nakajima, K.; Maegawa, Y.; Inagaki, S.; Fukuoka, A.

Catal. Today **2017**, *298*, 258–262.

14) Transfer hydrogenation of nitrogen heterocycles using a recyclable rhodium catalyst immobilized on bipyridine-periodic mesoporous organosilica

Matsui, K.; Maegawa, Y.; Waki, M.; Inagaki, S.; Yamamoto, Y.

Catal. Sci. Technol. **2018**, *8*, 534–539.

15) Re(bpy)(CO)₃Cl Immobilized on Bipyridine-Periodic Mesoporous Organosilica for Photocatalytic CO₂ Reduction.

Waki, M.; Yamanaka, K.-i.; Shirai, S.; Maegawa, Y.; Goto, Y.; Yamada, Y.; Inagaki, S.

Chem. Eur. J. **2018**, *24*, 3846–3853.

16) Heterogeneous hydrosilylation reaction catalyzed by platinum complexes immobilized on bipyridine-periodic mesoporous organosilicas.

Naganawa, Y.; Maegawa, Y.; Guo, H.; Suryabhan, S.; Tanaka, S.; Sato, K.; Inagaki, S.; Nakajima, Y.

Dalton Trans. **2019**, *48*, 5534–5540.

17) Well-controlled radical-based epoxidation catalyzed by copper complex immobilized on bipyridine-periodic mesoporous organosilica

Ishikawa, S.; Maegawa, Y.; Waki, M.; Inagaki, S.

Applied Catalysis A, General **2019**, *575*, 87–92.

18) Effects of Pore Surfaces on the Electronic States of Metal Complexes Formed on Bipyridine Periodic Mesoporous Organosilica

Shirai, S.; Waki, M.; Maegawa, Y.; Yamada, Y.; Inagaki, S.

New J. Chem. **2019**, *43*, 2471–2478

3. Reviews

1) Visible-light Emission from Dye-doped Mesostructured Organosilica Hybrid Films

Mizoshita, N.; Goto, Y.; Maegawa, Y.; Tani, T.; Inagaki, S.

R&D Review of Toyota CRDL, **2011**, *42*, 19–26.

2) Organic-bridged Allylsilane Precursors for the Synthesis of Functional Organosilica Hybrids

Maegawa, Y.; Mizoshita, N.; Waki, M.; Tani, T.; Shimada, T.; Inagaki, S.

R&D Review of Toyota CRDL, **2012**, *43*, 69–75.

3) Bipyridine-PMO; Innovative Solid Chelating Support for Metal Complex Catalyst (Japanese)

Maegawa, Y.; Inagaki, S.

Zeolite, **2015**, *21*, 10–15

4) Functional Design of Periodic Mesoporous Organosilicas (Japanese)

Maegawa, Y.; Inagaki, S.

Nanospace Materials Handbook, Chapter 1, Section 10 (S&T, 2016)

5) Pyridyl Ligand-bridged Mesoporous Organosilicas for Metal Complex Formation on the Pore Surfaces

Waki, M., Maegawa, Y., Mizoshita, N., Tani, T.; Inagaki, S.

R&D Review of Toyota CRDL, **2016**, *47*, 57–66.

6) Synthesis and Applications of Periodic Mesoporous Organosilicas

Goto, Y.; Mizoshita, N.; Ikai, M.; Waki, M.; Maegawa, Y.; Inagaki, S.

Chemistry of Silica and Zeolite-based Materials, Chapter 1 (Elsevier, 2019)

7) Catalysis of Metal Complexes Immobilized in Periodic Mesoporous Organosilicas

Maegawa, Y.

R&D Review of Toyota CRDL, **2019**, *50*, 9–20.